LIght activated mechanisms in proteins and engineering nanoparticle bioconjugates for biomedical applications

Correia, Manuel Guilherme Laranjeira Pedrosa Martins

Publication date:
2015

Document Version
Early version, also known as pre-print

Light activated mechanisms in proteins and engineering nanoparticle bioconjugates for biomedical applications

PhD Dissertation

PREPRINT

Manuel Guilherme Laranjeira Pedrosa Martins Correia

Department of Physics and Nanotechnology, Aalborg University
Skjernvej 4A, 9220 Aalborg Ø, Denmark

LIGHT ACTIVATED MECHANISMS IN PROTEINS AND ENGINEERING NANOPARTICLE BIOCONJUGATES FOR BIOMEDICAL APPLICATIONS

Published and Distributed by:
Department of Physics and Nanotechnology, Aalborg University
Skjernvej 4A, DK-9220 Aalborg Øst, Denmark.
Phone: +45 99409215; Fax: +4599409235.

ISBN 87-89195-35-3

Light activated mechanisms in proteins and engineering nanoparticle bioconjugates for biomedical applications

PhD Student: Manuel Guilherme Laranjeira Pedrosa Martins Correia

Supervisors:

Professor Steffen B. Petersen, PhD
Department of Health Science and Technology, Aalborg University, Denmark

Principal Investigator Teresa Neves Petersen, PhD
Leader of the Biophotonics Group, International Iberian Nanotechnology Laboratory, Braga, Portugal

Paper Contributions:

- **Paper 1:** Correia, Manuel; Neves-Petersen, Maria Teresa; Parracino, Antonietta; di Gennaro, Ane Kold; Petersen, Steffen B. (2012) "Photophysics, photochemistry and energetics of UV light induced disulphide bridge disruption in apo-α-lactalbumin". *Journal of fluorescence*, *22*(1), 323–37.
- **Paper 2:** Correia, Manuel; Neves-Petersen, Maria Teresa; Jeppesen, Per Bendix; Gregersen, Søren; Petersen, Steffen B. (2012) "UV-light exposure of insulin: pharmaceutical implications upon covalent insulin dityrosine dimerization and disulphide bond photolysis". *PloS One*, *7*(12), e50733.
- **Paper 3:** Correia, Manuel; Thiagarajan, Viruthachalam; Coutinho, Isabel; Gajula, Gnana Prakash; Petersen, Steffen B., Neves-Petersen, Maria Teresa (2014) "Modulating the structure of EGFR with UV light: new possibilities in cancer therapy". *PloS One*, 9 (11), e111617.
- **Paper 4:** Parracino, Antonietta; Gajula, Gnana Prakash; di Gennaro, Ane Kold; Correia, Manuel; Neves-Petersen, Maria Teresa; Rafaelsen, Jens, Petersen, Steffen B. (2011) "Photonic immobilization of BSA for nanobiomedical applications: creation of high density microarrays and superparamagnetic bioconjugates". *Biotechnology and bioengineering*, *108*(5), 999–1010.
- **Paper 5:** Galloway, Christopher M.; Kreuzer, Mark P.; Aćimović, Srdjan S.; Volpe, Giorgio; Correia, Manuel; Petersen, Steffen B.; Neves-Petersen, Maria Teresa; Quidant, Romain (2013). "Plasmon-assisted delivery of single nano-objects in an optical hot spot". *Nano letters*, *13*(9), 4299–304.

Supporting paper contribution:

- **Paper 6:** Correia, Manuel; Snabe, Tørben; Thiagarajan, Viruthachalam; Petersen, Steffen B., Neves-Petersen, Maria Teresa (2014) "Photonic Activation of Plasminogen induced by low dose UVB". *PloS One*, submitted September 2014.

This thesis has been submitted for assessment in partial fulfillment of the PhD degree. The thesis is based on the submitted or published scientific papers, which are listed above. Parts of the papers are used directly or indirectly in the extended summary of the thesis. As part of the assessment, co-author statements have been made available to the assessment committee and are also available at the Faculty. The thesis is not in its present form acceptable for open publication but only in limited and closed circulation as copyright may not be ensured.

Preface

The research presented in this PhD thesis represents the work carried out at Aalborg University, Denmark, during the doctoral degree research scholarship SFRH/BD/61012/2009 granted by "Fundação para a Ciência e Tecnologia" (FCT, Ministry for Science, Technology and Higher Education, Portugal) for the period 01/10/2009-31/09/2013.

The PhD work was fully funded by FCT under the program "Programa Operacional Potencial Humano" (POPH) in the framework of "Quadro de Referência Estratégico Nacional" (QREN) and co-financed by the European Social Fund ("Fundo Social Europeu", FSE).

The research was mainly carried out in the laboratories of Professor Steffen B. Petersen (Nanobiotechnology Group, at the Department of Physics and Nanotechnology, and later on at the Department of Health Science and Technology, Aalborg University). Other activities were performed in the laboratories of Assoc. Prof. Per Bendix Jeppesen and Assoc. Prof. Søren Gregersen (Department of Medicine and Endocrinology, Aarhus Sygehus THG, Aarhus University Hospital). Part of the work was also performed in the laboratories of Dr. Teresa Neves Petersen (Biophotonics Group, Nanomedicine Department, International Iberian Nanotechnology Laboratory, Braga, Portugal). Additionally, part of the experimental work was done in coordination with the laboratories of Prof. Romain Quidant (Plasmon NanoOptics Group, ICFO - Institut de Ciencies Fotoniques, Barcelona, Spain).

Acknowledgements

First of all, I would like to acknowledge Prof. Steffen B. Petersen and Dr. Teresa Neves-Petersen for their exceptional supervision, guidance and support during this PhD project. I also gratefully acknowledge Assoc. Prof. Per Bendix Jeppesen and Assoc. Prof. Søren Gregersen for their excellent supervision and for taking care of me during my several stays at their laboratory at the Aarhus University Hospital. I would also like to thank my colleagues Ane Kold Di Gennaro, Antonietta Parracino, Gnana Prakash Gajula, Isabel Coutinho, and Viruthachalam Thiagarajan for the productive collaboration and their help, friendship and joyful moments in the lab.

I want to express my gratitude to Prof. Kjeld Pedersen, Head of the Department of Physics and Nanotechnology, for his support during my stay at this Institution. I also greatly acknowledge Ulla Ponsaing and Jette Lynggaard Christensen for their sympathy and help with administrative tasks. Special thanks to Kim Houtved Jensen for his constant help and creative suggestions in several technical laboratory matters and to Dorthe Rasmussen and Lene Trudsø for their skilled technical assistance during my stays at the Århus University Hospital. I would also like to express my sincere gratitude to Jens Rafaelsen and Peter Kjær Kristensen for their kindness and help in several microscopy analyses. Thanks to all my colleagues at the Department of Physics and Nanotechnology at Aalborg University for all the positive scientific discussions and the pleasant social gatherings.

I am also grateful to all the people I have collaborated and learned from over the years during this PhD project, in particular to my colleagues at the International Iberian Nanotechnology Laboratory in Braga and the members of the Plasmon NanoOptics Group of the Institut de Ciencies Fotoniques in Barcelona.

I am thankful to my family for their support, love and visits to this faraway land that is my home. And of course, a special thanks to all my friends all over the world for the continuous cheering in my life.

Last but not least, a special world to Liana Madaleno, Marco Maduro, Dimitris Raptis and Thøger Kari Jensen for their endless support and help over this period!

Summary

The exciting properties of new nanomaterials have brought to nanomedicine innovative possibilities, such as the use of nanoparticles for optical bioimaging and diagnostics, and light activated therapies. The overall aim of this PhD research was to acquire knowledge for developing novel approaches to diagnosis and therapeutics through merging nanobiotechnology and biophotonics. This PhD dissertation gives insight into UV light induced mechanisms in proteins and their usefulness for developing protein based therapies and the construction of bioconjugates of nanomaterials and proteins for biosensing, bioseparation and targeted drug delivery.

Several protein candidates were used to probe light activated mechanisms in biomolecules. Disulphide bond disruption is one of the main mechanisms that can be activated upon UV excitation of proteins. Alpha-lactalbumin and insulin were used as models to study the photophysics and photochemistry involving this mechanism. The study on human insulin showed not only UV mediated disruption of insulin's disulphide bonds but also insulin UV dimerization via dityrosine cross-linking. These structural modifications occurred within hours of insulin UV exposure to irradiance levels close to the found in sunlight and lead to almost complete inactivation of insulin hormonal function *in vitro*. These findings are relevant to the pharmaceutical industry and alert to the importance of shielding drug formulations containing insulin from solar and indoor lighting.

The herein described research of UV light induced mechanisms in proteins also involved the investigation of a light-induced protein switch in view of a new photonic therapy. This approach was based on disabling the epidermal growth factor receptor (EGFR), which overexpression has been is associated with tumor progression. UV illumination resulted in structural changes in EGFR that impair EGF binding and thus stop receptor activation. The findings presented in this work suggest that UV light can be used to modulate EGFR structure and thereby halt the EGFR signaling pathway as a new cancer photonic therapy.

The knowledge acquired on light activated reactions was also applied to engineer bioconjugates of nanomaterials and proteins. Bovine serum albumin (BSA) was used as a model protein to demonstrate light assisted molecular immobilization (LAMI) onto gold coated iron oxide nanoparticles. This technique is based on the UV disruption of disulphide bridges leading to surface immobilization of biomolecules via thiol-metal linkage. Biofunctionalization of superparamagnetic nanoparticles with LAMI can lead to the creation of novel optical biosensors and drug delivery constructs. For the first time LAMI was also carried out using infrared light in order immobilize BSA onto gold gap-antennas arrays. The enhanced localized near field generated by the coupled gold dimers was exploited to trigger light induced coupling of BSA upon multi-photon excitation. The results showed protein immobilization on the nanometer sized gaps (20-30 nm) and the process was best when the gold dimers resonated at the same wavelength required

for three-photon wavelength (800 nm). The immobilized protein can later be used as scaffold to attach additional nanoscale objects.

This PhD work also demonstrated proof of concept for a novel nanoparticle carrier to be used in biomedical applications. A magnetic nanocarrier was engineered upon controlled agglomeration of several individual iron oxide nanoparticles onto colloidal nanoparticle clusters (CNCs). This self-assembly approach results in CNCs nanocarriers with superior magnetic properties, which retain the superparamagnetic nature of the individual iron oxide nanoparticles. Insulin was immobilized onto iron oxide nanoparticles using carbodiimide chemistry aiming at targeting the insulin receptor in cells. The CNCs-insulin bioconjugates could be easily controlled using external magnetic fields and thereby could be efficiently separated from solution within minutes. The superparamagnetic behavior, high magnetization and high water dispersibility of CNCs bioconjugates makes them promising candidates for future use in e.g. targeted drug delivery and bioseparation.

Resumé

Nye nanomaterialer og deres spændende egenskaber har bragt innovative muligheder til nanomedicin, såsom brugen af nanopartikler til biologisk afbildning og diagnose samt lysaktiverede terapimetoder. Hovedmålet med forskningen på denne PhD var at opsamle viden til udvikling af innovative diagnose- og terapimetoder ved at koble nano-bioteknologi og biofotonik. Denne PhD afhandling giver et indblik i UV aktiverede mekanismer i proteiner og hvordan de kan bruges til at udvikle proteinbaserede terapier samt at konjugere nanomaterialer og proteiner til biosensorer, bioseperation og målrettet medicinlevering.

Adskillige proteinkandidater blev brugt til at undersøge lysaktiverede mekanismer i biomolekyler. UV aktiverede brud af di-sulfid bindinger i proteiner er en af hovedmekanismerne i denne forbindelse. Alfa-lactalbumin og menneskelig insulin blev brugt som basis for at studere den optiske fysik og kemi bag denne mekanisme. Studiet af insulin viste ikke blot UV aktiveret brud af di-sulfid-bindinger, men også UV formidlet dannelse af insulin-dimerer via krydskobling af dityrosin. Disse strukturelle modifikationer skete indenfor få timers UV eksponering, på et strålingsniveau der svarer til det der findes i sollys, og førte til næsten fuldstændig inaktivering af insulinens hormonelle funktioner *in vitro*. Disse resultater er relevante for medicinindustrien og advarer om vigtigheden af at beskytte medikamenter der indeholder insulin mod sollys og indendørs belysning.

Forskningen beskrevet i denne afhandling involverer også en lysinduceret protein-afbryder i lyset af en ny fotonisk terapi. Denne metode var baseret på at afbryde den epidermiske vækstfaktor-receptor (EGRF) hvis overudtryk er forbundet med kræftvækst. UV belysning resulterede i strukturelle ændringer i EGFR der svækker epidermisk vækstfaktor-binding og dermed kunne stoppe receptor-aktivering. De resultater der præsenteres heri indikerer at UV lys kan blive brugt som en ny fotonisk kræftterapi ved at modulere EGFR-strukturen, og dermed stoppe EGFR signalvejen.

Den viden om lysaktiverede reaktioner som blev opsamlet i forskningen, blev også brugt til at skabe biokonjugeringer af nanomaterialer og proteiner. Bovinsk blodalbumin (BSA) blev brugt som basis for at at demonstrere lysassisteret molekyleimmobilisering (LAMI) på guldcoatede jernoxid-nanopartikler. Denne teknik er baseret på UV brydning af disulfid-broer i proteiner hvilket fører til overfladeimmobilisering af biomolekyler via thiol-metal-binding. Biofunktionalisering af superparamagnetiske nanopartikler med LAMI kan lede til opfindelsen af optiske biosensorer og målrettede medicineringsmetoder. For første gang var LAMI også udført med infrarødt lys for at immobilisere BSA på guldpartikel-antennerækker. Det forstærkede nærfelt genereret af de komblede gulddimerer blev udnyttet til at aktivere lysinduceret kobling af BSA gennem multi-foton excitering. Resultaterne viste proteinimmobilisering på de nanometer-størrelse antennegab (20-30 nm) og processen var bedst når gulddimererne resonerede på den bølgelængde der er

påkrævet for tre-foton-excitering (800 nm). Det immobiliserede protein kan senere bruges som et fundament hvortil der kan kobles yderligere objekter i nanostørrelse.

Arbejdet i denne PhD demonstrerede også proof-of-concept for en innovativ nanopartikelbærer til brug i biomedicin. En magnetisk nanobærer blev fabrikeret via kontrolleret agglomerering af adskillige individuelle jerndioxid-nanopartikler til klynger af nanopartikel-kolloider (CNC). Denne selvsamlende metode resulterede i CNC-nanobærere med overlegne magnetiske egenskaber som bibeholder de individuelle jernoxid-nanopartiklers superparamagnetisme. Insulin blev immobiliseret på jerndioxid-nanopartikler via carbo-diimid-kemi rettet imod cellers insulinreceptorer. CNC-insulin-biokonjugaterne kunne let blive kontrolleret ved brug af eksterne magnetfelter og derved blive separeret effektivt fra en opløsning i løbet af sekunder. CNC-biokonjugaters superparamagnetiske opførsel, høje magnetiseringsgrad og stærke dispersion i vand gør dem til lovende kandidater for fremtidig brug i f.eks. målrettet medicinlevering og bioseperation.

Abbreviations

BSA	Bovine serum albumin
CNCs	Colloidal nanoparticle clusters
Cys	Cysteine
DLS	Dynamic light scattering
DTT	Dithiothreitol
EDX	Energy Dispersive X-ray Spectroscopy
EGF	Epidermal growth factor
EGFR	Epidermal growth factor receptor
ELS	Electrophoretic light scattering
Fe_3O_4@Au	Magnetite gold coated nanoparticles
LAMI	Light assisted molecular immobilization
LSPR	Localized surface plasmon resonance
MRI	Magnetic resonance imaging
NTA	Nanoparticle tracking analysis
PAA	Polyacrylic acid
PDT	Photodynamic therapy
Phe	Phenylalanine
SEM	Scanning electron microscopy
SPIONs	Superparamagnetic iron oxide nanoparticles
Trp	Tryptophan
Tyr	Tyrosine

Table of contents

1. Introduction

Many of the advances on the medical field are associated with the emergence of novel technologies. The high economical, but more importantly social value of delivering proper medical care led to the production of new medical devices, the exploration of new materials and a constant research effort to design, test and evaluate novel products. Within this context, nanobiotechnology emerged, a multidisciplinary field that covers a wide span of technologies from engineering, physics, chemistry and biology. Nanobiotechnology is defined by its growing research interest and ability to work at the molecular level, atom by atom, combining biological materials and the rules of physics, chemistry, and biotechnology to fabricate minute synthetic structures (between 1-100nm). Thus, nanobiotechnology evolves as a research field both as it produces and researches the behavior of new materials as well as it takes advantage of technological advances in areas like optical components, hardware and laser systems, to do so.

For the last few decades, research efforts have been focused on the development of new materials at the atomic, molecular and macromolecular levels in order to build materials at the nanoscale and to explore the novel properties that nano-structures, -devices and -systems have. Since biomolecules such as nucleic acids and proteins are nanosized, materials at nanoscale are crucial in understanding the molecular mechanisms underlying disease processes. Nanoparticles constitute the core of nanomaterials developed for analysis of biomolecules. Due to their size, nanoparticles possess unique physical and chemical properties as compared to their larger counterparts. It has been shown that it is possible to tune precisely the physico-chemical properties of materials at nanoscale by modifying the size, shape and composition of their basic building blocks. The surface area to volume ratio makes nanoparticles a convenient platform for molecular assembly and they may be composed of inorganic or polymeric materials. They can be efficiently used as molecular carriers and if needed their surface can be pre-modified to use in biological applications, to render them biocompatible and to avoid the immune system response. Examples of novel biological and medical applications involving the use of nanoparticles are drug targeting and delivery, cell labeling and separation, cancer therapy, magnetic resonance image (MRI) contrast agents, bio-sensors and bio-imaging.

Simultaneously, the recent technological advances in optical components, hardware and laser systems have paved the way to the development of bionanophotonics, which merges biomedical science, technology and nanophotonics. Fluorescence spectroscopy and confocal microscopy provide nowadays high sensitivity and un-precedent optical resolution. The use of nanoparticles for optical bioimaging, optical diagnostics and light guided and activated therapy, are examples of new areas within bionanophotonics. The combination of biophotonics and nanofabrication of biological systems offers new possibilities in the areas of protein-based diagnostics, therapeutics, bioimaging, protein based nano-carriers and biomarker identification. Within this context light

represents a unique external control element as light-responsive biological compounds offer unique possibilities for the control and regulation of biological processes. With the light-sources and optics available nowadays (lamps, lasers, and microscopes) it is possible precisely control the area, time and dosage of the irradiating light. At the core of this PhD thesis is the study of light induced reactions. As nature uses UV light to initiate reactions, it is of major interest to describe and to better understand what it can induce in the structure and function of protein and cells, by uncovering the reaction mechanisms and dynamics.

The NanoBiotechnology Group at Aalborg University has been focusing its research onto UV light activated mechanisms in proteins and other biomolecules. In the recent years, the group has developed a new photonic technology, UV light assisted molecular immobilization (LAMI), which results in covalent coupling of biomolecules onto thiol reactive surfaces. This technology relies on a specific light induced mechanism in proteins, UV light mediated disruption of disulphide bonds. Using UV light, it is possible to open disulphide bridges in proteins, upon excitation of neighboring aromatic residues (e.g. tryptophan, Figure 1). The free thiol moieties yielded from disulphide bond breakage are very reactive and can be used to immobilize proteins onto thiol reactive surfaces (e.g. gold, thiol derivatized silica, Figure 1).

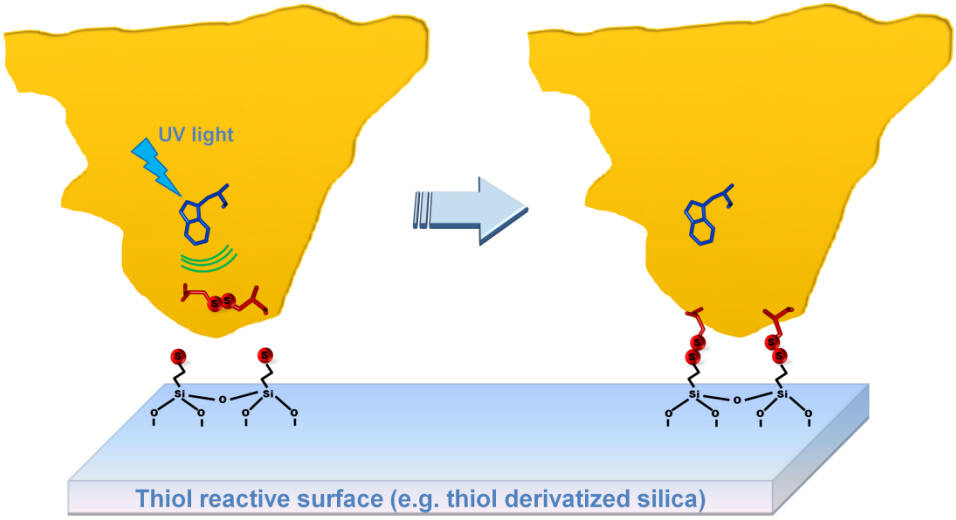

Figure 1. Principle of light assisted molecular immobilization (LAMI). In proteins (yellow), excitation of aromatic residues, here tryptophan (blue), leads to breakage of spatial neighboring disulphide bridges (red). The yielded reactive thiol groups can be used to immobilize the protein onto a thiol reactive surface.

Since aromatic residues are known to be conserved spatial neighbors of disulphide bonds in proteins [1], disulphide bond photolysis is likely to occur throughout nature. In this respect, several proteins were successfully immobilized onto thiol derivatized quartz slides by the Nanobiotechnology Group using LAMI, such as cutinase, lysozyme, major histocompatibility

complex, alkaline phosphatase, Fab fragments, and prostate specific antigen [2–4]. This photonic technology has been applied to build microarrays and biosensor technologies [4–7].

Within this context, the overall aim of this PhD project was to combine the methodologies and features offered both by nanobiotechnology and biophotonics for the development of new approaches to diagnosis and therapeutics. The present project was dedicated to two main research themes. The first part of the PhD work involved the investigation of UV light induced mechanisms in proteins and their usefulness for developing protein-based therapies. The second research focus regarded the construction of bioconjugates of nanomaterials and proteins for biosensing, bioseparation and targeted drug delivery. Both research themes will be presented in detail in the following sections.

1.1 Investigation of light induced switches in proteins

The first part of this PhD project studies disulphide bond disruption and other UV light triggered mechanisms on medically interesting protein molecules that were not previously analyzed by the Nanobiotechnology Group. This was in line with the group's ambition to further expand the database of protein molecules that carry the necessary features for protein immobilization using the LAMI technology. The main purpose of this investigation was to find out more about the molecular mechanisms triggered upon UV illumination of proteins and their implications to the structure and function of biomolecules.

In this research work, three criteria were taken into consideration in order to evaluate UV mediated disulphide bond disruption on different protein models:

- ❒ The protein candidate has to contain the structural features required for disruption of disulphide bonds upon excitation of the protein aromatic residues. This reaction mechanism depends both on the number as well as the geometric position of the aromatic residues and the disulphide bonds.
- ❒ The reaction mechanism depends on several experimental conditions, which have to be considered, such as the ionic strength of the solution, the pH, or the temperature.
- ❒ UV excitation of protein aromatic residues can also lead to other amino acid chemical modifications and conformational changes, which, in combination with disulphide bond disruption can affect the overall fold and function of the protein. Therefore, it is required to probe the effects of UV illumination and disulphide bond disruption on protein structure and function.

Two main protein candidates were used as models to evaluate disulphide bond disruption in proteins: alpha-lactalbumin and insulin. Furthermore, this research work focused also on the

study of the UV light induced inactivation of a protein receptor, the epidermal growth factor receptor (EGFR) in the perspective of a new photonic cancer therapy. More details are presented in chapter 2.

1.2 Construction of nanoparticle based bioconjugates

The second part of this PhD project dealt with the development of novel bioconjugates of proteins and nanoparticles, intended to be used in biomedical applications (e.g. as biosensors, nanocarriers for targeted protein therapeutics and drug delivery). It explored as well combined the function of a bioconjugate (e.g. protein, hormone) and the unique characteristics of nanomaterials, such as nanoparticles and other nanostructures. Among the various types of nanoparticles, superparmagnetic nanoparticles were selected for developing protein nanocarriers, as due to their properties they can be controlled using external magnetic fields without the risk of permanent agglomeration. This makes them makes them easily separable as well as provides transporter capabilities applicable for targeted protein therapeutics.

The development of nanoparticle bioconjugates for biomedical applications involves a number of procedures, from the synthesis of the nanomaterial to testing its functionality for the determined application. In this respect, the following features were addressed during the design and engineering of the nanoparticle bioconjugates:

- ❒ Type of biomolecule used - characteristics, stability, and biological function;
- ❒ Nanoparticle/nanostructure – synthesis/fabrication and characteristics;
- ❒ Coating/activation of the nanomaterial surface for protein coupling – surface chemistry involved and stability in those conditions;
- ❒ Bioconjugation – immobilization technique used, stability of the bioconjugate, retention of the biological function;
- ❒ Application for drug delivery/biosensor – *in vitro* behavior, biocompatibility, etc.

Aforementioned, the LAMI technology had been already successfully used to immobilize proteins onto flat surfaces, such as thiol-derivatized quartz slides. Herein it was intended to apply the LAMI technology to immobilize proteins onto new types of surfaces, such as nanoparticles. Iron oxide gold coated superparamagnetic nanoparticles (Fe_3O_4@Au) were selected for protein immobilization with LAMI, due to its interesting magnetic, optical and chemical properties. Furthermore, gold was a convenient coating for LAMI bioconjugation, since it has affinity towards biomolecules with thiol terminal groups. Bovine Serum Albumin (BSA) was used as a model protein to test and apply LAMI immobilization on magnetic nanoparticles.

Within the same scope, the LAMI technology was also applied to build new types of nanoconstructs upon protein immobilization onto plasmonic hot spots located in the interface of nanosized gold dimers. LAMI was applied for the first time with infrared light (3 photon excitation) to immobilize BSA onto the plasmonic surfaces (dimers) in regions as small as 20-30 nm. The immobilized protein can later be used as scaffold to attach additional nanoscale objects.

The magnetic properties of magnetic nanoparticle carriers are critical for its practical use in targeted therapy and guidance under external magnetic field gradients. In this respect, this PhD project also aimed at the construction of superparamagnetic nanoparticle carriers of strong magnetic response for future use in targeted protein therapeutics and magnetic separation technologies. A particular type of magnetic nanocarrier was engineered, based on the agglomeration of several individual Fe_3O_4 nanoparticles onto colloidal nanoparticle clusters (CNCs). This bottom-up approach results in CNCs nanocarriers with superior magnetic properties, which retain the superparamagnetic nature of individual Fe_3O_4 nanoparticles. Insulin was selected as a model protein to couple to the superparamagnetic CNCs aiming at targeting the insulin receptor in cells. More details are presented in chapter 3.

1.3 Objectives

The main objectives of the PhD project were to:

- ❒ Study UV light induced reactions mechanisms in proteins:
  - Study the structural features of each protein using bioinformatics and database mining tools;
  - Study the effects of UV illumination and disulphide bond disruption on the stability and function of the protein candidates;
  - Get insight into UV light induced reactions in biomolecules.
- ❒ Investigate light induced molecular switches in proteins (e.g. UV inactivation of EGFR).
- ❒ Use the novel photonic technology (LAMI) to immobilize proteins onto new types of surfaces such as nanoparticles:
  - Synthesize/fabricate superparamagnetic nanoparticles and other types of nanostructures containing the appropriate features for immobilization with LAMI;
  - Immobilize the protein candidate(s) using LAMI technology onto superparmagnetic nanoparticles and other types of nanostructures;

- Characterize the engineered bioconjugates (using spectroscopy, microscopy techniques) and demonstrate that the immobilization was successful.

❒ Construct nanoparticles carriers of strong magnetic response for practical use targeted protein therapeutics and magnetic separation technologies.

- Synthesize/engineer superparamagnetic nanoparticles of strong magnetic response;
- Test the behavior of the magnetic nanocarrier in the presence of external magnetic fields;
- Immobilize a functional protein onto the magnetic nanocarriers;
- Detect and quantify the presence of the protein on the surface of the nanocarriers.

1.4 Structure of the thesis

This chapter introduced the research area of this thesis and showed that it evolves around two themes: the investigation of UV light induced switches in proteins and the construction of nanoparticle based bioconjugates. The following two chapters (Chapters 2 and 3) present in detail the core theoretical foundations behind these two themes. Chapter 4 introduces the paper contributions of this thesis while Chapter 5 discusses the main findings and compares them to the related work. Chapter 6 briefly summarizes the main conclusions of this research work and it is followed by the bibliography that is cited in this dissertation and an Appendix. The Appendix includes supplementary information to Chapters 2 and 3 as well as a supporting scientific publication.

2 Investigation of light induced switches in proteins

Among biomolecules, proteins have the most diverse and dynamic roles in the human body. They catalyze biochemical reactions, form cell receptors and channels, participate in the activation and inhibition of receptors and pathways, provide scaffold support and act as molecular transporters [8]. Because of their versatility and wide number of functions proteins have been extensively used as therapeutics in order to develop new kinds of drugs and medicines. Protein based therapeutics include antibody-based drugs, anti-coagulants, blood factors, bone morphogenetic proteins, engineered protein scaffolds enzymes, growth factors, hormones, interferons, interleukins, and thrombolytics [9]. In protein therapeutics, proteins can have diverse roles and mechanisms of action such as:

- ❒ Replacement of an abnormal or deficitary native protein;
- ❒ Increasing the activity of a molecular pathway;
- ❒ Enabling a new function;
- ❒ Interfering other biomolecules or pathogens;
- ❒ Acting as delivery vehicle for other proteins or compounds (e.g. radionuclide, cytotoxic drug, effector proteins).

Proteins are also used to build therapeutics and other medicines in combination with other nano-sized objects, such as nanoparticles, which can be used e.g. as molecular carriers. Nanoparticle based therapeutics also benefit from the characteristics and biological properties of proteins and their therapeutic advantages and will be addressed in Chapter 3.

Proteins can be simple single domain globular proteins like hormones, growth factors or cytokines, or more complex multi-domain macromolecules, such as antibodies or receptors [10]. Besides complexity and size, proteins also differ in isoelectric point, surface charge, solubility, thermal stability, and optimal working pH (activity) [10–12]. In order to use a protein for a determined application it is necessary to understand its specific structural features and characteristics as well as to analyze its conformation and stability in the appropriate experimental conditions. For instance, to employ a specific protein as a therapy or drug, it is required it remains stable during its lifetime (from production and storage to administration) retaining both structure and activity.

During this PhD work five different proteins were studied and analyzed upon illumination with UV light: bovine alpha-lactalbumin, human insulin, human plasminogen, human epidermal growth factor receptor (EGFR) and bovine serum albumin (BSA). The structure and characteristics of each these proteins is described in Figure 2.

Protein	Species	Function(s)	Sequence length # Amino acids (aa) # Domains	pI	# Trp	# Tyr	# Disulphide bridges	Protein data bank (PDB)	Structure
Alpha-lactalbumin	Bovine	•Milk globular protein •Biosynthesis of lactose •Component of the lactose synthase complex	14.2 kDa 123 aa 1 domain (2 sub-domains)	4-5	4	4	4	1F6S Bovine	
Insulin	Human	•Hormone •Glucose homeostasis; Carbohydrate and lipid metabolism •Interacts w/insulin receptors (muscle cells, liver and adipose tissue)	6 kDa 51 aa	5.4	0	4	3	4INS Pig	
Plasminogen	Human	•Protease (inactive form of plasmin) •Blood coagulation - role in thrombolysis; Tissue remodeling; angiogenesis •Plasmin dissolves fibrin in blood cloths	92 kDa 791 aa 7 domains	6.2	19	30	24	4A5T Human	
Epidermal growth factor receptor (EGFR)	Human	•Receptor protein; tyrosine kinase •Regulation cell survival, proliferation migration; •Binds to EGF family ligands activating signaling cascades to trigger appropriate cellular responses	132 kDa 1186 aa 3 domains •Extracellular (621 aa) •Transmembrane (23 aa) •Cytoplasmic (542 aa)	5-7	6 (extracell. domain)	16 (extracell. domain)	25 (extracell. domain)	1IVO (extracell. domain) 2JWA (transm. domain) 1M17 (cytoplasmic domain) Human (all)	
Serum Albumin	Bovine	•Plasma globular protein •Regulation of the colloidal osmotic pressure of blood •Carrier protein for steroids, fatty acids, hormones and zinc	67 kDa 583 aa 3 domains	5.3	2	20	17 (and 1 free Cys)	3V03; 4F5S Bovine 1AO6 Human	

Figure 2. Characteristics and structural features of the protein molecules studied during the PhD work, including function, size, isoelectric point (pI), number of amino acids, domains, disulphide bridges, tryptophan (Trp) and tyrosine (Tyr) residues, and three-dimensional structural representation. The information regarding the structural and physicochemical characteristics was collected from the following sources and using considering the corresponding ProtParam sequences: Alpha-lactalbumin - [13, 14]**, UniProt Entry P00711 [AA 20-142]; Insulin -** [15–20]**, UniProt Entry P01308 [AA 25-54; 90-110]; Plasminogen -** [21–23]**, UniProt Entry P00747 [AA 20-810];EGFR -** [24–26]**, UniProt Entry P00533 [25-1210] and P00533 [25-645]; Serum albumin:** [27, 28]**, UniProt Entry P02679 [25-607]. The crystallography data used for three-dimensional protein structure display was extracted from the PDB files 1F6S (Bovine Alpha-lactalbumin), 4INS (Pig Insulin), 4A5T (human plasminogen), 1IVO (extracellular domain of Human EGFR) and 1AO6 (Human Serum Albumin). The three-dimensional structures were displayed using Accelrys Discovery Studio Visualizer 2.5.**

The five proteins are quite distinct in size, structure and physicochemical characteristics and are important for a wide number of biological processes. Alpha-lactalbumin is a small globular protein present in the milk whey of mammalians, which plays an important role in lactose biosynthesis [13, 14, 29]. Insulin is a small and important peptide hormone mostly known for its role in regulating the glucose levels in the blood. It is also involved in a wide span of cellular processes such as cell growth, cell differentiation, membrane transfer of nutrients and metabolism [16, 17]. Plasminogen is the inactive form of plasmin, a trypsin-like serine protease, which is a key enzyme in thrombolysis. Plasmin ensures blood fluidity by dissolving fibrin that forms blood clots [21, 22]. The epidermal growth factor receptor (EGFR) is a member of the ErbB family of receptor tyrosine kinases and plays a critical role in regulating cellular processes e.g. cell survival, proliferation and migration. EGFR overactivation is associated with tumor progression [24–26]. Bovine serum albumin (BSA) is a globular plasma protein and is essential for the regulation of the osmotic pressure in the blood. It also acts as a transport protein for certain hormones, steroids, fatty acids and binds to metals e.g. zinc [27, 28].

The response of proteins to UV light is quite dependent on its amino acid composition and certain structural features. Of particular relevance is the presence and location of UV absorbing groups such as the aromatic residues (e.g. tryptophan and tyrosine), and other relevant structural elements such as its disulphide bonds. As will be discussed in section 2.2, distinct processes can be triggered upon UV excitation of proteins, which can result in the formation of reactive radical species and structural modifications such as disulphide bond disruption. In particular, the photophysical and photochemical mechanisms that lead to disulphide bond photolysis are strongly dependent on the number and geometric position of the aromatic residues and the disulphide bonds. All the proteins analyzed during this PhD work contained a considerable number of aromatic residues, some of which located in close proximity to disulphide bonds (Figure 2).

In this chapter the main structural features of different types of proteins will be reviewed and in particular, the structural and functional properties of disulphide bonds. Subsequently, the most important processes triggered upon UV excitation of proteins will be described, as well as, the consequences to the structure and function of medically relevant proteins. In that scope, the application of some naturally occurring light-induced mechanisms for the development of new therapies will be discussed.

2.1 Protein Structure and function

2.1.1 Protein folding and stability

The conformation (three dimensional structure or overall fold) of a protein is of outmost importance for the function and biological activity. The specific fold of a protein is largely determined by the distribution of amino-acids in the primary amino acid sequence [12]. Namely,

patterns of hydrophobic and hydrophilic residues define to a high extent the structure of a fold. In several small globular proteins the internal core is mostly formed by hydrophobic amino acids held together by Van der Waals forces, whereas the surface is formed by polar and charged amino acids [12, 30]. This happens due to the hydrophobic effect, which can be viewed as a combined effect of hydration and van der Waals interactions between solute molecules, which results in a rapid collapse of the polypeptide chain. Proteins usually exist in this condensed state, while their specific conformation is determined by the flexibility of the polypeptide backbone and the specific intermolecular interactions of the amino acid side-chains [12]. The native conformation must be energetically stable. From a thermodynamic point of view, the four major stabilizing energetic contributions to protein stability are: the hydrophobic effect, the formation of hydrogen bonds, the formation of electrostatic interactions, and the conformational entropy due to restricted motion of the main chain and side-chains [12].

The side-chains of individual amino acids also play a major role in protein folding as they are related to the complexity, specificity and stability of individual proteins [31]. Several of the characteristics that contribute to protein stability have been identified on thermal stability studies of small mesophylic and thermophylic enzymes [32]. Some of these characteristics include entropic stabilization by introduction of prolines or disulphide bridges, which are often used in protein engineering to increase the stability of protein and enzymes in industry [32, 33]. Other strategies used for protein stabilization include helix optimization, introduction of salt bridges and clusters of aromatic interactions [32]. Hence, the overall fold of a protein is determined by the wide range of interactions between the amino-acids constituting the protein structural elements and the surrounding solvent environment [11, 12]. We can organize the different elements influencing the protein fold according to the levels of structural protein organization:

- ❒ The secondary structure elements – on which amino acids residues are organized, defined by configuration of the peptide backbone: alpha helix, beta sheet, turns, unordered structure;

- ❒ The tertiary structure organization - defined by short or long distance interactions between amino acids and interactions with the surrounding environment (e.g. buffer ions), including van der Waals, hydrophobic, charge-charge interactions, hydrogen bonds, salt bridges, disulphide bridges;

- ❒ The quaternary structure level – interaction/association of more than one polypeptide chain, usually required in larger proteins, such as antibodies, to form a fully functional protein.

In the complex biological environment, the native protein conformation is maintained by wide number of external agents, such other proteins, ions, lipids [34]. Outside of this natural environment protein conformation is more labile and the native conformation has to be stabilized

using appropriate solution conditions (e.g. low temperature) and appropriate buffer conditions [35]. Proteins can be unfolded by a wide number of stress agents including changes in pH, low or high ionic strength, heat, pressure, chemical agents [11, 35–37]. Protein unfolding can lead to reversible or irreversible protein denaturation, impairing protein function. The amino acid residues that constitute a protein can also undergo chemical modifications that can affect or not the overall function of the biomolecule [11].

The simplest model for unfolding and refolding of proteins involves a single cooperative transition step, in which native (N) and unfolded (U) states of the protein interconvert. In the native state, the protein has a distinct single conformation, while in the unfolded state the protein fold is denaturated and characterized by a high degree of disorder. The native state of a protein is characterized by the lowest free-energy. To pass between the unfolded and the native low free-energy states, the protein must cross the transition state, a higher free-energy barrier [12, 38]. This simple mechanism describes well the folding and unfolding mechanisms of small globular proteins (less than 100 residues) [30]. For such cases, the intermediates formed between the two steps are transient species that are not thermodynamically stable and the mechanism can be simplified to a “all or none” process (cooperative unfolding) [12, 38, 39].

The unfolding and refolding process of larger proteins is not as straightforward. For instance, the folding process of larger proteins usually involves the formation of partly folded protein intermediates, prior to formation of the completely folded native state. These intermediate structures are observed to accumulate during the folding of various proteins, and have a distinct conformation compared to the native and unfolded states [12, 38]. One of the most studied folding intermediates is the *molten globule*, which occurs in globular proteins (e.g. alpha-lactalbumin). The molten globule is a stabilized intermediate state formed in the early stages of folding, upon the collapse of the hydrophobic core [12, 40]. A molten globule is defined as a relatively compact folding state of the protein, which retains a native-like secondary structure and an overall backbone-folding topology, but lacks some of the specific side-chain interactions of the native structure that permit the existence of a clear tertiary arrangement [12, 38, 41, 42]. Molten globule states can also be generated at equilibrium during the unfolding of proteins under mild denaturing conditions e.g. high or low pH, moderate concentrations of denaturants, or upon removal of protein-bound prosthetic groups or metal ions [41, 42].

Furthermore, proteins have also the tendency to self associate and aggregate under appropriate solution conditions. The simplest form of this reaction is a concentration dependent thermodynamic equilibrium, that can lead to the formation of dimers, tetramers, and higher order protein aggregates [11, 35]. One example of concentration dependent self-protein aggregation is of insulin, that at physiological concentration (< 1 nM, in the blood) exists as a monomer, but that at higher concentrations and in specific solvent conditions self-associates to form dimeric, and even hexameric species [43, 44].

2.1.1.1 Disulphide Bonds

Disulphide bonds or bridges are covalent links between sulfur atoms of two cysteine residues in proteins, also named cystine residues. They are present in a considerable number of proteins in nature and are mostly found in proteins of the extra-cellular environment. In mammalian cells, around 10 % of the proteins (~3000) contain disulphide bonds [45, 46]. The ability of cysteine to form disulphide bonds is unique among the 20 essential amino acids. The thiol side chain on cysteine also affords this amino acid a wide range of functional roles, such as metal binding, electron donation and redox catalysis [47]. In isolation disulphide bonds are chemically stable (S-S bond energy of 60 kcal.mol^{-1}) [48, 49]. Only at extreme conditions such as 100 °C and alkaline pH they spontaneously break, or rearrange [50]. The formation and breakage of disulphide bonds is an oxidation-reduction process and requires the presence of electron acceptors, or donors [51]. Disulphide bonds can be reduced by thiol-disulphide exchange with other thiol groups (e.g. from small molecules like dithiothreitol (DTT) or from other proteins/enzymes) and by reducing agents (e.g. phosphite esters) [52, 53]. Disulphide bond formation or reduction depends on the reactivity of the involved chemical groups. The thiolate form S^- is the reactive cysteine form and therefore both the specific pK_a of the cysteine and the pH of the local environment control the thiol/disulphide exchange reaction. The general assumption is that basic environments promote disulphide formation/reduction, while acidic medium inhibit them [48, 51, 54].

After the peptide bonds, disulphide bonds are by far the second most common covalent bonds in proteins and peptides and one of the most common post translational covalent modifications that occurs during oxidative folding [55]. The prevailing view has been that disulphide bonds were a product of evolution to enhance the stability of proteins working in the varying physicochemical conditions of the extra-cellular environment [1, 53]. This is true for the majority of the disulphide bonds, which are called structural disulphide bonds. These disulphide bridges confer extra rigidity and stability to the resident protein, by stabilizing tertiary and quaternary protein structure and are also thought to assist protein folding by decreasing the entropy of the unfolded form [46, 53, 56]. Furthermore, they have a role in protecting proteins from oxidants (such as reactive oxygen species), nitrogen and sulphur species, electrophiles and proteolytic enzymes in the extra-cellular environment, and increasing their half-life [53, 55]. This structural properties of disulphide bonds has been used to increase the thermal stability of genetically engineered proteins, by introduction of cysteine pairs in the amino-acid sequence [33].

However, not all disulphide bonds have a structural role and not all of these bridges remain inert during the life of a protein. It has been experimentally verified that though many of disulphide bonds are essential to retain the structure and function of a protein, there are others than can be broken without affecting radically the behavior of a protein [1, 57]. In addition, another type of disulphide bonds that are redox active and are cleaved in mature proteins was recently discovered. These are functional disulphide bonds that regulate protein function, and can be

either catalytic or allosteric disulphide bonds [46, 47, 56, 58]. Catalytic disulphide bonds are usually at the active sites of enzymes, which mediate thiol/disulphide exchange in other proteins, called oxyreductases. Allosteric disulphide bonds have been recently identified and they control protein function by triggering a conformational change when they form and/or break [46, 56].

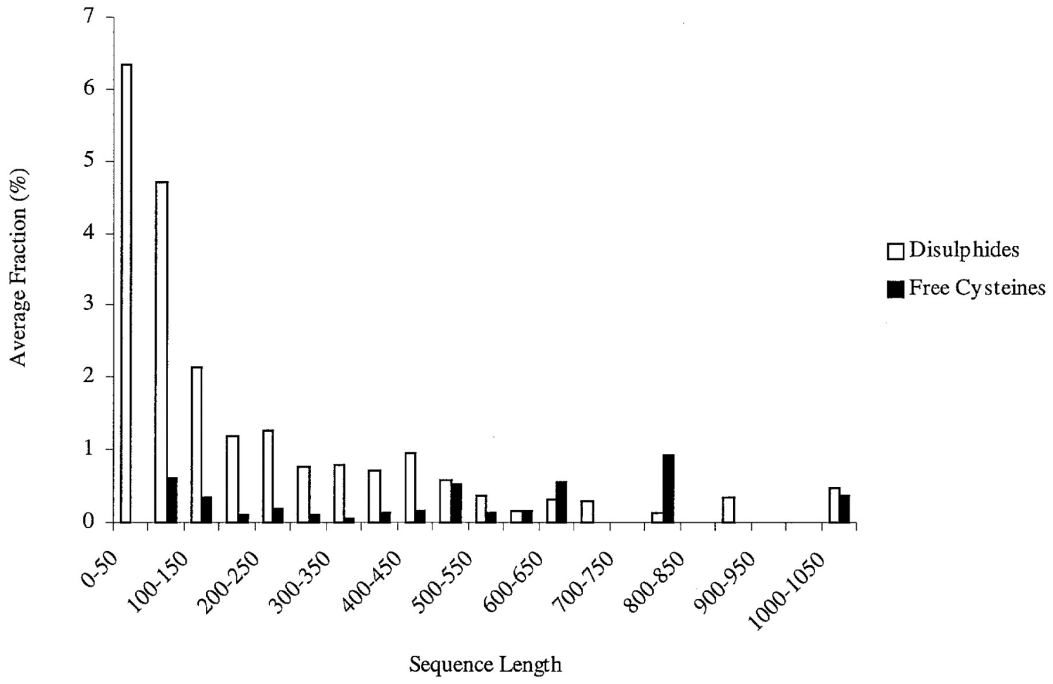

Figure 3. Dependence of the average fraction of disulphide bridges and free cysteines on the protein sequence length. The fraction of disulphide bridges was calculated as the number of disulphide bridges found in a protein divided by the protein sequence length (number of amino acids) X100. The same approach was applied to determine the fraction of free cysteines. Reprinted with permission from [1]**. Copyright © 1999 Oxford University Press.**

Considering their importance for protein structure and function, it does not come as a surprise that disulphide bonds are highly conserved throughout evolution [57]. A recent study involving all structurally validated disulphide bonds from the Protein Data Bank showed elevated conservation of disulfide bound cysteines (half-cystines) compared to unpaired cysteines and other amino-acids. Half-cystines were found to be even more conserved than the most conserved amino-acid, tryptophan [47].

The conformation and stability of a disulphide bond is much determined by its geometry and the interactions with the rest of the protein [1]. For instance, structural disulphide bridges decrease the entropy of the unfolded form and increase the stability of the native structure by cross-linking of distant regions in the polypeptide sequence. Therefore the stability of the native structure is favored with the increase in the number of residues between the bound cysteines [58, 59]. Another critical observation is that small proteins (less than 70 residues) are usually richer in disulphide bonds. Indeed, Petersen et al. made the observation, for a sub-set of 131 non-

homologous proteins, that the average fraction of disulphide bonds per protein decreases exponentially with the length of the amino acid sequence (Figure 3) [1]. This observation can be explained by the higher contribution and importance of disulphide bonds in the structural stability in small proteins rather than in larger ones [1, 60]. As small proteins usually lack a strong hydrophobic core [61], disulphide bonds may have a critical structural role in these short polypeptides.

Disulphide bridges are located in specific three-dimensional spatial environments. For instance, disulphide bridges are known to have preferential spatial neighbors, such as hydrophobic amino acid residues like valine, leucine, isoleucine and methionine, and in particular the aromatic amino acids tryptophan, tyrosine and phenylalanine [1]. The spatial proximity between disulphide bonds and aromatic residues in the three-dimensional structure of proteins has been extensively observed among proteases, hydrolytic enzymes and the immunoglobulin superfamily, which indicates that this structural arrangement might have been conserved throughout evolution [1, 62].

2.2 Light induced mechanisms and UV light effects on proteins

As it was discussed previously, proteins and peptides are prone to denaturation and structural damage when isolated from the complex biological environment. Proteins undergo structural changes when exposed to certain solvent conditions, such as extremes of pH, elevated temperature and pressure. For several years it has been acknowledged that the exposure of proteins to light can also have direct impact on protein structure and function [63–65].

Most of Earth's life forms and living organisms are in regular contact with sunlight. In the majority of cases this light exposure is crucial for viability and health. Despite the positive effects of light exposure, there is a wide concern regarding the exposure of biological systems and components to UV (100-400 nm) radiation. Even though atmospheric gases block most of the UV solar radiation, still a non-negligible amount of near-UV light goes through to the surface. Since, cells, proteins, and genes are all sensitive to UV light, in several organisms, the exposure to UV light can lead to reduction in growth and survival, protein photo-oxidation, pigment bleaching and photoinibition of photosynthesis [66]. On the human body, depending on the type of UV radiation and duration of exposure, UV light can have different effects, such as sunburn, suntan, cell-aging, and photocarcinogenesis on the skin, or welderflash and blindness [67].

Among biomolecules, proteins are major targets for the activation of light-induced mechanisms, due to the presence of endogenous chromophores within their structure (including amino-acid side-chains and bound prosthetic groups such as flavin and heme) and their fast reaction rates with other excited species [65, 68]. For proteins that do not contain prosthetic groups, most of these photo-activated processes are triggered upon UV radiation below 320 nm, where the amino-

acid side-chains absorb [68]. Their excitation leads to the formation of electronically-excited states and photo-ionization reactions. The photochemical and photophysical mechanisms that follow can involve the formation of reactive radicals and other species, which may result in changes in the primary, secondary and tertiary structure of the protein. In the worst case scenarios, these protein modifications can result in protein unfolding, aggregation and/or inactivation.

2.2.1 Effects of UV light exposure on proteins

In proteins, the main absorbing groups in the UV region are the aromatic side-chains of tryptophan (Trp, 280-305 nm), tyrosine (Tyr, 260-290 nm) and phenylalanine (Phe, 240-270 nm), cysteine (Cys) and cystine (250-300 nm), along with the peptide backbone (180-230 nm) [64, 65, 68]. This PhD work focused on the photophysics and photochemistry of the aromatic residues tryptophan (Trp) and tyrosine (Tyr), which will be described in detail in the following sections.

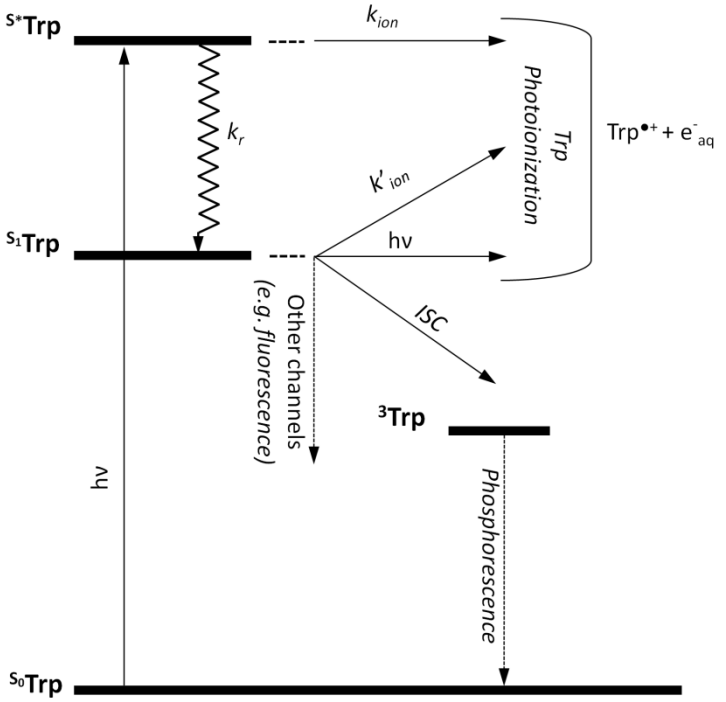

Figure 4. Schematic representation of the various processes triggered upon Trp excitation to higher energy states. Adapted from [69]**.**

Excitation of Trp and Tyr to higher energy states is usually followed by distinct processes which are influenced by the surrounding environment, such as pH, temperature, polarity, and proximity of other side chains (see example for Trp in Figure 4). The main relaxation channels of Trp and Tyr are fluorescence and intersystem crossing to the triplet state. In the absence of quenchers the main channel of triplet state decay is the transition to the ground state by phosphorescence. The fluorescence and phosphorescence of tryptophan and tyrosine have been extensively used for

probing the structure and dynamic processes in proteins. Besides these two main relaxation pathways, Trp and Tyr may undergo excited state photochemical and photophysical processes from the singlet and triplet states (e.g. photoionization, reaction with molecular oxygen to form peroxy radicals).

2.2.1.1 Tryptophan photophysics and photochemistry

The indole side-chain of Trp is the strongest UV absorbing group in proteins. In water, Trp has the highest absorption at 278 nm (ε^{278nm} = 5579 $M^{-1}.cm^{-1}$) and 287 nm (ε^{287nm} = 4594 $M^{-1}.cm^{-1}$) [70] (see Appendix 8.1). Additionally, in proteins Tyr and Phe can also transfer the excited state energy to Trp [71]. Therefore, despite of its low abundance in proteins [68], Trp has a major role in the photo-activated mechanisms of proteins.

The major photophysical and photochemical pathways that lead to Trp photooxidation are described in Figure 5 and are summarized below. Two main non-radiative relaxation channels have been identified upon excitation of Trp to higher energy states and involve Trp photoionization and inter-system crossing to the triplet state ^{3}Trp, respectively [64, 65, 68, 72–74].

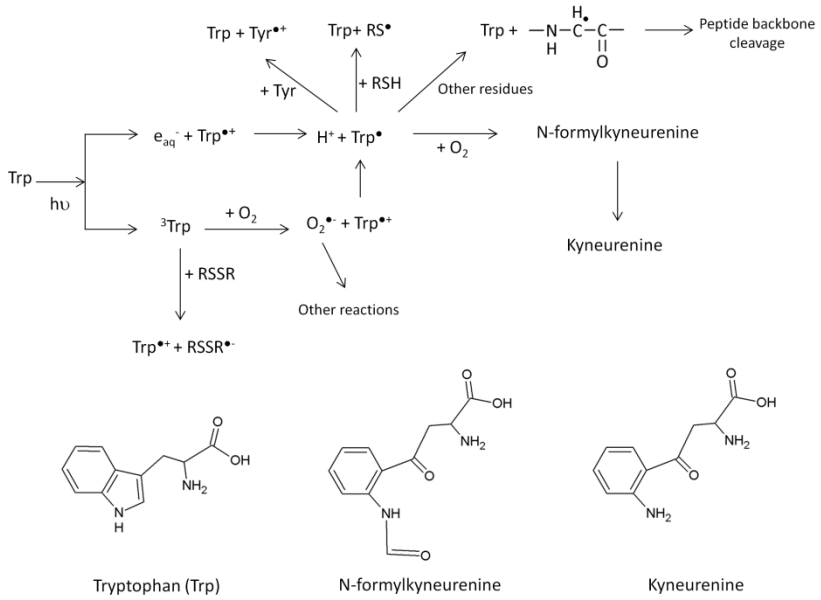

Figure 5. Major photophysical and photochemical pathways of Trp in proteins upon UV excitation and structure of Trp and its most abundant photoproducts. Adapted from [64]**.**

Trp photoionization is a major photoxidation pathway of many proteins [68]. Upon Trp photoionization there is ejection of an electron from the residue, yielding a electron, and a radical cation $Trp^{\bullet+}$, which rapidly deprotonates forming the neutral radical $Trp^{\bullet}$ [72, 74]. The ejected electron may become solvated forming an aqueous electron e_{aq}^- [75, 76] and react with molecular oxygen forming strong reactive oxygen radical $O_2^{\bullet-}$ and with electrophylic species, such as cystines,

as will be described in section 2.2.1.3. The tryptophan neutral radical $Trp^{\bullet}$ can react with Tyr, or with neighboring amino acids, ultimately leading to peptide chain cleavage [64]. One example is the reaction with cystine residues, which will be reviewed in section 2.2.1.3. In the presence of oxygen, $Trp^{\bullet}$ can form Trp based peroxy radicals that can further react yielding N-formylkyneurenine and kyneurenine [64, 68] (chemical structures displayed in Figure 5). These two species also absorb in the UV region, but at higher wavelengths than Trp. They are stronger photosenstitizers than the parent Trp and can generate reactive oxygen species upon UV absorption, eventually leading to further photo-degradation mechanisms [65, 77, 78]. The absorbance and fluorescence properties of N-formylkyneurenine and kyneurenine are described in Appendix 8.1.

Besides photoionization, Trp can undergo intersystem crossing to the triplet state (^3Trp). The resulting triplet states are characterized by much longer lifetimes (μs) than the short lived singlet states, and they are prone to undergo electron transfer and hydrogen abstraction mechanisms, besides solely energy transfer processes [65, 73, 79]. ^3Trp can transfer an electron to a nearby cystine (disulphide bridge) yielding $Trp^{\bullet+}$ and a disulphide electron adduct $RSSR^{\bullet-}$, eventually leading to disulphide bond cleavage [74, 80] (see section 2.2.1.3). Under aerobic conditions the ^3Trp might also react with molecular oxygen to give once more $Trp^{\bullet+}$ and a strong reactive oxygen radical $O_2^{\bullet-}$ [64].

2.2.1.2 Tyrosine photophysics and photochemistry

After tryptophan, tyrosine is the most absorbing protein residue in the near-UV region. At neutral pH (Tyr-OH) absorbs maximally at 275 nm (ε^{275nm} = 1400 $M^{-1}.cm^{-1}$) [79] . At alkaline pH the hydroxyl group of the tyrosine side chain deprotonates (pKa ~ 10.2) [71], resulting in tyrosinate ($Tyr\text{-}O^-$), which has a red-shifted absorption compared to tyrosine, with maximum at 290 nm (ε^{290nm} = 2300 $M^{-1}.cm^{-1}$) [64, 65, 68, 72–74] (see Appendix 8.1).

The non-radiative relaxation pathways that follow Tyr excitation are similar to those described for Trp: relaxation by fluorescence to ground state, triplet state (^3Tyr) formation and relaxation by nonradiative processes. At neutral pH, tyrosine can be photoionized through a biphotonic process that involves absorption of a second photon from the triplet state ^3Tyr [64, 65, 68, 72, 79, 81]. The most important photophysical and photochemical pathways leading to Tyr photo-oxidation are shown in Figure 6 and will be described below.

Photoionization of Tyr-OH from ^3Tyr leads to the formation of a solvated electron e_{aq}^- and a radical cation $Tyr\text{-}OH^{\bullet+}$, which quickly deprotonates [64, 72]. The resulting tyrosyl radical ($Tyr\text{-}O^{\bullet}$) is an important precursor for further photo-oxidation reaction mechanisms [82–84]. One of the most important mechanisms involves the cross-linking of tyrosyl radicals, which can yield dityrosine, isodityrosine (Tyr dimers), trityrosine or pulcherosine (Tyr trimers) [82, 83, 85, 86] (chemical

structures displayed in Figure 6). Typically, the most abundant of these products is dityrosine, which is cross-linked at the C_{ortho}-C_{ortho} positions [82, 83, 87]. Dityrosine cross-linking can occur within the same protein (intramolecular), or between two protein molecules (intermolecular) [82, 83]. Intermolecular dityrosine cross-linking is an important pathway for protein aggregation [88–91]. Like Tyr, dityrosine and some of the other Tyr cross-linking products are also strong absorbing groups in UV region [82, 85, 92, 93]. The formation of dityrosine cross-links in proteins can be easily monitored because dityrosine displays unique fluorescence properties, emitting strongly at 400-409 nm [82]. The absorbance and fluorescence properties of Tyr photo-products are described in Appendix 8.1.

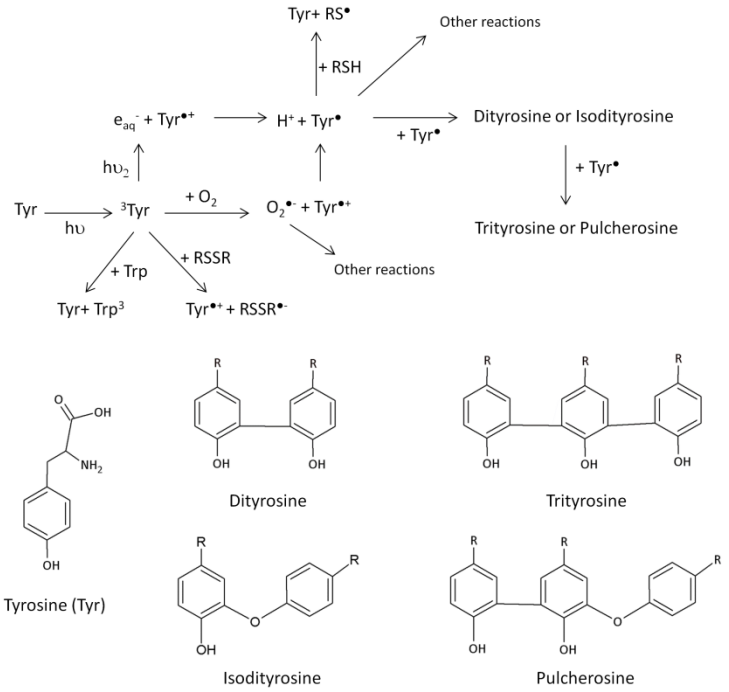

Figure 6. Major photophysical and photochemical pathways of Tyr in proteins upon UV excitation and structure of Tyr and its most abundant photoproducts. Adapted from [64]**.**

Other reactions can occur from the triplet state ^{3}Tyr, including energy transfer to a vicinal Trp to yield Trp^3. Similarly to tryptophan, ^{3}Tyr can also react with cystines (disulphide bonds) to form the disulphide electron adduct $RSSR^{\bullet-}$ (see section 2.2.1.3) and molecular oxygen to yield strong reactive oxygen radical $O_2^{\bullet-}$ [81]. These two reactions are alternative pathways for formation of the dityrosine precursor Tyr-$O^{\bullet}$.

2.2.1.3 UV light mediated disulphide bond disruption

One important photochemical mechanism occurring in proteins upon UV irradiation is the reduction of disulphide bonds. Photolysis of disulphide bonds can occur either directly by absorption of UV light by cystines, or indirectly via electron transfer from the protein aromatic residues (Trp, Tyr and Phe).

UV light absorption by cystines is pH dependent and generally takes place at wavelengths below 300 nm. Nonetheless, it should be taken in consideration that cystine absorption is sensitive to the dihedral bond angles and can be red-shifted to higher wavelengths [64, 94, 95]. The contribution of cystines to protein absorption in the UV range is lower compared to Trp or Tyr absorption. Dimethylsulfide, a linear disulphide compound that is used as model for cystine, absorbs maximally at ~250 nm (ε^{250nm} = 330 $M^{-1}.cm^{-1}$) [95]. Light absorption by cystines followed by disulphide bond disruption can either happen between the R-S, or the S-S bonds, yielding the radicals $RS^{\bullet}$ or $RSS^{\bullet}$, respectively (schemes 1 and 2). These reactive radicals can undergo further reactions with other amino acids and molecular oxygen [64].

$$RSSR \overset{h\upsilon}{\Leftrightarrow} 2RS^{\bullet} \quad (1)$$

$$RSSR \overset{h\upsilon}{\Leftrightarrow} RSS^{\bullet} + R^{\bullet} \quad (2)$$

The other main photochemical route for disulphide bond disruption is mediated upon excitation of the protein aromatic residues (Trp, Tyr and Phe) and involves electron transfer mechanisms that facilitate the formation of the disulphide electron adduct $RSSR^{\bullet-}$. Cystines can capture solvated electrons e_{aq}^- generated upon Trp and Tyr photoionization (scheme 3), or undergo direct electron transfer from ^{3}Trp and ^{3}Tyr triplet states formed upon UV excitation [72, 80, 87] (schemes 4 and 5). Electron capture by cystines results in the formation of $RSSR^{\bullet-}$, which can subsequently cleave to form a thiyl radical ($RS^{\bullet}$) and a deprotonated thiol (RS^-) [72, 74, 80, 81] (scheme 6). Protonation of the disulphide electron adduct can also lead to disulphide bond disruption [80] (scheme 7).

$$e_{aq}^- + RSSR \rightarrow RSSR^{\bullet-} \quad (3)$$

$$^3Trp + RSSR \rightarrow RSSR^{\bullet-} + Trp^{\bullet+} \quad (4)$$

$$^3Tyr + RSSR \rightarrow RSSR^{\bullet-} + Tyr^{\bullet+} \quad (5)$$

$$RSSR^{\bullet-} \Leftrightarrow RS^{\bullet} + RS^- \quad (6)$$

$$RSSR^{\bullet-} + H^+ \Leftrightarrow RS^{\bullet} + RS^- \quad (7)$$

The solvated electrons e_{aq}^- formed upon Trp and Tyr excitation can have a different fate and interact with the peptide chain to form hydroxide ions and ketyl radicals (scheme 8), which can propagate along the peptide chain [74, 81]. If the ketyl radical gets entrapped by a disulfide bridge, it can lead once more to the formation of the disulphide electron adduct $RSSR^{\bullet-}$ and likely disulphide bond cleavage.

$$e_{aq}^- + \text{-CONH-} \rightarrow OH^- + \text{-}\dot{C}(OH)NH\text{-} \quad (8)$$

The thiyl radicals $RS^\bullet$ generated upon disulphide bond disruption can undergo reaction with other amino acids, oxygen, or with a second thiyl radical resulting the reformation of disulphide bond either within a protein or between proteins, leading to aggregation [64].

Reduction of disulphide bridges upon UV excitation of aromatic residues has been shown for several proteins such as lysozyme [2, 6, 96, 97], cutinase [63, 72, 98], somatropin [99], bovine serum albumin [6], alpha lactalbumin [100–102], prostate specific antigen [4] and antibody Fab fragments [3]. In most cases, the breakage of disulphide bridges in the above mentioned proteins led to conformational changes, but did not necessarily result to loss of function or inactivation. Despite the growing number of studies on distinct proteins and the abundant of available information about the impact of UV radiation on amino acids in solutions, in proteins the photochemistry of Trp/Tyr mediated disulphide bond photolysis is not yet fully understood.

Fusarium solani pisi cutinase is one of the best characterized and understood protein models for Trp mediated disulphide bond photolysis. Disulphide bond photolysis in cutinase is associated with an increase in Trp fluorescence quantum yield and protein conformational changes [63, 98]. Cutinase is a good model for studying this UV activated mechanism, as it contains only one tryptophan in van der Waals contact of a disulphide bond (~3.8 Å). Photolysis of this disulphide bond can be directly related with the excitation of the single Trp residue, since the second disulphide bond of cutinase is located on the other side of the protein and remains intact upon UV excitation [98]. Neves Petersen et al. demonstrated that the observed increase in Trp fluorescence quantum yield in cutinase was correlated with Trp-mediated breakage of this disulphide bond [63]. Since disulphide bridges are excellent quenchers of the excited state of aromatic residues, this indicates that the induced disruption could be mediated by direct electron transfer from the excited state Trp. Once disrupted by UV light, the disulphide bridge could no longer quench the Trp residue. Furthermore, Neves Petersen et al. have shown that disulphide bond disruption and associated protein conformational changes (and eventual loss of enzymatic activity) were strongly dependent on the extent of Trp excitation, in particular the power and duration used for UV irradiation [63].

More recently, flash photolysis studies on cutinase have shown the formation of e_{aq}^-, $RSSR^{\bullet-}$, and Trp based radicals and Trp triplet states upon Trp excitation [72], supporting the evidence that disulphide bond photolysis occurs by electron transfer from excited state Trp to the neighboring disulphide bond (schemes 3, 4 and 5). Direct electron transfer mechanisms are known to consist on short range interactions, which decay exponentially as the distance between donor and acceptor increases [103, 104]. Therefore, it is possible to assume that Trp/Tyr mediated photolysis of disulphide bonds depends also on the proximity between the aromatic residues and the disulphide bridges. Since aromatic residues are known to be conserved spatial neighbors of disulphide bonds in proteins (see section 2.1.1.1), this type of electron transfer mechanisms and disulphide bond photolysis is likely to occur in nature.

Due to its small size (22kDa, 213 amino acids) and its ideal Trp-cystine configuration cutinase is still a simple model of UV mediated disulphide bond disruption. For proteins that contain a larger number of aromatic residues and cystines the mechanisms involving disulphide bond photolysis may be more complex. Additionally, there are other factors that can dictate and influence the mechanisms that lead to photolysis of disulphide bonds, such as the experimental conditions (temperature, pH), the presence of other electron acceptors in vicinity of Trp and Tyr side-chains, and the local protein environment [72]. Considering the importance of aromatic amino acid residues and disulphide bonds in the mediation of UV induced mechanisms in proteins, it is essential to obtain key information regarding the packing and their structural features within the protein.

2.2.2 Consequences of UV light exposure to the structural stability of proteins

The mechanisms described in the previous sections illustrate the diversity of structural modifications that can occur in proteins upon exposure to UV light, including photo-degradation and alterations of the resident amino acids, or even cleavage of the peptide chain. These processes can have deleterious consequences on the structural stability and function of proteins, e.g. modification of its physicochemical properties (*e.g.* hydrophobicity and charge), inter-protein cross-linking and protein fragmentation.

Upon prolonged exposure to UV light, some proteins are prone to unfolding and undergo conformational changes (e.g. increased exposure of its hydrophobic residues) [100, 102, 105–107]. These conformational changes often concur with modifications on their scattering and optical rotation properties. It is known that the extent of photo-induced damage depends greatly on the structure and conformation of individual proteins. Within milk proteins, random coil proteins (e.g. casein) are more susceptible to UV induced individual amino-acid damage than tightly-packed globular proteins (e.g. alpha-lactalbumin). In contrast, globular proteins display the most pronounced changes in secondary and tertiary structure under UV exposure. The tertiary structure

of proteins may have a protecting role towards particular residues in globular proteins that are more susceptible to UV induced damage [105].

Photo-induced aggregation of proteins (dimers and higher order aggregates) is another possible effect of UV illumination and has been documented in several proteins [106–108]. As previously discussed, the formation of aggregates can be driven by radical-radical reactions, such as inter-molecular dityrosine cross-linking [89, 91]. Other photo-induced mechanisms can also lead to protein aggregation, such as disulphide bond photolysis [64], or the indirect oxidation of histidine residues in the presence of reactive oxygen species (e.g. formed upon UV excitation) [78, 109, 110].

For several years it has also been acknowledged that the function of enzymes and hormones can altered, or even abolished upon exposure to UV light [63, 64, 111, 112]. Enzymes and hormones, which contain UV sensitive amino-acids such as Trp, Tyr, Cys in their active site(s) are more susceptible to UV inactivation. Furthermore, there might be other mechanisms that lead to the inactivation of these proteins, such as UV induced conformational changes, protein aggregation, or reaction with reactive oxygen species. Disulphide bonds are important for maintaining protein structure and in some proteins they even have a functional role (see section 2.1.1.1). Therefore, photolysis of certain disulphide bridges in proteins can likely lead to loss of function and inactivation, as was verified for cutinase [63].

Considering the deleterious effects that UV light can have on proteins and enzymes, it is of outmost importance to infer and identify which are the UV triggered mechanisms that ultimately lead to protein damage. Modulation of protein structure and function may influence a wide number of biochemical and cellular responses, e.g. cellular signalling, redox mechanism, cell survival and death. Understanding the molecular processes triggered upon UV radiation of proteins is essential for identifying the routes of photo-oxidative damage in human diseases. The major targets for protein photo-oxidation are the tissues regularly exposed to sunlight, such as skin and eyes. Some of the known side-effects of UV exposure in skin (e.g. pigmentation and decreased elasticity) are believed to be due to photo-oxidation of some structural proteins, like collagen or elastin, and to repetitive induction of the inflammatory response [113–116]. These processes may also be involved in the development of skin cancers upon long-term exposure to UV radiation [117]. While DNA damage is without doubt a major factor in development of skin cancer, photo-induced damage of some critical proteins (resulting for example in altered cell signalling, inactivation of DNA repair enzymes, and inhibition of apoptosis) can also play an important role [118].

Understanding the effects of UV light on proteins is also of particular relevance for the safety of food and pharmaceutical products. Thereby, the structural and functional integrity of proteins is crucial in their role as drugs and nutrients. For instance in the pharmaceutical industry, protein

products (e.g. insulin) can be exposed to UV light from natural or artificial light sources during production, formulation, visual inspection, fill and finish operations, packaging, storing and delivery of the drug. Therefore, UV light induced protein damage is likely to occur during the life-cycle of pharmaceutical compounds [64, 119, 120]. Similar issues are likely to occur in the food industry, since food products are prone to photo-induced damage during UV sterilization procedures, which are commonly used in food processing [121].

It is not yet clear which UV activated molecular mechanisms contribute the most for UV light mediated denaturation and inactivation of proteins. These processes depend on several experimental factors, such as the wavelength and power of the exposing radiation, temperature, pH and aeration (presence of molecular oxygen). In order to prevent and control protein photooxidation and to use UV based technologies for technological applications, it is essential to understand these mechanisms.

During this PhD work, two main protein candidates were used to probe the molecular mechanisms triggered upon UV illumination of proteins: bovine alpha-lactalbumin and human insulin. The effects of UV light exposure on the structure and function of these proteins were studied in detail using a wide number of spectroscopy techniques (e.g. fluorescence spectroscopy and circular dichroism spectroscopy) and other biological assays (e.g. binding immunoassays). The three-dimensional structure of these two proteins was analysed using bioinformatic tools, in order to understand the packing of the aromatic residues and disulphide bonds and to identify the most relevant structural features that could be affected upon UV illumination. This work will be described in detail in Chapter 4.

2.2.3 Potential of light based protein therapeutics

The damaging effects of UV and visible radiation on biomolecules are well publicized and the knowledge gathered on the mechanisms involved in these processes can help to prevent and control the impact of protein photo-degradation in disease and technological applications. In parallel, some of the naturally occurring light-induced processes in proteins have been beneficially used for medical and biological applications. Light-responsive biological compounds offer unique possibilities for the control and regulation of biological processes, which require high spatial and temporal specificity. In this context, light represents a unique external control element.

The most notable example of light-based applications is the technique of photodynamic therapy (PDT), which exploits the photo-degradation of proteins for medical treatment. PDT has been established several decades ago, and is still the subject of undergoing research and development [122, 123]. The principle of PDT is to administer a photosensitizing agent (or a precursor) prior to illumination with a light source (e.g. lamp, laser or light emitting diode) in the presence of O_2. Excitation of the photosensitizer results in the formation of singlet oxygen $^1O_2$ and radical species,

and the process can be spatially controlled to induce the photo-degradation of the neighboring proteins and biomolecules [122, 123]. PDT has been is employed for the treatment of a wide number of cancers [122, 124] and a variety of skin disorders, such as psioriasis and acne [122], as well as for photoangioplasty [125] and bacterial inactivation in dentistry [126].

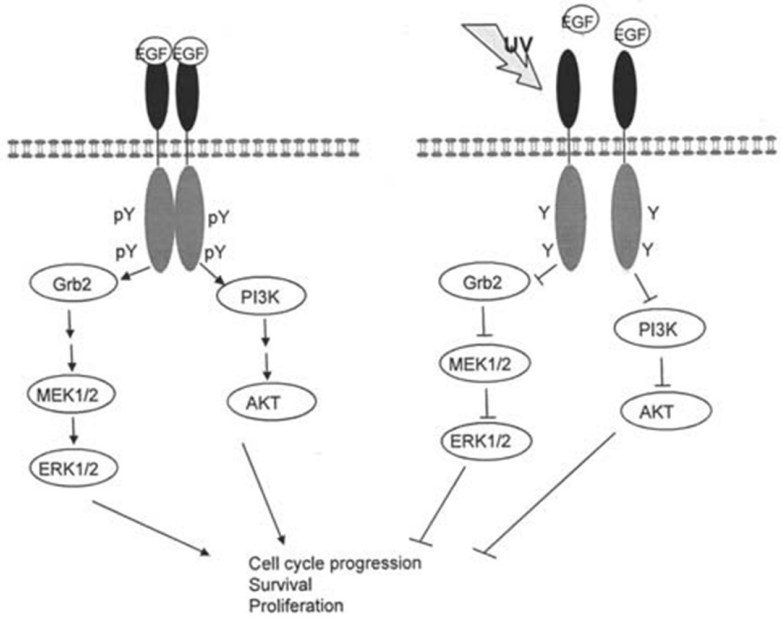

Figure 7. Overview of the cellular pathways affected upon low dose UVB illumination of EGFR. The extracellular domain of EGFR is shown in black and the intracellular receptor kinase domain in gray. Upon UVB illumination the extracellular domain of EGFR may undergo disulphide bond disruption and suffer conformational changes that prevent dimerization and activation of the EGFR signaling pathway, e.g. structural changes in the EGF binding site of EGFR. ***Reprinted from*** [132] ***(Open access).***

Light based molecular switches have also been used to control and regulate the conformation and function of proteins. Most of the undergoing work makes use of photocaging groups, which are photo-labile protecting groups (usually comprised of aromatic rings) [127–129]. Caging groups can be linked to specific amino acid residues in the protein in a way that their native role is inhibited. Upon light irradiation (usually UV light), the caging groups suffer photolytical cleavage and expose the amino acid in its natural form, thus inactivating or activating the protein [128, 129]. Naturally existing photoresponsive proteins have also been employed to control the function of other proteins using light. These systems rely on the fusion of the protein of interest to a photoactive domain, e.g. light-, oxygen- and voltage-sensitive domains. The protein activity can be modulated upon conformational change of the photoactive domain upon light irradiation [128]. Photochemical modulation of protein function can be a powerful tool to control precisely (in space) and timely the activation of a diversity of cellular processes. The photochemical strategies described above have already been applied with success to control important cellular processes, such as protein phosphorilation [130], or to induce protein-protein interactions in living cells *in vitro* [131]. Although most of these techniques require the use of external agents that may involve

photo-activated mechanisms, which are not necessarily found in nature, they do illustrate the potential of photophysical approaches to mediate and control protein function.

This PhD work investigated a photo-induced switch in view of a possible cancer photonic therapy: UV light induced inactivation of epidermal growth factor receptor (EGFR). As previously mentioned, EGFR is a member of the ErbB family of receptor tyrosine kinases and has an important role in regulation of cellular processes such as cell survival, proliferation and migration. EGFR binding to ligands, such as epidermal growth factor (EGF), leads to receptor dimerization and to the activation of the intracellular tyrosine kinase domain (Figure 7, scheme on the left). EGFR overactivation results in cell signaling cascades that promote tumor growth [24–26]. For this reason, the inhibition of EGFR function is a rational treatment approach for cancer and this receptor has been the target of many chemotherapeutical approaches [133].

The NanoBiotechnology group had previously shown that low dose UVB illumination of cancer cells overexpressing EGFR prior to adding EGF halted the EGFR signaling pathway [134] (Figure 7). This suggested that UV light could be used to modulate the inactivation of EGFR and thereby explored as an alternative treatment approach for cancer. This hypothesis is further investigated in this PhD work. The extracellular domain of EGFR (sEGFR), where the EGF binding site is located, is exceedingly rich in disulphide bridges (25 in total). As previously discussed in section 2.1.1.1, large proteins such as sEGFR (621 aa) are observed to have lower fraction of disulphide bridges compared to smaller proteins (becoming more noticeable for proteins comprising <70 aa) (Figure 3). sEGFR has an average disulphide bond fraction of ~4 % compared to the expected ~0.3 % for a protein of its size (600-650 aa) (Figure 3), implying that sEGFR contains ~13 times more disulphide bridges than what is expected for a protein of its length. Furthermore, EGFR contains a considerable number of aromatic residues in close proximity to disulphide bonds, leading to the belief that disulphide bond disruption may be one of main mechanisms triggered upon UVB light excitation. More interestingly, the aromatic residues and disulphide bridges have a critical role at the dimer interface of sEGFR, indicating that the disulphide bond disruption could induce conformational changes that impair EGFR dimerization and thereby cause the attenuation of the EGFR signaling cascade. It is also possible that that UVB-light induces structural changes in the EGF binding site of EGFR that could impair the correct binding to ligands, such as EGF, and thus prevent the dimerization of EGFR (Figure 7).

This work presented in this PhD dissertation aimed at understanding the mechanisms that are involved in the inactivation of sEGFR with UVB-light. For that purpose different spectroscopy techniques (e.g. steady-state and time-resolved fluorescence spectroscopy and circular dichroism spectroscopy) and a binding immuno-assay were used to analyze the UVB-induced conformational changes on sEGFR and its binding site. These experiments were also relevant for identifying the photophysical and photochemical mechanisms that lead to the UV inactivation of the receptor. This work will be described in detail in Chapter 4.

3 Construction of nanoparticle based bioconjugates

Nanoparticles are sub-micron entities composed of inorganic or organic materials, which can be either biodegradable or not [135]. The standing definition of a nanoparticle restricts the term to a material that has all of its three external dimensions at the nanoscale (1-100 nm) [136]. This terminology is inherently related to the unique physicochemical properties that materials exhibit at the nanoscale, such as ultra small size, large surface area to mass ratio, high reactivity, and distinct magnetic and electronic properties [137, 138]. In biotechnology and biomedical applications it is seldom to find particles and particle agglomerates with sizes in the order of a few hundred nanometers which retain the desired characteristics inherent to the nanoscale [139]. In that sense, in this work the term nanoparticle is not always restricted by the upper size limit of 100 nm.

Currently, several types of nanoparticles are being used for biomedical applications, including inorganic and metallic nanoparticles, polymeric nanoparticles, liposomes, nanocrystals, carbon nanotubes, or dendrimers [140]. These nanoparticles can have different shapes and forms, and can be composed of several layers and elements: inorganic, organic, or polymeric [140]. In biomedical applications, nanoparticles are usually used as a nanocarrier, serving to transport and protect functional biomolecules in solution. Different strategies exist to achieve nanoparticle-facilitated transport of biomolecules, which depend on the type of application that follows. Biomolecules can be carried inside the nanoparticles in restricted pockets or vesicles (nanocapsules, e.g. liposomes), can be loaded onto a porous matrix (e.g. polymer, mesopourous silica), or can be attached to the surface of the nanospheres [135, 141–143]. On the other hand, nanoparticles can also be coupled with surfaces and solid supports to build new ordered nanostructures, such as microarrays for electronic, optical, and molecular sensing applications [144].

In this PhD work, superparmagnetic nanoparticles were selected for the development of protein nanocarriers. Their magnetic properties enable to control their movement and position using magnetic field gradients, which makes them easily separable as well as provide transporter capabilities applicable for targeted protein therapeutics. Moreover, since they are superparamagnetic, they can easily be redispersed in solution after the field is removed and thus do not loose their properties due to agglomeration. Magnetic nanoparticles are usually constituted by a metallic magnetic core, surrounded by an inorganic, organic or polymeric coating, which renders the nanoparticles stable and can be served as a support to attach biomolecules [135, 145].

Similarly to the interesting properties that nanoparticles provide compared to their bulk counterparts, ensembles of nanoparticles can display new properties that differ from individual

nanoparticles and bulk samples [146, 147]. Assembling nanoparticles into secondary structures allows not only the combination of their individual properties but also takes advantage of the interactions between neighboring nanoparticles. The emerging interest in ensembles of inorganic nanoparticles has been driven by the ability to explore these collective properties and to use them in functional devices [146, 147]. Herein, the collective properties of secondary nanoparticle clusters were also explored to design functional nanoparticle bioconjugates. During this PhD this approach was used to built superior magnetic nanoparticle nanocarriers upon controlled assembly of several individual superparamagnetic nanoparticles onto colloidal nanoparticle clusters (CNCs). These magnetic CNCs possess a much higher magnetization than individual superparamagnetic nanoparticles, but retain the original superparamagnetic behavior of their building blocks.

Another well-known example of secondary nanoparticle structures that were also applied during this work, is the assembly of gold nanoparticles, which induces near field coupling of surface plasmons between adjacent particles. Through them new optical properties can be obtained, such as the formation of optical hot spots in gaps between coupled gold dimer nanostructures (also called gap antennas). Light excitation of the nanostructures at the surface plasmon resonance frequency generates electromagnetic fields that are strongly enhanced and highly restricted/focused in the hotspot region. The localized near fields can be used to increase the sensitivity of bio-sensors and to control light-activated reactions in the nanosized volumes surrounding the hotspot.

Three different types of nanoparticle constructs were developed during this PhD work and are presented in Figure 8. These nanoparticles constructs were designed to have the necessary features for coupling proteins and to address specific biomolecular applications.

Core-shell gold iron oxide nanoparticles (Fe_3O_4@Au) were developed to test the immobilization of proteins with the light assisted molecular immobilization (LAMI) technique developed by the Nanobiotechnology Group (Figure 8A). These magnetic nanoparticles comprise a superparamagnetic iron oxide core (Fe_3O_4), which provides the magnetic functionality. The Fe_3O_4 core is surrounded with a gold shell, which is a convenient coating for LAMI bioconjugation, since gold has affinity towards biomolecules with thiol terminal groups.

Magnetic colloidal nanoparticle clusters (CNCs, Fe_3O_4@PAA), were engineered to use as superior magnetic nanocarriers for biomedical applications (Figure 8B). These magnetic CNCs consist of a core, comprised by several individual superparamagnetic iron oxide nanoparticles (SPIONs, Fe_3O_4), capped by a layer of polyacrylic acid (PAA) that provides functional carboxylic groups to attach proteins and other biomolecules. The presence of several iron oxide nanoparticles in the core provides high magnetization and enhances the response of magnetic nanoparticles to external magnetic fields (when compared with constructs with a single superparamagnetic core).

The last nanostructure consisted on arrays of gold gap-antennas on glass to immobilize proteins with the LAMI technique by three-photon excitation of protein aromatic residues (Figure 8C). The dimensions of the identical gold cylinders and of the nm-sized gap were tuned in order to achieve a plasmon resonance of 800 nm. This resonance wavelength enabled three-photon excitation of tryptophan and tyrosine upon laser-illumination at 810 nm, thus initiating the LAMI process. Protein immobilization was confined to gold surfaces within the hotspot region (~20 nm), where the electromagnetic field is localized.

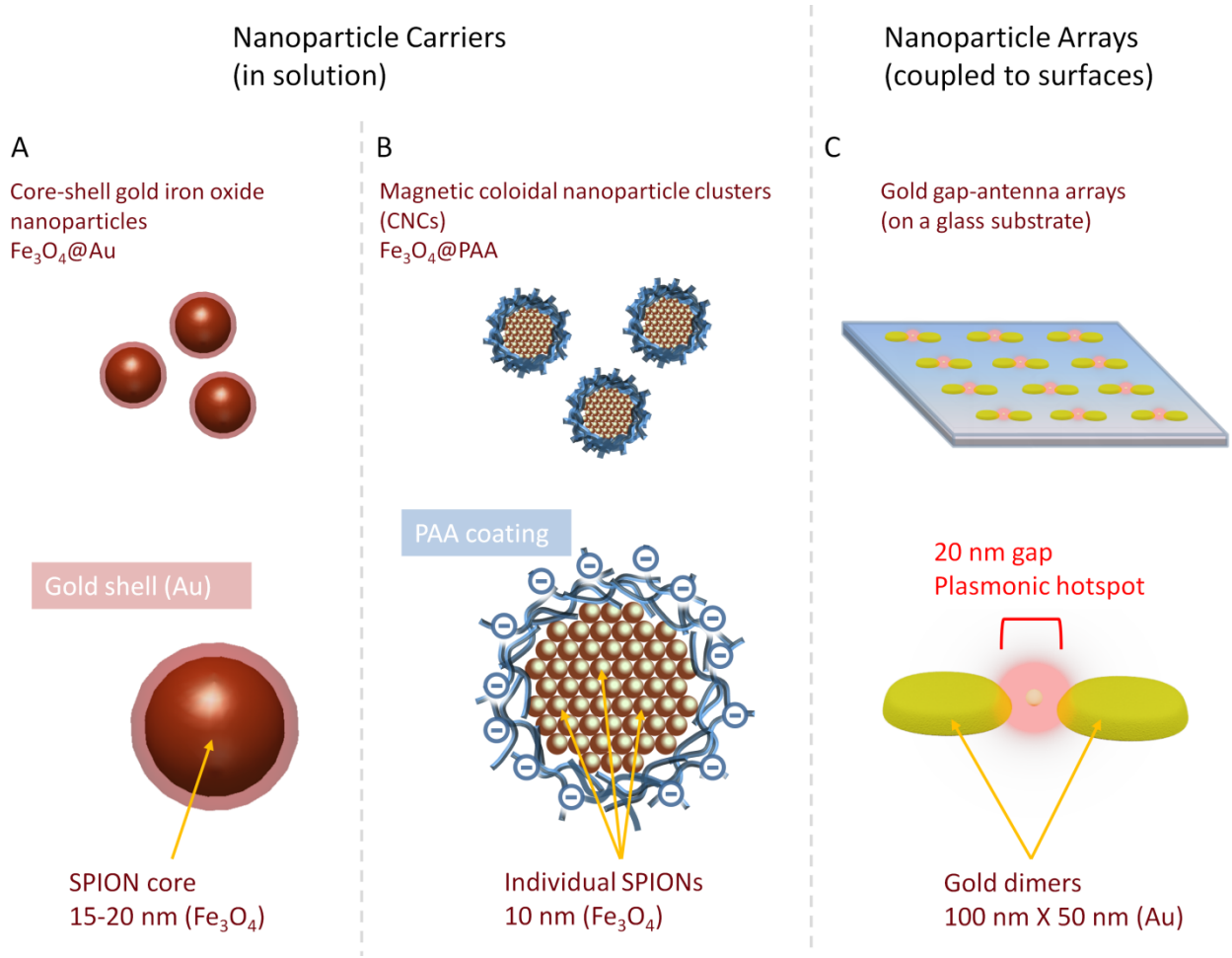

Figure 8. Schematic representation of nanoparticle constructs developed during the PhD work.

In this chapter the characteristics and physicochemical properties of nanoparticles and nanoparticle nanostructures will be described, with particular emphasis on the nanomaterials that were used in this work (magnetic and gold nanoparticles), as well as their current application in biomedicine and other biological sciences. The design and construction process of nanoparticle bioconjugates will also be reviewed, focusing on the synthesis and the bioconjugation techniques that were developed and applied during this PhD work.

3.1 Nanoparticles and nanostructures in biomedicine

3.1.1 Characteristics of nanoparticles and their use in biomedical applications

The size-dependent optical, electrical, and magnetic properties of nanoparticles render these systems promising candidates for biological and biomedical applications. Nanoparticle bioconjugates emerge as interesting constructs for *in vivo* imaging, bio-sensing, therapeutics, and cell targeting, among others.

Due to their size, nanoparticles are optimal vectors to protect and carry therapeutical molecules such as proteins, enzymes and specific polypeptides. The use of nanoparticles as protein carriers present numerous advantages for therapeutics: it improves the solubility of poorly water soluble proteins, prolongs the half-life of drug systemic circulation by reducing immunogenicity, and nanoparticles can be used to deliver drugs in a targeted manner reducing systemic side-effects [135, 137]. Reversibly, some proteins can also be used as active ligands to help functional nanoparticles to reach particular sites in the body (e.g. cell labeling), or target cancer cells and pathogens, such as bacteria [148–150]. Albumin, monoclonal antibodies, growth factors, transferrins, and cytokines are some examples of proteins that have been used to target and guide nanoparticles loaded with chemotherapeutic or other drugs [138, 149].

The use of nanoparticles as platforms to immobilize proteins has also other practical advantages. By immobilizing proteins such as enzymes onto the surface of nanoparticles it is possible to increase their pH and thermal stability, thus optimize their activity and specificity [151]. For example, immobilization of trypsin and putative feruloyl esterase onto superparamagnatic nanoparticles has led to higher activity than the corresponding free enzyme in solution with the same concentration [152, 153]. Enzyme glucose oxidase was found to be more thermally stable when bound to gold nanoparticles than free in solution [154].

By coupling active biomolecules like proteins and enzymes to nanoparticles, it is possible to benefit from the inherent characteristics of the nanomaterials and to implement additional biological functions to nanoconstructs, making them suitable to interact with other biomolecules and biological systems.

3.1.1.1 Superparamagnetic iron oxide nanoparticles (SPIONs)

Among magnetic nanoparticles, superparamagnetic iron oxide nanoparticles (SPIONs, e.g. magnetite, Fe_3O_4, or maghemite, γFe_2O_3) are a convenient choice to develop biomedical nanoconstructs, due to their unique characteristics. This class of magnetic nanoparticles is usually preferred due to their low toxicity profile [135, 145]. SPIONs are the only class of magnetic nanoparticles that have been approved for clinical use (for medical imaging and therapeutical

applications) [145] Their reactive surface can be easily derivatized with biocompatible coatings, targeting, therapeutic and imaging molecules [145, 155]. Due to their small size (10-20 nm), SPIONs are superparamagnetic and therefore it is possible to control these nanoparticles using magnetic fields without the risk of agglomeration as they retain no residual magnetism after the field is removed [135, 155]. Furthermore, their intrinsic magnetic properties make them good contrast agents for magnetic resonance imaging (MRI). In most cases, SPIONs are employed for signal reduction on T2-weighted images (negative contrast) [156, 157]. SPIONs can also be used as hyperthermia agents, as they can be selectively heated by applying a high frequency magnetic field [135]. This property has been used to target and kill selective cells, by heating up the tissues containing the magnetic nanoparticles to 43-45 °C [156, 157].

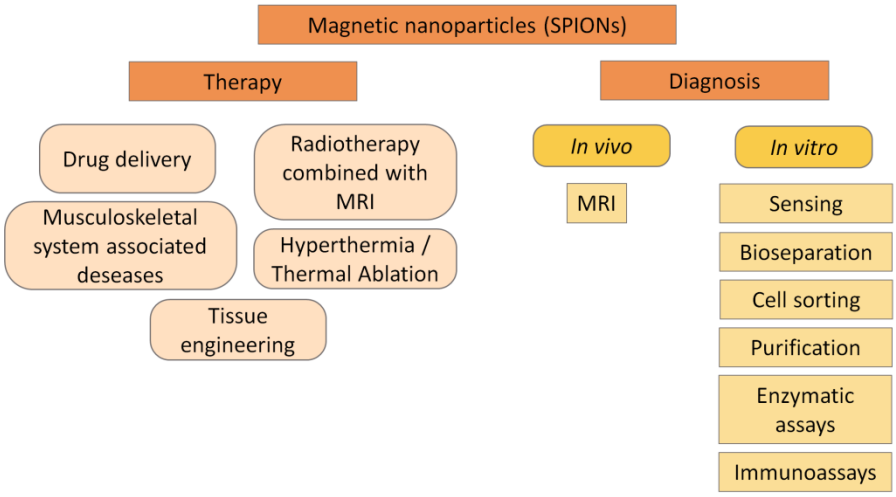

Figure 9. Biomedical applications of SPIONs. Adapted from [135]**.**

Due to these flexible properties, SPIONs have been used for a wide number of *in vivo* and *in vitro* biomedical applications (Figure 9). Their magnetic properties have been exploited in medicine to detect and target disease and for tissue engineering. Their magnetism has also been used to develop *in vitro* magnetic separation assays.

Magnetic nanoparticles are a promising platform to develop drug delivery vehicles. Ideally, external magnetic fields or internal magnetic implants can be used to drive and target magnetic nanoparticle bioconjugates to specific tissues and cells and thereby deliver or concentrate therapeutical molecules (e.g. proteins, enzymes and specific polypeptides) [135, 158, 159]. Currently, the practical use of magnetic drug delivery is mainly applicable to well-defined tumors, and using small molecule drugs. For instance 100 nm SPIONs derivatized with epirubicin (small molecule drug used for chemotherapy) have been used with success in mice to induce the regression of targeted solid tumors [160], and have been also tested in human clinical trials [161]. Much effort has still to be done in the field of magnetic drug delivery, mostly because it depends on several factors, such as the concentration and amount of particles, strength and geometry of

the magnetic field, and the vascular support of the targeted tissues [135, 158], as will be described in section 3.1.2.

Magnetic nanoparticles can also be targeted and located to tumoral regions by coupling active ligands (e.g. monoclonal antibodies) to their surface. Using this approach it is possible to use their properties for imaging and diagnosis (e.g. MRI) and for treatment (e.g. thermal ablation of tumors by hyperthermia) [156, 158, 162].

Protein functionalized SPIONs have proven to be very useful tools for magnetic separation techniques both in clinics and in industry and they have replaced other separation technologies [158, 159]. By using SPIONs coupled with antibodies it is easy to isolate and detect microorganisms in medical and clinical diagnostics. The interaction of antigens and antibodies is routinely used in biosensing to measure concentrations of biological markers [158]. Moreover, it is a practical approach to isolate relevant proteins and peptides (e.g. receptor proteins) from cell lysates [159] or to remove toxic compounds from biological fluids [150]. These techniques are more practical and easier than traditional separation techniques that usually require several steps (antibody/antigens immobilized onto solid phases on filters, tubular structures, plastic spheres or plates) and dispense the use of expensive liquid chromatography [158, 159].

3.1.1.2 Gold nanoparticles

Gold is an interesting material to use for nanoparticles construction/engineering and other nanostructures for biomedical applications. This is mostly due to the surface chemistry properties that gold provides, such as inertness and nontoxic nature towards cells, which makes it a good candidate for *in vitro* and *in vivo* applications [163–165]. The low toxicity of gold nanostructures has been shown in a number of studies and gold nanoparticles of sizes above 5 nm are considered to be safe and biocompatible [165]. Despite being non-reactive in most situations, gold has affinity towards amine, thiol and carboxylic terminal groups, which allows functionalization with biomolecules [141, 166]. Specifically, gold is known to form strong and stable covalent gold–thiolate bonds (Au–S, ~50 kcal/mol) to molecules with thiol (SH) groups [164, 167, 168].

In the nanoscale gold structures display interesting optical and electrical properties. Gold nanostructures are known for their localized surface plasmon resonance (LSPR), an optical phenomenon that occurs upon interaction between an electromagnetic wave and the conduction electrons in a metal. Upon irradiation with light of an appropriate wavelength, the delocalized conduction electrons of a gold nanostructure start to oscillate collectively relative to the lattice of positive nuclei at the frequency of the incoming light. At this resonant frequency, the incident light is absorbed by the nanostructure and part of the photons are scattered with the same frequency in all directions. The light is absorbed by the gold nanostructure as phonons and the vibrations of the lattice are typically observed as heat. The extinction of a LSPR is the sum of the absorption and

scattering components. Additionally, LSPR produces strong electrical near fields in the vicinity of the particle's surface [164, 165, 169].

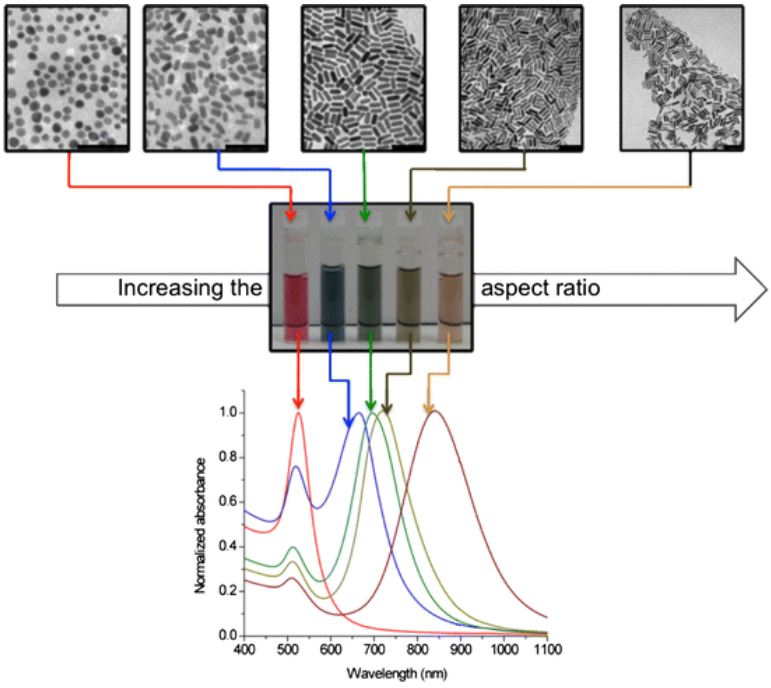

Figure 10. Gold nanospheres and nanorods of different aspect ratios display distinct colors in solution and tunable ultraviolet, visible and near infrared spectra. The scale bars in the transmission electron microscopy images at the top panels represent 100 nm. ***Reprinted with permission from*** [165]***. Copyright © 2010 SpringerLink.***

The specific properties of the LSPR response and the optimal resonance wavelength depend on the size, shape and morphology of the gold nanostructures (e.g. nanospheres, nanorods, nanodisks) and the dielectric environment [163, 165, 169, 170]. In the case of spherical nanoparticles with sizes up to 50 nm a single plasmon band is observed at ~ 520 nm, which is responsible for the ruby red colour displayed by conventional gold nanospheres (see Figure 10). This peak is red-shifted and becomes broader with the increase of particle diameter to 100 nm [169]. If the nanoparticles have an anisoptropic shape (e.g. a rod) two plasmon bands occur due to the electron oscillation along the two axes: The transverse plasmon gold band occurs at 520 nm (short axis) and the longitudinal plasmon band. The latter is located at higher wavelengths and depends on the aspect ratio (length to width ratio) of the nanoparticles (Figure 10). Thus the wavelength of the longitudinal LSPR band can be tuned by controlling the dimensions of gold nanorods. The controlled design of gold nanostructures allows obtaining LSPR responses in a considerable range of wavelengths in the near-infrared region (800-1200 nm) [163, 165, 169, 170].

All three interactions generated by LPSR (absorption, scattering, and electrical near field) can be tuned to be used for biomedical applications [169, 170]. For these applications it is beneficial to operate in the near-infrared region because it is a transparent window for blood and other types of biological samples and the background fluorescence is low and few chromophores absorb [165,

169]. As near infrared light can penetrate deep into tissues, gold nanorods and other gold anisotropic nanoparticles can be applied for *in vivo* biomedical imaging, relying on its strong absorption and light scattering properties [164, 165]. The heat generated by LSPR absorption has been exploited to develop new medical therapies, such as photo-thermal ablation of tumors or photo-sensitive drug delivery [165, 166, 169].

Moreover, gold nanostructures are also extremely interesting for the development of molecular sensors. Binding of chemical or biological analytes (e.g. proteins, enzymes, antigens, antibodies and microorganisms) to gold surfaces can lead to changes in the local refractive index or aggregation state of gold nanoparticles, resulting in a red-shift of the LPSR band. Thus, it is possible to detect the presence of these analytes by monitoring the output LSPR resonance frequency [148, 165, 171]. Gold nanoparticles are also convenient labels for biosensors as they can be detected by numerous techniques, due to their high optical extinction and electrical conductivity [164, 172]. These methods can be carried out in solution or can also involve the binding of the gold nanoparticles to a physical support (e.g. an array), leading to a change in a property, e.g. conductivity of the support, electrical signal [148].

Another method for modulating the optical plasmonic response of gold nanostructures is to assemble gold nanoparticles into secondary structures. [147, 173, 174]. A relevant example is the coupling of nearby gold nanostructures on flat surfaces (e.g. metal films) to generate local optical hotspots [173]. In optically coupled gold nanostructures, such as bold tie gold antennas, nanorod dimers and disk pairs, it is possible to localize the plasmonic near field to local hotspots in the nm-sized gap between nanostructures [175, 176] The electromagnetic fields generated by plasmon resonance are strongly enhanced so that light and energy can be confined in the sub-wavelength gap [176–178]. LSPR confinement to such small regions is useful to improve the sensitivity of LSPR sensing. It enables to probe local changes in refractive index induced by the presence of few or single molecules and other nano-objects on the hotspot location [177, 179, 180]. The highly focused electromagnetic field (sub-diffraction limited volume) can also be used as a nanolight source to control light induced mechanisms at the nanoscale: e.g. to enable multi-photon absorption of other molecules at the hotspot location [181], or to enhance of the excitation and emission of quantum emitters [182, 183].

3.1.1.3 Core-shell nanoparticles

As depicted before, the physicochemical properties of individual metallic nanoparticles (iron oxide, gold) can be precisely tuned by adjusting their size and shape. By combining two distinct nanomaterials into a unique modular nanoconstruct like a core-shell nanoparticle, it is also possible to exploit their collective magnetic, optical, electrical, and catalytical characteristics. Among core-shell nanoparticles, magnetite gold coated nanoparticles (Fe_3O_4@Au, Figure 8A) are of particular interest for the protection, stability, and functionality that a gold coating offers to the

iron oxide core (see previous section). Furthermore, by covering the surface of magnetic nanoparticles with gold, it is also possible to tune the magnetic nanoparticles to absorb light in the near infrared region, which is highly desired for applications that rely on light absorption, such as medical imaging and therapy [184]. While the gold shell enables distinct optical properties, the magnetic iron oxide core presents the potential for noninvasive MRI imaging, hyperthermia therapeutics, and magnetic drug targeting. Hence, by combining the magnetic functions of the iron oxide core and the optical properties of the gold-shell the resultant multifunctional platform can potentially find applications in multimodal imaging and therapeutic combinations, such as drug delivery and photothermal therapy and image-guided, minimally invasive interventions[184–186].

3.1.2 Design considerations and requirements for biomedical applications

During the engineering process of nanoparticle bioconjugates, there are several design parameters that need to be considered and optimized in relation to its applicability in biomedical applications. For instance, most of the biomedical and biological applications require that engineered nanoparticles are dispersible and chemically stable in aqueous solutions. These design considerations are mostly relevant in applications where the nanoparticles are exploited as colloidal carriers in solution, such as the magnetic nanoparticle carriers that were developed in this work (core-shell Fe3O4@Au and the CNCs Fe3O4@PAA). Therefore I will not extend these design considerations for nanoparticles immobilized onto solid supports or flat surfaces (e.g. the gold gap-antennas used in this PhD work).

Several physicochemical parameters dictate the behavior of nanoparticles in solution, including its morphology, hydrodynamic size, physicochemical stability, surface properties (charge, hydrophobicity, etc) and magnetic properties (magnetic moment, remanence, coercitivity) [135, 145, 187]. Nanoparticle functionalization with proteins will also change its physicochemical properties (e.g. surface charge) and has to be taken in consideration.

Among these various aspects, nanoparticle size is a critical parameter to control during the engineering of nanoparticle bioconjugates. It is desirable that nanoparticles retain a large surface area for coupling of biomolecules. Moreover, control of monodisperse nanoparticle size is also very important because the properties of the nanocrystals (such as the magnetic properties as we will see below) depend strongly on their dimensions [159].

In that sense, the dispersibility and colloidal stability of magnetic nanoparticles in aqueous solutions is of major importance when developing magnetic nanocarriers. Bare iron oxide nanoparticles (single iron oxide core) are stable at high and low pH aqueous solutions, but not at intermediate pH values, or at physiological pH, which is required in many biomedical and biological applications [145]. SPIONs have a large surface to area volume and possess high surface

energies and thus tend to aggregate in neutral aqueous solutions [188]. Naked iron oxide nanoparticles have also high chemical activity and can be easily oxidized in air, resulting in decrease of magnetism and dispersibility [188, 189]. To overcome nanoparticle agglomeration and to properly disperse and protect SPIONs in neutral aqueous solutions it is required to coat their surface with an inorganic layer (e.g. silica, carbon, precious metals), surfactants, or polymers [159, 189]. Surface coating of SPIONs has also an additional function that is to provide chemical handles (chemical function groups) for conjugation of biomolecules [145]

Gold is a highly adequate inorganic coating both for improving the stability of SPIONs (and other nanoparticles) in aqueous dispersions and implementing functionality [159]. The outer gold shell improves the mechanical stability of SPIONs and can act as a barrier that protects the magnetic core from oxidation and enzymatic degradation [150, 190]. The gold surface provides also the possibility to couple SPIONS to biomolecules and other chemical agents [186, 191]. Surfactants and polymers can be used to passivate the nanoparticle surface and avoid agglomeration by electrostatic and steric repulsion. Depending on its chemical and physical properties, each surfactant or polymer has a preferable adsorption to particle surfaces. For instance, thiol functional group molecules adsorb strongly to gold and silver, while carboxylic functional groups agents bond to aluminium and iron oxide [192]. Polyacrylic acid is an aqueous soluble polymer with a high density of reactive functional carboxylic groups. It is an attractive coating for SPIONs because of the strong coordination of carboxylate groups with iron cations [192, 193]. The polyacrylic acid acts as a surfactant, as the extent of uncoordinated carboxylate groups on the polymer chain confer these nanoparticles a high degree of dispersibility in water solutions [193]. The carboxylate groups also provide anchoring points for covalent attachment of biomolecules [194, 195].

The performance of the nanoparticles should be extended to the different media and biological fluids that the nanocarrier will encounter. For instance, the design of nanoparticle carriers for *in vivo* applications (e.g. diagnosis, targeted therapy, drug delivery) has to consider the vasculature, the anatomic features and the biological barriers of the human body. For example, magnetic nanoparticles constructs (e.g. MRI contrast agents) are usually designed for intravenous administration. Since blood is a high ionic strength heterogenous solution, it can induce nanoparticle aggregation, influencing its magnetic properties and leading to its sequestration [145]. While in the bloodstream, nanoparticles can also interact non-specifically with plasma proteins (opsonization), and thus trigger a response from the adaptative immune system, extracellular matrices, and non-targeted cell surfaces [140, 142, 145, 196].

Tuning the size of the nanoparticle constructs is also a major concern for *in vivo* applications. The size of the nanoparticles influences their fate in the body and their distribution. The smallest capillaries in the body are ~5-6 μm and it is imperative that the hydrodynamic size of the nanoparticles is significantly lower than this limit, and that they do not form μm-sized

agglomerates, that can obstruct blood vessels and cause an embolism [142]. Small nanoparticles (< 20 nm) are characterized by higher diffusion rates, which leads to an increase of the concentration at the center of the blood vessels and limits the interactions with endothelial cells, leading to longer circulatory residence times [140, 145]. Small nanoparticles are usually excreted renally [145]. Larger nanoparticles (150-300 nm) are more easily recognized by the reticuloendothelial system and by phagocytes, and are cleared through the liver and spleen [145]. In order to target particular tissues or organs, nanocarrier drug delivery systems usually require the engineering of nanoparticles with sizes in the range 30-100 nm [140]. These size limits ensure that the nanoparticles are large enough to avoid leaking into capillaries and small enough to avoid clearance by the reticuloendothelial system.

The development and optimization of magnetic nanoparticle carriers for biomedical application also requires a careful design of its magnetic properties. Magnetic nanoparticles must be endowed with the specific characteristics required for their practical in biomedical applications.

One usual pre-requisite of magnetic nanoparticle carriers is their superparamagnetism. As previously mentioned, in biomedical applications superparamagnetism is necessary to avoid nanoparticle agglomeration in the presence of magnetic fields. This is particularly relevant for *in vivo* applications, where nanoparticle agglomeration could lead to embolization of blood vessels as well as for *in vitro* magnetic separation procedures, where the proper recovery of the magnetic nanoparticles is desired upon removal of the magnetic field [135]. Superparamagnetism occurs in magnetic materials constituted of very small crystallites. The size threshold depends on the nature of the material. Iron oxide nanoparticles (magnetite) show superparamagnetism at sizes < 26 nm. Below this critical size, each nanoparticle becomes a single magnetic domain and exhibits superparamagnetic behavior when the temperature is above the blocking temperature. These individual nanoparticles have a large constant magnetic moment, perform as a paramagnetic atom with fast response to applied magnetic fields and they are characterized by negligible remanence (residual magnetism) and coercitivity (field required to bring the magnetization to zero) [150, 189].

Another key feature for magnetic nanoparticle carriers is their magnetic response to external magnetic fields. It is desired that the final nanocarrier construct has high magnetization so that it can be practically used in biomedical applications. For instance in magnetic drug delivery applications it is required that the magnetization of the nanoparticles is strong enough in order to withstand the drag of the blood flow, and keep the nanoparticles in proximity of the target [135]. The magnetic properties of magnetic nanoparticles are dictated by the composition, size and shape of their magnetic core [145, 197]. However, the magnetic behavior of nanoparticles is also sensitive to the environment, including interparticle interations, temperature and applied magnetic fields [198]. The nature of the coating will also influence the magnetic properties of the nanoparticles [189].

A usual limitation in developing magnetic nanoparticle carriers is related to the small size required for superparamagnetism, which implies a magnetic response of reduced strength, making it difficult to control the movement of nanoparticles by moderate magnetic fields [135, 193]. This restricts their usage in practical applications such as targeted magnetic delivery or magnetic separation (which takes longer time periods). One way of obtaining increased magnetic responses without compromising superparamagnetism is to assemble several SPIONs into a single magnetic nanocarrier. This approach, that was mentioned earlier, relies on the controlled agglomeration of individual SPIONs to form secondary CNCs. In these clusters, the magnetic interactions among crystallites are sufficiently disturbed. The result is that the individual constituent SPIONs are still single domains and that the superparamagnetic-ferromagnetic transition is suppressed [147].

3.2 Engineering of nanoparticle bioconjugates

The construction of nanoparticle bioconjugates is usually carried out in distinct steps/procedures that have to be taken into consideration during the overall design of the nanoparticle bioconjugates (Figure 11).

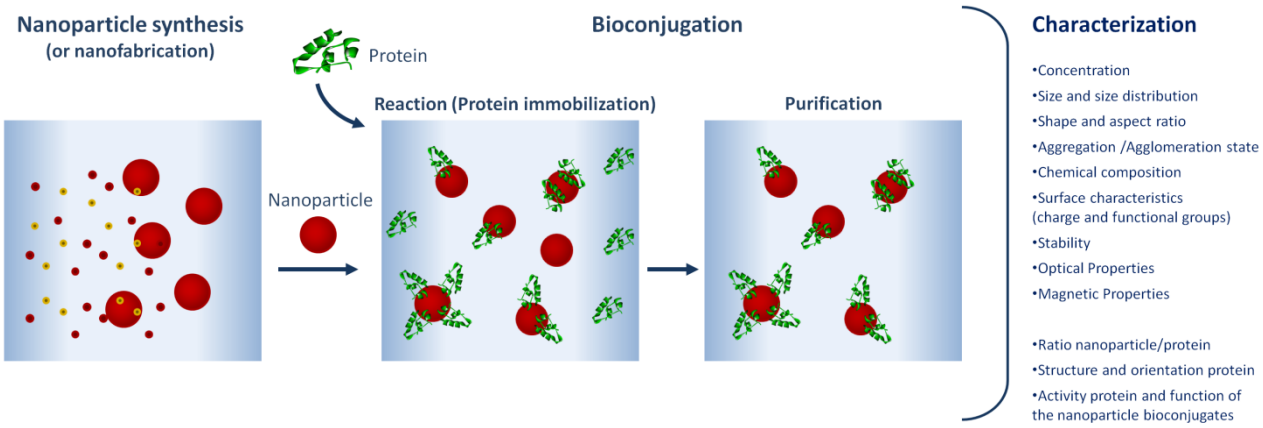

Figure 11. The distinct steps/procedures required for the engineering of nanoparticle bioconjugates.

The first step usually involves the synthesis, or nanofabrication of the nanoparticles (e.g. for magnetic nanoparticles the synthesis of the iron oxide core). Within this step it might be required to coat the nanoparticle surface for protection of the core, and to activate the surface groups for subsequent biofunctionalization. The second step is the bioconjugation procedure, which is carried out upon protein immobilization onto the nanoparticle surface. In some cases it is then required to separate the functionalized nanoparticles from the free proteins and non-functionalized nanoparticles.

An essential part of the engineering process of nanoparticle bioconjugates is the characterization procedure, which is used to verify if the nanoconstruct and its parts fit the design expectations. The main goals of the characterization procedure are to verify the physicochemical characteristics

of the nanoparticles and the confirm the presence of the protein molecules after bioconjugation. Thorough characterization of the nanoparticle bioconjugates should be done along the different steps of the engineering process of the nanocontructs. A short description of some techniques used to characterize nanoparticle bioconjugates during this PhD work can be found in Appendix 8.2. Therein, the operating principle of these methods is described, as well as their potential to characterize nanoparticle bioconjugates and the challenges that are associated to their analysis.

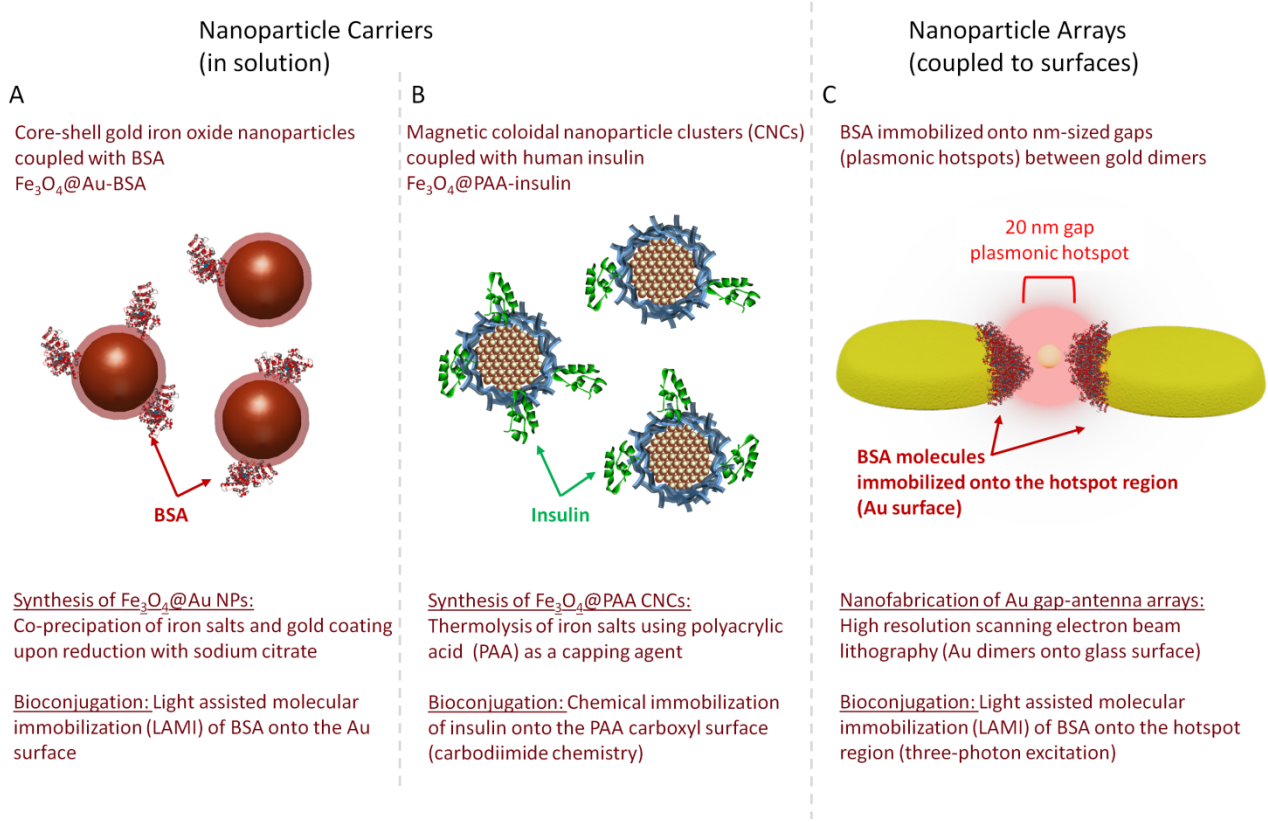

Figure 12. Schematic representation of the three types of nanoparticle bioconjugates developed during the PhD work and description of the synthesis/nanofabrication and bioconjugation techniques that were used.

The three types of nanoparticle bioconjugates developed during this PhD work and the synthesis/nanofabrication and bioconjugation techniques used for their construction are summarized in Figure 12. Fe_3O_4@Au nanoparticles were derivatized with BSA molecules using the light assisted molecular immobilization (LAMI) technique (Figure 12A). Magnetic colloidal nanoparticle clusters (CNCs, Fe_3O_4@PAA) were coupled to insulin using carbodiimide chemistry. (Figure 12B). BSA was immobilized onto the nm-size gaps of Au gap-antennas (Figure 12C) using a modified protocol for the LAMI technique where the aromatic residues of the proteins undergo three-photon excitation.

In the following sections, the techniques used to construct and engineer nanoparticle bioconjugates will be reviewed, with particular attention to the three nanoparticle constructs that were described above.

3.2.1 Engineering nanoparticles and nanostructures

3.2.1.1 General methods for preparing nanoparticles and nanoparticle structures

There are two basic approaches for the preparation and assembly of nanoparticles like the metallic nanoparticles used in this work: “top down” and “bottom up” [199, 200]. The top-down approach relies on micromachining materials down to the desired size and patterns and is generally subtractive in nature [200]. On the other hand, in the bottom-up approach the structure is built up from small constituents (atoms, molecules, clusters, the building blocks) up to a final structure [199, 201]. The bottom-up approach relies on the energetics of the assembly process to direct the formation of the pretailored architecture [200].

Typical examples of top-down approaches include mechanical machining/polishing, lithography, laser beam and electron beam processing and electrochemical removal (etching) [200]. With the development and advances of lithography processes (photo-lithography, X-ray lithography, high resolution e-beam lithography, near-field optical lithography, and multi-photon optical lithography) it is now possible to obtain minute structures with sizes and features down to 20 nm and below [202–204]. These techniques are ideal to construct patterns and nanostructures with high resolution and throughput on a wafer from a master. One example is nanosphere lithography, which is a cheap and extensively used process to fabricate large arrays of LSPR sensors (e.g. gold nanoparticle arrays). High resolution scanning electron beam lithography can be exploited to fabricate versatile arrays of gold, or other metallic nanostructures of different shapes while retaining a high reproducibility [180]. This approach was exploited to fabricate the gold gap-antenna arrays that are presented in this PhD work (Figure 13). After depositing a gold film on a substrate, e-beam lithography combined with reactive ion etching was used to fabricate the periodic arrays of gold dimers on glass, with gaps between dimers down to a few nanometers. Figure 13B shows a scanning electron microscopy (SEM) image of a 5X5 array of gold dimers obtained by this technique, where it is possible to clearly distinguish the nm-sized gaps between the gold dimers.

Mechanical attrition and milling (e.g. ball milling) are other typical top-down processes that have been used for the production of nanoparticles and involve the fracturing of larger coarse-grained materials to form individual nanoparticles [199, 205]. Attrition can produce fine nanoparticles in a size range of tens to several hundred nanometers. However, nanoparticles produced by attrition

have a broad size distribution and heterogeneous shapes or geometries. Furthermore, the milling process can introduce impurities and generate defects on the crystal structures [205].

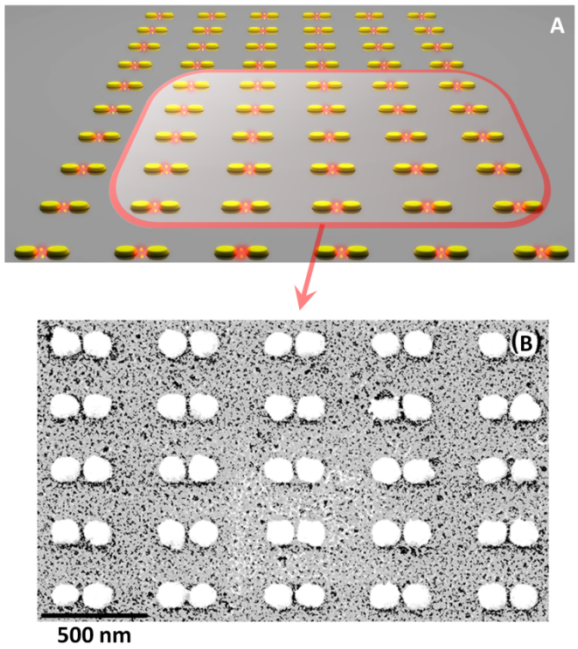

Figure 13. Gold gap-antenna arrays used in this PhD work for 3-photon immobilization of BSA with LAMI. The gold dimers arrays were fabricated by high resolution scanning electron beam lithography. The SEM image of a 5X5 array of gold dimers clearly shows the nm-sized gaps between the cylinders.

Bottom-up approaches are widely preferred for the production of nanoparticles, as they generate nanostructures with less defects, and with uniform chemical composition and size. There are several bottom-up methods to produce nanoparticles, which include synthesis in liquid and gas phases, or by solid state reactions [200, 205]. Solution chemical synthesis routes frequently constitute the most indicate methods for nanoparticle production, due to the enhanced homogeneity from the molecular level and the cost effective bulk quantity production [198]. The preparation of nanoparticles by chemical synthesis in solution is also highly convenient for use in biomedical and biological applications since surface modification of the particles is easily accomplished during or after synthesis [198]. Chemical synthesis also allows a facile control of particle size and size distribution, morphology and agglomerate size by manipulating the reaction parameters, such as temperature, pH, concentration of the reagents, or order of addition of the reagents [198].

In the remainder of this section I will focus on the chemical solution methods used for production of magnetic nanoparticle carriers, in particular the SPIONs nanoconstructs (Figure 12) that were assembled in this PhD work.

3.2.1.2 Chemical synthesis of superparamagnetic iron oxide nanoparticles

Synthesis of the iron oxide core

The first part of the engineering process of superparamagnetic iron oxide nanoparticles typically involves the fabrication of the iron oxide core, which is usually composed of magnetite (Fe_3O_4). There are several solution methods to prepare individual magnetite (Fe_3O_4) nanoparticles including co-precipitation of iron salts, microemulsion methods, thermolysis (thermal decomposition), hydrothermal and solvothermal synthesis, sol-gel and polyol synthesis [145, 155, 159, 188, 192]. Two of these methods will be described in detail as they were used to synthesize the magnetic nanoparticle carriers described in this work: the co-precipitation of iron salts and thermolysis techniques.

The co-precipitation of iron salts is the most common and simple chemical preparation method to obtain magnetite (Fe_3O_4) nanoparticles. It is a cost effective and a convenient method: the reaction is fast (less than one hour), can be carried out at low temperatures (20-90 °C) in a standard reactor vessel and a large number of nanoparticles can be obtained per batch. Additionally, it is a favorable technique for biological applications, as the synthesis can be done in aqueous phase in contrast to other synthesis methods, such as microemulsion or thermolysis, which require the use of organic solvents. This can lead to unwanted chemical impurities in the final products [192].

The experimental procedure usually involves the co-precipitation of Fe^{2+} and Fe^{3+} salt solutions upon addition of base in an inert atmosphere [145]. The chemical reaction of Fe_3O_4 formation from a stoichiometric mixture of ferrous and ferric salts is described in scheme 9.

$$Fe^{2+} + 2Fe^{3+} + 8OH^- \rightarrow Fe_3O_4 + 4H_2O \qquad (9)$$

The size and shape of the magnetite nanoparticles can be tailored by adjusting pH, ionic strength, nature of the salts (chlorides, sulfates, nitrates, or perchlorates), or the Fe^{2+}/Fe^{3+} concentration ratio and other reaction parameters (temperature, stirring rate, reaction time, dropping speed of the basic solution) as well as growth inhibitors [159, 188, 189, 192]. SPIONs with sizes ranging from 2 nm to 17 nm can be obtained in this manner [159].

A major disadvantage of traditional co-precipitation procedures is that it is difficult to obtain SPIONS with consistent size, shape and polydispersibility. Control of particle size distribution is limited because the crystal growth is only controlled by kinetic factors. To overcome this problem, one can add polymers and chelating organic anions (polyelectrolytes) during co-precipitation in order to control the size, shape and crystallinity of SPIONs. This approach is quite convenient because these agents can act as coatings/surfactants after the synthesis is done (coating *in situ*,

see next section). The coating allows recovering the iron oxide nanoparticles in neutral aqueous solutions [159].

Another inconvenience of the co-precipitation technique is the difficulty to obtain perfect crystalline magnetite structures. The magnetic saturation values obtained experimentally by co-precipitation for SPIONs are in the range 30-50 emu.g^{-1}, which are lower than corresponding bulk magnetic value obtained for Fe_3O_4 of 90 emu.g^{-1} [189]. Furthermore, magnetite nanoparticles are not very stable in ambient conditions and if the iron oxide surface is exposed to oxygen during the synthesis, it can be partially oxidized to maghemite that is still superparamagnetic, but yields a lower magnetic saturation [188, 189, 206].

The thermolysis approach, also known as thermal decomposition, involves generally more complex procedures than the traditional co-precipitation methods, but provides size-controllable and monodisperse magnetic nanoparticles with regular and excellent crystal morphology [159, 207]. As the name indicates, thermolytic synthesis relies on the thermal decomposition of organometallic precursors in high boiling point organic solvents containing fatty acids, or amines as stabilizing surfactants [207].

Different inorganic precursors have been used to produce iron oxide nanoparticles by thermal decomposition, e.g. $Fe(Cup)_3$, $Fe(CO)_5$, $Fe(acac)_3$, and $FeCl_3$. The critical reaction components are the ratios of the precursors, the solvents, the surfactants (which act as capping ligands), the temperature and the reaction time. Heating of the reaction solution to a sufficiently high temperature (150-320 °C) leads to the chemical transformation of the precursors to their active atomic or molecular species, which subsequently condense to form nanoparticles. Nanoparticle size can be controlled by stopping the reaction at different growth stages or by changing the concentration of capping ligands, which limit the crystal growth.

The major inconvenience of these routes is the high temperature needed for the reaction (requiring often special equipment, e.g. reactors and autoclaves) together with the fact that the nanoparticles are finally dispersed in non polar organic solvents [159, 188]. Some progress has been done in order to develop greener hydrolysis methods that can be potentially applied for biomedical applications. Several research groups have proposed the use of non toxic iron chloride salts (e.g. $FeCl_3$) as precursors [208, 209]. Furthermore, there are currently strategies being developed to overcome the required suspension in organic solvents by making the nanocrystals water-soluble (e.g use of hydrophilic capping agents such as PAA) [210, 211].

Assembly of SPIONs secondary structures – Colloidal Nanoparticle Clusters

Some of the conventional nanoparticle synthesis methods that were described above can also be adapted in order to prepare magnetic colloidal nanoparticle clusters (CNCs) with superior magnetic properties (Figure 14) [147, 207]. CNCs can be formed in a one-step process that involves both synthesis and controlled agglomeration of individual nanoparticles. Alternatively, the formation of CNCs can be directed in two-steps by self-assembly of already synthesized surfactant-coated nanoparticles (two-step route) [147, 207]. CNC assembly by thermolysis is one of the best studied approaches to assemble metallic oxide CNCs and has been used in this work to develop Fe_3O_4@PAA CNCs. This procedure consists of a one–step reaction, which requires two growth stages: firstly the primary nanoparticles nucleate and grow in a supersaturated solution, and secondly they agglomerate forming larger secondary structures [147].

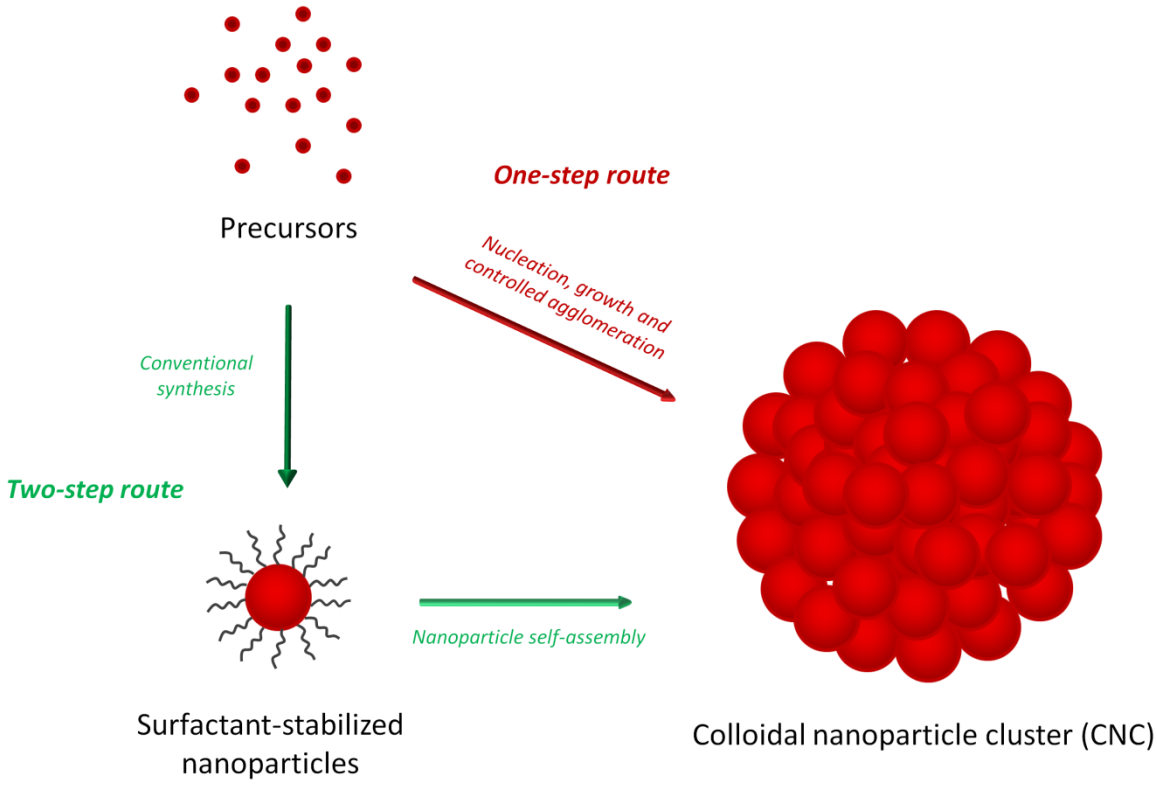

Figure 14. Preparation strategies for assembling colloidal nanoparticle clusters (CNCs). Adapted from [147].

In a standard thermolysis process, the concentration of the capping agents (surfactants) is optimized in order to prevent interparticle agglomeration through steric interactions and thereby obtain individual nanoparticles of uniform sizes. In contrast, the thermolysis approach to assemble CNCs relies on reducing the degree of protection conferred by the capping agent to induce the agglomeration of primary nanoparticles. The first event in the synthesis of metal oxide nanoparticles is nucleation upon thermolysis of the precursors. In the absence of capping agents,

the spherically shaped nanoparticles further grow at 250 °C upon the temperature increase. Ultimately, the nanospheres agglomerate into flower like clusters given the lack of protection from ligands. The key feature to assemble CNCs is to maintain an appropriate concentration of capping ligands, not sufficient to protect the primary nanoparticle spheres from agglomeration, but enough to stabilize the formed 3D nanostructures. The size of the crystal nanoclusters can be tuned by changing reaction conditions, such as the concentration of the capping ligands and the reaction time [147]. This approach has been used to build complex 3D CNCs of metal oxides with different compositions (e.g. In_2O_3, ZnO, CoO, and MnO_2) and sizes [147].

In this PhD work a high temperature thermolysis process based on a method developed by Ge et al. [193] was used to build the Fe_3O_4@PAA CNCs (Figure 12). In this process, $FeCl_3$ and sodium hydroxide (NaOH) were used as precursors, diethylene glycol (DEG) as solvent, and a short-chain polyacrylic acid (PAA) as a surfactant/capping agent. The size of the CNCs was easily tuned by adjusting the concentration of NaOH, resulting in CNCs of selected sizes between 30 nm and 500 nm. These magnetic CNCs show high magnetization in solution and superparamagnetic properties, since they encompass several magnetite nanoparticles of ~10 nm. This would not be the case for a single magnetite crystallite in the same size range (30-500 nm).

Coating of the nanoparticle surface

As previously mentioned, in order to use SPIONs in biomedical applications it is generally required to coat the surface of the iron oxide core. Coatings can have multiple functions in the magnetic nanoparticle carrier e.g. to improve the nanoparticle stability and dispersibility at intermediate pH aqueous solutions, or to provide anchoring chemical sites for protein bioconjugation. The coating procedure can be done during (*in situ* coating) or after synthesis (post-synthesis adsorption and post synthesis end grafting) [145, 159].

In general, surfactants and polymers are added during the synthesis (*in situ* coating) and in many cases are also active participants in the synthesis procedure. As mentioned before, it is common to add polymers and chelating organic anions to control co-precipation procedures. During thermolysis procedure the surfactants have also an active role as capping agents. For example, during the synthesis and assembly of Fe_3O_4@PAA CNCs (*vide supra*), PAA is a critical component, as it stabilizes the three-dimensional CNC structures. PAA is simply added during the synthesis procedure and is usually adsorbed onto the magnetite surface by electrostatic interaction. The carboxylate groups of PAA coordinate strongly with iron cations on the magnetite surface. Charges at the carboxylate ion de-localize between the two oxygen atoms because of the resonance effect. This resonance effect is expected to provide more stability to the carboxylate ion [192].

On the other hand, the deposition of inorganic coatings is usually done after the synthesis procedure (post synthesis end grafting), e.g. deposition of a silica shell by Stöber methods or a sol–

gel process, or the reduction of a single metal on the magnetite surface. Gold is often employed to passivate the surface of magnetite and avoid its oxidation and is usually coated immediately after fabrication of the magnetite core. The method used for gold deposition is related to the previous Fe_3O_4 core synthesis procedure. Gold can be coated onto magnetic nanoparticles through reactions in microemulsion [212–214], redox transmetalation, iterative hydroxylamine seeding [206, 215], or other methods [184, 190, 216, 217].

A simple and practical approach aiming at the subsequent bio-functionalization consists on carrying out both iron oxide core synthesis and gold coating in an aqueous phase. It can be achieved by direct reduction of a gold salt ($HAuCl_4$) on the magnetite surface (using a weak reducing agent, e.g. hydroxylamine or sodium citrate) [206, 215]. The thickness of the gold shell can be tuned by controlling the ratio of the reducing agent to gold salt [169, 218]. The use of citrate as reducing agent to produce Fe_3O_4@Au is quite convenient, because citrate has different functionalities during the whole synthesis procedure and it is not required to introduce other chemicals. First citrate acts as a surfactant for freshly synthesized Fe_3O_4 nanoparticles, then it works as a reducing agent for gold coating, and finally it serves as an anionic stabilizer/stabilizing agent for Fe_3O_4@Au nanoparticles.

In this PhD work, the core-shell Fe_3O_4@Au nanoparticles (Figure 12) were synthesized in aqueous phase, following the approach described above. Firstly, the magnetite nanoparticles (core) were synthesized by the conventional method of iron salts co-precipitation in aqueous solution, with sodium citrate as a stabilizer. Subsequently, these iron oxide nanoparticles were used as seeds for gold reduction with sodium citrate.

3.2.2 Immobilization techniques for protein bioconjugation

During the synthesis and nanofabrication procedures of nanoparticles, their surface is already prepared for further functionalization with biomolecules, e.g. by the introduction of functional coatings such as gold and carboxylic groups. The next step in constructing nanoparticle bioconjugates is the immobilization of proteins on the activated nanoparticle surface. A wide range of techniques has been developed for the biofunctionalization of solid nanoparticles, such as the magnetic nanoparticles and gold dimers that were used in this PhD work. The initial selection on which approach to use is normally determined by different factors such as the type, shape, size of the nanoparticle, its surface ligands or available functional groups, together with the characteristics of the protein, its size, surface charges, and available functional groups, and finally the application of the bioconjugate [219]. Due to their extremely high surface to volume ratio, nanoparticles have a highly active surface chemistry compared to their bulk materials. For this reason the interaction between proteins and the surface of nanoparticles surfaces is quite different than what occurs when proteins are attached to a flat surface of the same bulk material. The attachment of proteins to nanoparticles results in the formation of a dynamic biological

corona, whose thickness and composition depends greatly on the characteristics of the attached protein [151, 196, 220].

Another important part of the bioconjugation procedure is the washing and purification of the nanoparticle bioconjugates. During the functionalization procedure several washing steps are often required, in order to remove the excess reagents used as linkers or reactants, before adding the protein. Additionally, after biofunctionalization, the uncoupled free biomolecules should be removed from the colloidal suspension. The separation of the excess reagents or biomolecules from the nanoparticles can be done by the use of separation techniques such as centrifugation, dialysis or magnetic separation by applying external magnetic fields (for magnetic nanoparticles). The type of washing and separation procedure should be selected depending on the type of nanoparticle bioconjugate in construction.

Furthermore, the immobilization procedures should prevent the loss of activity and stability of the proteins, considering their sensitivity towards pH, temperature and chemical environments. It is also possible that other reagents employed during the functionalization process may contribute to protein denaturation and activity loss [138]. For all the reasons above, close monitoring of the quality and quantity of the conjugated protein and control of the biological function is extremely important, and should be part of the characterization process of the bioconjugates (see Appendix 8.2)

Herein the two types of immobilization techniques that were used in this work, chemical and photochemical immobilization, will be described in detail in the following section, as well as the advantages and disadvantages inherent to these methods.

3.2.2.1 Chemical immobilization of proteins on nanoparticle surfaces

There are several chemical approaches for immobilizing proteins onto the surfaces of nanoparticles, which usually fall into two categories: non covalent interactions and covalent chemistry. Non covalent bioconjugations are usually simpler procedures and can be subdivided in the techniques based on electrostatic/hydrophobic interactions and those consisting on biological recognition, binding, affinity interactions or enzyme activity [219]. Proteins can adsorb on surfaces such as nanoparticles through electrostatic interactions (Figure 15A) and through hydrophobic and polar interactions. The type of interaction will depend on the particular protein and surface involved and requires that both display appropriate cognate surfaces to mediate attachment [219, 221]. In either case protein adsorption frequently results in a heterogenous and randomly oriented protein layer, as each protein molecule can form different contact sites with the nanoparticle surface [138]. Another major disadvantage of bioconjugation via electrostatic/hydrophobic interactions is that proteins can be easily detached from the surface upon changes in pH, salt concentration, or temperature [219].

Other non-covalent protein attachment strategies involve the use of intermediary biomolecules (e.g. antibodies, enzymes, co-factors) that work as a linker and promote the binding of protein to the nanoparticles [222]. The most known linking strategy is based on the strongest non-covalent interaction that is known, streptavidin binding to its co-factor biotin [219]. As there are a wide number of linkers/biomolecules that can be functionalized with biotin, it is a simple and versatile technique to achieve a specific linkage [219, 222]. Depending on the strategy used, streptavidin can be coupled to the nanoparticles and used as a linker to bind biotinilated target biomolecules (Figure 15B) or reversibly biotinilated biomolecules can be used to couple streptavidin.

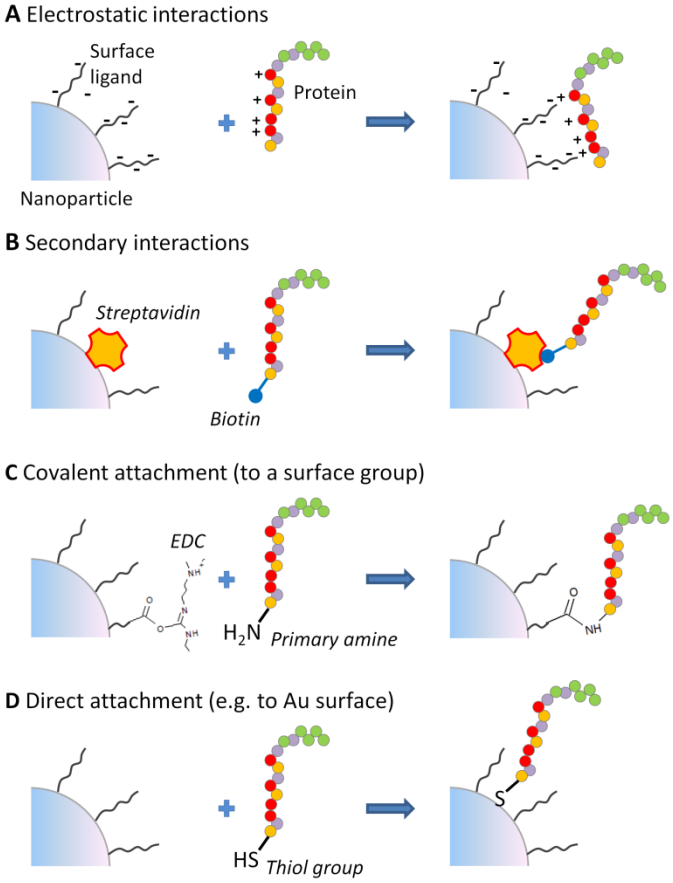

Figure 15. Distinct chemical approaches used for immobilizing proteins onto the surface of nanoparticles. Adapted from [219]**.**

Covalent chemistry strategies are preferable due to the high stability of covalent bounds [138]. This type of interaction is much stronger and thus convenient for the long-term stability of nanoparticle bioconjugates. These techniques can involve the direct attachment of proteins to the nanoparticles surface, or the use of an intermediary or spacer, which is usually a surface attached stabilizing ligand. Most of the covalent protein immobilization techniques rely on the existence of active functional groups provided by the protein amino acids including amino NH_2, carboxylic acid COOH, hydroxyl OH and thiol SH [138].

Proteins can be chemically coupled to different kinds of nanoparticles using established reagent such as bifunctional cross-linker molecules. There are several covalent cross-linker reagents found in literature, which link proteins to functional groups of nanoparticles such as carboxylic acid, hydroxyl, sulphydryl and amino groups, and are used according to the specific needs (chemical specificity, spacer arm between nanoparticle and protein, cleavability of the link) [138, 219]. For instance, carbodiimide reagents, such as the cross-linker 1-ethyl-3-(3-dimethylaminopropyl) carbodiimide (EDC), are used to link carboxyl modified surfaces of nanoparticles and the primary amines of biomolecules (Figure 15C). Proteins usually have several primary amines in the side-chains of lysine residues and N-terminus of each polypeptide, which are available as targets. EDC is a zero-length cross-linker and is widely used for bioconjugation as it allows covalent bound between nanoparticles and proteins without the insertion of an exogenous spacer [138]. Nonetheless, care should be taken when using these approaches, as direct attachment of a protein to a surface can result in a steric constraint that can modify protein reactivity compared to the protein in solution [138, 219]. As mentioned in the previous chapter, proteins containing cysteine residues can also be directly attached to some metal nanoparticle surfaces such as gold by stable Au-S bonds (50 kcal/mol) (Figure 15D) [164, 167, 168]. Metal-thiol interactions are more resistant than non-covalent bonds, which are in the range of 1-5 kcal/mol [223]. When a protein does not contain free cysteine residues (or other suitable residues required for the specific conjugation), the most common strategy is to chemically introduce sulphydril groups. One way of obtaining free thiol groups is by reducing the disulphide bonds of the proteins with mild reducing agents, such as dithiothreitol (DTT), 2-mercaptoethanol, or tris(2-carboxyethyl)phosphine hydrochloride [138, 224, 225].

Considering the nature of all the chemistries described above it is important to recall that the bioconjugation of nanoparticles usually occurs via a stochastic process and in the end it is possible that not all nanoparticles have the same number/nature of proteins immobilized to their surface. Bioconjugates may consist of nanoparticles with and without attached biomolecules and depending on the biofunctionalization methods that are used there might exist heterogeneity in the orientation of the attached proteins [219]. This is particularly relevant in cases where the chemistry can react with different groups on the protein. For instance, when applying a carbodiimide (EDC) chemistry for bioconjugation one should consider that there may be different primary amines available in proteins (lysine residues and N-terminus of each polypeptide) to form amide bonds with the carboxylic target groups in nanoparticles [219]. These type of reactions have also high propensity for cross-linking and formation of higher order structures and agglomerates [219].

In this work a chemical immobilization procedure based on carbodiimide chemistry with EDC was used to immobilize insulin onto the polyacrilic acid surface of the magnetic CNCs (Figure 12). Insulin was selected as a model protein to couple to superparamagnetic CNCs aiming at targeting

the insulin receptor in cells. Human insulin contains only three accessible primary amines as suitable targets for coupling to carboxyl groups with carbodiimide chemistry, which restricts the possible number of orientations of the immobilized insulin molecules on the CNCs surface. This work will be described in detail in Chapter 4.

3.2.2.2 Photochemical immobilization of proteins and light assisted molecular immobilization (LAMI)

A disadvantage of most of the chemical protein immobilization methods is that they require one or more chemical/thermochemical steps and in some cases the use of hazardous chemicals. Often it is also needed to introduce exogenous chemical groups in the protein to promote the bioconjugation. All of these conditions and constraints can affect the stability and conformation of the conjugated protein and thus lower its biological activity/function. Furthermore, chemical immobilization procedures are also laborious and time-consuming, as they can include several preliminary and washing steps. To overcome the drawbacks of classic immobilization procedures, noninvasive coupling techniques and mild reaction conditions are of major interest. In that sense, photochemical reactions are appropriate alternatives for the development of new immobilization technologies. Photochemical immobilization does not usually require prior chemical modification of the proteins (except for the appropriate energy light dose) and the reaction conditions (e.g. pH, temperature) can be adapted to the needs of the coupling protein [221, 226, 227]. Furthermore, light-dependent protocols enable to experimentally choose the time of initiation and the extent of biomolecule binding [226].

Most of the light-dependent immobilization procedures require mediating photosensitive reagents, which are activated by the incident light of appropriate wavelength. These reagents are usually previously coupled to the material surfaces, to the biomolecules or to the synthetic polymers. The immobilization of the biomolecules is mediated by the light activation of the photosensitive reagents. The photochemical reactions triggered by activation and subsequent chemical transformation of the reagents ultimately lead to the formation of covalent bonds between the photogenerated intermediates/photospecies and the target molecules, or material surfaces [221, 226]. Currently used photoreagents for immobilization on material surfaces include substituted arylazides, diazirines, benzophenones, and nitrobenzyl groups. Most of these reagents can be activated through irradiation at wavelengths ≥ 350 nm, for which most biomolecules are transparent, thus avoiding harmful interactions with the protein chromophores [221, 226].

The light assisted molecular immobilization (LAMI) technique (Figure 1) uses a similar operating principle to the methods described above and shares many of its advantages. However, it does not require the use of external photosensitive reagents, as it relies on light activation of endogenous photosensitive groups of the proteins: the aromatic residues tryptophan, tyrosine and phenylalanine. Aforementioned, the LAMI technique explores the natural photo-mechanism in

proteins and peptides, where a disulphide bridge is disrupted upon UV excitation of nearby aromatic residues (see section 2.2.1.3). The thiol groups generated by light induced disulphide bond disruption are used to attach the proteins onto a thiol reactive substrate (e.g. gold, thiol derivatized glass and quartz surfaces). This procedure results in covalent coupling between the biomolecules and the thiol reactive surfaces via covalent bond, or thiol-Au bond. In principle, this technique can be applied to most of the proteins containing disulphide bonds since aromatic residues are preferred spatial neighbors of disulphide bridges [1]. Several proteins were successfully immobilized onto thiol reactive surfaces (e.g. quartz derivatized slides) using the LAMI technology such as cutinase, lysozyme, major histocompatibility complex, alkaline phosphatase, Fab fragments, and prostate specific antigen [2–4].

Another advantage of light-dependent immobilization techniques such as LAMI is that the protein coupling can be controlled by the irradiation procedure. In the case of LAMI, the disruption of disulphide bonds and subsequent immobilization onto thiol reactive surfaces is dependent on the UV excitation of the aromatic residues. Therefore, the immobilization only occurs where the UV photons are present. This is particularly relevant for protein immobilization onto flat surfaces. Using a beam of UV light it is possible to restrict the coupling area to the size of the focal spot. The pattern of immobilized molecules on the surface can be controlled by shaping the pattern of the UV light used for molecular immobilization. This is extremely relevant for the development of functional protein microarrays and protein biochips. Protein microarrays have become essential for medical diagnostics and drug research, as the microarray format allows high throughput analysis of assays in a parallel fashion. Usually, the construction of microarrays is limited by printing and spotting of proteins on a planar substrate. Printing and spotting of proteins is feasible by various techniques, such as pin dispensing and piezo electric injectors that are used to dispense tiny amounts of liquids [228–231], or upon pre-treatment of the surface using nanofabrication techniques. These procedures are used to form spots, or large protein microarrays (by chemical immobilization). Photochemical immobilization methods bypass the use of micro-dispenser techniques and associated technical difficulties to build protein spots. Furthermore, these techniques ensure high lateral resolution of protein immobilization as the proteins are only immobilized on the zones exposed to light [221].

Based on the LAMI technique the Nanobiotechnology Group at Aalborg University developed a set up for large scale immobilization of proteins onto thiosilane-functionalized glass slides. The immobilization procedure is carried out by simply focusing a UV laser beam onto the glass slide surface where a droplet of protein solution was deposited. The LAMI process is relatively fast and is determined by physicochemical parameters as well as the light fluency (power per unit area). The exposure process is carried out using 100 ms illumination per spot with ~1mW 280 nm 8MHz femtosecond pulses [3]. The setup includes a computer controlled shutter and stage, where the slide is positioned, and the computer is programmed to create an array with micrometer

resolution by automatic exposure of the programmed areas with the laser beam. Using this setup it was possible to obtain spot sizes of ~3-5 micron [2, 3, 5]. This procedure is used to build microarrays of active biosensors, such as e.g. a prostate specific antigen (cancer marker) detection biosensor [4]. The spot size resolution is further improved by combining the UV light assisted immobilization procedure with the Fourier transforming properties of lenses. By inserting a spatial mask into the UV light beam, it is possible to shape the pattern of the UV light used for protein immobilization of the thiol-reactive surface. This approach enables to simultaneously produce multiple spots of immobilized protein with an individual spot size of ~700 nm [6, 7].

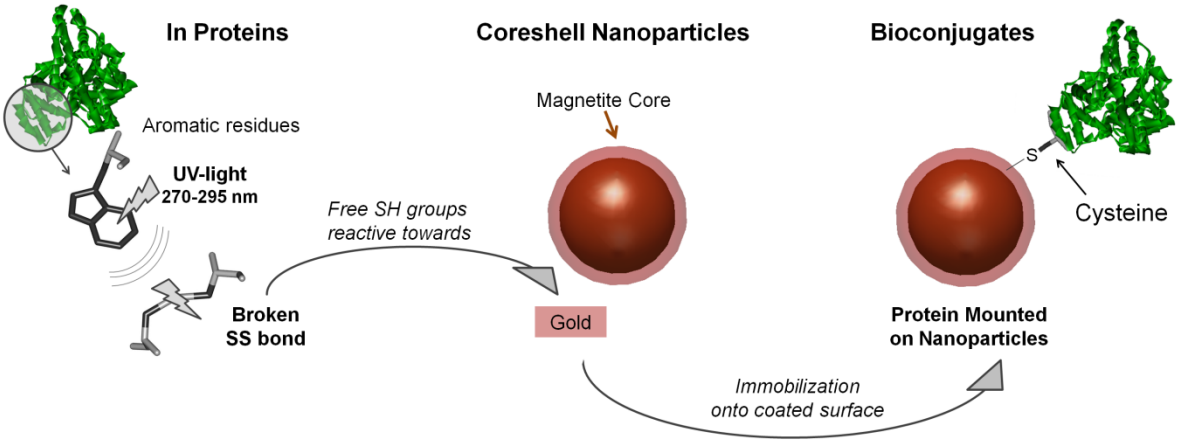

Figure 16. LAMI of proteins onto core-shell Fe_3O_4@Au nanoparticles.

In this PhD work the LAMI technology was exploited to immobilize proteins on nanoparticle surfaces, instead of flat surfaces. Among nanoparticles, magnetite gold coated nanoparticles (Fe_3O_4@Au) were selected for protein immobilization with LAMI, due to its interesting magnetic, optical and chemical properties and its chemical stability, good biocompatibility, low toxicity, and easy dispersibility. Furthermore, gold was a convenient coating for LAMI bioconjugation, since it has affinity towards biomolecules with thiol terminal groups. Bovine Serum Albumin (BSA) was used as a model protein to test and apply LAMI immobilization on magnetic nanoparticles, at it is rich in disulphide bonds, making it a good candidate for LAMI conjugation onto thiol reactive surfaces (Figure 16). The immobilization process was carried out in solution upon irradiation of sample of BSA and Fe_3O_4@Au nanoparticles with 295 nm light using a standard fluorescence spectrometer equipped with a 75-W Xenon arc lamp coupled to a monochromator. This work will be described in detail in Chapter 4.

This PhD work also looked into improving some aspects of the LAMI procedure, in particular the enhancement of the spatial resolution obtained for protein based arrays. As previously mentioned, the LAMI technique had been so far applied to create high-density protein arrays with a resolution restricted to the focusing ability of the light source, i.e. allowing spot sizes of a few hundred nanometers. In this work the plasmonic properties of gold gap-antennas (see Section

3.1.1.2) were exploited to confine the electromagnetic field used for immobilization to a sub-wavelength scale (hotspot region) and thereby enable the light induced immobilization of proteins onto nm-sized gaps between gold dimers (Figure 12). While gold nanostructures are typically resonant in the near-infrared, the excitation of the aromatic residues of proteins, required for initiation of the LAMI process, typically takes place in the UV (Trp and Tyr absorb maximally at ~278 nm and Tyr at ~275 nm, respectively). In order to compensate for the energy mismatch, the phenomenon of multi-photon excitation of fluorophores was explored. In the process of multi-photon excitation, the excited fluorophore interacts simultaneously with multiple long-wavelength photons (from the same light source, e.g. laser beam) in order to be excited to its first singlet state (Figure 17). Multiphoton excitation requires the use of high energy fs lasers since a high peak power is necessary in order to increase the probability that multiple photons are available for absorption [71, 232]. In three-photon excitation, a fluorophore that usually absorbs at λ can be excited at at a wavelength 3xλ when subjected to a high intensity radiation. Trp can be excited at wavelengths ~850 nm using a fs-pulsed Ti:sapphire laser [233, 234].

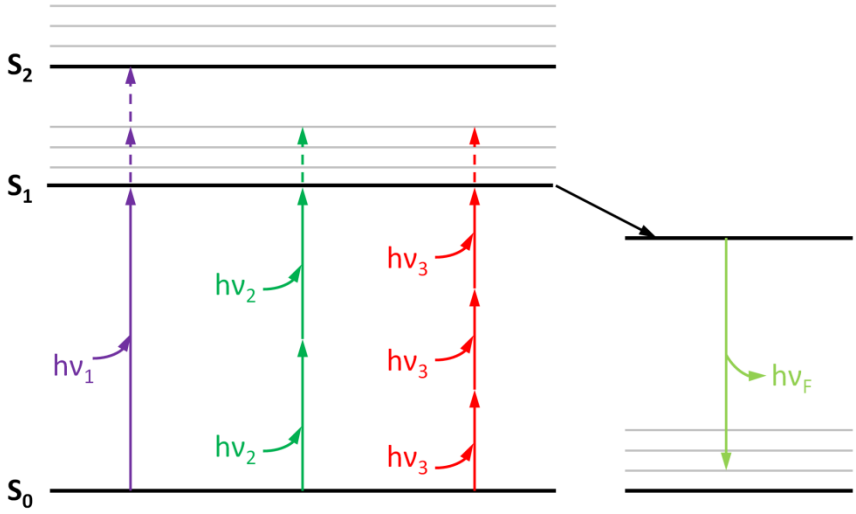

Figure 17. Jablonski diagram depicting multiphoton excitation of a fluorophore. The fluorophore is excited to higher energy states upon one- ($h\nu_1$), two- ($h\nu_2$), and three-photon ($h\nu_3$) excitation. The absorption of two $h\nu_2$ or three $h\nu_3$ photons occurs simultaneously. Adapted from [71]**.**

Herein, the absorption of multiple photons from the optical near field was exploited to excite the aromatic residues of BSA and thereby enable the LAMI of this protein onto the gold surfaces located in the hotspot region upon thiol-gold covalent bonding. The experimental procedure used to immobilize BSA onto the hotspot surfaces of gold-antenna arrays is summarized in Figure 18.

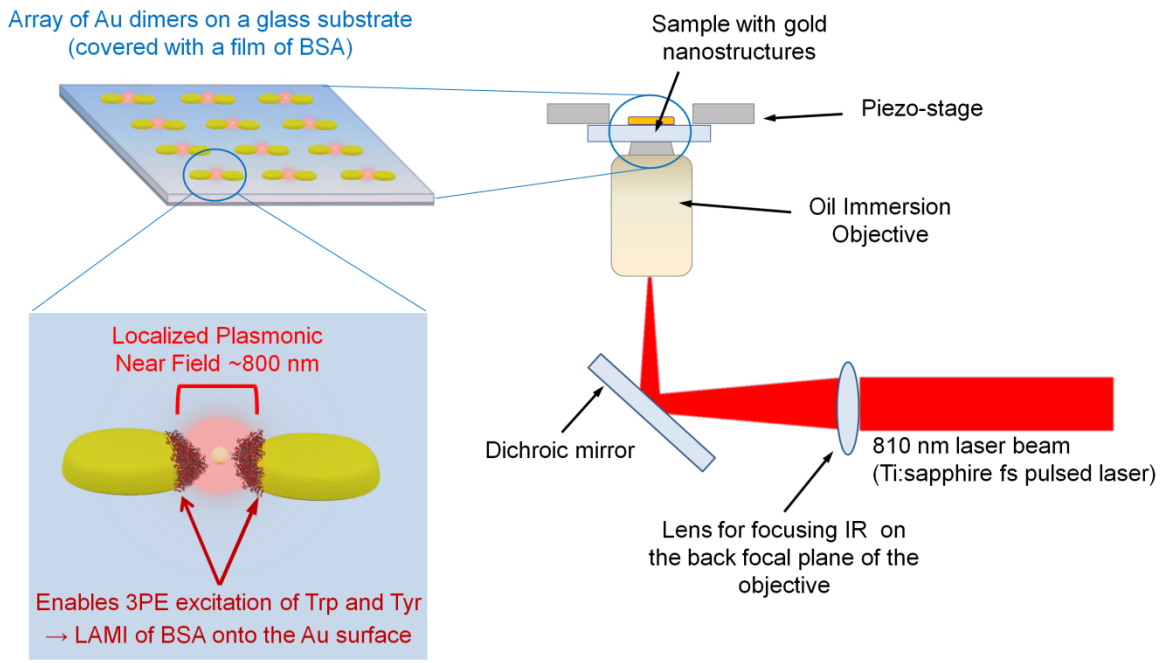

Figure 18. Experimental set-up used for LAMI of BSA onto nm-sized gaps of gold dimers upon three-photon excitation (3PE) of Trp and Tyr. The sample comprising the array of gold dimers covered with BSA was mounted onto a x-y translation piezo staged and placed on a Olympus IX71 inverted microscope. The microscope was coupled to a Coherent Mira 900 Ti:Sapphire laser. For illumination, the laser beam (810-840 nm, 200 fs, 76 MHz) was focused on the back focal plane of a 100x, 1.25 NA oil immersion objective using a 1 m focusing lens. This resulted in a beam width of ~12 µm at the sample's location. Each sample was exposed for 30 min (average power 100 µW-10 mW) in order to initiate the LAMI process.

First, a droplet of BSA solution was allowed to dry over the array of gold gap-antennas in order to promote a high protein concentration in the vicinity of the gold surfaces. During the array fabrication process (see section 3.2.1.1), the dimensions of the identical gold cylinders and of the nm-sized gap were tuned in order to obtain a plasmon resonance of 700 nm in the air. After protein coverage the plasmon resonance of the gold dimers shifted to 800 nm. This resonance wavelength allows three-photon absorption of the protein aromatic's upon illumination using a pulsed Ti:sapphire laser (set at 810 nm) and it enables the LAMI process to initiate. This work will be described in detail in the following chapter.

4 Results

This chapter includes the five main scientific papers that contribute to this PhD dissertation and one additional scientific unpublished work. The chapter is divided into two sections, which correspond to the two parts of this PhD study: a) Investigation of light induced switches in proteins and b) Construction of nanoparticle based bioconjugates.

The first section (4.1) presents the papers that focus on the investigation of light induced mechanisms and UV light effects on proteins. It includes three studies of UV light induced effects on three proteins: bovine alpha-lactalbumin (Paper 1), human insulin (Paper 2), and EGFR (Paper 3). The outcome of these papers will be further discussed in chapter 5. This first section includes the papers:

- **Paper 1:** "Photophysics, photochemistry and energetics of UV light induced disulphide bridge disruption in apo-α-lactalbumin". Correia, Manuel; Neves-Petersen, Maria Teresa; Parracino, Antonietta; di Gennaro, Ane Kold; Petersen, Steffen B. (2012) *Journal of fluorescence*, *22*(1), 323–37.
- **Paper 2:** "UV-light exposure of insulin: pharmaceutical implications upon covalent insulin dityrosine dimerization and disulphide bond photolysis". Correia, Manuel; Neves-Petersen, Maria Teresa; Jeppesen, Per Bendix; Gregersen, Søren; Petersen, Steffen B. (2012) *PloS One*, *7*(12), e50733.
- **Paper 3:** "Modulating the structure of EGFR with UV light: new possibilities in cancer therapy". Correia, Manuel; Thiagarajan, Viruthachalam; Coutinho, Isabel; Gajula, Gnana Prakash; Petersen, Steffen B., Neves-Petersen, Maria Teresa (2014) *PloS One*, PloS One, 9 (11), e111617.

The second section (4.2) encompasses the papers and one additional scientific unpublished work that discuss the construction of nanoparticle bioconjugates for biomedical applications. This section includes the papers:

- **Paper 4:** "Photonic immobilization of BSA for nanobiomedical applications: creation of high density microarrays and superparamagnetic bioconjugates". Parracino, Antonietta; Gajula, Gnana Prakash; di Gennaro, Ane Kold; Correia, Manuel; Neves-Petersen, Maria Teresa; Rafaelsen, Jens, Petersen, Steffen B. (2011) *Biotechnology and bioengineering*, *108*(5), 999–1010.
- **Paper 5:** "Plasmon-assisted delivery of single nano-objects in an optical hot spot". Galloway, Christopher M.; Kreuzer, Mark P.; Aćimović, Srdjan S.; Volpe, Giorgio; Correia, Manuel; Petersen, Steffen B.; Neves-Petersen, Maria Teresa; Quidant, Romain (2013). *Nano letters*, *13*(9), 4299–304.

- **Unpublished scientific work:** "Superparamagnetic colloidal nanoparticle clusters for use in targeted protein therapeutics and magnetic separation technologies".

4.1 Paper 1

Photophysics, photochemistry and energetics of UV light induced disulphide bridge disruption in apo-α-lactalbumin

Manuel Correia, Maria Teresa Neves Petersen, Antonietta Parracino, Ane Kold di Gennaro, and Steffen B. Petersen

Journal of Fluorescence, 2012, 22(1), 323–37

J Fluoresc (2012) 22:323–337
DOI 10.1007/s10895-011-0963-7

ORIGINAL PAPER

Photophysics, Photochemistry and Energetics of UV Light Induced Disulphide Bridge Disruption in apo-α-Lactalbumin

Manuel Correia · Maria Teresa Neves-Petersen · Antonietta Parracino · Ane Kold di Gennaro · Steffen B. Petersen

Received: 6 June 2011 / Accepted: 30 August 2011 / Published online: 14 October 2011

Abstract Continuous 295 nm excitation of whey protein bovine apo-α-lactalbumin (apo-bLA) results in an increase of tryptophan fluorescence emission intensity, in a progressive red-shift of tryptophan fluorescence emission, and breakage of disulphide bridges (SS), yielding free thiol groups. The increase in fluorescence emission intensity upon continuous UV-excitation is correlated with the increase in concentration of free thiol groups in apo-bLA. UV-excitation and consequent SS breakage induce conformational changes on apo-bLA molecules, which after prolonged illumination display molten globule spectral features. The rate of tryptophan fluorescence emission intensity increase at 340 nm with excitation time increases with temperature in the interval 9.3–29.9 °C. The temperature-dependent 340 nm emission kinetic traces were fitted by a 1st order reaction model. Native apo-bLA molecules with intact SS bonds and low tryptophan emission intensity are gradually converted upon excitation into apo-bLA molecules with disrupted SS, molten-globule-like conformation, high tryptophan emission intensity and red-shifted tryptophan emission. Experimental Ahrrenius activation energy was 21.8±2.3 kJ.mol^{-1}. Data suggests that tryptophan photoionization from the S_1 state is the likely pathway leading to photolysis of SS in apo-bLA. Photoionization mechanism(s) of tryptophan in proteins and in solution and the activation energy of tryptophan photoionization from S_1 leading to SS disruption in proteins are discussed. The observations present in this paper raise concern regarding UV-light pasteurization of milk products. Though UV-light pasteurization is a faster and cheaper method than traditional thermal denaturation, it may also lead to loss of structure and functionality of milk proteins.

Keywords Photophysics and photochemistry of α-lactalbumin · Protein fluorescence quenching · UV-light induced disulphide bridge disruption · Activation energy of photoionization · Tryptophan photoionization in proteins

Abbreviations

A_0	Ahrrenius pre-exponential factor
apo-bLA	Ca^{2+}-depleted bovine α-lactalbumin

M. Correia · A. Parracino · A. K. di Gennaro
Department of Physics and Nanotechnology, Aalborg University, Skjernvej 4A, DK-9220 Aalborg, Denmark

M. Correia
e-mail: mc@nano.aau.dk

A. Parracino
e-mail: m.parracino@yahoo.it

A. K. di Gennaro
e-mail: ak@nano.aau.dk

M. T. Neves-Petersen (✉)
INL Int Iberian Nanotechnol Lab,
P-4715310 Braga, Portugal
e-mail: teresa.petersen@inl.int

M. T. Neves-Petersen
NanoBiotechnology Group, Department of Biotechnology, Chemistry and Environmental Sciences, Aalborg University, Sohngaardsholmsvej 57, DK-9000 Aalborg, Denmark
e-mail: tnp@bio.aau.dk

S. B. Petersen
NanoBiotechnology Group, Department of Health Science and Technology, Aalborg University,
Fredrik Bajers vej 7, DK-9220 Aalborg, Denmark
e-mail: sp@hst.aau.dk

S. B. Petersen
The Institute for Lasers, Photonics and Biophotonics, University at Buffalo, The State University of New York Buffalo, Buffalo, NY 14260-3000, USA

apo-LA	Ca^{2+}-depleted α-lactalbumin
bLA	bovine α-lactalbumin
CD	circular dichroism
Cys	C, cysteine
DTNB	5,5′-dithiobis-2-nitrobenzoic acid
E_a	Ahrrenius activation energy
e^-_{aq}	solvated electron
k	rate fluorescence emission intensity increase at 340 nm
Gly	Glycine
LA	α-lactalbumin
LAMI	light assisted molecular immobilization
Phe	phenylalanine
S_1	relaxed first electronic singlet state
S*	non-relaxed pre-fluorescent first electronic singlet state
SS	disulphide bridge(s)
TNB^{2-}	2-nitro-5-thiobenzoate ion
Trp	W, tryptophan
^{T}Trp	tryptophan triplet state
Tyr	tyrosine
UV	ultraviolet
Δλ	difference in wavelength
λ_{max}	wavelength at maximum fluorescence emission
MG	molten globule

Introduction

Several reviews have been published on the photochemistry and photophysics of tryptophan (Trp) [1, 2] tyrosine (Tyr) [3, 4] phenylalanine (Phe) [5] and cystine [6]. Excitation to higher energy states is followed by relaxation to ground state (e.g. fluorescence, phosphorescence) or to excited state photochemical or photophysical processes, such as photoionization [2]. Since in this work the protein has been excited at 295 nm, we will focus on Trp photochemistry. Trp side-chain has the highest absorption at 280 and 287 nm [7]. Upon Trp excitation the following intermediates are formed [1, 8, 9]: excited singlet state S_1 and/or higher S^* excited states (schemes 1, 2); solvated electrons e^-_{aq}, formed upon electron ejection to the solvent (scheme 3–6); tryptophan radical cation $Trp^{\bullet+}$ which rapidly deprotonates yielding the neutral radical $Trp^{\bullet}$ (scheme 7) which can react with molecular oxygen, Tyr or cystine leading to peptide chain cleavage; ^{T}Trp, formed upon intersystem crossing from S_1 into triplet-state (scheme 8); protonated triplet state formed after intramolecular proton transfer from protonated NH_3^+ group to the indole ring (scheme 9).

$$^{S_0}Trp + h\nu \rightarrow {}^{S_1}Trp \quad (1)$$

$$^{S_0}Trp + h\nu \rightarrow {}^{S^*}Trp \quad (2)$$

$$^{S^*}Trp \rightarrow Trp^{\bullet+} + e^-_{aq} \quad (3)$$

$$^{S^*}Trp \rightarrow {}^{S_1}Trp \quad (4)$$

$$^{S_1}Trp \rightarrow Trp^{\bullet+} + e^-_{aq} \quad (5)$$

$$^{S_1}Trp + h\nu \rightarrow {}^{S_1}Trp^{\bullet+} + e^-_{aq} \quad (6)$$

$$Trp^{\bullet+} \rightarrow Trp^{\bullet} + H^+ \quad (7)$$

$$^{S_1}Trp \rightarrow {}^{T}Trp \quad (8)$$

$$^{S_1}Trp + H^+ \rightarrow {}^{T}TrpH^+ \quad (9)$$

Trp photoionization, a major photo-oxidation pathway of many proteins [10, 11], can take place from the pre-

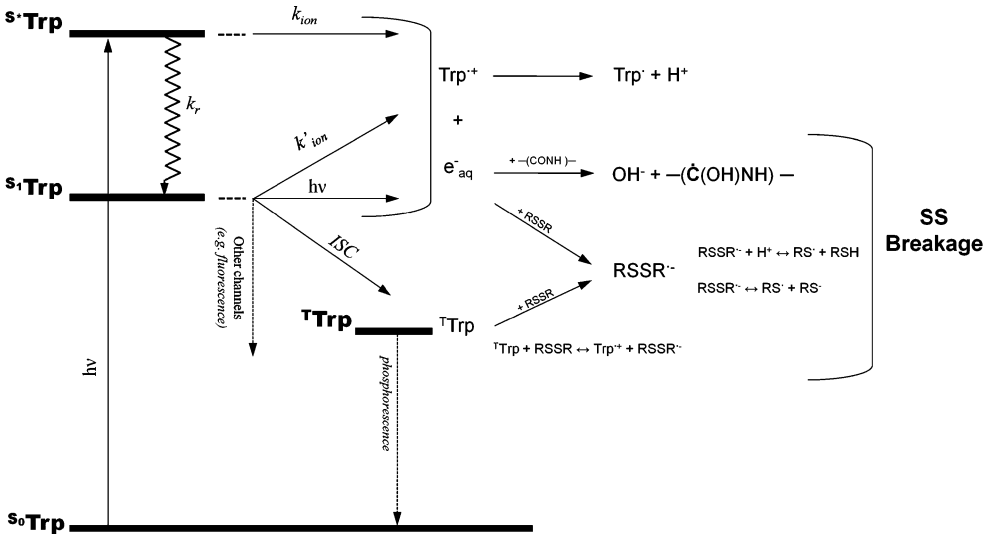

Fig. 1 Photophysical and photochemical pathways of Trp in proteins upon UV excitation. Pathways were assembled from articles from Bent and Hayon [1], Neves-Petersen et al. [10], Sherin et al. [14, 15] and Kerwin and Remmele [16]

fluorescent state S^* and/or from S_1 (Fig. 1). Ionization from S^* (rate constant k_{ion}) will compete with relaxation to S_1. Ionization from S^* has been proved by flash photolysis studies of Trp in solution, being solvated electrons observed within 200 fs after excitation [12, 13]. Photoionization from S_1 (rate constant k'_{ion}) has been reported to have an Arrhenius activation energy E_a~50 kJ.mol^{-1} [14]. Ionization quantum yield from S^* has been observed to decrease with temperature increase, in sharp contrast with the yield of ionization from S_1 state, which increases with temperature increase [15].

An important photochemical mechanism in proteins involves reduction of disulphide bridges (SS) upon UV excitation of Trp and Tyr side chains [10, 16, 17]. UV-excitation of these residues leads to photoionization and generation of solvated electrons [1–4, 10, 16]. These can subsequently undergo fast geminate recombination with their parent molecule or can be captured by electrophilic specii like cystines, molecular oxygen or H_3O^+. Capture of the solvated electrons by cystines leads to the formation of $RSSR^{\bullet-}$ (disulphide electron adduct) and likely SS breakage (schemes 10, 11) [18]. Solvated electrons can also interact with the peptide chain creating hydroxide ions and ketyl radicals (scheme 12), which can propagate along the peptide chain [1]. If a ketyl radical gets trapped by a disulfide bridge, this again results in a disulphide anion and likely SS breakage. ^{T}Trp can react with molecular oxygen to yield $Trp^{\bullet+}$ and $O_2^{\bullet-}$ [16] or it can transfer an electron to a nearby SS to give $Trp^{\bullet+}$ and $RSSR^{\bullet-}$ (scheme 13) [1]. Protonation of disulphide anion can also lead to SS disruption (scheme 14) [18].

$$e^-_{aq} + RSSR \rightarrow RSSR^{\bullet-} \tag{10}$$

$$RSSR^{\bullet-} \Leftrightarrow RS^{\bullet} + RS^- \tag{11}$$

$$e^-_{aq} + -CONH- \rightarrow OH^- + -\dot{C}(OH)NH- \tag{12}$$

$$^T Trp + RSSR \rightarrow Trp^{\bullet+} + RSSR^{\bullet-} \tag{13}$$

$$RSSR^{\bullet-} + H^+ \Leftrightarrow RS^{\bullet} + RSH \tag{14}$$

Reduction of SS upon UV excitation of aromatic residues has been shown for proteins such as cutinase and lysozyme [10, 17, 19], bovine serum albumin [20, 21] prostate specific antigen [22], and antibody Fab fragments [23]. This phenomenon has lead to a new technology for protein immobilization (LAMI, light assisted molecular immobilization) since the created thiol groups can bind thiol reactive surfaces leading to oriented covalent protein immobilization [19–31].

α-lactalbumin (LA) is a small (~14.2 kDa), acidic (isoelectric point ~4–5) protein present in the milk whey of mammalians. Most mammalian LAs share a highly conserved 3D structure [32, 33]. Expressed exclusively during lactation, LA plays an important role in lactose biosynthesis [32–34]. LA unfolding has been extensively studied since the protein adopts molten globule (MG) conformations under mild denaturating conditions [35, 36]. In the MG state the protein is still compact, with native-like secondary structure, but lacks well defined tertiary interactions, and the hydrophobic regions are more solvent accessible [36]. Calcium-bound LA is the major form under physiological conditions [33]. The Ca^{2+} depleted form of LA (apo-LA) herein studied is involved in other functions besides lactose synthase regulation, such as interaction with lipid membranes [37] and oleic acid [36]. The latter can give rise to a multimeric form that can induce apoptosis in tumor cells [38–40]. Apo-LA conformation is extremely sensitive to experimental conditions, particularly pH and ionic strength. It is known to adopt different conformations in solution such as molten globule forms void of cooperative thermal transition or partly native folded states showing cooperativity upon thermal denaturation [32, 36, 41–45]. At high ionic strength bovine apo-LA (apo-bLA) shows minor structural differences compared to native calcium-bound LA [32, 45]. Upon Ca^{2+} removal, the electrostatic interactions at the Ca^{2+} binding site are disrupted, leading to local structural destabilization of the protein structure [32]. Positively charged ions (e.g. Na^+, K^+) will interact with the negatively charged residues of the Ca^{2+} binding site and stabilize the protein structure [32, 45, 46]. Bovine LA (bLA) displays a marginal thermodynamic folding barrier, which is apparently modulated by protein electrostatics in its apo-form [47]. This low folding barrier explains the conformational flexibility of apo-LA in solution [47]. Apo-LA can be perceived as a continuum of conformational states, an ensemble of conformations whose population distribution depends strongly on electrostatic interactions.

Apo-bLA has 4 Trp residues in close spatial proximity of disulphide bridges, making it a good candidate for studying light induced SS disruption mediated by Trp excitation. UV light induced SS disruption in LA upon Trp excitation has been verified for Ca^{2+} bound and apo-versions of bovine and human LA [48], and goat LA [49, 50]. Mass-spectroscopy confirmed light induced SS disruption in human and goat LA [48–50]. SS disruption was correlated with a red-shift in fluorescence emission as well as with an increase in fluorescence yield [48, 49]. We here show for the first time the correlation between fluorescence emission increase and UV-light induced breakage of SS in apo-bLA. We report the photophysics, photochemistry, structural and fluorescence spectral changes induced by 295 nm excitation

of Trp residues in apo-bLA. The studies have been carried out at different temperatures in order to obtain the Arrhenius activation energy of such process. For the first time to our knowledge we here report the activation energy of photochemical process(es) leading to SS disruption upon excitation of aromatic residues in proteins. Trp photoionization mechanism(s) and consequent induced disruption of disulphide bridges in apo-bLA are discussed.

Materials and Methods

Protein and Buffer Solutions

Apo-bLA from bovine milk type III was purchased from Sigma-Aldrich (product L6010). Apo-bLA concentrations were determined by Abs_{280nm} using an extinction molar coefficient of 28500 $M^{-1}.cm^{-1}$ [48, 51]. Trizma base (Sigma) was used for preparation of Tris HCl buffers. pH adjustments were carried out by addition of 2.5 M HCl. Tris HCl buffer displays a minimal pH drift with temperature changes. Milli-Q water with conductivity below 0.2 $\mu S.cm^{-1}$ was used.

Fluorescence Emission of apo-bLA as a Function of 295 nm Excitation Time

UV-light triggered reaction mechanisms in apo-bLA were probed by monitoring the time-dependent fluorescence emission intensity at 340 nm of LA upon 295 nm excitation. 1.86 μM apo-bLA was prepared in 25 mM Tris HCl pH 8.55. 3 ml were placed in a quartz macro cuvette (1 cm path length) and excited at 295 nm during 1 h, 2 h, 3 h, 4 h, and 5 h. A fresh sample was used for each time based study. Excitation was carried out in a RTC 2000 PTI spectrometer (Photon Technology International, Canada, Inc.347 Consortium Court London, Ontario N6E 2S8) with a T-configuration, using a 75-W Xenon arc lamp coupled to a monochromator. Cuvette temperature was kept at 25 °C using a peltier element. Samples were magnetically stirred at 900 rpm in order to secure homogeneous excitation. All slits were set to 5 nm. Lamp power at 295 nm was 252 μW at the focal point in the sample holder location. After each illumination, emission and excitation spectra were recorded. Emission spectra were acquired with 295 nm and 280 nm excitation. Emission was fixed at 340 nm in detector-1 and at 320 nm in detector-2 while acquiring the excitation spectra. The same emission and excitation spectra were acquired for a non-illuminated solution and for the buffer. Raman signal was subtracted from each emission spectrum.

Detection of Free Thiol Groups Formed Upon UV Illumination of apo-bLA

Detection of free thiol groups was carried out using the Ellmann assay [17, 52]. Ellmann's reagent, 5,5′-dithiobis-2-nitrobenzoic acid (DTNB) was purchased from Invitrogen. 1 mM solution was prepared in Tris HCl, 100 mM at pH 6.6 in order to favor dissolution. The supernatant phase was used as stock solution and stored at 4 °C. The stock concentration (0.7 mM) was determined by absorbance at 324 nm using an extinction molar coefficient for DTNB in Tris HCl of 16600 $M^{-1}.cm^{-1}$ [53].

An excess of DTNB (100 μL of 0.7 mM stock solution) was added to 900 μL of illuminated solution immediately after each time-dependent 295 nm excitation, and to 900 μL of non-illuminated apo-bLA. Absorbance at 412 nm by the released 2-nitro-5-thiobenzoate ion (TNB^{2-})was monitored with a UV/Visible spectrophotometer (UV1 VWR International—Thermo Electron Corporation, Thermo Fisher Scientific Inc. 81 Wyman Street Waltham, MA 02454), using 1 cm path quartz cuvette. Absorbance at 412 nm, proportional to the amount of thiol groups present in solution, was monitored immediately after mixing the two components and a reading was obtained upon signal stabilization. The sample was kept in the dark between measurements and manually stirred before each reading. Abs_{412nm} stabilized after ~20 min of reaction. Abs_{412nm} at 22 min of reaction was used. The values were corrected for the contributions of apo-bLA and DTNB for Abs_{412nm}. Abs_{412nm} was monitored for a protein blank (900 μL of fresh 1.86 μM apo-bLA solution and 100 μL of 100 mM Tris HCl, pH 6.7) and a reagent blank (900 μL of 25 mM Tris HCl pH 8.5 and 100 μL of 0.7 mM stock solution of DTNB in Tris HCl). Concentration of thiol groups was determined using an extinction molar coefficient for TNB^{2-} of 14150 $M^{-1}.cm^{-1}$ at 412 nm [52]. The average number of free thiol groups detected per protein molecule was then estimated for each illuminated and non-illuminated samples, by dividing the concentration of detected thiol groups with the apo-bLA concentration used.

Time-Dependent Fluorescence Emission of apo-bLA at Different Temperatures

Time-based fluorescent emission kinetic traces (340 nm) obtained upon continuous 295 nm excitation of the protein solution were carried out at different temperatures (9.3, 12.9, 15.6, 20.4, 24.9 or 25.2, 29.9 or 34.6 °C) in the same RTC 2000 PTI spectrometer setup. 3 ml of 1.85 μM (runs at 9.3, 12.9, 15.6, 20.4, 24.9, 29.9 or 34.6 °C) and 3 ml of 1.66 μM (run at 25.2 °C) apo-bLA solutions (in 25 mM Tris-HCl pH 8.5) were continuously illuminated during 3.5 h in a 1 cm path quartz cuvette with constant magnetic stirring at 900 rpm.

Real-time correction was enabled in order to correct for oscillations in lamp intensity (gain set at 1.81 V). Emission spectra were acquired after each run (exc. 295 nm) at the run's temperature. Correspondent emission spectra were carried out for non-illuminated apo-bLA solutions at the same temperatures, and for the buffer, in order to Raman correct each emission spectrum. Solution temperature was previously set using a peltier element. Slits were set at 5 nm.

Circular Dichroism Measurements

Circular Dichroism (CD) spectroscopy was used to monitor the relative changes in ellipticity after 295 nm excitation of apo-bLA up to 2.8 h illumination. A solution of apo-bLA (11.5 μM in 10mM Tris HCl pH 8.55, 3.5 mL initial volume) was excited in the previously described RTC 2000 PTI spectrometer setup, using the same excitation slit width, and magnetic stirring speed. At discrete times in the excitation session, 300 μl of illuminated apo-bLA were removed and placed in a quartz microcuvette with a path length of 0.1 cm. Far-UV CD spectra (200–240 nm) of fresh and illuminated protein were acquired using the following parameters: 0.5 nm band width, resolution 1.0, 3 accumulations, scan speed 5 nm/min, 100 mdeg sensitivity, 1 s response time. Each measurement was controlled by the JASCO J-700 hardware manager (JASCO Corporation, 2967–5 Ishikawa-cho Hachioji-shi, Tokyo, Japan). The buffer signal was subtracted from all spectra.

Protein Three-Dimensional Structure Representation, Accessible Surface Area of Trp Residues and Trp-SS Distances

The crystallography data used for 3D protein representation, accessible surface area (ASA) and distance calculations was extracted from the PDB files 1F6S (apo-bLA crystallized at high ionic strength) and 1F6S.pdb (native bLA) [32]. Apo-bLA 3D structure was displayed using Accelrys Discovery Studio Visualizer 2.5. The ASA values for each Trp residue were calculated using the program *Surface Racer*© considering the probe radius of 1.4 Å (approximate value for a water molecule radius), and the van der Vaals radii sets of Richards—1977 [54, 55]. The ASA of Trp in the tripeptide Gly-Trp-Gly estimates the total ASA of this residue with the main chain in an extended conformation. The value used as Trp ASA in Gly-Trp-Gly was 217 $Å^2$, according to Miller et al. [56]. Distances between Trp residues and potential quenching groups were calculated in Rasmol 2.6 using the "monitor" tool.

Data Analysis

All smoothing procedures were carried out by adjacent averaging in Origin 8.0. Fluorescence emission and far-UV CD spectra were smoothed using a 5 points adjacent average, while excitation spectra were smoothed using 2 points adjacent average prior to normalization. Normalized emission and excitation spectra were obtained by dividing each data point by the maximum intensity value in each spectrum. Normalized time-based fluorescence measurements were obtained by dividing each data point (emission intensity) by the time zero emission. Normalized fluorescence kinetic traces obtained upon 295 nm excitation for 3.5 h at different temperatures were fitted with an exponential function $F(t) = C_1 - C_2 e^{-kt}$, where *F(t)* is the fluorescence emission intensity at 340 nm at the 295 nm excitation time t, C_1 and C_2 are constants and k is the rate constant fluorescence emission intensity increase. The first 800 s were excluded while fitting all kinetic traces since an initial decrease in fluorescence emission intensity is observed. Fittings were carried out from 800 s till the time corresponding to 95% of maximum fluorescence emission in order to avoid the region where fluorescence emission intensity peaks. The temperature dependence of the rate constant for fluorescence emission increase at 340 nm (k) was studied by fitting the data values with the logarithmic form of the Arrhenius equation $\ln k = \ln A_0 + \frac{E_a}{RT}$, where A_0 is the pre-exponential factor, E_a the activation energy, R the universal constant for perfect gases and T the temperature . The fitting took into account the standard errors determined for each previously calculated k value. Each data point was associated with a weight, $w_i = 1/\sigma_i^2$, where σ_i is the error bar size for each data point. Data fitting and plotting were done in Origin 8.0.

Results

Three-Dimensional Structure of bLA

Apo-bLA 3D structure obtained upon crystallization at high ionic strength [32] is displayed in Fig. 2. Apo-bLA 3D structure has high structural homology with the crystallized structure of native Ca^{2+}-bound bLA. The root mean square deviation obtained after superimposition of the two structures is of only 0.68 Å [32]. LA fold displays two sub-domains separated by a cleft: a large α-helical sub-domain (Fig. 2, in red on the online color version, and in light grey on the black and white version) formed by three main α-helices and two short 3_{10} helices, and a small β-sheet sub-domain (Fig. 2, in blue on the online color version, and in dark grey on the black and white version) constituted by non-structured loops, a small three-stranded anti-parallel β-pleated sheet and a short 3_{10} helix [32] (Fig. 2). The tertiary structure of LA is further stabilized by four SS (Fig. 2, stick configuration, in green on the online color version, and in white on the black and white version). Cys73-Cys91 holds together the two sub-domains. Cys61-Cys77 links nonstructured loops, connect-

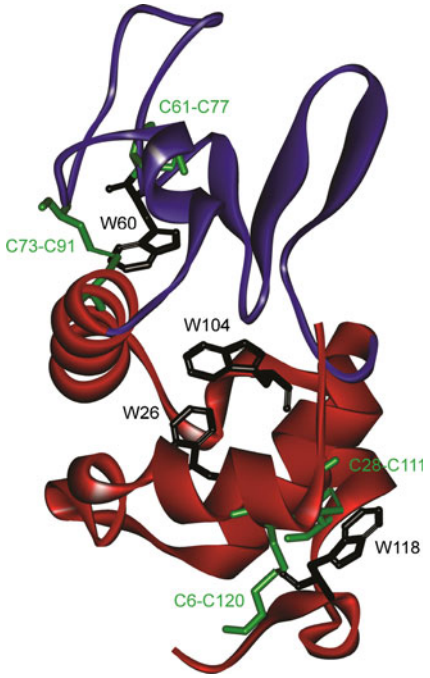

Fig. 2 3D structure of bovine apo-α-lactalbumin crystallized at high ionic strength (1F6S.pdb) [32]. 4 Trp (W) and 8 Cys (C) involved in 4 disulphide bridges (SS) are displayed (color online)

ing both sub-domains as well and is located in the β-sheet subdomain. Cys6-Cys120 and Cys28-Cys111 are situated in the α-helical sub-domain [33].

bLA contains four Trp residues (Fig. 2, stick configuration, in black) that are located within the two hydrophobic clusters of the protein, being part of two separate aromatic clusters [57]. Trp26, Trp60, and Trp104 belong to the aromatic cluster II. In the 3D structure of native bLA, the accessible solvent areas (ASA) of these Trp residues account for respectively 0.95, 2.70 and 13.96% of the total ASA of Trp in the tripeptide Gly-Trp-Gly. The correspondent values in crystallized apo-bLA are 0, 0.06 and 4.35%. The low relative values of ASA indicate that in the crystallized lattice of bLA these Trp residues are buried, even when the protein is Ca^{2+}depleted. Trp118 is situated in aromatic cluster I and is more solvent exposed, displaying 13.96 and 12.32% of the ASA of Trp in Gly-Trp-Gly for native and apo-bLA respectively.

In the apo-bLA 3D crystal structure Trp residues are surrounded by potential fluorescence quenching groups (Table 1). Trp60 is in van der Waals contact (≤ 5.2 Å as defined by Li and Nussinov [58]) with Cys73-Cys91 (4.20 Å) and 6.24 Å away from Cys61-Cys77. Trp118 is in van der Waals contact with Cys28-Cys111 (4.74 Å). The closest distance between Trp104 and a SS bond is 7.93 Å. Trp 60 and Trp104 are also in van der Waals contact to other potential quenching groups, the peptide bonds of Lys94-Ile95 (4.09 Å) and Val92-Lys93 (5.08 Å) respectively. Similarly, Trp118 is direct contact with imizidole ring of His32

Table 1 Distances between Trp residues and its potential quenchers in the 3D crystallized structures of native and apo-bLA (at high ionic strength).The values correspond to the shortest distances between the atoms involved in the quenching of Trp residues and the indole side-chain atoms of Trp residues. In bold are highlighted the Trp-quencher pairs for which there is direct van der Vaals contact (≤ 5.2 Å as defined by Li and Nussinov [58])

Pair		Distance (Å)	
Tryptophan	Potential Quencher	Apo-bLA	Native bLA
Trp26	**Trp104**	**3.61**	**3.78**
Trp26	Cys28-Cys111	8.38	8.37
Trp26	Cys6-Cys120	13.36	14.81
Trp60	Cys61-Cys77	6.24	6.43
Trp60	**Cys73-Cys91**	**4.20**	**4.67**
Trp60	**Peptide bond of Lys94-Ile95**	**4.09**	**3.76**
Trp104	**Peptide bond of Val92-Lys93**	**5.08**	**5.06**
Trp104	Cys28-Cys111	8.95	9.06
Trp104	Cys73-Cys91	7.93	7.80
Trp118	Cys6-Cys120	8.07	9.60
Trp118	**Cys28-Cys111**	**4.74**	**5.15**
Trp118	**His32**	**4.12**	**3.86**
Trp118	Peptide bond of Val27-Cys28	5.70	5.70

(4.12 Å) and close to the peptide bond Val27-Cys26 (5.70 Å). In its protonated form, the imidazole ring of histidine is known to quench substantially Trp fluorescence in proteins [59, 60]. The indole side-chains of Trp26 and Trp104 are also in van der Waals contact (3.61 Å), allowing for resonance energy transfer. Similar distances are observed for the structure of native bLA. The same structural features have been pointed out by Vanhooren et al. for native goat LA [61].

Steady State Fluorescence Emission

Fluorescence emission intensity of apo-bLA (340 nm) upon continuous 295 nm excitation is displayed in Fig. 3. A rapid increase in fluorescence emission intensity (~17%) is observed after 1.7 h of illumination, peaking at ~2.7 h.

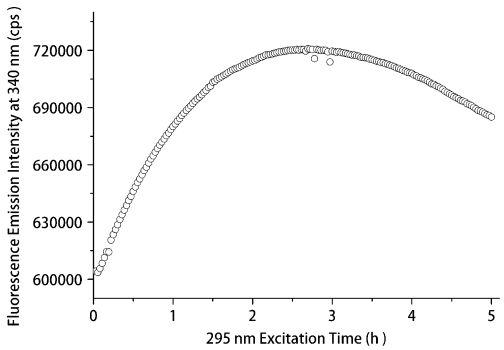

Fig. 3 Fluorescence emission intensity of apo-bLA versus 295 nm illumination time. Emission was monitored at 340 nm

Afterwards, fluorescence emission intensity decreases with further illumination.

Excitation spectra (em. 340 nm) and emission spectra (exc. 295 nm) were acquired prior and after 1–5 h excitation at 295 nm. The observed increase in fluorescence excitation intensity is correlated with an increase in fluorescence emission intensity for the first 2 h of 295 nm excitation (Fig. 4a). Furthermore, the longer the illumination time the larger the fluorescence emission red-shift (Fig. 4a and d).

Normalized excitation spectra with emission set at 340 nm and 320 nm acquired after apo-bLA 295 nm excitation for different illumination times are displayed in Fig. 4b and c, respectively. A progressive decrease in

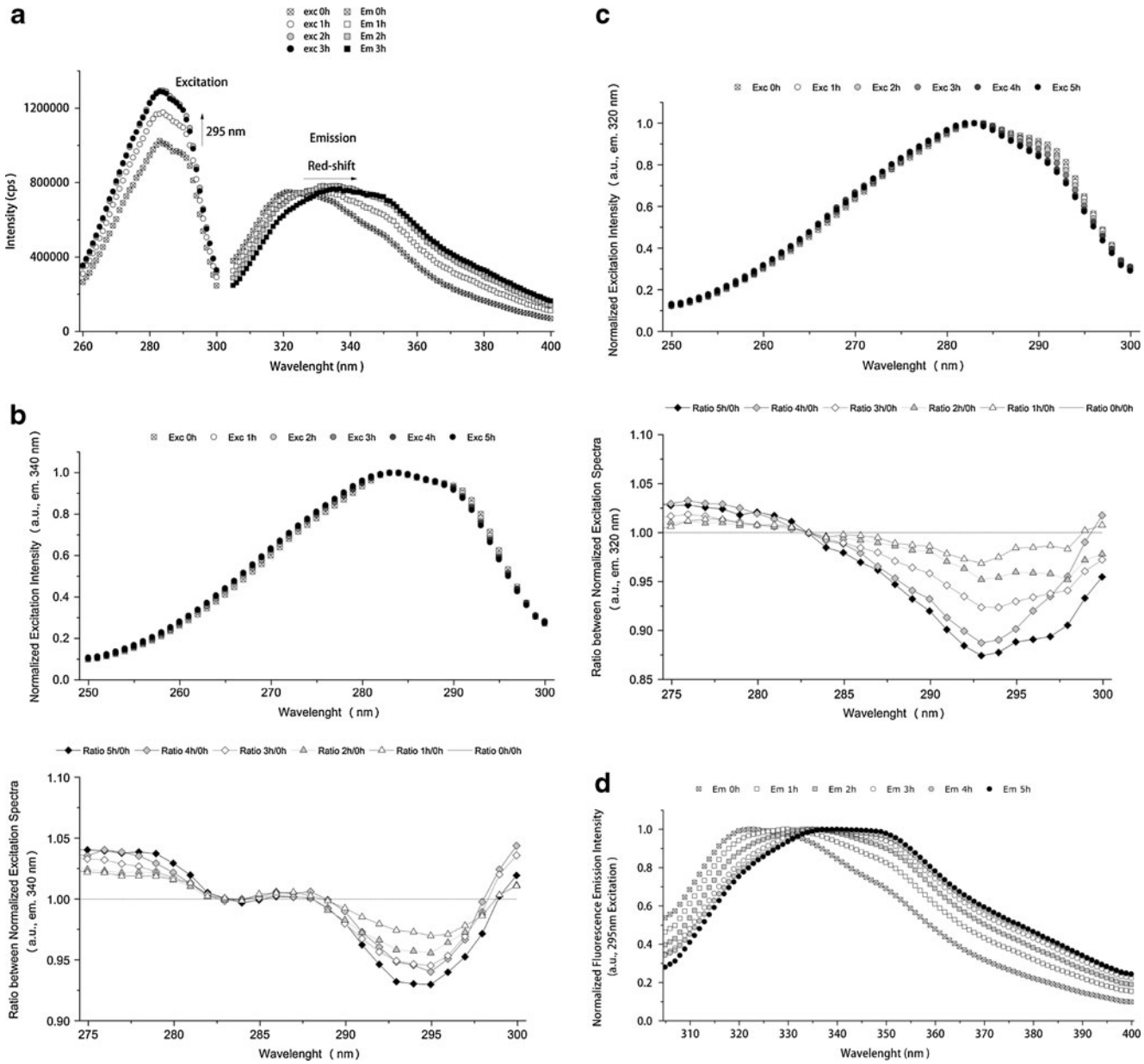

Fig. 4 **a**. Effect of 295 nm excitation time on excitation and emission intensity spectra. Excitation spectra were acquired fixing emission at 340 nm and emission spectra were acquired upon excitation at 295 nm. **b**. Top panel: Normalized excitation spectra of apo-bLA acquired after 0–5 h 295 nm illumination with emission at 340 nm; bottom panel: ratio between normalized excitation spectra displayed in the top panel (ratio between each excitation spectrum acquired after a specific illumination time and the excitation spectrum of non-illuminated apo-bLA sample). **c** Top panel: Normalized excitation spectra of apo-bLA acquired after 0–5 h 295 nm illumination with emission at 320 nm, respectively; bottom panel: ratio between normalized excitation spectra displayed in the top panel (ratio between each excitation spectrum acquired after a specific illumination time and the excitation spectrum of non-illuminated apo-bLA sample). **d** Normalized emission spectra of apo-bLA illuminated for different time periods and non-illuminated apo-bLA. Excitation was carried out at 295 nm

normalized excitation intensity with increasing illumination time is observed at 290–297 nm, wavelengths that only excite Trp (Fig. 4b, bottom panel). Figure 4c (top panel) shows a progressive decrease in normalized excitation intensity with increasing illumination time for wavelengths higher than 283 nm. The ratio between normalized excitation spectra (Fig. 4c, bottom panel) shows a progressive loss of intensity between 285 nm and 300 nm, wavelengths where Trp and Tyr are excited. After 5 h illumination, the ratio between normalized excitation spectra shows a 7.0% decrease in normalized excitation intensity at 295 nm when emission has been set at 340 nm (Fig. 4b) compared to 11.2% decrease when emission has been set at 320 nm (Fig. 4c).

A progressive red-shift in fluorescence emission is observed upon illumination (Fig. 4d). Non-illuminated apo-bLA displays maximum fluorescence emission at ~322.9 nm. After 5 h of excitation, this maximum is red-shifted to ~339.9 nm (Table 3 and Fig. 4d).

Thiol group's Quantification

The concentration of solvent accessible thiol groups in apo-bLA has been determined with Ellmann's reaction for a non-illuminated sample and for samples previously illuminated at 295 nm during 1–5 h at 25 °C. An increase in the average number of detected thiol groups per protein molecule is correlated with the increase in fluorescence emission intensity as a function of 295 nm illumination time (Fig. 5). The average number of detected thiol groups rapidly increases in the first 3 h of illumination, which is correlated with an exponential increase in fluorescence emission intensity (Fig. 5). After fluorescence maximum intensity is reached, a further increase in the average number of thiol detected thiol groups is observed (between 3 and 4 h of illumination). Data confirms that excitation of Trp residues in apo-bLA induces SS disruption. Ellmann's reaction also confirmed the presence of thiol formation in apo-bLA illuminated for 3.5 h with 295 nm light at different temperatures (9.3, 12.9, 15.6, 20.4, 24.9, 29.9 and 34.6 °C).

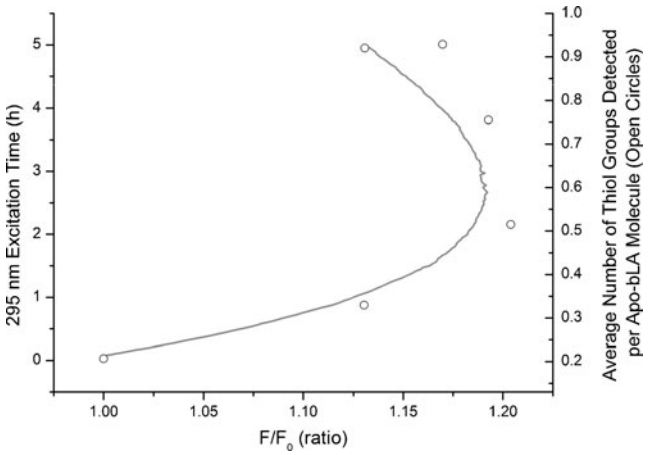

Fig. 5 Average number of free thiol groups detected per apo-bLA molecule (open circles) *versus* relative increase in fluorescence emission intensity (F/F_0) of apo-bLA with 295 nm excitation time. In gray is displayed fluorescence emission increase at 340 nm (F/F_0) versus 295 nm excitation time. Detection of free thiol groups was carried out using the Elmann's assay. The average number of free thiol groups formed upon UV-excitation the protein was estimated from the absorbance of the product of the Elmann's Assay reaction, TNB^{2-}, at 412 nm

CD Measurements

Far-UV CD spectra of fresh and 295 nm illuminated apo-bLA show that progressive Trp excitation (2.8 h) results only in minor changes in the secondary structure of the protein (12.33% signal loss at 222 nm, data not shown).

Temperature Dependent Studies

In order to study the temperature dependence of photoinduced reaction mechanisms in apo-bLA, fluorescence emission kinetic traces have been acquired at different temperatures. Kinetic traces recorded at 9.3, 12.9, 15.6, 20.4, 25.2 and 29.9 °C are displayed in Fig. 6a (gray and black lines). All traces display a strong initial increase in fluorescence emission intensity, peaking after a few hours. Afterwards, the fluorescence emission intensity is observed to decay upon further 295 nm illumination. At 34.6 °C, apo-bLA fluorescence emission intensity decreases upon excitation (data not shown). In Fig. 6a it can be observed that the largest total fluorescence emission increase is observed after illumination at the lowest temperature (9.3 °C). For the three lowest temperatures fluorescence emission increases more than 25%. Additionally, the higher the temperature the lower the maximum fluorescence emission intensity is. On the other hand, the higher the temperature, the steeper the initial slope of fluorescence emission increase is, indicating an increase in the rate of fluorescence emission increase k (see paragraph below and Table 2).

Fitted kinetic traces are displayed in Fig. 6a (color traces on the online version, and black lines on the black and white version). Fitted parameters and root mean square deviation (R^2) are displayed in Table 2. Both constants C_1 and C_2 decrease with temperature increase, whereas the rate constant k increases with temperature. In the exponential model used the constant C_1 defines the maximum fluorescence intensity emission. The fluorescence emission intensity is directly proportional to the value of C_1 in the whole time-trace. C_2 affects both the initial value of fluorescence emission intensity (value at time zero) and the steepness of the slope of fluorescence emission intensity increase. The

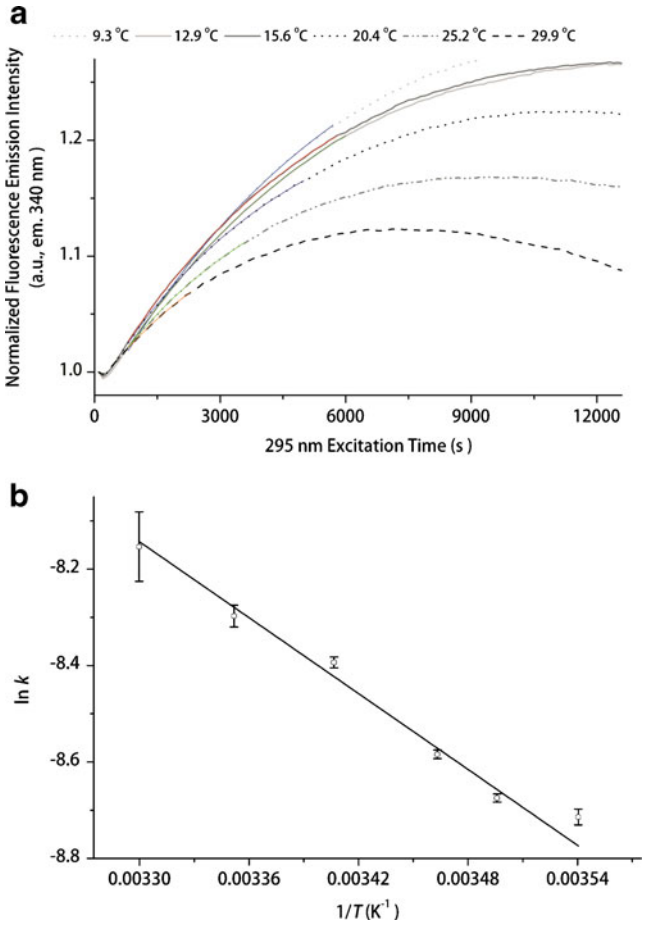

Fig. 6 **a** Black and white kinetic traces: apo-bLA experimental fluorescence emission intensity (em 340 nm) as a function of 295 nm illumination time at different temperatures (9.3, 12.9, 15.6, 20.4, 25.2, and 29.9 °C). Highlighted traces: fitting of experimental data from 800 s till the time corresponding to 95% of maximum fluorescence emission intensity. Fitting was carried out using an exponential function $F(t)=C_1\text{-}C_2.e^{-kt}$. Fitted parameter values and correspondent errors, and root mean square error value were obtained after fitting each kinetic trace. **b** Arrhennius plot showing the linear correlation between the logarithm of the rate constant ln k and the inverse of temperature $1/T$ (R^2=0.98429). Calculated parameters: E_a=21.8± 2.3 kJ.mol^{-1} and A_0=1.67±1.57 s^{-1}. Uncertainty errors for ln k values are displayed with error bars

higher the value of C_2 the fastest the fluorescence emission intensity increase is. The rate constant k does not influence the magnitude of the fluorescence emission intensity increase. The highest the rate constant k, the fastest the fluorescence emission intensity increase is. In Fig. 6b is displayed the Arrhenius plot of the experimental k values. The observed linear regression shows that k is temperature dependent following Arrhenius law. Activation energy (Ea) and pre-exponential factor (A_0) calculated from the slope ($-Ea/R$) and the $ln\ A_0$ were respectively 21.8±2.3 kJ. mol^{-1} and 1.67±1.57 s^{-1}.

In Fig. 7 are displayed the fluorescence emission spectra (exc 295 nm) for non-illuminated apo-bLA (A) and after 3.5 h of 295 nm illumination (B) at each temperature. Maximum fluorescence intensity of non-illuminated apo-bLA is observed at 322.9 nm at temperatures between 9.3 and 29.9 °C (A, Table 3). Fluorescence emission at 34.6 °C becomes 11 nm red-shifted (A, Table 3). Fluorescence emission intensity at 340 nm increases linearly with decreasing temperature between 9.3 and 29.9 °C: F_{340nm}=−6742 T+ 765787, R^2=0.95. After 3.5 h of 295 nm illumination, fluorescence emission becomes red-shifted at all temperatures (B). The largest shifts are observed between 12.9 and 29.9 °C, ranging between 13 and 17 nm (Table 3). A 5 nm red shift is observed at 34.6 °C.

Discussion

Non-illuminated apo-bLA at pH 8.55 and 25 °C shows maximum Trp fluorescence emission at 322.9 nm (295 nm excitation, Fig. 4a and Table 3), a value close to the maximum of emission of Ca^{2+}-bound bLA at 325 nm (300 nm excitation and neutral pH) [62]. The aromatic clusters I and II contain approximately half of the residues involved in the packing of the two hydrophobic clusters of bLA, which makes Trp suited to serve as solvent accessibility reporter group to study structural changes in hydrophobic regions of the protein [57]. In native goat LA Trp26 is the strongest contributor for Trp fluorescence, due to the lack of direct quenching compared to the other Trp residues [61]. Trp26 belongs to the aromatic cluster II, which includes also Trp60 and Trp104. These Trp residues are quite protected from the solvent in native bLA as shown by the calculated ASA values (see Results section) and previous crystallography, NMR and hydrogen exchange

Table 2 Fitted parameter values and correspondent errors, and root mean square value obtained after fitting each temperature dependent 340 nm fluorescence emission kinetic trace displayed in Fig. 6a to the equation $F(t) = C_1 - C_2e^{-kt}$

T (°C)	C_1	C_2	k (s^{-1})	R^2
9.3	1.37±0.004	0.402±0.003	1.64E-04±2.73E-06	0.99986
12.9	1.33±0.002	0.356±0.001	1.71E-04±1.44E-06	0.99995
15.6	1.32±0.002	0.340±0.001	1.87E-04±1.67E-06	0.99994
20.4	1.25±0.002	0.274±0.001	2.26E-04±2.57E-06	0.99992
25.2	1.20±0.003	0.221±0.002	2.49E-04±5.64E-06	0.99989
29.9	1.16±0.008	0.174±0.007	2.88E-04±2.07E-05	0.99977

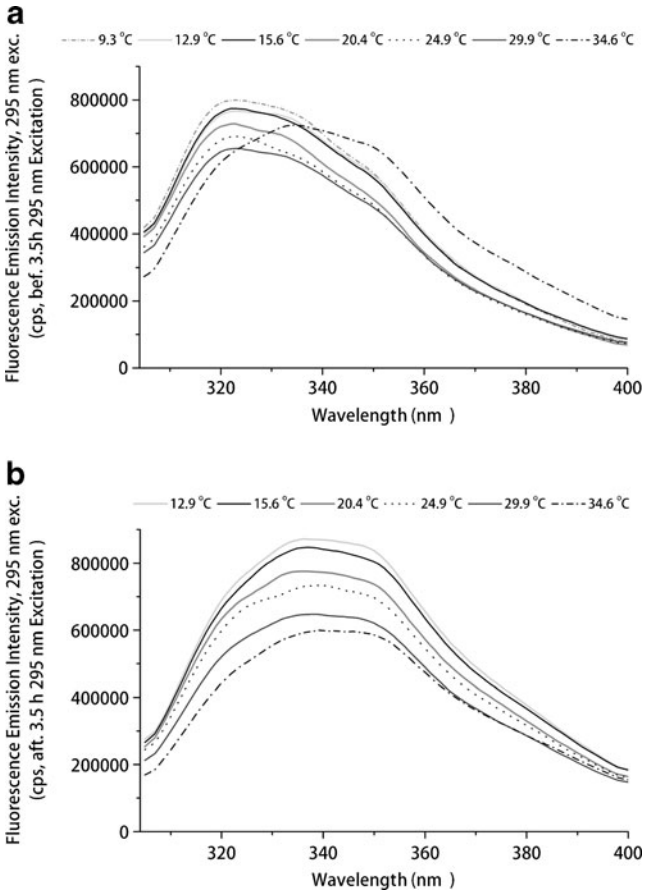

Fig. 7 **a** Emission spectra (exc 295 nm) of apo-bLA acquired before 295 nm illumination (fresh solutions) at different temperatures (9.3, 12.9, 15.6, 20.4, 24.9, 29.9 and 34.6 °C). **b** Fluorescence emission intensity spectra (exc 295 nm) of apo-bLA acquired after 3.5 h of 295 nm illumination at different temperatures (9.3, 12.9, 15.6, 20.4, 24.9, 29.9 and 34.6 °C)

Table 3 Effect of 295 nm excitation time and temperature on the wavelength at maximum fluorescence emission ($\lambda_{max\ emission}$) of apo-bLA (data displayed in Fig. 4d, 9A and 9B). Data was acquired at pH 8.55

Fig. 4d	Illum. time (h)	$\lambda_{max\ emission}$ (nm)	$\Delta\lambda$ ($\lambda_{after\ illumination} - \lambda_{0h\ illumination}$) (nm)
	0	322.9	-
	1	329.9	7
	2	333.9	11
	3	334.9	12
	4	336.9	14
	5	339.9	17
Fig. 7a	T (ºC)	$\lambda_{max\ emission}$ (nm)	$\Delta\lambda$ ($\lambda_{Ti} - \lambda_{T=9.3\,°C}$) (nm)
	9.3	322.9	0
	12.9	322.9	0
	15.6	322.9	0
	20.4	322.9	0
	24.9	322.9	0
	29.9	322.9	0
	34.6	333.9	11
Fig. 7b	T (ºC)	$\lambda_{max\ emission}$ (nm)	$\Delta\lambda$ ($\lambda_{after\ 3.5h\ exc.} - \lambda_{0h\ exc}$) (nm)
	9.3	-	-
	12.9	335.9	13
	15.6	336.9	14
	20.4	335.9	13
	24.9	339.9	17
	29.9	337.9	15
	34.6	338.9	5

experiments studies [32, 45]. There is no major shift in wavelength of maximum Trp fluorescence emission or considerable changes in the spectrum shape for apo-bLA reported here compared to the native Ca^{2+} bound protein [62]. This indicates that the Trp residues remain buried.

At high ionic strength there are no significant differences in Trp solvent exposure between native and apo-bLA, as suggested by the calculated ASA values and previously mentioned crystallography and NMR hydrogen exchange experiments [32, 45]. The crystallography study shows small structural changes in the aromatic cluster II, due to disruption of some of the native interactions in apo-bLA. In order to maintain high values of ionic strength in the experiments above mentioned, NaCl was added to the buffer. Tris, present in the buffer in our experiments, stabilizes LA conformation by simple charge screening effect [46]. Near-UV CD experiments carried out in Tris HCl pH 8.0 with similar charge screening conditions (number of Tris molecules per number of protein molecules) show minor losses of ellipticity of apo-bLA (less than 6% at 270 nm) relatively to native bLA at 5 °C [46]. The observations above indicate that, before UV-illumination, the majority of the apo-bLA molecules in our experiments are in a native-like conformation. The wavelength at maximum Trp fluorescence emission in apo-bLA is the same between 9.3 and 29.9 °C (Fig. 7a and Table 3). It suggests that there should be no considerable differences in the structural stability of apo-bLA molecules in this temperature range.

Continuous 295 nm Trp excitation of apo-bLA leads to an increase in fluorescence emission intensity at 340 nm in the first hours of illumination (Figs. 3 and 6a). Cutinase [17] and horseradish peroxidase [63] display similar fluorescence behavior upon Trp excitation: an increase in fluorescence yield was directly related to light induced damage of strong protein fluorescence quenchers located in close spatial proximity of the proteins' aromatic residues. Fluorescence yield increase in cutinase was caused by light induced cleavage of disulphide bridges mediated by Trp excitation, resulting in a 10-fold increase of fluorescence emission [17]. Free thiol groups are formed upon continuous 295 nm Trp excitation of apo-bLA (Fig. 5), indicating that Trp irradiation induces SS bond breakage. The average

number of thiol groups formed per apo-bLA molecule may be higher than the detected by the Elmann's assay and shown in Fig. 5 (maximum of 0,92 thiol groups formed per apo-bLA molecule) . Previous reports have shown incomplete reaction of protein sulfhydryls with DTNB, due to steric or electrostatic constraints [64–67]. Light induced disruption of SS bonds is correlated with the observed fluorescence emission intensity increase of apo-bLA. Disulphide bridge disruption mediated by UV excitation of aromatic residues in proteins has been previously reported for Ca^{2+} bound goat LA [49, 50]. In calcium bound and apo-goat-LA thiol formation is observed upon continuous Trp excitation but no direct correlation was made between the kinetics of thiol formation and the kinetics of fluorescence emission intensity increase upon UV illumination [49]. Breakage of Cys61-Cys77, Cys73-91 and Cys6-Cys120 has been verified upon continous UV-irradiation of goat LA [49, 50]. All Trp residues contributed to the photolytic cleavage of goat SS bonds. UV-excitation of human LA only yields the disruption of Cys61-Cys77 and Cys73-91 [48]. Breakage of Cys28-Cys111 was not found either in goat or in human LA [48–50].

Trp fluorescence emission is significantly red-shifted upon prolonged 295 nm excitation. The longer the 295 nm excitation time the larger the red-shift: from 7 nm after 1 h to 17 nm after 5 h excitation. This observation is consistent with one or more Trp residues becoming more solvent accessible with illumination time. It suggests a conformational change in apo-LA molecules with Trp excitation, leading to solvent exposure of the protein aromatic clusters. After 5 h of 280 nm (data not shown) and 295 nm illumination, maximum fluorescence emission intensity is observed at ~340 nm (Table 3), a value close to the wavelength of maximum fluorescence emission intensity of partly denaturated bLA at pH 2 (frequently termed classical MG) of ~343 nm [68]. The red shift observed in bLA fluorescence emission when it adopts the mentioned molten globule conformation is due to the movement of the Trp residues into a more solvent-exposed environment compared with native bLA [68]. Far-UV CD spectra of 295 nm illuminated apo-bLA show only minor loss of secondary structural features after 2.8 h of illumination (see Results section). Vanhooren at al. [49] reported similar results for apo-goat-LA in the far-UV region (200–250 nm). It was not feasible to carry out near-UV CD studies in this work, due to the excessive protein concentration required. For such high apo-bLA concentrations, we did not manage to obtain fluorescence emission kinetics similar to the ones here presented. Near-UV CD spectrum of apo-goat-LA showed profound losses of ellipticity (maximally around 270 nm) after excitation of the protein with UV-light [49]. These observations indicate that Trp excitation of apo-bLA and subsequent cleavage of SS bonds induces conformational changes preferentially in the protein's aromatic clusters and that the protein's secondary structure is less affected.

The gradual increase in fluorescence emission intensity here observed can result from conformational changes suffered by apo-bLA upon continuous 295 nm illumination. Quenching groups surround Trp residues in apo-bLA structure including SS bonds, peptide bonds and one histidine residue (see Fig. 1 and Results section). Trp26 is not prone to direct quenching from nearby groups but is subject to indirect quenching by energy transfer to Trp104, through resonance energy transfer. This is supported by experimental observations in goat LA [61]. Trp60 and Trp118 are strongly quenched by nearby SS bonds in goat [61] and human LA [69], which is consistent with the apo-bLA structural features here presented (see Table 1 and Results section). Disulphide bridges are the strongest Trp fluorescence quenching groups [60]. Once broken, SS no longer efficiently quench protein fluorescence. This would explain e.g. an increase in Trp60 fluorescence, upon continuous UV-excitation, assuming that neighbor Cys73-Cys91 and Cys61-Cys77 are also disrupted in apo-bLA. Conformational changes in the aromatic clusters of apo-bLA induced upon UV-excitation may also contribute to an increase in Trp emission intensity due to disruption of the resonance couple Trp26-Trp104, or changes of Trp residues spatial position relatively to the quenching groups.

The observations presented here are correlated with similar fluorescence changes (fluorescence emission increase and red-shift in fluorescence emission spectra) observed upon dithiothreitol chemical reduction of two SS bonds (Cys6-Cys120 and Cys28-Cys111) and all SS bonds in native and apo-bLA [70]. These fluorescence changes have been associated with conformational changes of the protein and formation of MG-like structures [70]. Furthermore, Cys depleted mutant of human LA forms a MG conformation, maintaining most of the native-like structure, more precisely a compact α-domain, showing that the architecture of compact α-helical sub-domain of the protein is determined by the polypeptide sequence and not a direct result of SS bond cross-linking [71]. The correlation between fluorescence emission intensity increase and formation of thiol groups upon 295 nm excitation suggests that the conformational changes on the protein are caused by disulphide bridge disruption, which leads to fluorescence intensity increase. Furthermore, increase in the fluorescence emission intensity and red-shift of the fluorescence emission has also been previously observed when bLA is partly denaturared at pH 2 or when native bLA suffers partial heat denaturation in comparison with native bLA [68]. In these experiments these spectral changes were related to the transition of the protein to MG-like conformations. Fluorescence emission intensity increase as well as a red-shift in fluorescence emission spectra has also

been observed upon UV illumination of Ca^{2+} bound and apo bovine, human and goat LA [48–50], for which light induced cleavage of SS bonds was verified. Trp irradiation of hen egg white lysozyme (a protein structurally homologous to α-lactalbumin [72] induces similar fluorescence changes, which are also related to photolysis of SS bonds of the protein [73].

The progressive loss in normalized excitation intensity upon continuous 295 nm excitation of apo-bLA observed at wavelengths where Trp absorbs (Fig. 4b and c) indicates likely photo-bleaching and/or chemical photo-degradation of Trp specii. The observed red-shift in apo-bLA Trp emission with illumination time also contributes to the observed loss in excitation intensity when emission is set at 320 nm.

As previously mentioned, constant λ_{max} fluorescence emission observed from 9.3 to 29.9 °C indicates that no conformational change has occurred in apo-bLA in this temperature range. The observed 11 nm red-shift in emission of non-illuminated apo-bLA between 29.9 and 34.6 °C (Table 3, Fig. 7a) indicates that a conformational change occurs in apo-bLA before illumination in this temperature interval. Data present in Table 3 and Fig. 7b demonstrates that UV illumination of apo-bLA induced local conformational changes at all temperatures, leading to the same fluorescence emission changes reported at 25 °C: fluorescence emission intensity increase and red-shift in Trp fluorescence emission. The kinetics of fluorescence emission intensity increase at 340 nm upon continuous Trp excitation is faster at higher temperatures (Fig. 7a and Table 2). On the other hand the observed increase in fluorescence emission intensity upon illumination is lower at higher temperatures due to dynamic solvent quenching (Results and Fig. 6a). At 34.6 °C a continuous decrease in fluorescence emission intensity is observed upon 295 nm illumination of apo-bLA, which should be correlated with the conformational transition observed between 29.9 and 34.6 °C in non-illuminated apo-bLA.

The physical interpretation of the exponential equation used for fitting the temperature dependent fluorescence emission time traces is that Trp excited specii are involved in a first order reaction and that the reaction constant is proportional to the rate constant of fluorescence increase (k). For the photo-induced cleavage of SS bonds in cutinase, Neves-Petersen et al. [17] described the fluorescence emission increase using a model that assumes a chemical conversion (1st order photo-induced reaction) of low quantum yield native Trp specii to high quantum yield Trp specii. We consider a similar mechanism for apo-bLA involving the chemical conversion between one pool of molecules with intact disulphide bonds and low fluorescence emission intensity and another with broken SS bonds, MG-like intermediate conformations, and high fluorescence emission intensity. This chemical conversion between the Trp molecules is associated with the increase in Trp fluorescence emission intensity. Thus, the rate of fluorescence emission intensity increase k should be related to the kinetic rate of conversion between the two pools of molecules.

Neves-Petersen et al. have previously reported that the UV-light induced disruption of SS in a protein upon Trp excitation is mediated by the presence of solvated electrons originated from the photoionization of aromatic residues such as Trp and Tyr [10]. Trp photoionization, a major photo-oxidation pathway of many proteins [10, 11] can take place from the pre-fluorescent state S^* and from S_1 giving rise to transient specii (see schemes 1–14) which in proteins will lead to disulphide bridge disruption and free thiol formation. The 21.8 $kJ.mol^{-1}$ Arrhenius activation energy obtained is smaller but comparable to previously reported 50 $kJ.mol^{-1}$ activation energy of thermal photoionization from the singlet excited S_1 of Tryptophan in solution [14]. The presence of other groups (e.g. proton transfer groups, electron acceptors such as disulphide bridges) nearby Trp residues can favor Trp photoionization, lowering the energy barrier required for the reaction, which is correlated with a lower E_a value for Trp photoionization in apo-bLA. Only two decay pathways of excited Trp are known to be favored by a temperature increase: photoionization from S_1 and intramolecular proton transfer from the protonated amino group to the indole ring, not possible in proteins due to the presence of the peptide bond [14]. Photoionization yield has been determined upon measurement of the concentration of generated solvated electron or the concentration of Trp radical formed at each temperature [14]. On the other hand, photoionization yield from higher excited states S^* is known to decrease with temperature [15] and ionization rate constant from S^* is reported to be temperature independent [14]. Furthermore, ^{S*}Trp photoionization in solution yields e_{aq-} within 200 fs after irradiation [12, 13]. ^{S*}Trp photoionization competes with relaxation to S_1. Flash photolysis studies of cutinase and lysozyme show formation of aqueous e_{aq-} within 12 ns after excitation [10]. These observations suggest that Trp photoionization in apo-bLA occurs from S_1. However, delayed detection of solvated electrons after UV excitation of proteins could be due to the fact that Trp is initially buried in the 3D lattice of the protein and not solvent exposed.

Conclusions

Prolonged excitation of Trp residues in apo-bLA induces an increase in fluorescence emission at 340 nm coupled with a red-shift in Trp emission and SS bond disruption. We show that Trp fluorescence spectral changes and disulphide

bridge disruption in apo-bLA are correlated with a chemical conversion between two pools of molecules. Native apo-bLA molecules with intact SS and low fluorescence emission intensity Trp emission are gradually converted into apo-bLA molecules with disrupted disulphide bridges, MG-like conformation, high fluorescence emission intensity and red-shifted Trp emission. A 1st order reaction was an excellent model for the temperature-dependent 340 nm emission kinetic traces. Data suggests that photoionization from the S_1 state is one of the major mechanisms involved in the photolysis of SS in apo-bLA and in the reaction mechanism above described. These studies provide a deeper insight into the photophysical and photochemical processes activated upon UV-illumination proteins.

In the latest years, UV-light (mostly UVC-light – 200–280 nm) has been explored as an alternative method for microbial disinfection of liquid foods, beverages and growth media [74]. Thermal treatment is the traditional method for pasteurization of cheese whey, but has been found to be time consuming and cause denaturation of the whey protein [75, 76]. UV-light continuous sterilization technique of cheese whey and milk has been shown to be effective in eliminating certain microorganisms [75–77]. However, no considerable attention has been given to the potential effects of UV-light on the nutrients present in the UV-pasteurized products. LA constitutes 20–25% of the whey protein [78]. The observations reported in the present paper together with previous reports [48–50] show that UV-light exposure induces structural changes on native and apo-LA. Loss of structure most likely leads to loss in activity, as reported by Vanhooren et al, where ~35% of the original lactose synthase regulatory activity of native goat-LA has been lost after 3 h of 290 nm illumination [50]. Furthermore, Elmnaser et al. recently reported some structural changes upon light treatment (including UV-light) of milk proteins [79]. A more careful analysis should be undertaken when studying UV-light as an alternative for pasteurization and sterilization processes in whey and other milk derivatives where LA is present since the biological function of the protein might also be affected, and protein denaturation may occur as well. Experimental parameters such as UV-irradiation power and illumination time of the medium should be optimized in order to ensure microorganism destruction but avoiding affecting the structure and the function of whey protein. This same concern should be extended to all protein containing food products.

Acknowledgments M.C. acknowledges the support from "Fundação para a Ciência e Tecnologia" (FCT) for the PhD grant (SFRH/BD/61012/2009) supported by "Programa Operacional Potencial Humano" (POPH) in the framework of "Quadro de Referência Estratégico Nacional" (QREN) and co-financed by the European Social Fund ("Fundo Social Europeu", FSE).

References

1. Bent DV, Hayon E (1975) Excited-state chemistry of aromatic amino-acids and related peptides .3. tryptophan. J Am Chem Soc 97(10):2612–2619
2. Creed D (1984) The photophysics and photochemistry of the near-UV absorbing amino-acids .1. Tryptophan and its simple derivatives. Photochem Photobiol 39(4):537–562
3. Bent DV, Hayon E (1975) Excited-state chemistry of aromatic amino-acids and related peptides .1.tyrosine. J Am Chem Soc 97 (10):2599–2606
4. Creed D (1984) The photophysics and photochemistry of the near-uv absorbing amino-acids .2. Tyrosine and its simple derivatives. Photochem Photobiol 39(4):563–575
5. Bent DV, Hayon E (1975) Excited-state chemistry of aromatic amino-acids and related peptides .2.phenylalanine. J Am Chem Soc 97(10):2606–2612
6. Creed D (1984) The photophysics and photochemistry of the near-UV absorbing amino-acids.3. Cystine and its simple derivatives. Photochem Photobiol 39(4):577–583
7. Du H, Fuh RA, Li J, Corkan A, Lindsey JS (1998) PhotochemCAD: a computer-aided design and research tool in photochemistry. Photochem Photobiol 68(2):141–142
8. Robbins RJ, Fleming GR, Beddard GS, Robinson GW, Thistlethwaite PJ, Woolfe GJ (1980) Photophysics of aqueous tryptophan: pH and temperature effects. J Am Chem Soc 102(20):6271–6279
9. Tsentalovich YP, Snytnikova OA, Sagdeev RZ (2004) Properties of excited states of aqueous tryptophan. J Photochem Photobiol A: Chem 162(2–3):371–379
10. Neves-Petersen MT, Klitgaard S, Pascher T, Skovsen E, Polivka T, Yartsev A, Sundström V, Petersen SB (2009) Flash photolysis of cutinase: identification and decay kinetics of transient intermediates formed upon UV excitation of aromatic residues. Biophys J 97(1):211–226
11. Devies MJ, Truscott RJW (2001) Photo-oxidation of proteins and its role in cataractogenesis. J Photochem Photobiol B: Biol 63(1–3):114–125
12. Mialocq JC, Amouyal E, Bernas A, Grand D (1982) Picosecond laser photolysis of aqueous indole and tryptophan. J Phys Chem 86(16):3173–3177
13. Peon J, Hess GC, Pecourt J-ML, Yuzawa T, Kohler B (1999) Ultrafast photoionization dynamics of indole in water. J Phys Chem 103(14):2460–2466
14. Sherin PS, Snytnikova OA, Tsentalovich YP (2004) Tryptophan photoionization from prefluorescent and fluorescent states. Chem Phys Lett 391(1–3):44–49
15. Sherin PS, Snytnikova OA, Tsentalovich YP (2006) Competition between ultrafast relaxation and photoionization in excited prefluorescent states of tryptophan and indole. J Chem Phys 125 (14):144511
16. Kerwin BA, Remmele RL Jr (2006) Protect from light: photodegradation and protein biologics. J Pharmac Sci 96(6):1468–1479
17. Neves-Petersen MT, Gryczynski Z, Lakowicz J, Fojan P, Pedersen S, Petersen E, Petersen SB (2002) High probability of disrupting a disulphide bridge mediated by an endogenous excited tryptophan residue. Protein Sci 11(3):588–600
18. Hoffman MZ, Hayon E (1972) One-electron reduction of the disulfide linkage in aqueous solution. Formation, protonation, and decay kinetics of the RSSR- radical. J Am Chem Soc 94(23):7950–7957

19. Neves-Petersen MT, Snabe T, Klitgaard S, Duroux M, Petersen SB (2006) Photonic activation of disulfide bridges achieves oriented protein immobilization on biosensor surfaces. Protein Sci 15(2):343–351
20. Skovsen E, Kold AB, Neves-Petersen MT, Petersen SB (2009) Photonic immobilization of high-density protein arrays using Fourier optics. Proteomics 9(15):3945–3958
21. Parracino A, Gajula GP, Gennaro AK, Correia M, Neves-Petersen MT, Rafaelsen J, Petersen SB (2010), Photonic immobilization of BSA for nanobiomedical applications: creation of high density microarrays and superparamagnetic bioconjugates. Biotechnol Bioeng. 2010 Dec 1. [Epub ahead of print]
22. Parracino A, Neves-Petersen MT, di Gennaro AK, Pettersson K, Lövgren T, Petersen SB (2010) Arraying prostate specific antigen PSA and Fab anti-PSA using light-assisted molecular immobilization technology. Protein Sci 19(9):1751–1759
23. Duroux M, Skovsen E, Neves-Petersen MT, Duroux L, Gurevich L, Petersen SB (2007) Light-induced immobilisation of biomolecules as a replacement for present nano/micro droplet dispensing based arraying technologies. Proteomics 7(19):3491–3499
24. Snabe T, Røder GA, Neves-Petersen MT, Petersen SB, Buus S (2006) Oriented coupling of major histocompatibility complex (MHC) to sensor surfaces using light assisted immobilisation technology. Biosens Bioelectron 21(8):1553–1559
25. Neves-Petersen MT, Snabe T, Klitgaard S, Duroux M, Petersen SB (2006) Photonic Biosensors: UV light induced molecular switch allows sterically oriented immobilisation of biomolecules and the creation of protein nanoarrays. Protein Sci 15(2):343–351
26. Duroux M, Duroux L, Neves-Petersen MT, Skovsen E, Petersen SB (2007) Novel photonic technique creates micrometer resolution protein arrays and provides a new approach to coupling of genes, peptide hormones and drugs to nanoparticle carriers. Appl Surf Sci 253(19):8125–8129
27. Duroux M, Gurevich L, Neves-Petersen MT, Skovsen E, Duroux L, Petersen SB (2007) Using light to bioactivate surfaces: a new way of creating oriented, active immunobiosensors. Appl Surf Sci 254(4):1126–1130
28. Skovsen E, Duroux M, Neves-Petersen MT, Duroux L, Petersen SB (2007) Molecular printing using UV-assisted immobilization of biomolecules. Int J Optomechatronics 1(4):383–391
29. Neves-Petersen MT, Duroux M, Skovsen E, Duroux L, Petersen SB (2009) Printing novel architectures of nanosized molecules with micrometer resolution using light. J Nanosci Nanotechnol 9 (6):3372–3381
30. Skovsen E, Neves-Petersen MT, Kold A, Duroux L, Petersen SB (2009) Immobilizing biomolecules near the diffraction limit. J Nanosci Nanotechnol 9(7):4333–4337
31. Skovsen E, Kold A, Neves-Petersen MT, Petersen SB (2009) Photonic immobilization of high density protein arrays using fourier optics. Proteomics 9(15):1–4
32. Chrysina ED, Brew K, Acharya KR (2000) Crystal structures of apo- and holo-bovine alpha-lactalbumin at 2.2-Å resolution reveal an effect of calcium on inter-lobe interactions. J Biol Chem 275 (47):37021–37029
33. Permyakov EA, Berliner LJ (2000) α-Lactalbumin: structure and function. FEBS Lett 473(3):269–274
34. Ramakrishnan B, Qasba PK (2001) Crystal structure of lactose synthase reveals a large conformational change in its catalytic component, the b1,4-Galactosyltransferase-I. J Mol Biol 310 (1):205–218
35. Kuwajima K (1996) The molten globule state of α-lactalbumin. FASEB J 10(1):102–109
36. Laureto PP, Frare E, Gottardo R, Fontana A (2002) Molten globule of bovine α-Lactalbumin at neutral pH induced by heat, trifluoroethanol, and oleic acid: a comparative analysis by circular dichroism spectroscopy and limited proteolysis. PROTEINS: Structure, Function, and Genetics 49(3):385–397
37. Cawthern KM, Permyakov E, Berliner LJ (1996) Membrane-bound states of alpha-lactalbumin: implications for the protein stability and conformation. Protein Sci 5(7):1394–1405
38. Aits S, Gustafsson L, Hallgren O, Brest P, Gustafsson M, Trulsson M, Mossberg AK, Simon HU, Mograbi B, Svanborg C (2009) HAMLET (human alpha-lactalbumin made lethal to tumor cells) triggers autophagic tumor cell death. Int J Cancer 124(5):1008–1019
39. Rammer P, Groth-Pedersen L, Kirkegaard T, Daugaard M, Rytter A, Szyniarowski P, Høyer-Hansen M, Klitgaard Povlsen L, Nylandsted J, Larsen JE, Jäättelä M (2010) BAMLET Activates a lysosomal cell death program in cancer cells. Mol Cancer Ther 9 (1):24–32
40. Pettersson-Kastberg J, Mossberg AK, Trulsson M, Yong YJ, Min S, Lim Y, O'Brien JE, Svanborg C, Mok KH (2009) alpha-Lactalbumin, engineered to be nonnative and inactive, kills tumor cells when in complex with oleic acid: a new biological function resulting from partial unfolding. J Mol Biol 394(5):994–1010
41. Hendrix TM, Griko YV, Privalov PL (1996) Energetics of structural domains in α-lactalbumin. Protein Sci 5(5):923–931
42. Pfeil W (1998) Is the molten globule a third thermodynamic state of proteins? The example of alpha-lactalbumin. Prot Struct Funct Genet 30(1):43–48
43. Veprintsev DB, Permyakov SE, Permyakov EA, Rogov VV, Cawtherm KM, Berliner LJ (1997) Cooperative thermal transitions of bovine and human apo-lactalbumins: evidence for a new intermediate state. FEBS Lett 412(3):625–628
44. Wilson G, Ford SJ, Cooper A, Hecht L, Wen ZQ, Barron LD (1995) Vibrational Raman optical activity of a-lactalbumin: comparison with lysozyme, and evidence for native tertiary folds in molten globule states. J Mol Biol 254(4):747–760
45. Wijesinha-Bettoni R, Dobson CM, Redfield C (2001) Comparison of the structural and dynamical properties of holo and apo bovine alpha-lactalbumin by NMR spectroscopy. J Mol Biol 307(3):885–898
46. Griko YV, Remeta DP (1999) Energetics of solvent and ligand-induced conformational changes in alpha-lactalbumin. Protein Sci 8(3):554–561
47. Jr O, Halskau R, Perez-Jimenez B, Ibarra-Molero J, Underhaug V, Muñoz AM, Sanchez-Ruiz JM (2008) Large-scale modulation of thermodynamic protein folding barriers linked to electrostatics. Proc Natl Acad Sci U S A 105(25):8625–8630
48. Permyakov EA, Permyakov SE, Deikus GY, Morozova-Roche LA, Grishchenko VM, Kalinichenko LP, Uversky VN (2003) Ultraviolet Illumination-induced Reduction of α-Lactalbumin disulfide bridges. PROTEINS: Structure, Function, and Genetics 51(4):498–503
49. Vanhooren A, Devreese B, Vanhee K, Van Beeumen J, Hanssens I (2002) Photoexcitation of tryptophan groups induces reduction of two disulfide bonds in goat α-Lactalbumin. Biochemistry 41 (36):11035–11043
50. Vanhooren A, De Vriendt K, Devreese B, Chedad A, Sterling A, Van Dael H, Van Beeumen J, Hanssens I (2006) Selectivity of tryptophan residues in mediating photolysis of disulfide bridges in goat α-Lactalbumin. Biochemistry 45(7):2085–2093
51. Masaki K, Masuda R, Takase K, Kawano K, Nitta K (2000) Stability of the molten globule state of a domain-exchanged chimeric protein between human and bovine α-lactalbumins. Protein Engineering 13(1):1–4
52. Riener CK, Kada G, Gruber HJ (2002) Quick measurement of protein sulfhydryls with Ellman's reagent and with 4,4′-dithiodipyridine. Anal Bioanal Chem 373:266–276
53. Riddles PW, Blakeley RL, Zerner B (1983) Reassessment of Ellman's reagent. Meth Enzymol 91:49–60
54. Tsodikov OV, Record MT Jr, Sergeev YV (2002) A novel computer program for fast exact calculation of accessible and molecular surface areas and average surface curvature. J Comput Chem 23(6):600–609

55. Richards FM (1977) Areas, volumes, packing and protein structure. Annu Rev Biophys Bioeng 6:151–176
56. Miller S, Janin J, Lesk AM, Chothia C (1987) Interior and surface of monomeric proteins. J Mol Biol 196(3):641–656
57. Mok KH, Nagashima T, Day IJ, Hore PJ, Dobson CM (2005) Multiple subsets of side-chain packing in partially folded states of alpha-lactalbumins. Proc Natl Acad Sci U S A 102(25):8899–8904
58. Li A-J, Nussinov R (1998) A set of van der waals and coulombic radii of protein atoms for molecular and solvent-accessible surface calculation, packing evaluation, and docking. PROTEINS: Structure, Function, and Genetics 32(1):111–127
59. Loewenthal R, Sancho J, Fersht AR (1991) Fluorescence spectrum of barnase: contributions of three tryptophan residues and a histidine-related pH dependence. Biochemistry 30 (27):6775–6779
60. Van Gilst M, Hudson BS (1996) Histidine-tryptophan interactions in T4 lysozyme: 'Anomalous' pH dependence of fluorescence. Biophys Chem 63(1):17–25
61. Vanhooren A, Illyes E, Majer Z, Hanssens I (2006) Fluorescence contributions of the individual Trp residues in goat alpha-lactalbumin. Biochim Biophys Acta 1764(10):1586–1591
62. Engel MFM, van Mierlo CPM, Visser AJWG (2002) Kinetic and Structural Characterization of Adsorption-induced Unfolding of Bovine α-Lactalbumin. J Biol Chem 277(13):10922–10930
63. Neves-Petersen MT, Klitgaard S, Carvalho ASL, Petersen SB, de Barros MRA, Pinho e Melo E (2007) Photophysics and Photochemistry of Horseradish Peroxidase A2 upon Ultraviolet Illumination. Biophys J 92(6):2016–2027
64. Grassetti DR, Murray JF Jr (1967) Determination of sulfhydryl groups with 2,2'- or 4,4'-dithiodipyridine. Arch Biochem Biophys 119(1):41–49
65. Han MK, Roseman S, Brand L (1990) Sugar transport by the bacterial phosphotransferase system. Characterization of the sulfhydryl groups and site-specific labeling of enzyme I. J Biol Chem 265(4):1985–1895
66. Wilson JM, Wu D, Motiu-DeGrood R, Hupe DJ (1980) A spectrophotometric method for studying the rates of reaction of disulfides with protein thiol groups applied to bovine serum albumin. J Amer Chemic Soc 102(1):359–363
67. Woodward J, Tate J, Herrmann PC, Evans BR (1993) Comparison of Ellman's reagent with N-(1-pyrenyl)maleimide for the determination of free sulfhydryl groups in reduced cellobiohydrolase I from Trichoderma reesei. J Biochem Biophys Methods 26(2–3):121–129
68. Wijesinha-Bettoni R, Gao C, Jenkins JA, Mackie AR, Wilde PJ, Mills EN, Smith LJ (2007) Heat treatment of bovine alpha-lactalbumin results in partially folded, disulfide bond shuffled states with enhanced surface activity. Biochemistry 46(34):9774–9784
69. Chakraborty S, Ittah V, Bai P, Luo L, Haas E, Peng ZY (2001) Structure and dynamics of the alpha lactalbumin molten globule: fluorescence studies using proteins containing a single tryptophan residue. Biochemistry 40(24):7228–7238
70. Ewbank JJ, Creighton TE (1993) Structural characterization of the disulfide folding intermediates of bovine alpha-lactalbumin. Biochemistry 32(14):3694–3707
71. Redfield C, Schulman BA, Milhollen MA, Kim PS, Dobson CM (1999) Alpha-lactalbumin forms a compact molten globule in the absence of disulfide bonds. Nat Struct Biol 6(10):948–952
72. Qasba PK, Kumar S (1997) Molecular divergence of lysozymes and alpha-lactalbumin. Crit Rev Biochem Mol Biol 32(4):255–306
73. Wu L-Z, Sheng Y-B, Xie J-B, Wang W (2008) Photoexcitation of tryptophan groups induced reduction of disulfide bonds in hen egg white lysozyme. J Molec Struct 882(1–3):101–106
74. Koutchma T (2009) Advances in ultraviolet light technology for non-thermal processing of liquid foods. Food Bioprocess Technol 2(2):138–155
75. Mahmoud NS, Ghaly AE (2004) On-line sterilization of cheese whey using ultraviolet radiation. Biotechnol Prog 20(2):550–560
76. Singh JP, Ghaly AE (2006) Reduced fouling and enhanced microbial inactivation during online sterilization of cheese whey using UV coil reactors in series. Bioprocess Biosyst Eng 29 (4):269–281
77. Altic LC, Rowe MT, Grant IR (2007) UV light inactivation of Mycobacterium avium subsp. paratuberculosis in milk as assessed by FASTPlaqueTB phage assay and culture. Appl Environ Microbiol 73(11):3728–3733
78. Hong Y-H, Creamer LK (2002) Changed protein structures of bovine β-lactoglobulin B and α-lactalbumin as a consequence of heat treatment. Int Dairy J 12:345–359
79. Elmnasser N, Dalgalarrondo M, Orange N, Bakhrouf A, Haertlé T, Federighi M, Chobert JM (2008) Effect of pulsed-light treatment on milk proteins and lipids. J Agric Food Chem 56(4):1984–1991

4.2 Paper 2

UV-light exposure of insulin: pharmaceutical implications upon covalent insulin dityrosine dimerization and disulphide bond photolysis

Manuel Correia, Maria Teresa Neves Petersen, Per Bendix Jeppesen, Søren Gregersen, and Steffen B. Petersen

PloS One, 2012, 7(12), e50733

OPEN ACCESS Freely available online

PLOS ONE

UV-Light Exposure of Insulin: Pharmaceutical Implications upon Covalent Insulin Dityrosine Dimerization and Disulphide Bond Photolysis

Manuel Correia[1], Maria Teresa Neves-Petersen[2,3]*, Per Bendix Jeppesen[4], Søren Gregersen[4], Steffen B. Petersen[2,5,6]

1 Department of Physics and Nanotechnology, Aalborg University, Aalborg, Denmark, **2** International Iberian Nanotechnology Laboratory (INL), Braga, Portugal, **3** NanoBiotechnology Group, Department of Biotechnology, Chemistry and Environmental Sciences, Aalborg University, Aalborg, Denmark, **4** Aarhus University Hospital, Aarhus Sygehus THG, Department of Medicine and Endocrinology MEA, Aarhus C, Denmark, **5** NanoBiotechnology Group, Department of Health Science and Technology, Aalborg University, Aalborg, Denmark, **6** The Institute for Lasers, Photonics and Biophotonics, University at Buffalo, The State University of New York, Buffalo, New York, United States of America

Abstract

In this work we report the effects of continuous UV-light (276 nm, ~2.20 W.m^{-2}) excitation of human insulin on its absorption and fluorescence properties, structure and functionality. Continuous UV-excitation of the peptide hormone in solution leads to the progressive formation of tyrosine photo-product dityrosine, formed upon tyrosine radical cross-linkage. Absorbance, fluorescence emission and excitation data confirm dityrosine formation, leading to covalent insulin dimerization. Furthermore, UV-excitation of insulin induces disulphide bridge breakage. Near- and far-UV-CD spectroscopy shows that UV-excitation of insulin induces secondary and tertiary structure losses. In native insulin, the A and B chains are held together by two disulphide bridges. Disruption of either of these bonds is likely to affect insulin's structure. The UV-light induced structural changes impair its antibody binding capability and *in vitro* hormonal function. After 1.5 and 3.5 h of 276 nm excitation there is a 33.7% and 62.1% decrease in concentration of insulin recognized by guinea pig anti-insulin antibodies, respectively. Glucose uptake by human skeletal muscle cells decreases 61.7% when the cells are incubated with pre UV-illuminated insulin during 1.5 h. The observations presented in this work highlight the importance of protecting insulin and other drugs from UV-light exposure, which is of outmost relevance to the pharmaceutical industry. Several drug formulations containing insulin in hexameric, dimeric and monomeric forms can be exposed to natural and artificial UV-light during their production, packaging, storage or administration phases. We can estimate that direct long-term exposure of insulin to sunlight and common light sources for indoors lighting and UV-sterilization in industries can be sufficient to induce irreversible changes to human insulin structure. Routine fluorescence and absorption measurements in laboratory experiments may also induce changes in protein structure. Structural damage includes insulin dimerization via dityrosine cross-linking or disulphide bond disruption, which affects the hormone's structure and bioactivity.

Citation: Correia M, Neves-Petersen MT, Jeppesen PB, Gregersen S, Petersen SB (2012) UV-Light Exposure of Insulin: Pharmaceutical Implications upon Covalent Insulin Dityrosine Dimerization and Disulphide Bond Photolysis. PLoS ONE 7(12): e50733. doi:10.1371/journal.pone.0050733

Editor: Rajagopal Subramanyam, University of Hyderabad, India

Received June 19, 2012; **Accepted** October 24, 2012; **Published** December 5, 2012

Funding: MC acknowledges the support from "Fundação para a Ciência e Tecnologia" (FCT) for the PhD grant (SFRH/BD/61012/2009) supported by "Programa Operacional Potencial Humano" (POPH) in the framework of "Quadro de Referência Estratégico Nacional" (QREN) and co-financed by the European Social Fund ("Fundo Social Europeu", FSE). The funders had no role in study design, data collection and analysis, decision to publish, or preparation of the manuscript.

Competing Interests: The authors have declared that no competing interests exist.

* E-mail: teresa.petersen@inl.int

Introduction

For several years, there has been significant interest on the effects of UV-light excitation on the structure and function of proteins [1–4]. This is particularly relevant for the food and pharmaceutical industries, and for the medical field where structural stability and activity of proteins as drugs or nutrients, is of nuclear importance. In the pharmaceutical industry, UV-light induced damage of proteins can occur during production, formulation, visual inspections, fill and finish operations, packaging, storage and delivery of the drug, since protein products will most likely be exposed to UV-light from natural or artificial light-sources [2,5]. The same may occur during handling and administration of pharmaceuticals to patients, in hospitals and clinics (e.g. use of intravenous bags for administration of drugs) [2,6]. A summary of possible UV-light induced reactions will be presented.

In proteins, the main targets of UV-light induced photo-degradation are the peptide backbone, tryptophan, tyrosine (Tyr, Y), phenylalanine, and cystine. In this work we will focus on Tyr photochemistry. The protein studied, insulin, does not contain any tryptophan residues. Furthermore, in this work insulin has been excited at 276 nm. At this wavelength and at neutral pH, Tyr absorption ($\varepsilon_{276\ nm} = 1362\ cm^{-1}.M^{-1}$ [7]) is higher than the absorption by cystine ($\varepsilon_{276\ nm} = 220\ cm^{-1}.M^{-1}$ for dimethylsulfide, model for cystine absorption [8]) or by phenylalanine ($\varepsilon_{276\ nm} = 3\ cm^{-1}.M^{-1}$ [7]).

Excitation of Tyr to higher electronic energy states is followed by distinct processes including relaxation by fluorescence to ground state, triplet state (^{3}Tyr) formation, reaction with oxygen to

form peroxy radicals, or excited state photochemical or photophysical processes, such as photoionization. Photoionization leads to the ejection of an electron from the residue, possibly yielding a solvated electron (e^-_{aq}), and a radical cation (^{1}Tyr-OH$^{\bullet+}$) followed by deprotonation resulting in formation of an uncharged radical (^{1}Tyr-O$^\bullet$) [2,3]. These processes are influenced by the pH of the solution, the temperature, the neighboring side-chains and the protein structure itself [2,3]. Furthermore, in proteins Tyr can transfer their excited state energy to tryptophan [2]. A complete overview of the photophysical and photochemical mechanisms of Tyr can be found in our previous publication [2] and other literature [2,9,10].

The tyrosine radical ^{1}Tyr-O$^\bullet$ can also be involved in cross-linking through the ortho position leading to the formation of dityrosine (see Figure 1A) [2,11]. Dityrosine is formed upon radical isomerization followed by diradical reaction, and finally enolization [12,13]. Dityrosine is found in numerous proteins as a result of aging [13], exposure to oxygen free radicals [13,14], nitrogen dioxide, peroxynitrite, and lipid hydroperoxides [13], enzymatic reaction with peroxidases [13,15,16], γ-irradiation [17], and UV-irradiation [18–20]. In these cases dityrosine cross-linking (C_{ortho}-C_{ortho}) can be either intramolecular or intermolecular [2,12,20] (see Figure 1B). Dityrosine is one of the specific markers for protein oxidation. The intermolecular cross-linking may result in protein aggregation [14,15,21] (See Figure 1B). Dityrosine formation upon UV-irradiation has been shown with fluorescence spectroscopy in L-dityrosine solutions [22], calmodulin [18,20] and elastin hydrolysates (1 h excitation at 254 nm, power fluency of 43.8 W.m^{-2}) [19]. The yield of dityrosine formation obtained in UV-irradiation of calmodulin (which contains a perfectly oriented Tyr pair and no tryptophan nor cysteine (Cys, C) is low (intermolecular cross-linking). There is only ~6% conversion of Tyr to dityrosine and the reaction appears to be self-limiting [20]. Dityrosine displays unique fluorescence properties emitting strongly at 400–409 nm [20]. The deprotonated and protonated forms of dityrosine have absorption maxima at ~315 nm and ~283 nm respectively [22,23]. The pK_a of the phenolic hydroxyl groups ionized group that deprotonates first in free dityrosine is ~7.0–7.1 [22,23]. It is only the single deprotonated form of dityrosine (in which one of the two phenolic hydroxyl groups is deprotonated) that emits at 400–409 nm [22,24]. When dityrosine in is in the singlet excited state it has an apparent pK_a below 3. Thus, dityrosine fluorescence can be also seen in solutions with pH below 7, upon excitation of the protonated form (max at ~283 nm), because deprotonation of the first phenolic hydroxyl group takes place in the excited state [20].

In proteins, another important photochemical mechanism which follows Tyr excitation is the reduction of disulphide bridges (SS) [1–3]. The solvated electrons generated upon Tyr excitation (either through photoionization or biphotonic absorption in the triplet state) can be captured by cystines leading to the formation of RSSR$^{\bullet-}$ (disulphide electron adduct) and likely SS breakage (schemes 1, 2) [3,25]. Solvated electrons can also interact with the peptide chain creating hydroxide ions and ketyl radicals (scheme 3), which can propagate along the peptide chain [10,26]. If a ketyl radical gets trapped by a disulfide bridge, this again results in a disulphide anion and likely SS breakage. ^{3}Tyr can also transfer an electron to a nearby SS forming Tyr$^{\bullet+}$ and RSSR$^{\bullet-}$ (scheme 4) [11]. Protonation of the disulphide anion can also lead to SS disruption (scheme 5) [25]. Photolysis of SS can also take place through direct excitation of cystine residues at ~254 nm, with similar formation of the electron adduct RSSR$^{\bullet-}$

$$e^-_{aq} + RSSR \rightarrow RSSR^{\bullet-} \quad (1)$$

$$RSSR^{\bullet-} \Leftrightarrow RS^\bullet + RS^- \quad (2)$$

$$e^-_{aq} + -CONH- \rightarrow OH^- + -\dot{C}(OH)NH- \quad (3)$$

$$^3Tyr + RSSR \rightarrow Tyr^{\bullet+} + RSSR^{\bullet-} \quad (4)$$

$$RSSR^{\bullet-} + H^+ \Leftrightarrow RS^\bullet + RSH \quad (5)$$

Reduction of SS upon UV excitation of aromatic residues has been shown for proteins such as cutinase and lysozyme [1,3,27], bovine serum albumin [28,29], prostate specific antigen [30], alpha-lactalbumin [4] and antibody Fab fragments [31].

Insulin is a small and important peptide hormone for the mammals involved in processes such as cell growth, cell differentiation, membrane transfer of nutrients and metabolism [32]. Insulin interacts with the insulin receptors in muscle cells, liver, and adipose tissue [33]. It stimulates glucose uptake, glucose oxidation, glycolysis, glycogenesis, lypogenesis, protein synthesis and inhibits gluconeogenesis, lipolysis, fatty acid oxidation and protein degradation [32,33]. In almost all the species, including human, it has 51 amino-acids and a molecular weight of ~6000 Da [34]. The human insulin molecule is constituted by two polypeptide chains, an A chain and a B chain, containing 21 and 30 amino acid residues, respectively [35]. The two chains are linked together by two inter-chain SS (CysA7-CysB7 and CysA20-CysA19) and an additional SS connects CysA6 and CysA11 within the A chain (Figure 2A). The amino-acids of the two chains are also involved in numerous non-covalent interactions [35].

Although insulin binds to its receptor as a monomer, it assumes different forms both physiologically and in solution [36–38]. It forms dimers, double dimers (or tetramers), triple dimers (or hexamers), and higher-order aggregates [39]. The insulin form in solution dependents on e.g. insulin concentration, pH, and solvent composition, and metal ion concentration, which can also affect the charge and solubility of the insulin molecule [36,39]. At physiologic pH, monomeric human insulin molecules in solution only exist at very low concentrations ($<1\times10^{-9}$ M), while dimers are formed at concentrations of about 1×10^{-6} M [36,39]. In the blood, the physiological concentration of insulin is generally $<1\times10^{-9}$ M, which ensures the circulation of insulin and its biological effects as a monomer [36]. Insulin aggregation is initiated upon concentration increase and several models have been proposed for describing the phenomenon in the absence of metal ions [39,40]. In the presence of zinc or other metal ions, three human insulin dimers readily associate into hexamers [39,41]. 2Zn hexameric insulin assembles through the coordination of two zinc ions and has a similar structure to the natural storage species of the peptide in pancreatic beta-cells [41].

The stability of insulin molecule in either of its aggregation states has been extensively studied over the years, due to its importance for pharmaceutical preparations. Several studies have been reported on the effects of pH, temperature and other environmental stresses on the structure and function of the peptide (for review see: [42]) but little attention has been given to insulin

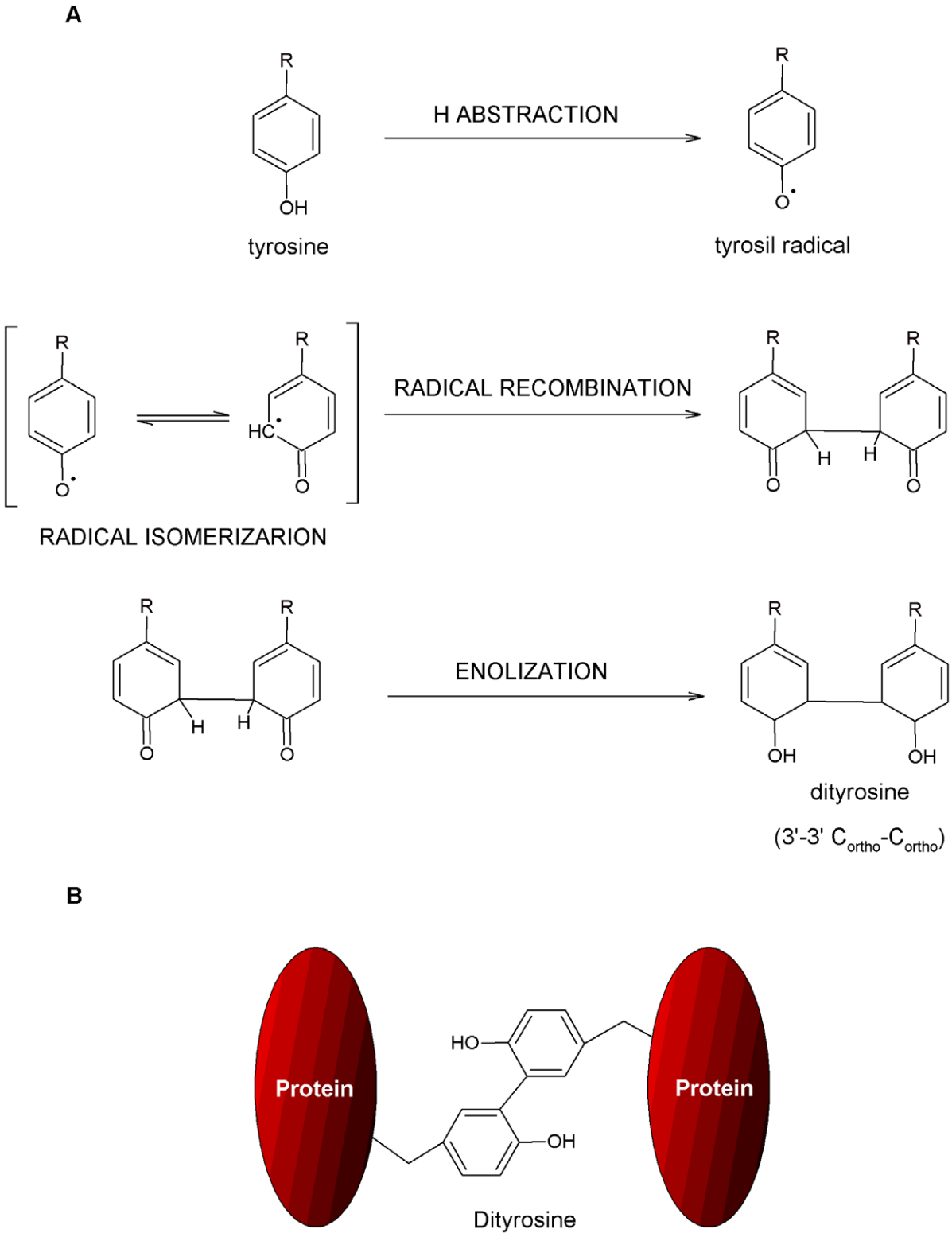

Figure 1. Molecular mechanisms of dityrosine cross-linking (C_{ortho}-C_{ortho}). (A) Reaction mechanism for the formation of dityrosine. (B) Intermolecular dityrosine cross-linking in proteins.
doi:10.1371/journal.pone.0050733.g001

exposure to UV-light. Here we show that prolonged exposure of human insulin to 276 nm UV-light has dramatic consequences on the absorption, fluorescence, structure and biofunctionality of human insulin. Continuous UV-exposure of insulin leads to SS breakage mediated by tyrosine excitation, covalent insulin dimerization via dityrosine cross-linking, and considerable losses

A

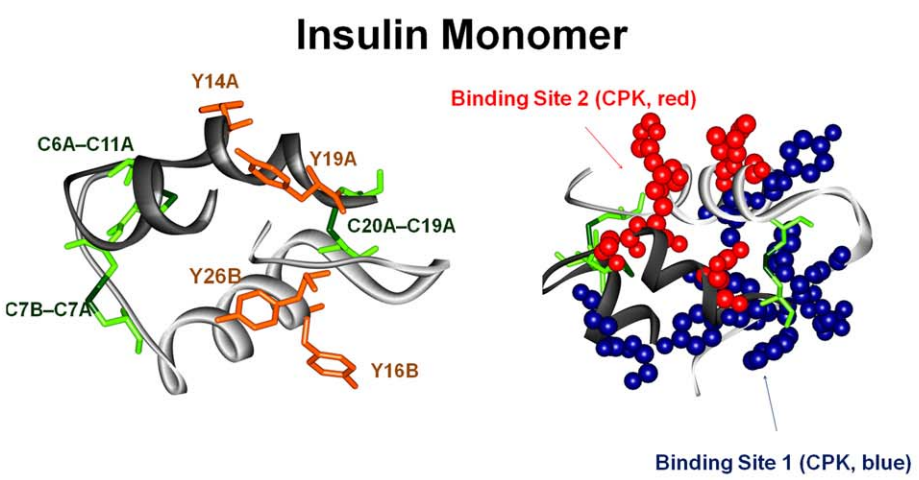
Insulin Monomer
Y14A
C6A–C11A
Y19A
C20A–C19A
Y26B
C7B–C7A
Y16B
Binding Site 2 (CPK, red)
Binding Site 1 (CPK, blue)

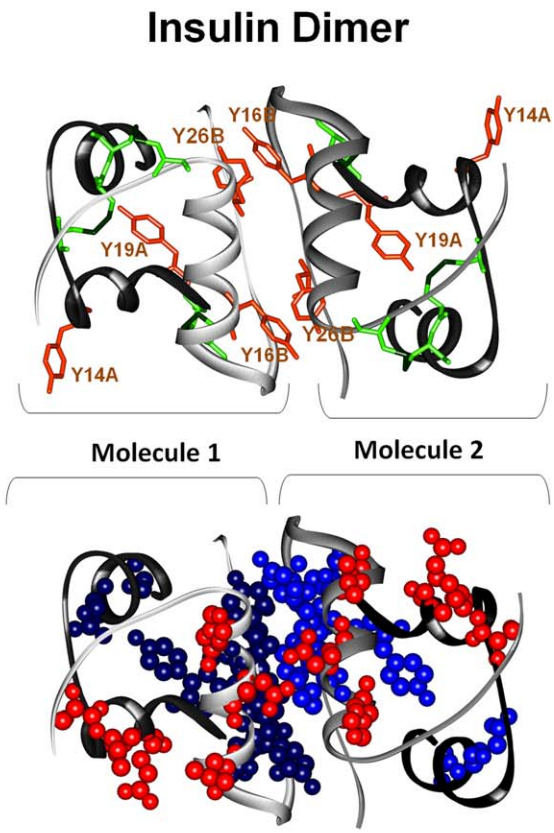
Insulin Dimer
Y16B
Y26B
Y14A
Y19A
Y19A
Y26B
Y16B
Y14A
Molecule 1
Molecule 2

B

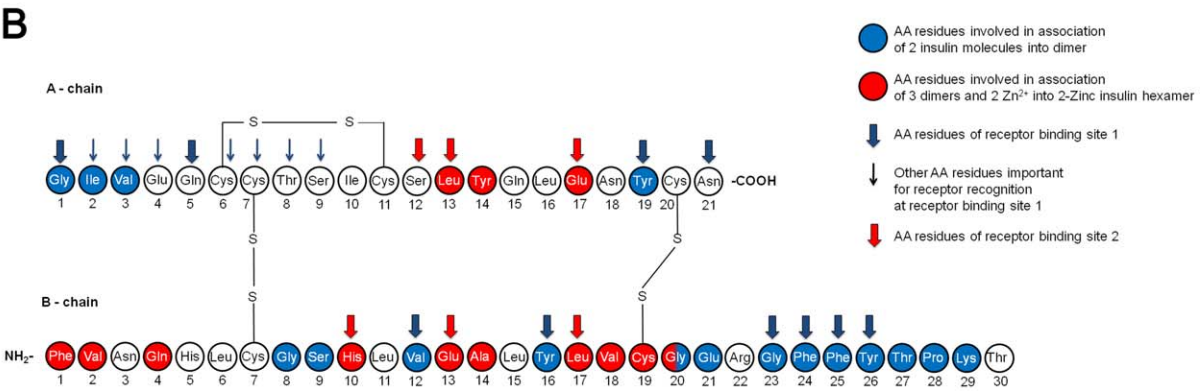
AA residues involved in association of 2 insulin molecules into dimer
AA residues involved in association of 3 dimers and 2 Zn2+ into 2-Zinc insulin hexamer
AA residues of receptor binding site 1
Other AA residues important for receptor recognition at receptor binding site 1
AA residues of receptor binding site 2
A - chain
Gly Ile Val Glu Gln Cys Cys Thr Ser Ile Cys Ser Leu Tyr Gln Leu Glu Asn Tyr Cys Asn -COOH
1 2 3 4 5 6 7 8 9 10 11 12 13 14 15 16 17 18 19 20 21
B - chain
NH2- Phe Val Asn Gln His Leu Cys Gly Ser His Leu Val Glu Ala Leu Tyr Leu Val Cys Gly Glu Arg Gly Phe Phe Tyr Thr Pro Lys Thr
1 2 3 4 5 6 7 8 9 10 11 12 13 14 15 16 17 18 19 20 21 22 23 24 25 26 27 28 29 30

Figure 2. Tertiary and primary structures of insulin, dimer and 2Zn hexamer forms and receptor binding sites. (A) 3D structures of insulin monomer and dimer extracted from the crystallized structured of the 2Zn pig insulin hexamer (4INS.pdb) [37]. Insulin A chains of insulin are displayed in gray (two different shades in the insulin dimer) and B chains are displayed in black. The 4 Tyr residues of insulin (Y, orange) and the 6 Cys (C, green) involved in 3 disulphide bridges (SS) are displayed in orange and green, respectively (left-side structure for insulin monomer and top structure for insulin dimer). The two insulin binding sites are displayed in CPK (0.5 Å radius) in blue (binding site 1) and red (binding site 2) (right side structure for insulin monomer and bottom structure for insulin dimer). (B) Primary structure of human insulin. The amino acid residues involved in the association of 2 insulin molecules into a dimer (blue residues) and in the molecular assembly of 3 dimers into 2Zn insulin hexamer (red residues) are displayed. The amino acid residues belonging to insulin receptor binding sites 1 and 2 are indicated by wide blue and red arrows, respectively. Amino acid residues important for insulin receptor recognition of the binding site 1 but not belonging to this site are displayed with thin blue arrows (adapted from [36], information regarding dimer association, hexamer formation, and insulin receptor binding sites extracted from [35,36,38,48–51]).
doi:10.1371/journal.pone.0050733.g002

in secondary and tertiary structural features. This structural modification impairs both insulin antibody recognition and biological function in *vitro*. For the first time to our knowledge we quantify the functional losses in insulin activity and we relate it to the irradiance levels used in our experiments. The effects of prolonged exposure of insulin pharmaceutical preparations to sunlight and artificial lighting,-and the implications for pharmaceutical industry are discussed.

Materials and Methods

Protein and Buffer Solutions

Human insulin was purchased from Sigma-Aldrich (product I2643, Sigma-Aldrich Danmark A/S, Copenhagen, Denmark) (MW = 5807.57 $g.mol^{-1}$; Zinc, Zn $\leq$1%, dried basis). Stock solutions of insulin were prepared by dissolving the powder in 10 mM Phosphate Buffer pH 8.0 and stored at 4°C until use. Insulin concentrations were determined by Abs_{276nm} using a molar extinction coefficient of 1.0675 $cm^{-1}.(mg/ml)^{-1}$ [43]. Milli-Q water with conductivity below 0.2 $\mu S.cm^{-1}$ was used.

UV-excitation of Insulin Samples

Throughout the work insulin samples were excited on a RTC 2000 PTI spectrometer (Photon Technology International, Canada, Inc.347 Consortium Court London, Ontario, Canada) with a T-configuration, using a 75-W Xenon arc lamp coupled to a monochromator. For each experiment 2 mL of 17.7 µM insulin in 10 mM PBS pH 8.0 was placed in a quartz macro cuvette (1 cm path length) and continuously excited with UV-light over selected time periods. A fresh sample was used for each excitation session. Samples were magnetically stirred at 750 rpm in order to secure homogeneous excitation. Slits (bandpass) were always set to 5 nm. Lamp power at 276 nm was 142 µW and the same lamp was used throughout the experiments.

UV-absorption Studies and Elmanns Assay

Before analyzing the insulin samples by UV-absorption and quantifying the number of free thiol groups with the Elmann's assay, insulin was continuously excited at 276 nm during 0.25 h, 0.5 h, 0.75 h, 1 h, 2 h, or 2.5 h. After each illumination, 1 mL of the illuminated solution was placed in 1 cm path length cuvette and an absorbance spectrum was recorded with UV/Visible spectrophotometer (UV1 VWR International–Thermo Electron Corporation, Thermo Fisher Scientific Inc. 81 Wyman Street Waltham, MA, USA). Absorbance spectra were acquired between 200 and 500 nm. A reference spectrum was acquired for a fresh insulin sample (time 0 h, control).

Detection of free thiol groups was carried out using the Ellman's assay [1,44]. Ellman's reagent, 5,5′-dithiobis-2-nitrobenzoic acid (DTNB) was purchased from Molecular Probes (product D8451, Life Technologies, Naerum, Denmark). One hundred mM DTNB stock solution was prepared in DMSO and stored at 4°C. After each excitation session, 990 µL of illuminated insulin solution was mixed with an excess of DTNB (10 µL of 100 mM stock solution). The molar ratio DTNB/insulin was ~57. Two minutes after mixing the two components, the absorbance intensity at 412 nm was monitored with a UV/Visible spectrophotometer (UV1 VWR International–Thermo Electron Corporation, Thermo Fisher Scientific Inc. 81 Wyman Street Waltham, MA, USA), using a 1 cm path length quartz cuvette. The sample was kept in the dark during the 2 min incubation period. Absorbance at 412 nm is due to the release of the product 2-nitro-5-thiobenzoate ion (TNB^{2-}) and is proportional to the amount of thiol groups present in solution. Concentration of thiol groups was determined using an extinction molar coefficient for TNB^{2-} of 14150 $M^{-1}.cm^{-1}$ at 412 nm [44].

Fluorescence Studies

Insulin samples were continuously excited at 276 nm during 0.5 h, 1 h, 1.5 h, 2.5 h, 3.5 h, and 7 h using the RTC 2000 PTI spectrometer setup as described above. Time-based fluorescent emission kinetic traces (emission fixed at 405 nm in detector 1 and 303 nm in detector 2) were obtained during continuous 276 nm excitation. Real-time correction was enabled in order to correct for oscillations in lamp intensity (gain set at 1 V).

Before and after each illumination, emission and excitation spectra were recorded. Emission spectra were acquired with 276 nm and 320 nm excitation. Excitation spectra were recorded with the emission fixed at 303 nm and 405 nm. The same emission and excitation spectra were acquired for the buffer. Slits (bandpass) were always set to 5 nm. During the whole procedure samples were magnetically stirred at 750 rpm in order to secure homogeneous excitation. Solution temperature was set at 21°C using a Peltier element at the cuvette holder location.

Circular Dichroism Measurements

Circular Dichroism (CD) spectroscopy was used to monitor the relative changes in ellipticity after prolonged 276 nm excitation of insulin. Near- and far-UV CD spectra were immediately recorded after each excitation session described in the previous session (0 h, 0.5 h, 1 h, 1.5 h, 2.5 h, 3.5 h, and 7 h 276 nm excitation). Two hundred µl of illuminated insulin (17.7 µM in 10 mM PBS pH 8.0) was placed in a quartz microcuvette with a path length of 0.1 cm. Far-UV CD spectra (190–260 nm) were acquired using the following parameters: 1.0 nm band width, resolution 1.0 nm, 9 accumulations, scan speed 50 nm/min, 20 mdeg sensitivity, 4 s response time. Near-UV CD spectra (250–310 nm) were recorded using the following parameters: 10 nm band width, resolution 1.0 nm, 32 accumulations, scan speed 100 nm/min, 1 mdeg sensitivity, 4 s response time. Far-UV and near-UV CD were also acquired for a fresh insulin sample and for the buffer. The buffer signal was subtracted from all spectra. Each measurement was controlled by the JASCO J-700 hardware manager (JASCO Corporation, Ishikawa-cho Hachioji-shi, Tokyo, Japan). Temperature was kept constant at 21°C throughout all the measurements using a Peltier element.

Radioimmunoassay

Insulin samples were continuously excited at 276 nm during 1.5 h or 3.5 h. As a control, in parallel, 2 mL of the same 17.7 μM insulin stock was placed in a quartz macro cuvette and left in the dark under 750 rpm during 1.5 or 3.5 h.

After excitation, the illuminated sample and the non-illuminated sample (positive control, PC) were diluted 500000 times. One hundred μL of each diluted sample was pre-incubated with a surplus (100 μL) of guinea pig anti-porcine insulin antibody serum (Novo Nordisk, Bagsvaerd, Denmark). During the incubation period (~48 h) the guinea-pig anti porcine insulin antibodies bind to the intact insulin molecules forming a complex. After incubation an excess of labeled ^{125}I-Insulin (100 μL with specific radioactivity of ~371 mCi/mg, Novo Nordisk) is added to the reacting mixture and binds to the remaining antibodies in solution, forming a ^{125}I-Insulin-antibody complex. To separate free insulin (non-bound) and ^{125}I-Insulin excess from the antibody-bound insulin, the mixture is washed two times with 96% ethanol and subsequently FAM/ethanol. After mixing, antibody-bound insulin and antibody-bound ^{125}I-Insulin precipitate immediately, while free insulin and free ^{125}I-Insulin stay in the supernatant phase. The free ^{125}I-Insulin concentration is then determined by measuring the radioactivity in the supernatant or the radioactivity of antibody-bound ^{125}I-Insulin in the precipitate. The intensity of the radioactive-bound ^{125}I-Insulin measured is directly proportional to the insulin concentration in the analyzed sample. Rat insulin is used as a standard sample. Insulin concentration is calculated from a standard curve obtained using the radioactivity intensity measurements of rat insulin (known concentrations) and their input in Multicalc.

Glucose Uptake Assay

The effect of UV-light exposure of insulin on its *in vitro* function was tested using a bioassay based on glucose uptake in proliferating human skeletal muscle cells (SkMC) (Promocell, Heidelberg, Germany). The cells were prepared according to the Promocell manual and protocol. The cells were then seeded in 24 wells ($0.3.10^6$ cells/well) containing 1 mL growth medium. Once 70–90% confluence was reached, the growth medium was replaced by 1 mL differentiation medium (Promocell) inducing the fusion of skeletal cells to myotubes with typical multinucleated syncytia. The differentiation medium was changed every 2nd to 3rd day. Once extensive formation of multinucleated syncytia was visible under the microscope (after 8–14 days), the cells were ready for the glucose uptake assay.

As a preliminary step for the glucose uptake assay, an insulin sample was continuously excited at 276 nm during 1.5 h using the RTC 2000 PTI spectrometer setup as described above. As a control, in parallel, 2 mL of the same 17.7 μM insulin stock was placed in a quartz macro cuvette and left in the dark under 750 rpm during 1.5 h. After excitation, the illuminated sample and the non-illuminated sample (positive control, PC) were diluted to the concentration to be used in the assay (~100 nM).

After 8–14 days of culture in differentiation medium the 24 wells plate was washed twice with 1 mL Dullbecco's Phosphate Buffer saline (D-PBS) without $CaCl_2$ and $MgCl_2$ (GIBCO, Paisley, UK). Afterwards 300 μL M-KRB supplemented with 0.1% BSA, 0.1 mM glucose (5 μCi/ml) or 1.5 μCi/well deoxy-d-glucose 2-[1,2–3H(M)], referred as deoxy-d-glucose (Nen, Perkin Elmer, 2740 Skovlunde, Denmark) was added to the plates. Additionally, for the wells where glucose uptake was being stimulated, insulin was supplemented to the medium. Three types of wells were prepared: one type with no insulin (control), a second with 100 nM illuminated insulin, and another with 100 nM of non-illuminated insulin (PC). In the last two cases insulin was directly diluted to the medium down to a concentration of 100 nM. Of the 24 wells, 6 wells were not supplemented with insulin (controls), 9 were stimulated with 100 nM of illuminated insulin, and 9 with the PC 100 nM insulin. The plates were kept on ice during the addition of medium. After 15 minutes incubation at 37°C the plates were placed on ice, and the incubation was stopped by washing twice with 1 ml M-KRB supplemented with 0.1% BSA and 50 mM glucose. Two hundred μl of 0.1 M NaOH was added to each well, and after 30 minutes at room temperature 100 μl was transferred to a 24 well counting plate (Wallac Oy, Turku, Finland) and 900 μL of Hisafe II scintillator (Perkin Elmer, 2740 Skovlunde, Denmark) was added. After ~12 h the plates were counted using a micro beta counter TriLUX (Wallac Oy, Turku, Finland). Counts per minute is a direct measure of the glucose taken up by the muscle cells.

The assay was repeated maintaining all the experimental conditions except the following. Of the 24 wells, 6 wells were not supplemented with insulin (control), 12 were stimulated with 100 nM of illuminated insulin, and 6 wells with the PC 100 nM insulin.

3D Protein Structure

The crystallography data used for 3D protein structure display (Figure 2A), and distance calculations was extracted from the PDB file 4INS (2Zn hexameric pig insulin [37]). 3D structures of the insulin monomer and dimer were displayed using Accelrys Discovery Studio Visualizer 2.5. Distances between Tyr residues, and between Tyr residues and SS were calculated in Accelrys Discovery Studio Visualizer 2.5 using the "monitor" tool.

Data Analysis

Absorbance Spectra. Absorbance spectra were first smoothed using a 7 points adjacent averaging and the baseline was corrected using the baseline tool of Origin Pro 8.0. Fitting of peaks at 276 and ~314 nm was carried out using a 2 Gaussian function and the peak finder from Origin Pro 8.0. The peak at 276 nm was fixed. The fitting procedure was carried out between 260 and 400 nm.

Emission and Excitation Spectra. All spectra obtained were first Raman corrected by subtracting the corresponding spectra recorded for the buffer alone in solution. Emission spectra recorded upon 276 nm were smoothed using a 7 points adjacent averaging. Excitation spectra obtained with emission fixed at 405 nm were smoothed using a 5 points adjacent averaging.

Since the emission and excitation spectra recorded at excitation time 0 h were different for each excitation session (0.17 h, 0.33 h, 0.5 h, 0.75 h, and 1.5 h) a correction factor had to be applied to each spectrum. Each spectrum obtained after each excitation session (0.17 h, 0.33 h, 0.5 h, 0.75 h, and 1.5 h) was divided by the maximum intensity value of the corresponding 0 h emission or excitation spectrum. The emission spectra acquired upon 276 nm were divided respectively by the 300 nm emission intensity values of the corresponding 0 h emission spectra. Each emission spectrum obtained upon 320 nm excitation was divided by the 300 nm emission intensity value of the corresponding 0 h emission spectra obtained upon 276 nm excitation. It was not possible to use the 0 h emission spectra recorded at 320 nm for correction since there is emission peak at 0 h for this excitation wavelength. The excitation spectra acquired with emission fixed at 303 nm was divided by the 278 nm excitation intensity values of the corresponding 0 h emission spectra. The excitation spectra obtained with emission fixed at 405 nm were divided by the 278 nm emission intensity value of the corresponding 0 h

excitation spectra obtained with emission fixed at 303 nm. Zero h emission and excitation spectra obtained before 1 h excitation were normalized using the respective correction factors mentioned above and used for representation of the non-illuminated insulin spectra.

Normalized emission and excitation spectra were obtained by dividing each data point by the maximum intensity value in each spectrum.

Time-based fluorescence emission kinetic traces (vs 276 nm exc. time). Time-based fluorescence emission kinetic traces obtained with emission set at 303 nm and 405 nm, and excitation fixed 276 nm were normalized by dividing each data point by the emission intensity value at 1 h excitation time.

The emission intensity values at 405 nm used for plotting the kinetic trace of fluorescence emission intensity at 405 nm with excitation fixed at 320 nm were obtained directly from the emission spectra recorded upon 320 nm excitation. The time-based fluorescence kinetic trace was then normalized by dividing each data point (emission intensity) by the 1 h excitation emission.

CD spectra. All spectra were obtained in mdeg directly from the instrument and further treated in Origin Pro 8.0. The ellipticities of the samples after different excitation periods were all corrected for the buffer contribution. Near-UV CD spectra were smoothed using a 5 points adjacent averaging.

Radioimmunoassay and glucose uptake assay. For both assays data was represented as the mean ± standard error of mean.

In the radioimmunoassay the concentration detected for the insulin samples has been normalized in order to compare the two sets of experiments (1.5 and 3.5 h exc. and dark). Normalization was carried out using as reference the non-illuminated PC insulin detected concentration values (individually for each set of experiments, 1.5 h and 3.5 h) and setting these values to 1.

Unpaired student t-tests were used to compare the samples in the glucose uptake assay. The students t-tests were carried out in Origin Pro 8.0. A p-value <0.05 was considered significant.

Fitting Procedures. Normalized fluorescence kinetic traces obtained upon 276 nm illumination (emission set at 303 nm and/or 405 nm, excitation set at 276 nm or 320 nm) were fitted with an exponential function $F(t) = C_1 - C_2.e^{-kt}$, where $F(t)$ is the fluorescence emission intensity at 303 nm or 405 nm (a.u.) at the 276 nm excitation time t (h), C_1 and C_2 are constants and k is the rate constant of fluorescence emission intensity increase (h^{-1}).

The kinetics of thiol group formation versus 276 nm excitation time have also been fitted according to an exponential function $y = y_0 - A.e^{-R0t}$, where y is the concentration of thiol groups (μM) at the 276 nm excitation time t (h), y_0 and A are constants and $R0$ is the rate of thiol group formation (h^{-1}).

Smoothing procedures, data fitting and plotting were done in Origin Pro 8.0.

Results

Three-dimensional Structure of Insulin

In Figure 2A the 3D crystal structures of native pig insulin monomer and dimer in the hexamer 2Zn structure are presented. Human and pig insulin differ just in one amino acid (human: ThrB30, pig: AlaB30), implying that they share the same protein fold and structure. The insulin monomer contains 4 Tyr residues and as previously mentioned 3 SS. The closest distances between Tyr and Cys residues involve Tyr19 A. TyrA19 is ~5.4 Å away from CysA6-CysA11 and ~6.9 Å from CysB19-CysA20. In the insulin monomer, no Tyr residue is in direct contact with another Tyr residue. The shortest distance between Tyr residues is ~7.5 Å (Tyr19A-Tyr26B). In the insulin dimer Tyr26B from one molecule is in direct Van der Vaals contact (≤5.2 Å as defined by Li and Nussinov [45]) with Tyr16B in the second molecule: for TyrB26 (molecule 1) and TyrB16 (molecule 2) distance is ~3.8 Å, and for TyrB26 (molecule 2) and TyrB16 (molecule 1) distance is ~4.1 Å (see Figure 2A).

UV-Absorption (Prior and after 0.25–2.5 h 276 nm exc., Power Fluency of 2.20 $W.m^{-2}$)

Absorbance spectra were acquired prior and after 0.25–2.5 h excitation at 276 nm (Figure 3A). UV-excitation of insulin leads to an increase in absorbance intensity at 240–285 nm, (where Tyr absorbs) and at 285–330 nm. Fitting the absorbance values between 240 nm and 400 nm with a 2-Gaussian peak function shows the presence of two peaks centered at ~276 nm and at ~315 nm (Figure 3B and Table 1). The area under each peak tends to increase with UV-excitation time (fitted area, Table 1).

Steady State Fluorescence Emission (Prior and after 0.5–7 h 276 nm exc., Power Fluency of 2.20 $W.m^{-2}$)

Emission Spectra (excitation 276 nm). In Figure 4A is shown the emission spectra of insulin acquired upon excitation at 276 nm (absorption maximum wavelength for Tyr) prior and after 276 nm excitation. A pronounced decrease in emission intensity (centered at 301 nm) is observed after UV-excitation. After 7 h continuous 276 nm excitation the emission intensity of the insulin tyrosine residues at 303 nm is only ~60% of the initial fluorescence emission intensity. The observed decrease in emission intensity at 303 nm is correlated with an increase in fluorescence emission intensity at 405 nm (Figure 4A, insert). After 7 h of excitation a peak is clearly visible at ~405 nm and a 6.2 fold intensity increase is observed. Normalization of the emission spectra (data not shown) shows no shift in the wavelength of the most intense peak centered at 301 nm. The change in fluorescence emission intensity at 303 nm and 405 nm upon prolonged 276 nm excitation time is displayed in Figure 4B. Fitting the experimental curves show that both changes are exponential. The results are listed in the section below.

Emission spectra (excitation 320 nm). After exciting insulin with 276 nm light, emission spectrum of the protein were recorded upon 320 nm excitation in order to verify if the species that absorbs at these wavelengths is also fluorescent (Figure 5A). Before 276 nm excitation, no fluorescence emission is observed at 330–500 nm upon 320 nm excitation. With the increase in 276 nm excitation time, we observe the progressive formation of a peak centered at ~400 nm (exc. 320 nm). After 7 h of excitation, the emission intensity at 405 nm is 31.4 fold higher compared to non-illuminated insulin. The kinetics of the fluorescence emission intensity increase at 405 nm versus 276 nm exc. time is exponential (Figure 5B and Table 2). In Table 2 are summarized the fitted parameters and root mean square errors obtained upon fitting the kinetic traces displayed in Figures 4B and 5B with an exponential model ($F(t) = C_1 - C_2.e^{-kt}$). After prolonged excitation with 276 nm light, there is an exponential increase of fluorescence emission intensity at 405 nm (Figures 4B and 5B) and an exponential decrease of fluorescence emission intensity at 303 nm (Figure 4B) upon 276 nm excitation. The kinetics traces have been fitted in the same time window (1–7 h) and normalized to the emission value at 1 h of 276 nm excitation.

In Table 2 we observe that the kinetics of emission intensity increase at 405 nm upon 276 nm or 320 nm excitation are similar with comparable kinetic constant k (constant that determines

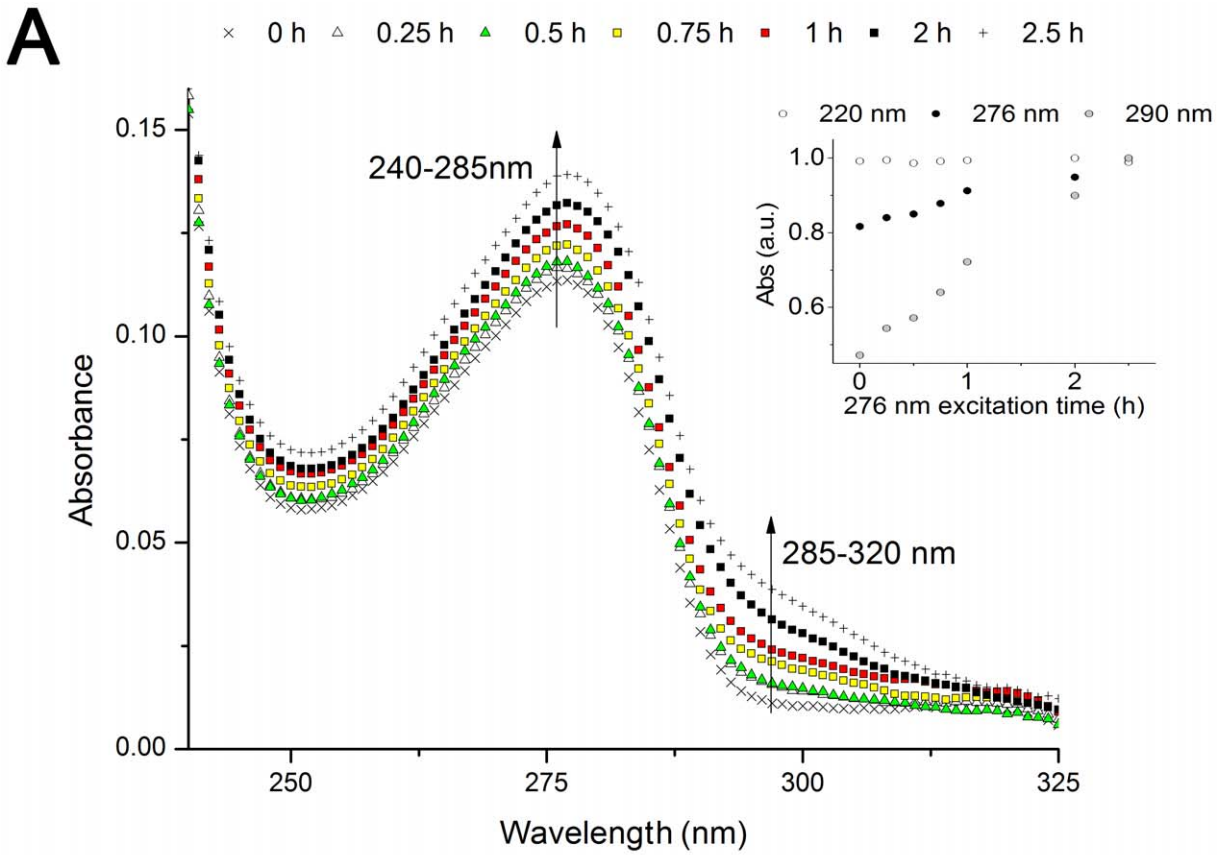
A
0 h
0.25 h
0.5 h
0.75 h
1 h
2 h
2.5 h
240-285nm
285-320 nm
Absorbance
Wavelength (nm)
220 nm
276 nm
290 nm
Abs (a.u.)
276 nm excitation time (h)

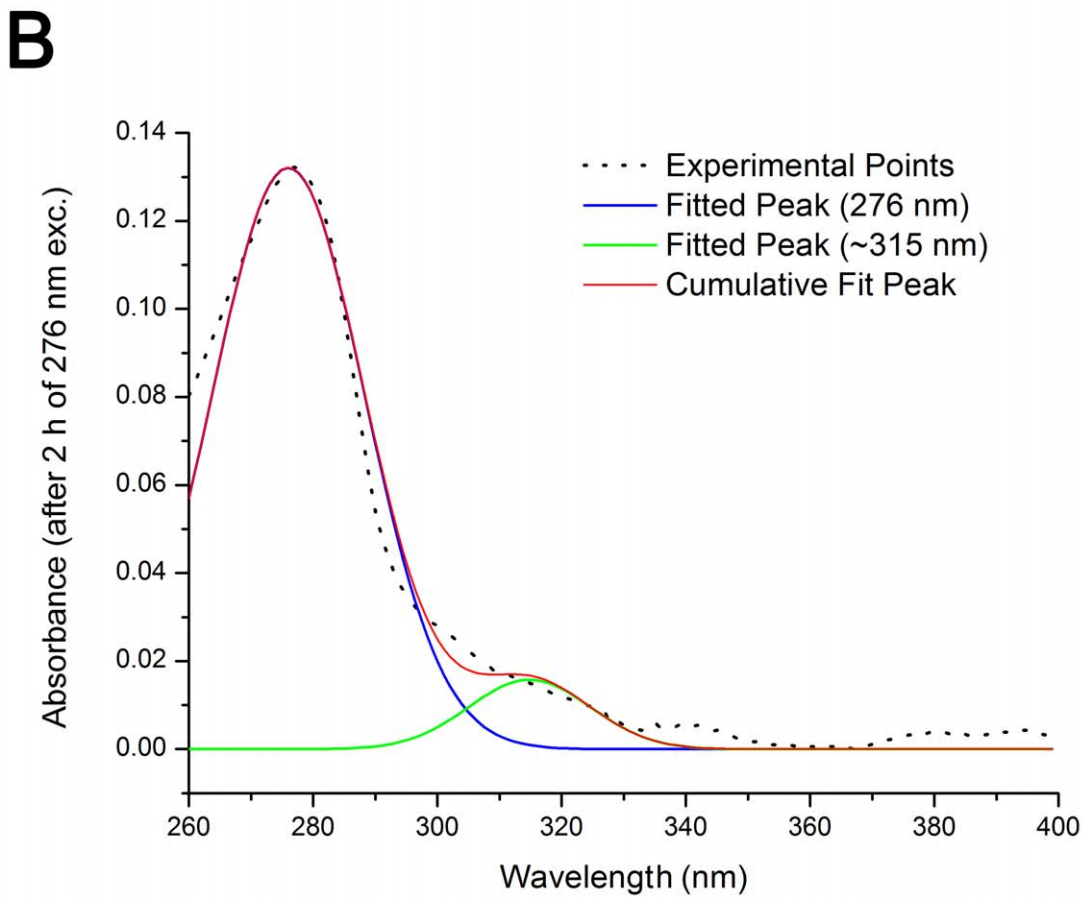
B
Experimental Points
Fitted Peak (276 nm)
Fitted Peak (~315 nm)
Cumulative Fit Peak
Absorbance (after 2 h of 276 nm exc.)
Wavelength (nm)

Figure 3. Absorbance spectra of human insulin after prolonged 276 nm UV-excitation. (A) Absorbance spectra obtained before and after 276 nm light continuous exc. (0.25 h, 0.5 h, 0.75 h, 1 h, 2 h, and 2.5 h) of human insulin in solution. In the insert, are plotted the absorbance values at 220, 276 and 290 nm *vs* 276 nm exc. time. Absorbance at 276 and 290 nm increase linearly with 276-nm excitation time (linear fitting, $R^2 = 96.78\%$ for $Abs_{276\ nm}$ and $R^2 = 99.28\%$ for $Abs_{290\ nm}$). (B) Fitting of the absorbance spectrum (obtained after 2 h exc. with 276 nm light) with a 2 gaussian peak function. The peak at 276 nm was fixed. The original experimental spectrum, the two individual fitting curves obtained for each peak and the cumulative curve of the two fittings are displayed.
doi:10.1371/journal.pone.0050733.g003

exponential fluorescence emission increase over 276 nm exc. time) values ($1.59.10^{-1}$ h^{-1}, exc. 276 nm and $1.62.10^{-1}$ h^{-1}, exc. 320 nm). However, the fluorescence emission intensity increase at 405 nm upon 320 nm excitation is faster (higher C_2 value). The kinetics of fluorescence emission intensity decrease at 303 nm (exc. 276 nm) are distinct and slower, with a lower k value ($1.08.10^{-1}$ h^{-1}).

Excitation spectra (emission 303 nm). In Figure 6 is shown the excitation spectra of insulin acquired by fixing the emission at 303 nm, where Tyr should emit, prior and after 276 nm excitation. It can be observed that the excitation emission intensity decreases over the illumination time, which is correlated with the previously described decrease in emission intensity at 303 nm (Figure 4A). Normalization of the excitation spectra shows no shift in the wavelength where maximum excitation intensity is observed (~277 nm), matching the absorption maximum of Tyr (data not shown).

Excitation spectra (emission 405 nm). In order to analyze the species that contribute to the increase of fluorescence emission intensity at 405 nm after continuous 276 nm excitation, excitation spectra (emission fixed at 405 nm) were acquired after each continuous excitation session (Figure 7). Upon 276 nm excitation, a progressive increase in the excitation intensity centered around 320–325 nm is observed. After 7 h, excitation intensity increases ~22 fold at 320 nm. Normalization of the excitation spectra shows no shift with excitation time on the peak formed at ~320–325 nm (data not shown).

Table 1. Parameter values obtained upon fitting of the insulin absorbance spectra with a 2 Gaussian peak function.

Exc. time (276 nm)	λ_{max} (nm)	Fitted area	FWHM (nm)	R^2
0 h	Peak 1 276	3.070±0.065	25.08±0.66	0.95566
	Peak 2 315.6 ±2.0	0.22±0.050	17.99±4.77	
0.25 h	Peak 1 276	3.259±0.064	25.95±0.64	0.96477
	Peak 2 315.9±1.8	0.262±0.049	19.62±4.31	
0.5 h	Peak 1 276	3.319±0.069	26.11±0.69	0.96078
	Peak 2 315.3±2.2	0.231±0.053	19.62±5.24	
0.75 h	Peak 1 276	3.521±0.068	26.97±0.67	0.96948
	Peak 2 316.5±1.7	0.329±0.053	22.34±4.23	
1 h	Peak 1 276	3.725±0.069	27.50±0.65	0.97289
	Peak 2 314.4±1.3	0.361±0.05	20.04±3.22	
2 h	Peak 1 276	4.089±0.068	29.08±0.63	0.98307
	Peak 2 314.8±1.4	0.387±0.049	23.04±3.29	
2.5 h	Peak 1 276	4.436±0.08	30.26±0.68	0.98496
	Peak 2 316.7±1.5	0.519±0.059	27.72±3.41	

Fitting parameters and corresponding errors (standard error), and root mean square errors were obtained after fitting each insulin absorbance spectrum (spectra in Figure 3A and fitting example in Figure 3B) with a 2 Gaussian peak function. λ_{max} is the wavelength of maximum emission for each absorbance peak. The peak at 276 nm was fixed.
doi:10.1371/journal.pone.0050733.t001

Thiol group's quantification (Prior and after 0.25–2.5 h 276 nm exc., Power Fluency of 2.20 $W.m^{-2}$)

The concentration of free thiol groups increases with 276 nm excitation time, following an exponential kinetic (Figure 8). After 2.5 h the concentration of free thiol groups in insulin is ~4.47 µM. Assuming that the formation of free thiol groups follows a first order kinetics (as indicates the 1st order exponential model used) it is possible that more thiol groups are formed with increased 276 nm excitation time. The maximum value of thiol concentration can be estimated from the exponential model ($y = y_0 - A.e^{-R0t}$) used for fitting and is given by y_0, which is of 5.04 µM.

CD measurements (Prior and after 0.5 h –7 h 276 nm exc., Power Fluency of 2.20 $W.m^{-2}$)

The far-UV CD spectrum of the non-illuminated sample (exc. 0 h) displays the classical far-UV features characterizing protein secondary structure (Figure 9). There is a peak at ~195 nm, representative of β-sheet organization and a double minimum at 222 nm and 210–208 nm, characteristic of α-helical content [46]. Prolonged excitation with 276 nm light leads to a progressive decrease of ellipticity at 195, 210–208, and 222 nm (Figure 9). After 7 h of illumination, there is a decrease of 58.5%, 18.1% and 37.15% of ellipticity signal at 195, 209 and 202 nm, respectively.

Prolonged excitation of insulin with 276 nm light results in a loss in near-UV CD ellipticity signal. After 3.5 h of 276 nm excitation there is a 66.2% decrease ellipticity signal at 273 nm (data not shown).

Radioimmunoassay (1.5 h, 3.5 h 276 nm exc., Power Fluency of 2.20 $W.m^{-2}$)

Continuous UV-excitation leads to a progressive decrease in insulin concentration detected by the guinea-pig anti-porcine insulin antibodies (Figure 10). After 1.5 h of illumination the detected insulin concentration is 25.6% lower than the one for the positive control sample (non-illuminated insulin, PC). After 3.5 h of excitation, the concentration of insulin molecules detected was 65.0% lower than for the PC sample.

Glucose Uptake Assays (1.5 h 276 nm exc., Power Fluency of 2.20 $W.m^{-2}$)

Figure 11 shows the glucose uptake (counts per minute) by skeletal muscle cells after 1 hour of incubation at three different conditions: no insulin, insulin kept in the dark (positive control, PC), and pre-treated UV-illuminated insulin (1.5 h excitation at 276 nm). As expected, there is a considerable increase in glucose uptake (15.4±4.1%) for the cells that have been stimulated with insulin (non-illuminated, positive control, PC) when compared to the cells void of insulin ($p<0.05$). When the cells were stimulated with the same concentration of insulin previously illuminated with 276 nm light, the increase in glucose uptake relative to the cells void of insulin is 5.9±3.3% ($p<0.05$). The difference in glucose uptake between the positive control samples (PC) and the excited samples (1.5 h excitation at 276 nm) is significant ($p<0.05$). After 1.5 h of excitation with 276 nm light, insulin retains only 38.3% of

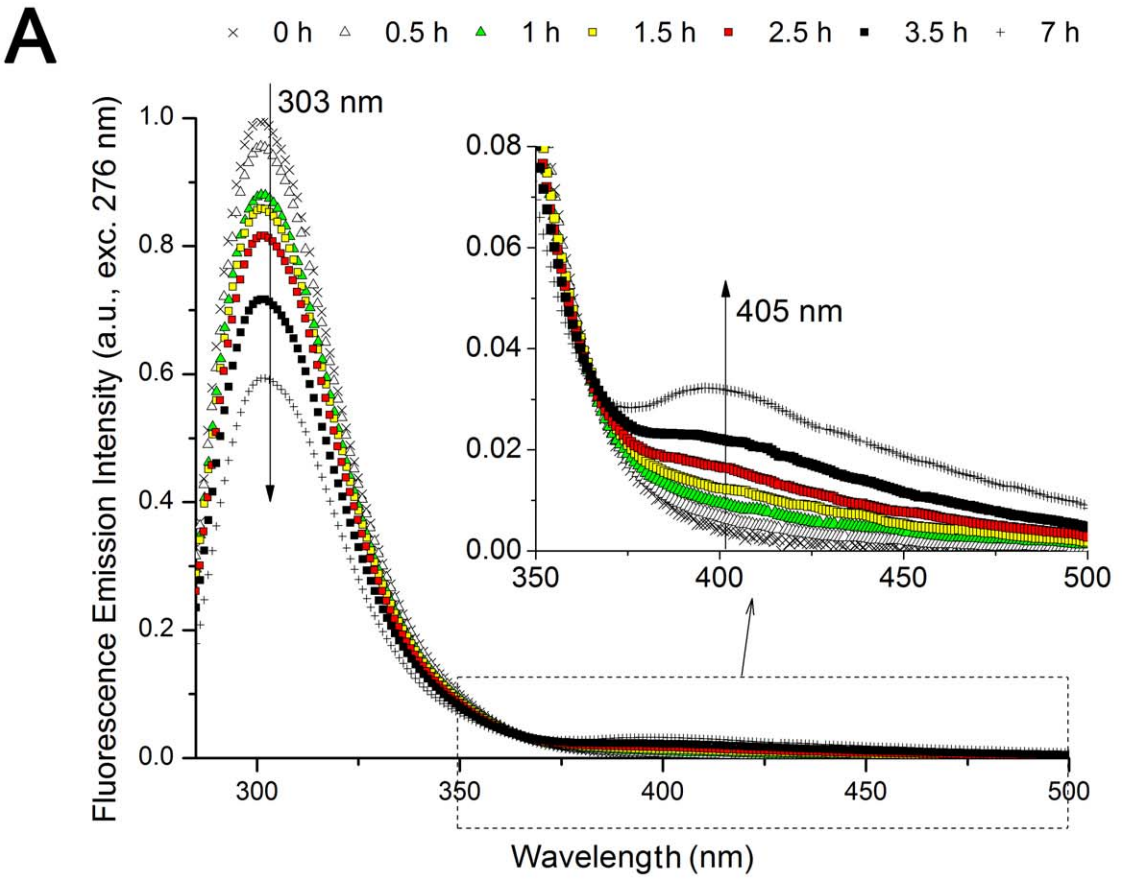
A
0 h
0.5 h
1 h
1.5 h
2.5 h
3.5 h
7 h
303 nm
405 nm
Fluorescence Emission Intensity (a.u., exc. 276 nm)
Wavelength (nm)

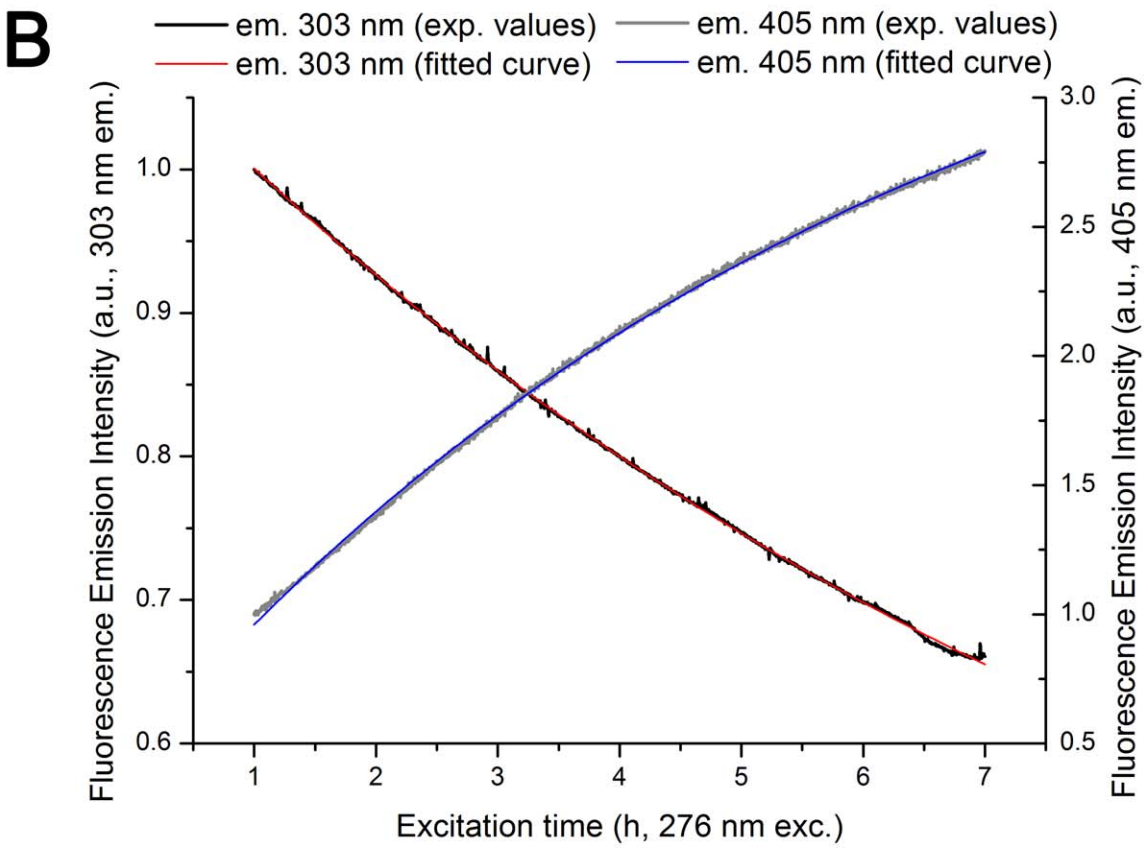
B
em. 303 nm (exp. values)
em. 303 nm (fitted curve)
em. 405 nm (exp. values)
em. 405 nm (fitted curve)
Fluorescence Emission Intensity (a.u., 303 nm em.)
Fluorescence Emission Intensity (a.u., 405 nm em.)
Excitation time (h, 276 nm exc.)

Figure 4. Fluorescence emission of human insulin (276 nm excitation) upon prolonged 276 nm UV-excitation. (A) Fluorescence emission spectra (276 nm exc.) obtained before and after 276 nm light continuous exc. (0.5 h, 1 h, 1.5 h, 2.5 h, 3.5 h, and 7 h) of human insulin in solution. There is a continuous decrease in emission intensity at 303 nm with 276 nm exc. time. The insert shows a zoom of the emission spectra between 350 and 550 nm. Emission intensity at ~405 nm increases progressively with 276 nm excitation time. (B) Fluorescence emission intensity kinetic traces obtained at 330 and 405 nm (exc. fixed at 276 nm) upon continuous of human insulin with 276 nm light. Fitting of the experimental traces was carried out using an exponential function $F(t) = C_1 - C_2 e^{-kt}$. Fitted parameter values and corresponding errors, and root mean square error values were obtained after fitting each kinetic trace (Table 2).
doi:10.1371/journal.pone.0050733.g004

its normal activity *in vitro*. The same experiment was repeated in similar conditions yielding comparable results (data not shown). Such data shows that stimulation of cells with non-illuminated and 1.5 h 276 nm excited insulin resulted respectively in 16.2±7.2% and 3.3±6.1% increase in glucose uptake. Only 20.2% of the insulin hormonal function was retained after exposure with UV-light.

Discussion

The response of insulin molecules to UV-light and the interaction between illuminated insulin molecules will depend greatly on which form insulin will be in solution (monomer, dimer, or higher order aggregational states). In our experiments, human insulin is present at a 17.7 μM concentration. Currently a widely accepted model for concentration-dependent association of insulin in zinc-free solutions is the one of Pekar and Frank [47]. It assumes that two insulin monomers form a dimer, three dimers form a hexamer, and subsequently self-association proceeds with addition of hexamers (the model does not consider tetramer formation). Using the equilibrium constants determined by Attri et al. (2010) [40] for insulin self-association (20 mM Phosphate, 0.1 M NaCl, 5 mM EDTA, pH 8.0) in the model for a concentration of 17.7 μM we obtain relative populations of monomer, dimer, and hexamer of 1.66%, 97.75% and 0.59%, respectively (we excluded aggregation states of higher order than hexamer). Thus, it is expected that in our experiments, insulin is mainly present in its dimeric form.

The structural interaction between the insulin peptide and its membrane receptor is a key process in the biological and physiological action of the hormone. It is well established that insulin molecules bind to its receptor in its monomeric form, but the mechanisms of binding are not completely understood. The classical receptor binding surface in insulin is constituted by a number of residues: GlyA1, GlnA5, TyrA19, AsnA21, ValB12, TyrB16, GlyB23, PheB24, PheB25 and TyrB26 (Figure 2A, CPK in blue) [38,48]. For convenience we will refer this binding surface as binding site 1. Furthermore, it has been shown that the N-terminal α-helix of the insulin A chain (amino acids A1-A8) is relevant for achieving high affinity insulin receptor activation for insulin recognition [38,48]. A second cluster of residues has been proposed to be important for insulin receptor binding: SerA12, LeuA13, GluA17, HisB10, GluB13 and LeuB17 (Figure 2A, residues displayed as CPK in red) [38]. We will name this second binding region as binding site 2. It is proposed that these two separate binding zones in insulin allow the interaction with two separate binding sites in the insulin receptor [38,49].

In its aggregated forms insulin is inactive and does not bind to the insulin receptor [50]. In fact, in the physiologically present aggregated forms of insulin (dimer conformation and 2Zn hexamer), several residues relevant for insulin receptor binding (sites 1 and 2) are involved in dimer interaction and thus blocked from insulin receptor recognition (see Figure 2B). In the insulin dimer conformation (Figure 2A) the key interactions between insulin molecules 1 and 2 are complementary (anti-symmetric) and involve hydrogen bonding between residues of the classical receptor binding site 1: TyrB26 of one molecule and PheB24 of the other molecule [50,51]. Other important residues of the classical receptor binding site 1 that also participate in dimerization are PheB25, TyrA19 and TyrB16 [50,51]. Upon dimer formation, almost all the residues of the receptor binding site 1 are either blocked or solvent shielded (Figure 2B, in blue). It is also relevant to mention that Tyr A14 is involved in dimer interaction to form the insulin 2Zn hexamer [35], and that 5 of the 6 residues of the binding site 2 are either blocked or solvent shielded (Figure 2B, in red). In the case of permanent dimerization of the insulin dimer it is expected that some of the binding site 1 protein residues remain inaccessible for receptor recognition, which would result in permanent loss of insulin functionality.

The changes in fluorescence emission of insulin induced by continuous UV-excitation concur with the progressive formation of a new species that emits strongly at ~405 nm (Figure 4A). This species is excited at 276 nm and more strongly at 320 nm (Figure 7), which correlates well with the fluorescence characteristics of dityrosine formed upon cross-linking of two tyrosine molecules (*vide supra*, introduction). The progressive increase in excitation intensity at 276 and 320 nm upon continuous 276 nm excitation also confirms that new dityrosine molecules are constantly formed upon UV-excitation. Dityrosine formation is also correlated with the observed increase in absorption of insulin at 276 and 314 nm upon UV-excitation (Figures 3A, 3B and Table 1). The two fitted absorption peaks correspond to the absorption maxima of dityrosine species, at 284 and 315 nm (vide

Table 2. Parameter values obtained upon fitting the insulin fluorescence emission kinetic traces recorded with emission fixed at 303 nm (exc. 276 nm) and 405 nm (exc. 276 or 320 nm).

Fitting Fig.	Exc. (nm)	Em. (nm)	C_1	C_2	k (h^{-1})	R^2
Fig. 4B	276	303	0.277±0.002	−0.806±0.002	1.08E−01±4.04E−04	0.99979
	276	405	3.935±0.007	3.489±0.006	1.59E−01±6.05E−04	0.99955
Fig. 5B	320	405	9.191±0.161	9.622±0.135	1.62E−01±5.08E−03	0.99992

Fitting parameter values and corresponding errors (standard errors), and root mean square errors were calculated after fitting the fluorescence emission kinetic traces recorded with emission fixed at 303 nm (exc. fixed at 276 nm, Figure 4B) and 405 nm (exc. fixed at 276 nm and 405 nm, Figures 4B and 5B) upon continuous 276 nm excitation to the equation $F(t) = C_1 - C_2 e^{-kt}$.
doi:10.1371/journal.pone.0050733.t002

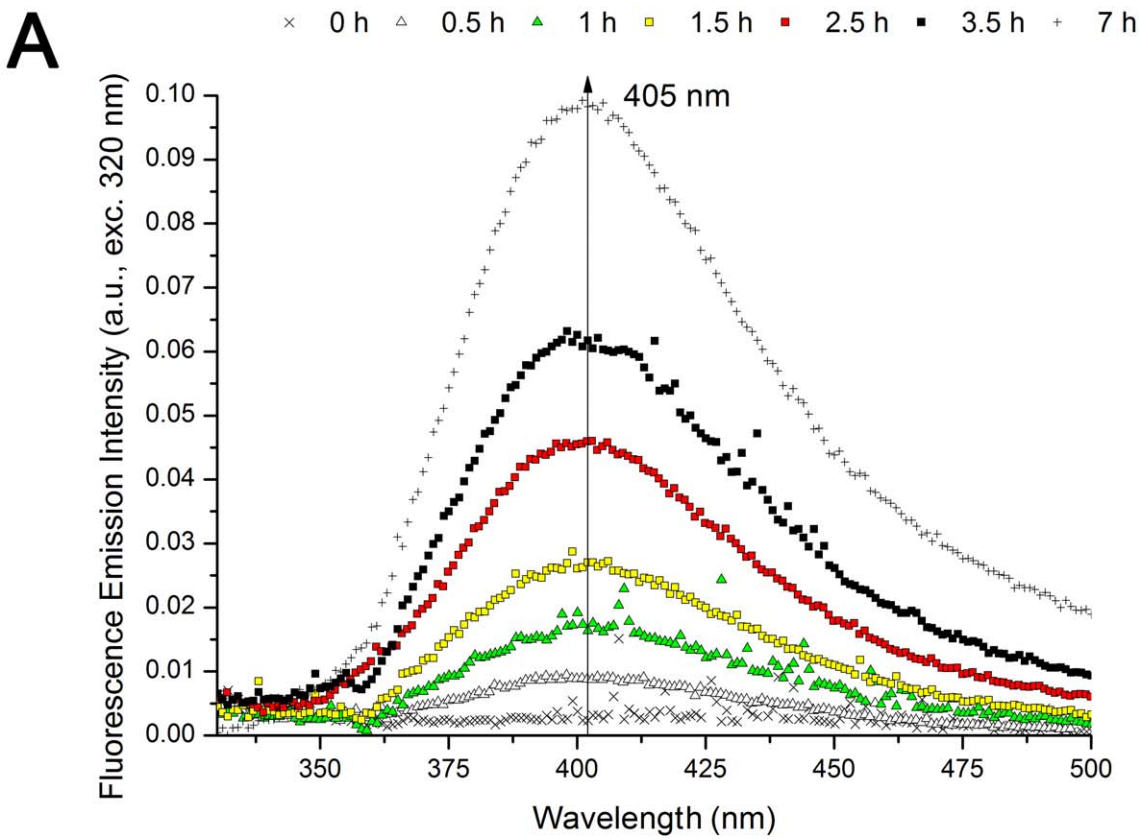
A
0 h
0.5 h
1 h
1.5 h
2.5 h
3.5 h
7 h
405 nm
Fluorescence Emission Intensity (a.u., exc. 320 nm)
0.10
0.09
0.08
0.07
0.06
0.05
0.04
0.03
0.02
0.01
0.00
350
375
400
425
450
475
500
Wavelength (nm)

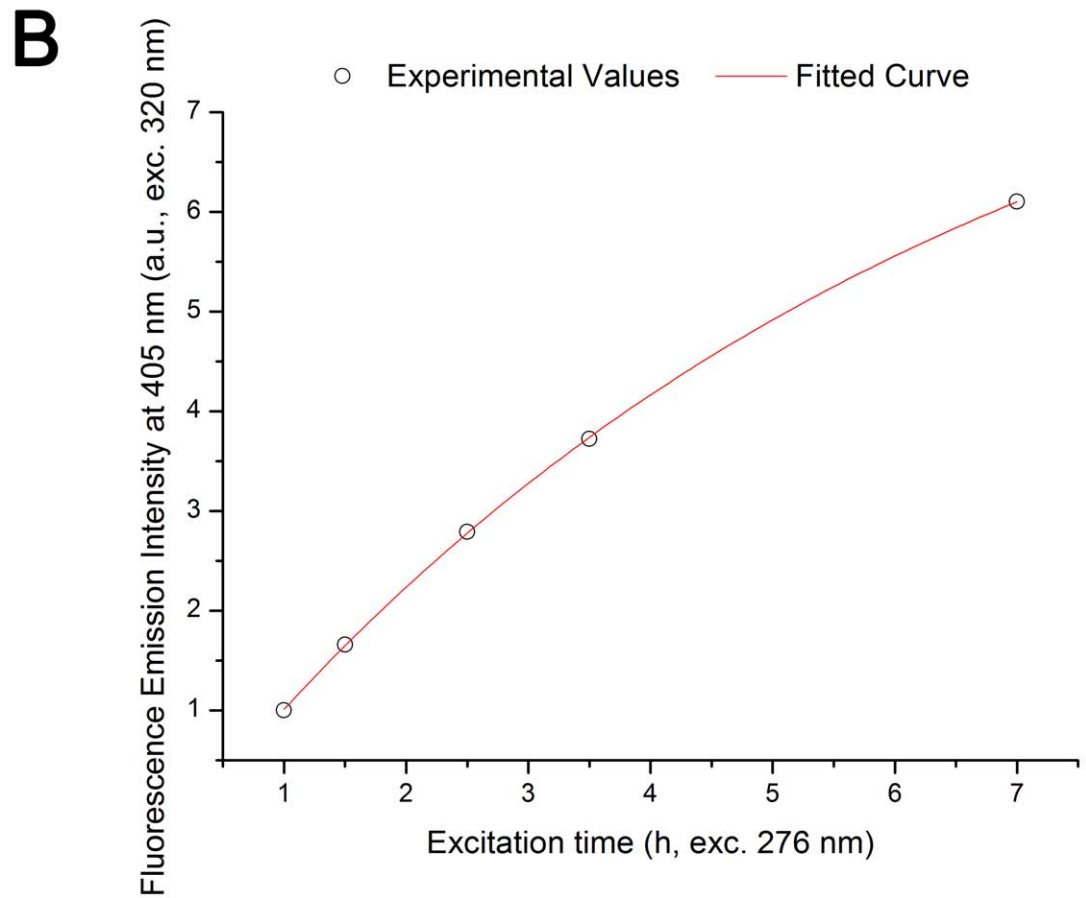
B
Experimental Values
Fitted Curve
Fluorescence Emission Intensity at 405 nm (a.u., exc. 320 nm)
7
6
5
4
3
2
1
1
2
3
4
5
6
7
Excitation time (h, exc. 276 nm)

Figure 5. Fluorescence emission of human insulin (320 nm excitation) upon prolonged 276 nm UV-excitation. (A) Fluorescence emission spectra (320 nm exc.) recorded before and after 276 nm light continuous exc. (0.5 h, 1 h, 1.5 h, 2.5 h, 3.5 h, and 7 h) of human insulin in solution. There is a continuous increase in emission intensity at 405 nm with 276 nm exc. time. (B) Fluorescence emission intensity kinetic trace obtained at 405 nm (exc. at 320 nm) upon continuous of human insulin with 276 nm light. Fitting of the experimental traces was carried out using an exponential function $F(t) = C_1 - C_2 e^{-kt}$. Fitted parameter values and corresponding errors, and root mean square error values were obtained after fitting each kinetic trace (Table 2).
doi:10.1371/journal.pone.0050733.g005

supra, *introduction*). Tyrosil radicals may also be involved in other reactions than dityrosine coupling. Some of the tyrosil radicals disproportionate (reaction between radicals to originate non-radical products) to tyrosine and dihydroxyphenylalanine (DOPA) [19,20]. Furthermore, other products of tyrosine oxidation may be present such as isodityrosine, trityrosine, pulcherosine, dopamine, dopamine quinone, 5,6-dihydroxyindol and 5,6-dihydroxy-3-oxo-indol [12,20]. The yields of formation of these products are usually lower compared to dityrosine [12].

Dityrosine formation has been observed previously in insulin upon oxidation with H_2O_2/peroxidase [15], metal-catalyzed oxidation with H_2O_2/Cu [52], ozone [53], carbon electrodes [54], and exposure to γ-radiation [17]. Inter-molecular dityrosine cross-linking is indicated by two of these studies [15,52], while carbon electrode oxidation suggests intra-molecular dityrosine cross-linking of insulin [54]. The minimum distance between tyrosine residues within an insulin monomer is 7.5 Å which does not favor direct Van der Vaals contacts (Results and Figure 2A). Thus, it is more likely that tyrosine cross-linking occurs between two different insulin molecules. In the dimer conformation (Figure 2A), Tyr26B from one molecule is in direct Van der Vaals contact (≤5.2 Å [45]) with Tyr16B in the second molecule and *vice-versa*. These two residue pairs are also involved in the dimer stabilization via hydrogen bonding. This geometry favors direct dityrosine cross-linking, indicating that excitation of insulin with UV-light leads to progressive covalent cross-linking of the insulin molecules in the dimer. In the dityrosine insulin dimer the classical binding region would not be available for receptor recognition, resulting in permanent loss of function, as observed in our study (Figure 10). Since the tyrosil radical $Tyr^{\bullet}$ is relatively stable, with a lifetime in the microsecond timescale [2], we cannot exclude that the cross-linking occurs differently between insulin molecules of different dimers.

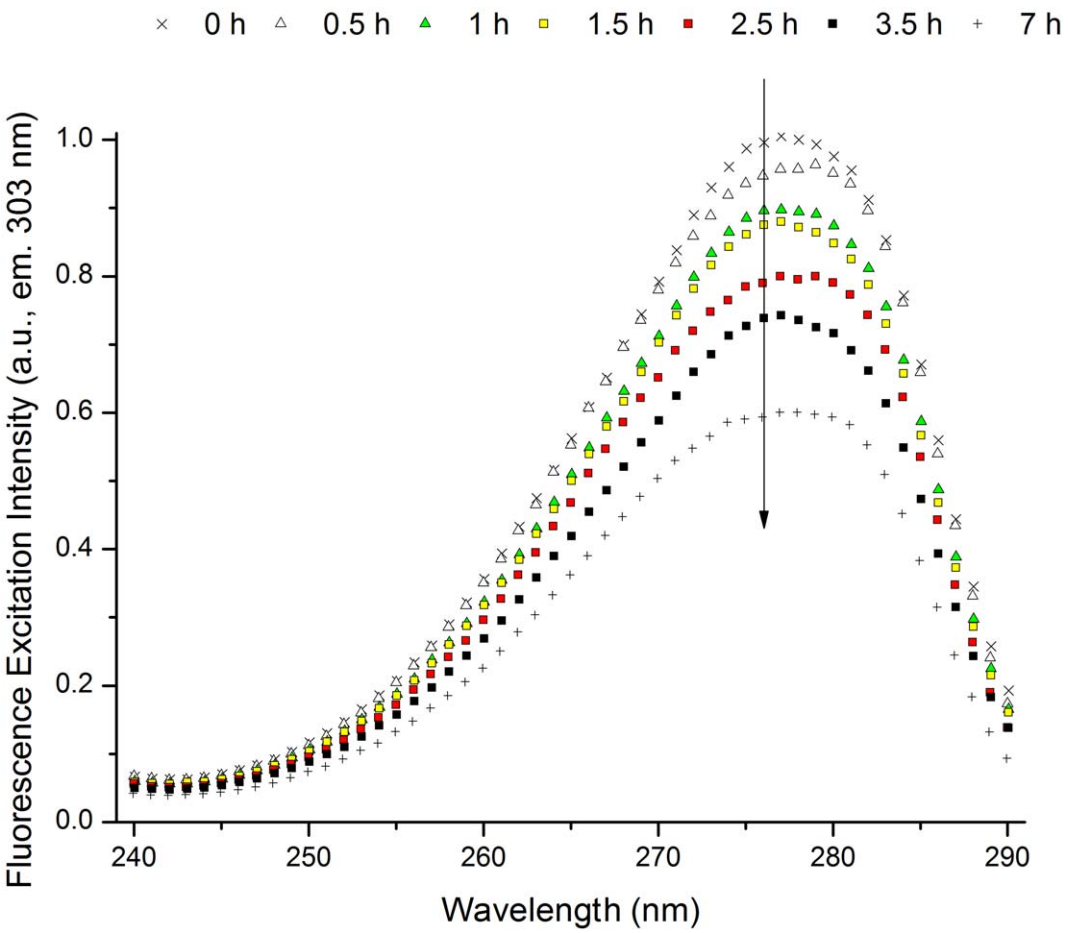

Figure 6. Fluorescence excitation spectra of human insulin (emission fixed at 303 nm) upon prolonged 276 nm UV-excitation. The excitation spectra (em. 303 nm) were obtained before and after 276 nm light continuous exc. (0.5 h, 1 h, 1.5 h, 2.5 h, 3.5 h, and 7 h) of human insulin in solution. There is a continuous decrease in excitation intensity at 276 nm with 276 nm exc. time.
doi:10.1371/journal.pone.0050733.g006

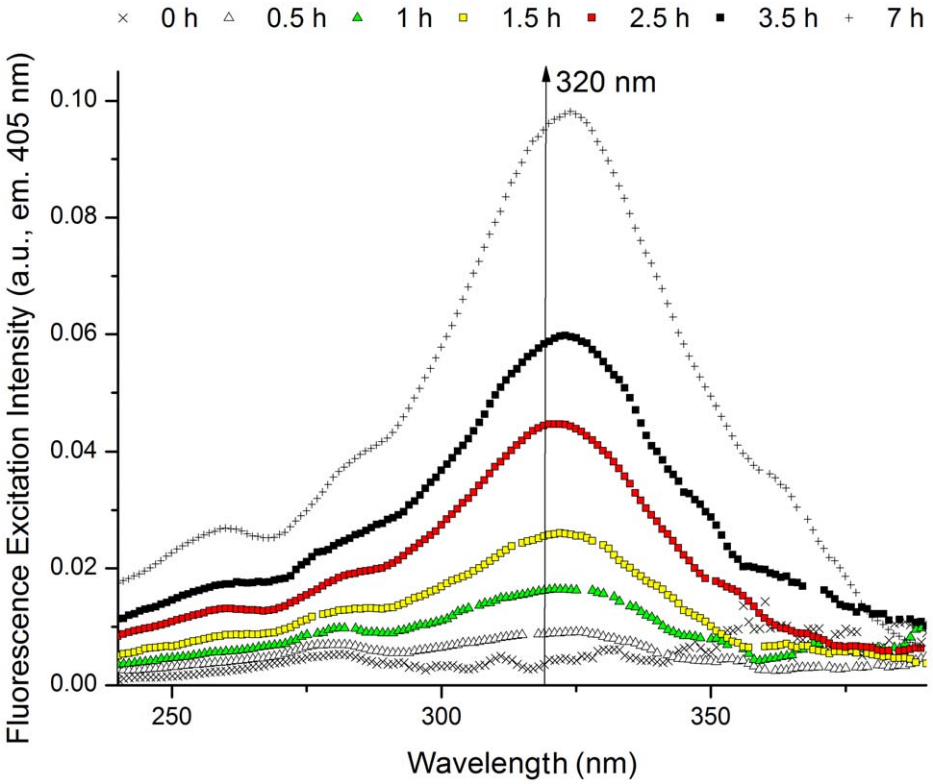

Figure 7. Fluorescence excitation spectra of human insulin (emission fixed at 405 nm) upon prolonged 276 nm UV-excitation. Fluorescence excitation spectra (emission fixed at 405 nm) obtained before and after 276 nm light continuous exc. (0.5 h, 1 h, 1.5 h, 2.5 h, 3.5 h, and 7 h) of human insulin in solution. There is a continuous increase in excitation intensity at 320 nm with 276 nm exc. time.
doi:10.1371/journal.pone.0050733.g007

The fluorescence emission intensity at 405 nm upon insulin 276 nm prolonged illumination follows a single exponential increase for excitation wavelength either at 276 nm (Figure 4B and Table 2) or 320 nm (Figure 5B and Table 2). The fitted constant *k* (constant for exponential fluorescence emission intensity increase) is similar at the two excitation wavelengths which indicate that it is the same process that occurs in both cases. The two excitation wavelengths (276 nm and 320 nm) can excite separately the protonated and single deprotonated forms of dityrosine (absorption maxima of 284 and 314 nm, respectively, *vide supra* introduction). Upon excitation to its singlet excited states, both of these species fluoresce at ~400–409 nm. This can be interpreted as if dityrosine is formed upon UV-excitation of tyrosine following a 1st order reaction, and that upon continuous excitation of its protonated and single deprotonated forms, dityrosine fluoresces at 405 nm. This is in agreement with the photochemical reaction mechanism for dityrosine cross-linking from tyrosine radical described previously (*vide supra*, introduction, Figure 1A).

A new molecular species is formed upon UV excitation of insulin: dityrosine. Simultaneously with the formation of dityrosine, tyrosines must disappear. Upon prolonged illumination at 276 nm, tyrosine emission at 303 nm diminishes (Figure 4A) Furthermore, tyrosine excitation intensity at 276 nm (303 nm em., Figure 6) decreases. This contrasts with the already mentioned decrease of 276 nm absorbance with excitation time (Figure 3A). At 276 nm the extinction coefficient of dityrosine is higher than the summed extinction coefficients of the forming two tyrosine molecules (at 276 nm – tyrosine, extinction coefficient of 1362 $cm^{-1}.M^{-1}$ [7]; dityrosine extinction coefficient of 3068 $cm^{-1}.M^{-1}$ (extracted from [55]). Since dityrosine is also progressively formed upon continuous UV-excitation, the replacement of tyrosine molecules with dityrosine will lead to an increase of absorption intensity at 276 nm. The formation of other tyrosine derivatives upon UV-excitation (please see discussion above) may also contribute to the increase in absorption intensity at 276 nm, (e.g. for DOPA: $\varepsilon_{280\ nm} = 2692\ M^{-1}.cm^{-1}$,in buffer, pH 5.6 and 6.8 [56]). The decrease in fluorescence emission intensity at 303 nm follows a single exponential decay kinetics upon continuous 276 nm excitation (Figure 4B). The exponential model is consistent once more with a 1st order reaction, which is in agreement with the mechanisms that precede tyrosine depletion, such as Tyr photoionization and intersystem crossing to the triplet state.

The depletion of tyrosine molecules and formation of dityrosine cross-linking with UV-light is correlated with growing amounts of free thiol (SH) groups with the Ellman's assay (Figure 8). This is consistent with the breakage of the protein's SS bonds upon UV-excitation of tyrosine, a well-described mechanism in proteins [2,3,27,28]. As previously observed (*vide supra* results – *three-dimensional structure of insulin*) in the insulin monomer (Figure 2A) no Tyr residue is in direct Van der Vaals contact with SS bonds. Nonetheless, TyrA19 is close to CysA6-CysA11 (~5.9 Å) and CysB19-CysA20 (~6.5 Å), which would favor direct electron transfer to these residues after formation of ^{3}Tyr (*vide supra* – introduction, scheme 4). Photoionization of Tyr and formation of solvated e^{-}_{aq} may also be a mechanism involved in breakage of SS in insulin, which could be the case for longer distances between Tyr and SS (*vide supra* – Introduction, schemes 1 and 2). The formation of free SH groups upon continuous 276 nm excitation

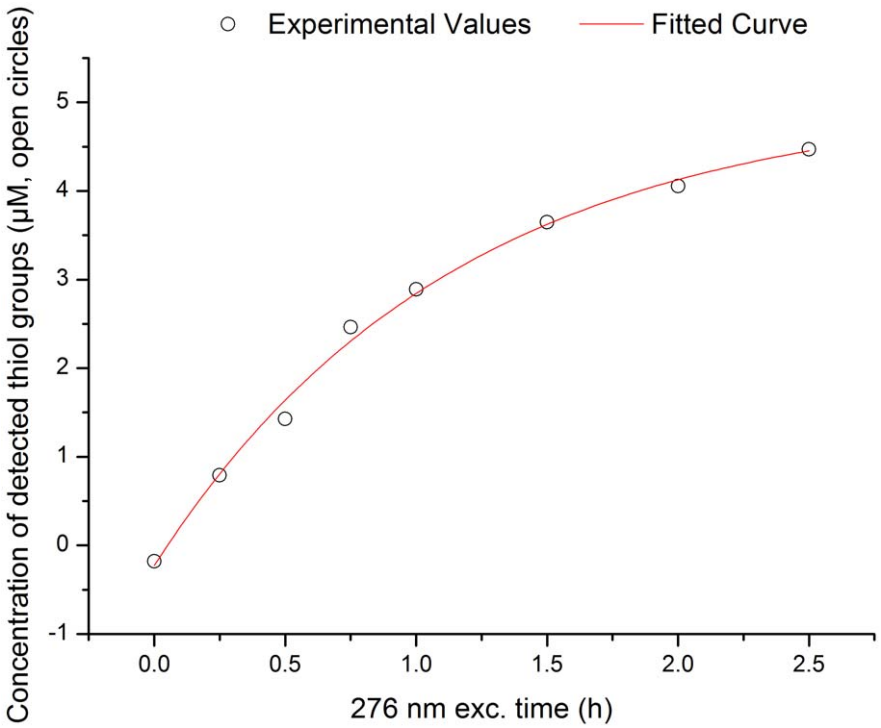

Figure 8. Concentration of detected free thiol groups (open circles) in human insulin *vs* 276 nm exc. time. Detection of free thiol groups was carried out using the Ellman's assay before and after 276 nm light continuous exc. (0.25 h, 0.5 h, 0.75 h, 1 h, 2 h, and 2.5 h) of human insulin in solution. The concentration of free thiol groups was estimated from the absorbance of the Ellman's assay reaction product, TNB^{2-}, at 412 nm ($\varepsilon_{412\ nm} = 14150\ M^{-1}.cm^{-1}$ [44]). The experimental values were fitted using an exponential function $y = y_0 - A.e^{-R0t}$ (fitted curve in red), where y is the concentration of thiol groups (μM) at the 276 nm excitation time t (h), y_0 and A are constants and $R0$ is the rate of thiol group formation (h^{-1}). Fitted experimental parameters were: $y_0 = 5.04 \pm 0.24$ μM, $A = 5.27 \pm 0.22$ μM, $R0 = 0.87 \pm 0.09\ h^{-1}$. Root mean square error was 99.41%.
doi:10.1371/journal.pone.0050733.g008

of insulin follows a single exponential kinetics which would indicate that the breakage of SS bonds is consistent with a first order reaction. The maximum value of free SH concentration is 5.04 μM. Considering that the protein concentration in the experiments is 17.7 μM and that insulin has 3 SS, the maximum concentration of free thiol groups that could be present would be of 106.2 μM. Thus, we conclude that at least one SS in insulin has been disrupted in the insulin molecules after 276 nm excitation. The number of SS broken may be higher than the estimated by the Ellman's assay.

Moziconacci et al. reported UV light (253.7 nm) induced photolysis of the SS bonds in human insulin [57]. At this wavelength photolysis of SS occurs both via direct cystine excitation and via tyrosine or phenylalanine excitation. Mozziconaci et al. report that 67% of the thiols formed were generated through direct homolysis of the SS and 33% through solvated electrons yielded from tyrosine and phenylalanine excitation [57]. In total, all of the 3 SS in insulin were prompt to cleavage upon insulin continuous 253.7 nm excitation. The authors reported the existence of different photo-products with SS bonds broken upon 253.7 nm excitation [57]. More relevantly, one of the photo-products yielded from Tyr excitation had a cross-link between TyrA19 and CysB19 resulting from CysB19-CysA20 breakage. The breakage of this CysB19-CysA20 upon TyrA19 excitation is in agreement with our previous observation on the proximity between TyrA19 and this SS. Breakage of SS CysB7-CysB19, and the cross-link TyrA19-CysB19 were also observed in insulin after 253.7 nm excitation. It is likely that breakage of these SS bonds and the above mentioned cross-link also occur in our experiments. TyrA19 belongs to binding site 1. If it is cross-linked with CysB19 it might be blocked and not be able to participate in receptor binding.

Disruption of CysA7-CysB7 and/or CysA20-CysB19 may result in the rearrangement of the native interactions between the A and B chains and the native structural secondary organization. Electrolytic reduction of the intrachain disulfide bonds of crystalline beef zinc-insulin results in losses of α-helix and β-sheet organization content [58]. Dithiothreitol (DTT) reduction of the three SS leads to a conformational transition in insulin, thermodynamically of the same nature as in the thermal denaturation of globular proteins [59]. The CD results described in our study confirm that continuous UV-excitation of insulin leads to loss of secondary structure. The losses in secondary structural content of the protein (Figure 9) can result from breakage of SS, leading to a gradual unfolding of insulin. The major decrease in ellipticity is consistent with a loss of β-content upon UV-excitation. Curiously, the β-strand of insulin is located in the region of dimer interaction. Upon dityrosine cross-linking between the two monomers (through the two tyrosine pairs Tyr26B and Tyr16B), it is possible that some of the native fold is rearranged in this region, resulting in a structural rearrangement of the antiparallel β-sheet. The dramatic losses in near-UV CD can be explained by the rearrangement of the native interactions of the aromatic residues in insulin.

The structural modifications resulting from UV-excitation are correlated with the observed loss in insulin detection by specific insulin antibodies and in the function of insulin as a hormone. The number of insulin molecules detected by the insulin antibodies decreases progressively with the 276 nm excitation time of the insulin solution. After 1.5 h and 3.5 h of excitation the concen-

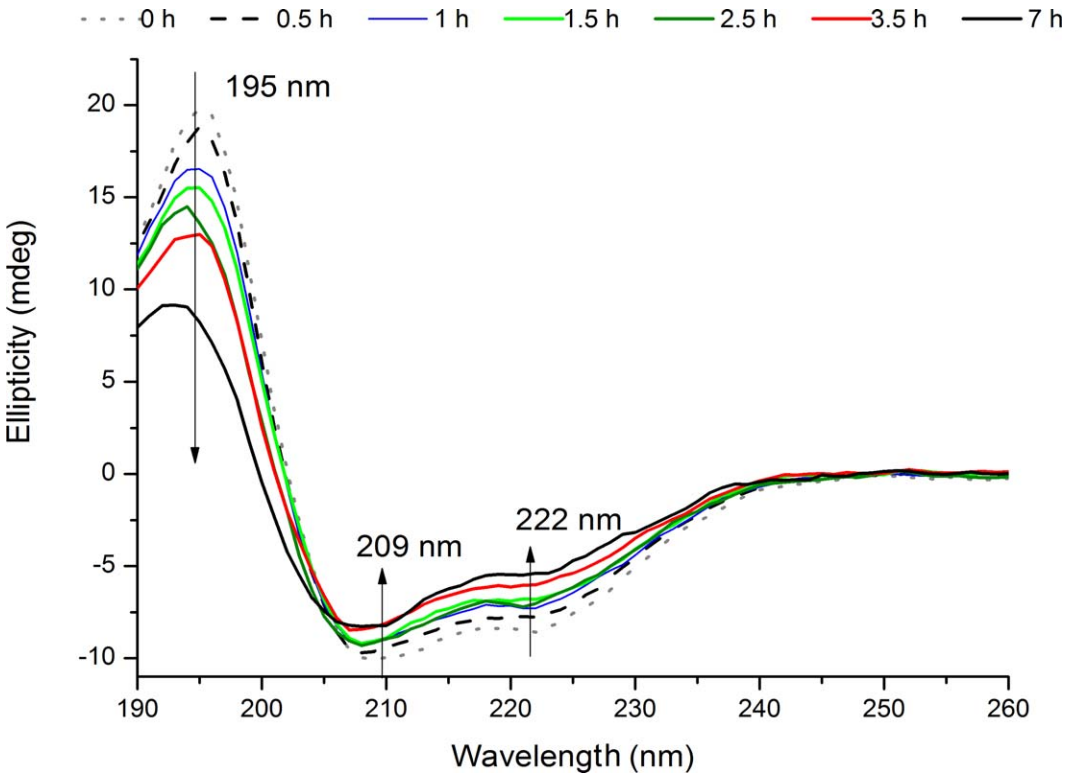

Figure 9. Far-UV CD spectra of human insulin recorded before upon prolonged 276 nm UV-excitation. The far-UV CD spectra were obtained before and after 276 nm light continuous exc. (0.5 h, 1 h, 1.5 h, 2.5 h, 3.5 h, and 7 h) of insulin in solution. There is a progressive loss of ellipticity signal with 276 nm exc. time at 195, 209 and 222 nm.
doi:10.1371/journal.pone.0050733.g009

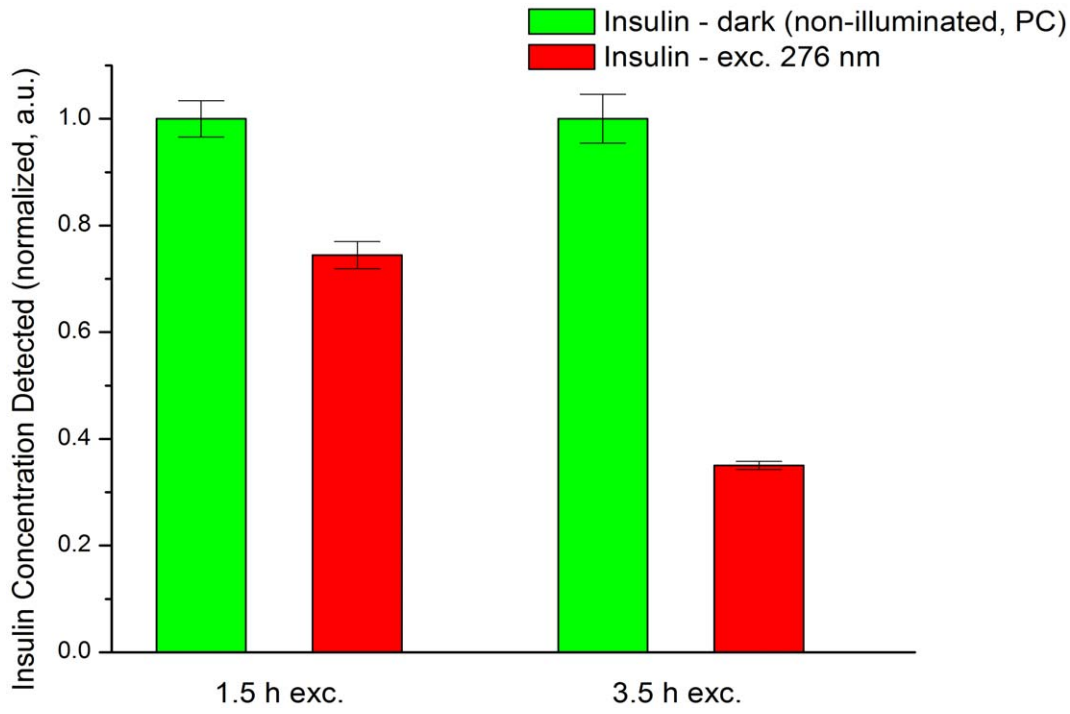

Figure 10. Effect of continuous 276 nm light exposure of human insulin on its recognition by guinea-pig anti-insulin antibodies. Human insulin concentration was detected using a radioimmunoassay. Insulin samples were previously excited with 276 nm light during 1.5 and 3.5 h. A positive control (PC) was carried out for each excitation duration, where insulin was left in the dark for the same time period (1.5 and 3.5 h). Uncertainty values (standard errors) for the detected insulin concentration are displayed with error bars.
doi:10.1371/journal.pone.0050733.g010

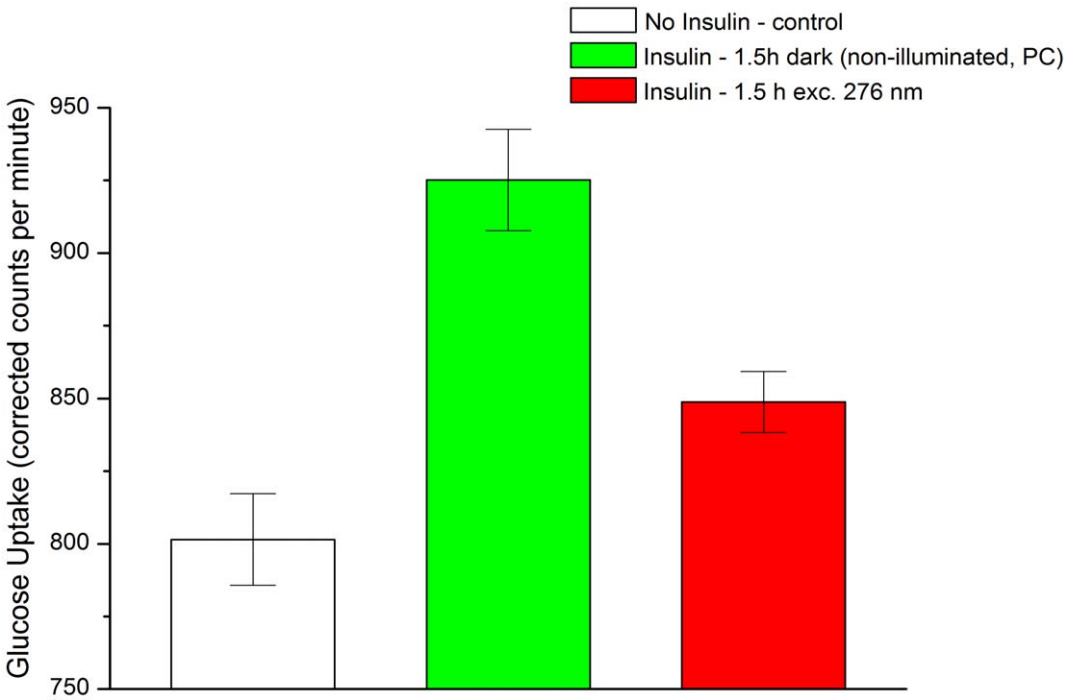

Figure 11. Effect of continuous 276 nm light exposure of human insulin on its hormonal function *in vitro*. The glucose uptake by human skeletal muscle cells was measured after 1 hour of incubation at three different conditions: no insulin (control), insulin kept in the dark (positive control, PC), and UV-illuminated insulin (1.5 h exc. at 276 nm). Uncertainty values (standard errors) for the concentration of glucose (uptake) are displayed with error bars. The students t-tests resulted in the following p-values: p (control *vs* PC) = $27.6.10^{-4}$; p (control *vs* 1.5 h exc. at 276 nm) = 0.002165; p(PC *vs* 1.5 h exc. at 276 nm) = 0.00179.
doi:10.1371/journal.pone.0050733.g011

tration of insulin molecules detected decreases by 25.6% and 65.0%, respectively (Figure 9). It implies that UV-light excitation induces 3D structural changes in insulin, which impair the binding of the insulin antibodies to the peptide hormone.

The antibody serum used in this work for radioimmunodetection consists on a mixture of polyclonal antibodies prepared by immunization of guinea pigs with porcine insulin. The specificity of this polyclonal mixture has been tested positively for human insulin. Since we are using a polyclonal antibody serum it is expected that separate regions of the insulin molecule can be used as attachment sites for the different insulin antibodies present in the serum [60,61]. In human insulin epitopes involving the residues GluA4, ThrA8, SerA9, IleA10, AsnB3, ProB28, LysB29 and ThrB30 have been indicated as possible antigenic sites [60]. The insulin antibodies are added as an excess to the insulin in the radioimmunoassay. Thus, it is expected that if there are any structural changes in a single epitope, insulin can still be detected, because antibody molecules could still bind to alternative epitopes/sites would still be plentiful. The insulin molecules that are not detected by the insulin antibodies have probably suffered structural modifications in all or almost all of the epitopes recognized by the antibodies. In that context several regions of the non-detected insulin molecules must have lost their native conformation upon continuous UV-excitation. Within the amino acid residues reported to be part of likely antibody binding sites, Glu4 is part of an α-helix and ThrA8, SerA9 and IleA10 are part of a loop between the 2 α-helices in the A chain of insulin. Any loss of structure nearby these residues is likely to distort the 2 A chain α-helices. This is positively correlated with the decrease in α-ellipticity reported by our far-UV CD studies. Residues ProB28 and LysB29 are involved in the association of 2 insulin molecules into a dimer (see Figure 2B, in blue). If these residues cannot be recognized by the insulin antibodies it may indicate that these insulin molecules have covalently dimerized via dityrosine cross-linking as we will discuss ahead. The glucose uptake assay allows monitoring the efficiency of insulin binding to the insulin receptor, which occurs through specific binding sites. In this case it is easier to identify the structurally modified regions in the insulin molecule upon UV excitation. Glucose uptake has been reduced 61.7% when stimulation has been done with insulin previously excited during 1.5 h with 276 nm (Figure 10). This implies that 1.5 h of UV illumination has induced 3D structural changes in insulin which impaired binding to the receptor. After 1.5 h of 276 nm excitation the number of insulin molecules that are impaired for insulin receptor recognition is quite higher than the number of insulin molecules impaired for antibody recognition (61.7% decrease in glucose uptake *vs* 25.6% decrease in detected insulin by antibodies). After this UV-excitation period, part of the pool of insulin molecules may have suffered structural modifications in the binding sites regions but can still be recognized by the polyclonal antibodies due to the presence of several epitopes. In the radioimmunoassay and glucose uptake assays the insulin used for the experiments (illuminated or not) has been diluted down respectively to 0.0354 and 100 nM concentrations to allow receptor binding to monomeric insulin. During 1.5 h of continuous 276 nm excitation dityrosine has been formed, leading to likely insulin dimerization (Figure 1B). Upon dilution of the illuminated solution down to 0.0354 and 100 nM any dityrosine cross-linked dimers will remain as dimers. As previously discussed, covalent insulin dimerization would lead to loss of the binding capability and consequently loss of functional insulin, which is the monomeric form of insulin. As previously mentioned, metal-

catalyzed oxidation of insulin with H_2O_2/Cu leads to the formation of dityrosine [52]. In this case, formation of dityrosine is correlated with the formation of insulin aggregates (probably resultant from inter-molecular cross-linking) and loss of the peptide biological function [52]. According to the kinetics of fluorescence emission increase at 405 nm not even half of the dityrosine molecules are formed after 7 h of continuous excitation at 276 nm (Figure 5B, Table 2). As previously mentioned, the yield of dityrosine formation upon UV-excitation of proteins is rather low [20]. Thus, there is/are probably other population(s) of molecules whose native structural fold has suffered conformational changes via other mechanisms, such as SS disruption. After 1.5 h of 276 nm excitation the concentration of SH groups formed is 71.7% of the maximum detected concentration (Figure 8). It means that a considerable number of insulin molecules have had their SS disrupted. The integrity of the three native SS of insulin is essential for the hormone's biological activity. Disruption or rearrangement of any of these SS results in low or absent bioactivity [48]. Substitution of CysA6 and CysA11 in insulin with a serine or alanine pair reduces the binding affinity to the receptor to 0.1 and 5% of native insulin [48]. Other analogs with group substitutions of CysA7 or CysB7 showed also lower bioactivity than native insulin [48]. Therefore, considering these two major structural modifications it is not surprising that 25.6% of the insulin molecules are no longer detected by polyclonal antibodies and that ~61.7% have lost their function after 1.5 h of UV-excitation.

Conclusions

The present study advances conclusions that are of global importance to the shelf life of pharmaceutical products and preparations containing proteins. The majority of proteins contain several tyrosine residues, such as the pharmaceutical relevant proteins insulin, insulin growth factors, nerve growth factors, and tumor necrosis factors. If pharmaceutical preparations are exposed to ambient and artificial UV-light, long-term inter-molecular aggregation may occur via dityrosine cross-linking.

The irradiance level used in our experiments (2.20 W. m^{-2} at 276 nm) is similar to the total irradiance of sunlight in the UVB region (~0.78 W. m^{-2}, 280–315 nm) (See Table S1). UV sterilization lamps (Hg), which can be used during disinfection of the drug products, have irradiance levels ranging from 10 to 2400 W. m^{-2} at 254 nm, wavelength at which Tyr still absorbs (Table S1). Commercially available indoor light sources used commonly in industry, hospitals, warehouses, such as fluorescent tubes, quartz halogen lamps and even tungsten filament incandescent lamps can provide UVB (280–315 nm) and even UVC (200–280 nm) emission [62]. For instance, energy efficient compact fluorescent lamps (CFL) [63,64] provide irradiance levels up to $2–3\times10^{-2}$ W.m^{-2} in UVB and 8.15×10^{-3} W.m^{-2} in UVC (see Table S1). Though the irradiation levels of CFL and other light sources are still lower than the used in our experiments and that the distance of measurement is still quite short (0.1–0.2 m), it would not be surprising that long exposure times of insulin preparation to the above cited light sources will also induce partial degradation of the protein.

The FDA (Food and Drug Administration) ICH Q1B (Photostability Testing of New Drug Substances and Products) guideline for industry does not include any recommendation for carrying out photostability tests for light sources below 320 nm, which excludes testing for Tyr absorption in drugs containing proteins [5]. Furthermore, in the "confirmatory study" approach present in the ICH Q1B guideline, an illumination level with an integrated near-UV energy of 200 Wh. m^{-2} (0.055 W. m^{-2}) or more is recommended [5]. These irradiation levels might not represent accurately the exposure to UV-light suffered by drug products in industry.

It is important to include photostability studies of protein drug candidates prior to final formulation as also recommended by Rathore and Rajan [5]. The exposure time and spectral outputs of the light sources used should be investigated. During production, it is important to avoid the use of UV-light sources, including natural sunlight. The pharmaceutical preparations should be packed with UV-blocking materials.

Supporting Information

Table S1 Irradiance and other properties - experimental set-up, solar light and commonly used commercial light sources.
(DOCX)

Acknowledgments

The authors wish to thank Dorthe Rasmussen, Lene Trudsø and Kim Houtved Jensen for their skilled technical assistance.

Author Contributions

Conceived and designed the experiments: MC MTNP SP PBG SG. Performed the experiments: MC. Analyzed the data: MC MTNP SP PBJ SG. Contributed reagents/materials/analysis tools: MC MTNP SP PBJ SG. Wrote the paper: MC MTNP SP.

References

1. Neves-Petersen MT, Gryczynski Z, Lakowicz J, Fojan P, Pedersen S, et al. (2002) High probability of disrupting a disulphide bridge mediated by an endogenous excited tryptophan residue. Prot Sci 11:588–600.
2. Kerwin BA, Remmele RL (2007) Protect from Light: Photodegradation and Protein Biologics. J Pharm Sci 96: 1468–1479.
3. Neves-Petersen MT, Klitgaard S, Pascher T, Skovsen E, Polivka T, et al. (2009) Flash photolysis of cutinase: identification and decay kinetics of transient intermediates formed upon UV excitation of aromatic residues. Biophys J 97: 211–226.
4. Correia M, Neves-petersen MT, Parracino A, Kold A, Petersen SB (2012) Photophysics, Photochemistry and Energetics of UV Light Induced Disulphide Bridge Disruption in apo-α-Lactalbumin. J Fluor 22: 323–337.
5. Rathore N, Rajan RS (2008) Current Perspectives on Stability of Protein Drug Products during Formulation, Fill and Finish Operations. Biotechnol Prog 24: 504–514.
6. Hawe A, Wiggenhorn M, van de Weert M, Garbe JH, Mahler HC, et al. (2012) Forced Degradation of Therapeutic Proteins. J Pharm Sci 101: 895–913.
7. Dixon JM, Taniguchi M, Lindsey JS (2007) PhotochemCAD 2: A Refined Program with Accompanying Spectral Databases for Photochemical Calculations. Photochem Photobiol 81: 212–213.
8. Klitgaard S, Neves-Petersen MT, Petersen SB (2006) Quenchers induce wavelength dependence on protein fluorescence lifetimes. J Fluor 16: 595–609.
9. Creed D (1984) The Photophysics and Photochemistry of the Near-UV Absorbing Amino acids - II. Tyrosine and its Simple Derivatives. Photochem Photobiol 39: 563–575.
10. Bent DV, Hayon E (1975) Excited state chemistry of aromatic amino acids and related peptides. I. Tyrosine. J Am Chem Soc 97: 2599–2606.
11. McCormick ML, Gaut JP, Lin TS, Britigan BE, Buettner GR, et al. (1998) Electron paramagnetic resonance detection of free tyrosyl radical generated by myeloperoxidase, lactoperoxidase, and horseradish peroxidase. J Biol Chem 273: 32030–32037.
12. Giulivi C, Traaseth NJ, Davies KJ (2003) Tyrosine oxidation products: analysis and biological relevance. Amino Acids 25: 227–232.
13. Giulivi C, Davies KJ (1994) Dityrosine: a marker for oxidatively modified proteins and selective proteolysis. Methods Enzymol 233: 363–371.
14. Tew D, Montellano PR (1988) The Myoglobin Protein Radical. The myoglobin protein radical. Coupling of Tyr-103 to Tyr-151 in the H2O2-mediated cross-linking of sperm whale myoglobin. J Biol Chem 263: 17880–17886.

15. Aeschbach R, Amadoò R, Neukom H (1976) Formation of dityrosine cross-links in proteins by oxidation of tyrosine residues. Biochim Biophys Acta 439: 292–301.
16. Malencik DA, Anderson SR (1996) Dityrosine formation in calmodulin: cross-linking and polymerization catalyzed by Arthromyces peroxidase. Biochemistry 35: 4375–4386.
17. Terryn H, Vanhelleputte J-P, Maquille A, Tilquin B (2006) Chemical analysis of solid-state irradiated human insulin. Pharm Res 23: 2141–2148.
18. Malencik DA, Anderson SR (1987) Dityrosine formation in calmodulin. Biochemistry 26: 695–704.
19. Sionkowska A, Skopinska J, Wisniewski M, Leznicki A, Fisz J (2006) Spectroscopic studies into the influence of UV radiation on elastin hydrolysates in water solution. J Photochem Photobiol B 85: 79–84.
20. Malencik DA, Anderson SR (2003) Dityrosine as a product of oxidative stress and fluorescent probe. Amino acids 25: 233–247.
21. Balasubramanian D, Kanwar R (2002) Molecular pathology of dityrosine cross-links in proteins: structural and functional analysis of four proteins. Mol Cell Biochem 234–235: 27–38.
22. Lehrer SS, Fasman GD (1967) Ultraviolet irradiation effects in poly-L-tyrosine and model compounds. Identification of bityrosine as a photoproduct. Biochemistry 6: 757–767.
23. Malencik DA, Anderson SR (1991) Fluorometric characterization of dityrosine: complex formation with boric acid and borate ion. Biochem Biophys Res Commun 178: 60–67.
24. Gross AJ, Sizer IW (1959) The oxidation of tyramine, tyrosine, and related compounds by peroxidase. J Biol Chem 234: 1611–1614. Available: http://www.ncbi.nlm.nih.gov/pubmed/13654426. Accessed 2012 Apr 25.
25. Hoffman MZ, Hayon E (1972) One-electron reduction of the disulfide linkage in aqueous solution. Formation, protonation, and decay kinetics of the RSSR-radical. J Am Chem Soc 94: 7950–7957.
26. Bent DV, Hayon E (1975) Excited state chemistry of aromatic amino acids and related peptides. III. Tryptophan. J Am Chem Soc 97: 2612–2619.
27. Neves-Petersen MT, Snabe T, Klitgaard S, Duroux M, Petersen SB (2006) Photonic activation of disulfide bridges achieves oriented protein immobilization on biosensor surfaces. Protein Sci 15: 343–351.
28. Skovsen E, Kold AB, Neves-Petersen MT, Petersen SB (2009) Photonic immobilization of high-density protein arrays using Fourier optics. Proteomics 9: 3945–3948.
29. Parracino A, Gajula GP, di Gennaro AK, Correia M, Neves-Petersen MT, et al. (2011) Photonic immobilization of BSA for nanobiomedical applications: creation of high density microarrays and superparamagnetic bioconjugates. Biotechnol Bioeng 108: 999–1010.
30. Parracino A, Neves-Petersen MT, di Gennaro AK, Pettersson K, Lövgren T, et al. (2010) Arraying prostate specific antigen PSA and Fab anti-PSA using light-assisted molecular immobilization technology. Protein Sci 19: 1751–1759.
31. Duroux M, Skovsen E, Neves-Petersen MT, Duroux L, Gurevich L, et al. (2007) Light-induced immobilisation of biomolecules as an attractive alternative to microdroplet dispensing-based arraying technologies. Proteomics 7: 3491–3499.
32. Melmed S, Conn PM (2005) Endocrinology: Basic and Clinical Principles. Humana Press. 456 p.
33. LeRoithn D, Olefsky JM, Taylor SI (2003) Diabetes Mellitus: A Fundamental and Clinical Text. Lippincott Williams & Wilkins. p.1200.
34. Steiner DF, Chan SJ, Welsh JM, Kwok SC (1985) Structure and evolution of the insulin gene. Annu Rev Genet 19: 463–484.
35. Derewenda U, Derewenda Z, Dodson GG, Hubbard RE, Korber F (1989) Molecular structure of insulin: the insulin monomer and its assembly. Br Med Bull 45: 4–18.
36. Brange J, Owens DR, Kang S, Vølund a (1990) Monomeric insulins and their experimental and clinical implications. Diabetes Care 13: 923–954.
37. Baker EN, Blundell TL, Cutfield JF, Cutfield SM, Dodson EJ, et al. (1988) The structure of 2Zn pig insulin crystals at 1.5 A resolution. Philos Trans R Soc Lond Biol Sci 319: 369–456.
38. De Meyts P (2004) Insulin and its receptor: structure, function and evolution. Bioessays 1351–1362.
39. Becker RH (2007) Insulin glulisine complementing basal insulins: a review of structure and activity. Diabetes Technol Ther 9: 109–121.
40. Attri AK, Fernández C, Minton AP (2010) pH-dependent self-association of zinc-free insulin characterized by concentration-gradient static light scattering. Biophys Chem 148: 28–33.
41. Dunn MF (2005) Zinc-ligand interactions modulate assembly and stability of the insulin hexamer – a review. Biometals 18: 295–303.
42. Brange J, Langjær L (1993) Insulin Structure and Stability (Chapter 11). In: Pearlman R, Wang YJ,editors. Stability and Characterization of Protein and Peptide Drugs: Case Histories. Springer. 315.
43. Manno M, Mauro M, Craparo EF, Podestà A, Bulone D, et al. (2007) Kinetics of different processes in human insulin amyloid formation. J Mol Biol 366: 258–274.
44. Riener CK, Kada G, Gruber HJ (2002) Quick measurement of protein sulfhydryls with Ellman's reagent and with 4,4′-dithiodipyridine. Anal Bioanal Chem 373: 266–276.
45. Li AJ, Nussinov R (1998) A set of van der Waals and coulombic radii of protein atoms for molecular and solvent-accessible surface calculation, packing evaluation, and docking. Proteins 32: 111–27.
46. Pain R (2005) Determining the CD spectrum of a protein. Curr Protoc Protein Sci Chapter 7: Unit 7.6.
47. Pekar AH, Frank BH (1972) Conformation of proinsulin. A comparison of insulin and proinsulin self-association at neutral pH. Biochemistry 11: 4013–4016.
48. Mayer JP, Zhang F, Dimarchi RD (2007) Insulin Structure and Function. Biopolymers 88: 687–713.
49. De Meyts P (2008) The insulin receptor: a prototype for dimeric, allosteric membrane receptors? Trends Biochem Sci 33: 376–384.
50. Zoete V, Meuwly M, Karplus M (2004) A comparison of the dynamic behavior of monomeric and dimeric insulin shows structural rearrangements in the active monomer. J Mol Biol 342: 913–929.
51. Antolíková E, Žáková L, Turkenburg JP, Watson CJ, Hančlová I, et al. (2011) Non-equivalent role of inter- and intramolecular hydrogen bonds in the insulin dimer interface. J Biol Chem 286: 36968–36977.
52. Olivares-Corichi IM, Ceballos G, Medina-Santillan R, Medina-Navarro R, Guzman-Grenfell AM, et al. (2005) Oxidation by reactive oxygen species (ROS) alters the structure of human insulin and decreases the insulin-dependent D-glucose-C14 utilization by human adipose tissue. Front Biosci 10: 3127–3131.
53. Verweij H, Christianse K, Van Steveninck J (1982) Ozone-induced formation of O,O′-dityrosine cross-links in proteins. Biochim Biophys Acta 701: 180–184.
54. Zhang M, Mullens C, Gorski W (2005) Insulin oxidation and determination at carbon electrodes. Anal Chem 77: 6396–6401.
55. Heinecke JW, Li W, Daehnke III HL, Goldstein JA (1993) Dityrosine, a specific marker of oxidation, is sinthesized by the myeloperoxidase-hydrogen peroxide system of human neutrophils and macrophages. J Biol Chem 268: 4069–4077.
56. Mason HS (1948) The chemistry of melanin; mechanism of the oxidation of dihydroxyphenylalanine by tyrosinase. J Biol Chem 172: 83–99.
57. Mozziconacci O, Williams TD, Kerwin BA, Schöneich C (2008) Reversible intramolecular hydrogen transfer between protein cysteine thiyl radicals and alpha C-H bonds in insulin: control of selectivity by secondary structure. J Phys Chem B 112: 15921–15932.
58. Markus G (1964) Electrolytic Reduction of the Disulfide Bonds of Insulin. J Biol Chem 239: 4163–4170.
59. Fukada H, Takahashi K (1982) Enthalpy and heat capacity changes for the reduction of insulin. Biochemistry 21: 1570–1574.
60. Diaz JL, Wilkin TJ (1988) Effect of iodination site on binding of radiolabeled ligand by insulin antibodies and insulin autoantibodies. Clin Chem 34: 356–359.
61. Potter KN, Wilkin TJ (2000) The molecular specificity of insulin autoantibodies. Diabetes Metab Res Rev 16: 338–353.
62. Sayre RM, Dowdy JC, Poh-Fitzpatrick M (2004) Dermatological risk of indoor ultraviolet exposure from contemporary lighting sources. Photochem Photobiol 80: 47–51.
63. Khazova M, O'Hagan JB (2008) Optical radiation emissions from compact fluorescent lamps. Radiat Prot Dosimetry 131: 521–525.
64. Sharma P, Jaiswal VK, Kandpal HC (2009) Ultraviolet radiation emitted by compact fluorescent lamps. Mapan 24: 183–191.
65. ASTM Subcommittee G03.09 (2003) ASTM G173–03 Standard Tables for Reference Solar Spectral Irradiance Direct Normal and Hemispherical on 37° Tilted Surface. Annual Book of ASTM Standards. West Conshohocken, PA: ASTM International, Vol. 14.04.
66. Sen Lights Corporation (n.d.) Low-Pressure Mercury Lamps. Available: http://www.senlights.com/lamp/lplamp/lamp.htm.
67. Nuzum-Keim AD, Sontheimer RD (2009) Ultraviolet light output of compact fluorescent lamps: comparison to conventional incandescent and halogen residential lighting sources. Lupus 18: 556–560.

SUPPORTING INFORMATION: TABLE S1

Source	Light source / Lamp type	Purpose	Wavelength (nm)	Irradiance ($W.m^{-2}$)	Measurement Position
Our experiments	Xenon Arc Lamp	-	276* 280* 285*	2.20 2.31 2.39	At cuvette position
Reference solar spectrum – Direct + Circunsolar Solar Spectral Irradiance ASTM G173-03 Air Mass 1.5 Reference Spectra, American Society for Testing and Materials (ASTM) [65]	Sun	-	282.5** 285** 280-315	$1.16x10^{-16}$ $4.6x10^{-13}$ 0.78	Surface of earth
Sen Lights Corporation [66]	Low and High Pressure Hg Lamps	UV sterilization	254***	10 to 2400	1 meter distance from lamp
	Cold Cathode Lamps	Illumination, neon signs	254***	11 to 240	
Study on Compact Fluorescent Lamps from Khazova and O'Hagan [63] 73 commercial Compact Fluorescent Lamps were acquired from UK major retailers and tested	Compact Fluorescent Lamps Single Envelope (1 lamp)	Commercial, household, indoor lighting	254** 289**	~$2.6x10^{-3}$ ~$3.6x10^{-4}$	0.2 m distance from lamp
	Compact Fluorescent Lamps Single Envelope (53 lamps tested)		313***	>0.01 (24 % of lamps tested) 0.005-0.01 (30%) 0.001-0.005 (21%) 0.0001-0.005 (21%) <0.0001 (4%)	0.2 m distance from lamp
	Compact Fluorescent Lamps Double Envelope (20 lamps tested)		313***	0.001-0.005 (20% of lamps tested) 0.0001-0.005 (40%) <0.0001 (40%)	0.2 m distance from lamp
Study on Compact Fluorescent Lamps from Sharma et al. [64] 18 commercial Compact Fluorescent Lamps were tested	Compact Fluorescent Lamps Single Envelope		280-315 200-280	$2.87x10^{-3}$ to $28.15x10^{-3}$ $1.39x10^{-3}$ to $8.15x10^{-3}$	0.1 m distance from lamp

	Compact Fluorescent Lamps Double Envelope	280-315	$0.55x10^{-3}$ to $1.57x10^{-3}$	
		200-280	$0.21x10^{-3}$ to $0.53x10^{-3}$	
Study on Compact Fluorescent Lamps from Nuzum-Keim and Sontheimer [67] 12 commercial Lamps were tested	Incandescent lamps (3 out of 5 lamps tested)	280-315	$2x10^{-11}$ to $3x10^{-11}$	0.1 m distance from lamp
	Halogen lamp (1 out of 2 lamps tested)		~$2.5x10^{-11}$	
	Unshielded Compact Fluorescent Lamps (5 lamps tested)		$1x10^{-11}$ to $4.5x10^{-11}$	
	Shielded Compact Fluorescent Lamps (1 out of 2 lamps tested)		~$1x10^{-11}$	

[1]The irradiance value was measured/calculated from the power measured in the instrument at each wavelength and considering the exposition area of the cuvette. The bandwidth in the excitation slit was 5 nm.
[2]The irradiance value at each specific wavelength (e.g. 276 nm) was calculated by integration the spectral irradiation values over bandwidth of 5 nm.
[3]The calculation or measurement method was not stated in the source.

4.3 Paper 3

Modulating the structure of EGFR with UV light: new possibilities in cancer therapy

Manuel Correia, Viruthachalam Thiagarajan, Isabel Coutinho, Gnana Prakash Gajula, Steffen B. Petersen, and Maria Teresa Neves-Petersen

PloS One, PloS One, 9 (11), e111617

OPEN ACCESS Freely available online

PLOS ONE

Modulating the Structure of EGFR with UV Light: New Possibilities in Cancer Therapy

Manuel Correia[1☯], Viruthachalam Thiagarajan[2,3], Isabel Coutinho[2], Gnana Prakash Gajula[2], Steffen B. Petersen[4,5], Maria Teresa Neves-Petersen[2*☯]

1 Department of Physics and Nanotechnology, Aalborg University, Aalborg, Denmark, **2** BioPhotonics Group, Department of Nanomedicine, International Iberian Nanotechnology Laboratory (INL), Braga, Portugal, **3** School of Chemistry, Bharathidasan University, Tiruchirappalli, India, **4** Department of Health Science and Technology, Aalborg University, Aalborg, Denmark, **5** The Institute for Lasers, Photonics and Biophotonics, University at Buffalo, The State University of New York, New York, United States of America

Abstract

The epidermal growth factor receptor (EGFR) is a member of the ErbB family of receptor tyrosine kinases. EGFR is activated upon binding to e.g. epidermal growth factor (EGF), leading to cell survival, proliferation and migration. EGFR overactivation is associated with tumor progression. We have previously shown that low dose UVB illumination of cancer cells overexpressing EGFR prior to adding EGF halted the EGFR signaling pathway. We here show that UVB illumination of the extracellular domain of EGFR (sEGFR) induces protein conformational changes, disulphide bridge breakage and formation of tryptophan and tyrosine photoproducts such as dityrosine, N-formylkynurenine and kynurenine. Fluorescence spectroscopy, circular dichroism and thermal studies confirm the occurrence of conformational changes. An immunoassay has confirmed that UVB light induces structural changes in the EGF binding site. A monoclonal antibody which competes with EGF for binding sEGFR was used. We report clear evidence that UVB light induces structural changes in EGFR that impairs the correct binding of an EGFR specific antibody that competes with EGF for binding EGFR, confirming that the 3D structure of the EGFR binding domain suffered conformational changes upon UV illumination. The irradiance used is in the same order of magnitude as the integrated intensity in the solar UVB range. The new photonic technology disables a key receptor and is most likely applicable to the treatment of various types of cancer, alone or in combination with other therapies.

Citation: Correia M, Thiagarajan V, Coutinho I, Gajula GP, Petersen SB, et al. (2014) Modulating the Structure of EGFR with UV Light: New Possibilities in Cancer Therapy. PLoS ONE 9(11): e111617. doi:10.1371/journal.pone.0111617

Editor: Federico Quaini, University-Hospital of Parma, Italy

Received May 18, 2014; **Accepted** October 6, 2014; **Published** November 11, 2014

Data Availability: The authors confirm that all data underlying the findings are fully available without restriction. All relevant data are within the paper.

Funding: MC acknowledges the support from "Fundaço para a Ciência e Tecnologia" (FCT) for the PhD grant (SFRH/BD/61012/2009) supported by "Programa Operacional Potencial Humano" (POPH) in the framework of "Quadro de Referência Estratégica Nacional" (QREN) and co-financed by the European Social Fund ("Fundo Social Europeu", FSE). The funders had no role in study design, data collection and analysis, decision to publish, or preparation of the manuscript.

Competing Interests: The authors have declared that no competing interests exist.

* Email: nevespetersen@gmail.com

☯ These authors contributed equally to this work.

Introduction

The ErbB family of receptor tyrosine kinases (RTKs) plays a key role in regulating normal cellular processes such as cell survival, proliferation and migration [1,2] and have a critical role in the development and progression of cancers [3]. The epidermal growth factor receptor (EGFR; ErbB1) is a member of this family [4]. EGFR binding to ligands such as epidermal growth factor (EGF) or transforming growth factor alpha (TGF-α) leads to receptor dimerization and to the activation of the intracellular tyrosine kinase domain [1,2]. The extracellular domain of EGFR (sEGFR, soluble extracellular region of EGFR) comprises 4 subdomains: 2 large homologous binding domains (I and III), and 2 homologous furin-like cysteine rich domains (II and IV). Domains I, II and III have been found to be directly involved in ligand binding and dimer formation that precede the mechanism of signal transduction by RTKs [1,5,6]. Cancer progression has been correlated with the increase in the number of EGFR molecules on the cell surface [7]. High expression of EGFR is generally associated with invasion, metastasis, late-stage disease, chemotherapy resistance, hormonal therapy resistance and poor general therapeutic outcome. EGFR overexpression has been found to be a strong prognostic indicator in head and neck, ovarian, cervical, bladder and oesophageal cancers, a modest prognostic indicator in breast, colorectal, gastric and endometrial cancer and a weak prognostic indicator in non-small-cell lung cancer [7]. EGFR is the target of many chemotherapeutical approaches because EGFR activation results in cell signaling cascades that promote tumor growth. Inhibition of EGFR function is therefore a rational treatment approach. Typical chemotherapeutical agents are EGFR tyrosine kinase inhibitors which compete with ATP at the intracellular tyrosine kinase domain, and monoclonal antibodies (mAbs) that prevent ligand-binding or receptor dimerization. Blocking the binding of EGF to EGFR can abolish cancer proliferation, invasion, metastasis, angiogenesis and inhibition of apoptosis [8].

We have previously reported that UVB illumination (280 nm, 0.35 W/m^2 for 30 min) of cancer cells overexpressing EGFR led

to the arrest of the EGFR signaling pathway [9]. Proof-of-concept has been documented on cell lines A431 (human epidermoid carcinoma cells) and Cal39 (derived from human vulva squamous cell carcinoma cells). The irradiance used was lower than the total UVB solar irradiance [10]. UVB prevented EGF induced activation of EGFR, abolishing phosphorylation of the EGFR intracellular domain and of other key downstream signaling proteins such as AKT (Protein Kinase B) and the mitogen activated protein kinases (ERK1 and 2). AKT plays a key role in e.g. glucose metabolism, apoptosis, cell proliferation, transcription and cell migration. AKT is involved in cellular survival pathways by inhibiting apoptotic processes [11–16]. The ERK kinases act in a signaling cascade that regulates cellular processes such as proliferation, differentiation, and cell cycle progression [17].

One of the possible reasons for the observed UV light induced arrest of the EGFR signaling pathway is the UVB induced photochemistry, leading to conformational changes in EGFR which most likely prevent the correct binding to EGF. Our previous work on UVB induced photochemistry in proteins (wavelengths used 275–295 nm) [18–22] supports this hypothesis. UVB excitation of aromatic residues in proteins leads to the disruption of disulphide bridges and to the formation of photoproducts, such as N-formylkynurenine (NFK), kynurenine (Kyn) [23,24] and dityrosine (DT) [25–27] (see Figure 1). Such reactions will most likely induce structural changes in proteins which may impair their activity [22]. Proteins that are rich in aromatic residues and disulphide bridges are likely to have their structure considerably impaired upon prolonged UVB excitation. sEGFR is extremely rich in disulphide bridges when compared to the natural average abundance of disulphide bridges in protein structures of the size of sEGFR, as will be shown in the results section. The % of disulphide bridges in sEGFR is approximately 13 times higher than expected for a protein of its size. The expected average results have been previously reported by our group after a comprehensive analyses of the features of the disulphide bridges present in 131 non-homologous single chain protein structures [28]. Furthermore, the extracellular domain of sEGFR has 40 aromatic residues and 25 disulphide bridges per monomer and many of the aromatic residues are in close proximity of disulphide bridges (see Figure 2). Therefore, it is likely that UV illumination of this protein will lead to disulphide bridge breakage and to photoproducts. This hypothesis will be tested in our present paper.

Whereas the dangers of overexposure to sunlight have been well publicized, less attention has been given to the health benefits of UV-exposure. The effects of UV light on biomolecules, cells and tissues will depend on the energy delivered per unit area. UVB (280–315 nm) radiation is the primary contributor to vitamin D production, which has a protective effect in colon, prostate, and breast cancer [29,30]. Exposure to sunlight in low doses has also been linked to improved cancer survival rates [31,32]. UV light has been used to successfully treat rickets, psoriasis, lupus vulgaris, vitiligo, atopic dermatitis and localized scleroderma and jaundice (World Health Organization. The known health effects of UV. *Ultrav. Radiat. INTERSUN Program. - FAQ* at http://www.who.int/uv/faq/uvhealtfac/en/index1.html). There is no direct and conclusive evidence to suggest an increased risk of skin cancer from UVB treatments for psoriasis if radiation doses are respected. UV light is currently being used to treat cutaneous T-cell lymphoma (American Cancer Society, 2011 at http://www.cancer.org). This therapy has been improved by the Food and Drug Administration (FDA, USA). The protective effects of regular weekend sun exposure have been reported, particularly in the case of limb tumors [33]. Melanoma is more frequent among people with indoor occupations than among people having outdoor activities (without sunburn) such as farmers, fishermen, and kids that play outdoors [34,35]. Skin cancer is still on the increase but this is a result of exposure to UV light both by acute overdosing (causing sunburn) and lifelong cumulative exposure [36]. It is mainly the UVB fraction of solar radiation that gives erythema, melanogenesis (melanin production, which acts as a sunscreen protecting against DNA photodamage and erythema), vitamin D synthesis, and non-melanoma skin cancer, while melanoma is likely to be caused by UVA [37]. Jones et al (1987) found that among the UVA wavelengths, 365 nm had the highest mutagenic effect [38]. UVA fluency rates are several times higher for sunbeds than in the case of direct solar radiation [39]. The above examples document that the health effects of UV exposure are dose and wavelength dependent.

The goal of the present work is to investigate if a low dose of UVB light can induce structural changes in the EGF binding site of EGFR that could impair the correct binding of molecules, such a specific antibody that is known to compete with EGF for EGFR binding. If observed, this will give us insight into why UVB illumination (280 nm) of cancer cells overexpressing EGFR led to the arrest of the EGFR signaling pathway [9]. The UVB irradiance used is in the same order of magnitude as the total irradiance of solar UVB. Fluorescence spectroscopy and circular dichroism studies were carried out in order to detect UVB induced conformational changes. Thermal unfolding studies have been done in order to determine the melting point of the protein prior to and after illumination. Light induced breakage of disulphide bridges has been quantified and the formation of Trp/Tyr photoproducts has been detected. A binding immunoassay was carried out in order to infer the effects of UVB illumination on the structure of the EGF binding site. Our study confirms that low dose UVB (280 nm) illumination of sEGFR induced structural changes in the EGFR binding domain that impaired the binding of a specific antibody known to compete with EGF for EGFR binding to that particular domain. We address the beneficial effects of UV light, its present application in the treatment of diseases and the potential of our putative new photonic therapy for the treatment of localized tumors associated with the overexpression of UV sensitive cellular receptors.

Results

Three-dimensional structure of monomeric and dimeric sEGFR

In Figure 2A is displayed the 3D structure of monomeric sEGFR (1ivo.pdb, chain A) bound to Epidermal Growth Factor (EGF, in red). sEGFR contains 25 SS bridges, 6 Trp residues, 16 Tyr residues, and 18 Phe residues, displayed as CPK: SS bridges in yellow, Trp in green, Tyr in violet (Tyr246 and Tyr251 in pink) and Phe in cyan. Only 18 out of 25 SS bridges, 5 out of 6 Trp residues, 13 out of 16 Tyr residues and 17 out of 18 Phe residues are displayed since some residues are missing in the pdb file. Several aromatic residues are located in close spatial proximity of SS bonds.

In Figure 2B is displayed the 3D structure of the EGFR dimer (1ivo.pdb, chains A and B) formed upon binding EGF (in red). The dimer interface is rich in disulphide bridges and aromatic residues (Fig. 2B). Residues Tyr246 and Tyr251 (Figure 2B, in pink) from one chain, are intertwined with the same residues from the other chain. A zoom into one of the chains is displayed in Figure 2C and distances between aromatic residues and disulphide bridges are shown. EGF docking to EGFR is displayed in Figure 2D (EGFR monomer). The interaction between EGFR and EGF appears to

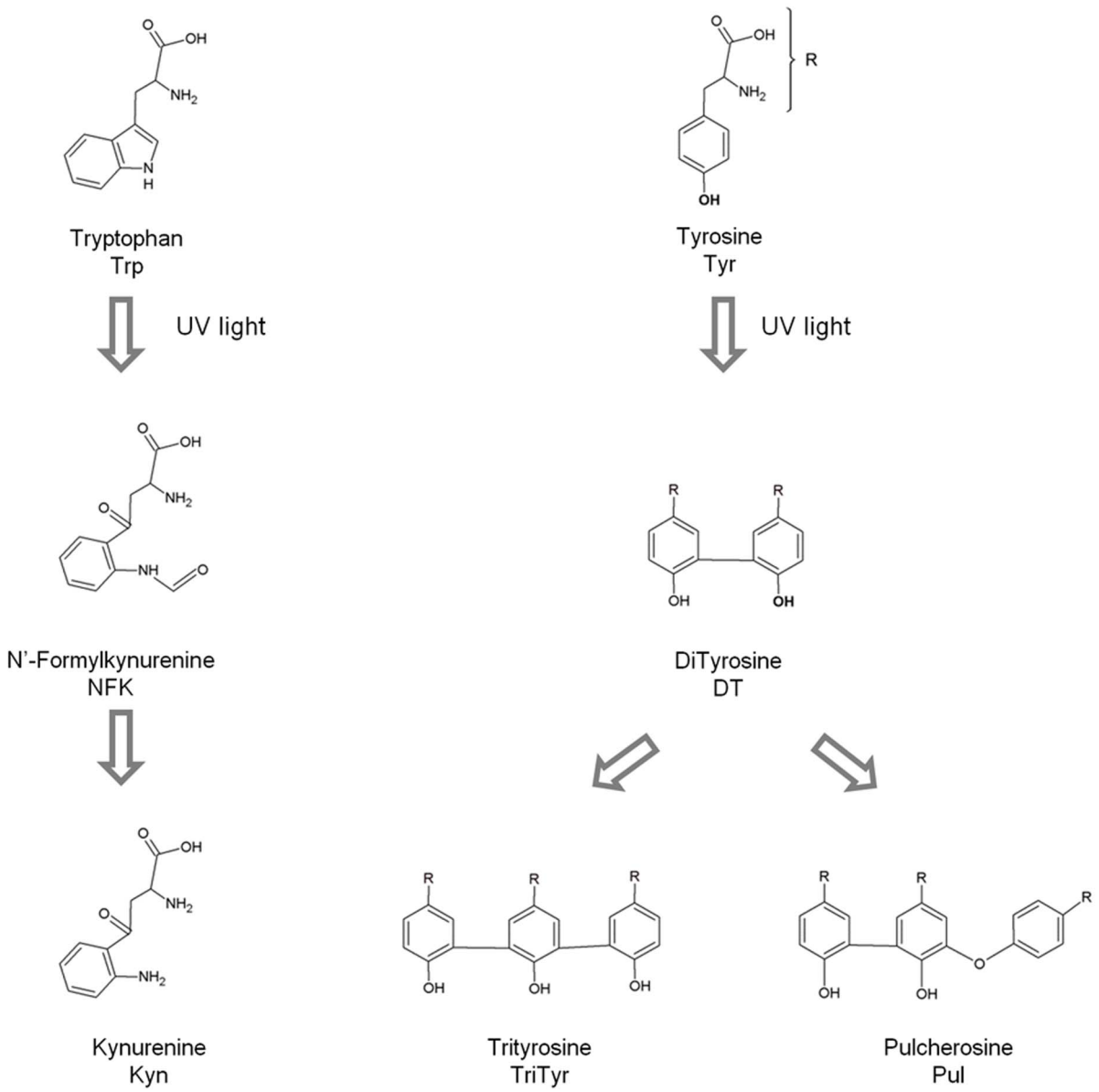

Figure 1. Typical photoproducts generated upon UV illumination of the aromatic residues Trp and Tyr.
doi:10.1371/journal.pone.0111617.g001

be strongly dependent on Van der Waals interactions. Some of those interactions are π-π interactions, such as the interaction between Phe357 (in cyan) of sEGFR and Tyr13 (in violet) of EGF (5 Å).

Protein Bioinformatics

In Figure 3 is displayed the fraction of disulphide bridges present in sEGFR and the dependence of the average fraction of disulphide bridges on the protein chain length [28]. The expected average fraction of disulphide bridges for proteins with sequence length of 600–650 residues is ~0.3%, while in sEGFR (622 aa) it is ~4%, confirming that this protein is exceedingly rich in disulphide bridges. The expected average results has been previously reported by our group after doing a comprehensive analyses of the features of the disulphide bridges present in 131 non-homologous single chain protein structures [28].

Steady State Fluorescence

The fluorescence emission intensity of sEGFR at 350 nm decreases upon continuous 280 nm excitation (Figure 4A). The kinetic trace is best fitted by a bi-exponential model (Figure 4A and methods). The root mean square error R^2 was 0.99774. The values recovered from the fitting for C1 and C2 were 367240.44±1182.23 and 208449.95±1054.90, respectively. The rate constants of fluorescence emission intensity decrease k1 and k2 fitted values were 117.63±0.71 min-1 and 12.20±0.10 min-1, respectively.

Emission Spectra (excitation 280 nm and 295 nm). Emission spectra of sEGFR were recorded upon 280 nm excitation before and after continuous 280 nm illumination (15 min, 30 min, 45 min and 75 min at 2.5 W/m^2) (not shown). A decrease in the intensity of the fluorescence emission at ~337 nm, where Trp and Tyr emit, is observed due to continuous illumination. The emission intensity at 337 nm decreases by 43%

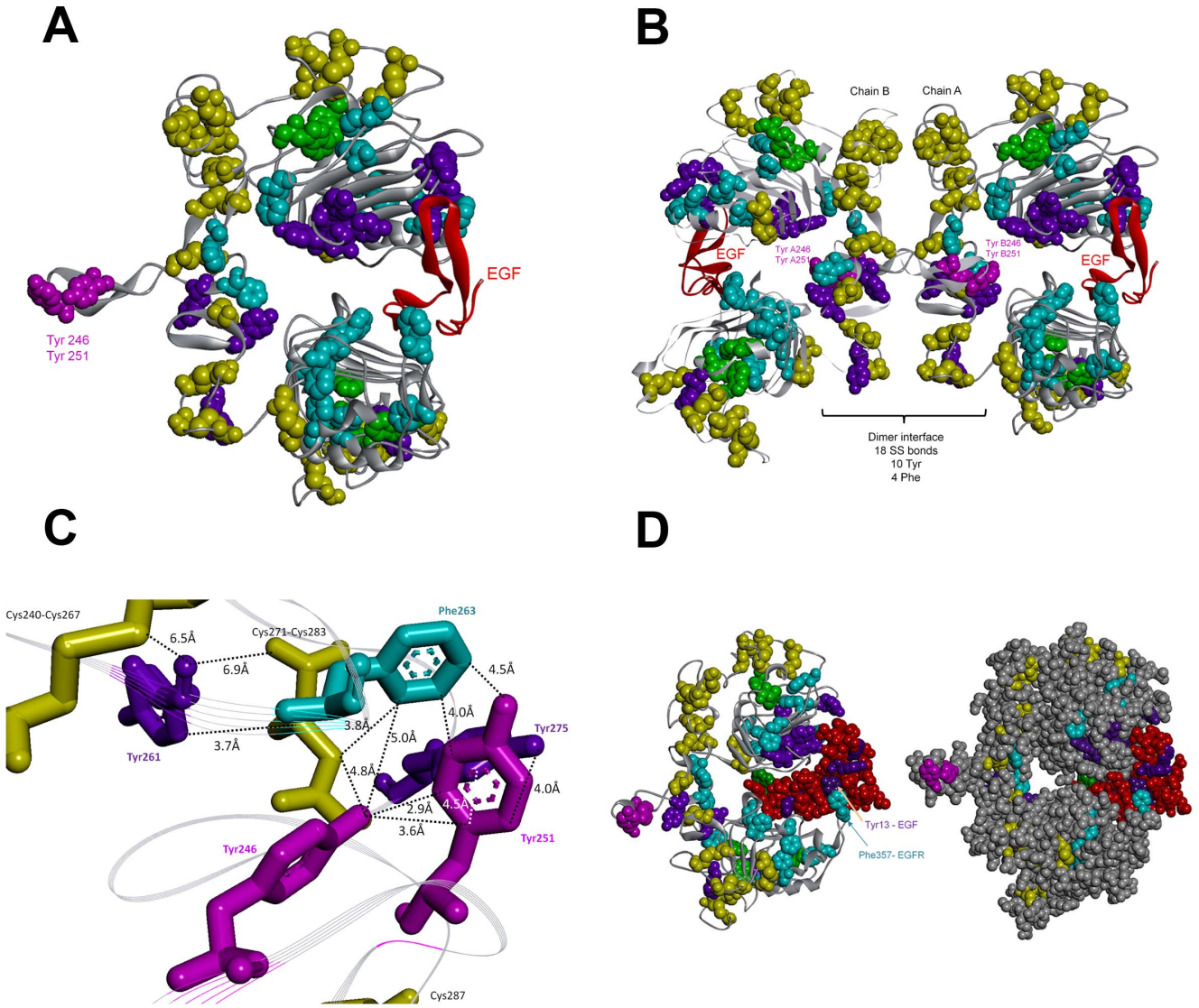

Figure 2. Structural analysis of the EGFR extracellular domain and interactions with EGF upon dimerization. (A) Crystal structure of EGFR extracellular domain (1ivo.pdb, chain A) [1]. The disulphide bridges and aromatic residues atoms are displayed as CPK: SS bridges in yellow, Trp in green, Tyr in violet (Try 246 and Tyr 251 are displayed in pink) and Phe in cyan. Only 18 out of 25 SS bridges, 5 out of 6 Trp residues, 13 out of 16 Tyr residues and 17 out of 18 Phe residues are displayed since some residues are missing in the pdb file. (B) Crystal structure of a 1:1 complex between human EGF and the dimeric form of EGFR extracellular domain (1ivo.pdb, chain A and B and 2 EGF molecules [1]). EGF is displayed in red. (C) Zoom into interface region present in the dimeric of EGFR (extracellular domains). Distances among some of the aromatic residues and the nearby disulphide bridges are also displayed. (D) Crystal structure of a 1:1 complex between human EGF and the dimeric form of EGFR extracellular domain. (1ivo.pdb, chain A and B and 2 EGF molecules [1]) EGF is shown in red. In the right panel all atoms are displayed as CPK. EGF docking to sEGFR involves extensive non-covalent contacts.
doi:10.1371/journal.pone.0111617.g002

and 74% after 15 min and 75 min of continuous 280 nm illumination, respectively. The wavelength of the most intense peak centered at 337 nm remains constant.

The emission spectra of sEGFR recorded upon 295 nm excitation before and after of continuous 280 nm illumination (15 min, 30 min, 45 min and 75 min) are shown in Figure 4B. A decrease in the intensity of the fluorescence emission at ~337 nm, where Trp emits, is observed. The emission intensity of sEGFR at 337 nm decreases by 42% and 77% after 15 min and 75 min of continuous 280 nm illumination, respectively. The wavelength of the most intense peak centered at 337 nm is observed to red-shift to 343 nm after 75 min of illumination.

Excitation Spectra (emission 334 nm). In Figure 4C is displayed the excitation spectra of sEGFR with fluorescence emission fixed at 334 nm, before and after continuous 280 nm illumination of the protein for different time periods: 15 min, 30 min, 45 min, 60 min and 75 min. Trp and Tyr absorption contribute to this spectrum. Continuous 280 nm illumination leads to a progressive decrease in the fluorescence excitation intensity. After 15 min and 75 min of illumination, the excitation intensity at 282 nm decreases by 40% and 71%, respectively. The correspondent normalized excitation spectra (not shown) show no shift in the wavelength at maximum excitation intensity (~282 nm).

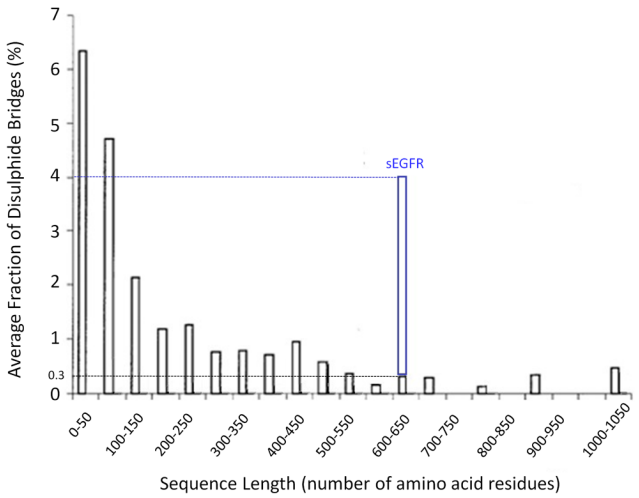

Figure 3. Dependence of the average fraction of disulphide bridges on the protein chain length. The fraction of disulphide bridges was calculated as the number of disulphide bridges found in a protein divided by the protein sequence length (number of amino acids) x 100. The fraction of disulphide bridges present in the monomeric extracellular domain of EGFR is displayed.
doi:10.1371/journal.pone.0111617.g003

Fluorescence based protein thermal unfolding studies. The fluorescence emission intensity at 330 nm (exc. 295 nm) of a fresh sEGFR sample (non-illum.) and illuminated sEGFR sample (75 min at 280 nm) was monitored from 4°C to 90°C and from 90°C to 4°C (see Fig. 5). For both samples the fluorescence emission intensity decreases upon heating. A transition between 65–75°C is observed for the non-illuminated sEGFR. Data has been fitted using a modified Boltzmann function (see methods). The root mean square error for the fitting R^2 was 0.99774. The values recovered from the fitting for $A1$, $B1$, $A2$, $B2$ and dx were 1.06202±0.0014, 0.45482±0.02255, −0.00426± 5.41E-04, -0.00296±2.72E-04 and 1.74±0.17, respectively. The recovered parameter $x0$ (69.7°±0.24°C C) corresponds to the mid-point of transition, i.e. to the melting temperature of the protein. This value is in agreement with the inflection point values obtained from the second derivative of the fitted data (not shown). The second derivative is zero (inflection point) within the interval 68.3–69.2°C. Such transition is not observed for the illuminated sample. Furthermore, no transition is observed for both samples when cooling the protein from 90°C to 4°C.

Time Resolved Fluorescence. The decay times (τ_i) and pre-exponential factors (f_i) recovered from the time resolved intensity decays for the control sEGFR sample (75 min in the dark, negative control, NC) and the illuminated sEGFR sample (illum. for 75 min

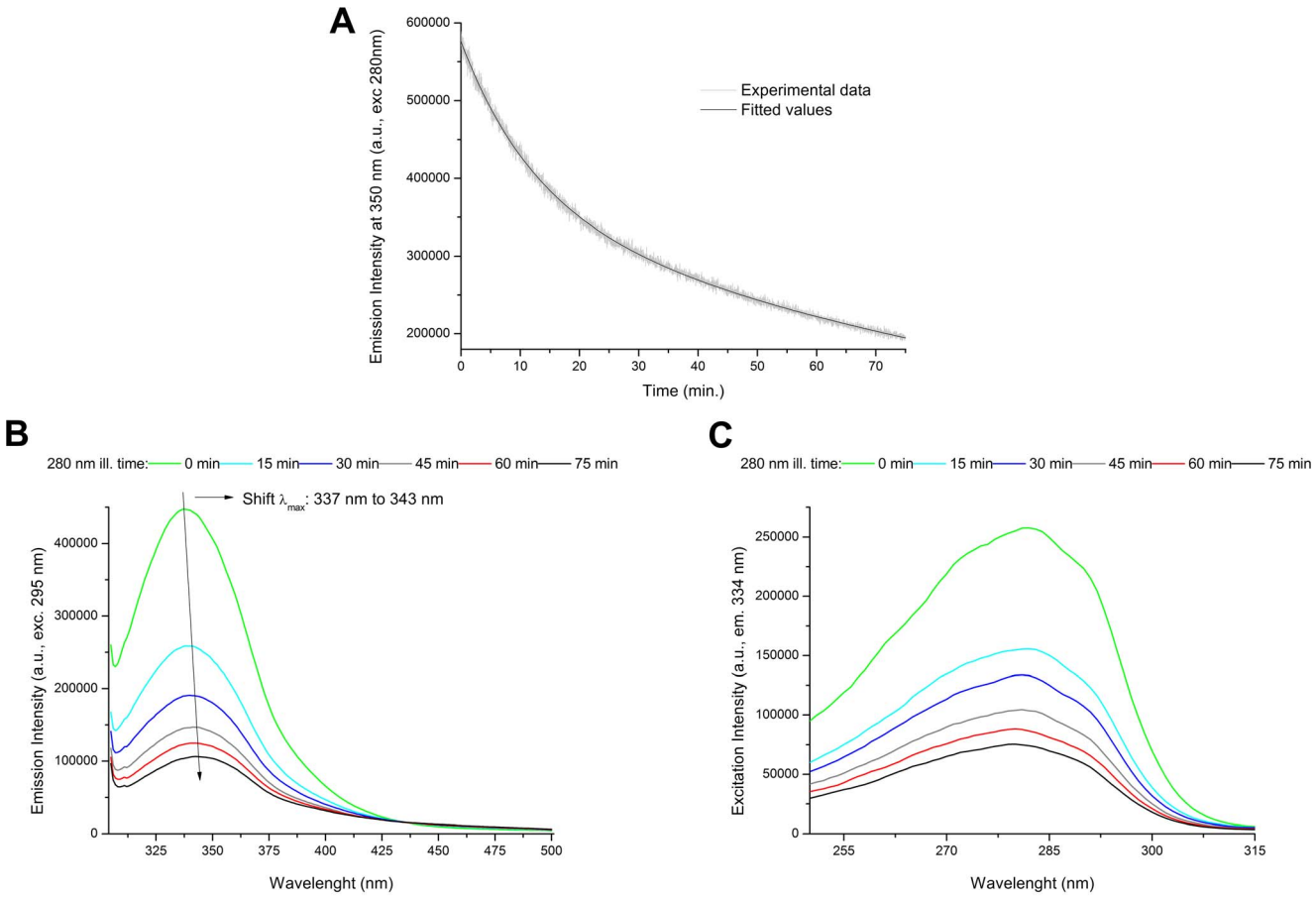

Figure 4. Effects of UV illumination on the intrinsic fluorescence emission of human extracellular EGFR. (A) Fluorescence emission intensity kinetics at 350 nm of human extracellular EGFR (sEGFR) sample during 75 min UV illumination at 280 nm. (B) Fluorescence emission spectra of sEGFR samples obtained upon 295 nm excitation after 280 nm illumination for 0 min, 15 min, 30 min, 45 min, 60 min and 75 min. (C) Fluorescence excitation spectra of sEGFR samples recorded with emission fixed at 334 nm excitation after 280 nm illumination for 0 min, 15 min, 30 min, 45 min, 60 min and 75 min.
doi:10.1371/journal.pone.0111617.g004

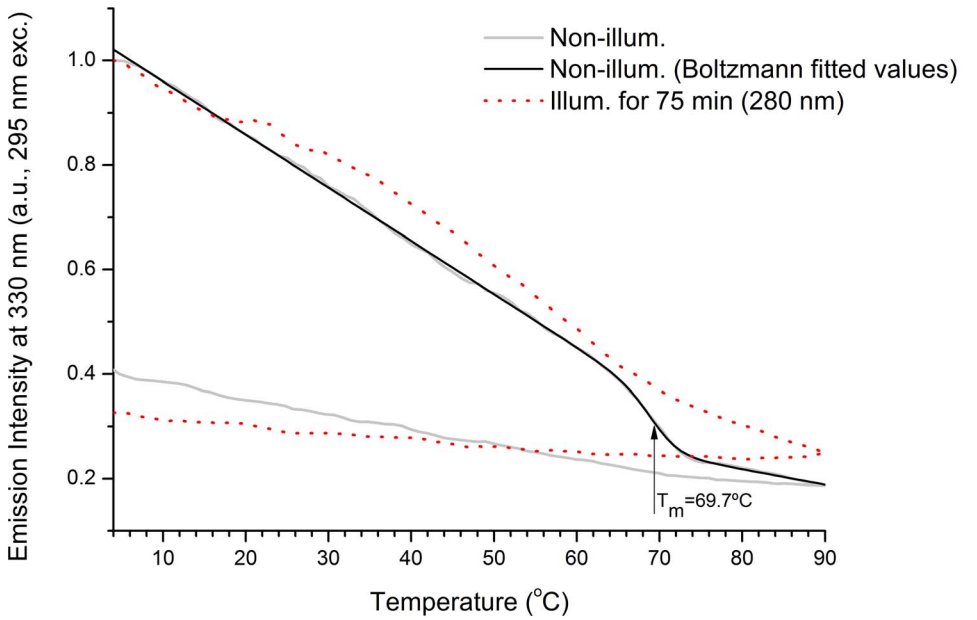

Figure 5. Temperature dependent fluorescence emission intensity at 330 nm upon 295 nm excitation. Non illuminated (non illum.) and UV illuminated (illum. for 75 min) human extracellular EGFR (sEGFR) samples were heated from 4 °C to 90 °C. Fitted values (non-illuminated sample) were obtained using a modified Boltzmann function (see Results section). The transition mid-point recovered from the fitting was at 69.72±0.24°C.
doi:10.1371/journal.pone.0111617.g005

at 280 nm) at pH 7.5 are given in Table 1. Figure 6 shows the experimental data, the fit and residuals assuming three lifetime decays for sEGFR control sample (NC). The value of χ^2 dropped significantly when progressing from a one lifetime component fit to two and to three components. The fluorescence mean lifetime of sEGFR is shown in Table 1. Non-illuminated sEGFR displays three lifetimes: 1.04 ns, 2.74 ns and 6.23 ns with intensity fractions of 25.6%, 53.1% and 21.1%, respectively. Upon illumination, the contribution of the shortest lived 1.04 ns species increased from 25.6% to 30.6%, the contribution of the 2.74 ns species was kept constant and the contribution of the longer lived species decreased from 21.1% to 16.4%. Furthermore, the lifetime of the longer lived component increased from 6.2 ns to 7.0 ns while the lifetime of the other two components remained constant.

Excitation Spectra (emission 400 nm). In Figure 7A are displayed the excitation spectra (emission at 400 nm) obtained before and after continuous 280 nm illumination (0 min, 15 min, 30 min, 45 min, 62 min and 75 min). Spectra were recorded in order to verify the presence of NFK, dityrosine and Kyn (Fig. 1). In Table 2 are displayed their absorbance and fluorescence emission properties. At 0 min, one excitation peak is observed centered at ~281 nm. Its intensity decays upon UV illumination of sEGFR, decreasing 52% after 75 min. However, illumination of sEGFR leads to an increase of fluorescence excitation above 305 nm. After 75 min, fluorescent excitation intensity increased 115% at 315 nm, where dityrosine maximally absorbs (Abs^{max} at 316 nm, [40], see Table 2), 149% at 322 nm, where NFK maximally absorbs (Abs^{max} at 321 nm, [23], see Table 2) and 173% at 360 nm, where Kyn maximally absorbs (Abs^{max} at 360 nm, [23], see Table 2).

Emission Spectra (excitation 320 nm). In order to verify the formation of dityrosine (DT) and NFK, emission spectra were obtained upon 320 nm excitation before and after 280 nm illumination (Fig. 7B). An increase in fluorescence emission intensity at 400–405 nm (exc. 320 nm) is observed. The fluorescence emission maximum is centered ~400 nm, corresponding to the emission maximum of DT (Em^{max} at 400–409 nm, [25,40], see Table 2) and to a spectral region where NFK can also emit (for NFK, Em^{max} at 400–440 nm [23], Table 2). After 75 min, fluorescence emission intensity at 400 nm increases by 129%. A small emission peak at ~368 nm is observed in the spectra

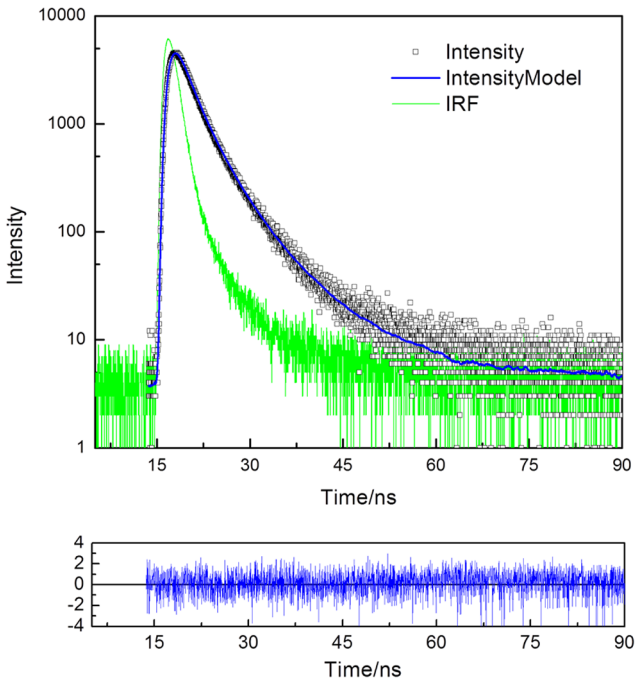

Figure 6. Time-resolved fluorescence measurements. Time-resolved intensity decay data, fitting curve and residuals obtained using the ISS routine for the control sEGFR sample (kept in the dark for 75 min, negative control, NC).
doi:10.1371/journal.pone.0111617.g006

Table 1. Lifetimes (τ_i) and pre-exponential values (α_i) for sEGFR (negative control and UV illuminated samples) at pH 7.5 obtained by a nonlinear fit (see Figure 6 for example, negative control sEGFR) using the ISS software.

Lifetime (ns)		Intensity fraction		Pre-exponential	
sEGFR Dark for 75 min (negative control, NC)					
τ_1	1.04±0.06	f_1	0.258±0.02	α_1	24.8
τ_2	2.74±0.1	f_2	0.531±0.01	α_2	19.4
τ_3	6.23±0.2	f_3	0.211 Fixed	α_3	3.38
$<\tau>_{f\ \text{weighed}}$	3.04				
sEGFR Illum. for 75 min (at 280 nm)					
τ_1	1.02±0.04	f_1	0.306±0.02	α_1	30
τ_2	2.88±0.1	f_2	0.53±0.01	α_2	18.4
τ_3	7.0±0.2	f_3	0.164 Fixed	α_3	2.34
$<\tau>_{f\ \text{weighed}}$	2.99				

doi:10.1371/journal.pone.0111617.t001

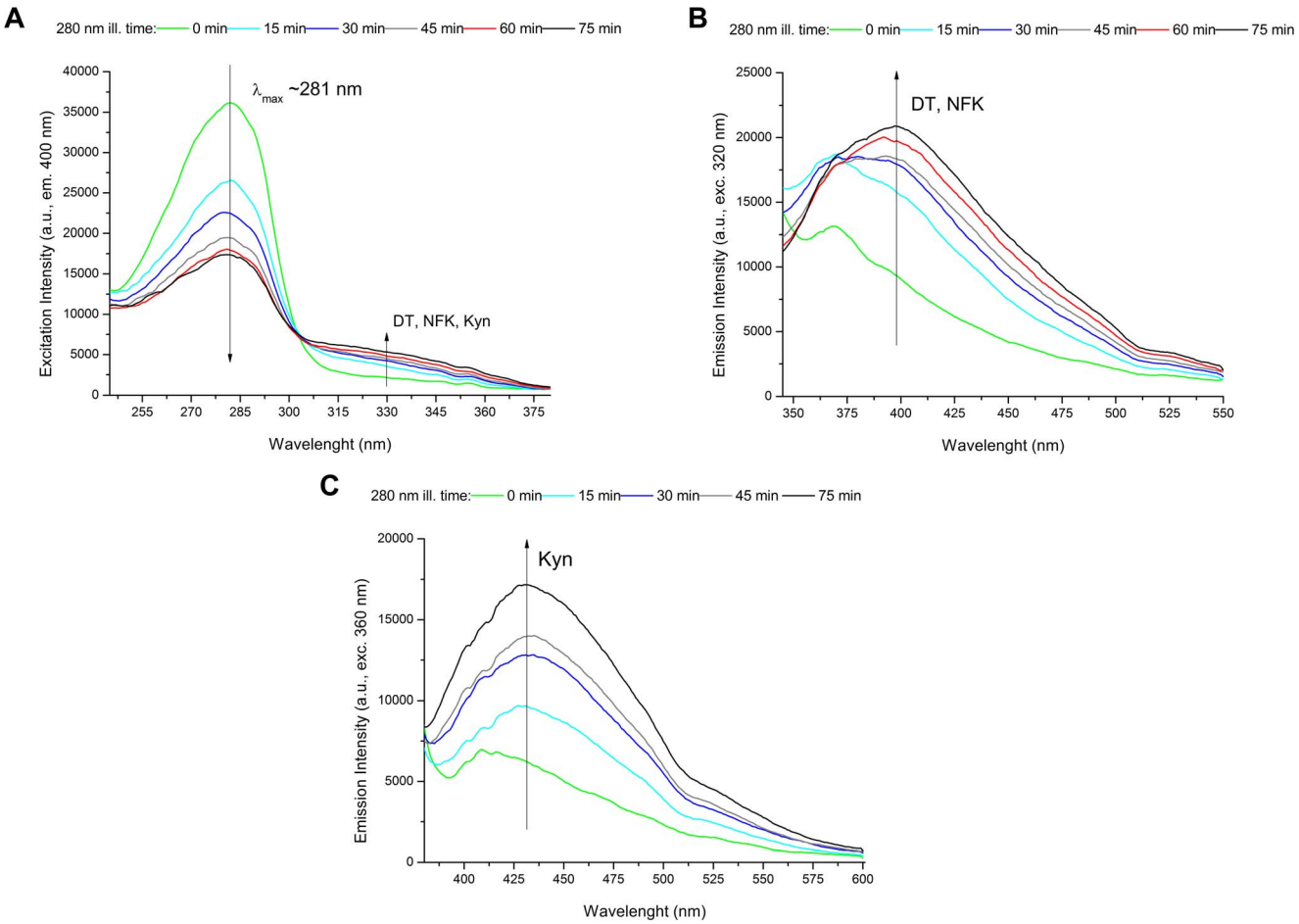

Figure 7. Formation of new fluorescence species and changes in thermal unfolding of the human extracellular EGFR upon UV illumination. (A) Fluorescence emission spectra of human extracellular EGFR (sEGFR) samples recorded upon 320 nm excitation after 280 nm illumination for 0 min, 15 min, 30 min, 45 min, 60 min and 75 min. (B) Fluorescence emission spectra of sEGFR recorded upon 360 nm excitation after 280 nm illumination for 0 min, 15 min, 30 min, 45 min and 75 min. (C) Fluorescence excitation spectra of sEGFR obtained with fluorescence emission fixed at 400 nm after 280 nm illumination for 0 min, 15 min, 30 min, 45 min, 60 min and 75 min.
doi:10.1371/journal.pone.0111617.g007

Table 2. Absorption and fluorescence spectral characteristics of N-formylkynurenine (NFK), dityrosine (DT) and kynurenine (Kyn) [23,25,40].

	Absorption (λ_{max}, nm)	Fluor. Em. (λ_{max}, nm)
NKF	261, 322	400–440[a]
DT	284, 316	400–409
Kyn	258, 360	434–480[a]

[a]Depending on solvent characteristics (e.g. polarity).
doi:10.1371/journal.pone.0111617.t002

obtained at 0 min and 15 min of illumination due to the Raman contribution of water. Raman spectral corrections did not completely remove this peak.

Emission Spectra (excitation 360 nm). In order to verify the presence of kynurenine (Kyn) (Abs^{max} at 360 nm, [23], Table 2) in sEGFR, emission spectra were obtained upon 360 nm excitation before and after 15 min, 30 min, 45 min, 60 min and 75 min of 280 nm illumination (Fig. 7C). Kyn absorbs maximally at 360–365 nm and fluoresces maximally at ~434–480 nm ([23], Table 2). Continuous UVB illumination of sEGFR leads to an increase of fluorescence centered at ~430–435 nm. The fluorescence intensity at 430 nm increased 53% and 172 after 15 min and 75 min illumination, respectively.

Thiol group's quantification

In order to confirm that UV illumination of sEGFR has led to SS disruption, the concentration of solvent accessible thiol groups has been determined with the Ellman's assay for a control sEGFR sample kept in the dark for 75 min (negative control, NC) and for a sample previously illuminated at 280 nm for 75 min. The detected concentration of free thiol groups is 2.9 fold higher in the illuminated sample (Fig. 8). Free thiol groups in illuminated sEGFR is ~1 μM.

Circular dichroism studies

In Figure 9A are displayed the CD spectra of fresh sEGFR (non-illum.) and illuminated sEGFR (75 min at 280 nm). The far-UV CD spectrum of the non-illuminated sEGFR displays some of the classical far-UV features of protein secondary structure, with the presence of a double minimum at 208–210 nm and 220–222 nm, characteristic of α-helical content. β-sheet structural content (characteristic minimum at ~218 nm) may also contribute for the second minimum at 220–222 nm [41]. Prolonged excitation with UVB light leads to a decrease in the ellipticity intensity at 205–225 nm and to a spectral shift. The ellipticity at 207.5 nm and at 220 nm has decreased by 9% and 20%, respectively. Furthermore, the first negative peak has shifted from 207.5 nm to 203 nm.

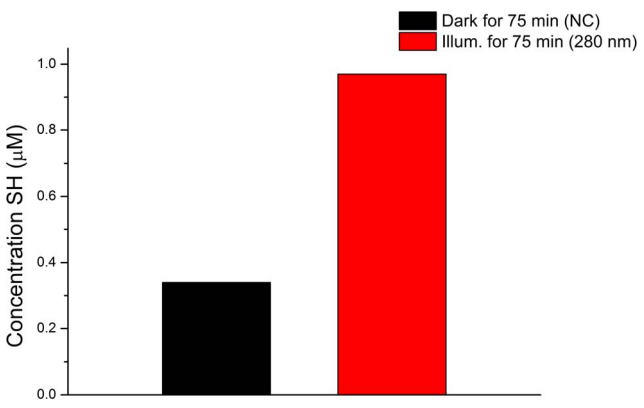

Figure 8. Increase in the concentration of free thiol groups detected in sEGFR upon UV illumination for 75 min. The control sample of sEGFR was kept in the dark for 75 min (negative control, NC). Free thiol groups have been detected using the Ellmann's assay.
doi:10.1371/journal.pone.0111617.g008

Circular dichroism based protein thermal unfolding studies. The ellipticity intensity at 220 nm of fresh sEGFR (non illum.) and of illuminated sEGFR (75 min at 280 nm) was continuously monitored from 4°C to 90°C (Fig. 9B). For both samples the ellipticity intensity at 220 nm decreases upon heating. A transition with mid-point between 60–70 °C is observed for the non-illuminated sEGFR sample. Data has been fitted by a Boltzmann function (see methods). The root mean square error for the fitting R^2 was 0.99921. The values recovered from the fitting for $A1$, $A2$ and dx were -0.96 ± 9.97E-4, -0.83 ± 0.002, and 2.59 ± 0.08, respectively. The temperature of mid-transition $x0$ fitted value was 64.70 ± 0.07 °C, corresponding to the melting temperature of the protein. This value is in agreement with the value recovered by fluorescence spectroscopy displayed in Figure 5. Such transition is not observed for the illuminated sample.

EGFR binding immunoassay

A binding immunoassay was used to indirectly access the effects of UV illumination on the structure of the sEGFR binding site to EGF/TGF-α. Results displayed in Figure 10 show that non-illuminated sEGFR binds LA1 anti-EGFR (lanes "No-UV", fresh sample; and "NC", negative control, sample kept in the dark for 75 min). sEGFR sample illuminated with 280 nm light for 75 min no longer binds LA1 anti-EGFR, confirmed by the complete disappearance of the sEGFR band (Figure 10, lanes "UV"). Two sets of duplicate samples were analysed. Signal intensity profiles along the protein bands are shown. The intensity observed in the regions where illuminated sEGFR was present ("UV" lanes) is within the observed noise level (noise intensity from ~0.02 to 0.2).

Discussion

UVB excitation of aromatic residues leads to the formation of photoproducts. Tryptophan may form tryptophanyl cation radical, N-formylkynurenine (NKF) and kynurenine (Kyn) (Fig. 1). NFK and Kyn are of particular importance as they are photosensitizers that can generate reactive oxygen species (ROS) upon UV absorption [42], further contributing to protein structural damage. Tyrosine residues are known to be converted into e.g. tyrosil radicals, dityrosine, trityrosine and pulcherosine (Fig. 1). These reactions are likely to lead to changes or to complete loss of protein structure and function [22,43]. UVB excitation also leads to

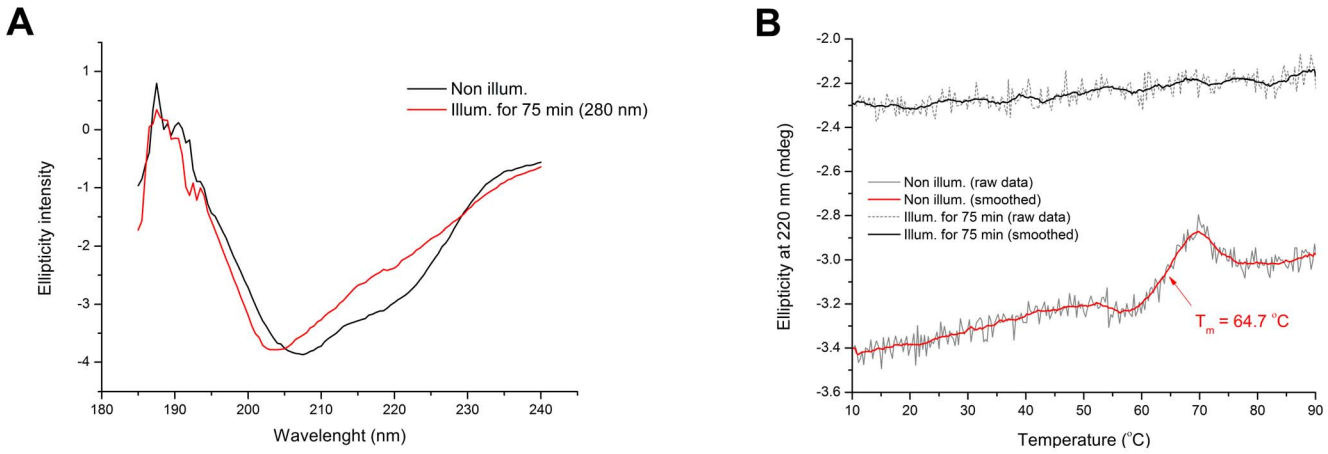

Figure 9. Effect of UVB illumination on the far UV circular dichroism features of sEGFR. (A) Far UV CD spectra were recorded for a fresh sEGFR solution (non illum.) and a sEGFR sample that was previously illuminated at 280 nm (illum. for 75 min). (B) Circular dichroim thermal unfolding curves of fresh sEGFR (non-illum.) and UVB illuminated sEGFR (illum. for 75 min) were obtained upon heating from 4 °C to 90 °C (1 °C.min^{-1}). The ellipticity signal was constantly monitored at 220 nm. The melting temperature of non illuminated sEGFR, which corresponds to the transition mid-point of the curve, was recovered upon fitting the curve with a Boltzmann function (see methods).
doi:10.1371/journal.pone.0111617.g009

electron ejection from the side chains of aromatic residues [20,24,44–46]. The electron can be captured by disulphide bridges, leading to the formation of a transient disulphide electron adduct RSSR$^{\bullet-}$ (see schemes 1–8, [49]), which upon dissociation will form free thiol groups (scheme 9, [47]). Nature has kept aromatic residues in spatial close proximity to disulphide bridges

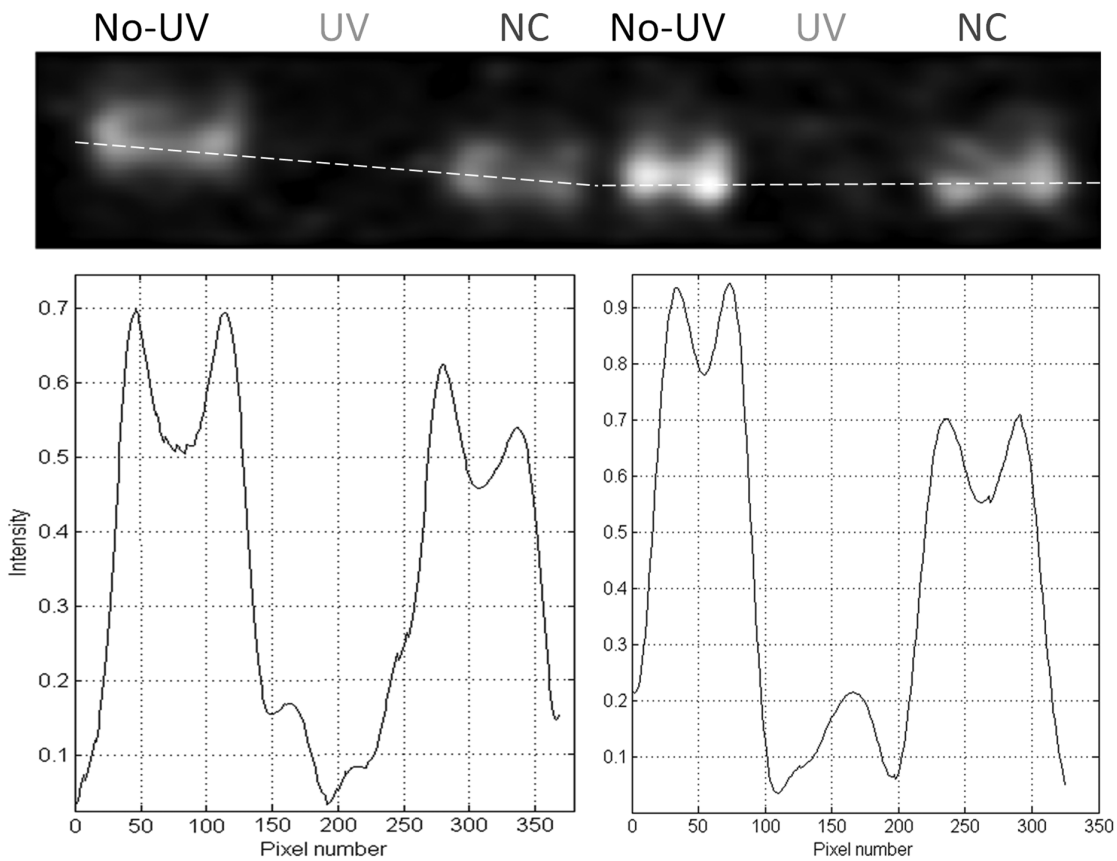

Figure 10. UV illumination of sEGFR prevents binding of anti-EGFR neutralizer antibody LA1 to its target antigen. In each well, exactly 1.4 μg of non illuminated ("No-UV"), UV illuminated for 75 min ("UV") and negative control ("NC") sEGFR samples was loaded. Samples loaded on well 1–3 are duplicates of samples 4–6, but were treated independently after UV illumination. The intensity profile along the wells shows that signal is observed in the wells with non-illuminated protein but no signal is present in the wells containing UV illuminated protein samples.
doi:10.1371/journal.pone.0111617.g010

(SS) in proteins [19,28], making the disruption of SS a likely event upon UV excitation. The schemes below summarize some of the photoproducts formed which contribute to SS disruption, leading to conformation changes that can lead to loss of protein function. For further details please see referenced literature [21,22,24].

$$^1\text{Tyr-OH} + h\nu \rightarrow {}^1\text{Tyr-OH}^{\bullet +} + e_{aq}^- \quad (1)$$

$$^1\text{Trp} + h\nu \rightarrow {}^1\text{Trp}^{\bullet +} + e_{aq}^- \quad (2)$$

$$^1\text{Tyr-OH} + h\nu \rightarrow {}^3\text{Tyr-OH} \quad (3)$$

$$^1\text{Tyr-O}^- + h\nu \rightarrow {}^1\text{Tyr-O}^{\bullet} + e_{aq}^- \quad (4)$$

$$^1\text{Trp} + h\nu \rightarrow {}^1\text{Trp}^{*} \quad (5)$$

$$^1\text{Trp}^{*} \rightarrow {}^3\text{Trp} \quad (6)$$

$$e_{aq}^- + \text{RSSR} \rightarrow \text{RSSR}^{\bullet -} \quad (7)$$

$$^3\text{Trp} + \text{RSSR} \rightarrow \text{Trp}^{\bullet +} + \text{RSSR}^{\bullet -} \quad (8)$$

$$\text{RSSR}^{\bullet -} \Leftrightarrow \text{RS}^{\bullet} + \text{RS}^{-} \quad (9)$$

Proteins rich in aromatic residues and disulphide bridges are most vulnerable to photochemistry and damage. sEGFR is such a protein. It has a total of 6 Trp, 16 Tyr, 18 Phe residues and 25 disulphide bridges (Figure 2A). Interestingly, aromatic residues and disulphide bridges play a critical structural role at the dimer interface (Figures 2B, 2C, and 2D) indicating that UVB induced photochemistry will most likely impair EGFR dimerization. The close proximity between aromatic residues and disulphide bridges (Figure 2C) promotes electron transfer from the aromatic residues to the bridges, leading to their disruption. UV-induced protein inactivation involves fast and short-range electron transfer between photoexcited aromatic residues and nearby disulphide bridges [20,44,45,48]. Zhi Li et al. [49] showed that fast electron transfer is consistent with direct electron transfer between triplet tryptophan and a nearby disulphide bridge, leading to $RSSR^{\bullet -}$ and likely bridge breakage (schemes 8 and 9). As displayed in Figure 3, proteins as large as sEGFR (600–650 aa) are observed to have an average fraction of disulphide bridges no larger than ~0.3%. This is presumably due to the stabilizing effect of the large hydrophobic core. A short protein has a much smaller hydrophobic core and depends to a larger extent on the structural stability provided by disulphide bridges. An example of this is insulin, a molecule formed by two polypeptide chains containing 21 and 30 residues, respectively, and that has 3 disulphide bridges (SS average fraction of 5.9%). Two disulphide bridges are the only covalent links between the chains. sEGFR displays an average SS fraction of ~4% compared to the expected ~0.3%, which means that disulphide bridges in sEGFR are ~13 times more abundant than expected for a protein of this length. Due to the fact that disulphide bridges are good acceptors of the electrons produced upon UV excitation of the protein, several disulphide bridges might be disrupted during illumination, compromising the structure of sEGFR. Data confirms that UVB illumination of sEGFR leads to the disruption of disulphide bridges (Fig. 8).

Receptors that are not as rich in aromatic residues and disulphide bridges as EGFR is are known be less sensitive of UV light. Huang et al. have reported that PDGF receptors did not appear to be involved in the cells response to UVC illumination, contrary to what they observed with EGFR [50]. They observed that PDGF-B was able to stimulate the tyrosine phosphorylation of the UV illuminated receptor, confirming that the 3D structure of the PDGFR binding domain remained intact after UV illumination. PDGFR lower sensitivity to UV light compared to EGFR might be due to a considerably lower number of disulphide bridges (3 per monomer) and Trp residues (2 per monomer), and lower number of aromatic residues in close spatial proximity to disulphide bridges.

Our previous work on the UV illumination effects on native and W69A mutant cutinase (Trp-depleted mutant) with 280 nm and 295-nm light also documents the crucial interplay between the aromatic residue and the disulphide bridge [51]. Cutinase has a single Trp residue in very close spatial proximity to a disulphide bridge. 280 nm and 295 nm excitation of theTrp residue is known the lead to the disruption of the disulphide bridge mediated by an electron transfer process [20]. This mechanism is severely impaired in the mutant cutinase. In our present study, the ultimate control control would be a sEGFR mutant that did not have aromatic residues and/or disulphide bridges in its structure or at least that did not have aromatic residues in close spatial proximity of disulphide bridges. Those mutants are not available for the simple reason that so many residues would have to be mutated and most certainly the structure of such mutant would no longer be the same as the native structure of the extracellular domain of EGFR. Therefore, studies done with EGFR depleted mutant cells are important in asserting the important of EGFR in UV mediated responses. Evidence is found in literature that strengthens the knowledge that most of the signal pathways involved in UV-induced processes are thought to originate at plasma membrane receptors such as EGFR. Zhang et al. showed that UVA stimulation of the epidermal growth factor receptor (EGFR) may lead to activation of kinases ($p70^{S6K}/p90^{RSK}$) through phosphatidyl isositol (PI)-3 kinase and extracellular receptor-activated kinases (ERKs) [52]. Evidence is provided that phosphorylation and activation of $p70^{S6K}/p90^{RSK}$ induced by UVA were prevented in Egfr-/- cells (in which basal EGFR expression and its tyrosine phosphorylation induced by UVA were absent) and were also markedly inhibited by EGFR-specific tyrosine kinase inhibitors. Hence, data suggest that UVA-induced $p70^{S6K}/p90^{RSK}$ signalling activation is initiated by EGFR-dependent pathways. Furthermore, Xu et al. reported that B82 mouse L cells devoid of EGFR confirmed the key role of EGFR in UVB-dependent signal transduction [53].

Data displayed in Figures 7A, 7B and 7C confirms that UVB illumination of sEGFR leads to the progressive conversion of Trp and Tyr residues into species such as NKF, Kyn and DT. The longer the illumination time the larger such conversion is. Kyn formation is very clear since it absorbs at 360 nm [23] (Table 2). Figure 4B confirms that UVB induces conformational changes in sEGFR due to the observed spectral shift observed upon illumination (solvent relaxation effect). Such red shift is due to the fact that the Trp pool in this protein became more solvent accessible upon illumination. Temperature dependent fluores-

cence studies (Fig. 5) confirm that illumination of sEGFR induces conformation changes. Prior to illumination a clear thermal transition around 69.7°C was observed. Such transition is due to conformation changes that happen in the Trp moiety of the protein and is associated with changes in solvent accessibility of these residues. The transition is absent if the protein previously has been illuminated for 75 min. This is correlated with the observation that UV illumination renders Trp residues in sEGFR more solvent accessible (Fig. 4B). The cooling experiments have shown that the sEGFR could not refold into its native 3D structure in our *in vitro* experiments. It is also likely that protein aggregation could have occurred upon heating the protein, contributing also to preventing protein refolding. However, the typical formation of a turbid solution associated with protein aggregation was not observed. CD data also confirms that UVB induced protein conformational changes leading to the loss of secondary structural content. As can be seen in Figure 9A, UVB illumination lead to the loss of ellipticity intensity at 207.5 nm (9%) and 220 nm (20%), characteristic of α-helical content and possibly β-sheet structural content. It is likely that the large amount of disulphide bridges in the protein has prevented further loss of ellipticity. The temperature dependent CD data (Figure 9B) shows that non-illuminated sEGFR has a melting temperature around 64.7°C. This value is in good agreement with the value recovered from the temperature dependent fluorescence studies (69.7°C). After 75 min illumination at 280 nm, the observed transition disappears, confirming that UVB has induced protein denaturation. The observed structural changes induced in sEGFR as well as the observed photochemistry are likely causes for the observed changes in fluorescence lifetime distribution in sEGFR (Table 1). Conformational changes that alter the environment surrounding the aromatic residues will most likely induce changes in their lifetimes' distribution. The protein immunoassays displayed in Figure 10 confirm that the UVB illumination of sEGFR induces structural changes in the EGFR binding site to EGF/TGF-α. After illumination, sEGFR no longer binds LA1 anti-EGFR antibody, confirmed by the complete disappearance of the band corresponding to sEGFR (Figure 10). The monoclonal antibody used competes with EGF and TGF-α for binding to EGFR [54]. This demonstrates that UV-illumination of sEGFR compromises the 3D structure of the EGF binding site in the protein. EGF docking to sEGFR is dependent on extensive non-covalent and Van der Vaals interactions between the two molecules, including π-π interactions (see Results, Fig. 2D). It is likely that UV induces conformational changes, disrupting the native tertiary fold that promotes sEGFR-EGF contacts.

The mechanisms through which EGF binds and induces receptor dimerization are not fully understood and the standing model is based on structural studies [1,55,56]. Inactive EGFR is kept in its closed conformation via interactions between two sEGFR disulphide rich domains (II and IV) [56]. EGF binding occurs primarily through interactions with domains I and III [1,55]. Ligand binding requires a change in the relative positions of domains I and III and dimerization occurs upon interaction of subdomains II of two EGFR monomers [1,5,55,56]. It is believed that domain IV has a role in high affinity binding and signal transduction [6]. Considering that the mechanisms of EGF binding and posterior EGFR dimerization can involve all four domains of sEGFR, it is not surprising that UV induced conformational changes will most likely impair binding to EGF. UV induced SS disruption in domain II will likely impair correct EGFR dimerization, but may also affect EGF binding as it is involved in the change of the relative position of domains I and III. Furthermore, domains I and III also contain disulphide bonds, though in lower extent, and SS breakage in these regions can also impair EGF binding. It has also been reported by several groups that EGFR exists as a preformed dimer on the cell-surface [57]. Also in this case, UV induced photochemistry and consequent structural changes in the EGF binding site will most likely impair EGF binding.

Our data confirms that low dose UVB leads to conformational changes in sEGFR, impairing its ability to bind an EGFR specific antibody that competes with EGF for binding EGFR, confirming that the 3D structure of the EGFR binding domain suffered conformational changes upon UV illumination. The present molecular level *in vitro* studies allow us to predict that UV light will most likely also change the structure/function of the extracellular domain of EGFR when present in the cell surface of cancer cells overexpressing EGFR, halting this way EGF-EGFR activation and EGFR dependent key metabolic pathways. Our most recent studies on the UVB (280 nm) illumination of lung cancer cells overexpressing EGFR confirm our predictions (paper in preparation). The present data also supports our previously publish results showing that low dose UVB illumination of cancer cells overexpressing EGFR (A431 and Cal39) led to the arrest of the EGFR signaling pathway [9]. The irradiance used in the present study (2.5 $W.m^{-2}$) and in the previous study (0.35 $W.m^{-2}$) is in the same order of magnitude or lower, respectively, than the total irradiance of sunlight in the UVB region, reported to be 1.75 $W.m^{-2}$ in summer and 0.4 $W.m^{-2}$ in winter (below 313 nm) [10]. The total amount of energy given to the protein solution after 75 min illumination at 280 nm is 90 mJ. This energy is lower than the limit values recommended by the British Photodermatology Group (1000 J, Psoriasis and Psoriatic Arthritis Alliance (PAPAA), 2008, available online at http://www.nhs.uk/ipgmedia/national/psoriasis) in order to prevent cancer. We envision that low dose UVB light can be used as a new photonic therapeutical approach used in order to stop the development of localized cancer, which cells overexpress EGFR or another receptor which structure will be labile to UV light. The treatment could be easily applicable to epidermal skin cancer because UVB light penetrates the skin down to 150–200 μm [37] (online information from the Department of Dermatology School of Medicine, University of California, San Francisco. UV Radiation. at http://www.dermatology.ucsf.edu/skincancer/General/prevention/UV_Radiation.aspx). The thickness of the stratum corneum of our skin is 10–20 μm, the thickness of the epidermis can vary from 50 to 150 μm [37] (online information from the Department of Dermatology School of Medicine, University of California, San Francisco. UV Radiation. at http://www.dermatology.ucsf.edu/skincancer/General/prevention/UV_Radiation.aspx) while the thickness of the dermis varies from 30 to 300 μm (Brannon, H. Skin Anatomy. at http://dermatology.about.com/cs/skinanatomy/a/anatomy.htm). If the localized tumor is located deeper location, UVB light could be delivered to those locations my means of an optical fiber or generated via multiphoton excitation using e.g. IR light. This possible new photonic therapy can also be applied during a surgical intervention.

The role of UV light on the activation or deactivation of EGFR and in promoting cell death or cell survivel remains controversial. We have previously described the attenuation of EGFR signaling as detected by the phosphorylation status of key downstream molecules i.e. AKT and the mitogen activated protein kinases ERK1 and 2 [9]. In response to UV (280 nm) illumination phosphorylation of AKT and ERK1/2 is not detectable upon activation with EGF. Given the observed upregulation of p21WAF1 in our previous work [9], which is a cyclin dependent kinase inhibitor, we must assume that UV illumination causes the

cells to arrest the cell cycle in G1 phase, which would be beneficial in inhibiting the proliferative potential of EGFR overexpressing cells. Adachi S. et al have also recently shown that UV irradiation can induce evasion of colon cancer cells from stimulation of epidermal growth factor [58]. They report that UV (254 nm) caused inhibition of cell survival and proliferation, concurrently inducing the decrease in cell surface EGFR and subsequently its degradation. Furthermore, the same team has reported that UV (254 nm) significantly inhibited platelet-derived growth factor PDGF-BB-induced phosphorylation of Akt on pancreatic cancer cells [59]. Several reports exist, describing how UV light can activate the EGF receptor hence activating the AKT and MAPK pathway (43–50 from ref. 9). These observations are in contrast to our results. Wan et al. have reported that UVB irradiation stimulated PI 3-kinase activity in human skin *in vivo* [60]. UV also stimulated phosphorylation of the downstream AKT effectors, S6 kinase and BAD. Inhibitors of EGFR and PI 3-kinase blocked UV-induced phosphorylation of BAD, suggesting that EGFR mediates UV-activated cell survival pathway. They concluded that both positive and negative roles for UV activation of the PI 3-K/AKT pathway in human skin can be envisioned. The PI 3-K/AKT pathway likely plays a critical role in balancing UV-induced apoptotic signals, thereby preventing widespread skin cell death. Conversely UV activation of the PI 3-K/AKT pathway may enhance survival of mutated cells, thereby promoting skin cancer, as has been found in several other types of cancer. Cao et al. [61] have concluded that UV (>290 nm, UVB/UVA2 source peaking we believe at 445 nm) induces multiple signalling pathways mediated by EGFR trans-activation leading to possible maturation, apoptosis and survival, and EGFR activation protects against UV-induced apoptosis in cultured mouse dendritic cells. Authors also report that most of the UV responses are mediated by the production of reactive oxygen species (ROS) and can be blocked by antioxidants. UVC is reported to induce rapid and transient expression of early growth response-1 gene (Egr-1) encoding a transcription factor that plays a role in cell survival. UVC irradiation causes tyrosine phosphorylation of EGFR in mouse NIH 3T3 fibroblasts and HC11 mouse mammary cells [50]. Possible reasons for the reported discrepancies could be found in the wavelength used in the experiments (from 254 nm to 445 nm), in the illumination power per unit of illuminated area and in the type of cells used (mutated vs non-mutated cells). Unfortunately these values are not accurately reported in all papers in order to make comparisons possible.

The present paper has provided unequivocal evidence for a UVB induced structural modification in EFGR, resulting in structural changes in the EGF binding site and loss of function. Interestingly, these changes were observed at a photonic power level approximately in the same order of magnitude as the integrated power in the solar UVB range. Therefore, it is reasonable to believe that UVB possesses therapeutic properties, especially towards skin and other superficial types of cancer. Clearly there must be a threshold irradiance level and illumination time, below which UVB light can be used for cancer treatment. Our most recent studies on the on the UV (280 nm) effects on EGF-EGFR activation of A549 lung carcinoma cells overexpressing EGFR (paper in preparation) confirm the hypothesis raised in this study that 280 nm light will most likely also change the structure/function of the extracellular domain of EGFR when present in the cell surface of cancer cells overexpressing EGFR, preventing this way EGF-EGFR binding and activation.

Materials and Methods

Structure Analysis

The crystallography data used for the display of the 3D protein structure (Figure 2) was extracted from 1ivo.pdb (extracellular domain of human epidermal growth factor receptor complexed with EGF, 3.3 Å resolution [1]). Accelrys Discovery Studio Visualizer 3.5 was used for displaying the 3D structure. Distances between protein residues were obtained by using the monitor tool in the program to determine the distance between atoms in the 3D structure. The fraction of disulphide bridges was calculated as the number of disulphide bridges found in a protein divided by the protein sequence length (number of amino acids) x 100 (Figure 3). The pdb dataset used in order to display the dependence of the average fraction of disulphide bridges on the protein chain length has been published previously by our group [28].

Fluorescence Studies

Fluorescence studies were carried out in order to analyze the effects of 280 nm excitation on the structure of the extracellular domain of human EGFR (sEGFR). sEGFR was purchased from Speed Biosystems (YCP1031). This protein was expressed in human embryonic kidney (HEK) 293 cells. The amino acid sequence corresponds to sEGFR (Leu25-Ser645) with a C-terminal polyhistidine (His) tag. The protein was dissolved directly in 10 mM Sodium Phosphate Buffer (NaPB) at pH 7.5 (stock solutions). Milli-Q water with conductivity below 0.2 $\mu S.cm^{-1}$ was used. sEGFR concentration was determined by Abs^{280nm} using a molar extinction coefficient of 60,000 $M^{-1}cm^{-1}$ estimated using the bioinformatic tool ProtParam (Expasy, [62], entry: sequence of extracellular domain of EGFR (Leu25-Ser645) with a C-terminal polyhistidine (His) tag). Stock solutions were used within 2-3 days after dissolution in buffer and was kept desiccated and protected from light at 4°C. Before each experiment the stock solution was diluted to 3.9 μM. Unless stated otherwise, this was the concentration used in all the fluorescence studies.

Steady state studies

UVB illumination of sEGFR was carried out in a ChronosBH spectrometer (ISS) with a T-configuration, using a 300-W Xenon arc lamp coupled to a monochromator. Excitation and emission slits were set to 4 nm and 8 nm, respectively. Lamp power at the sample location was 89 μW (at 280 nm). The illumination spot was 0.35 cm^2. Irradiance was 2.5 $W.m^{-2}$. The temperature of the solution was kept at 20°C using a Peltier element at the cuvette holder location. One hundred L of sEGFR stock solution was placed in a quartz cuvette (2 mm×10 mm×6 mm excitation volume) and excited at 280 nm during a maximum time of 75 min. Samples were illuminated through the 2 mm×6 mm window and fluorescence collected from the 10 mm×6 mm window. A fresh sample was used for each illumination session. Emission spectra were acquired with 280 nm, 295 nm, 320 nm and 360 nm excitation. Excitation spectra were recorded with the emission fixed at 320 nm, 334 nm, 350 nm, and 400 nm. Each of the previous spectra was recorded before illumination (0 min), and after 15 min, 30 min, 45 min, 60 min and 75 min of illumination. The same emission and excitation spectra were acquired for the buffer. The emission and excitation intensity values obtained were corrected in real-time for oscillations in the intensity of the excitation lamp. Buffer Raman signal was subtracted from each emission spectrum. The 350 nm fluorescence emission intensity upon continuous 280 nm excitation was recorded during 75 min of illumination.

Fluorescence based protein thermal unfolding studies. Trp emission is sensitive to the extent of solvent accessibility. The more solvent accessible Trp is the more red shifted its fluorescence emission will be. Therefore, Trp emission is usually used as a probe for protein conformational changes and can be used to determine the melting temperature of the protein.

The 330 nm fluorescence emission intensity (exc. 295 nm) of a fresh sEGFR sample (3.49 μM) and of a 280 nm illuminated for 75 min sEGFR sample (3.07 μM) was monitored from 4 °C to 90 °C. The sEGFR sample was continuously illuminated at 280 nm and as it was previously described. The heating rate was 1°C/min. A point was acquired every minute. After reaching 90 °C the protein samples were cooled from 90 °C to 4 °C at a cooling rate of 1 °C/min and the fluorescence intensity at 330 nm was monitored (exc. 295 nm).

Time resolved studies. A sEGFR sample was continuously illuminated at 280 nm during 75 min. The experimental set-up and parameters used for UVB illumination were the same as previously described. As negative control, a freshly prepared sEGFR sample was kept in the dark for 75 min. After UV illumination or dark period (negative control), the sample was kept in the cuvette and lifetime measurements were carried out at magic angle conditions using TCSPC method. A 283 nm light emitting diode from ISS (FWHM = 9 nm) was used to excite the samples. The fluorescence emission at magic angle (54.7°) was counted by a GaAs detector (Hamamatsu H7422P-40), and a 300 nm long-pass filter (Semrock) was employed in order to stray light. A solution of Ludox in Millipore water was used as a reference sample. The instrument response function for this system is 180 ps.

Detection of thiol groups' concentration formed upon UV illumination of sEGFR

Preparation of sEGFR solutions and buffers was carried as described in the previous section. One hundred L of sEGFR work solution (3.9 μM) was placed in a quartz macro cuvette (1 cm path length) and illuminated at 280 nm during 75 min. 280 nm illumination was carried out as described in the previous section. In parallel, 100 μL of the same sEGFR work solution was kept in the dark for 75 min (negative control sample, dark NC). Ellman's assay was used in order to detect free thiol groups formed upon UVB induced disruption of disulphide bridges in sEGFR [19,21,22,63]. Ellman's reagent, 5,5′-dithiobis-2-nitrobenzoic acid (DTNB) was purchased from Molecular Probes (product D8451, Life Technologies, Naerum, Denmark). One hundred mM stock solution was prepared in DMSO and stored at 4°C. After illumination, 150 μL of 2 times diluted illuminated or control sEGFR solution was mixed with an excess of DTNB (1.5 μL of 100 mM stock solution). The molar ratio DTNB/sEGFR was 5.13. Four minutes after mixing the two components (sample kept in the dark), the absorbance intensity at 412 nm was measured in a UV/Visible spectrophotometer (Shimadzu Corporation, 3. Kanda-Nishikicho 1-chome, Chiyoda-ku, Tokyo 101–8448, Japan), using a 1 cm path length quartz cuvette. The product of the reaction is the 2-nitro-5-thiobenzoate ion (TNB^{2-}), which absorbs at 412 nm. Abs_{412nm} is proportional to the amount of thiol groups present in solution. The concentration of thiol groups was determined using an extinction molar coefficient for TNB^{2-} of 14150 $M^{-1}.cm^{-1}$ at 412 nm [63].

Circular dichroism studies

The circular dichroism spectrum of a fresh sEGFR sample and of a 280 nm illuminated for 75 min sEGFR sample was acquired in order to monitor the UVB loss of secondary structural elements. Preparation of sEGFR solutions and buffers was carried as previously described. One hundred μL of sEGFR work solution (3.9 μM) was placed in a quartz macro cuvette (1 cm path length) and illuminated at 280 nm during 75 min. The experimental set-up, conditions and parameters used during the illumination procedure were the same as previously described. Immediately after the illumination, 200 μL of 3 times diluted illuminated sEGFR solution was placed in a quartz microcuvette with a path length of 0.1 cm and cooled to 4°C using a Peltier element at the cuvette holder's location. Afterwards, a far-UV CD spectrum was recorded. Temperature was kept constant at 4°C during the measurement. The same was done for a fresh sEGFR sample. Far-UV CD spectra (190–240 nm) were acquired using the following parameters: 1.0 nm band width, resolution 0.5 nm, 4 accumulations, scan speed 20 nm/min, sensitivity high, 16 s response time. Far-UV CD spectrum was also acquired for the buffer. The buffer signal was subtracted from all spectra. The measurements were carried out on a JASCO J-815 CD spectrometer (JASCO Corporation, Ishikawa-cho Hachioji-shi, Tokyo, Japan).

Circular dichroism based protein thermal unfolding studies. The ellipticity intensity at 220 nm of a fresh sEGFR sample and of a 280 nm illuminated for 75 min sEGFR sample (both solutions 3.9 μM) was continuously monitored from 4°C to 90°C. The experimental set-up, conditions and parameters used during the illumination procedure were the same as described in the previous sections. The heating rate was 1 °C/min. A point was acquired every minute. Far-UV CD spectra (190–240 nm) were acquired at 4°C (before heating) and at 90°C. Afterwards the protein samples were cooled from 90°C to 4°C at a cooling rate of 1 °C/min and the ellipticity intensity at 220 nm was monitored every minute. At the end, far-UV CD spectra (190–240 nm) were acquired at 4°C. Far-UV CD spectra (190–240 nm) were recorded using the parameters described in the previous section.

Immunoassay

A binding immunoassay was carried out in order to analyze the effects of 75 min of UV illumination at 280 nm on the structure of the EGF-sEGFR binding site. The primary mouse monoclonal antibody anti-EGFR neutralizer antibody LA1 from Milipore (05–101), which competes with EGF and TGF-α for binding EGFR [54] was used.

For each experiment, 1.4 μg of fresh non-illuminated protein sample, 1.4 μg of a 280 nm illuminated sample for 75 min and 1.4 μg of a protein sample that has been in the dark for 75 min (negative control, NC) were analyzed by Western blot. The experimental set-up, conditions and parameters used during UV illumination procedure were the same as described in the previous sections. Samples were resolved by reduced sodium dodecyl sulfate polyacrylamide gel electrophoresis (SDS-PAGE), 7.5% polyacrylamide from Bio-Rad (4561023) and transferred to a 0.2 μm nitrocellulose membrane from Whatman (10402495). Then, the membrane was probed with 11000 dilution of LA1 primary antibody followed by incubation with 15000 dilution of goat anti-mouse horseradish peroxidase (HRP)-conjugated secondary antibody from Santa Cruz Biotech (SC-2005). Immune complexes were visualized on nitrocellulose by enzyme-linked enhanced chemiluminescence (ECL) from GE Healthcare (RPN2232) and detected using the CCD camera of G:Box chemi XT4 controlled by Genesys software from Syngene. Band intensities were quantified using the gel analysis software GeneTools from Syngene. The immunoassay was carried out twice.

Data Analysis

All data analysis, plotting and fitting procedures were done using Origin 8.1.

Emission Spectra and Excitation Spectra. Emission Spectra (280 nm, 295 nm, 320 nm, and 360 nm excitation) were first smoothed using a 12 points adjacent averaging. Excitation Spectra (emission fixed at 334 nm and 400 nm excitation) were smoothed using a 5 points adjacent averaging. All fluorescence spectra obtained were first Raman corrected by subtracting the spectra recorded for the buffer in solution. Normalized emission and excitation spectra were obtained by dividing each data point by the maximum intensity value in each spectrum.

Fitting Procedures. *Fluorescence emission kinetic trace at 350 nm upon 280 nm exc*: The fluorescence emission kinetic trace (em. 350 nm, Fig. 4A) was fitted using a bi-exponential function $F(t) = y_0 + C1.e^{-k1.t} + C2.e^{-k2.t}$. $F(t)$ is the fluorescence emission intensity at 350 nm (a.u.) at 280 nm excitation time t (min), y_0, $C1$ and $C2$ are constants and $k1$ *and* $k2$ is the rate constant of fluorescence emission intensity decrease (min^{-1}). y_0 value was fixed to 0.

Fluorescence based protein thermal unfolding studies: The fluorescence emission intensity thermal curves (Fig. 5) were first smoothed using a 5 points adjacent averaging. The fluorescence emission intensity values were afterwards normalized by dividing each value by the initial 330 nm emission intensity value. The curve corresponding to the non-illuminated sEGFR sample (non illum.) was then fitted using a modified Boltzmann function:

$$y = A2 + B2.x + \frac{(A1 + B1.x - A2 + B2.x)}{\left(1 + \exp\left(\frac{x - x0}{dx}\right)\right)}$$

where y (a.u.) is the 330 nm fluorescence emission intensity at the temperature x (°C), $A1$, $B1$, $A2$, $B2$ and dx are constants. The fitting parameter $x0$ (°C) corresponds to the inflection point of the Boltzmann curve and the corresponding temperature is the temperature of mid-transition determined upon probing Trp fluorescence emission.

Fluorescence lifetimes: The fluorescence decay was analyzed by an ISS routine based on the Marquardt least-squares minimization. The governing equations for the time-resolved intensity decay data were assumed to be a sum of discrete exponentials as in:

$$F(t) = \sum_i \alpha_i . \exp(-t/\tau_i)$$

where $F(t)$ is the intensity decay, α_i is the amplitude (pre-exponential factor), τ_i the fluorescence lifetime of the i-th discrete component, and $\sum \alpha_i = 1.0$.

The fractional intensity fi of each decay time is given by:

$$f_i = \frac{\alpha_i \tau_i}{\sum_i \alpha_i \tau_i}$$

and the mean lifetime is:

$$\langle \tau \rangle = \sum_i f_i \tau_i$$

Circular dichroism based protein thermal unfolding studies. Only the data values obtained above 10°C were then considered for analysis. The ellipticity intensity values were first smoothed using a 12 points adjacent averaging. The data values were then normalized by dividing each ellipticity intensity value by the initial ellipticity intensity value (i.e. first data point above 10°C). The curve corresponding to the non-illuminated sEGFR sample (non illum.) was then fitted using a Boltzmann function:

$$y = A2 \frac{(A1 - A2)}{\left(1 + \exp\left(\frac{x - x0}{dx}\right)\right)}$$

where y (a.u.) is the 220 nm ellipticity intensity values at the temperature x (°C), $A1$, $A2$, and dx are constants. The fitting parameter $x0$ (°C) is the inflection point of the Boltzmann curve and its value corresponds to the temperature of mid-transition of the curve. The fitting was done for the interval 57.12–69.48°C, which comprises the thermal transition part of the curve.

Author Contributions

Conceived and designed the experiments: MC VT IC GPG SBP MTNP. Performed the experiments: MC VT IC. Analyzed the data: MC VT IC SBP MTNP. Contributed reagents/materials/analysis tools: MC VT IC GPG SBP MTNP. Wrote the paper: MC VT IC SBP MTNP.

References

1. Ogiso H, Ishitani R, Nureki O, Fukai S, Yamanaka M, et al. (2002) Crystal structure of the complex of human epidermal growth factor and receptor extracellular domains. Cell 110: 775–787.
2. Han W, Lo HW (2012) Landscape of EGFR signaling network in human cancers: biology and therapeutic response in relation to receptor subcellular locations. Cancer Lett 318: 124–134.
3. Suzuki S, Dobashi Y, Sakurai H, Nishikawa K, Hanawa M, et al. (2005) Protein overexpression and gene amplification of epidermal growth factor receptor in nonsmall cell lung carcinomas. An immunohistochemical and fluorescence in situ hybridization study. Cancer 103: 1265–1273.
4. Yarden Y (2001) The EGFR family and its ligands in human cancer. Signalling mechanisms and therapeutic opportunities. Eur J Cancer 37 Suppl 4: S3–8.
5. Liu P, Cleveland TE, Bouyain S, Byrne PO, Longo PA, et al. (2012) A single ligand is sufficient to activate EGFR dimers. Proc Natl Acad Sci U S A 109: 10861–10866.
6. Macdonald J, Li Z, Su W, Pike LJ (2006) The membrane proximal disulfides of the EGF receptor extracellular domain are required for high affinity binding and signal transduction but do not play a role in the localization of the receptor to lipid rafts. Biochim Biophys Acta 1763: 870–878.
7. Nicholson RI, Gee JM, Harper ME (2001) EGFR and cancer prognosis. Eur J Cancer 37 Suppl 4: S9–15.
8. Noonberg SB, Benz CC (2000) Tyrosine kinase inhibitors targeted to the epidermal growth factor receptor subfamily: role as anticancer agents. Drugs 59: 753–767.
9. Olsen BB, Neves-Petersen MT, Klitgaard S, Issinger OG, Petersen SB (2007) UV light blocks EGFR signalling in human cancer cell lines. Int J Oncol 30: 181–185.
10. Pirie A (1971) Formation of N′-formylkynurenine in proteins from lens and other sources by exposure to sunlight. Biochem J 125: 203–208.
11. Casanova ML, Larcher F, Casanova B, Murillas R, Fernández-Aceñero MJ, et al. (2002) A critical role for ras-mediated, epidermal growth factor receptor-dependent angiogenesis in mouse skin carcinogenesis. Cancer Res 62: 3402–3407.
12. Kiguchi K, Beltrán L, Rupp T, DiGiovanni J (1998) Altered expression of epidermal growth factor receptor ligands in tumor promoter-treated mouse epidermis and in primary mouse skin tumors induced by an initiation-promotion protocol. Mol Carcinog 22: 73–83.
13. Sibilia M, Fleischmann A, Behrens A, Stingl L, Carroll J, et al. (2000) The EGF receptor provides an essential survival signal for SOS-dependent skin tumor development. Cell 102: 211–220.
14. Segrelles C, Ruiz S, Perez P, Murga C, Santos M, et al. (2002) Functional roles of Akt signaling in mouse skin tumorigenesis. Oncogene 21: 53–64.

15. Budiyanto A, Bito T, Kunisada M, Ashida M, Ichihashi M, et al. (2003) Inhibition of the epidermal growth factor receptor suppresses telomerase activity in HSC-1 human cutaneous squamous cell carcinoma cells. J Invest Dermatol 121: 1088–1094.
16. Kim YN, Dam P, Bertics PJ (2002) Caveolin-1 phosphorylation in human squamous and epidermoid carcinoma cells: dependence on ErbB1 expression and Src activation. Exp Cell Res 280: 134–147.
17. Roux PP, Blenis J (2004) ERK and p38 MAPK-activated protein kinases: a family of protein kinases with diverse biological functions. Microbiol Mol Biol Rev 68: 320–344.
18. Neves-Petersen MT, Petersen S, Gajula GP (2012) UV Light Effects on Proteins: From Photochemistry to Nanomedicine. In: Saha S (Dr., editor.Molecular Photochemistry - Various Aspects.InTech. pp.125–158.
19. Neves-Petersen MT, Gryczynski Z, Lakowicz J, Fojan P, Pedersen S, et al. (2002) High probability of disrupting a disulphide bridge mediated by an endogenous excited tryptophan residue. Protein Sci 11: 588–600.
20. Neves-Petersen MT, Klitgaard S, Pascher T, Skovsen E, Polivka T, et al. (2009) Flash photolysis of cutinase: identification and decay kinetics of transient intermediates formed upon UV excitation of aromatic residues. Biophys J 97: 211–226.
21. Correia M, Neves-Petersen MT, Parracino A, di Gennaro AK, Petersen SB (2012) Photophysics, photochemistry and energetics of UV light induced disulphide bridge disruption in apo-α-lactalbumin. J Fluoresc 22: 323–337.
22. Correia M, Neves-Petersen MT, Jeppesen PB, Gregersen S, Petersen SB (2012) UV-light exposure of insulin: pharmaceutical implications upon covalent insulin dityrosine dimerization and disulphide bond photolysis. PLoS One 7: e50733.
23. Fukunaga Y, Katsuragi Y, Izumi T, Sakiyama F (1982) Fluorescence characteristics of kynurenine and N′-formylkynurenine. Their use as reporters of the environment of tryptophan 62 in hen egg-white lysozyme. J Biochem 92: 129–141.
24. Kerwin BA, Remmele RL (2007) Protect from light: photodegradation and protein biologics. 96: 1468–1479.
25. Malencik DA, Anderson SR (2003) Dityrosine as a product of oxidative stress and fluorescent probe. Amino Acids 25: 233–247.
26. Malencik DA, Anderson SR (1987) Dityrosine formation in calmodulin. Biochemistry 26: 695–704.
27. Giulivi C, Traaseth NJ, Davies KJ (2003) Tyrosine oxidation products: analysis and biological relevance. Amino Acids 25: 227–232.
28. Petersen MT, Jonson PH, Petersen SB (1999) Amino acid neighbours and detailed conformational analysis of cysteines in proteins. Protein Eng 12: 535–548.
29. Grant WB (2002) An estimate of premature cancer mortality in the U.S. due to inadequate doses of solar ultraviolet-B radiation. Cancer 94: 1867–1875.
30. Banwell CM, Singh R, Stewart PM, Uskokovic MR, Campbell MJ (2003) Antiproliferative signalling by 1,25(OH)2D3 in prostate and breast cancer is suppressed by a mechanism involving histone deacetylation. Recent Results Cancer Res 164: 83–98.
31. Gorham ED, Garland CF, Garland FC, Grant WB, Mohr SB, et al. (2005) Vitamin D and prevention of colorectal cancer. J Steroid Biochem Mol Biol 97: 179–194.
32. Garland CF, Garland FC, Gorham ED, Lipkin M, Newmark H, et al. (2006) The role of vitamin D in cancer prevention. Am J Public Health 96: 252–261.
33. Newton-Bishop JA, Chang YM, Elliott F, Chan M, Leake S, et al. (2011) Relationship between sun exposure and melanoma risk for tumours in different body sites in a large case-control study in a temperate climate. Eur J Cancer 47: 732–741.
34. Pukkala E, Martinsen JI, Lynge E, Gunnarsdottir HK, Sparén P, et al. (2009) Occupation and cancer - follow-up of 15 million people in five Nordic countries. Acta Oncol 48: 646–790.
35. Kaskel P, Sander S, Kron M, Kind P, Peter RU, et al. (2001) Outdoor activities in childhood: a protective factor for cutaneous melanoma? Results of a case-control study in 271 matched pairs. Br J Dermatol 145: 602–609.
36. Webb AR, Engelsen O (2006) Calculated ultraviolet exposure levels for a healthy vitamin D status. Photochem Photobiol 82: 1697–1703.
37. Moan J (2001) Visible Light and UV radiation. In: Brune D, Hellborg R, Persson B, Paakkonen R, editors. Radiation at Home, Outdoors and in the Workplace. Oslo: Scandinavian Publisher. pp.69–85.
38. Jones CA, Huberman E, Cunningham ML, Peak MJ (1987) Mutagenesis and cytotoxicity in human epithelial cells by far- and near-ultraviolet radiations: action spectra. Radiat Res 110: 244–254.
39. Nilsen LTN, Aalerud TN, Hannevik M, Veierød MB (2011) UVB and UVA irradiances from indoor tanning devices. Photochem Photobiol Sci 10: 1129–1136.
40. Jacob JS, Cistola DP, Hsu FF, Muzaffar S, Mueller DM, et al. (1996) Human phagocytes employ the myeloperoxidase-hydrogen peroxide system to synthesize dityrosine, trityrosine, pulcherosine, and isodityrosine by a tyrosyl radical-dependent pathway. J Biol Chem 271: 19950–19956.
41. Greenfield NJ (2006) Using circular dichroism spectra to estimate protein secondary structure. Nat Protoc 1: 2876–2890.
42. Finley EL, Dillon J, Crouch RK, Schey KL (1998) Identification of tryptophan oxidation products in bovine alpha-crystallin. Protein Sci 7: 2391–2397.
43. Finley EL, Busman M, Dillon J, Crouch RK, Schey KL (1997) Identification of photooxidation sites in bovine alpha-crystallin. Photochem Photobiol 66: 635–641.
44. Bent DV, Hayon E (1975) Excited state chemistry of aromatic amino acids and related peptides. I. Tyrosine. J Am Chem Soc 97: 2599–2606.
45. Bent DV, Hayon E (1975) Excited state chemistry of aromatic amino acids and related peptides. III. Tryptophan. J Am Chem Soc 97: 2612–2619.
46. Creed D (1984) The photophysics and photochemistry of the near-uv absorbing amino acids–I. Tryptophan and its simple derivatives. Photochem Photobiol 39: 537–562.
47. Hoffman MZ, Hayon E (1972) One-electron reduction of the disulfide linkage in aqueous solution. Formation, protonation, and decay kinetics of the RSSR-radical. J Am Chem Soc 94: 7950–7957.
48. Bent DV, Hayon E (1975) Excited state chemistry of aromatic amino acids and related peptides. II. Phenylalanine. J Am Chem Soc 97: 2606–2612.
49. Li Z, Lee WE, Galley WC (1989) Distance dependence of the tryptophan-disulfide interaction at the triplet level from pulsed phosphorescence studies on a model system. Biophys J 56: 361–367.
50. Huang RP, Wu JX, Fan Y, Adamson ED (1996) UV Activates Growth Factor Receptors via Reactive Oxygen Intermediates. The Journal of Cell Biology 133 (1): 311–220.
51. Neves-Petersen MT, Snabe T, Klitgaard S, Duroux M, Petersen SB (2006) Photonic activation of disulfide bridges achieves oriented protein immobilization on biosensor surfaces. Protein Science 15: 343–351.
52. Zhang Y, Dong Z, Dode AM, Ma WY, Chen, Dong Z (2001) Induction of EGFR-Dependent and EGFR-Independent Signaling Pathways by Ultraviolet A Irradiation. DNA and Cell Biology 20(12): 769–777.
53. Xu Y, Voorhees JJ, Fisher GJ (2006) Epidermal growth factor receptor is a critical mediator of ultraviolet B irradiation-induced signal transduction in immortalized human keratinocyte HaCaT cells. The American Journal of Pathology 169(3): 823–830.
54. Kawamoto T, Kishimoto K, Takahashi K, Matsumura T, Sato JD, et al. (1992) Polymorphonuclear leukocytes-mediated lysis of A431 cells induced by IgG1 mouse anti-epidermal growth factor receptor monoclonal antibodies. In Vitro Cell Dev Biol 28A: 782–786.
55. Garrett TPJ, McKern NM, Lou M, Elleman TC, Adams TE, et al. (2002) Crystal structure of a truncated epidermal growth factor receptor extracellular domain bound to transforming growth factor alpha. Cell 110: 763–773.
56. Ferguson KM, Berger MB, Mendrola JM, Cho HS, Leahy DJ, et al. (2003) EGF activates its receptor by removing interactions that autoinhibit ectodomain dimerization. Mol Cell 11: 507–517.
57. Tao RH, Maruyama IN (2008) All EGF(ErbB) receptors have preformed homo- and heterodimeric structures in living cells. Journal of Cell Science 121: 3207–3217.
58. Adachi S, Yasuda I, Nakashima M, Yamauchi T, Kawaguchi J (2011) Ultraviolet Irradiation Can Induce Evasion of Colon Cancer Cells from Stimulation of Epidermal Growth Factor. The Journal of Biological Chemistry 286: 26178–26187.
59. Kawaguchi J, Adachi S, Yasuda I, Yamauchi T, Yoshioka T, et al. (2012) UVC irradiation suppresses platelet-derived growth factor-BB-induced migration in human pancreatic cancer cells. Oncology Reports 27(4): 935–939.
60. Wan YS, Wang ZQ, Shao Y, Voorhees JJ, Fisher GF (2001) Ultraviolet irradiation activates PI 3-kinase/AKT survival pathway via EGF receptors in human skin in vivo. International Journal of Oncology 18(3): 461–466.61.
61. Cao C, Lu S, Jiang Q, Wang WJ, Song X, et al. (2008) EGFR activation confers protections against UV-induced apoptosis in response to UV radiation in cultured mouse skin dendritic cells. Cell Signal. 20(10): 1830–1838.
62. Gasteiger E, Hoogland C, Gattiker A, Duvaud S, Wilkins MR, et al. (2005) Protein Identification and Analysis Tools on the ExPASy Server. In: Walker JM, editor. The Proteomics Protocols Handbook. Humana Press. pp.571–607.
63. Riener CK, Kada G, Gruber HJ (2002) Quick measurement of protein sulfhydryls with Ellman's reagent and with 4,4'-dithiodipyridine. Anal Bioanal Chem 373: 266–276.

4.4 Paper 4

Photonic immobilization of BSA for nanobiomedical applications: creation of high density microarrays and superparamagnetic bioconjugates

Antonietta Parracino, Gnana Prakash Gajula, Ane Kold di Gennaro, Manuel Correia, Maria Teresa Neves Petersen, Jens Rafaelsen, and Steffen B. Petersen

Biotechnology and bioengineering, 2011, 108(5), 999–1010

ARTICLE

BIOTECHNOLOGY and BIOENGINEERING

Photonic Immobilization of BSA for Nanobiomedical Applications: Creation of High Density Microarrays and Superparamagnetic Bioconjugates

Antonietta Parracino,[1] Gnana Prakash Gajula,[1] Ane Kold di Gennaro,[1] Manuel Correia,[1] Maria Teresa Neves-Petersen,[2] Jens Rafaelsen,[1] Steffen B. Petersen[3,4]

[1]Department of Physics and Nanotechnology, Aalborg University, Skjernvej 4A, Aalborg, Denmark

[2]Nanobiotechnology Group, Department of Biotechnology, Chemistry and Environmental Sciences, Aalborg University, Sohngaardsholmsvej 49, Aalborg, Denmark

[3]Nanobiotechnology Group, Department of Health Science and Technology, Aalborg University, Frederik Bajers Vej 7D2, Aalborg, Denmark; telephone: +45-99408469; fax: 98154008; e-mail: sp@hst.aau.dk

[4]University at Buffalo, The State University of New York Buffalo, The Institute for Lasers, Photonics and Biophotonics, New York, New York

Received 30 June 2010; revision received 27 September 2010; accepted 1 November 2010

Published online 1 December 2010 in Wiley Online Library (wileyonlinelibrary.com). DOI 10.1002/bit.23015

ABSTRACT: Light assisted molecular immobilization has been used for the first time to engineer covalent bioconjugates of superparamagnetic nanoparticles and proteins. The technology involves disulfide bridge disruption upon UV excitation of nearby aromatic residues. The close spatial proximity of aromatic residues and disulfide bridges is a conserved structural feature in proteins. The created thiol groups bind thiol reactive surfaces leading to oriented covalent protein immobilization. We have immobilized a model carrier protein, bovine serum albumin, onto Fe_3O_4@Au core–shell nanoparticles as well as arrayed it onto optically flat thiol reactive surfaces. This new immobilization technology allows for ultra high dense packing of different bio-molecules on a surface, allowing the creation of multi-potent functionalized active new biosensor materials, biomarkers identification and the development of nanoparticles based novel drug delivery system.

Biotechnol. Bioeng. 2011;108: 999–1010.

KEYWORDS: superparamagnetic core–shell nanoparticles; LAMI light assisted protein immobilization; protein bioconjugates; biosensor arrays; drug carrier protein

Introduction

Advanced clinical diagnostic methods have been developed in order to understand the molecular mechanisms underlying disease processes. Since biomolecules such as nucleic acids and proteins are nanosized, probes of equivalent dimensions are very efficient tools at the subcellular level. New nanotechnological applications have recently emerged such as drug targeting and delivery (Huang and Lee, 2006), cell labeling and separation (Park et al., 2007), cancer therapy (Chu et al., 2006), magnetic resonance image (MRI) contrast agents (Cho et al., 2006), bio-sensors (You et al., 2007), and bio-imaging (Sharma et al., 2006). Among nanomaterials, magnetic core–shell nanoparticles resulting from the combination of metals with relevant optical, electrical, magnetic and catalytic properties can be used for nano applications. Fe_3O_4@Au particles are widely used because of their chemical stability, easy dispersibility, affinity towards biomolecules and convenient preparation techniques (Daniel and Astruc, 2004; Laurent et al., 2008). Their magnetism is used extensively in biosciences even for tissue engineering and to build complex 1D–3D structures (Ito et al., 2004; Lee and Liddell, 2009; Safarik and Safarikova, 2002). Tuning their plasmonic properties, by changing shell thickness, physic-chemical environment or through interactions with fluorophores, can greatly contribute to the development of clinical diagnosis

Antonietta Parracino and Gnana Prakash Gajula contributed equally to the work.

Correspondence to: S.B. Petersen

Contract grant sponsor: Fundação para Ciência e Tecnologia (FCT)

Contract grant number: SFRH/BD/61012/2009

methods (Baptista et al., 2008; Imahori et al., 2001; Lyon et al., 2004).

Since biomolecules are highly sensitive to pH, temperature and chemical environment, immobilization protocols should secure high molecular activity and stability. Incorporation of chiral molecules onto nanoparticles leads to specific protein surface recognition (You et al., 2008). Trypsin immobilization onto super-paramagnetic nanoparticles allowed using high enzyme concentrations leading to shorter digestion times, facilitating the separation of derivatized nanoparticles from solution (Li et al., 2007). Immobilization of biomolecules not only easies their separation and manipulation but also increases enzyme stability towards pH, temperature, chemical denaturants and organic solvents as well as preventing auto proteolysis (Yang et al., 2004, 2008). Several proteins have been coupled to magnetic particles using organic agents (Koneracka et al., 2002; Mehta et al., 1997) or by carrying out the reaction through ligand exchange, metal ions affinity, electrostatic as well as hydrophobic interactions (Brewer et al., 2005; Ma et al., 2006; Park et al., 2007). The covalent bond between thiol groups and gold surfaces is stronger than electrostatic interactions (Di Felice and Selloni, 2004; Uvdal et al., 1992; Varghese et al., 2008).

UV light assisted molecular immobilization (LAMI) is a novel photonic technology that results in covalent and uniform orientated coupling of biomolecules onto thiol reactive surfaces (Duroux et al., 2007; Jonkheijm et al., 2008; Petersen et al., 2006; Neves-Petersen et al., 2009a,b; Skoven et al., 2009a,b). The technology involves formation of free, reactive thiol groups upon UV excitation of protein aromatic residues located in spatial proximity of disulfide bridges, a conserved structural feature in proteins. LAMI has been successfully used to array functional biomolecules of medical interest (Duroux et al., 2007). LAMI combined with the Fourier-transforming properties of lenses as well as with a simple millimeter scale feature spatial mask lead to high-density protein arrays with a spatial resolution of a few hundred nanometers. An improvement of tenfold over existing commercially available high-density protein arraying methods was demonstrated (Neves-Petersen et al., 2009b; Skoven et al., 2009a).

In this paper we report light assisted immobilization of a carrier protein, BSA, onto Fe_3O_4@Au core–shell nanoparticles for the first time, as well as arrayed BSA onto a thiol reactive surface using LAMI. BSA has aromatic residues in close spatial proximity of disulfide bridges making it a good candidate for LAMI. Furthermore, we report the synthesis of Fe_3O_4@Au core–shell nanoparticles and the characterization of the engineered bioconjugates using spectroscopy techniques. In house imaging software package was used for advanced analysis of the protein array images and also to understand the nanoparticle size distribution. Binding therapeutic molecules onto nanoparticles leads to sensitive nanoprobes for bio-medical applications such as bio-separation, bio-sensing, drug delivery, and cellular specific binding.

Materials and Methods

Preparation of Fe_3O_4@Au Core–Shell Nanoparticles

Successive precipitation of two metals from metal precursors is used for the preparation of magnetic core–shell particles. Acidic solutions of 0.1 M $FeSO_4.7H_2O$ and 0.2 M $FeCl_3$ (pH 1) were mixed in 1:1 ratio upon constant stirring at room temperature. pH was rapidly increased to 10 by adding 10 mL 25% aqueous ammonia. Ten minutes after the solution turned black, 10 mL 1.0 M sodium citrate was added and the solution was stirred for 30 min. These magnetite particles were used as seeds onto which gold was deposited by citrate reduction method. One milliliter of the above suspension was transferred into 100 mL 1 mM sodium citrate. The solution was heated with constant stirring. Upon boiling, 10 mL 0.01 M $HAuCl_4$ solution was rapidly added and stirred for 30 min. The solution turned deep red, the characteristic color of gold colloids indicating presence of metallic gold. The suspension was cooled to room temperature and washed twice with water and centrifuged (10,000 rpm for 10 min) in order to eliminate excess surfactant and reaction byproduct salts. The supernatant was decanted. Bottom agglomerated particles were re-dispersed in water and re-washed.

Protein Labeling

BSA-AF532 labeling was carried out according to the protein labeling kit (A10236) from Molecular Probes (Invitrogen, Leek, The Netherlands). After labeling, BSA was dialyzed against 10 mM Tris–HCl buffer pH 7.5. Labeled protein concentration and degree of labeling (DOL) were calculated measuring the Abs^{530nm} using 81,000 $cm^{-1}\,M^{-1}$ as the molar extinction coefficient of AF532 at 530 nm. DOL was 1.46. 0.02 M ANS solution in dimethylsulfonic acid (DMSO) was diluted to 70 μM in 10 mM Tris–HCl pH 7.5 buffer. Concentration was calculated using 5,000 $cm^{-1}\,M^{-1}$ as the extinction coefficient of ANS at 350 nm. Protein–nanoparticle bioconjugates were incubated with an excess of ANS (1:10 molar ratio). ANS protein binding was monitored upon measuring the characteristic ANS absorption peak at 350 nm. Characteristic protein absorption was monitored at 220 and 280 nm.

Photonic Immobilization of BSA Onto Functionalized Slide

Chemical modification of optically flat quartz slides and optical setup used for immobilization were carried out as previously described (Duroux et al., 2007). One microliter of 7 μM BSA/AF532 was placed and dried on the thiol functionalized slide. A UV laser beam (1 mW, 280 nm) was sent through a computer controlled shutter, a beam expander and an iris diaphragm and focused through a quartz lens onto the sample mounted on a computer controlled 3D translation stage. One hundred milliseconds exposure time was used. A 4×6 array with 20 μm spots

interspaced 150 μm was created. The slide was washed with 1% Mucasol for 1 h changing the mucasol solution every 15 min and scanned with a Tecan LS 200 scanner for protein array visualization (exc. 532 nm, 6 μm resolution).

Photonic Immobilization of BSA Onto Gold Coated Superparamagnetic Nanoparticles

A sample containing 8.0 μM BSA and 0.8 μM concentration of gold in the form of nanoparticles superparamagnetic nanoparticles in 10 mM Tris–HCl buffer pH 7.5 was illuminated for 1 h with 295 nm light in a RTC 2000 PTI spectrofluorimeter. Lamp power at the sample location was 142 nW. Slits were kept at 5 nm and temperature at 20°C. The sample was stirred every 10th minute during illumination. The uncoupled BSA was washed out by two centrifugations and particle-protein bioconjugates were re-dispersed in buffer and characterized. As a negative control, identical experiments were carried out in the absence of UV illumination.

UV–Visible Absorption Spectroscopy

Thermo scientific UV–visible spectrophotometer (VWK International UV1 v4.60, West Chester, PA) was used to characterize the free thiol groups in BSA, nanoparticles, protein, degree of labeling and protein coated nanoparticles. The path length of the quartz cuvette was 1 cm. Absorbance spectra were acquired between 220 and 700 nm.

Ellman's Reactions

Ellman's assay was used to determine the concentration of free thiol groups in BSA prior to and after 1 h 295 nm excitation upon measuring the intensity of the absorption at 412 nm (Riener et al., 2002). BSA concentration was 8.0 μM in 10 mM Tris–HCl buffer pH 7.5. Ellman's reagent (5,5′-dithiobis(2-nitrobenzoate), DTNB) concentration was 500 μM.

Fluorescence Spectroscopy

Fluorescence characterization of native BSA, BSA-AF532, and BSA-ANS coupled to nanoparticles were carried out in a RTC 2000 PTI spectrofluorimeter at 20°C. Quartz cuvette path length was 1 cm. Slits were set at 5 nm. Intrinsic protein fluorescence spectra were acquired upon 295 nm excitation. Extrinsic fluorescence emission spectra of BSA-AF532 were acquired upon 530 nm excitation. Intrinsic protein fluorescence spectra were acquired upon 295 nm excitation. ANS fluorescence spectra of BSA-ANS alone and coupled to nanoparticles were acquired upon 350 nm excitation.

Dynamic Light Scattering (DLS)

Measurements were carried out in a Zsizer Malvern with temperature controlled MicroSampler. Average hydrodynamic size and size distribution of the core–shell nanoparticles, protein, and protein tagged nanoparticles were estimated. Fifty microliters was transferred to a 1 cm path length cuvette for each measurement.

Scanning Electron Microscopy—Energy Dispersive X-Ray spectroscopy (SEM-EDS)

Carl Zeiss 1540XB SEM with Noran EDS system was used for particle's size estimation and composition. SEM images were collected upon optimizing the voltage between 5 and 12 kV on silicon substrate where dried magnetic core–shell particles were placed. The average size of core–shell nanoparticles and protein–particles bioconjugates were estimated. The electron beam was focused over the particle projection area during X-ray acquisition. The X-ray spectrum was acquired for 60 s, at an acceleration voltage of 12 kV. NORAN system six version 2.0 software from Thermo Fischer scientific was used to analyze the EDS data (particles' chemical composition).

Fluorescence Microscopy

Nanoparticles coupled to labeled proteins were visualized with a fluorescence microscope (Leica TCS SP5) in oil-immersion 60× objective and images recorded with CCD camera. Before imaging, the samples were dried over the glass slide surface at room temperature. In order to image AF532, N2.1 filter cube was used (exc 515–560 nm; long pass filter (LP) at 590 nm). For ANS, A4 filter cube was used (exc 340–380; LP 425 nm).

Particles and Protein Array Image Processing

MATLAB v7.8 was used to develop BNIP-Pro software package that allows for advanced image analysis. The SEM image was baseline corrected using manually placed multiple control points in the base of the image. The image was then converted to a binary image, using a threshold value that allowed for the observation of a maximum number of separated particles. Morphological erosion and dilation was applied to the binary image in order to break residual contacts between particles. The modified binary image was then multiplied with the original image, leading to an image where only the particles are visible. Contours were draw around all particles, and their individual area and intensity analyzed.

Pairwise Sequence Alignment

Clustal W, version 2, was used to carried out the pairwise sequence alignment of BSA (607 aa) and HSA (585 aa). The matrix used was EBLOSUM62 with gap penalty 10 and extended penalty 0.5.

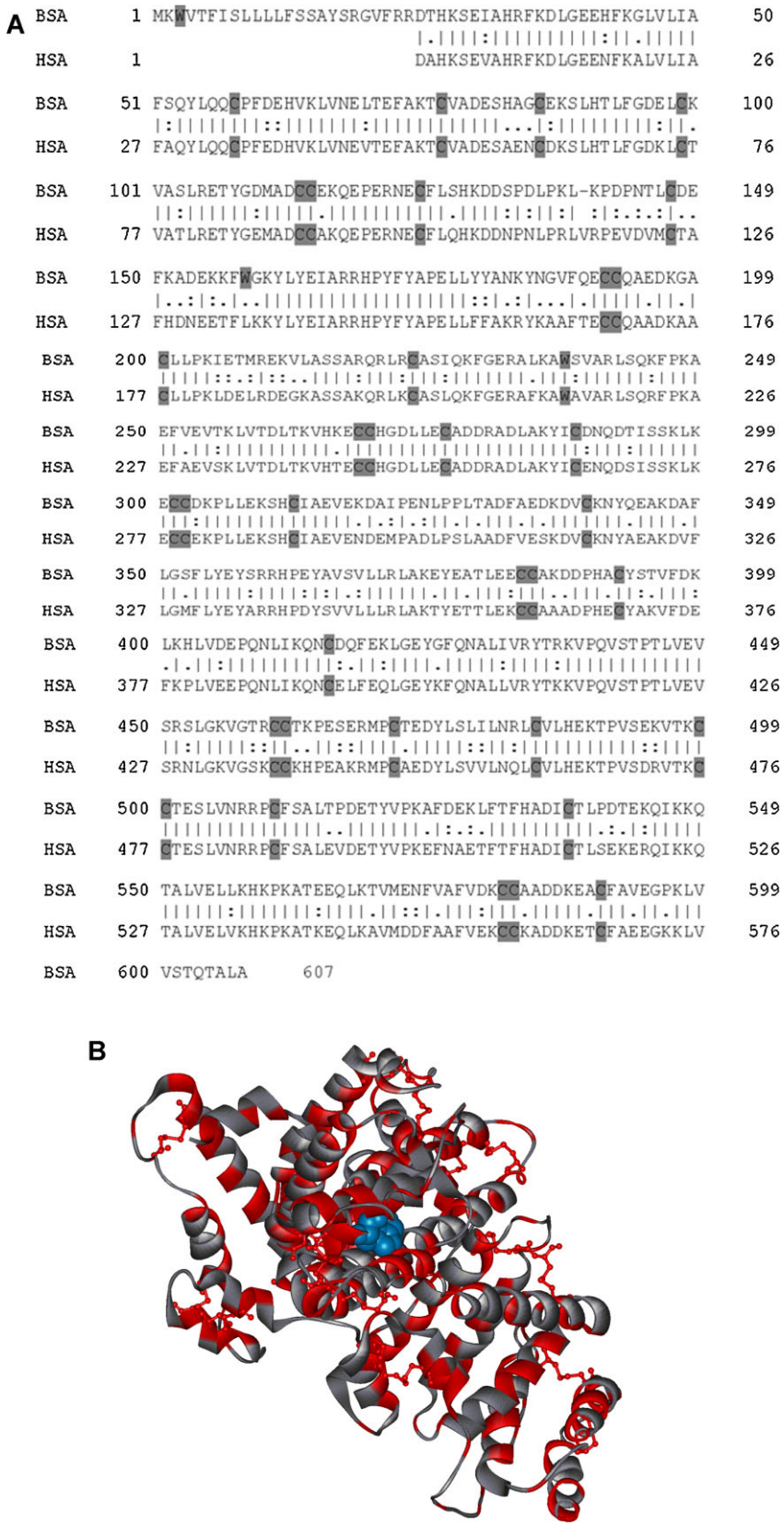

Figure 1. **A**: Pairwise sequence alignment of BSA and HSA. Standard one letter abbreviations are used for the amino acids; (|) Indicates identical amino acids; indicates similar (homologous) amino acids; (:) indicates unrelated amino acids. The cysteins (C) and tryptophans (W) are highlighted in gray and bold. Moreover, all 35 cysteins are conserved. **B**: 3D representation of HSA (PDB code: 1ao6) which displays identity, similarity, and gap of 72.6%, 84.2%, and 4.3%, respectively with BSA [http://www.ebi.ac.uk/Tools/emboss/align/]. Cysteines are highlighted in red ball and stick; W 214 is highlighted in blue CPK and the hydrophobic amino acids are highlighted in red.

Results and Discussion

Protein Characterization

Since BSA 3D structure is not available, a pairwise sequence alignment between BSA and human serum albumin (HSA) has been carried out, revealing identity, similarity and gap of 72.6%, 84.2%, and 4.3%, respectively. Alignment not only shows high identity between the two proteins but also reveals a consistently dispersed identity and similarity (Fig. 1A). Thus, structural homology can be inferred. It is likely that the distances between homologous Trp and disulfide bridges in HSA may be comparable to those in BSA. The shortest distance between conserved Trp214 chainA and the nearest disulfide bridge (Cys200–Cys246) in HSA is 11 Å. The 3D structure of HSA is shown in Figure 1B. HSA contains 1 tryptophan and 17 disulfide bridges. BSA contains 3 Trp residues and 17 disulfide bridges and one free thiol group Cys34. Cys34 has low or no solvent accessibility making it difficult to react with the nanoparticles' Au surface (Brahma et al., 2005; Wang et al., 2009; Zhu et al., 2001). The combined presence of 3 Trp and 17 disulfide bridges make BSA a good candidate for LAMI technology.

Thiol Groups Formation Upon 295 nm Irradiation

UV-light induced changes in amino acid residues of proteins have been reported (Bent and Hayon, 1975a,b; Creed, 1984a,b,c Kerwin and Remmele, 2007; Grossweiner and Usui, 1971; Li et al., 1989; Neves-Petersen et al., 2009b). Tryptophan (Trp) has the highest absorption coefficient in the near UV region. Since excitation has been carried out at 295 nm, we will focus on Trp photochemistry. Flash photolysis studies of lysozyme demonstrated that enzyme inactivation was due to the production of photo-oxidized tryptophan residue and due to electron transfer between Trp triplet state and a nearby disulfide bridges, resulting in SS disruption. Two non-radiative relaxation pathways were observed: (1) Electron ejection to the solvent, yielding solvated electrons e^-_{aq} ($Trp + h\nu \rightarrow Trp^{\bullet+} + e^-_{aq}$), (2) Intersystem crossing, yielding the triplet-state ^3Trp ($^1Trp + h\nu \rightarrow {}^1Trp^* \rightarrow {}^3Trp$). e^-_{aq} and ^3Trp can transfer an electron to a nearby disulfide bridge forming $RSSR^{\bullet-}$, which will lead to SS disruption (Sander et al., 1993):

$$RSSR^{\bullet-} \Leftrightarrow RS^{\bullet} + RS^-$$
$$RSSR^{\bullet-} + H^+ \Leftrightarrow RS^{\bullet} + RSH$$
$$H^{\bullet} + RSSR \rightarrow RS^{\bullet} + RSH$$

The resultant free thiol radicals/groups can then form a new disulfide bridge with other thiol groups or thiol reactive surfaces. This can be used to carry out LAMI of proteins onto thiol reactive surfaces. Therefore, LAMI is used to immobilize BSA onto thiol derivatized slides as well as superparamagnetic particles aiming at the development of nanoparticles based drug delivery system and biosensors. Our earlier work as well as Vanhooren's work verified the crucial role of Trp on the photolytic cleavage of disulfide bridge using protein engineering (Petersen et al., 2006; Vanhooren et al., 2006). The estimated concentration of free thiols in BSA before and after 1 h 295 nm illumination was 0.35 and 0.98 μM, respectively. The value for non-illuminated sample is due to the presence of Cys34 (though it is difficult to bind with Au surface, it can react with some probes (Brahma et al., 2005; Wang et al., 2009; Zhu et al., 2001)) and the observed increase in free thiol groups concentration after excitation indicates disulfide bridge disruption upon 295 nm excitation.

For LAMI we use energy per pulse $\leq$100 pJ, which is at least 10^7 times smaller than the energies required in the flash photolysis studies. No protein denaturation has been observed while carrying out the hereby presented illumination experiments. Circular dichroism, dynamic light scattering, steady state fluorescence and static light scattering experiments indicate that 295 nm excitation (excitation carried out at the spectrofluorimeter) did not induced structural changes, for example, denaturation and aggregation of BSA (data not shown).

Microarray Visualization

A 4 × 6 BSA array with 20 μm diameter spots and 150 μm pitch is displayed in Figure 2. BSA-AF532 extrinsic fluorescence can be observed. The spots are well resolved indicating that protein has been washed out from regions of the slide that have not been illuminated. The array shows uniform vertical and horizontal fluorescence intensity profiles (Fig. 2).

Fe_3O_4@Au Core–Shell Nanoparticles Characterization

Citrate stabilized magnetite nanoparticles dispersion is shown in Figure 3A (brown color dispersion, I). Magnetite nanoparticles were nucleated by simultaneous reaction of iron salts hydrolysis into Fe^{2+}-Ferrihydrite complex material (at pH < 8) and condensation of the complex into inverse spinel structure (pH > 8) (Tronc et al., 1992). Particles below critical size (~26 nm for magnetite) exhibit superparamagnetism where the coercivity and remenence of the hysteresis loop are zero. These particles can therefore be controlled by external magnetic fields but retain no residual magnetism after the field is removed since thermal energy overcomes the anisotropic energy barrier.

While preparing magnetic core–shell particles, citric acid plays four major roles: (1) Prevention of magnetite nanoparticles agglomeration immediately after nucleation due to affinity between carboxylic group and iron oxides (Lesnikovich et al., 1990), (2) Reduction of gold cations (Au^{3+}) into gold (Au^0), (3) Stabilization of Fe_3O_4@Au core–shell nanoparticles (magnetic nanoparticles were very stable with zeta potential of −75 mV at pH 9 (Lattuada and Hatton, 2007)), and (4) Easy replacement of citrate ions on the gold surface by thiol groups. Gold cation in the form

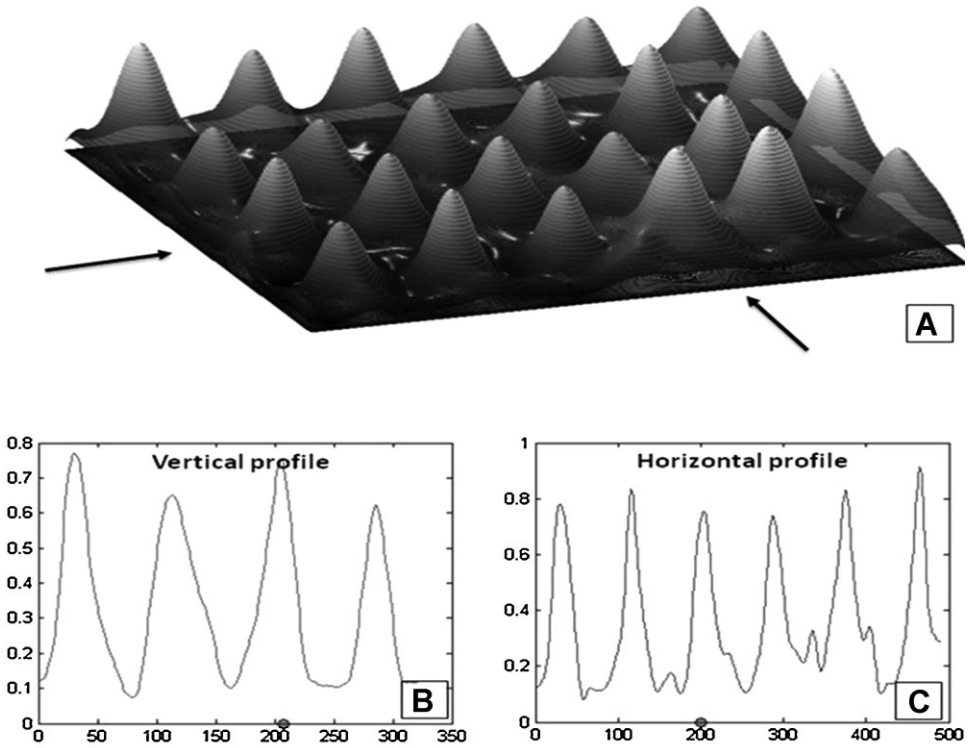

Figure 2. Microarray of BSA-Alexa-Fluor532 immobilized onto the SH functionalized optical flat surface through LAMI technique (**A**). The array contains 4 × 6 spots with 150 μm pitch and each spot is ~20 μm in diameter. Uniform vertical and horizontal fluorescence emission intensity profiles are displayed in **panels B and C**, respectively.

$AuCl_4^-$ is a strong oxidizing agent with $E^0 + 1.002$ (Cushing et al., 2004). Therefore, biocompatible weaker reducing agents such as carboxylates or alcohols can be used to reduce these cations. Since citrate ions are weak reducing agents, gold salt reduction process occurs at a slow reaction rate and precipitation onto existing seed magnetite particles is observed instead of primary nucleation. The use of borohydride as well as other strong reducing agents results in the formation of a large number of tiny gold particles due to high reaction rate (Gnanaprakash et al., 2007). In contrast, citrate reduction methodology leads to secondary nucleation on the magnetite core particles, resulting in the formation of Fe_3O_4@Au core–shell nanoparticles (Fig. 3A and II). The magnetic nature of the gold coated magnetite nanoparticles is shown in Figure 3A and III using a permanent magnet. Upon exposure to a permanent magnetic field, the wine-red (purple on dilution) color disappears leaving a clear solution behind and accumulating particles at the permanent magnet location (Fig. 3A and III). Upon magnetic field removal, the particles re-dispersed in solution.

Figure 3B displayed the SEM image of Fe_3O_4@Au core–shell nanoparticles. EDS experimental analysis qualitatively confirms the presence of the elements C, O, Fe, Na, Si, Au, and Cl (Fig. 3C). C, O, and Na peaks can be expected from sodium citrate surfactant; Si from substrate; Cl from buffer; Fe, Au, and O from Fe_3O_4@Au core–shell nanoparticles. The estimated average nanoparticle size observed with SEM was 22 nm. Using BNIP image analysis, the particles' size distribution was estimated (Fig. 3D). DLS measurements revealed an average hydrodynamic diameter (D_h) of 37.4 nm. The observed single peak confirmed that the particles dispersed in solution were isolated and not agglomerated (data not shown). The average size difference between the SEM and DLS measurements is due to the particles solvation by water and surfactant molecules in solution.

Absorption at 534 nm confirmed the presence of gold layer over the magnetite particles (Fig. 3E). Figure 3E displays the UV–visible absorption spectra of citrate stabilized particles of Fe_3O_4 (average size of 8 nm), Au nanoparticles (average size of 22 nm) and Fe_3O_4@Au nanoparticles (average size of 22 nm) in aqueous solution and of water (blank). Fe_3O_4 nanoparticles dispersion shows absorption band with maximum at 220 nm which extends into the visible region due to the charge transfer transitions involving Fe^{3+}–O and Fe^{2+}–Fe^{3+}(Schwertmann and Cornell, 1991). Plasmonic excitation of citrate stabilized 20 nm gold nanoparticles has a maximum at ~520 nm in agreement with literature (Brown et al., 2000). Fe_3O_4@Au particles show a clear surface plasmon absorption band at 534 nm (14 nm red shift compared to Au nanoparticles) and the suppression of the intense magnetite absorption peak in the UV region. Earlier works report similar shifts for gold

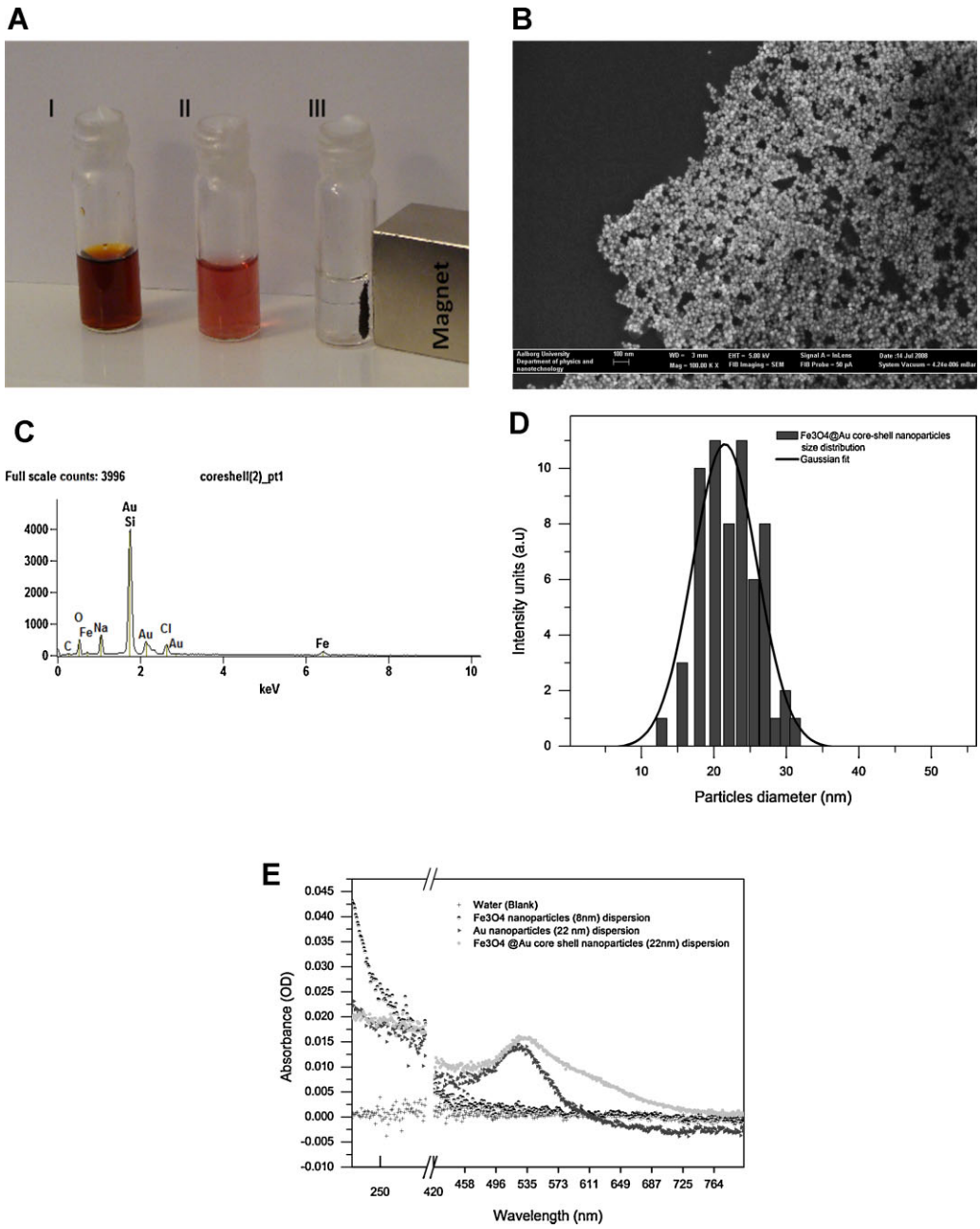

Figure 3. **A**: Display of samples containing (**I**) Magnetite dispersion (brown), (**II**) gold modified magnetite nanoparticles dispersion (purple) and (**III**) separation of superparamagnetic gold coated magnetite nanoparticles from solution using a permanent magnet, illustrating the separation potential of the technique. **B**: SEM image of Fe_3O_4@Au core–shell nanoparticles. The estimated average particle size is 22 nm. **C**: EDS analysis of gold covered superparamagnetic nanoparticles. **D**: Particles' size distribution obtained from BNIP image analysis. **E**: UV–visible absorption spectra of citrate stabilized particles of Fe_3O_4 (8 nm average size), Au nanoparticles (22 nm average size) and Fe_3O_4@Au nanoparticles (22 nm average size) in aqueous solution and of water (blank).

coated magnetite nanoparticles (Lyon et al., 2004; Wang et al., 2005). These previous studies revealed that the surface plasmon resonance property of the Au shell is dependent on its thickness. As the thickness of the gold layer increases the plasmon resonance peak gradually blue shifts towards 520 nm. The observed red shift (~14 nm) in the plasmon resonance peak, the suppression of magnetite absorption band in UV region for Fe_3O_4@Au nanoparticles (Fig. 3E) and the magnetic nature of the wine-red colored solution confirms the completely covered magnetite core with thick Au shell (more than 1 nm (Wang et al., 2005)).

At pH 7.5, gold covered magnetite nanoparticles (22 nm) are more stable than magnetite particles (8 nm) in solution. This is expected due to higher surface to volume ratio and magnetic dipole–dipole interactions in 8 nm magnetite dispersion than in 22 nm core–shell nanoparticles dispersion

(Lyon et al., 2004). Hence, depositing Au layer over magnetite particles is a better choice as compared to magnetite alone for the protein immobilization onto superparamagnetic nanoparticles.

Confirming BSA Immobilization Onto the Superparamagnetic Nanoparticles

At pH 7.5 the created free thiol groups will likely be partially deprotonated (typical pK_a in proteins from 8 to 11 (Creighton, 1993)), thus being more reactive towards gold. Since thiols bind stronger to gold than citrate does, citrate ions are usually substituted by thiols (Lim et al., 2008; Schmid and Corain, 2003). Therefore, Au–S bond is a likely bond between the protein and the core–shell nanoparticles. BSA and citrate stabilized gold nanoparticles interact electrostatically through carboxylate–ammonium salt bridges between the citrate and amino group of lysine and arginine on the protein surface (Brewer et al., 2005). Since the pI of BSA is 5.82, at pH 7.5 the protein will have a negative net charge. Therefore, it is likely that the protein molecules will replace citrate molecules and interact electrostatically with the positively charge Au surface. However, salt bridges interactions (2–15 Kcal/mol) are weaker than Au–S bonds (47 Kcal/mol). Thus, solvent accessible free thiol groups created in BSA are likely covalently bound to the gold nanoparticles surface. Thiol groups covalently bind gold surfaces through the sulfur atom (Bain et al., 1989; Uvdal et al., 1992). The reaction formally is considered an oxidative addition of the S–H bond to the gold surface, followed by reductive elimination of the hydrogen (Ullman, 1996; Varghese et al., 2008):

$$\text{R-S-H} + \text{Au}_n^0 \rightarrow \text{R-S}^-\text{Au}^+\text{Au}_\text{n}^0 + \frac{1}{2}\text{H}_2$$

Templeton et al. (1999) demonstrated that it is easy to replace one molecule with another present in higher concentration while providing enough heat and/or sonication. In order to optimize protein immobilization, protein concentration was kept 10-fold higher than the particles concentration. This will favor protein immobilization. Likewise the protein concentration should be higher than the citrate concentration. Finally, pH was adjusted to pH 7.5 in order to secure a significant proportion of deprotonated thiol groups and protein stability.

Binding of BSA onto the superparamagnetic nanoparticles was confirmed by DLS, SEM, UV–visible spectroscopy and fluorescent spectroscopy. Fluorescence emission spectra of the supernatant were acquired in order to monitor the removal of excess unbound protein from the nanoparticles after each washing step (Fig. 4A and B). Washing for a second time the derivatized nanoparticles lead to the removal of the majority of the unbound protein molecules. The intensity of the protein peak observed in the second wash was much smaller than the protein absorption peak of bottom settled particles, though the particles were diluted

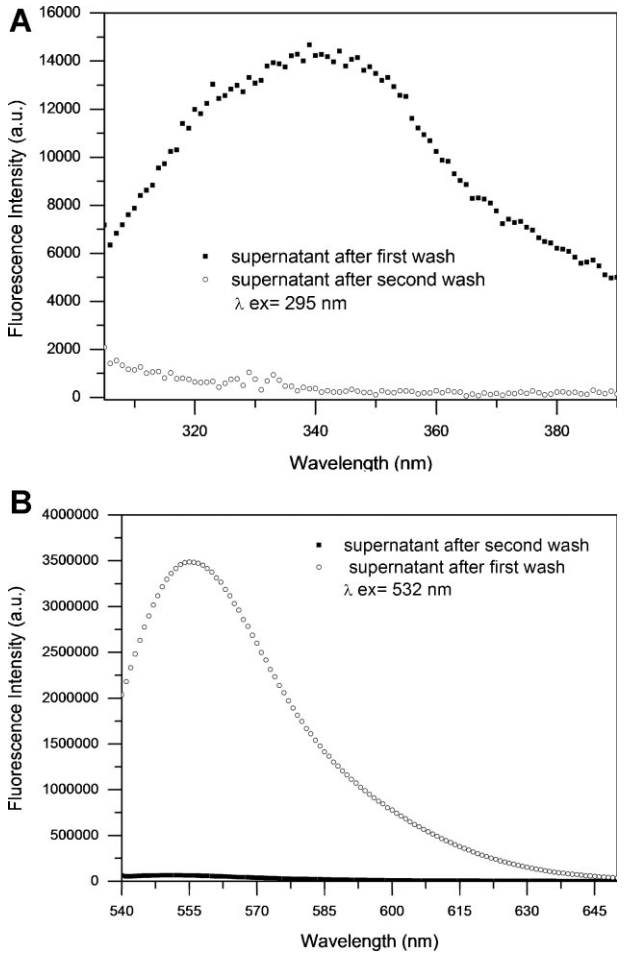

Figure 4. **A**: Fluorescence emission spectra of the supernatant recovered after the first and second washes. The proteins' intrinsic fluorescence was acquired upon 295 nm excitation. The spectra show the negligible amount of free protein present in the supernatant after the second wash. **B**: Fluorescence emission spectra of the supernatant recovered after the first and second washes. The proteins' extrinsic fluorescence was acquired upon 532 nm excitation. The spectra show the negligible amount of free protein present in the supernatant after the second wash.

500 times with buffer. Further washing did not show any significant change in the intensity of the protein absorption peak of the nanoparticle-BSA bioconjugates and of the supernatant. Data confirms that two washes were sufficient to remove non-immobilized protein from the solution (Fig. 4A and B). After two washing procedures, the bottom settled particles were re-dispersed in buffer and used characterized. BSA shows a hydrodynamic diameter (D_h) of 9.6 nm. The observed D_h values for the protein–particles bioconjugate showed a distinct dominant peak at 217 ± 63 nm in DLS, accounting for 95.5% of the signal. A smaller peak accounting for 3.3% of the signal has been observed centered at $1{,}029 \pm 309$ nm and a very small third peak centered at 5227 nm accounting for 1.2% of the signal (Fig. 5A). The polydispersity and the increase of the particles size indicates that aggregation of derivatized nanoparticles

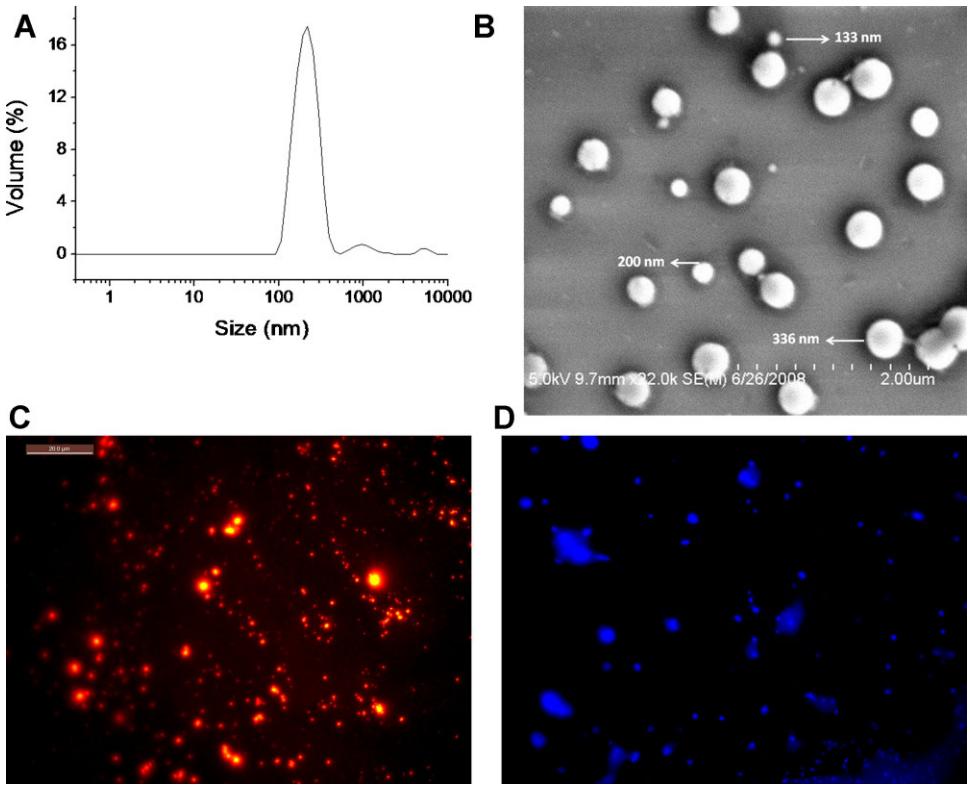

Figure 5. **A**: DLS data of BSA immobilized onto Fe_3O_4@Au core–shell nanoparticles showing a dominant peak at 217 ± 63 nm (95.5% volume). **B**: SEM image of BSA immobilized core–shell nanoparticles and observed sizes. **C**: Fluorescence microscopy images of BSA-AF532 immobilized onto Fe_3O_4@Au core–shell nanoparticles. **D**: ANS fluorescence from ANS molecules bound to BSA-Fe_3O_4@Au core–shell nanoparticles bioconjugates. ANS becomes fluorescent upon binding hydrophobic regions of BSA.

has occurred after protein immobilization. The protein derivatized nanoparticles were stable in solution and the particles–protein bioconjugate does not show any peak at 9.6 nm or 37.4 nm corresponding to free BSA or core–shell nanoparticles, respectively. When carefully observing the SEM data (Fig. 5B) we see bioconjugates at ~133, ~200, ~336 nm. All these peaks are located within the observed statistically relevant DLS peak at $\sim 217 \pm 63$ nm. The presence of 17 disulfide bridges in BSA makes it likely that upon UV excitation several bridges break, generating multiple free thiol groups. The reactivity of these groups induces aggregation among derivatized nanoparticles due to new SS bridges formed between several bioconjugates. Figure 5C displays the fluorescence of BSA-AF532 coupled to superparamagnetic gold coated nanoparticles, confirming the presence of labeled BSA onto the nanoparticles. In order to confirm protein immobilization onto the nanoparticles, ANS has been added to the derivatized nanoparticles. ANS is non-fluorescent in water and becomes fluorescent upon adsorption onto hydrophobic regions of the protein (Haugland, 2002). Figure 5D shows the fluorescence of the adsorbed ANS to the proteins bound onto the nanoparticles, confirming the presence of protein onto the core–shell nanoparticles.

Figure 6A displays the normalized fluorescence emission spectra of free (not immobilized) and immobilized protein, revealing a 15 nm blue shift in the fluorescence emission maximum after protein immobilization. A blue shift (~10 nm) in ANS fluorescence emission is also observed for Fe_3O_4@Au-BSA-ANS versus BSA-ANS (Fig. 6B). The blue shift is likely to be caused by the lower dielectric constant of the core–shell particles compared to the aqueous environment. Data confirms that ANS as well as the Trp becomes less solvent accessible upon BSA immobilization onto nanoparticles.

Figure 7A shows the UV–visible absorption spectra of nanoparticles with and without BSA-AF532. Core–shell particles show the single characteristic 534 nm gold absorption peak. The spectrum of functionalized nanoparticles shows characteristic protein absorption at 220 and 280 nm, and an enhanced peak at 530 nm. The peak at 280 nm is due to aromatic residues absorption, the peak around 220 nm is due to protein backbone absorption and the enhanced peak at 530 nm is due to the presence of gold and dye molecules attached to the protein. This clearly indicates the immobilization of protein onto the particles. The concentration of BSA tagged to nanoparticles was estimated to be 0.566 μM. The final molar ratio of coupled

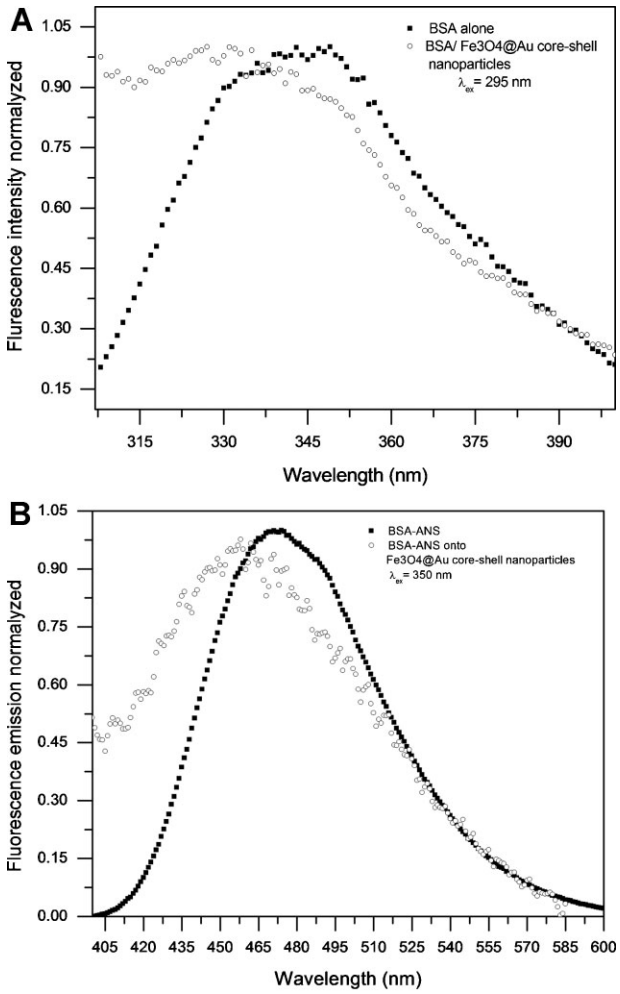

Figure 6. **A**: Normalized intrinsic fluorescence emission spectra of free BSA (not immobilized) and immobilized labeled BSA onto Fe_3O_4@Au core–shell nanoparticles. **B**: Normalized emission spectra of ANS bound to free BSA and ANS bound to BSA immobilized onto Fe_3O_4@Au core–shell nanoparticles. Spectra show a blue shift in the ANS fluorescence emission maximum when ANS is bound to the immobilized protein.

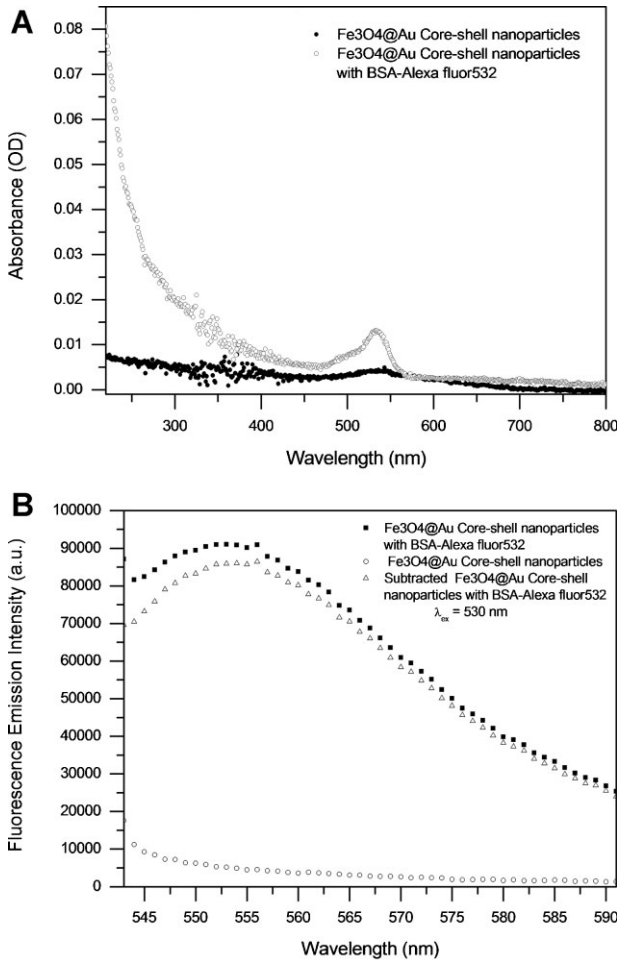

Figure 7. **A**: Absorption spectra of Fe_3O_4@Au core–shell nanoparticles with and without BSA-AF532. **B**: Fluorescence emission spectra of BSA-AF532 coupled Fe_3O_4@Au core–shell nanoparticles and of Fe3O4@Au core–shell nanoparticles. The difference spectrum is also displayed.

BSA-nanoparticles was 1:0.7 in solution indicating the successful immobilization of BSA onto Fe_3O_4@Au core–shell nanoparticles using LAMI. In Figure 7B it can be seen that nanoparticles alone do not show any significant fluorescence emission at 552 nm. However, when exciting BSA immobilized onto nanoparticles with 532 nm light a fluorescence emission peak is observed at 552 nm, confirming the presence of BSA on the nanoparticles' gold surface. The spectra obtained for the samples that were illuminated with UV light and for the non-illuminated samples (negative control) are displayed in Figure 8. The illuminated sample exhibits higher 552 nm fluorescence emission upon 532 nm excitation, while the non-illuminated sample shows low 552 nm fluorescence intensity, indicating that UV excitation has increased the immobilization yield of labeled protein onto the particles.

Conclusions

Immobilization of BSA on the surface of gold coated magnetite nanoparticles as well as on flat sensor surface has been achieved with LAMI. The protein–nanoparticles bioconjugates are more stable in solution than non-derivatised nanoparticles since it was always possible to re-disperse them into solution after centrifugation. The non-derivatised nanoparticles aggregated as a black pellet after two centrifugation/washing steps and no longer re-disperse. The photonic immobilization technology can lead to the creation of multi-potent covalently bio-functionalized new materials as well as drug and gene carriers. These results encourage future development of magnetic nanoparticle based protein carriers with targeted technological applications such as bioseparation, drug targeting, tissue engineering and to improve the enzyme stability towards pH, temperature and solvents.

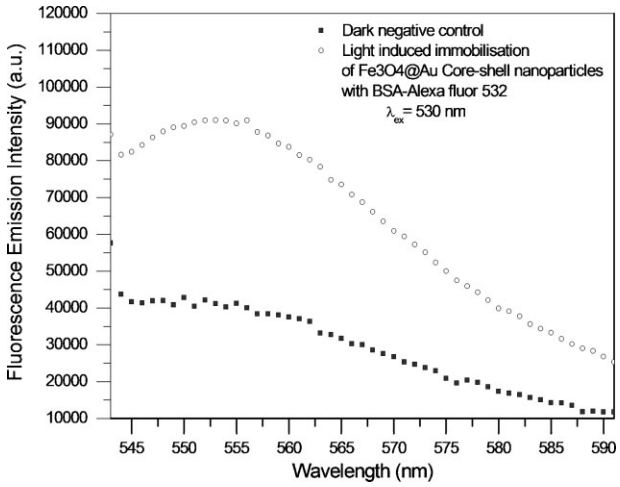

Figure 8. Fluorescence emission spectra of coupled Fe_3O_4@Au core–shell nanoparticles with BSAAF532 with and without light (negative control).

M.C. acknowledges the support from "Fundação para a Ciência e Tecnologia" (FCT) for the PhD grant (SFRH/BD/61012/2009) supported by "Programa Operacional Potencial Humano" (POPH) in the framework of "Quadro de Referência Estratégico Nacional" (QREN) and co-financed by the European Social Fund ("Fundo Social Europeu", FSE). G.P.G. acknowledges the support from the Danish National Advanced Technology Foundation (contract 010-2006-1).

References

Bain CD, Troughton EB, Tao YT, Evall J, Whitesides GM, Nuzzo RG. 1989. Formation of monolayer films by the spontaneous assembly of organic thiols from solution onto gold. J Am Chem Soc 111:321–335.

Baptista P, Pereira E, Eaton P, Doria G, Miranda A, Gomes I, Quaresma P, Franco R. 2008. Gold nanoparticles for the development of clinical diagnosis methods. Anal Bioanal Chem 391:943–950.

Bent DV, Hayon E. 1975a. Excited state chemistry of aromatic amino acids and related peptides. III. Tryptophan. J Am Chem Soc 97:2612–2619.

Bent DV, Hayon E. 1975b. Excited-state chemistry of aromatic amino-acids and related peptides. I. Tyrosine. J Am Chem Soc 97:2599–2606.

Brahma A, Mandal C, Bhattacharyya D. 2005. Characterization of a dimeric unfolding intermediate of bovine serum albumin under mildly acidic condition. Biochim Biophys Acta 1751(2):159–169.

Brewer SH, Glomm WR, Johnson MC, Kang MK, Franzen S. 2005. Probing BSA binding to citrate-coated gold nanoparticles and surfaces. Langumuir 21:9303–9307.

Brown KR, Walter DG, Natan MJ. 2000. Seeding of colloidal Au nanoparticle solutions. 2. Improved control of particle size and shape. Chem Mater 12:306–313.

Cho SJ, Jarrett BR, Louie AY, Kauzlarich SM. 2006. Gold-coated iron nanoparticles: A novel magnetic resonance agent for T1 and T2 weighted imaging. Nanotechnology 17:640–644.

Chu M, Song X, Cheng D, Liu S, Zhu J. 2006. Preparation of quantum dot-coated magnetic polystyrene nanospheres for cancer cell labelling and separation. Nanotechnology 17:3268–3273.

Creed D. 1984a. The photophysics and photochemistry of the near-uv absorbing amino acids—iii. Cystine and its simple derivatives. Photochem Photobiol 39:577–583.

Creed D. 1984b. The photophysics and photochemistry of the near-uv absorbing amino acids—i. Tryptophan and its simple derivatives. Photochem Photobiol 39:537–562.

Creed D. 1984c. The photophysics and photochemistry of the near-uv absorbing amino-acids .ii. Tyrosine and its simple derivatives. Photochem Photobiol 39:563–575.

Creighton TE. 1993. Proteins: Structures & molecular properties. 2nd edition. New York: W H Freeman & Co; pp. 293–296.

Cushing BL, Kolesnichenko VL, O'Connor CJ. 2004. Recent advances in the liquid-phase syntheses of inorganic nanoparticles. Chem Rev 104:3893–3946.

Daniel MC, Astruc D. 2004. Gold nanoparticles: Assembly, supramolecular chemistry, quantum-size-related properties, and applications toward biology, catalysis, and nanotechnology. Chem Rev 104:293–346.

Di Felice R, Selloni A. 2004. Adsorption modes of cysteine on Au (111): Thiolate, amino-thiolate, disulfide. J Chem Phys 120:4906–4914.

Duroux M, Skovsen E, Petersen MTN, Duroux L, Gurevich L, Petersen SB. 2007. Light-induced immobilisation of biomolecules as an attractive alternative to microdroplet dispensing-based arraying technologies. Proteomics 7:3491–3499.

Gnanaprakash G, Philip J, Jayakumar T, Raj B. 2007. Effect of digestion time and alkali addition rate on physical properties of magnetite nanoparticles. J Phys Chem B 111:7978–7986.

Grossweiner LI, Usui Y. 1971. Flash photolysis and inactivation of aqueous lysozyme.

Haugland RP. 2002. Handbook of fluorecent probes and research products. 9th edition. USA: Molecular Probes, Inc.

Huang CY, Lee YD. 2006. Core–shell type of nanoparticles composed of poly[(n-butyl cyanoacrylate)-co-(2-octyl cyanoacrylate)] copolymers for drug delivery application: Synthesis, characterization and in vitro degradation. Int J Pharm 325:132–139.

Imahori H, Fukuzumi S, Porphyrin S. 2001. Porphyrin monolayer-modified gold clusters as photoactive materials. Adv Mater 13:1197–1199.

Ito A, Hayashida M, Honda H, Hata K, Kagami H, Ueda M, Kobayashi T. 2004. Construction and harvest of multilayered keratinocyte sheets using magnetite nanoparticles and magnetic force. Tissue Eng 10:873–880.

Jonkheijm P, Weinrich D, Schröder H, Niemeyer CM, Waldmann H. 2008. Chemical stratergies for generating protein biochips. Angew Chem Int Ed Engl 47:9618–9647.

Kerwin BA, Remmele RL, Jr. 2007. Protect from light: Photodegradation and protein biologics. J Pharm Sci 96:1468–1479.

Koneracka M, Kopcansky P, Timko M, Ramchand CN, de Sequeira A, Trevan M. 2002. Direct binding procedure of proteins and enzymes to fine magnetic particles. J Mol Catal B: Enzym 18:13–18.

Lattuada M, Hatton TA. 2007. Functionalization of monodisperse magnetic nanoparticles. Langmuir 23:2158–2168.

Laurent S, Forge D, Port M, Roch A, Robic C, Elst LV, Muller RN. 2008. Magnetic iron oxide nanoparticles: Synthesis, stabilization, vectorization, physicochemical characterizations, and biological applications. Chem Rev 108:2064–2110.

Lee SH, Liddell CM. 2009. Anisotropic magnetic colloids: A strategy to form complex structures using nonspherical building blocks. Small 5:1957–1962.

Lesnikovich AI, Shunkevich TM, Naumenko VN, Vorobyova SA, Baykov MV. 1990. Dispersity of magnetite in magnetic liquids and the interaction with a surfactant. J Magn Magn Mater 85:14–16.

Li Z, Lee WE, Galley WC. 1989. Distance dependence of the tryptophan–disulfide interaction at the triplet level from pulsed phosphorescence studies on a model system. Biophys J 56:361–367.

Li Y, Xu X, Deng C, Yang P, Zhang X. 2007. Immobilization of trypsin on superparamagnetic nanoparticles for rapid and effective proteolysis. J Proteome Res 6:3849–3855.

Lim JK, Kim Y, Lee SY, Joo SW. 2008. Spectroscopic analysis of l-histidine adsorbed on gold and silver nanoparticle surfaces investigated by surface-enhanced Raman scattering. Spectrochim Acta Part A 69: 286–289.

Lyon JL, Fleming DA, Stone MB, Schiffer P, Williams ME. 2004. Synthesis of Fe oxide core/Au shell nanoparticles by iterative hydroxylamine seeding. Nano Lett 4:719–723.

Ma Z, Guan Y, Liu H. 2006. Superparamagnetic silica nanoparticles with immobilized metal affinity ligands for protein adsorption. J Magn Magn Mater 301:469–477.

Mehta RV, Upadhyay RV, Charles SW, Ramchand CN. 1997. Direct binding of protein to magnetic particles. Biotechnol Tech 11:493–496.

Neves-Petersen MT, Duroux M, Skovsen E, Duroux L, Petersen SB. 2009a. Printing novel molecular architectures with micrometer resolution using light. J Nanosci Nanotechnol 6:3372–3381.

Neves-Petersen MT, Klitgaard S, Pascher T, Skoven E, Polivka T, Yartsev A, Sundstrom V, Petersen SB. 2009b Flash Photolysys of cutinase: Identification and decay kinetics of transient intermediates formed upon UV excitation of aromatic residues. Biophys J 97:211–226.

Park HY, Schadt MJ, Wang L, Lim IIS, Njoki PN, Kim SH, Jang MY, Luo J, Zhong CJ. 2007. Fabrication of magnetic core@shell Fe oxide@Au nanoparticles for interfacial bioactivity and bio-separation. Langmuir 23:9050–9056.

Petersen MTN, Snabe T, Klitgaard S, Duroux M, Petersen SB. 2006. Photonic activation of disulfide bridges achieves oriented protein immobilization on biosensor surfaces. Protein Sci 15:343–351 (Photochem Photobiol 13:195–214).

Riener CK, Kada G, Gruber HJ. 2002. Quick measurement of protein sulfhydryls with Ellman's reagent and with 4,4′-dithiodipyridine. Anal Bioanal Chem 373:266–276.

Safarik I, Safarikova M. 2002. Magnetic nanoparticles and biosciences. Munatsh Chem 133:737–759.

Sander MU, Luther K, Troe J. 1993. Excitation energy dependence of the photoionization of liquid water. J Phys Chem 97:11489–11492.

Schmid G, Corain B. 2003. Nanoparticulated gold: Syntheses, structures, electronics, and reactivities. Eur J Inorg Chem 17:3081–3098.

Schwertmann U, Cornell RM. 1991. Iron oxides in the laboratory. Weinheim: VCH Verlagsgesellschaft, p. 137.

Sharma P, Brown S, Walter G, Santra S, Moudgil B. 2006. Nanoparticles for bioimaging. Adv Colloid Interface Sci 123–126:471–485.

Skoven E, Kold A, Petersen MTN, Petersen SB. 2009a. Photonic immobilization of high density protein arrays using Fourier optics. Proteomics 9:3945–3948.

Skoven E, Petersen MTN, Laurent D, Kold A, Petersen SB. 2009b. Immobilizing biomolecules near the diffraction limit. J Nanosci Nanotech 9:4333–4337.

Templeton AC, Cliffel DE, Murray RW. 1999. Redox and fluorophore functionalization of water-soluble, tiopronin-protected gold clusters. J Am Chem Soc 121:7081–7089.

Tronc E, Belleville P, Jolivet J-P, Livage J. 1992. Transformation of ferric hydroxide into spinel by iron (II) adsorption. Langmuir 8: 313–319.

Ullman A. 1996. Formation and structure of self-assembled monolayers. Chem Rev 96:1533–1554.

Uvdal K, Bodo P, Liedberg B. 1992. L-Cysteine adsorbed on gold and copper: An X-ray photoelectron spectroscopy study. J Colloid Interface Sci 149:162–173.

Vanhooren A, De Vriendt K, Devreese B, Chedad A, Sterling A, Dael HV, Beeumen JV, Hanssens I. 2006. Selectivity of tryptophan residues in mediating photolysis of disulfide bridges in goat α-lactalbumin. Biochemistry 45:2085–2093.

Varghese N, Vivekchand SRC, Govindaraj A, Rao CNR. 2008. A calorimetric investigation of the assembly of gold nanorods to form necklaces. Chem Phys Lett 450:340–344.

Wang L, Luo J, Fan Q, Suzuki M, Suzuki IS, Engelhard MH, Lin Y, Kim N, Wang JQ, Zhong CJ. 2005. Monodispersed core–shell Fe_3O_4@Au nanoparticles. J Phys Chem B 109:21593–21601.

Wang X, Guo L, Ma H. 2009. Analysis of local polarity change around Cys34 in bovine serum albumin during N→B transition by a polarity-sensitive fluorescence probe. Spectrochim Acta Part A: Mol Biomol Spectrosc 73:875–878.

Yang H, Zhang S, Chen X, Zhuang Z, Xu J, Wang X. 2004. Magnetite-containing spherical silica nanoparticles for biocatalysis and bioseparations. Anal Chem 76:1316–1321.

Yang Z, Si S, Zhang C. 2008. Magnetic single-enzyme nanoparticles with activity and stability. Biochem Biophys Res Commun 367:169–175.

You CC, Miranda OR, Gider B, Ghosh PS, Kim IB, Erdogan B, Krovi SA, Bunz U, Rotello VM. 2007. Detection and identification of proteins using nanoparticle-fluorescent polymer 'chemical nose' sensors. Nat Nanotechnol 2:318–323.

You CC, Agasti SS, Rotello VM. 2008. Isomeric control of protein recognition with amino- and dipeptide-functionalized gold nanoparticles. Chem Eur J 14:143–150.

Zhu Y, Cheng G, Dong S. 2001. The electrochemically induced conformational transition of disulfides in bovine serum albumin studied by thin layer circular dichroism spectroelectrochemistry. Biophys Chem 90: 1–8.

4.5 Paper 5

Plasmon-assisted delivery of single nano-objects in an optical hot spot

Christopher M. Galloway, Mark P. Kreuzer, Srdjan S. Aćimović, Giorgio Volpe, Manuel Correia, Steffen B. Petersen, Maria Teresa Neves-Petersen, and Romain Quidant

Nano letters, 2013, 13(9), 4299–304

NANO LETTERS

Letter

pubs.acs.org/NanoLett

Plasmon-Assisted Delivery of Single Nano-Objects in an Optical Hot Spot

Christopher M. Galloway,[†] Mark P. Kreuzer,[†] Srdjan S. Aćimović,[†] Giorgio Volpe,[†] Manuel Correia,[‡] Steffen B. Petersen,[∥] Maria Teresa Neves-Petersen,[§,*] and Romain Quidant*[,†,⊥]

[†]ICFO - Institut de Ciencies Fotoniques, Mediterranean Technology Park, 08860 Castelldefels (Barcelona), Spain

[‡]Department of Physics and Nanotechnology, Aalborg University, Skjernvej 4A. DK-9220, Aalborg, Denmark

[§]International Iberian Nanotechnology Laboratory (INL), P-4715-310 Braga, Portugal

[∥]NanoBiotechnology Group, Department of Health Science and Technology, Aalborg University, Fredrik Bajers vej 7, DK-9220, Aalborg, Denmark

[⊥]ICREA - Institució Catalana de Recerca i Estudis Avançats, Barcelona, Spain

Supporting Information

ABSTRACT: Fully exploiting the capability of nano-optics to enhance light-matter interaction on the nanoscale is conditioned by bringing the nano-object to interrogate within the minuscule volume where the field is concentrated. There currently exists several approaches to control the immobilization of nano-objects but they all involve a cumbersome delivery step and require prior knowledge of the "hot spot" location.[1−6] Herein, we present a novel technique in which the enhanced local field in the hot spot is the driving mechanism that triggers the binding of proteins via three-photon absorption. This way, we demonstrate exclusive immobilization of nanoscale amounts of bovine serum albumin molecules into the nanometer-sized gap of plasmonic dimers. The immobilized proteins can then act as a scaffold to subsequently attach an additional nanoscale object such as a molecule or a nanocrystal. This universal technique is envisioned to benefit a wide range of nano-optical functionalities including biosensing,[7−12] enhanced spectroscopy like surface-enhanced Raman spectroscopy[13,14] or surface-enhanced infrared absorption spectroscopy,[15] as well as quantum optics.[1,2,6]

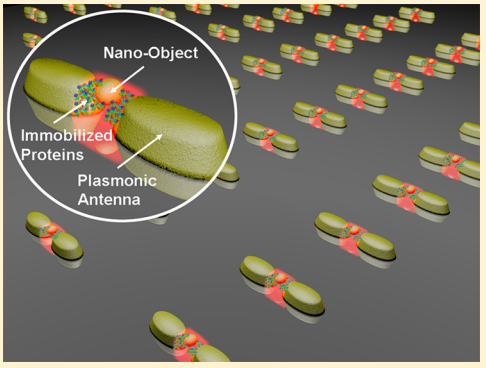

KEYWORDS: *Nanopositioning, fabrication, plasmonics, biosensing, quantum optics*

Recent advances in nano-optics and especially in plasmonics offer a unique capability to concentrate light fields well below the limit of diffraction. While nanoscale control of light opens up a huge potential that could benefit many different fields of science, its full exploitation raises major technical challenges. Indeed, the more confined is the optical field the more critical and challenging becomes the positioning of the specimen as a small spatial shift translates into a strong change of the interaction strength. With the aim to achieve a deterministic control of enhanced light-matter interaction in an optical "hot spot", researchers have recently proposed strategies to position few to single quantum emitters at a predefined location of plasmonic nanostructures. A first family of techniques consists in using scanning probes or optical tweezers to pick up one specimen and move it to its final destination.[16−18] Although accurate, these approaches are tedious and not scalable to a large number of structures. Alternatively, double-step lithography combined with surface chemistry was successfully used to immobilize few to single quantum dots at predefined locations of large arrays of optical antennas.[1,2,6] While the first lithography defines the plasmonic pattern, the second one opens binding sites where the quantum dots subsequently attach. Again, such a process is cumbersome and its precision is limited by the accuracy with which the sample is aligned for the second lithography, typically of the order of 20 nm. More importantly, all these approaches fully rely on a prior knowledge of the hot spot location, which is extremely sensitive to any morphological defect or irregularities of the optical nanostructure. The photochemical approach we propose here addresses the limitations of existing strategies by building upon the actual (and not the expected) near field optical response of the fabricated nanostructures.

Our strategy relies on light-assisted molecular immobilization (LAMI)[19−21] in which proteins can be immobilized onto a thiol-reactive surface[22−24] by absorption of UV photons. LAMI technology exploits an inherent natural property of proteins and peptides whereby a disulfide bridge is disrupted upon absorption of UV photons by the nearby aromatic amino acids. The created thiol groups are subsequently used to immobilize the protein or peptide to a substrate or nanoparticle. This

Received: June 7, 2013
Revised: July 16, 2013
Published: August 5, 2013

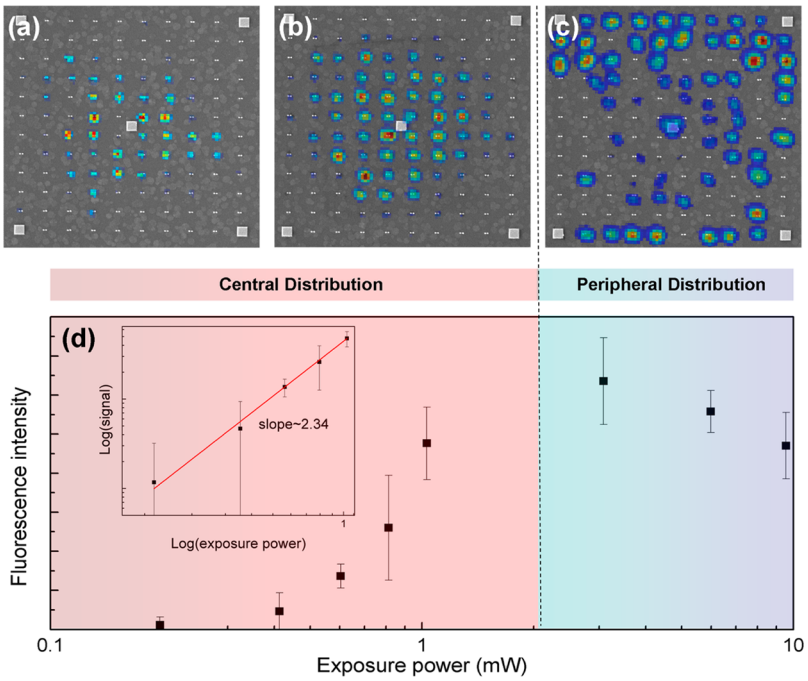

Figure 1. SEM images of three arrays illuminated at powers of (a) 600 μW, (b) 1 mW, and (c) 10 mW are superimposed with their corresponding fluorescence maps (note that the color scale is not constant) with red representing strong fluorescence and blue representing weak fluorescence. The dimers are separated by 1 μm in both directions and have dimensions as explained in the Supporting Information. (d) Plot of the dependence with exposure power of the average fluorescence of the 10 dimers with the largest fluorescent signal. The error bars represent the spread in those 10 values. Inset in (d) is a logarithmic plot of the power dependence of the average fluorescence for a central distribution demonstrating the multiphoton mechanism.

photonic protein immobilization technology has led to the development of microarrays of active biosensors and biofunctionalization of thiol reactive nanoparticles, aimed at drug delivery systems.[21,25] LAMI has so far been used to create high-density protein arrays with a resolution that is only restricted by the focusing ability of the light source, typically limited by diffraction to approximately half the wavelength of light. Therefore, the best-case scenario allowed protein spots of the order of a few hundred nanometers to be manufactured. The use of plasmonics could enable the immobilization of much smaller amounts of molecules by capitalizing on the capability of metallic nanostructures to concentrate light on the subwavelength scale. While the aromatic residue of proteins features an absorption peak centered at around 275 nm (274 nm for tyrosine and 278 nm for tryptophan), gold nanostructures are usually resonant in the near-infrared region of the spectrum. To compensate for this energy mismatch, we employ absorption of multiple infrared photons from the optical near field of the nanostructures. In addition, LAMI based on multiphoton absorption[26−28] is expected to further improve the spatial resolution of the immobilization by restricting the photochemical reaction to the region of most intense optical fields.[29]

In the present experimental implementation, periodic arrays of gold dimers were fabricated on glass by using standard e-beam lithography. The dimensions of the two identical cylinders forming the dimers were tuned to achieve a resonance centered ca. 700 nm in air. Scanning electron microscopy (SEM) shows an average gap size of 20 ± 5 nm in which most of the plasmonic field is expected to be confined upon illumination polarized along the dimer longitudinal axis. A 5 μL droplet containing Alexa-488 labeled bovine serum albumin (BSA) was allowed to evaporate over the structures in an incubator set to 31 °C in order to achieve a high concentration of proteins close to the gold surface (see Supporting Information for additional details). As a result of the protein coverage, the resonance of the dimers shift to ca. 800 nm, thus enabling three-photon absorption upon illumination with a pulsed titanium:sapphire laser (set at 810 nm) to initiate the LAMI process.

Figure 1 demonstrates how the spatial distribution of immobilized proteins varies with the laser power (illumination focus of 12 μm). Arrays of gold dimers were coated with Alexa-488 labeled BSA and exposed at differing powers before being cleaned of all unbound BSA (see Supporting Information for experimental details).

Three of the arrays imaged by SEM are shown in Figure 1a−c and overlaid with their corresponding fluorescence maps. The location of the fluorescence demonstrates how the proteins are arranged on the array surface while its intensity provides qualitative information on the local density of protein binding. Two spatial regimes are clearly apparent; central immobilization (red region of Figure 1d), in which the dimers with the largest fluorescence are located in the center of the array, and a peripheral immobilization (blue region of Figure 1d) where the inner structures show little or no fluorescence and the largest fluorescence come from the dimers at the periphery of the array. This phenomenon is due to the Gaussian intensity profile of the IR beam used to illuminate the arrays such that the central dimers experience the largest laser intensity. However, if the local intensity becomes too high, protein immobilization will cease resulting in the ringlike peripheral pattern. We postulate that the main contributing factor here is heating of the gold to temperatures that lead to the breaking of the thiol bond that anchors the protein to the gold. The local temperature is expected to become rapidly homogeneous

dx.doi.org/10.1021/nl402071p | Nano Lett. 2013, 13, 4299−4304

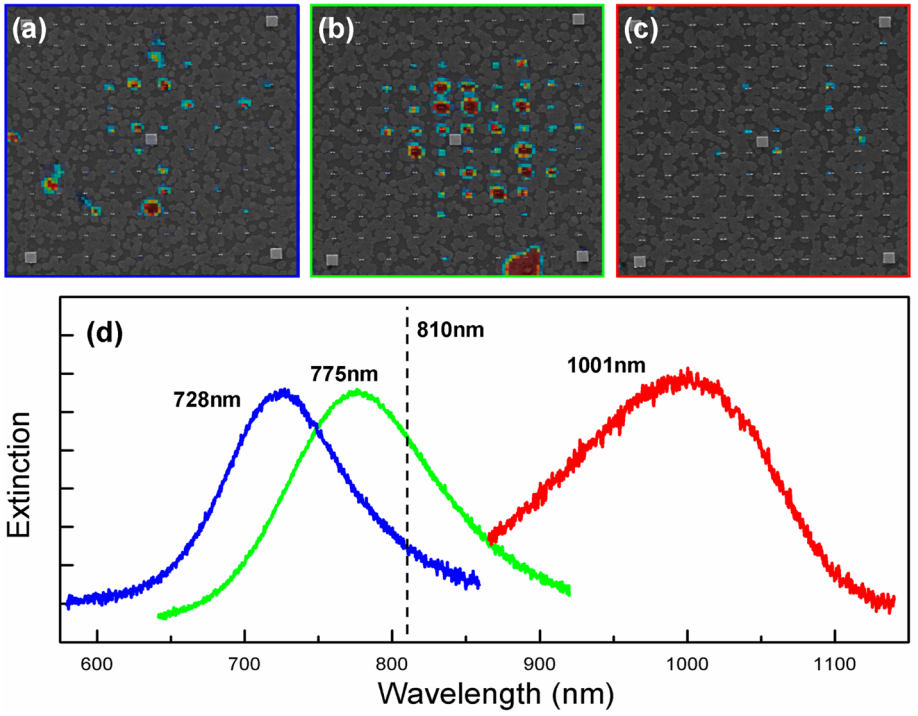

Figure 2. SEM images of arrays with resonance wavelengths (when coated with BSA) of (a) 728 nm, (b) 775 nm, and (c) 1001 nm are superimposed with their fluorescence maps (the color scale is kept constant). (d) Extinction spectra for the three different dimer arrays. The dashed line at 810 nm represents the wavelength at which the structures were illuminated.

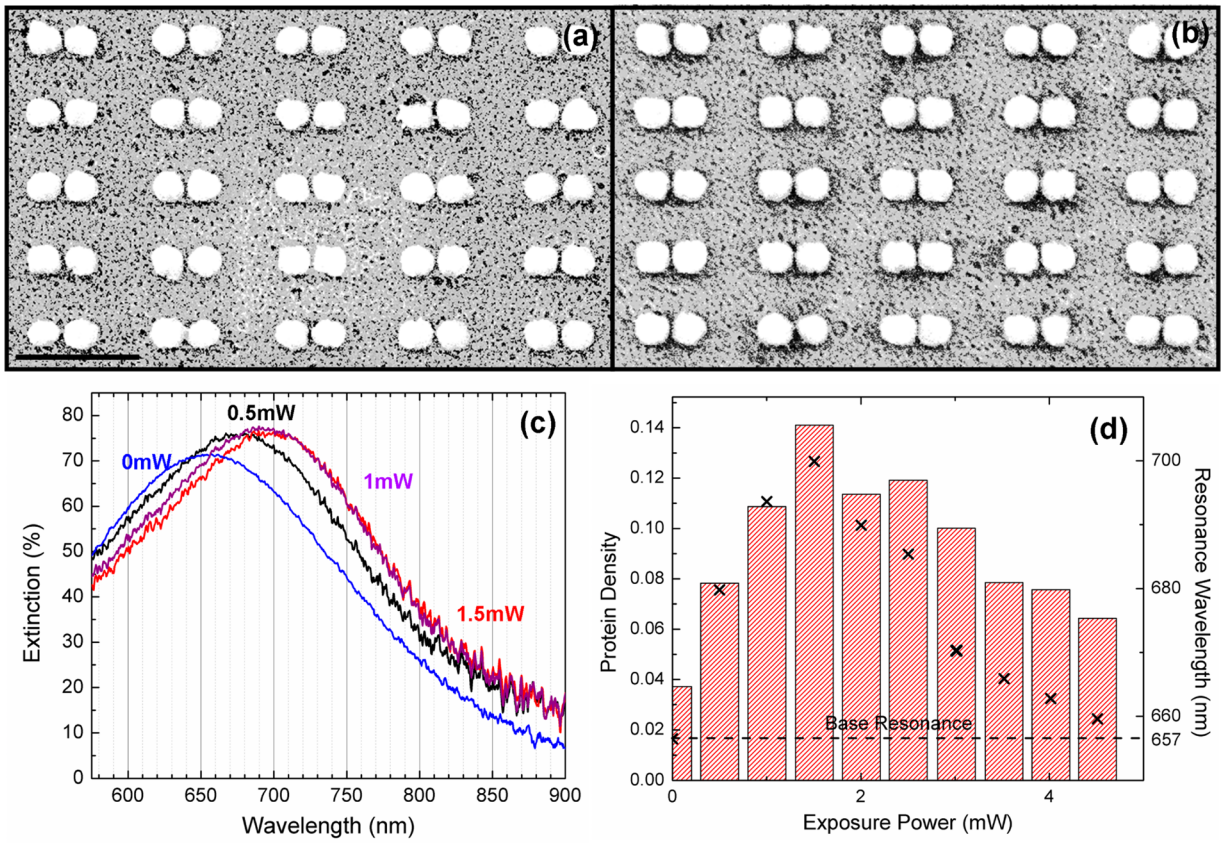

Figure 3. Processed SEM images of a set of 5 × 5 gold dimers (scale bar = 500 nm) (a) unexposed and (b) after exposure at 1 mW. (c) Shift of the extinction spectrum of the arrays for increasing exposure powers. (d) Evolution with the exposure power of the protein density extracted from SEM imaging (bars) and the peak resonance wavelengths (crosses).

dx.doi.org/10.1021/nl402071p | *Nano Lett.* 2013, 13, 4299−4304

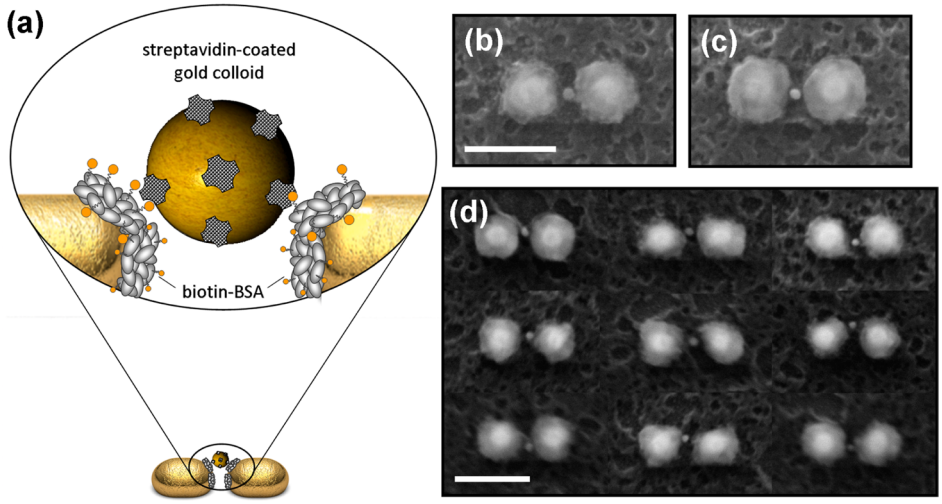

Figure 4. (a) Schematic of the chemical modification used to bind a gold colloid to the immobilized protein. (b,c) SEM images showing binding of a single gold nanoparticle in the gap of homogeneous gold dimers. (d) Series of SEM images that illustrates self-alignment of the gold colloid in the hot spot despite the morphological irregularities of the hosting dimers (scale bar = 150 nm).

over the structure; hence any disruption to the binding process is not expected to be dependent on the position. For those maps with central immobilization (those where the central structures are not overexposed), the integrated fluorescence intensity (see Supporting Information) varies nonlinearly with power as demonstrated from the inset logarithmic plot in Figure 1d. A slope of ca. 2.34 is achieved demonstrating that the immobilization involves the absorption of more than two infrared photons. The reason we do not observe a slope closer to three is while the excitation of the aromatic amino acids in the BSA proteins occurs upon absorption of three-photons and thus follows a cubic power dependence, the power dependence of the BSA binding process itself is more complicated as an immobilized protein may still undergo three photon absorption by its amino acids without affecting the fluorescence signal from the Alexa-488 molecule.

In order to verify that the protein binding is triggered by the enhanced plasmonic fields produced by the dimer at its localized surface plasmon resonance (LSPR), arrays with different resonant wavelengths were exposed under identical excitation conditions (see Supporting Information). The array with a resonance closest to the exposing wavelength, set at 810 nm (Figure 2b), shows a larger fluorescence signal as compared to the arrays whose resonance is shifted (see Figure 2d for the extinction spectra). It is interesting to note that the array with the longest resonance wavelength has the largest surface area of gold but shows the least amount of fluorescence. This confirms that the optical near field governs the proteins immobilization independently of the geometry of the gold structure.

The susceptibility of the immobilization to the resonant optical properties of the gold antenna suggests that under the right conditions, proteins can be exclusively bound to the regions of highest field enhancement. However, due to the small dimensions of the plasmonic structure, techniques other than conventional confocal microscopy need to be utilized to determine the spatial distribution of proteins on the gold surface. Fortunately, the protein localization can be observed as a dark "clouding" using SEM microscopy.[30] In Figure 3, panel a is an unexposed array, while panel b was exposed with 1 mW (see Supporting Information for details on visualizing proteins clouds). For convenience, these arrays feature a higher density (lower pitch) so that the illumination seen by each structure is as homogeneous as possible. Compared to the nonexposed array, there is substantially more clouding in the exposed case, particularly in the gap region of the structures. Furthermore, there is very little sign of clouding at other locations of the gold surface. To complement this initial visual effect, we exploit the intrinsic sensitivity of LSPR resonances to the binding of proteins at the gold surface. The shift in the resonance peak depends on both the number of proteins and their location.[3,31] In particular, it will be more pronounced when the molecules overlap with the regions where the near field is the most concentrated. Figure 3c displays the evolution in the dimers resonance as the power of the exposing beam increases.

Upon increasing incident power, the LSPR wavelength rapidly shifts from 657 nm to a maximum of 700 nm for a power of 1.5 mW before decreasing back to the initial level. This is because for low laser intensities (when local heating is not significant) the area encompassed by the proteins will increase, beginning with the gap region, as a function of power resulting in a red-shift of the plasmon resonance frequency. However, once the heating effect does start to play a role, the ability of the protein to bind at any position on the surface is reduced until the temperature is high enough that the binding completely ceases. The protein density extracted from SEM imaging is well correlated to the resonance shift, featuring a similar resonant behavior (Figure 3d). Interestingly, though, for powers larger than 1.5 mW the decay is slower, indicating that the immobilized proteins have a decreasing influence on the dimer resonance. For example, the protein density at 0.5 and 3.5 mW are very similar, however, the resonance shift at 0.5 mW is approximately twice that at 3.5 mW. This confirms that at low powers, the proteins are mainly located in the gap region of the structures where they have a larger influence on the LSPR wavelength.[31]

At this stage, we propose to exploit the proteins immobilized in the region of most intense field as a scaffold to attach any additional nano-objects of interest. The latter would then be automatically located at the position at which the interaction with the plasmonic field is optimum. To demonstrate this we chose to modify the immobilized BSA protein with biotin with 0.5 mW and then allow streptavidin-coated gold colloids to

dx.doi.org/10.1021/nl402071p | *Nano Lett.* 2013, 13, 4299−4304

interact with the system[32,33] (see Figure 4a and Supporting Information for more details). The choice of gold colloids over quantum emitters such as a quantum dot is because the colloids can be easily imaged via SEM. Figure 4b,c shows two high-resolution examples in which a highly symmetric dimer has bound a single 20 nm colloid very close to the gap center. However, most of nanofabricated structures feature morphological imperfections that lead to a hot spot that is not exactly located in the very center of the gap between the two gold particles forming the dimer. The strength of our approach is that it automatically accounts for these slight variations such that the hosting protein scaffold builds where the field is actually concentrated. Despite the unique fine geometrical features of each of the dimers shown in Figure 4d, the gold colloid attaches in or very close to the region of smallest gap. Such self-alignment makes the process directly transposable to more complex architectures without any need for a prior knowledge of the hot spot location.

It is important to note that the ability to position nanoparticles is largely dependent on a number of sequential steps (uniform evaporation of protein, consistent postlabeling of protein by biotin, multiple wash steps, and finally appropriate reaction time of modified nanoparticles with the protein-labeled substrate), each with its own efficiency. The overall yield is thus the product of all these steps. At this point in time, 10−20% of the dimers showed nanoparticle binding, however, of those structures, the nanoparticles were always positioned in the hot spot position and it was only a single particle in a majority of those cases (<1% multiple nanoparticle attachment).

Beyond the present proof of concept, we envision this approach to benefit a wide range of research areas involving the interaction of an inhomogeneous optical near field with tiny amounts of matter. This includes plasmon-enhanced optical spectroscopy techniques such as surface-enhanced Raman spectroscopy and infrared absorption spectroscopy in which the magnitude of the signal directly depends on analyte/hot spot overlap. Also, our technique may improve the sensitivity in biosensing, whereby the precise positioning of receptors in the most sensitive region remains both allusive and technologically challenging.[3] Finally, it may also be useful in quantum optics where the strong coupling between quantum emitters and strongly confined optical modes is a crucial condition to fulfill in many quantum functionalities.

■ ASSOCIATED CONTENT

Supporting Information

Additional information and figures. This material is available free of charge via the Internet at http://pubs.acs.org.

■ AUTHOR INFORMATION

Corresponding Author

*E-mail: (M.T.N.-P.) teresa.petersen@inl.int; (R.Q.) romain.quidant@icfo.es.

Notes

The authors declare no competing financial interest.

■ ACKNOWLEDGMENTS

This work was partially supported by the Spanish Ministry of Sciences under Grants FIS2010-14834 and CSD2007-046-NanoLight.es, the European Community's Seventh Framework Program under Grant ERC-Plasmolight (259196), and Fundació privada CELLEX. M.C. acknowledges the support from "Fundação para a Ciência e Tecnologia" (FCT) for the Ph.D. Grant (SFRH/BD/61012/2009).

■ REFERENCES

(1) Bermúdez Ureña, E.; Kreuzer, M. P.; Itzhakov, S.; Rigneault, H.; Quidant, R.; Oron, D.; Wenger, J. Excitation enhancement of a quantum dot coupled to a plasmonic antenna. *Adv. Mater.* **2012**, *24*, OP314−OP320.

(2) Curto, A. G.; Volpe, G.; Taminiau, T. H.; Kreuzer, M. P.; Quidant, R.; van Hulst, N. F. Unidirectional emission of a quantum dot coupled to a nanoantenna. *Science* **2010**, *329*, 930−933.

(3) Feuz, L.; Jonsson, M. P.; Höök, F. Material-selective surface chemistry for nanoplasmonic sensors: Optimizing sensitivity and controlling binding to local hot spots. *Nano Lett.* **2012**, *12*, 873−879.

(4) Kramer, R. K.; Pholchai, N.; Sorger, V. J.; Yim, T. J.; Oulton, R.; Zhang, X. Positioning of quantum dots on metallic nanostructures. *Nanotechnology* **2010**, *21*, 145307.

(5) Pfeiffer, M.; Lindfors, K.; Atkinson, P.; Rastelli, A.; Schmidt, O. G.; Giessen, H.; Lippitz, M. Positioning plasmonic nanostructures on single quantum emitters. *Phys. Status Solidi B* **2012**, *249* (4), 678−686.

(6) Dregely, D.; Lindfors, K.; Dorfmüller, J.; Hentschel, M.; Becker, M.; Wrachtrup, J.; Lippitz, M.; Vogelgesang, R.; Giessen, H. Plasmonic antennas, positioning, and coupling of individual quantum systems. *Phys. Status Solidi B* **2012**, *249* (4), 666−677.

(7) Anker, J. N.; Hall, W. P.; Lyandres, O.; Shah, N. C.; Zhao, J.; Van Duyne, R. P. Biosensing with plasmonic nanosensors. *Nat. Mater.* **2008**, *7*, 442−453.

(8) Chen, S.; Svedendahl, M.; Käll, M.; Gunnarsson, L.; Dmitriev, A. Ultrahigh sensitivity made simple: Nanoplasmonic label-free biosensing with an extremely low limit-of-detection for bacterial and cancer diagnostics. *Nanotechnology* **2009**, *20*, 434015.

(9) Hoa, X. D.; Kirk, A. G.; Tabrizian, M. Towards integrated and sensitive surface plasmon resonance biosensors: A review of recent progress. *Biosens. Bioelectron.* **2007**, *23*, 151−160.

(10) Kabashin, A. V.; Evans, P.; Pastkovsky, S.; Hendren, W.; Wurtz, G. A.; Atkinson, R.; Pollard, R.; Podolskiy, V. A.; Zayats, A. V. Plasmonic nanorod metamaterials for biosensing. *Nat. Mater.* **2009**, *8*, 867−871.

(11) Hendry, E.; Carpy, T.; Johnston, J.; Popland, M.; Mikhaylovskiy, R. V.; Lapthorn, A. J.; Kelly, S. M.; Barron, L. D.; Gadegaard, N.; Kadodwala, M. Ultrasensitive detection and characterization of biomolecules using superchiral fields. *Nat. Nanotechnol.* **2010**, *5*, 783−787.

(12) Lee, J.; Hernandez, P.; Lee, J.; Govorov, A. O.; Kotov, N. A. Exciton−plasmon interactions in molecular spring assemblies of nanowires and wavelength-based protein detection. *Nat. Mater.* **2007**, *6*, 291−295.

(13) De Angelis, F.; Gentile, F.; Mecarini, F.; Das, G.; Moretti, M.; Candeloro, P.; Coluccio, M. L.; Cojoc, G.; Accardo, A.; Liberale, C.; Zaccaria, R. P.; Perozziello, G.; Tirinato, L.; Toma, A.; Cuda, G.; Cingolani, R.; Di Fabrizio, E. Breaking the diffusion limit with super-hydrophobic delivery of molecules to plasmonic nanofocusing SERS structures. *Nat. Photonics* **2011**, *5*, 682−687.

(14) Hu, M.; Suong, Ou, F.; Wu, W.; Naumov, I.; Li, X.; M. Bratkovsky, A. M.; Williams, R. S.; Li, Z. Gold nanofingers for molecule trapping and detection. *J. Am. Chem. Soc.* **2010**, *132*, 12820−12822.

(15) Adato, R.; Yanik, A. A.; Amsden, J. J.; Kaplan, D. L.; Omenetto, F. G.; Hong, M. K.; Erramilli, S.; Altug, H. Ultra-sensitive vibrational spectroscopy of protein monolayers with plasmonic nanoantenna arrays. *Proc. Natl. Acad. Sci. U.S.A.* **2009**, *106* (46), 19227−19232.

(16) Kühn, S.; Håkanson, U.; Rogobete, L.; Sandoghdar, V. Enhancement of single-molecule fluorescence using a gold nanoparticle as an optical nanoantenna. *Phys. Rev. Lett.* **2006**, *97*, 017402.

(17) Schietinger, S.; Barth, M.; Aichele, T.; Benson, O. Plasmon-enhanced single photon emission from a nanoassembled metal-diamond hybrid structure at room temperature. *Nano Lett.* **2009**, *9* (4), 1694−1698.

(18) Geiselmann, M.; Juan, M. L.; Renger, J.; Say, J. M.; Brown, L. J.; de Abajo, F. J. G.; Koppens, F.; Quidant, R. Three-dimensional optical manipulation of a single electron spin. *Nat. Nanotechnol.* **2013**, *8*, 175−179.
(19) Snabe, T.; Røder, G. A.; Neves-Petersen, M. T.; Buusb, S.; Petersen, S. B. Oriented coupling of major histocompatibility complex (MHC) to sensor surfaces using light assisted immobilisation technology. *Biosens. Bioelectron.* **2006**, *21*, 1553−1559.
(20) Neves-Petersen, M. T.; Snabe, T.; Klitgaard, S.; Duroux, M.; Petersen, S. P. Photonic activation of disulfide bridges achieves oriented protein immobilization on biosensor surfaces. *Protein Sci.* **2006**, *15*, 343−351.
(21) Duroux, M.; Skovsen, E.; Neves-Petersen, M. T.; Duroux, L.; Gurevich, L.; Petersen, S. B. Light-induced immobilisation of biomolecules as an attractive alternative to microdroplet dispensing-based arraying technologies. *Proteomics* **2006**, *7*, 3491−3499.
(22) Collioud, A.; Clémence, J.-F.; Sänger, M.; Sigrist, H. Oriented and covalent immobilization of target molecules to solid supports: Synthesis and application of a light-activatable and thiol-reactive cross-linking reagent. *Bioconjugate Chem.* **1993**, *4* (6), 528−536.
(23) Jonkheijm, P.; Weinrich, D.; Schröder, H.; Niemeyer, C. M.; Waldmann, H. Chemical strategies for generating protein biochips. *Angew. Chem., Int. Ed.* **2008**, *47*, 9618−9647.
(24) Sigrist, H.; Collioud, A.; Clémence, J.-F.; Gao, H.; Luginbühl, R.; Sänger, M.; Sundarababu, G. Surface immobilization of biomolecules by light. *Opt. Eng.* **1995**, *34* (8), 2339−2348.
(25) Parracino, A.; Gajula, G. P.; di Gennaro, A. K.; Correia, M.; Neves-Petersen, M. T.; Rafaelsen, J.; Petersen, S. B. Photonic immobilization of BSA for nanobiomedical applications: Creation of high density microarrays and superparamagnetic bioconjugates. *Biotechnol. Bioeng.* **2011**, *108* (5), 999−1010.
(26) Gryczynski, I.; Malak, H.; Lakowicz, J. R. Three-photon excitation of a tryptophan derivative using a fs-Ti: sapphire laser. *Biospectroscopy* **1996**, *2* (1), 9−15.
(27) Gryczynski, I.; Malak, H.; Lakowicz, J. R.; Cheung, H. C.; Robinson, J.; Umeda, P. K. Fluorescence spectral properties of troponin C mutant F22W with one-, two-, and three-photon excitation. *Biophys. J.* **1996**, *71*, 3448−3453.
(28) Maiti, S.; Shear, J. B.; Williams, R. M.; Zipfel, W. R; Webb, W. W. Measuring serotonin distribution in live cells with Three-Photon Excitation. *Science* **1997**, *275*, 530−532.
(29) Volpe, G.; Noack, M.; Aćimović, S. S.; Reinhardt, C.; Quidant, R. Near-field mapping of plasmonic antennas by multiphoton absorption in poly(methyl methacrylate). *Nano Lett.* **2012**, *12*, 4864−4868.
(30) López, G. P.; Biebuyck, H. A.; Härter, R.; Kumar, A.; Whitesides, G. M. Fabrication and imaging of two-dimensional patterns of proteins adsorbed on self-assembled monolayers by scanning electron microscopy. *J. Am. Chem. Soc.* **1993**, *115* (23), 10774−10781.
(31) Aćimović, S. S.; Kreuzer, M. P.; González, M. U.; Quidant, R. Plasmon near-field coupling in Metal dimers as a step toward single-molecule sensing. *ACS Nano* **2009**, *3* (5), 1231−1237.
(32) Caswell, K. K.; Wilson, J. N.; Bunz, U. H. F.; Murphy, C. J. Preferential end-to-end assembly of gold nanorods by biotin-streptavidin connectors. *J. Am. Chem. Soc.* **2009**, *125* (46), 13914−13915.
(33) Fu, Y.; Zhang, J.; Lakowicz, J. R. Plasmon-enhanced fluorescence from single fluorophores end-linked to gold nanorods. *J. Am. Chem. Soc.* **2009**, *132* (16), 5540−5541.

SUPPLEMENTARY INFORMATION

Plasmon-assisted delivery of single nano-objects in an optical *hot-spot*

Christopher M. Galloway [1], Mark P. Kreuzer [1], Srdjan S. Aćimović [1], Giorgio Volpe [1], Manuel Correia [2], Steffen B. Petersen [4], Maria Teresa Neves-Petersen [3, *], Romain Quidant [1, 5, *]

1. Substrate Fabrication

Our structures were fabricated by standard *e*-beam lithography and reactive ion etching (RIE) on glass-ITO-SiO_2 substrates. The initial substrate for the lithography is a glass cover slide on which a 10 nm layer of ITO is deposited by e-beam deposition, followed by a second deposition of a 50nm thick SiO_2 layer. Electrically conductive and optically transparent, ITO prevents the electric charging of substrates during the scanning electron microscopy characterization. The SiO_2 spacing layer decouples the resonance of the metallic nanoparticles from optically dense ITO, which would otherwise both red-shift and dampen the resonance. On such substrates, a thin adhesive Ti layer is deposited (1nm) followed by a 50nm thermally evaporated gold layer. An e-beam negative tone resist AR N 7520.073 is then spin-coated onto the substrate. At this point, the resist is patterned by an electron beam (acceleration voltage of 30kV), and developed in recommended developer (AR 300-47) immediately after. The patterned resist is baked for 1h at 130^{o}C. Finally, the exposed pattern is transferred to the underlying metal film by the RIE process in Ar gas, followed by a gentle O_2 plasma etching which removes the remaining resist debris.

Our samples consist of gap-antenna arrays of varying arm lengths (100 nm to 160 nm) and gap size (5 nm to 30 nm). Their thickness is determined by the pre-deposited gold layer thickness i.e. 50nm. The distance between adjacent antennas was tuned according to the particular application.

2. Protein Conjugation with Fluorophores

Bovine serum albumin (BSA) was purchased from Sigma-Aldrich as a lyophilized powder and used with no further preparation. A stock solution of BSA was prepared in 0.1 M sodium bicarbonate, pH 8.34 (Merck) and the concentration determined by absorbance at 279 nm and extinction coefficient of 0.667 cm^{-1} (197.5 µM).[1] Milli-Q water with a conductivity below 0.2 µS cm^{-1} was used throughout. BSA was labeled with Alexa Fluor® 488 carboxylic acid, 2,3,5,6-tetrafluorophenyl ester *5-isomer* (AF488) from Molecular Probes, Invitrogen (Holland) as per the supplier manual. Briefly, 25 µl of an 11.3 mM AF488 stock solution in dimethylsulphoxide was added to 1 ml of BSA stock solution. The molar ratio of AF488/BSA was 1.43 which was left to react in the dark for 1 h under slight stirring. Thereafter, unreacted AF488 was separated from labeled-BSA (BSA-

AF488) using gel filtration. The gel filtration column was prepared and packed in-house using the media Sephadex G-25 Coarse from Amersham Biosciences (GE Healthcare). Sodium bicarbonate was used for swelling the gel, washing, equilibration and elution steps. After separation, the fractions containing BSA-AF488 were collected. Labeled protein concentration and degree of labeling (DOL) were calculated measuring the ABS_{279nm} and ABS_{494nm}, using 78,000 $cm^{-1}M^{-1}$ as the molar extinction coefficient of AF488 at 494 nm.[2] The degree of labeling (DOL) was found to be 1.9. Finally the conjugate solution was further dialyzed to 10mM carbonate buffer, pH 8.34 to avoid crystal interference during the protein evaporation process.

3. Plasmon Assisted 3-photon Protein Binding & Fluorescence Characterization

A 5 µL droplet containing 50 µM BSA-AF488 in 10 mM carbonate buffer, pH 8.34, is evaporated at 31 °C, on an e-beam lithography prepared nano-antenna substrate. The resonances of the BSA-coated nanostructures are then determined using a standard optical microscope in bright-field mode, coupled to an Andor spectrometer. Next, the sample is mounted on an x-y translation piezo-stage and placed on an Olympus IX71 inverted microscope which is coupled to a Coherent Mira 900 Ti-Sapphire laser with repetition rate of 76 MHz and pulse width near 200 fs with wavelength between 810-840 nm (see fig. S1). The pulsed beam is focused on the back focal plane of an Olympus 100x, 1.25 NA oil immersion objective using a 1m focusing lens resulting in a beam width, at the sample, of approximately 12 µm. Each array of structures is exposed to an average power between 100 µW and 10 mW and for a period of 30 minutes in order to initiate the LAMI process[1-10]. Following the infra-red (IR) exposures, the sample is immersed in a 1% mucasol solution in di-ionized water (DIW) in order to remove any BSA which is not covalently bound to the structures. Frequent changes of this solution are made every 15min up to 60min and then finally left overnight at room temperature (RT). The following day the sample is removed, rinsed in de-ionized water and dried under a flow of nitrogen.

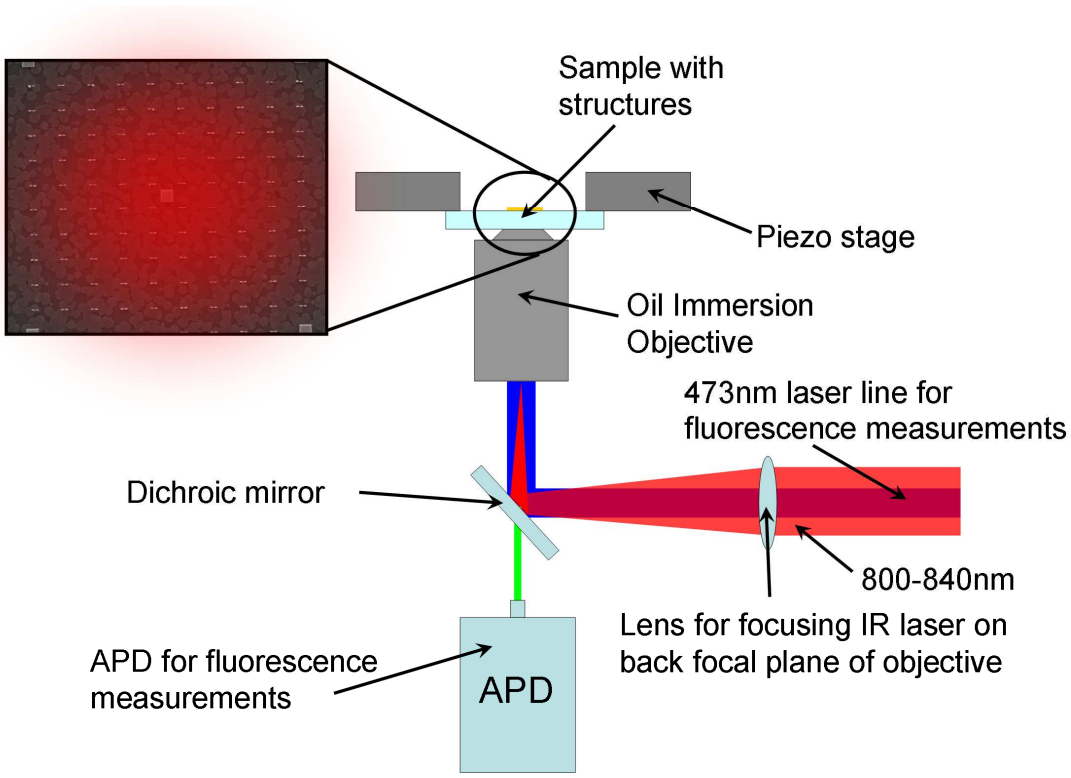

Figure S1. Experimental setup.

The fluorescence from the BSA-AF488 proteins was imaged using the same microscope set-up as for the original IR exposures. However, a 473 nm continuous wave laser is now coupled to the objective (see fig. S1). In the sample plane, the laser focus is approximately 400-500 nm with an average power of ca. 100 µW. The fluorescence signal is filtered using a dichroic mirror, a 473 nm long pass filter and focused on an avalanche photo-diode (APD). The 473 nm laser is scanned over the area of the array by steps of 150 nm (in both the x and y direction) using the piezo-stage and at each position the fluorescence signal integrated for 50 ms.

4. Three photon immobilization on flat gold surface

Initial tests of protein immobilization via three-photon absorption were performed on samples consisting of 50 µm x 50 µm gold squares. In addition, these measurements allowed us to determine what illumination powers and exposure times would be required and also whether any changes needed to be made to the BSA solution. Figure S2 shows 3D and 2D fluorescence maps, being the fluorescence emitted by labeled BSA molecules that were immobilized on the surface upon focusing 840nm laser light, with a power of 622 µW, onto the gold substrate, for 1.5 hours on each spot. The location of each exposure was separated by 5 µm and arranged in a square layout which is in agreement with what is observed in the fluorescence maps. However, it was also observed that the maximum signal could vary drastically between spots as shown in the 3D plot. Nevertheless, these results proved that proteins could be immobilized to the gold surface at a wavelength that was approximately three times longer than the absorption peak of BSA.

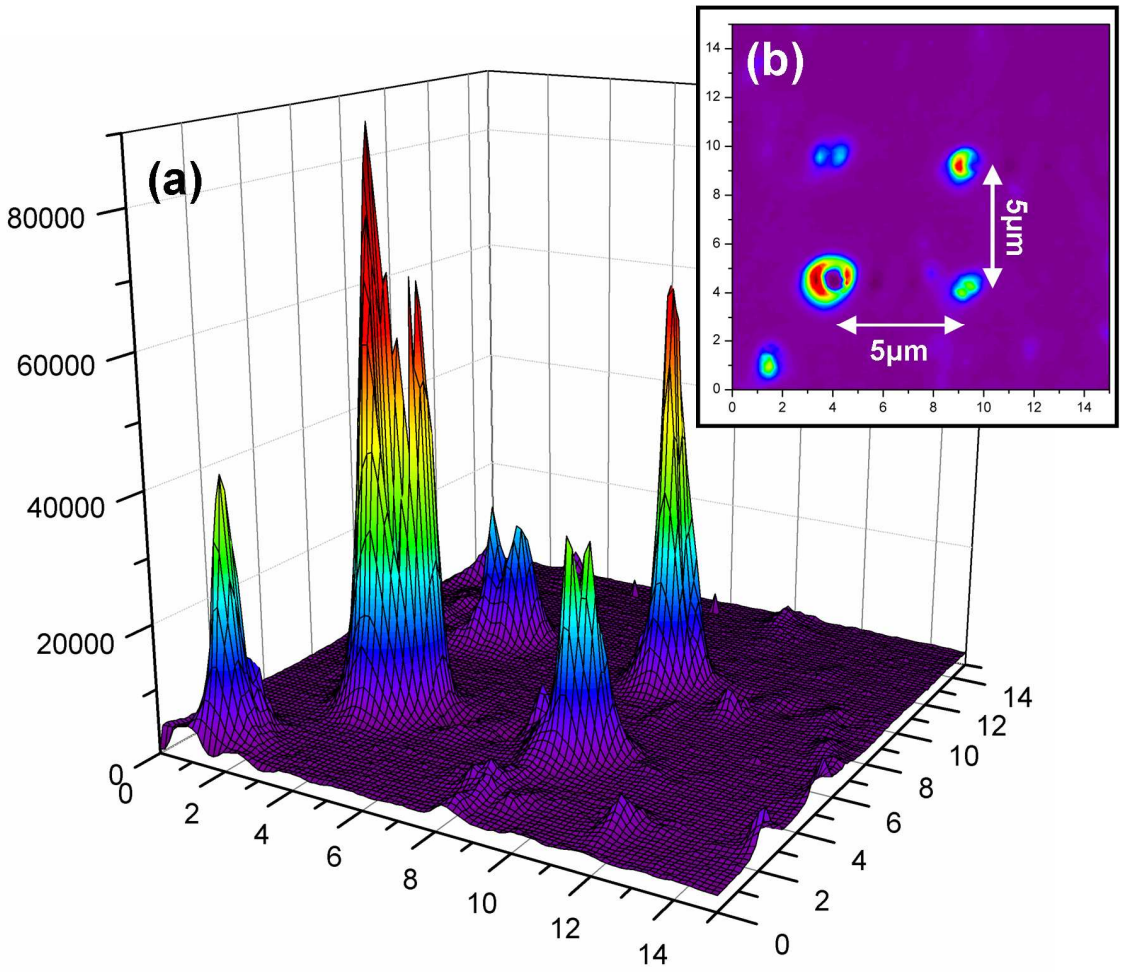

Figure S2. (a) 3D and (b) 2D fluorescence intensity maps which cover the 4 locations where the flat gold surface was exposed during 90min by a focused 840nm laser beam at 622 µW.

Throughout these preliminary experiments it was discovered that the concentration of proteins used in one-photon absorption experiments carried out by *Neves-Petersen et al*.[1,4] was insufficient in order to observe immobilization through a three-photon absorption process. Furthermore, in the early stages of testing on dimer structures, we found out that the salt concentration also needed to be reduced because salt crystals would form during evaporation preventing the BSA proteins from properly coating the gold surface. At the time of these preliminary experiments on a flat gold surface, the importance of the salt concentration was not known and too high a concentration may have been the cause of the difference in fluorescence intensity between the four exposures.

5. Protein imaging via SEM

In order to clearly demonstrate that the clouding observed in the SEM images is due to the presence of the BSA protein, it is helpful to compare the SEM image and the fluorescence map of a given region showing significant levels of binding. Figure S3 shows the same SEM image as in fig. 3(c) of the manuscript but with the fluorescence map separated. The only sources of fluorescence in these experiments are the labeled protein and a small amount of auto-fluorescence from the gold. The four circled regions demonstrate that both the intensity and distribution of the fluorescence correlate very well with the clouding observed in the SEM image. For example, in the region labeled as "4", two dimers show significant binding but in one case the clouding extends to the right of the structure and in the other to the left. This is also observed in the fluorescence map. In regions 1, 2 and 3, the clouding has very distinct patterns, especially in the case of region 2 where the protein surrounds the central square. These different patterns are as well restituted by the fluorescent map. It is interesting to note that while the proteins can bind directly to the gold surface, they can also bind to each other as shown by the fact that the clouds extend away from the gold. For high powers, when the localized surface plasmon resonance (LSPR) is no longer the only contributing effect, BSA proteins will bind together in large agglomerates. If these agglomerates are also bound to the gold, they will not be removed in the post-illumination cleaning process. Thus, for highly localized protein positioning, it is of paramount importance to use illumination powers where the binding is directed only by the LSPR field distribution.

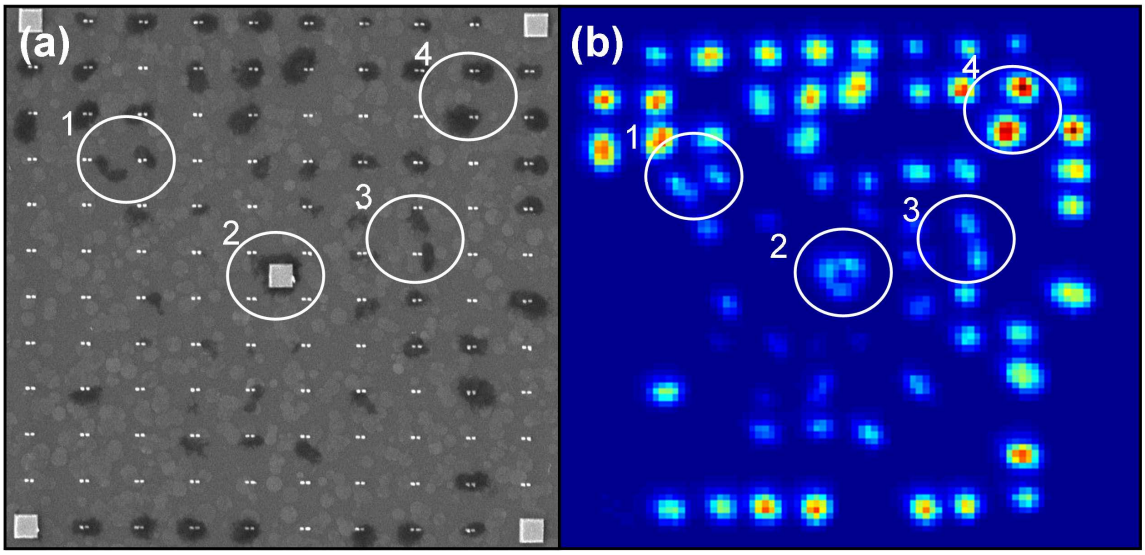

Figure S3. SEM image (a) and corresponding fluorescence (b) map of an array of dimers that was exposed at 10mW of power. The four regions that are circled and labeled from 1-4 demonstrate how well the fluorescence and clouded regions are correlated.

While the clouding can be easily imaged when the structures are over-exposed, this is not necessarily the case for lower powers. In this case, proteins are very close to the gold surface and some processing of the SEM image is needed in order to accurately determine their location. Figure S4 documents the process used in order to visualize the low quantities of immobilized proteins. Fig. S4(a) shows the SEM data prior to image processing while fig. S4(b) shows the processed data. Firstly, the lightest components in the original image are selected and the remainder of the image is cropped out. The brightness is then increased as shown in fig. 3(c) where a plain gray background is placed beneath the image. The same is repeated for the darkest components of the image but in this case the brightness is decreased after cropping (fig. S4(d)). Finally, both the light and dark components are overlaid on a plain gray background shown in fig. S4(b).

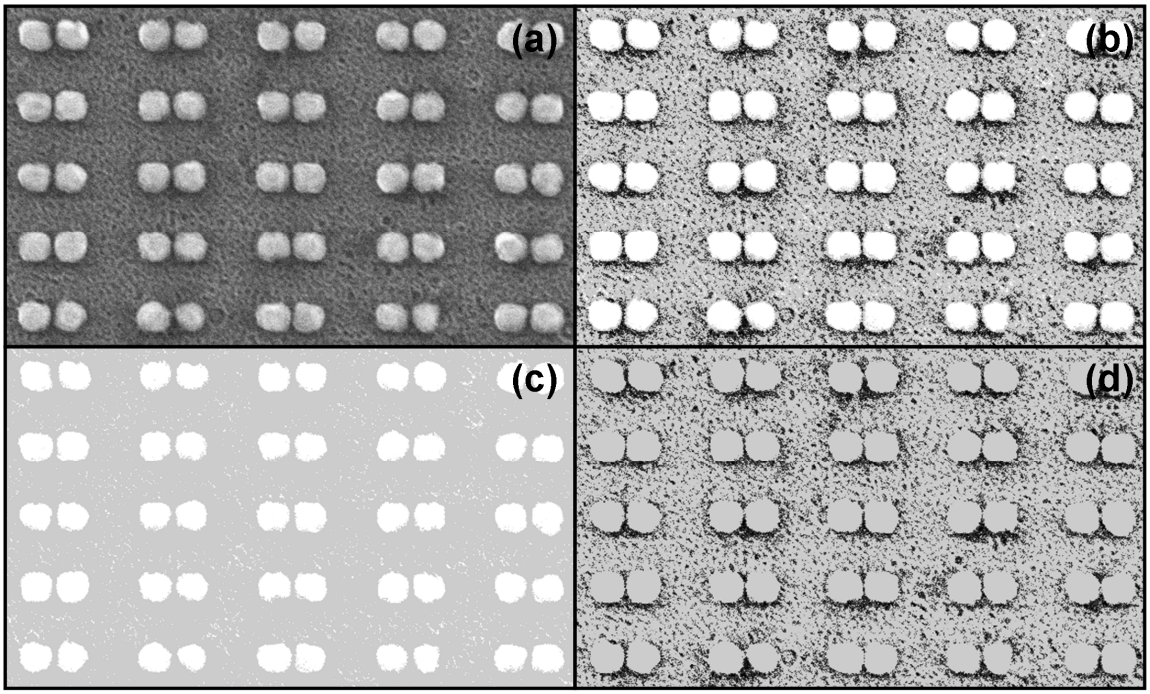

Figure S4. Illustration of SEM image processing: SEM image (a) before and (b) after image processing. (c) The lightest components of the image in (a) are overlaid on a gray background and further brightened. (d) The darkest components of the image in (a) are overlaid on a gray background and further darkened. The final modified image is obtained when both the light and dark components are overlaid on the gray background.

6. Protein density estimation

An approximate estimation of the protein density can be done directly from the processed SEM images (see section 6). While the value is not a real estimate of the number of proteins, it does give us a way to compare SEM images. This value is taken from the number of dark pixels in the processed image (see fig. S5). Firstly, a background value is found by counting the number of dark pixels in the background region. This background count is then normalized with respect to the total number of pixels in that region. Next, the dark pixels are counted in the binding region and normalized with respect to the total number of pixels minus those that correspond to the gold structure (the white pixels). The protein density is then taken as the difference between the binding region density minus the background region density. This can also be expressed as:

$$protein\_density = \frac{Dark_{BD}}{Total_{BD} - White_{BD}} - \frac{Dark_{BG}}{Total_{BG}}$$

where *BD* and *BG* correspond to the binding region and background region, respectively.

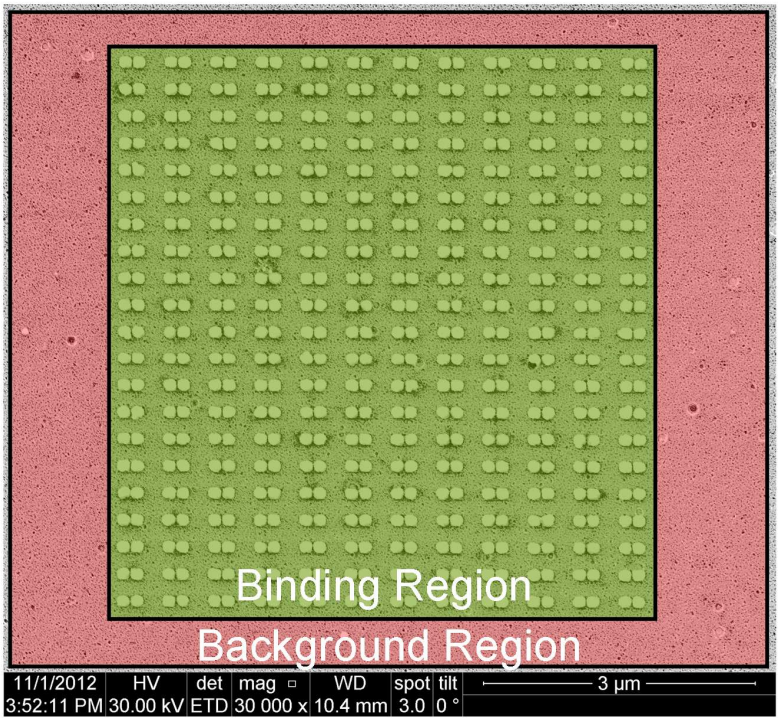

Figure S5. A SEM image, after image processing, is showing the two regions that are considered in the estimation of the protein density.

7. Immobilization of single gold colloid

BSA was evaporated on a nano-antenna substrate, exposed and subsequently washed in order to remove non-bound protein (as described above). Next, a 10 µL drop of 13 mM biotin-N-hydroxysuccinimide in 20 mM HEPES buffer, pH 7.5 was added to the substrate and allowed to interact for 90min at RT. This allowed the labeling of any remaining BSA molecules with biotin. At this point the drop was removed, substrate rinsed in de-ionized water and again immersed in 1% mucasol for 30min under constant stirring, in order to remove any unbound biotin-NHS. Once completed and dried, the substrate was further exposed to streptavidin-coated gold nanospheres (20nm), prepared in 20 mM HEPES buffer (as above) and left for 2.5 h at RT. The rinse, wash and drying was repeated prior to imaging the sample with a scanning electron microscope (SEM) in order to identify the location of the bound gold colloids.

References

(1) Duroux, M.; Skovsen, E.; Neves-Petersen, M. T.; Duroux, L.; Gurevich, L.; Petersen, S. B. Light-induced immobilisation of biomolecules as an attractive alternative to microdroplet dispensing-based arraying technologies. *Proteomics* **2006**, 7, 3491-3499.

(2) Duroux, M.; Duroux, L.; Neves-Petersen, M.T.; Skovsen, E.; Petersen, S.B. Novel photonic technique creates micrometer resolution protein arrays and provides a new approach to coupling of genes, peptide hormones and drugs to nanoparticle carriers. *Appl*. *Surf*. *Sci*. **2007**, 253, 8125-8129.

(3) Duroux, M.; Skovsen, E.; Neves-Petersen, M. T.; Duroux, L.; Petersen, S. B. Photonics and immobilisation of biomolecules. *2007 Asia Optical Fiber Communication and Optoelectronics Conference. IEEE*. **2007**, 293-295.

(4) Neves-Petersen, M. T.; Snabe, T.; Klitgaard, S.; Duroux, M.; Petersen, S. P. Photonic activation of disulfide bridges achieves oriented protein immobilization on biosensor surfaces. *Protein Sci*. **2006**, 15, 343-351.

(5) Neves-Petersen, M. T.; Crookshanks, M.; Skovsen, E.; Duroux, L.; Petersen, S. B. Printing novel molecular architectures with micrometer resolution using light. *J*. *Nanosci*. *Nanotechnol*. **2009**, 9 (6), 3372-3381.

(6) Parracino, A.; Neves-Petersen, M. T.; di Gennaro, A. K.; Pettersson, K.; Lövgren, T.; Petersen, S. B. Arraying prostate specific antigen PSA and Fab anti-PSA using light-assisted molecular immobilization technology. *Protein Sci*. **2010**, 19, 1751-1759.

(7) Petersen, S. B.; di Gennaro, A. K.; Neves-Petersen, M. T.; Skovsen, E.; Parracino, A. Immobilization of biomolecules onto surfaces according to ultraviolet-light diffraction patterns. *Appl*. *Opt*. **2010**, 49 (29), 5344-5350.

(8) Skovsen, E.; Neves-Petersen, M. T.; Kold, A.; Duroux, L.; Petersen, S. B. Immobilizing biomolecules near the diffraction limit. *J*. *Nanosci*. *Nanotechnol*. **2009**, 9 (7), 4333–4337.

(9) Skovsen, E.; Kold, A. B.; Neves-Petersen, M. T.; Petersen, S. B.; Photonic immobilization of high-density protein arrays using Fourier optics. *Proteomics* **2009**, 9, 3945–3948.

(10) Snabe, T.; Røder, G. A.; Neves-Petersen, M. T.; Buusb, S.; Petersen, S. B. Oriented coupling of major histocompatibility complex (MHC) to sensor surfaces using light assisted immobilisation technology. *Biosens*. *Bioelectron*. **2006**, 21, 1553–1559.

4.6 Unpublished scientific work.

Superparamagnetic colloidal nanoparticle clusters for use in targeted protein therapeutics and magnetic separation technologies

---

Abstract

The aim of this work was to develop superparamagnetic nanoparticle carriers of strong magnetic response for future use in targeted protein therapeutics and magnetic separation technologies. A self-assembly thermolysis synthesis procedure was used to prepare Fe_3O_4 colloidal nanoparticle clusters (CNCs) of selected sizes in the range 30-500 nm. These CNCs show high magnetization in aqueous solution and superparamagnetic properties, since they encompass several magnetite nanoparticles of ~10 nm. Human insulin was selected as a model protein to couple to Fe_3O_4 CNCs and to test the obtained CNCs bioconjugates aiming at their use in targeted drug delivery and magnetic bioseparation. Insulin was immobilized onto the polyacrilic acid surface of Fe_3O_4 CNCs using two different carbodiimide chemistry approaches. Insulin immobilization on the CNCs surface was confirmed using both an adapted Coomassie assay for nanoparticles and a radioimmunoassay. The obtained CNCs bioconjugates in aqueous solution were characterized for hydrodynamic particle size, agglomeration state, and magnetic separation. The CNCs-insulin could be efficiently separated within minutes by using a permanent magnet. A strong magnetic response is essential feature for the practical use of magnetic nanoparticle carriers for biomedical applications. The superparamagnetic behavior, high magnetization and high water dispersibility of the CNCs renders them as promising nanocarrier vehicles for active biomolecules to use in biomedical and biological applications. This includes e.g. drug delivery of therapeutic proteins to specific cells, monitoring of metabolic pathways, or their use as biomarkers to isolate specific molecules or cells.

Abbreviations

BSA	Bovine serum albumin
CNCs	Colloidal nanoparticle cluster(s)
DEG	Diethylene glycol
DLS	Dynamic light scattering
EDC	1-ethyl-3-(3-dimethylaminopropyl) carbodiimide
ELS	Electrophoretic light scattering
MES	2-(*N*-morpholino)ethanesulfonic acid
MRI	Magnetic resonance imaging
NaPB	Sodium phosphate
NTA	Nanoparticle tracking analysis
PAA	Polyacrylic acid
SEM	Scanning electron microscope/microscopy
SPIONs	Superparamagnetic iron oxide nanoparticles
Sulfo-NHS	N-hydroxylsulfosuccinimide
TGA	Thermo gravimetric analysis
VSM	Vibrating sample magnetometer

Introduction

In the latest years, superparamagnetic nanoparticles have been intensively investigated for use in various biomedical and pharmaceutical applications such as drug delivery, hyperthermia, magnetic resonance imaging (MRI), tissue engineering and repair, biosensing, bioseparations, and biochemical analysis [1–5]. Superparamagnetic iron oxide nanoparticles (SPIONs, e.g. magnetite, Fe3O4, or maghemite, γFe2O3) have received a considerable amount of attention due to their stability and low toxicity profile in physiological conditions [2,3]. Their superparamagnetic properties allow controlling their position by using magnetic fields without the risk of permanent agglomeration because they do not retain any magnetism after the field is removed. This is an essential feature for the development of magnetic nanoparticle carriers for in vivo applications, where the agglomeration of nanoparticles could be restrictive to its practical use, as it could lead to the clogging/blocking of blood capillaries and vessels [3]. For other biological applications, such as bioseparation assays, it is also desired that upon removal of the magnetic field, the magnetic nanoparticles can be recovered in their original size/form.

Since superparamagnetism only occurs in magnetic materials constituted of very small crystallites, the development of superparamagnetic nanoparticles is restricted to an upper size limit (e.g. SPIONs show superparamagnetism at sizes < 26 nm) [6,7]. Over the years, several synthesis techniques have been developed to synthesize SPIONs aiming at a narrow size distribution together with high magnetization values (sizes ranging from several to 20 nm) [2,4,8–10]. Nevertheless, due to the size limit required for superparamagnetism, the nanoparticles obtained by these methods still display a magnetic response of reduced strength. Usually, the reduced magnetic response is not sufficient to readily separate them from solution, or to efficiently control their movement in against strong flows (e.g. blood) using moderate magnetic fields [3,11]. This restricts their practical usage in several applications, e.g. targeted drug delivery.

In light of the challenges described above, new approaches have been developed in order to obtain more magnetically responsive superparamagnetic nanoparticle constructs [12–16], e.g. by assembling individual superparamagnetic nanoparticles onto secondary nanoparticle structures. A straightforward strategy consists on the self-assembly of magnetite colloidal nanoparticle clusters (CNCs) upon controlled agglomeration of several individual superparamagnetic iron oxide nanoparticles in conditions that limit the protection degree conferred by the capping agent [13]. By assembling superparamagnetic nanoparticles onto CNCs, one obtains a construct that possesses much higher overall saturated magnetization than the individual components, even though the cluster size may exceed the size threshold for the superparamagnetic-ferromagnetic transition (26 nm for SPIONs). In these clusters the magnetic interactions between the small individual crystallites are still sufficiently disturbed so that they behave as single domains, thus supressing the superparamagnetic-ferromagnetic transition [13,17]. Another advantage of forming clusters of SPIONs that it is possible to tune their overall size (from 30 nm to several hundred of nm) and thereby increase the magnetization in a controllable manner [13,17]. Being able to tailor

the overall CNCs dimensions is also relevant for the development of magnetic nanocarriers for *in vivo* applications, since the size of the constructs will determine their fate in the body and their distribution [2,18,19].

In this work the strategy of forming clusters of SPIONs was used to build magnetic nanoparticle bioconjugates with superior magnetic properties. Polyelectrolyte capped Fe_3O_4 CNCs of distinct sizes (20-500 nm) were prepared using a high temperature thermolysis process initially developed by Ge et al. [17]. The obtained Fe_3O_4 CNCs are capped with polyacrylic acid, which confers high water dispersibility and provides carboxyl moieties for subsequent conjugation to biomolecules. In order to couple proteins to the carboxyl surface of the Fe_3O_4 CNCs, a conventional chemistry based on a carbodiide reagent, 1-ethyl-3-(3-dimethylaminopropyl) carbodiimide (EDC) and N-hydroxylsulfosuccinimide (sulfo-NHS) was used. The EDC/sulfo-NHS coupling approach is a standard approach for linking NH_2-containing biomolecules onto carboxyl-derivatized surfaces via covalent amide bond as it presents several advantages: mild reaction conditions, high conversion efficiency, and good biocompatibility with reduced influence on the bioactivity of the biomolecules [20,21].

Human insulin was used as a model protein to couple to Fe_3O_4 CNCs and to test the obtained CNCs bioconjugates in the context of biomedical applications. Insulin is a small peptide (6 kDa, 51 amino acids), which has an important role for controlling the glucose levels in the blood. Insulin stimulates glucose uptake by binding to insulin receptors located in the plasma cell membrane [22,23]. Human insulin contains three accessible primary amines (two in the N-terminus of A-chain and B-chain and one from Lys29B) as suitable targets for coupling to carboxyl groups with EDC/sulfo-NHS chemistry. From the protein residues comprising the primary amines, only GlyA1 from the A-chain N-terminus is involved in binding to the insulin receptor [24–27]. Therefore, it is reasonable to say that carboxyl group coupling to either of the two remaining primary amines should not affect the biological activity of insulin (binding to the insulin receptor). The fact that in insulin there are only three possible targets for bioconjugation with EDC/sulfo-NHS chemistry is also an advantage because it restricts to three the possible number of orientations of the immobilized peptide molecules. Furthermore, insulin is also convenient protein model as its activity can be easily tested by monitoring the glucose uptake by skeletal muscle cells upon binding to the insulin receptor.

The behavior and magnetic properties of obtained CNCs-insulin in aqueous solution were analyzed upon characterization for hydrodynamic particle size, agglomeration state, and magnetic separation. Insulin coupling to the CNCs surface was verified using both an adapted Coomassie assay (Bradford assay) for nanoparticles and a radioimmunoassay. The superparamagnetic behavior, high magnetization and high water dispersibility of CNCs bioconjugates makes them promising candidates for future use in biomedical applications such as targeted drug delivery and bioseparation.

Results and discussion

Synthesis of superparamagnetic colloidal nanoparticle clusters

The magnetite (Fe_3O_4) CNCs were synthesized by one-pot thermolysis polyol reaction following a method initially developed by Ge et al. [17]. The Fe_3O_4 CNCs were prepared by hydrolyzing iron (III) chloride ($FeCl_3$, precursor) in NaOH at 220 °C in a diethylene glycol (DEG) solution using a short-chain polyacrylic acid (PAA) as surfactant/capping agent. DEG is a suitable polar solvent for the reaction due to its high boiling point (245 °C) and since it allows to efficiently solubilize a wide variety of polar inorganic and organic compounds. The reductive environment provided by DEG at high temperature leads to the partial transformation of the intermediate species $Fe(OH)_3$ to $Fe(OH)_2$, and Fe_3O_4 nanoparticles are formed through dehydration. Under optimized conditions and low PAA concentration, the individual Fe_3O_4 nanocrystals (~10 nm) spontaneously agglomerate to form flowerlike three-dimensional CNCs (Figure 1).

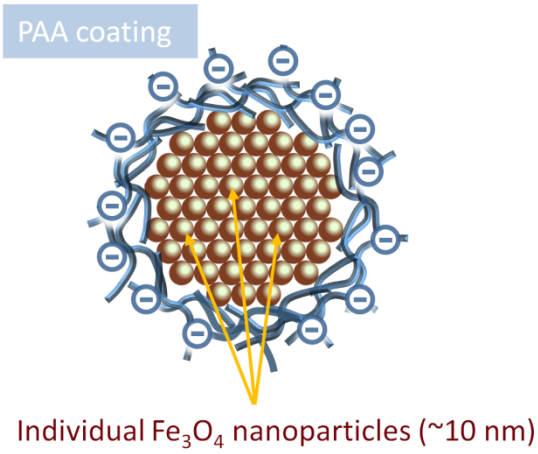

Figure 1. Schematic representation of PAA capped Fe_3O_4 CNCs.

By adjusting the concentration of NaOH, it was possible to obtain magnetite CNCs of different sizes within the range 30-500 nm (data not shown). A batch containing magnetite CNCs of ~30-40 nm was selected for further characterization and biofunctionalization with insulin. This particle size is in the range 30-100 nm, which is a suitable size for developing drug delivery systems and for use in biomedical applications. This size range ensures longer circulatory residence times of nanoparticles in the bloodstream, since the nanoparticles are large enough to avoid leaking into capillaries, but also small enough to avoid clearance by the reticuloendothelial system [19].

The synthesized dispersion of magnetite CNCs was characterized by scanning electron microscope (SEM) analysis. The obtained SEM images are shown in Figure 2. The synthesized nanoparticle suspension was composed by evenly sized round-shaped magnetite CNCs of 30-40 nm.

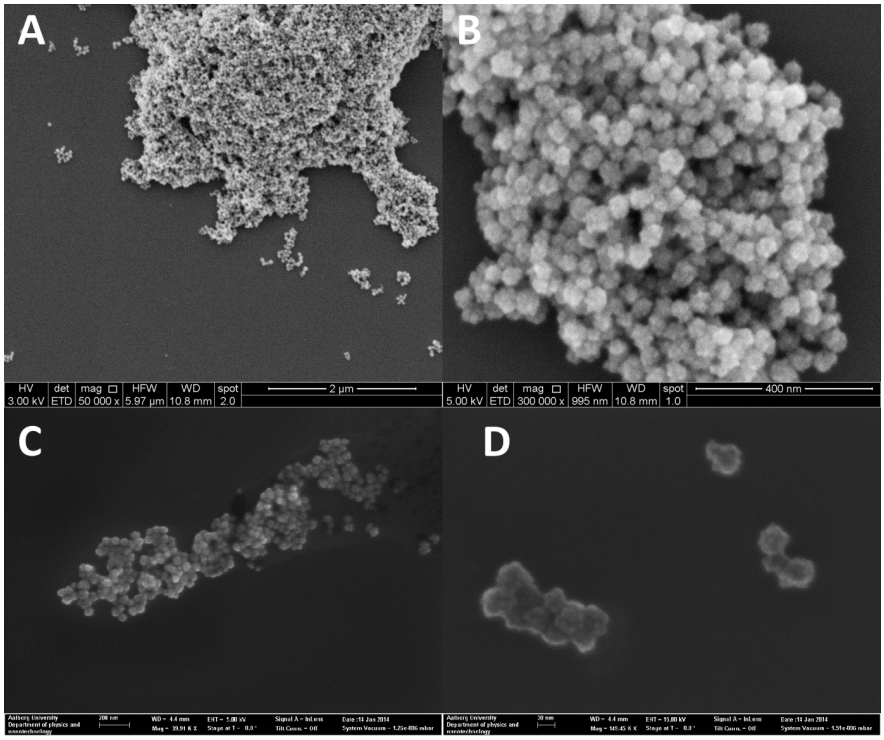

Figure 2. SEM images of the synthesized Fe_3O_4 CNCs. The average size of each individual CNC was 30-40 nm.

Upon close analysis of the SEM micrograph displayed in Figure 2D, it is possible to observe that each individual CNC is composed of many interconnected primary nanoparticles (expected size ~10 nm). The CNCs are formed through a two-stage growth process: firstly primary nanoparticles nucleate and grow in a supersaturated solution, and secondly agglomerate onto larger secondary particles [17]. The PAA serves as a surfactant for the CNCs, coordinating with the iron groups on the magnetite surface through its carboxylate groups, and limiting further agglomeration. PAA was selected as a surfactant because it confers to the CNCs a high degree of dispersibility in aqueous solutions, which was convenient for carrying out the subsequent bioconjugation procedure. The introduced carboxylate groups could also be subsequently used for further functionalization with biomolecules. The concentration of PAA was determined by thermo gravimetric analysis (TGA) was 8.6 % (m/m) (data not shown). After synthesis, the Fe_3O_4 CNCs were highly water dispersible, even after multiple washes with ethanol and water, due to the surface coating with PAA.

The magnetic properties of the magnetite CNCs were analyzed by vibrating sample magnetometer (VSM, data not shown). The CNCs did not show remanence or coercivity at 300 K, confirming their superparamagnetic behavior. The saturation magnetization of the CNCs was determined to be 64.2 emu.g^{-1}, which is higher than the usual saturation magnetization values obtained for superparamagnetic Fe_3O_4 nanoparticles prepared by conventional synthesis methods, such as co-precipitation (30-50 emu.g^{-1}) [6].

Behavior and magnetic properties of CNCs in water

Prior to protein immobilization, the behavior and magnetic properties of the CNCs in Milli-Q water were analyzed. A CNCs stock suspension was withdrawn from the synthesized CNCs batch. The hydrodynamic size of the CNCs in Milli-Q suspension was determined using dynamic light scattering (DLS) and nanoparticle tracking analysis (NTA) with NanoSight. The size distributions obtained by DLS and NTA are shown in Figure 3.

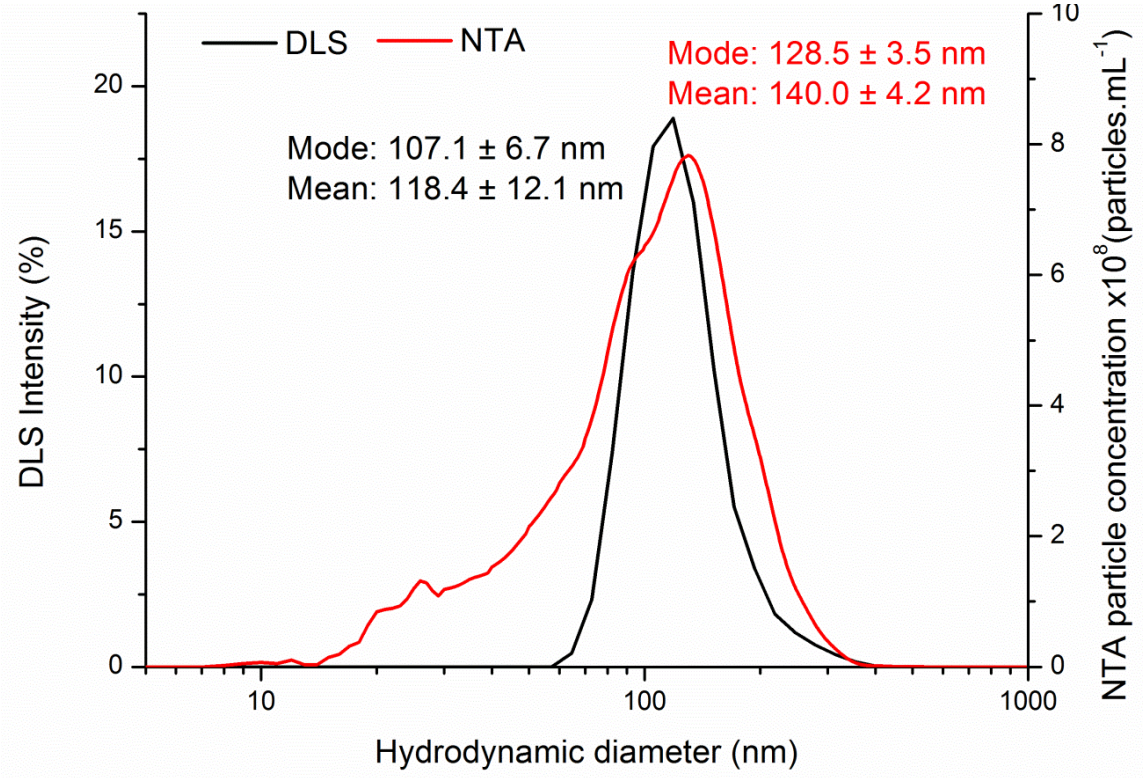

Figure 3. Hydrodynamic diameter measurements of the CNCs suspension obtained by DLS (N=3) and NTA with NanoSight (N=2). The uncertainty values correspond to the standard deviation of the repeated measurements.

Both measurements demonstrated that the CNCs suspension in Milli-Q was fairly monodisperse. The DLS and NTA size distributions show individual peaks in the size distributions with mean sizes of 118.4 nm and 140.0 nm for DLS and NTA, respectively (Figure 3). The mean hydrodynamic diameters obtained by the two techniques are within the same size range. The small differences observed between the two distributions (e.g. broader size distribution obtained by NTA) are inherent to the distinct measurement principles of the two techniques. In particular the NTA number based size distribution shows the presence of smaller particles (< 60 nm), which are not visible in the DLS intensity based distribution. Particle size measurements by DLS depend on the light scattering of the particles in solution and the intensity based distribution provided by DLS may omit the presence of smaller particles in samples containing different size populations. On the other hand, in NTA each scattering source is tracked separately during analysis and not as an

ensemble, and therefore it provides a direct number based frequency distribution [28,29]. Small deviations in the mean hydrodynamic size could also be resultant of distinct dilution factors used in the two measurements.

The mean hydrodynamic size values determined by DLS and NTA (118.4 nm and 140 nm) were larger than the average size of the individuals CNCs obtained by SEM imaging, which was around 30-40 nm (Figure 2). This average size difference might be resultant of the interaction of two or more 30-40 nm CNCs-PAA in aqueous suspension, resulting in larger and loosely bound CNCs agglomerates. This would explain the larger hydrodynamic diameter values obtained by DLS and NTA. The determined hydrodynamic size values are still close to the size range of 30-100 nm, which is desirable for drug delivery applications. The stability of the colloidal suspension was evaluated upon zeta potential measurement by electrophoretic light scattering (ELS). The determined zeta potential of the CNCs suspension was -66.5 mV, which is above -30mV, indicating good colloidal stability [28,30]. The elevated surface charge leads to electrostatic repulsion between individual nanoparticles, preventing permanent agglomeration.

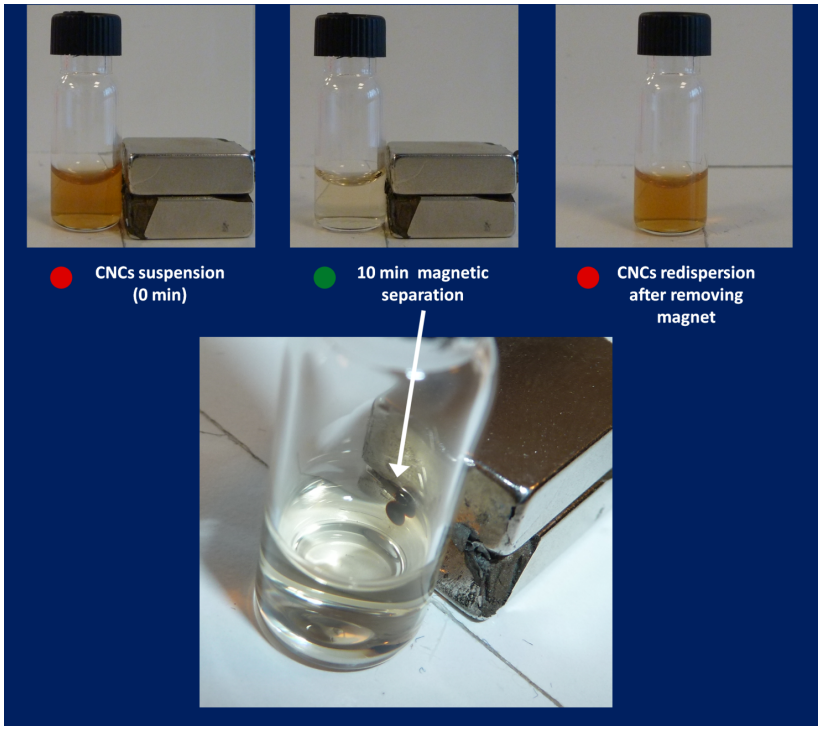

Figure 4. Separation of CNCs from water solution using a permanent magnet.

The magnetic separation of CNCs aqueous suspensions was analyzed using a permanent magnet (Figure 4). A dispersion of the magnetite CNCs in Milli-Q water is shown on the left-side image (brown color suspension). After placing a permanent magnet, the CNCs were readily separated towards the magnetic field. After 10 min in the presence of the magnetic field, the solution was nearly transparent and a clear pellet was formed in vial region vicinal to the adjacent magnet. Based on these observations, separation times of ~10-15 min were selected for future magnetic

separations and nanoparticle washing procedures. This separation times were still short enough for experimental practical use and ensured that the majority of CNCs was properly separated from the solution. After removing the magnet the CNCs could be easily redispersed into aqueous solution, confirming their superparamagnetic properties.

The efficiency of CNCs separation by permanent magnet was analyzed by DLS and zeta potential measurements. A fresh suspension of CNCs in Milli-Q was subjected to magnetic separation (10 min) and the supernatant was removed. The CNCs pellet was then redispersed in newly added Milli-Q water of the same volume. The DLS and zeta potential measurements obtained for the redispersed CNCs (washed) and for the supernatant are summarized in Table 1. After magnetic separation and washing the CNCs were still stable in aqueous solution, with a measured zeta potential value of -59.2 mV. The DLS and zeta potential measurements have also shown the presence of smaller particles (~79.8 nm) in the supernatant. It is likely that a reduced fraction of smaller sized CNCs was not efficiently recovered after 10 min under the magnetic field. This would explain the increase in mean CNCs hydrodynamic diameter observed after separation and redispersion (from 118.4 nm to 159.0 nm), as larger CNCs are more responsive to the magnetic field. This also explains the observed decrease in the polydispersity index from 0.281 to 0.201.

Table 1. Effect of magnetic separation on the size and charge of CNCs in water. Measurements of hydrodynamic diameter and polydispersity index by DLS (N=3) and zeta potential (N=2) obtained for CNCs suspensions before and after wash upon 10 min magnetic separation, and for the supernatant. The uncertainty values correspond to the standard deviation of the repeated measurements.

Parameters	CNCs stock suspension	Washed CNCs suspension (10 min Magnetic Separation)	Supernatant
DLS hydrodynamic diameter (mean, nm)	118.4 ± 12.1	159.0 ± 9.6	79.8 ±0.5
Polydispersity Index	0.281 ± 0.02	0.201 ± 0.02	0.164 ± 0.014
Zeta Potential (mV)	-66.5 ± 0.85	-59.2 ± 1.13	-70.25 ± 0.49

Protein immobilization onto Fe_3O_4 CNCs

Protein immobilization onto the surface of the CNCs was carried out using EDC/sulfo-NHS chemistry, which is a standard approach for linking NH_2-containing biomolecules onto carboxyl-derivatized surfaces via covalent amide bond. The molecular coupling of proteins to carboxyl-derivatized nanoparticles (here CNCs-PAA) using EDC/sulfo-NHS consists on a two-stage reaction mechanism: carboxylic group activation and amidation reaction (Figure 5).

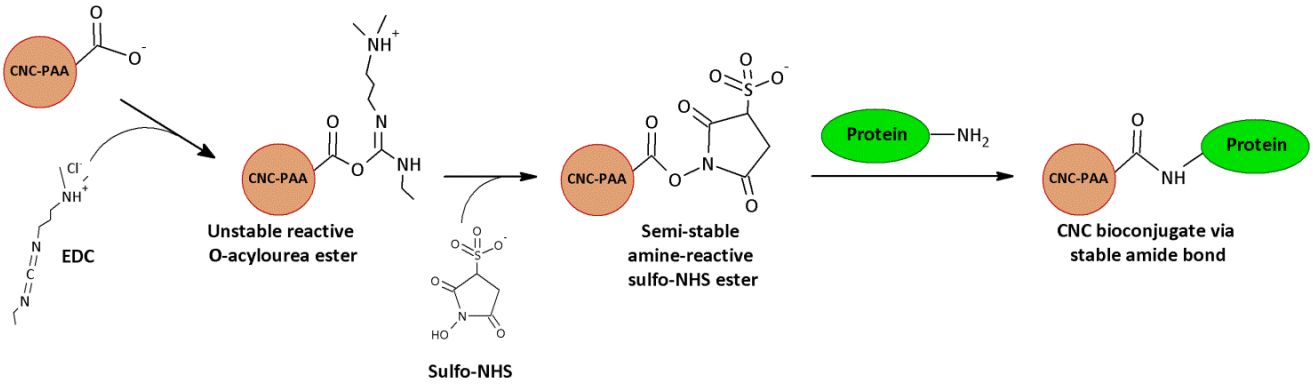

Figure 5. Protein immobilization onto CNCs by EDC/NHS chemistry: reaction mechanisms.

First EDC is used to active the carboxyl groups present in the surface of the nanoparticles, forming an unstable O-acylurea intermediate. Sulfo-NHS is included in the reaction as it forms a more stable amine reactive intermediate (sulfo-NHS ester) upon nucleophylic attack to O-acylurea. The sulfo-NHS ester then reacts with the protein's primary amines to form the final amide cross-link [20].

In this work the immobilization procedure was done in four steps (Figure 6). Step 1 involved the activation reaction with EDC and sulfo-NHS, which is most efficient at pH 4.5-7.2. After washing by magnetic separation, the CNCs were redispersed into the protein solution to allow the reaction between the activated sulfo-NHS esters and the primary protein amines (steps 2 and 3). The reaction of sulfo-NHS-activated molecules with primary amines is very efficient at pH 7-8. However, it is often required to include a pre-concentration step at a lower pH in order to bring the protein in close proximity of surface carboxyls. This is usually achieved by electrostatic attraction between the oppositely charged carboxyls and the protein's amino groups. The optimal pH for the pre concentration step depends on the isoelectric point of the protein. In order to obtain positive charges on the amino groups of the protein and still keep the protein as uncharged as possible, the pH has to be 0.5-1 units below the isolectric point of the protein [31]. The experimental conditions used for coupling between the protein amine groups and activated CNCs carboxyl groups (step 2 and 3) are described in detail in Table 2. A final washing procedure (step 4) was included to ensure that all free non-bound protein is removed from solution.

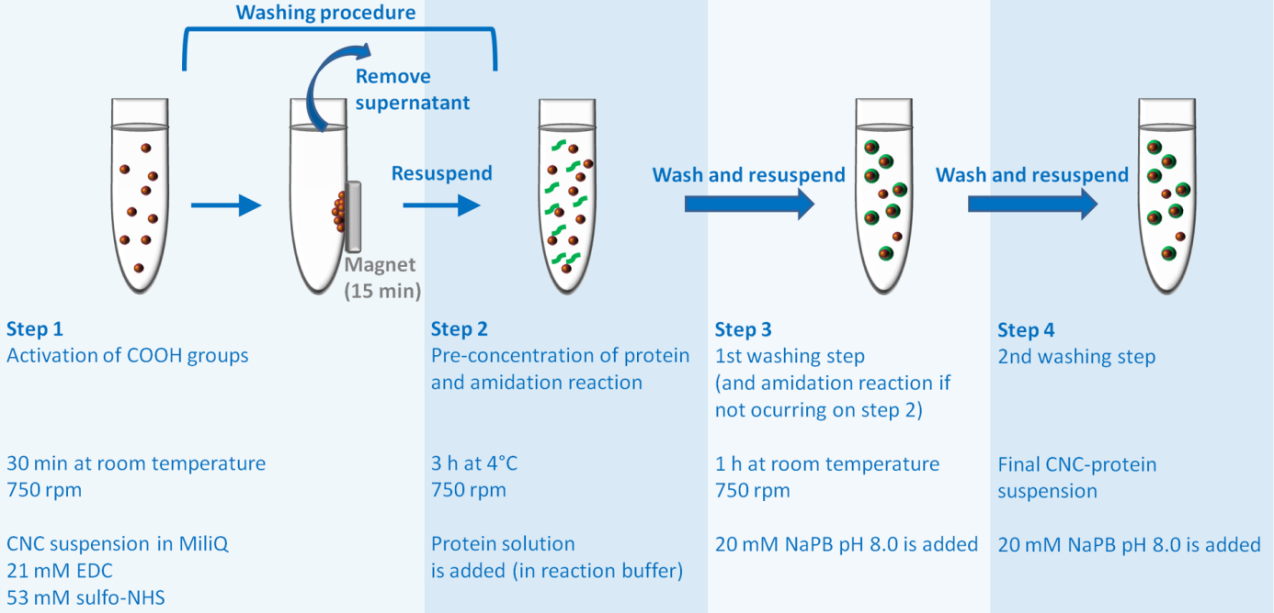

Figure 6. Summary of experimental procedure used for protein immobilization onto CNCs-PAA by EDC/sulfo-NHS.

Table 2. Experimental conditions used for protein protein immobilization onto CNCs-PAA by EDC/sulfo-NHS.

Immobilization	Solution added		Protein concentration	Nanoparticle concentration (estimated by NTA)	Initial number protein molecules per CNCs binding site
	Step 2	Step 3			
CNCs-BSA	BSA in Milli-Q	20 mM NaPB pH 8.0	3.7 µM 240 µg.mL^{-1}	75.2x10^{8} particles.mL^{-1}	9.1
CNCs-insulin (with pre-concentration)	Human insulin in 0.1 M MES 0.5 M NaCl pH 5.0		32.1 µM 186 µg.mL^{-1}		11.6
CNCs-insulin (without pre-concentration)	Human insulin in 20 mM NaPB pH 8.0		32.1 µM 186 µg.mL^{-1}		11.6
CNCs-blank	Milli-Q		-		-

For immobilization, a new stock suspension was collected from the synthesized CNCs batch. The mean hydrodynamic diameter and the initial concentration of nanoparticles (after 1:4 dilution, step 1) were 142 nm and 75.2×10^8 particles.mL^{-1}, as determined with NTA from NanoSight. The immobilization procedure was first tested and optimized (protein and reagent concentration, separation and reaction times) using bovine serum albumin (BSA) as a model protein (Table 2). Subsequently, the initial concentration of insulin was fixed in order to have a similar excess of insulin molecules per possible CNCs protein binding sites (Table 2). One binding site was considered to be the area occupied by a single protein molecule (disk area, see Materials and Methods). The immobilization of human insulin onto the CNCs-PAA was carried out using two approaches (Table 2), with inclusion or not of a pre-concentration-step. In one approach, human insulin was added using a reaction buffer at pH 5 (step 2), in order to allow the pre-concentration of insulin molecules on the surface prior to amidation reaction (done in step 3 where pH is raised to 8). The isoelectric point of insulin is 5.3, therefore at pH 5 its overall charge should be slightly positive [32]. In the second approach the human insulin solution was immediately added in buffer at pH 8, favoring immediate amidation reaction on step 2. The occurrence of non-specific protein binding (protein adsorption by electrostatic and/or hydrophobic interactions) was checked by performing controls experiments without the addition of EDC/sulfo-NHS on step 1 (and thus no activation of the carboxyl groups). Finally, a CNCs blank sample was also prepared, where no neither EDC/sulfo-NHS, nor protein was added. The CNCs blank was washed three times by magnetic separation, just like the CNCs-protein samples.

Confirming protein immobilization onto Fe_3O_4 CNCs

From previous experience, it was known the reaction of BSA molecules with activated sulfo-NHS ester (amidation reaction) in carboxylated nanoparticles occured successfully on Milli-Q water (pH should be 5-6 with BSA present). BSA immobilization onto the surface of CNCs was confirmed using the Coomassie Plus assay, which is based on the shift of absorbance maximum of the Coomassie dye from 465 nm to 595 nm upon binding to proteins. The concentration of protein is directly proportional to the absorbance value at 595 nm (A_{595nm}). The amount of BSA immobilized onto the CNCs was quantified by subtracting the assayed amount of unbound protein (supernatant or wash fraction after amidation reaction, occurring in step 2) from the initial amount of starting protein (initial BSA solution introduced in step 2). The concentration of BSA bound to CNCs estimated by the Coomassie Assay was 23.8 ± 5.6 µg.mL^{-1} (N=5)[a]. This value corresponds to ~0.91 coupled BSA molecules per binding site, indicating a high density of BSA coupling. The BSA concentration found in the control sample was 9.6 ± 5.6 µg.mL^{-1} (N=5)[a], corresponding to ~0.36 BSA molecules per binding site. The amount of non-specific BSA binding by adsorption onto CNC surface was less than half than the obtained by covalent EDC/sulfo-NHS

[a] The uncertainty values correspond to the standard error of mean of five independent measurements.

chemistry. These results demonstrate that BSA was successfully immobilized onto the CNC surface using the EDC-NHS chemistry and was not solely attached by non-specific interactions.

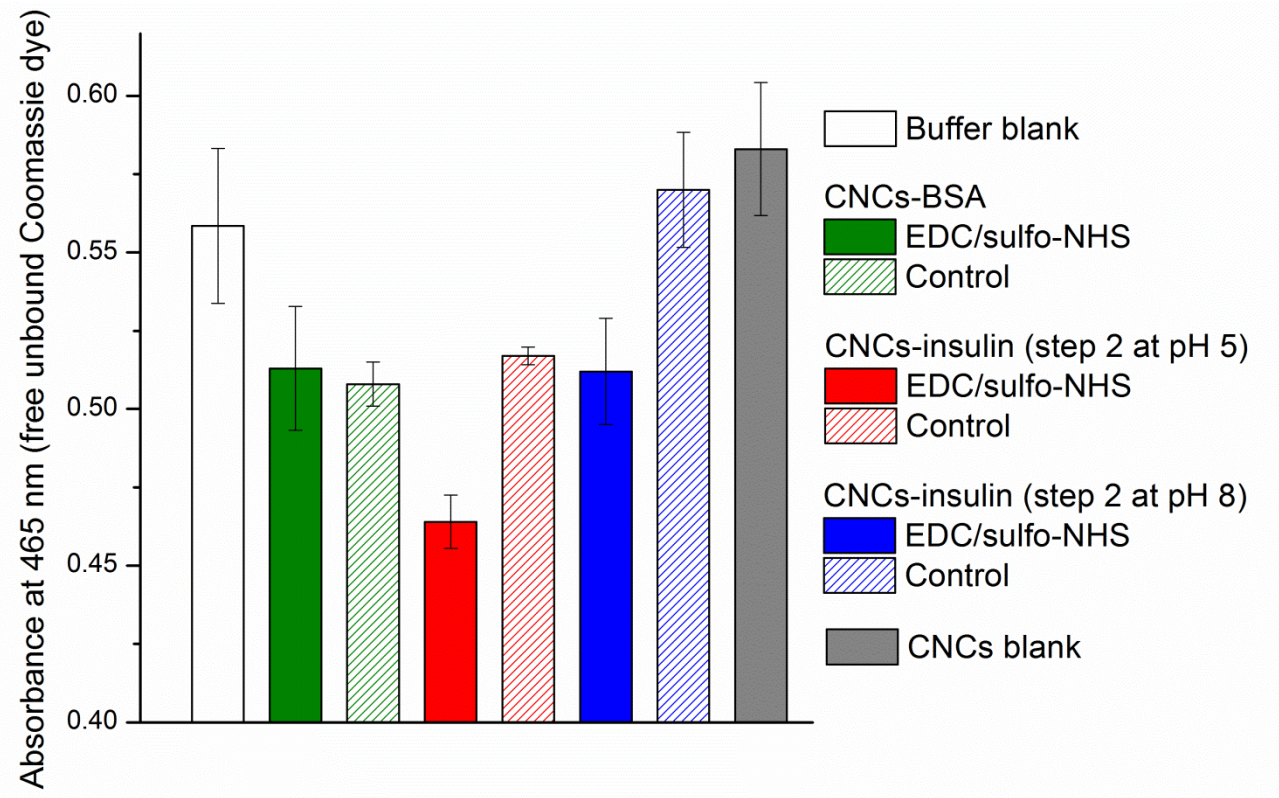

Figure 7. Confirmation of protein immobilization onto CNCs using an inverted Coomassie Plus assay. The absorbance at 465 nm is proportional to the amount of free unbound Coomassie dye. A decrease in absorbance at 465 nm indicates protein attachment to the surface (of CNCs). The uncertainty values (error bars) correspond to the standard error of mean of two independent measurements (N=2).

It was not possible to confirm the immobilization of insulin onto CNCs using the previous method. This could be due the lower sensitivity of the Coomassie dye towards insulin compared to BSA. Additionally, one of drawbacks of conventional colorimetric assays for detecting nanoparticle bioconjugation is that it is not possible to directly measure the amount of protein bound to nanoparticles, mostly due to interference of the nanoparticles at the absorption wavelength of the protein bound dye (for Coomassie dye at 595 nm). In order to directly assay the amount of protein immobilized onto the CNCs and to improve the limit of detection, an alternative Coomassie Plus assay was carried out. Instead of measuring the amount of protein bound dye at 595 nm, the assay was done inversely, by measuring the decrease in absorbance at 465 nm caused by removal of unbound dye from solution upon binding to BSA-CNCs [33]. The amount of free dye (proportional to A465nm) in solution can be easily accessed by separating the solution from the CNCs (where the protein bound dye is attached) by centrifugation. This value is inversely proportional to the amount of immobilized protein.

The results obtained using the inverted Coomassie Plus assay are shown in Figure 7. As expected, the highest A_{465nm} values were obtained for the buffer and for the CNCs blank (0.56 and 0.58, respectively), where no protein was present, and for one of the CNCs-insulin control samples. The two CNCs-insulin (step 2 at pH 5 or pH 8) samples and the CNCs BSA sample prepared by EDC/sulfo NHS chemistry displayed the lowest absorbance values (0.46, 0.512 and 0.513, respectively). As the coomassie dye binds to the proteins attached to the CNCs, the amount of unbound dye present in the separated solution is lower. These results indicated that like BSA, insulin was successfully immobilized onto the surface of the CNCs using the EDC/sulfo-NHS approach.

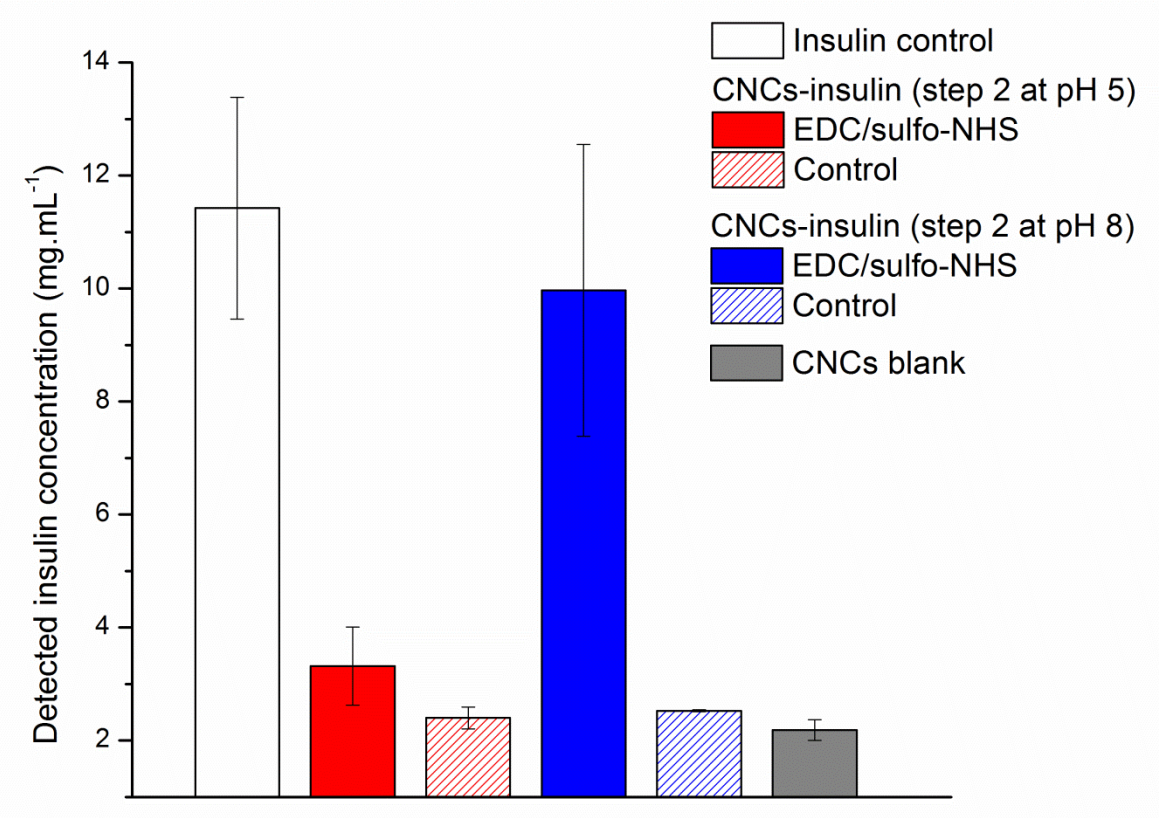

Figure 8. Quantification of insulin immobilization onto the surface of CNCs. Human insulin concentration was detected using a radioimmunoassay based on polyclonal insulin antibodies. The uncertainty values (error bars) correspond to the standard error of mean of three independent measurements (N=3).

A radioimmunoassay was used to quantify the amount of insulin bound to the CNCs. The antibody serum for radioimmunodetection consisted on a mixture of polyclonal antibodies, whose specificity has been previously tested for human insulin. The advantage of using a radioimmunoassay is that it allows direct quantification of insulin on the surface of nanoparticles and does not rely on a light-based detection method (such as UV-visible absorbance), which signal can be interfered by nanoparticle suspension. The results are summarized in Figures 8 and 9.

The radioimmunoassay data confirms the presence of insulin on the CNCs-insulin bioconjugates prepared by EDC/sulfo-NHS chemistry. The detected insulin concentration was found to be higher for the two samples prepared using EDC/sulfo-NHS (9.97 $mg.mL^{-1}$ with step 2 done at pH 8, and 3.32 $mg.mL^{-1}$ with step 2 done at pH 5) compared to the controls and the CNCs blank (Figure 8). The detected insulin concentration values obtained for the CNCs-insulin controls, CNCs blank, CNCs stock and CNCs-BSA samples were very similar (between 2.19 and 2.56 $mg.mL^{-1}$ Figure 8 and 9). No insulin was added to the CNCs blank and stock and in the CNCs-BSA samples. The detection of insulin in these CNCs samples may be due to non-specific binding of insulin antibodies to the CNCs surface.

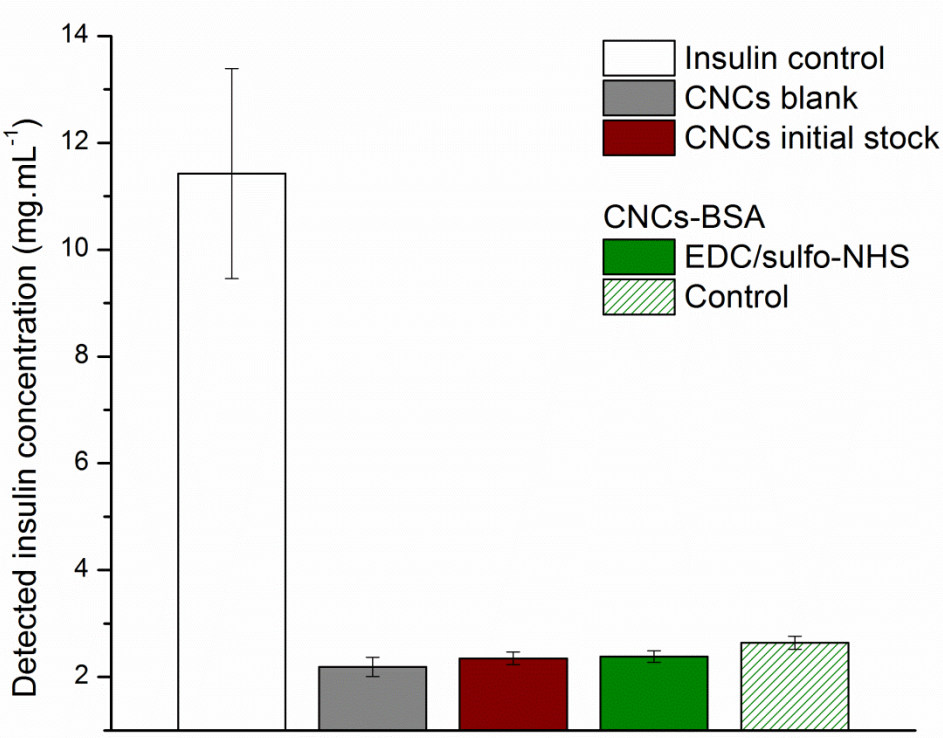

Figure 9. Quantification of insulin immobilization onto the surface of CNCs: control samples. Human insulin concentration was detected using a radioimmunoassay based on polyclonal insulin antibodies. The uncertainty values (error bars) correspond to the standard error of mean of three independent measurements (N=3).

The results also show that the immobilization procedure with EDC/sulfo-NHS was more efficient when the pre-concentration step (step 2 done at pH 5) was not included. The detected insulin concentration was about 3 times higher when the pre-concentration step was omitted (step 2 done at pH 8 favoring immediate amidation reaction). It is known that small neutral molecules (such as insulin) do not always pre-concentrate efficiently on the negatively carboxyl surfaces [31], which could be the case here. In this event, it is preferable to remove the pre-concentration step, since the sulfo-NHS molecules may actually lose stability after 3 h at pH 5.

The insulin concentration values detected using the radioimmunoassay values were most likely overestimated compared to the insulin concentrations in the samples. The concentration measured for the insulin control using the radioimmunoassay was about 24 times higher than the actual human insulin concentration present in this control. The same was verified for other human insulin control samples. This could be partly resultant of a higher sensitivity of the insulin antibodies toward human insulin, since rat insulin was used for calculating the standard concentration curve in the radioimmunoassay (see Materials and Methods).

Characterization of CNCs-insulin bioconjugates

The CNCs-insulin bioconjugates prepared by EDC/sulfo-NHS chemistry were further characterized for hydrodynamic size and particle concentration using NTA by NanoSight (Figure 10 and Table 3). First, the effect of the successive washing steps used during immobilization procedure (3 magnetic separations, 15 min each) on the size and number of CNCs in Milli-Q was tested (no protein or reagents added, CNCs blank). After 3 magnetic separations, there was a small increase in the mean hydrodynamic size of the CNCs, as the peak mean of the size distribution shifts from 142 nm to 157.7 nm (Figure 10 and Table 3). As previously discussed, this could be due to the partial loss of smaller sized CNCs to the supernatant upon successive washing steps. In fact, the concentration of recovered nanoparticles in the CNCs blank was 1.65 times lower round than the nanoparticle concentration present in the initial CNCs suspension (Table 3), which corresponds to a final particle recovery of 60.5 %.

The results obtained for the CNCs-insulin bioconjugates show that the EDC/sulfo-NHS immobilization procedure leads to an increase in CNC mean hydrodynamic size (Figure 10 and Table 3). Upon insulin immobilization with EDC/sulfo-NHS the mean hydrodynamic diameter of the CNCs is 49.3 nm higher that the CNCs blank (207.0 nm, peak mean, Table 3). A similar size difference was observed for the control CNCs-insulin, which showed a mean hydrodynamic diameter of 195.7 nm (peak mean, Table 3). These results indicate that insulin attachment to the surface of the CNCs (covalent or not) most likely leads to a moderate CNCs agglomeration in suspension. The estimated particle concentration obtained for the CNCs-insulin was considerably lower than the measured in the blank sample (6.4 times lower for the CNC-insulin prepared by the EDC/sulfo NHS approach and 2 times lower for the control CNCs-insulin, Table 3). This could be partly due to CNC agglomeration during the immobilization of insulin. As CNCs agglomerate in suspension, the number of particles also decreases. The decrease in particle concentration is more pronounced for the CNCs-insulin prepared by EDC/sulfo-NHS, which indicates that this chemistry may lead to extended particle loss during the overall immobilization procedure.

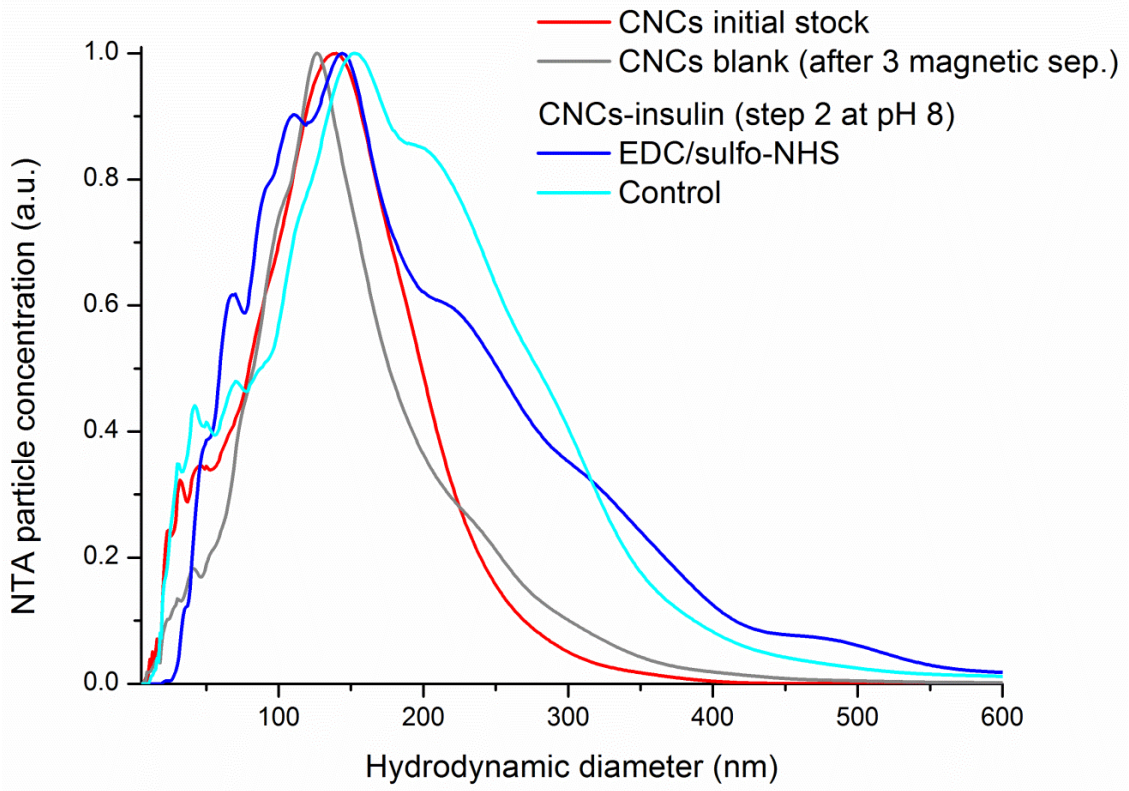

Figure 10. Hydrodynamic diameter measurements of the CNCs-insulin bioconjugates and CNCs suspensions obtained by NTA with NanoSight (N=3). The uncertainty values correspond to the standard deviation of the repeated measurements.

Table 3. Characterization of CNCs insulin bioconjugates with NTA from NanoSight. Measurements of hydrodynamic diameter and particle concentration by NTA (N=3) obtained for CNCs initial stock suspension, CNCs blank and the CNCs-insulin suspensions. The uncertainty values correspond to the standard deviation of the repeated measurements.

Parameters	**CNCs initial suspension**	**CNCs blank (after 3 magnetic separations)**	**CNCs-insulin (step 2 at pH 8)**	
			EDC/sulfo-NHS	**Control**
Peak mode (nm)	138.7 ± 9.6	126.7 ± 1.5	124.7 ± 17.5	154.0 ± 10.6
Peak mean (nm)	142.0 ± 1.7	157.7 ± 3.1	207.0 ± 6.2	195.7 ± 19.0
Estimated particle concentration $x10^8$ ($particles.mL^{-1}$)	75.2 ± 10.7[b]	45.5 ± 3.4	7.1 ± 1.8	23.1 ± 2.7

[b] For comparison purposes, this value corresponds to the particle concentration present in the diluted CNCs suspension used during step 1 of the immobilization procedure (stock suspension was diluted 1:4).

Conclusions

This work aimed at the development of novel Fe_3O_4 CNCs bioconjugates for future use in biomedical applications. Insulin was successfully immobilized onto the PAA surface of Fe_3O_4 CNCs using EDC/NHS chemistry.

The findings of this work point out some of the challenges related to the coupling of proteins to nanoparticles and bring forth some new solutions. It was observed that the optimal conditions for protein strongly coupling depend on the type and size of protein to immobilize. Immobilization procedures using EDC/sulfo-NHS chemistry usually include a pre-concentration step in order to bring the protein in close proximity of surface carboxyls. Herein, the immobilization procedure with EDC/sulfo-NHS was more efficient when the pre-concentration step (step 2 done at pH 5) was not included, which indicates that for small molecules, like insulin, it is preferable to omit this step and change other reaction parameters (e.g. increase the protein concentration).

Another usual challenge in the development of nanoparticle bioconjugates relates to the confirmation and quantification of protein immobilization. BSA and Insulin attachment to the CNCs was first confirmed using an inverted Coomassie assay, which overcomes some of the typical problems of standard colorimetric assays for protein detection, e.g. interference of nanoparticles in the absorption of the measured dye [28]. This inverted assay still needs be improved towards the quantification of the amount of immobilized protein. This could be achieved by including appropriate standard samples where the protein concentration is known. The radioimmunoassay was also an efficient method to confirm insulin immobilization onto the CNCs. We have observed non-specific binding of the insulin antibodies to the CNCs, resulting in residual detection of insulin for the blank samples. In the future this issue could be addressed by pre-treating the CNCs samples with a blocking agent, e.g. BSA or ethanolamine.

The behavior and magnetic properties of obtained CNCs-insulin in aqueous solution were analyzed upon characterization for hydrodynamic particle size, agglomeration state and magnetic separation. The CNCs-insulin show high magnetization in solution, while retaining superparamagnetic properties since they encompass several magnetite nanoparticles of ~10 nm. This would not be the case for a single magnetite crystallite of the same size (~200 nm). The CNCs-insulin could be easily controlled using external magnetic fields and by using a conventional magnet an efficient separation occurs within minutes. As previously mentioned, this is a key feature for the development of magnetic nanoparticle carriers for biomedical applications. The bioconjugation procedure still needs to be optimized, as the protein coupling and successive magnetic separations lead to considerable particle loss and moderate CNCs agglomeration. The next step would be to test the biological activity of the CNCs-insulin bioconjugates by monitoring the glucose uptake by skeletal muscle cells and to isolate specific cells by magnetic separation upon CNCs-insulin binding to the insulin receptor.

These findings encourage the development of CNCs Fe_3O_4 bioconjugates for biomedical and biological applications. By coupling the Fe_3O_4 CNCs nanocarriers to active biomolecules one could use them for example, to deliver therapeutic proteins to specific cells, or to isolate specific molecules or cells identified by a coupled biomarker.

Materials and Methods

Ultrapure Milli-Q water with conductivity below 0.2 $\mu S.cm^{-1}$ was used throughout the work. Unless stated otherwise, results based on repeated measurements are given as mean ± standard deviation and results based on independent measurements are given as mean ± standard error of mean, respectively. The number of measurements N is stated in parentheses.

Synthesis of Fe_3O_4 colloidal nanoparticle clusters

The Fe_3O_4 CNCs were synthesized in a DEG solution at high temperature. A stock solution of NaOH/DEG was prepared by dissolving 50 mM NaOH in 20 mL DEG and heating at 120 °C for 20-30 min in nitrogen atmosphere. For synthesis, 0.4 mmol of $FeCl_3$ was first dissolved in 17 mL of DEG and 4 mmol of polyacrylic acid (Average MW 1800) was added under vigorous mechanical stirring at 120 °C. Subsequently, this mixture was heated to 220 °C and kept for 1 more hour under continuous stirring forming a clear yellow solution. At this point, 1.6 mL of the stock solution was added to the mixture, which was kept for 1 more hour under stirring at 220 °C to form Fe_3O_4 CNCs. After synthesis the CNCs suspension was left to cool down and was subsequently transferred to Milli-Q water solution, upon multiple washing steps with water/ethanol (separation was carried out with a permanent magnet).

Characterization of CNCs suspensions

Scanning electron microscopy (SEM)

Samples were first prepared upon air-drying of CNCs suspensions onto silicon substrates. SEM images were acquired using a either a Quanta 650 FEG environmental SEM (FEI, Oregon, USA) or a Carl Zeiss 1540XB cross-beam SEM system (Carl Zeiss Microscopy GmbH, Oberkochen, Germany). SEM images were collected upon optimizing the voltage between 5 and 15 kV on the silicon substrate where the dried CNCs were placed. The average size of CNCs was estimated using the tools available on the instrument's software.

Dynamic light scattering (DLS) and laser Doppler velocimetry (zeta potential measurement)

CNCs suspensions were characterized by dynamic light scattering (DLS) and laser Doppler velocimetry using a SZ-100 nanoparticle analyzer (Horiba, Kyoto, Japan) for measurement of hydrodynamic diameter and zeta potential, respectively. Prior to measurement, the instrument

was warmed up for at least 30 minutes. For DLS and zeta potential measurements the CNCs stock suspension was diluted 1:4 and the washed CNCs suspensions and CNCs supernatants were diluted 1:8 (in Milli-Q water). For DLS measurement, 1 mL of the diluted suspensions was transferred to a dust-free disposable cuvette and the measurement was performed at a temperature of 25°C. The angle of detection was 90°. Three consecutive measurements were performed. The DLS characteristics of the measured sample, given as the mean of the peak in the intensity distribution and polydispersity index, were determined by averaging the result of the repeated measurements (N=3). For determination of the zeta potential, 600 µL of CNCs suspension were transferred to a disposable zeta cell. After equilibration to a temperature of 25°C, two consecutive measurements were performed. The zeta potential is given as the average of the repeated measurements (N=2).

Nanoparticle tracking analysis (NTA) with NanoSight

NTA measurements were performed using a NanoSight LM10 instrument (NanoSight, Amesbury, United Kingdom), equipped with a sample chamber with a 642-nm laser. Prior to measurement, CNCs samples were diluted with in Milli-Q water. CNCs stock suspensions were diluted 1:40, CNCs blank was diluted 1:10, and CNCs-insulin samples were diluted 1:4. The CNCs samples were injected into the sample chamber using sterile syringes until the liquid reached the tip of the nozzle. All measurements were carried out at room temperature. NTA 2.1 Build 329 software was used for data acquisition and analysis. All measurements were performed with semi-automatic shutter and gain adjustments. Two measurements of the same sample were done for testing the behavior of a CNCs stock suspension in water (90 s capture time) and three measurements were performed for the CNCs stock suspension, CNCs blank, and CNCs insulin samples prepared during the immobilization procedure (160 s capture time). The sample particle concentration is directly calculated by the software from the number of particles detected during capture. The NTA characteristics of the measured sample, given as mean or mode of the peak in the number based distribution and estimated particle concentration, were determined by averaging the results of the consecutive measurements (N=2 or N=3). The CNCs surface area was calculated using the average of mean hydrodynamic diameter.

Protein immobilization onto Fe_3O_4 CNCs

Protein solutions and reagents

BSA and human insulin were purchased from Sigma-Aldrich as lyophilized powders (Bovine Serum Albumin - product code A2153, MW = 66430 $g.mol^{-1}$; Human Insulin – product code I2643, MW = 5807.57 $g.mol^{-1}$; Sigma-Aldrich Danmark A/S, Copenhagen, Denmark). BSA stock solutions were prepared by directly dissolving the BSA powder into Milli-Q water. Two types of insulin stock solutions were prepared, at pH 5.0 in 2-(*N*-morpholino)ethanesulfonic acid (MES) buffer and at pH

8.0 in sodium phosphate (NaPB) buffer. Insulin stock solutions were prepared by gently dissolving the powder in 0.1 M MES 0.5 M NaCl pH 5.0 or 20 mM NaPB pH 8.0 by gentle overnight stirring at 4 °C. The insulin MES stock pH 5.0 solutions were further treated with filtration (0.2 µm) in order to remove any trace of unsolubilized protein. The mass of insulin recovered after the filtration step was ~91 %. After preparation protein stock solutions (BSA and insulin) were stored at 4 °C until use. Protein concentrations were determined by UV-vis absorbance. The extinction coefficients used for the calculations were: ε_{280nm} = 0.667 $cm^{-1}.(mg/mL)^{-1}$ for BSA [34] and ε_{276nm} = 1.0675 $cm^{-1}.(mg/ml)^{-1}$ for human insulin [35].

EDC and sulfo-NHS were acquired from Thermo Scientific (EDC - 1-Ethyl-3-[3-dimethylaminopropyl]carbodiimide hydrochloride, product code 22980; Sulfo-NHS - N-Hydroxysulfosuccinimide, product code 24510). Before each immobilization procedure, intermediate solutions of EDC (12 $mg.mL^{-1}$) and sulfo-NHS (33 $mg.mL^{-1}$) were freshly prepared in Milli-Q water.

Protein immobilization set-up and procedure

The immobilization procedure was carried out in protein low-binding tubes (Lo-bind, Eppendorf), which were placed in a mixer incubator (Thermomixer® R, Eppendorf) during reaction for temperature control and mixing. In total, seven CNCs samples were prepared in parallel: three CNCs-protein bioconjugates using EDC/sulfo-NHS chemistry (CNCs-BSA and CNCs-insulin using or not a pre-activation step), three corresponding control experiments where no EDC/sulfo-NHS was added, and one CNCs blank where neither EDC/sulfo-NHS nor protein was added.

Typically, the immobilization procedure was carried out in four steps (Figure 5). First, 125 µL of CNCs stock suspension (particle concentration = $300.6x10^8$ $particles.mL^{-1}$) were mixed with 25 µL of Milli-Q and equal volumes (2 X 175 µL) of freshly prepared intermediate solutions of EDC (12 $mg.mL^{-1}$) and sulfo-NHS (33 $mg.mL^{-1}$). For the CNCs-protein control samples and for the CNCs blank, 350 µL of Milli-Q water were added instead of the EDC and sulfo-NHS solutions. The 500 µL mixture was left to react at 750 rpm for 30 min at room temperature (step 1, activation of COOH groups). Subsequently, the CNCs sample was washed by magnetic separation. Generally, the washing procedures consisted on 15 min CNCs separation using a permanent magnet stand (DynaMag™-2, Molecular Probes, Invitrogen, Leek, The Netherlands), after which the supernatant was removed. The remaining CNCs pellet was then directly redispersed by adding 500 µL of the appropriate protein solution and left to react for 3 h at 750 rpm and 4 °C (step 2, pre-concentration of protein and amidation reaction, see Figure 5 and Table 2). The added protein solutions were as follows: CNCs-BSA – 240.17 $\mu g.mL^{-1}$ BSA in Milli-Q; CNCs-insulin with pre-concentration – 186.44 $\mu g.mL^{-1}$ in 0.1 M MES 0.5 M NaCl; CNCs-insulin without pre-concentration – 186.44 $\mu g.mL^{-1}$ in 20 mM NaPB pH 8.0. For the CNCs blank, 500 µL of Milli-Q water were added instead. The CNCs suspension was again washed using magnetic separation and the CNCs pellet was redispersed into 500 µL of 20 mM NaPB pH 8.0. The redispersed CNCs suspension was left to

react at pH 8.0 for 1 h at 750 rpm and room temperature (step 3, 1st washing step and amidation reaction if not occurring in step 2). Afterwards, the CNCs suspension was washed once more with magnetic separation and the CNCs pellet was redispersed into 500 µL of 20 mM NaPB pH 8.0 to obtain the final CNCs-protein suspension (step 4, 2nd washing step).

The number of protein molecules per CNCs binding site was determined as follows. One binding site was considered to be the CNCs area occupied by one protein molecule (corresponding to the protein disk area). The protein disk areas used were 38.5 nm^2 for BSA and 5.7 nm^2 for insulin (BSA diameter ~7 nm [36] and insulin diameter ~2.7 nm [37]). The total number of CNCs protein binding sites was estimated by dividing the area occupied by one protein molecule by the total CNCs surface area available. The number of protein molecules per CNCs binding site is then estimated by dividing the number of protein molecules (initial or detected) by the number of CNCs protein binding sites.

Confirming protein immobilization onto Fe_3O_4 CNCs

Coomassie Plus assay

The Coomassie Plus Protein Assay (Pierce Biotechnology, Rockford, USA) was used to quantify BSA attachment onto the CNCs. After the immobilization step 2, (where BSA is incubated together with the CNCs and the amidation reaction occurs) the supernatant/wash fraction was collected. To quantify the amount of BSA bound to the CNCs, the total protein content present in the initial BSA stock solution (added in the beginning of step 2) and in the supernatant were assayed according to the supplier's instructions. The assay was carried out using a standard 96-well plate. After introducing 10 microliters of each sample to the appropriate wells, 300µL of the Coomassie Plus Reagent (Pierce Biotechnology, Rockford, USA), were added to each well, after which the plate was mixed with a plate shaker for 30 sec and left to incubate at room temperature for 10 min. After the incubation period, the absorbance at 595 nm (proportional to the concentration of the Coomassie protein-bound dye) was measured using a BioTek Synergy H1 plate reader (BioTek, Vermont, USA). The instrument automatically corrects the absorbance of the samples for a pathlenght of 1 cm. BSA concentration is calculated from a standard curve obtained using $A_{595\ nm}$ measurements of BSA Standard samples (known concentrations). For each of the samples under analysis (initial BSA stock concentration added in the beginning of step 2 and supernatant collected after step 2), five wells were prepared for measurement. The BSA concentration of each of the samples was determined by averaging of the five independent measurements (N=5). The final concentration of BSA present on the CNCs-BSA bioconjugates is given by the difference between the initial BSA stock concentration and the concentration of free unbound BSA measured in the supernatant.

Inverted Coomassie Plus assay

An inverted Coomassie Plus Assay (Quantitate immobilized protein, Pierce Biotechnology, Rockford, USA) was used to confirm protein immobilization onto the CNCs. This inverted assay relies on measuring the decrease in absorbance at 465 nm caused by removal of unbound dye from solution upon protein binding [33]. The amount of free unbound dye (proportional to A465nm) is inversely proportional to the amount of immobilized protein. In total, eight samples were assayed: the three final CNCs-protein bioconjugates prepared using EDC/sulfo-NHS chemistry (CNCs-BSA and CNCs-insulin using or not a pre-activation step), the three corresponding control samples where no EDC/sulfo-NHS was added, the CNCs blank, and a buffer blank containing only 20 mM NaPB pH 8.0. One hundred µL of each sample were mixed with 100 µL of Coomassie Plus Reagent (Pierce Biotechnology, Rockford, USA) and left to react for 5 min at 750 rpm and at room temperature. Subsequently, the samples were centrifuged for 2 min at 1500 x g to separate the unbound dye from the CNCs (which form a pellet). The collected supernatant (150 µL) was diluted 2X in 20 mM NaPB. One hundred µL this mixture (2X dilution) were then transferred to the appropriate wells in a standard 96-well plate. Duplicates were done for each of the assayed samples. The absorbance at 465 nm (proportional to the concentration of free unbound Coomassie dye) was measured using a BioTek Synergy H1 plate reader reader (BioTek, Vermont, USA). The final absorbance value A_{465nm} corresponds to the average of the two independent measurements (N=5).

Radioimmunoassay

A radioimmunoassay was used to quantify the amount of insulin bound to the CNCs. In total, nine samples were assayed: a sample containing 475.9 µg.mL^{-1} of human insulin in 20 mM Na PB pH 8.0 (used as a positive control), the three final CNCs-protein bioconjugates prepared using EDC/sulfo-NHS chemistry (CNCs-BSA and CNCs-insulin using, or not a pre-activation step), the three corresponding control samples where no EDC/sulfo-NHS was added, the CNCs blank and the initial CNCs stock (4 times more concentrated). Prior to the assay, the samples were diluted 16.10^6 times. One hundred µL of each diluted sample were mixed with a surplus (100 µL) of guinea pig anti-porcine insulin antibody serum (Novo Nordisk, Bagsvaerd, Denmark) and incubated for 48 h. Triplicates were done for each sample. During incubation the guinea-pig anti porcine insulin antibodies bind to the intact insulin molecules and form a complex. Subsequently, an excess of labeled ^{125}I-Insulin (100 µL with specific radioactivity of ~371 mCi/mg, Novo Nordisk) was added to the reacting mixture. The labeled ^{125}I-Insulin binds to the remaining antibodies in solution to form a ^{125}I-Insulin-antibody complex. This mixture was then washed two times with 96% ethanol and subsequently FAM/ethanol to separate unbound insulin and ^{125}I-Insulin excess from the antibody-bound insulin. Antibody-bound insulin and antibody-bound ^{125}I-Insulin precipitate immediately after mixing, while the unbound insulin and free ^{125}I-Insulin remain in the supernatant. The concentration of insulin in the samples was then determined by measuring the radioactivity of ^{125}I-

Insulin in the supernatant or of antibody-bound ^{125}I-Insulin in the precipitate. The intensity of the radioactive-bound ^{125}I-Insulin measured is inversely proportional to the insulin concentration in the analyzed sample. Rat insulin was used as a standard sample. Insulin concentration is calculated from a standard curve obtained using the radioactivity intensity measurements of rat insulin standards of known concentrations. The final detected insulin concentration for each of the samples was determined by averaging the results of the triplicates (three independent measurements, N=3).

References

1. Ito A, Shinkai M, Honda H, Kobayashi T (2005) Medical application of functionalized magnetic nanoparticles. J Biosci Bioeng 100: 1–11.

2. Veiseh O, Gunn JW, Zhang M (2010) Design and fabrication of magnetic nanoparticles for targeted drug delivery and imaging. Adv Drug Deliv Rev 62: 284–304.

3. Arruebo M, Fernández-Pacheco R, Ibarra MR, Santamaría J (2007) Magnetic nanoparticles for drug delivery. Nano Today 2: 22–32.

4. Reddy LH, Arias JL, Nicolas J, Couvreur P (2012) Magnetic nanoparticles: design and characterization, toxicity and biocompatibility, pharmaceutical and biomedical applications. Chem Rev 112: 5818–5878.

5. Pankhurst QA, Thanh NTK, Jones SK, Dobson J (2009) Progress in applications of magnetic nanoparticles in biomedicine. J Phys D Appl Phys 42: 224001.

6. Lu A-H, Salabas EL, Schüth F (2007) Magnetic Nanoparticles: Synthesis, Protection, Functionalization, and Application. Angew Chemie Int Ed 46: 1222–1244.

7. Gupta AK, Gupta M (2005) Synthesis and surface engineering of iron oxide nanoparticles for biomedical applications. Biomaterials 26: 3995–4021.

8. Laurent S, Forge D, Port M, Roch A, Robic C, et al. (2008) Magnetic iron oxide nanoparticles: synthesis, stabilization, vectorization, physicochemical characterizations, and biological applications. Chem Rev 108: 2064–2110.

9. Gnanaprakash G, Philip J, Jayakumar T, Raj B (2007) Effect of digestion time and alkali addition rate on physical properties of magnetite nanoparticles. J Phys Chem B 111: 7978–7986.

10. Wu W, He Q, Jiang C (2008) Magnetic iron oxide nanoparticles: synthesis and surface functionalization strategies. Nanoscale Res Lett 3: 397–415.

11. Pankhurst QA, Connolly J, Jones SK, Dobson J (2003) Applications of magnetic nanoparticles in biomedicine. J Phys D Appl Phys 36: R167.

12. Liu J, Qiao SZ, Hu QH, (Max) Lu GQ (2011) Magnetic Nanocomposites with Mesoporous Structures: Synthesis and Applications. Small 7: 425–443.

13. Lu Z, Yin Y (2012) Colloidal nanoparticle clusters: functional materials by design. Chem Soc Rev 41: 6874–6887.

14. Nie Z, Petukhova A, Kumacheva E (2010) Properties and emerging applications of self-assembled structures made from inorganic nanoparticles. Nat Nano 5: 15–25.

15. Jun Y-W, Seo J-W, Cheon J (2008) Nanoscaling laws of magnetic nanoparticles and their applicabilities in biomedical sciences. Acc Chem Res 41: 179–189.

16. Kolhatkar AG, Jamison AC, Litvinov D, Willson RC, Lee TR (2013) Tuning the magnetic properties of nanoparticles. Int J Mol Sci 14: 15977–16009.

17. Ge J, Hu Y, Biasini M, Beyermann WP, Yin Y (2007) Superparamagnetic magnetite colloidal nanocrystal clusters. Angew Chem Int Ed Engl 46: 4342–4345.

18. Singh R, Lillard JW (2009) Nanoparticle-based targeted drug delivery. Exp Mol Pathol 86: 215–223.

19. Faraji AH, Wipf P (2009) Nanoparticles in cellular drug delivery. Bioorg Med Chem 17: 2950–2962.

20. Wang C, Yan Q, Liu H-B, Zhou X-H, Xiao S-J (2011) Different EDC/NHS Activation Mechanisms between PAA and PMAA Brushes and the Following Amidation Reactions. Langmuir 27: 12058–12068.

21. Di Marco M, Shamsuddin S, Razak KA, Aziz AA, Devaux C, et al. (2010) Overview of the main methods used to combine proteins with nanosystems: absorption, bioconjugation, and encapsulation. Int J Nanomedicine 5: 37–49.

22. Melmed S, Conn PM (2005) Endocrinology: Basic and Clinical Principles (Google eBook). Humana Press.

23. Diabetes Mellitus: A Fundamental and Clinical Text (2003). Lippincott Williams & Wilkins.

24. Correia M, Neves-Petersen MT, Jeppesen PB, Gregersen S, Petersen SB (2012) UV-light exposure of insulin: pharmaceutical implications upon covalent insulin dityrosine dimerization and disulphide bond photolysis. PLoS One 7: e50733.

25. Derewenda U, Derewenda Z, Dodson GG, Hubbard RE, Korber F (1989) Molecular structure of insulin: the insulin monomer and its assembly. Br Med Bull 45: 4–18.

26. Brange J, Owens DR, Kang S, Vølund a (1990) Monomeric insulins and their experimental and clinical implications. Diabetes Care 13: 923–954.

27. De Meyts P (2008) The insulin receptor: a prototype for dimeric, allosteric membrane receptors? Trends Biochem Sci 33: 376–384.

28. Sapsford KE, Tyner KM, Dair BJ, Deschamps JR, Medintz IL (2011) Analyzing nanomaterial bioconjugates: a review of current and emerging purification and characterization techniques. Anal Chem 83: 4453–4488.

29. Figueiredo M (2013) Sizing Nanoparticles in Liquids: An Overview of Methods. In: Coelho J, editor. Drug Delivery Systems: Advanced Technologies Potentially Applicable in Personalised Treatment SE - 3. Advances in Predictive, Preventive and Personalised Medicine. Springer Netherlands, Vol. 4. pp. 87–107.

30. Couvreur P, Dubernet C, Puisieux F (1995) Controlled drug delivery with nanoparticles : current possibilities and future trends. Eur J Pharm Biopharm 41: 2–13.

31. Fischer MJE (2010) Amine coupling through EDC/NHS: a practical approach. Methods Mol Biol 627: 55–73.

32. Gualandi-Signorini a M, Giorgi G (2001) Insulin formulations--a review. Eur Rev Med Pharmacol Sci 5: 73–83.

33. Bonde M, Pontoppidan H, Pepper DS (1992) Direct dye binding--a quantitative assay for solid-phase immobilized protein. Anal Biochem 200: 195–198.

34. Putman FW, editor (1975) The Plasma Proteins: Structure, Function and Genetic Control. 2nd Editio. New York, NY, USA: Academic Press.

35. Manno M, Mauro M, Craparo EF, Podestà A, Bulone D, et al. (2007) Kinetics of different processes in human insulin amyloid formation. J Mol Biol 366: 258–274.

36. Yohannes G, Wiedmer SK, Elomaa M, Jussila M, Aseyev V, et al. (2010) Thermal aggregation of bovine serum albumin studied by asymmetrical flow field-flow fractionation. Anal Chim Acta 675: 191–198.

37. Baker EN, Blundell TL, Cutfield JF, Cutfield SM, Dodson EJ, et al. (1988) The structure of 2Zn pig insulin crystals at 1.5 A resolution. Philos Trans R Soc Lond B Biol Sci 319: 369–456.

5 Discussion

The main objective of this PhD project was to acquire knowledge for developing novel approaches to be later applied in diagnosis and therapeutics by merging nanobiotechnology and biophotonics. This PhD dissertation provides insights into two research topics: UV light induced mechanisms in proteins and their usefulness for developing protein based therapies, and the construction of bioconjugates of nanomaterials and proteins for biosensing, bioseparation and targeted drug delivery.

5.1 Investigation of light induced switches in proteins

The aim of the investigation of the first research topic was to find out more about the molecular mechanisms triggered upon UV illumination of proteins, in particular UV mediated disulphide bond disruption and their implications to the structure and function of biomolecules. For this purpose, three proteins were studied: bovine alpha-lactalbumin, human insulin and the epidermal growth factor receptor (EGFR).

The first two proteins were used as models to evaluate disulphide bond disruption in proteins. In order to probe the effects of UV light on their structure and function they were fully characterized using spectroscopy techniques (UV absorption, fluorescence, and circular dichroism spectroscopy). Furthermore, in the case of insulin, the impact of prolonged UV illumination on its biological function was also investigated. The results showed that prolonged UV illumination of these proteins lead to conformational changes, which were correlated with the disruption of disulphide bonds upon excitation of its pool of aromatic residues. The nature and extent of the UV induced conformational changes was found to be distinct in these two proteins. As discussed previously in section 2.1, these two proteins differ in size, amino acid content, structure and physicochemical characteristics. There were also some differences in the experimental procedures used during these investigations (e.g. the wavelength used for UV illumination). For this reason, one should be careful when comparing the results obtained for these two distinct protein models.

The study of bovine alpha-lactalbumin (Paper 1) focused on the photochemistry and photophysics of Trp, as this protein was selectively excited at 295 nm. Alpha-lactalbumin contains four Trp residues, two of them in close proximity to disulphide bonds. Prolonged excitation of the Trp pool of alpha-lactalbumin lead to conformational changes associated with the increased exposure of its Trp residues. The UV induced disruption of one or more of the disulphide bonds in alpha-lactalbumin upon Trp excitation was likely to be one of the causes for the observed conformational changes. This concurred with the findings from thermal-dependent fluorescence studies, which allowed to identify Trp photoionization from the S_1 state as one of the major photophysical mechanisms triggered upon UV excitation of alpha lactalbumin. As discussed in

section 2.1.1.1, Trp photoionization leads to the formation of solvated aqueous electrons, which can then be captured by disulphide bridges resulting in disulphide bond disruption. Continuous UV illumination of alpha-lactalbumin did not have a major impact on the secondary structure of the protein. Most likely, the conformational changes that occur upon UV illumination such as disulphide bond disruption only lead to partial unfolding of the protein, resulting in a molten-globule like conformation, which is usually adopted by the alpha-lactalbumin under mild denaturating conditions. In its molten globule state, alpha-lactalbumin is still compact and retains its overall backbone fold and native-like secondary structure, but lacks well defined tertiary interactions, and the hydrophobic regions are more solvent accessible. It would be interesting to figure out how the observed UV induced structural changes would affect its original biological function, i.e. the lactose synthase regulatory activity.

The study carried out with human insulin (Paper 2) also provided some important insights on UV light induced effects on proteins. Insulin does not contain Trp residues and thereby is an interesting molecule to evaluate the photophysics and photochemistry of Tyr. Insulin contains three Tyr residues, one of them (TyrA19) in close proximity to two disulphide bonds. As expected, continuous UV excitation of insulin resulted in disulphide bond breakage but also in the progressive formation of dityrosine, an important photo-oxidation product of Tyr. In contrast to the results obtained for alpha lactalbumin, the secondary structure and tertiary structure of insulin were severally impaired upon UV exposure. As discussed in section 2.1.1.1, small proteins like insulin lack a strong hydrophobic core, and for this reason disulphide bonds have a critical role in the stabilization of its tertiary structure. In native insulin, the A and B chains are held together by two disulphide bridges. Therefore, disruption of either of these bonds is likely to compromise the native three-dimensional fold of the protein, as verified in this study. The UV light induced structural changes observed in insulin also resulted in the concomitant loss of antibody binding capability and impaired its hormonal biological function. Both UV induced disulphide bond disruption and formation of dityrosine cross-links independently contribute to the loss of insulin's biological function. Since the three-dimensional structure of insulin is impaired upon photolysis of the disulphide bonds the hormone can no longer bind to the insulin receptor. On the other hand, the formation of dityrosine cross-links results in covalent insulin dimerization and inactivation, as in its dimer form the hormone is no longer recognized by its receptor.

The results of the work in insulin and alpha-lactalbumin also brought forth some important conclusions that are of global importance for the use of these proteins in pharmaceutical and food products, respectively. Only after a few hours of UV exposure, these two proteins undergo conformational changes, which can compromise their biological function. In particular, the hormonal activity of insulin decreased to more than half of its original value after only 1.5 h of UV illumination. The irradiance levels used during these two experimental works are comparable (3.94 W. m^{-2} at 295 nm for alpha-lactalbumin and 2.20 W. m^{-2} at 276 nm for insulin) and are

similar to the total irradiance of sunlight in the UVB region (~0.78 W. m^{-2}, 280-315 nm). These irradiance levels are also comparable to other artificial light sources that could be present during the production and storage of such products, e.g. UV sterilization lamps. This was demonstrated during the investigation done with human insulin. Considering the above, it can be expected that overdue exposure to the cited natural and artificial UV light sources may compromise some of the products containing these proteins, e.g. milk whey in the case of alpha lacalbumin, or pharmaceutical formulations containing insulin. These findings support the need for additional investigations in industry regarding the impact of light exposure on products containing proteins. This includes: the requirement of photostability tests for pharmaceutical products and the identification of exposure time and spectral outputs of the light sources used during life-cycle of these products, from production to distribution.

This PhD work also looked into the development of a light based therapeutical application for cancer treatment based on the UV induced inactivation of the epidermal growth factor receptor (EGFR), which was the third studied protein (Paper 3). The NanoBiotechnology group had previously shown that UVB illumination of cancer cells overexpressing EGFR resulted in the arrest the EGFR signaling pathway [134]. This suggested that UVB light could be used to modulate the inactivation of EGFR and the EGFR signaling pathway and thereby to explore as an alternative treatment approach for cancer. Herein, this hypothesis was further investigated. In particular, the work presented in this PhD dissertation provided further insight onto the mechanisms and the structural changes that result in the inactivation of EGFR with UVB-light. The findings demonstrated that prolonged UVB illumination of the extra-cellular domain of EGFR (sEGFR) lead to profound conformational changes on the protein concurrent with the progressive exposure of its Trp pool, loss of protein secondary structural content and loss of the native thermal unfolding behavior of the protein. These UVB-induced conformational changes were correlated with the cleavage of several of its disulphide bonds and the progressive formation of Trp and Tyr photoproducts such as dityrosine, N-formylkyneurenine and kyneurenine. These structural and chemical modifications can affect the native interactions of dimer interface of sEGFR, where aromatic residues and disulphide bonds are known to play a critical role, and therefore hinder the dimerization of EGFR. On the other hand, EGFR UVB inactivation could also be resultant of structural changes on the EGF binding site, which would impair the correct binding to ligands such as EGF and thus prevent the dimerization of EGFR. This was confirmed by using a protein immunoassay, which showed that UVB-illumination of sEGFR compromised the 3D structure of the EGF binding site in the protein. The docking of EGF to sEGFR is dependent on extensive non-covalent and Van der Vaals interactions between the two molecules, including π-π interactions that included one of the aromatic residues of the protein. Therefore, it is likely that chemical and structural changes mentioned above also contribute for disrupting the native tertiary fold that promotes sEGFR-EGF contacts.

These findings provide unambiguous evidence for the existence of UVB induced structural modifications in EFGR, resulting in structural changes in the EGF binding site and loss of function. For a protein of its size, sEGFR is unusually rich in disulphide bonds (see section 2.2.3). Together with the high number of aromatic residues that it contains, it makes this receptor as a major putative target of photoxidation in cells. These observations provide strong indications that EGFR is uniquely susceptible to UVB excitation and that UV light will most likely also change the structure/function of the extracellular domain of EGFR when present in the cell surface of cancer cells overexpressing EGFR, halting this way EGF-EGFR activation and EGFR dependent key metabolic pathways. This is supported by the previous results obtained by the Nanobiotechnology group that document the arrest of the EGFR pathway upon UVB illumination of cancer cells overexpressing EGFR [134]. There will still a long road ahead for the practical use of this approach as a therapy for the local treatment of cancer cells. In particular, it is essential to gather more information on the molecular mechanisms that are activated upon UV illumination of cells overexpressing EGFR. At the cellular level, the photochemical mechanisms are exceedingly more complex than at the scale of the single protein and may involve reactions with other UV sensitizers and other reaction intermediates (*e.g.* $^1O_2$, $O_2^{\bullet -}$, H_2O_2 and other peroxides) that are generated upon exposure to UV light [65].

It is important to emphasize that UV illumination does not always necessarily lead to protein denaturation and loss of activity. A striking example is human plasminogen, which was another protein studied during this PhD work. The results of this research demonstrate that it may be actually possible to induce the activation of this pro-enzyme with UV light. The investigation on the effects of the UV light on structure and function of human plasminogen is included as a supporting publication (Paper 6) and can be found in the Appendix, section 8.3. Plasminogen is a large and complex protein constituted by seven independently folded domains. It comprises a considerable number of aromatic residues (19 Trp and 30 Tyr), which are present in all seven domains of the protein. Plasminogen contains 24 disulphide bonds that serve different purposes within the protein, including the structural stabilization of the kringle domains or the restriction of the activation loop. The high number of aromatic residues and disulphide bonds makes this protein a likely target for photo-oxidation. In fact, the excitation of plasminogen with a low dose of UV light (10 min at 280 nm, 2.1 $W.m^{-2}$) resulted in UV mediated disulphide bond disruption and formation of products of photooxidation such as dityrosine and N-formylkynurenine. Despite the occurrence of chemical modifications and structural changes, most of the native fold of plasminogen was retained upon UV illumination. Most importantly, exposure to plasminogen to 280 nm light in similar illumination conditions resulted in an increase of its proteolytic activity *in vitro*. These findings suggest that this pro-enzyme can be activated upon UV exposure to its active form plasmin. This is a promising study that could have a potential impact for the development of alternatives to the existing plasminogen activators (e.g streptokinase) used in clinical therapy as thrombolytical agents for treatment of blood clotting disorders, e.g. myocardical infarction.

Further investigations are still required to uncover the mechanisms involved in the activation of this pro-enzyme upon UV excitation.

The overall results obtained during this PhD work show that the response of proteins to UV radiation strongly depends on the UV illumination conditions (e.g. exposure wavelength, power and illumination time) and on the type of protein that is being studied. In this respect, the native features of the protein are of particular importance, including the number and location of their UV absorbing groups and their microenvironment, as well as, the three-dimensional structure of the protein and adopted fold in solution. It was possible to identify some of the major molecular mechanisms that are activated upon excitation of its aromatic residues, including e.g. UV mediated disulphide disruption, dityrosine cross-linking and formation of other photo-products such as N-formylkyneurenine and kyneurenine. These photophysical and photochemical pathways largely determine the extent of the conformational changes suffered by the proteins, and how its structure and function will be affected upon exposure to UV light.

There are many challenges that need to be tackled to fully understand the molecular mechanisms addressed in this work and particularly disulphide bond disruption. These proteins contain several UV absorbing groups and disulphide bonds, which are located in particular microenvironments within the protein fold and thereby may undergo distinct photophysical and photochemical reactions. The resultant chemical species and local structural changes are complex and difficult to discriminate using spectroscopic tools, such as protein fluorescence and circular dichroism spectroscopy, which provide global information on the aromatic residues and protein structure. In this respect, it would be relevant to detect possible chemical modifications occurring in these specific protein residues upon UV excitation, e.g. identifying which specific disulphide bonds are broken upon UV excitation of the aromatic residues. This could be achieved by using mass-spectrometry tools such as MALDI-TOF-TOF-MS (Matrix-assisted laser desorption/ionization time-of-flight mass spectrometry). Such studies could provide detailed information to complement the results presented herein.

5.2 Construction of nanoparticle based bioconjugates

The second part of the PhD project consisted on developing novel bioconjugates of proteins and nanoparticles to be used in biomedical applications (e.g. as biosensors, nanocarriers for targeted protein therapeutics and drug delivery). It included the development of three functional nanoparticle bioconjugates (Papers 4, 5 and one unpublished scientific work). The nanoparticle constructs were designed and engineered to have the necessary features for coupling proteins and addressing specific biomolecular applications. This was thoroughly described in Chapter 3 and in the Chapter 4 (Results). In this section, the major achievements and results obtained during the development of the nanoparticle bioconjugates in this PhD project will be discussed.

One of the main objectives of this PhD work was to exploit the light-assisted immobilization (LAMI) technique for immobilizing proteins onto the surface of functional nanoparticles. This was successfully achieved by immobilizing a model protein, BSA, onto core-shell gold iron oxide nanoparticles (Fe_3O_4@Au) (Paper 4). BSA was selected as a model because it is a well-studied protein and contains 17 disulphide bonds and 3 Trp residues, characteristics that indicated that UV mediated disulphide bond disruption would be likely to occur. This study involved the structural characterization of BSA upon exposure to UV light, synthesis and characterization of Fe_3O_4@Au nanoparticles, the coupling procedure with LAMI, and the characterization of the obtained nanoparticle bioconjugates (in particular the detection of the immobilized protein to confirm the success of coupling procedure).

The immobilization procedure was carried out in solution upon continuous illumination of a sample of BSA and Fe_3O_4@Au nanoparticles with 295 nm light, using a standard fluorescence spectrometer. The experimental conditions were optimized in order to promote the binding of BSA to the gold surface of the Fe_3O_4@Au upon Au-S covalent linkage. The illumination conditions (power and UV excitation time) used during the coupling procedure ensured the formation of free thiol groups required for LAMI coupling upon continuous excitation of BSA's Trp pool. This was verified by studying the structural features of the free protein in solution under the same illumination conditions used for coupling. More importantly, these findings also demonstrated that most of the structural features of BSA were retained after the same exposure period to UV light. One important parameter that was considered for the coupling reaction was the pH of the coupling buffer. The coupling procedure was carried out at pH 7.5, which ensured the pre-concentration of BSA molecules on the gold surface. Considering that the isoelectric point of BSA is 5.3, at pH 7.5 it was expected that BSA would have an overall negative charge, and thereby would interact electrostatically with the positively charge Au surface. Furthermore, at this pH value the created solvent accessible thiol groups in BSA would be most likely partly deprotonated, favouring the subsequent reaction and formation of covalent bonds with the Au surface.

The biomolecular coupling of BSA was verified by steady state fluorescence spectroscopy and microscopy, and UV visible spectroscopy. The obtained results showed that BSA was successfully immobilized onto the Fe_3O_4@Au nanoparticles after light-induced coupling. The degree of immobilization was found to be lower when the procedure was performed in the absence of UV light. This proved that BSA was indeed covalently bound to the nanoparticles due to covalent coupling with LAMI and not only upon electrostatic interaction between the protein and the Fe_3O_4@Au nanoparticles. The final BSA-Fe_3O_4@Au nanoparticle bioconjugates were further characterized using dynamic light scattering (DLS) and scanning electron microscopy (SEM). The results showed that the obtained nanoparticle bioconjugates consisted on nanostructures with sizes of several hundred of nm (in the range of 100-300 nm), much larger than the initial citrate coated Fe_3O_4@Au nanoparticles (~22 nm). This indicated that the light-induced coupling with BSA

may have lead to the progressive agglomeration of multiple Fe_3O_4@Au nanoparticles. The formation of intra-protein disulphide bonds between the coupled BSA molecules upon UV light excitation may be one of the causes for the observed nanoparticle agglomeration.

The overall findings of this investigation show that it is possible to use the LAMI procedure in solution for coupling proteins onto functional nanocarriers. Core-shell Fe_3O_4@Au nanoparticles are attractive constructs to develop nanoparticle bioconjugates because they combine in a single construct the magnetic properties of the iron oxide core and the optical properties of the gold coating (see section 3.1.1.3). As will be discussed later, the Fe_3O_4@Au nanoparticles used in this particular investigation did not contain yet the optimal magnetic features for their practical use as magnetic nanoparticle carriers. Nevertheless, the results presented in this work do prove the usefulness of the LAMI coupling technique to build novel protein nanocarriers. This procedure presents some advantages compared to other chemical immobilization techniques for coupling proteins to nanoparticles (see section 3.2.2.2). It does not for instance require the introduction of exogenous chemical groups on the protein. Furthermore, the number of washing steps is quite reduced (two in this case), which minimizes the loss of protein during the whole procedure.

There is still some improvement to be done in order to use and apply the LAMI procedure for the development of a functional nanoparticle bioconjugate construct. Firstly, it is not yet clear how the coupling procedure will affect the structure and function of the immobilized proteins. This would require further characterization of the nanoparticle bioconjugates and in particular the structure of the coupled protein. This might not be an easy task to perform while using classical spectroscopy techniques (e.g. circular dichroism spectroscopy or fluorescence spectroscopy) due to interference of the nanoparticles in the optical signal [219][219]. One way of addressing this issue can be to use a protein which function can be easily quantified (it is not the case of BSA). Secondly, it is important to mention that the immobilization procedure may lead to different orientations of the BSA molecules on the nanoparticle surface, since the coupling may occur through distinct thiol groups formed upon UV excitation of the protein. Finally, one should further investigate the mechanisms that lead to the observed nanoparticle agglomeration. During the coupling procedure any sort of nanoparticle agglomeration should be minimized, considering the importance of achieving a controlled nanoparticle bioconjugate size in view of its practical use in biomedical applications (see section 3.1.2).

During this PhD research, the plasmonic properties of coupled gold nanostructures were also exploited to enable the LAMI of BSA onto selective regions located in the interface of gold dimer arrays (Paper 5). As thoroughly described in section 3.2.2.2 this approach relied on exploring the localized electromagnetic field generated by the gold nanostructures to trigger three-photon excitation of the protein's aromatic residues and thereby initiate the LAMI process on the hotspot regions. In order to prove this concept, a series of experiments was performed where one particular parameter was controlled: first the laser power and then the resonance wavelength of

the gold dimers. Prior to the experiments, BSA was labeled with the Alexa Fluor 488 fluorophore in order detect and spatially localize BSA coupling on the array of gold nanostructures. The results obtained at different laser powers demonstrated that the pattern obtained for BSA immobilization was dependent on the laser beam's intensity. In particular, the extrinsic fluorescence from the coupled BSA was generally localized to the regions of higher infrared exposure. Another relevant observation was that the integrated Alexa fluor 488 fluorescence intensity (which is related to the amount of coupled protein) varied non-linearly in relation to the laser power. This proved that the immobilization process occurred in fact upon absorption of multiple infrared photons. In order to show that the protein binding was triggered by the plasmonic field generated at the LPSR of the gold dimers, arrays of gold dimers with distinct resonance wavelengths were exposed under identical illumination conditions. The highest immobilization yield was obtained with the array with the resonance closest to the exposing wavelength (810 nm), confirming that the optical near field dictated the immobilization of the protein.

It was left to verify if the protein immobilization achieved with this process could be restricted to the zones of most intense plasmonic field. This was confirmed by analyzing the gold nanostructures with scanning electron microscopy (SEM), where the immobilized protein location could observed as a dark "clouding" in the SEM image. This analysis was complemented by monitoring the shift in the LSPR wavelength of the gold dimers, which is known to shift upon protein binding to these surfaces (see section 3.1.1.2). In particular, this shift should be more pronounced when the immobilized molecules overlap with regions of most intense fields (hotspots). The results of this parallel analysis shown under optimized conditions (low laser powers) the immobilization of BSA could in fact be restricted to the gap region of the structure, corresponding to the highest shift of LSPR of the gold dimers.

This investigation demonstrated that it is possible to initiate the LAMI process upon three-photon excitation of the aromatic residues of proteins, which was achieved for the first time. Most relevantly, by exploiting the localized plasmonic field of the gold dimers, it was possible to restrict the immobilization of proteins to a 20 nm gap region, which is a considerable improvement in spatial resolution obtained with the LAMI process. Up to now, the LAMI technique only allowed to create high-density protein arrays with spot sizes of a few hundred nanometers since the resolution was restricted to the focusing ability of the light source.

Another novelty of this approach is that it allows to precisely place the coupled biomolecules on the specific plasmonic hotspot region, without the requirement of previously knowing the position of these hotspots. In this work this feature was exploited to automatically place nano-objects of interest at the position of most intense optical fields, by using the immobilized proteins as attachment points. This approach allowed to successfully attach individual gold nanospheres in or close to the region of the smallest gap between dimers. The self-alignment of gold nanospheres could be verified all along the gold dimer array, which shows the strength of this technique.

This feature can be explored in a wide range of research fields that exploit the interaction of an optical near field with minute amounts of matter. One can mention plasmon-enhanced optical spectroscopy techniques, such as surface-enhanced Raman spectroscopy, or infrared absorption spectroscopy, where the magnitude of the signal greatly depends on the overlap between the analyte and the hotspot. In the context of biomedical applications this approach can be particularly relevant for developing highly sensitive biosensor technologies. Protein detection is vital in biological study and medical diagnosis (e.g. cancer detection) and the improvement of the sensitivity of the current assays is of outmost importance [235]. By coupling the capture agents and the detection system to plasmonic hotspots, such as gold antennas (where the electromagnetic field is enhanced), it is possible, for instance, to increase tremendously the fluorescence signal obtained in fluorescence immunoassays [180, 235].

Another aim of this PhD project was to construct superparamagnetic nanoparticle carriers of strong magnetic response in view of their practical use in biomedical applications. This was achieved by developing a new type of magnetic nanocarrier based on the controlled agglomeration of several individual iron oxide nanoparticles onto colloidal nanoparticle clusters (CNCs) (unpublished scientific work). Human insulin was chosen as a model protein to couple to polyacrylic acid coated iron oxide CNCs (Fe_3O_4@PAA CNCs) by means of a carbodiimide base chemistry aiming at targeting the insulin receptor in cells. This study involved the synthesis and characterization of Fe_3O_4@PAA CNCs, the carbodiimide coupling procedure with insulin and the characterization of the obtained nanoparticle bioconjugates.

The first part of this study involved the synthesis of the Fe_3O_4@PAA CNCs constructs and characterization of their physico-chemical properties. The Fe_3O_4@PAA CNCs were synthesized using a high-temperature thermolysis approach. The obtained nanoconstructs were characterized with scanning electron microscopy, which confirmed the formation of the flower-like CNCs structures encompassing multiple Fe_3O_4 nanoparticles. Prior to the immobilization procedure, it was required to verify if the synthesized Fe_3O_4@PAA CNCs would carry the necessary features to be practically used as magnetic nanocarriers. This was done by studying the behavior and magnetic properties of obtained CNCs-insulin in aqueous solution upon characterization for hydrodynamic particle size, agglomeration state and magnetic separation. The obtained results demonstrated that the obtained Fe_3O_4@PAA CNCs could be efficiently separated from aqueous solution in matter of minutes by using a permanent magnet. Most importantly, the Fe_3O_4@PAA CNCs could be efficiently re-dispersed after separation, which confirmed its superparamagnetic nature in solution.

The second part of the study involved the optimization of the coupling process of insulin with the Fe_3O_4@PAA CNCs. Insulin was immobilized onto the polyacrilic acid surface of Fe_3O_4@PAA CNCs using a conventional chemistry based on a carbodiide reagent, 1-ethyl-3-(3-dimethylaminopropyl) carbodiimide (EDC) and N-hydroxylsulfosuccinimide (sulfo-NHS). The optimization of the coupling

procedure involved the testing of two different EDC/ sulfo-NHS approaches, which differed in the inclusion of a pre-concentration step, prior to the coupling reaction. Immobilization procedures using EDC/sulfo-NHS chemistry usually include this pre-concentration step in order to bring the protein in close proximity of surface carboxyls and thereby promote the coupling between the protein and the surface. The biomolecular coupling of insulin was then verified using both an adapted Coomassie assay for nanoparticles and a radioimmunoassay. The obtained results demonstrated that the immobilization procedure with EDC/sulfo-NHS was more efficient when the pre-concentration step was not included, which indicates that for small molecules like insulin it is preferable to omit this step and change other reaction parameters. The detection techniques used in this study also addressed some of the limitations typically encountered during the characterization of nanoparticle bioconjugates. In particular, the inverted Coomassie assay may be an interesting alternative to standard colorimetric assays for detection of proteins, which are hampered in many cases by the interference of nanoparticles in the optical signal. Both of the detection techniques still require improvement, namely to allow to quantify the amount of immobilized protein.

The last part of the work involved the physico-chemical characterization of the obtained CNCs-insulin bioconjugates, namely the analysis of its behavior and magnetic properties of in aqueous solution. The obtained results demonstrated that the coupling procedure with EDC/sulfo-NHS resulted in an extended particle loss and moderate CNCs agglomeration (from an initial size of ~142 nm to a final size of ~207 nm). These findings indicate that bioconjugation procedure needs further optimization. Nonetheless, the final obtained CNCs-insulin still presented the desired physico-chemical properties, namely a high magnetization in solution, together with superparamagnetism. In order to illustrate the strength of the magnetic response of the Fe_3O_4 CNCs nanoparticle bioconjugates, one can refer to the Fe_3O_4@Au nanoparticles that were synthesized during the study described in Paper 4. In that study it was shown that the non-derivatized Fe_3O_4@Au nanoparticles (~22 nm) could be also separated with a permanent magnet. However, this process was time-consuming and in order to achieve an efficient separation several hours were needed. In the present study, by using Fe_3O_4 CNCs, it was possible to achieve an efficient magnetic separation within 10-15 minutes, even after bioconjugation.

The high magnetization and superparamagnetic behavior of the CNCs bioconjugates makes them promising candidates for future use in targeted drug delivery and bioseparation. In order to fully demonstrate the applicability of the CNCs bioconjugates for targeted protein therapeutics, it would still be required to test the *in vitro* function of the CNCs-insulin by monitoring their interaction with cellular components. The biological activity of the CNCs-insulin bioconjugates could be tested by monitoring the glucose uptake by skeletal muscle cells. Furthermore, one could try to isolate specific cells by magnetic separation upon binding of the CNCs-insulin to the insulin receptor.

It is important to mention that the magnetic nanoparticle carriers assembled during this PhD research are still far from being a final product that could be used in biomedical applications, such as targeted drug delivery. Herein, only the preliminary steps of the engineering process were addressed, namely the synthesis of the nanoparticle carriers and the bioconjugation with functional proteins. In order to be used for *in vivo* applications, these nanocarriers have to possess additional features. In particular it might be required to change the surface coating of the nanocarriers in order to avoid an adverse immune response. As discussed in section 3.1.2, when released into the blood stream, nanoparticles are prone to interaction with plasma proteins. The absorption of plasma proteins to the surface of the nanoparticles (opsonization) can lead to their recognition by the reticuloendothelial system and thereby to their removal from circulation [140, 142, 145, 196]. One way of addressing this issue is to modify the surface of the nanoparticles with hydrophilic molecules such as polytethylene glycol that can minimize opsonization through steric repulsion [145]. Another important issue regards the toxicity of the nanoconstructs, which should be of course tested in later stages of the process. In this respect, it is important to mention that there has been recently a wide concern about the long-term toxicity of iron oxide nanoparticles [185, 236]. Lately reports have shown that the degradation of iron oxide in physiological environments can increase the free radical production in cells and thereby lead to cell death [236, 237]. The overgrowing concerns on the toxicity of SPIONs even led to the removal of two of the iron oxide MRI agents present in the market [185]. These observations demonstrate the importance of performing toxicity studies in parallel with the development of magnetic nanoparticle constructs

To summarize, during this second part of this PhD project, it was possible to address several features related to the construction of nanoparticle bioconjugates, mostly related to the synthesis and bioconjugation procedures. It considered both the development of nanoparticle bioconjugates to be used as nanoparticle carriers (Paper 4 and unpublished scientific work) and the construction of nanoparticle based arrays (Paper 5). The overall results of this work illustrate some of the limitations related to the engineering of nanoparticle bioconjugates. In particular, the construction of nanoparticle carriers is challenging as these constructs are developed in solution, which makes them prone to agglomeration and changes in its physico-chemical properties. The bioconjugation procedures often also require distinct steps at particular experimental conditions, which may damage the coupled proteins, or again lead to nanoparticle agglomeration. The three studies herein presented also brought forth some new approaches and techniques, which can be valuable for further development of magnetic nanoparticle carriers and nanoparticle based biosensor arrays.

6 Conclusions

6.1 Investigation of light induced switches in proteins

The first part of this PhD project focused on the investigation of UV light switches in proteins and their usefulness for developing new protein-based therapies. The presented work provided new insights into some of mechanisms activated upon UV light excitation of proteins, in particular disulphide bond disruption and their implications to the structure of particular proteins. During the first part of the PhD research, three proteins were studied: bovine alpha-lactalbumin, human insulin and the epidermal growth factor receptor (EGFR)

The study on bovine alpha lactalbumin allowed to identify one of the main photophysical and photphysical mechanisms that leads to disulphide bond disruption in this protein, Trp photoionization from the S_1 state. Continuous UV exposure of alpha-lactalbumin results in conformational changes correlated with breakage of its disulphide bridges and leads to partial denaturation of this milk whey protein.

The study on human insulin demonstrated that exposure of this hormone to UV light can lead both to the disruption of its disulphide bonds and to permanent dimerization upon formation of dityrosine cross-links. Most importantly, these structural modifications result in the almost complete inactivation of the biological function of this hormone.

The results of the two previous studies are of particular relevance for the food and pharmaceutical industries. The observed UV induced structural modifications occurred within hours of UV exposure of alpha lactalbumin and insulin to irradiance levels close to the found in sunlight and other industrial lighting sources. These findings urge the need for additional investigations in industry regarding the impact of light exposure on products containing proteins.

Finally, the research of UV light induced mechanisms in proteins also involved the investigation of a light-induced protein switch in view of a new photonic therapy. This study focused on the UV inactivation of the epidermal growth factor receptor (EGFR), which overexpression has been is associated with tumor progression. The findings of this work provide evidence for the existence of UV induced structural changes in the EGF binding site that impair the dimerization and activation of the receptor. These results suggest that UV light can be used to modulate EGFR structure and thereby halt the EGFR signaling pathway as a new cancer photonic therapy.

6.2 Construction of nanoparticle based bioconjugates

The second research topic focused on the construction of bioconjugates of nanoparticles and proteins for biomedical applications, including biosensing, bioseparation and targeted drug delivery. The work showed a number of new nanotechological, chemical and photonic approaches which can be used for the construction of nanoparticle bioconjugates. It also addressed some of the challenges that are associated with the engineering process of different types of nanoconstructs. The experimental work included three different studies that involved the development of magnetic nanoparticle carriers or nanoparticle based arrays.

The first study involved the immobilization of a model protein, bovine serum albumin (BSA) onto the surface of gold coated iron oxide nanoparticles. The findings demonstrate that light assisted molecular immobilization (LAMI) can be successfully applied to couple proteins onto the surface of functional nanoparticles. This technique presents some advantages over other bioconjugation techniques. For instance, it does not require the introduction of foreign chemical groups onto the biomolecules. Biofunctionalization of superparamagnetic nanoparticles with LAMI can lead to the creation of novel optical biosensors and drug delivery constructs.

The LAMI technology was also exploited in the second study for immobilizing BSA onto plasmonic hot spots located in the interface of nanosized gold dimers. The enhanced near field generated by the coupled gold dimers was used to induce light induced coupling of BSA to the gold surface upon multi-photon excitation of its aromatic residues. Using this process it was possible obtain a relatively uniform array of gold dimer structures where BSA was selectively immobilized onto the 20 nm hotspot region between each dimer. Since the immobilized biomolecules are automatically placed in the zone of most intense plasmonic fields, this approach can be explored for developing highly sensitive biosensor arrays.

Finally, this PhD dissertation also showed proof of concept for a highly responsive superparamagnetic nanoparticle carrier, based on the agglomeration of several individual iron oxide nanoparticles onto colloidal nanoparticle clusters (CNCs). Insulin was coupled to the surface of the CNCs using carbodiimide chemistry aiming at targeting the insulin receptor in cells. The CNCs-insulin bioconjugates displayed a strong magnetic response in solution and could be efficiently separated within minutes. The superior magnetic properties of the CNCs bioconjugates are of outmost relevance for fields of drug delivery and bioseparation.

Summarizing, this PhD thesis provided relevant knowledge that can be most helpful for understanding UV light induced mechanisms in biomolecules and for the continuous development of new nanotehcnological approaches to diagnosis and therapeutics.

7 Bibliography

1. Petersen MT, Jonson PH, Petersen SB (1999) Amino acid neighbours and detailed conformational analysis of cysteines in proteins. Protein Eng 12:535–48.

2. Neves-Petersen MT, Snabe T, Klitgaard S, et al. (2006) Photonic activation of disulfide bridges achieves oriented protein immobilization on biosensor surfaces. Protein Sci 15:343–51. doi: 10.1110/ps.051885306

3. Duroux M, Skovsen E, Neves-Petersen MT, et al. (2007) Light-induced immobilisation of biomolecules as an attractive alternative to microdroplet dispensing-based arraying technologies. Proteomics 7:3491–9. doi: 10.1002/pmic.200700472

4. Parracino A, Neves-Petersen MT, di Gennaro AK, et al. (2010) Arraying prostate specific antigen PSA and Fab anti-PSA using light-assisted molecular immobilization technology. Protein Sci 19:1751–9. doi: 10.1002/pro.461

5. Neves-Petersen MT, Duroux M, Skovsen E, et al. (2009) Printing novel molecular architectures with micrometer resolution using light. J Nanosci Nanotechnol 9:3372–81.

6. Skovsen E, Kold AB, Neves-Petersen MT, Petersen SB (2009) Photonic immobilization of high-density protein arrays using Fourier optics. Proteomics 9:3945–8. doi: 10.1002/pmic.200800960

7. Petersen SB, Kold di Gennaro A, Neves-Petersen MT, et al. (2010) Immobilization of biomolecules onto surfaces according to ultraviolet light diffraction patterns. Appl Opt 49:5344–50.

8. Leader B, Baca QJ, Golan DE (2008) Protein therapeutics: a summary and pharmacological classification. Nat Rev Drug Discov 7:21–39. doi: 10.1038/nrd2399

9. Dimitrov DS (2012) Therapeutic proteins. Methods Mol Biol 899:1–26. doi: 10.1007/978-1-61779-921-1_1

10. Ruso JM, Piñeiro Á (2013) Proteins in Solution and at Interfaces: : Methods and Applications in Biotechnology and Materials Science. Proteins Solut Interfaces. doi: 10.1002/9781118523063.ch7

11. Narhi LO (2013) Chapter 1: Introduction. In: Narhi LO (ed) Biophys. Ther. Protein Dev. Springer New York, pp 1–5

12. Szilágyi A, Kardos J, Osváth S, et al. (2007) Protein Folding. In: Lajtha A, Banik N (eds) Handb. Neurochem. Mol. Neurobiol. SE - 10. Springer US, pp 303–343

13. Permyakov EA, Berliner LJ (2000) alpha-Lactalbumin: structure and function. FEBS Lett 473:269–74.

14. Chrysina ED, Brew K, Acharya KR (2000) Crystal structures of apo- and holo-bovine alpha-lactalbumin at 2. 2-A resolution reveal an effect of calcium on inter-lobe interactions. J Biol Chem 275:37021–9. doi: 10.1074/jbc.M004752200

15. Derewenda U, Derewenda Z, Dodson GG, et al. (1989) Molecular structure of insulin: the insulin monomer and its assembly. Br Med Bull 45:4–18.

16. Melmed S, Conn PM (2005) Endocrinology: Basic and Clinical Principles. 440.

17. (2003) Diabetes Mellitus: A Fundamental and Clinical Text. 1200.

18. Baker EN, Blundell TL, Cutfield JF, et al. (1988) The structure of 2Zn pig insulin crystals at 1.5 A resolution. Philos Trans R Soc Lond B Biol Sci 319:369–456.

19. Gualandi-Signorini a M, Giorgi G (2001) Insulin formulations--a review. Eur Rev Med Pharmacol Sci 5:73–83.

20. Haas J, Vöhringer-Martinez E, Bögehold A, et al. (2009) Primary steps of pH-dependent insulin aggregation kinetics are governed by conformational flexibility. Chembiochem 10:1816–22. doi: 10.1002/cbic.200900266

21. Booth NA, Bachmann F (2005) Plasminogen-Plasmin System. In: Colman RW, Marder VJ, Clowes AW, George JN (eds) Hemost. Thromb. Basic Princ. Clin. Pract. Lippincott Williams & Wilkins, pp 335–364

22. Collen D (2001) Ham-Wasserman Lecture: Role of the Plasminogen System in Fibrin-Homeostasis and Tissue Remodeling. Hematology 2001:1–9. doi: 10.1182/asheducation-2001.1.1

23. Robbins K, Summaria L (1976) Plasminogen and plasmin. Methods Enzymol 45:257.

24. Ogiso H, Ishitani R, Nureki O, et al. (2002) Crystal structure of the complex of human epidermal growth factor and receptor extracellular domains. Cell 110:775–87.

25. Han W, Lo H-W (2012) Landscape of EGFR signaling network in human cancers: biology and therapeutic response in relation to receptor subcellular locations. Cancer Lett 318:124–34. doi: 10.1016/j.canlet.2012.01.011

26. Suzuki S, Dobashi Y, Sakurai H, et al. (2005) Protein overexpression and gene amplification of epidermal growth factor receptor in nonsmall cell lung carcinomas. An immunohistochemical and fluorescence in situ hybridization study. Cancer 103:1265–73. doi: 10.1002/cncr.20909

27. Putman FW (1975) The Plasma Proteins: Structure, Function and Genetic Control, 2nd Editio. 141–147.

28. Kaplan LJ, Foster JF (1971) Isoelectric focusing behavior of bovine plasma albumin, mercaptalbumin, and beta-lactoglobulins A and B. Biochemistry 10:630–6.

29. Ramakrishnan B, Qasba PK (2001) Crystal structure of lactose synthase reveals a large conformational change in its catalytic component, the beta1,4-galactosyltransferase-I. J Mol Biol 310:205–18. doi: 10.1006/jmbi.2001.4757

30. Schultz CP (2000) Illuminating folding intermediates. Nat Struct Biol 7:7–10. doi: 10.1038/71197

31. Baker D (2000) A surprising simplicity to protein folding. Nature 405:39–42. doi: 10.1038/35011000

32. Eijsink VGH, Bjørk A, Gåseidnes S, et al. (2004) Rational engineering of enzyme stability. J Biotechnol 113:105–20. doi: 10.1016/j.jbiotec.2004.03.026

33. Trivedi M V, Laurence JS, Siahaan TJ (2009) The role of thiols and disulfides on protein stability. Curr Protein Pept Sci 10:614–25.

34. Bolen DW (2001) Protein Stabilization by Naturally Occurring Osmolytes. In: Murphy K (ed) Protein Struct. Stability, Fold. SE - 2. Humana Press, pp 17–36

35. Kendrick BS, Li T, Chang BS (2002) Physical stabilization of proteins in aqueous solution. Pharm Biotechnol 13:61–84.

36. Hovgaard L, Frokjaer S, van de Weert M (2012) Pharmaceutical Formulation Development of Peptides and Proteins, Second Edi. 2012:392.

37. Banga AK (2005) Therapeutic Peptides and Proteins: Formulation, Processing, and Delivery Systems, Second Edition. 376.

38. Allen G (1999) Protein: A Comprehensive Treatise, Jai Press . 318.

39. Chan HS, Bromberg S, Dill KA (1995) Models of cooperativity in protein folding. Philos Trans R Soc Lond B Biol Sci 348:61–70. doi: 10.1098/rstb.1995.0046

40. Li R, Woodward C (1999) The hydrogen exchange core and protein folding. Protein Sci 8:1571–90. doi: 10.1110/ps.8.8.1571

41. Kuwajima K (1996) The molten globule state of alpha-lactalbumin. FASEB J 10:102–9.

42. Polverino de Laureto P, Frare E, Gottardo R, Fontana A (2002) Molten globule of bovine alpha-lactalbumin at neutral pH induced by heat, trifluoroethanol, and oleic acid: a comparative analysis by circular dichroism spectroscopy and limited proteolysis. Proteins 49:385–97. doi: 10.1002/prot.10234

43. Brange J, Owens DR, Kang S, Vølund a (1990) Monomeric insulins and their experimental and clinical implications. Diabetes Care 13:923–54.

44. Becker RH a (2007) Insulin glulisine complementing basal insulins: a review of structure and activity. Diabetes Technol Ther 9:109–21. doi: 10.1089/dia.2006.0035

45. Schmidt B, Ho L, Hogg PJ (2006) Allosteric Disulfide Bonds. Biochemistry 45:7429–7433. doi: 10.1021/bi0603064

46. Chen VM, Hogg PJ (2006) Allosteric disulfide bonds in thrombosis and thrombolysis. J Thromb Haemost 4:2533–41. doi: 10.1111/j.1538-7836.2006.02236.x

47. Wong JWH, Ho SYW, Hogg PJ (2011) Disulfide Bond Acquisition through Eukaryotic Protein Evolution. Mol Biol Evol 28 :327–334. doi: 10.1093/molbev/msq194

48. Singh R, Whitesides GM (1993) Thiol—disulfide interchange. Sulphur-Containing Funct. Groups. John Wiley & Sons, Inc., pp 633–658.

49. Darby N, Creighton TE (1995) Disulfide Bonds in Protein Folding and Stability . Protein Stab Fold 40 :219–252.

50. Feige MJ, Buchner J (2009) The Role of Disulfide Bonds in Protein Folding and Stability. In: Moroder L, Buchner J (eds) Oxidative Fold. Pept. Proteins. RSC Publishing, Cambridge, United Kingdom, pp 179–191.

51. Ventura S, Chang RJY (2011) Oxidative Folding: Coupling Conformational Folding and Disulfide Formation. In: Ventura S, Chang RJY (eds) Fold. Disulfide Proteins. Springer, New York, NY, USA, pp 1–6.

52. Lo Conte M, Carroll K (2013) The Chemistry of Thiol Oxidation and Detection. In: Jakob U, Reichmann D (eds) Oxidative Stress Redox Regul. SE - 1. Springer Netherlands, pp 1–42

53. Hogg PJ (2003) Disulfide bonds as switches for protein function. Trends Biochem Sci 28:210–4. doi: 10.1016/S0968-0004(03)00057-4

54. Darby N, Creighton T (1997) Probing protein folding and stability using disulfide bonds. Mol Biotechnol 7:57–77. doi: 10.1007/BF02821544

55. Góngora-Benítez M, Tulla-Puche J, Albericio F (2013) Multifaceted Roles of Disulfide Bonds. Peptides as Therapeutics. Chem Rev. doi: 10.1021/cr400031z

56. Schmidt B, Hogg PJ (2007) Search for allosteric disulfide bonds in NMR structures. BMC Struct Biol 7:49. doi: 10.1186/1472-6807-7-49

57. Thornton JM (1981) Disulphide bridges in globular proteins. J Mol Biol 151:261–87.

58. Fass D (2012) Disulfide bonding in protein biophysics. Annu Rev Biophys 41:63–79. doi: 10.1146/annurev-biophys-050511-102321

59. Carugo O, Cemazar M, Zahariev S, et al. (2003) Vicinal disulfide turns. Protein Eng 16:637–9.

60. Creighton TE (1988) Disulphide bonds and protein stability. Bioessays 8:57–63. doi: 10.1002/bies.950080204

61. Dill KA (1985) Theory for the folding and stability of globular proteins. Biochemistry 24:1501–9.

62. Ioerger TR, Du C, Linthicum DS (1999) Conservation of cys–cys trp structural triads and their geometry in the protein domains of immunoglobulin superfamily members. Mol Immunol 36:373–386. doi: 10.1016/S0161-5890(99)00032-2

63. Neves-Petersen MT, Gryczynski Z, Lakowicz J, et al. (2002) High probability of disrupting a disulphide bridge mediated by an endogenous excited tryptophan residue. Protein Sci 11:588–600. doi: 10.1110/ps.06002

64. Kerwin BA, Remmele RL (2007) Protect from light : photodegradation and protein biologics. 96:1468–1479. doi: 10.1002/jps

65. Pattison DI, Rahmanto AS, Davies MJ (2012) Photo-oxidation of proteins. Photochem Photobiol Sci 11:38–53. doi: 10.1039/c1pp05164d

66. Sinha RP, Häder DP (2002) UV-induced DNA damage and repair: a review. Photochem Photobiol Sci 1:225–36.

67. Matsumura Y, Ananthaswamy HN (2004) Toxic effects of ultraviolet radiation on the skin. Toxicol Appl Pharmacol 195:298–308. doi: 10.1016/j.taap.2003.08.019

68. Davies MJ, Truscott RJW (2001) Photo-oxidation of proteins and its role in cataractogenesis. J Photochem Photobiol B Biol 63:114–125. doi: 10.1016/S1011-1344(01)00208-1

69. Correia M, Neves-Petersen MTM, Parracino A, et al. (2012) Photophysics, photochemistry and energetics of UV light induced disulphide bridge disruption in apo-α-lactalbumin. J Fluoresc 22:323–37. doi: 10.1007/s10895-011-0963-7

70. Fasman GD (1976) Handbook of Biochemistry and Molecular Biology, Proteins, Volume I, 3rd ed. 183–203.

71. Lakowicz JR (2006) Principles of Fluorescence Spectroscopy, 3rd ed. Springer

72. Neves-Petersen MT, Klitgaard S, Pascher T, et al. (2009) Flash photolysis of cutinase: identification and decay kinetics of transient intermediates formed upon UV excitation of aromatic residues. Biophys J 97:211–26. doi: 10.1016/j.bpj.2009.01.065

73. Creed D (1984) The photophysics and photochemistry of the near-uv absorbing amino acids–I. Tryptophan and its simple derivatives. Photochem Photobiol 39:537–562. doi: 10.1111/j.1751-1097.1984.tb03890.x

74. Bent D V, Hayon E (1975) Excited state chemistry of aromatic amino acids and related peptides. III. Tryptophan. J Am Chem Soc 97:2612–9.

75. Mialocq JC, Amouyal E, Bernas A, Grand D (1982) Picosecond laser photolysis of aqueous indole and tryptophan. J Phys Chem 86:3173–3177. doi: 10.1021/j100213a022

76. Peon J, Hess GC, Pecourt J-ML, et al. (1999) Ultrafast Photoionization Dynamics of Indole in Water. J Phys Chem A 103:2460–2466. doi: 10.1021/jp9840782

77. Fukunaga Y, Katsuragi Y, Izumi T, Sakiyama F (1982) Fluorescence characteristics of kynurenine and N'-formylkynurenine. Their use as reporters of the environment of tryptophan 62 in hen egg-white lysozyme. J Biochem 92:129–41.

78. Finley EL, Busman M, Dillon J, et al. (1997) Identification of photooxidation sites in bovine alpha-crystallin. Photochem Photobiol 66:635–41.

79. Creed D (1984) The photophysics and photochemistry of the near-uv absorbing amino acids–II. Tyrosine and its simple derivatives. Photochem Photobiol 39:563–575. doi: 10.1111/j.1751-1097.1984.tb03891.x

80. Hoffman MZ, Hayon E (1972) One-electron reduction of the disulfide linkage in aqueous solution. Formation, protonation, and decay kinetics of the RSSR- radical. J Am Chem Soc 94:7950–7957. doi: 10.1021/ja00778a002

81. Bent D V, Hayon E (1975) Excited state chemistry of aromatic amino acids and related peptides. I. Tyrosine. J Am Chem Soc 97:2599–2606.

82. Malencik D a, Anderson SR (2003) Dityrosine as a product of oxidative stress and fluorescent probe. Amino Acids 25:233–47. doi: 10.1007/s00726-003-0014-z

83. Giulivi C, Traaseth NJ, Davies KJ a (2003) Tyrosine oxidation products: analysis and biological relevance. Amino Acids 25:227–32. doi: 10.1007/s00726-003-0013-0

84. Giulivi C, Davies KJ (1994) Dityrosine: a marker for oxidatively modified proteins and selective proteolysis. Methods Enzymol 233:363–71.

85. Jacob JS, Cistola DP, Hsu FF, et al. (1996) Human phagocytes employ the myeloperoxidase-hydrogen peroxide system to synthesize dityrosine, trityrosine, pulcherosine, and isodityrosine by a tyrosyl radical-dependent pathway. J Biol Chem 271:19950–6.

86. Brady JD, Sadler IH, Fry SC (1996) Di-isodityrosine, a novel tetrametric derivative of tyrosine in plant cell wall proteins: a new potential cross-link. Biochem J 315 (Pt 1:323–7.

87. McCormick ML, Gaut JP, Lin TS, et al. (1998) Electron paramagnetic resonance detection of free tyrosyl radical generated by myeloperoxidase, lactoperoxidase, and horseradish peroxidase. J Biol Chem 273:32030–7.

88. Tew D, Ortiz de Montellano PR (1988) The myoglobin protein radical. Coupling of Tyr-103 to Tyr-151 in the H2O2-mediated cross-linking of sperm whale myoglobin. J Biol Chem 263:17880–6.

89. Aeschbach R, Amadoò R, Neukom H (1976) Formation of dityrosine cross-links in proteins by oxidation of tyrosine residues. Biochim Biophys Acta - Protein Struct 439:292–301. doi: 10.1016/0005-2795(76)90064-7

90. Kanwar R, Balasubramanian D (2000) Structural studies on some dityrosine-cross-linked globular proteins: stability is weakened, but activity is not abolished. Biochemistry 39:14976–83.

91. Shen H-R, Spikes JD, Smith CJ, Kopeček J (2000) Photodynamic cross-linking of proteins. J Photochem Photobiol A Chem 133:115–122. doi: 10.1016/S1010-6030(00)00228-8

92. Lehrer SS, Fasman GD (1967) Ultraviolet irradiation effects in poly-L-tyrosine and model compounds. Identification of bityrosine as a photoproduct. Biochemistry 6:757–67.

93. Malencik DA, Anderson SR (1991) Fluorometric characterization of dityrosine: complex formation with boric acid and borate ion. Biochem Biophys Res Commun 178:60–7.

94. Kahn PC (1979) The interpretation of near-ultraviolet circular dichroism. Methods Enzymol 61:339–78.

95. Klitgaard S, Neves-Petersen MT, Petersen SB (2006) Quenchers induce wavelength dependence on protein fluorescence lifetimes. J Fluoresc 16:595–609. doi: 10.1007/s10895-006-0081-0

96. Grossweiner LI, Usui Y (1971) Flash photolysis and inactivation of aqueous lysozyme. Photochem Photobiol 13:195–214.

97. Wu L-Z, Sheng Y-B, Xie J-B, Wang W (2008) Photoexcitation of tryptophan groups induced reduction of disulfide bonds in hen egg white lysozyme. J Mol Struct 882:101–106. doi: 10.1016/j.molstruc.2007.09.016

98. Prompers JJ, Hilbers CW, Pepermans HA (1999) Tryptophan mediated photoreduction of disulfide bond causes unusual fluorescence behaviour of Fusarium solani pisi cutinase. FEBS Lett 456:409–16.

99. Miller BL, Hageman MJ, Thamann TJ, et al. (2003) Solid-state photodegradation of bovine somatotropin (bovine growth hormone): evidence for tryptophan-mediated photooxidation of disulfide bonds. J Pharm Sci 92:1698–709. doi: 10.1002/jps.10418

100. Permyakov EA, Permyakov SE, Deikus GY, et al. (2003) Ultraviolet illumination-induced reduction of alpha-lactalbumin disulfide bridges. Proteins 51:498–503. doi: 10.1002/prot.10371

101. Vanhooren A, De Vriendt K, Devreese B, et al. (2006) Selectivity of tryptophan residues in mediating photolysis of disulfide bridges in goat alpha-lactalbumin. Biochemistry 45:2085–93. doi: 10.1021/bi0517638

102. Vanhooren A, Devreese B, Vanhee K, et al. (2002) Photoexcitation of tryptophan groups induces reduction of two disulfide bonds in goat alpha-lactalbumin. Biochemistry 41:11035–43.

103. Noronha M, Lima JC, Paci E, et al. (2007) Tracking local conformational changes of ribonuclease A using picosecond time-resolved fluorescence of the six tyrosine residues. Biophys J 92:4401–14. doi: 10.1529/biophysj.106.093625

104. Li Z, Lee WE, Galley WC (1989) Distance dependence of the tryptophan-disulfide interaction at the triplet level from pulsed phosphorescence studies on a model system. Biophys J 56:361–367. doi: http://dx.doi.org/10.1016/S0006-3495(89)82682-7

105. Dalsgaard TK, Otzen D, Nielsen JH, Larsen LB (2007) Changes in structures of milk proteins upon photo-oxidation. J Agric Food Chem 55:10968–76. doi: 10.1021/jf071948g

106. Redecke L, Binder S, Elmallah MIY, et al. (2009) UV-light-induced conversion and aggregation of prion proteins. Free Radic Biol Med 46:1353–61. doi: 10.1016/j.freeradbiomed.2009.02.013

107. Roy S, Mason BD, Schöneich CS, et al. (2009) Light-induced aggregation of type I soluble tumor necrosis factor receptor. J Pharm Sci 98:3182–99. doi: 10.1002/jps.21750

108. Wang W, Nema S, Teagarden D (2010) Protein aggregation--pathways and influencing factors. Int J Pharm 390:89–99. doi: 10.1016/j.ijpharm.2010.02.025

109. Agon V V, Bubb WA, Wright A, et al. (2006) Sensitizer-mediated photooxidation of histidine residues: evidence for the formation of reactive side-chain peroxides. Free Radic Biol Med 40:698–710. doi: 10.1016/j.freeradbiomed.2005.09.039

110. Shen HR, Spikes JD, Kopeceková P, Kopecek J (1996) Photodynamic crosslinking of proteins. I. Model studies using histidine- and lysine-containing N-(2-hydroxypropyl)methacrylamide copolymers. J Photochem Photobiol B 34:203–10.

111. Grossweiner LI, Blum A, Brendzel AM (1982) Primary Processes in the Photochemistry of Proteins. In: Hélène C, Charlier M, Montenay-Garestier T, Laustriat G (eds) Trends Photobiol. SE - 7. Springer US, pp 67–80

112. Kaplan EH, Campbell ED, McLaren AD (1950) Photochemistry of proteins VIII. Inactivation of insulin by ultraviolet light. Biochim Biophys Acta 4:493–500. doi: 10.1016/0006-3002(50)90055-2

113. Sander CS, Chang H, Salzmann S, et al. (2002) Photoaging is associated with protein oxidation in human skin in vivo. J Invest Dermatol 118:618–25. doi: 10.1046/j.1523-1747.2002.01708.x

114. Smith GJ (1995) New trends in photobiology (invited review) photodegradation of keratin and other structural proteins. J Photochem Photobiol B Biol 27:187–198. doi: 10.1016/1011-1344(94)07104-V

115. Wlaschek M, Tantcheva-Poór I, Naderi L, et al. (2001) Solar UV irradiation and dermal photoaging. J Photochem Photobiol B 63:41–51.

116. Wondrak GT, Jacobson MK, Jacobson EL (2006) Endogenous UVA-photosensitizers: mediators of skin photodamage and novel targets for skin photoprotection. Photochem Photobiol Sci 5:215–37. doi: 10.1039/b504573h

117. Black HS, deGruijl FR, Forbes PD, et al. (1997) Photocarcinogenesis: an overview. J Photochem Photobiol B 40:29–47.

118. Pattison DI, Davies MJ (2006) Actions of ultraviolet light on cellular structures. EXS 131–57.

119. Rathore N, Rajan RS (2008) Current Perspectives on Stability of Protein Drug Products during Formulation , Fill and Finish Operations. 504–514.

120. Hawe A, Wiggenhorn M, van de Weert M, et al. (2012) Forced degradation of therapeutic proteins. J Pharm Sci 101:895–913. doi: 10.1002/jps.22812

121. Koutchma T (2009) Advances in Ultraviolet Light Technology for Non-thermal Processing of Liquid Foods. Food Bioprocess Technol 2:138–155. doi: 10.1007/s11947-008-0178-3

122. Phillips D (2010) Light relief: photochemistry and medicine. Photochem Photobiol Sci 9:1589–96. doi: 10.1039/c0pp00237b

123. Pervaiz S, Olivo M (2006) Art and science of photodynamic therapy. Clin Exp Pharmacol Physiol 33:551–6. doi: 10.1111/j.1440-1681.2006.04406.x

124. Choudhary S, Nouri K, Elsaie ML (2009) Photodynamic therapy in dermatology: a review. Lasers Med Sci 24:971–80. doi: 10.1007/s10103-009-0716-x

125. Rockson SG, Lorenz DP, Cheong WF, Woodburn KW (2000) Photoangioplasty: An emerging clinical cardiovascular role for photodynamic therapy. Circulation 102:591–6.

126. Konopka K, Goslinski T (2007) Photodynamic therapy in dentistry. J Dent Res 86:694–707.

127. Curley K, Lawrence DS (1999) Light-activated proteins. Curr Opin Chem Biol 3:84–8.

128. Riggsbee CW, Deiters A (2010) Recent advances in the photochemical control of protein function. Trends Biotechnol 28:468–75. doi: 10.1016/j.tibtech.2010.06.001

129. Mayer G, Heckel A (2006) Biologically active molecules with a “light switch”. Angew Chem Int Ed Engl 45:4900–21. doi: 10.1002/anie.200600387

130. Lemke EA, Summerer D, Geierstanger BH, et al. (2007) Control of protein phosphorylation with a genetically encoded photocaged amino acid. Nat Chem Biol 3:769—772. doi: 10.1038/nchembio.2007.44

131. Yazawa M, Sadaghiani AM, Hsueh B, Dolmetsch RE (2009) Induction of protein-protein interactions in live cells using light. Nat Biotechnol 27:941–5. doi: 10.1038/nbt.1569

132. Neves-Petersen MT, Petersen S, Gajula GP (2012) UV Light Effects on Proteins: From Photochemistry to Nanomedicine. In: Saha S (ed) Mol. Photochem. - Var. Asp. InTech, pp 125–158

133. Noonberg SB, Benz CC (2000) Tyrosine kinase inhibitors targeted to the epidermal growth factor receptor subfamily: role as anticancer agents. Drugs 59:753–67.

134. Olsen BB, Neves-Petersen MT, Klitgaard S, et al. (2007) UV light blocks EGFR signalling in human cancer cell lines. Int J Oncol 30:181–5.

135. Arruebo M, Fernández-Pacheco R, Ibarra MR, Santamaría J (2007) Magnetic nanoparticles for drug delivery. Nano Today 2:22–32. doi: http://dx.doi.org/10.1016/S1748-0132(07)70084-1

136. ISO (2008) ISO/TS 27687 Nanotechnologies – Terminology and definitions for nano-objects – Nanoparticles, nanofibres and nanoplates. Geneva

137. Zhang L, Gu FX, Chan JM, et al. (2008) Nanoparticles in medicine: therapeutic applications and developments. Clin Pharmacol Ther 83:761–9. doi: 10.1038/sj.clpt.6100400

138. Di Marco M, Shamsuddin S, Razak KA, et al. (2010) Overview of the main methods used to combine proteins with nanosystems: absorption, bioconjugation, and encapsulation. Int J Nanomedicine 5:37–49.

139. Mody V V, Siwale R, Singh A, Mody HR (2010) Introduction to metallic nanoparticles. J Pharm Bioallied Sci 2:282–9. doi: 10.4103/0975-7406.72127

140. Faraji AH, Wipf P (2009) Nanoparticles in cellular drug delivery. Bioorg Med Chem 17:2950–62. doi: 10.1016/j.bmc.2009.02.043

141. Mishra B, Patel BB, Tiwari S (2010) Colloidal nanocarriers: a review on formulation technology, types and applications toward targeted drug delivery. Nanomedicine 6:9–24. doi: 10.1016/j.nano.2009.04.008

142. Singh R, Lillard JW (2009) Nanoparticle-based targeted drug delivery. Exp Mol Pathol 86:215–23. doi: 10.1016/j.yexmp.2008.12.004

143. Laurent S, Mahmoudi M (2011) Superparamagnetic iron oxide nanoparticles: promises for diagnosis and treatment of cancer. Int J Mol Epidemiol Genet 2:367–90.

144. Shipway AN, Katz E, Willner I (2000) Nanoparticle Arrays on Surfaces for Electronic, Optical, and Sensor Applications . ChemPhysChem 1:18–52. doi: 10.1002/1439-7641(20000804)1:1<18::AID-CPHC18>3.0.CO;2-L

145. Veiseh O, Gunn JW, Zhang M (2010) Design and fabrication of magnetic nanoparticles for targeted drug delivery and imaging. Adv Drug Deliv Rev 62:284–304. doi: 10.1016/j.addr.2009.11.002

146. Nie Z, Petukhova A, Kumacheva E (2010) Properties and emerging applications of self-assembled structures made from inorganic nanoparticles. Nat Nano 5:15–25.

147. Lu Z, Yin Y (2012) Colloidal nanoparticle clusters: functional materials by design. Chem Soc Rev 41:6874–6887. doi: 10.1039/C2CS35197H

148. Tiwari PM, Vig K, Dennis VA, Singh SR (2011) Functionalized Gold Nanoparticles and Their Biomedical Applications. Nanomaterials 1:31–63. doi: 10.3390/nano1010031

149. Wang L, Zhao W, Tan W (2008) Bioconjugated silica nanoparticles: Development and applications. Nano Res 1:99–115. doi: 10.1007/s12274-008-8018-3

150. Gupta AK, Gupta M (2005) Synthesis and surface engineering of iron oxide nanoparticles for biomedical applications. Biomaterials 26:3995–4021. doi: 10.1016/j.biomaterials.2004.10.012

151. Lynch I, Dawson KA (2008) Protein-nanoparticle interactions. Nano Today 3:40–47. doi: 10.1016/S1748-0132(08)70014-8

152. Parracino A, Gajula GP, di Gennaro AK, et al. (2011) Towards nanoscale biomedical devices in medicine: biofunctional and spectroscopic characterization of superparamagnetic nanoparticles. J Fluoresc 21:663–72. doi: 10.1007/s10895-010-0754-6

153. Li Y, Xu X, Deng C, et al. (2007) Immobilization of trypsin on superparamagnetic nanoparticles for rapid and effective proteolysis. J Proteome Res 6:3849–55. doi: 10.1021/pr070132s

154. Li D, He Q, Cui Y, et al. (2007) Immobilization of glucose oxidase onto gold nanoparticles with enhanced thermostability. Biochem Biophys Res Commun 355:488–93. doi: 10.1016/j.bbrc.2007.01.183

155. Reddy LH, Arias JL, Nicolas J, Couvreur P (2012) Magnetic nanoparticles: design and characterization, toxicity and biocompatibility, pharmaceutical and biomedical applications. Chem Rev 112:5818–78. doi: 10.1021/cr300068p

156. Ito A, Shinkai M, Honda H, Kobayashi T (2005) Medical application of functionalized magnetic nanoparticles. J Biosci Bioeng 100:1–11. doi: 10.1263/jbb.100.1

157. Pankhurst QA, Thanh NTK, Jones SK, Dobson J (2009) Progress in applications of magnetic nanoparticles in biomedicine. J Phys D Appl Phys 42:224001.

158. Neuberger T, Schöpf B, Hofmann H, et al. (2005) Superparamagnetic nanoparticles for biomedical applications: Possibilities and limitations of a new drug delivery system. J Magn Magn Mater 293:483–496. doi: http://dx.doi.org/10.1016/j.jmmm.2005.01.064

159. Laurent S, Forge D, Port M, et al. (2008) Magnetic iron oxide nanoparticles: synthesis, stabilization, vectorization, physicochemical characterizations, and biological applications. Chem Rev 108:2064–110. doi: 10.1021/cr068445e

160. Lübbe AS, Bergemann C, Brock J, McClure DG (1999) Physiological aspects in magnetic drug-targeting. J Magn Magn Mater 194:149–155. doi: 10.1016/S0304-8853(98)00574-5

161. Lübbe AS, Bergemann C (1997) Selected Preclinical and First Clinical Experiences with Magnetically Targeted 4'-Epidoxorubicin in Patients with Advanced Solid Tumors. In: Häfeli U, Schütt W, Teller J, Zborowski M (eds) Sci. Clin. Appl. Magn. Carriers SE - 35. Springer US, pp 457–480

162. Ghosh P, Han G, De M, et al. (2008) Gold nanoparticles in delivery applications. Adv Drug Deliv Rev 60:1307–15. doi: 10.1016/j.addr.2008.03.016

163. Khan MS, Vishakante GD, H S (2013) Gold nanoparticles: A paradigm shift in biomedical applications. Adv Colloid Interface Sci 199–200:44–58. doi: http://dx.doi.org/10.1016/j.cis.2013.06.003

164. Cobley CM, Chen J, Cho EC, et al. (2011) Gold nanostructures: a class of multifunctional materials for biomedical applications. Chem Soc Rev 40:44–56. doi: 10.1039/b821763g

165. Alkilany AM, Murphy CJ (2010) Toxicity and cellular uptake of gold nanoparticles: what we have learned so far? J Nanopart Res 12:2313–2333. doi: 10.1007/s11051-010-9911-8

166. Giljohann DA, Seferos DS, Daniel WL, et al. (2010) Gold nanoparticles for biology and medicine. Angew Chem Int Ed Engl 49:3280–94. doi: 10.1002/anie.200904359

167. Bain CD, Troughton EB, Tao YT, et al. (1989) Formation of monolayer films by the spontaneous assembly of organic thiols from solution onto gold. J Am Chem Soc 111:321–335. doi: 10.1021/ja00183a049

168. Uvdal K, Bodö P, Liedberg B (1992) l-cysteine adsorbed on gold and copper: An X-ray photoelectron spectroscopy study. J Colloid Interface Sci 149:162–173. doi: http://dx.doi.org/10.1016/0021-9797(92)90401-7

169. Hu M, Chen J, Li Z-Y, et al. (2006) Gold nanostructures: engineering their plasmonic properties for biomedical applications. Chem Soc Rev 35:1084–1094. doi: 10.1039/B517615H

170. Cobley CM, Skrabalak SE, Campbell DJ, Xia Y (2009) Shape-Controlled Synthesis of Silver Nanoparticles for Plasmonic and Sensing Applications. Plasmonics 4:171–179. doi: 10.1007/s11468-009-9088-0

171. Zeng S, Yong K-T, Roy I, et al. (2011) A Review on Functionalized Gold Nanoparticles for Biosensing Applications. Plasmonics 6:491–506. doi: 10.1007/s11468-011-9228-1

172. Sanvicens N, Marco MP (2008) Multifunctional nanoparticles--properties and prospects for their use in human medicine. Trends Biotechnol 26:425–33. doi: 10.1016/j.tibtech.2008.04.005

173. Taladriz-Blanco P, Buurma NJ, Rodriguez-Lorenzo L, et al. (2011) Reversible assembly of metal nanoparticles induced by penicillamine. Dynamic formation of SERS hot spots. J Mater Chem 21:16880–16887. doi: 10.1039/C1JM12175H

174. Lin S, Li M, Dujardin E, et al. (2005) One-Dimensional Plasmon Coupling by Facile Self-Assembly of Gold Nanoparticles into Branched Chain Networks. Adv Mater 17:2553–2559. doi: 10.1002/adma.200500828

175. Aizpurua J, Bryant GW, Richter LJ, et al. (2005) Optical properties of coupled metallic nanorods for field-enhanced spectroscopy. Phys Rev B 71:235420.

176. Ghenuche P, Cherukulappurath S, Taminiau TH, et al. (2008) Spectroscopic Mode Mapping of Resonant Plasmon Nanoantennas. Phys Rev Lett 101:116805.

177. Ye J, Van Dorpe P (2012) Plasmonic behaviors of gold dimers perturbed by a single nanoparticle in the gap. Nanoscale 4:7205–7211. doi: 10.1039/C2NR32353B

178. Lereu AL, Sanchez-Mosteiro G, Ghenuche P, et al. (2008) Individual gold dimers investigated by far- and near-field imaging. J Microsc 229:254–8. doi: 10.1111/j.1365-2818.2008.01895.x

179. Feuz L, Jonsson MP, Höök F (2012) Material-Selective Surface Chemistry for Nanoplasmonic Sensors: Optimizing Sensitivity and Controlling Binding to Local Hot Spots. Nano Lett 12:873–879. doi: 10.1021/nl203917e

180. Aćimović SS, Kreuzer MP, González MU, Quidant R (2009) Plasmon Near-Field Coupling in Metal Dimers as a Step toward Single-Molecule Sensing. ACS Nano 3:1231–1237. doi: 10.1021/nn900102j

181. Volpe G, Noack M, Aćimović SS, et al. (2012) Near-Field Mapping of Plasmonic Antennas by Multiphoton Absorption in Poly(methyl methacrylate). Nano Lett 12:4864–4868. doi: 10.1021/nl3023912

182. Muskens OL, Giannini V, Sánchez-Gil JA, Gómez Rivas J (2007) Strong Enhancement of the Radiative Decay Rate of Emitters by Single Plasmonic Nanoantennas. Nano Lett 7:2871–2875. doi: 10.1021/nl0715847

183. Curto AG, Volpe G, Taminiau TH, et al. (2010) Unidirectional Emission of a Quantum Dot Coupled to a Nanoantenna. Sci 329 :930–933.

184. Melancon M, Lu W, Li C (2009) Gold-Based Magneto/Optical Nanostructures: Challenges for In Vivo Applications in Cancer Diagnostics and Therapy. Mater Res Bull 34:415–421.

185. Hoskins C, Min Y, Gueorguieva M, et al. (2012) Hybrid gold-iron oxide nanoparticles as a multifunctional platform for biomedical application. J Nanobiotechnology 10:27. doi: 10.1186/1477-3155-10-27

186. Huang C, Jiang J, Muangphat C, et al. (2010) Trapping Iron Oxide into Hollow Gold Nanoparticles. Nanoscale Res Lett 6:43. doi: 10.1007/s11671-010-9792-x

187. Lin P-C, Lin S, Wang PC, Sridhar R (2013) Techniques for physicochemical characterization of nanomaterials. Biotechnol Adv. doi: 10.1016/j.biotechadv.2013.11.006

188. Wu W, He Q, Jiang C (2008) Magnetic iron oxide nanoparticles: synthesis and surface functionalization strategies. Nanoscale Res Lett 3:397–415. doi: 10.1007/s11671-008-9174-9

189. Lu A-H, Salabas EL, Schüth F (2007) Magnetic Nanoparticles: Synthesis, Protection, Functionalization, and Application. Angew Chemie Int Ed 46:1222–1244. doi: 10.1002/anie.200602866

190. Wang L, Luo J, Fan Q, et al. (2005) Monodispersed core-shell Fe3O4@Au nanoparticles. J Phys Chem B 109:21593–601. doi: 10.1021/jp0543429

191. Goon IY, Lai LMH, Lim M, et al. (2009) Fabrication and Dispersion of Gold-Shell-Protected Magnetite Nanoparticles: Systematic Control Using Polyethyleneimine. Chem Mater 21:673–681. doi: 10.1021/cm8025329

192. Gnanaprakash G, Philip J, Jayakumar T, Raj B (2007) Effect of digestion time and alkali addition rate on physical properties of magnetite nanoparticles. J Phys Chem B 111:7978–86. doi: 10.1021/jp071299b

193. Ge J, Hu Y, Biasini M, et al. (2007) Superparamagnetic magnetite colloidal nanocrystal clusters. Angew Chem Int Ed Engl 46:4342–5. doi: 10.1002/anie.200700197

194. Shao D, Xu K, Song X, et al. (2009) Effective adsorption and separation of lysozyme with PAA-modified Fe3O4@silica core/shell microspheres. J Colloid Interface Sci 336:526–32. doi: 10.1016/j.jcis.2009.02.061

195. Piñeiro-Redondo Y, Bañobre-López M, Pardiñas-Blanco I, et al. (2011) The influence of colloidal parameters on the specific power absorption of PAA-coated magnetite nanoparticles. Nanoscale Res Lett 6:383. doi: 10.1186/1556-276X-6-383

196. Mahmoudi M, Lynch I, Ejtehadi MR, et al. (2011) Protein−Nanoparticle Interactions: Opportunities and Challenges. Chem Rev 111:5610–5637. doi: 10.1021/cr100440g

197. Kolhatkar AG, Jamison AC, Litvinov D, et al. (2013) Tuning the magnetic properties of nanoparticles. Int J Mol Sci 14:15977–6009. doi: 10.3390/ijms140815977

198. Willard MA, Kurihara LK, Carpenter EE, et al. (2004) Chemically prepared magnetic nanoparticles. Int Mater Rev 49:125–170. doi: 10.1179/095066004225021882

199. Muhammed M (2003) Engineering of Nanostructured Materials. In: Tsakalakos T, Ovid'ko IA, Vasudevan AK (eds) Nanostructures Synth. Funct. Prop. Appl. Springer Netherlands, Dordrecht, The Netherlands, pp 37–79

200. Reiss G, Hütten A (2010) Magnetic Nanoparticles. In: Sattler KD (ed) Handb. Nanophysics Vol. 3 Nanoparticles Quantum Dots. CRC Press, Boca Raton, USA, p 716

201. Ghosh P (2009) Colloid And Interface Science. PHI Learning Pvt. Ltd., New Dehli, India

202. Zhang X, Sun C, Fang N (2004) Manufacturing at Nanoscale: Top-Down, Bottom-up and System Engineering. J Nanoparticle Res 6:125–130. doi: 10.1023/B:NANO.0000023232.03654.40

203. Manfrinato VR, Zhang L, Su D, et al. (2013) Resolution Limits of Electron-Beam Lithography toward the Atomic Scale. Nano Lett 13:1555–1558. doi: 10.1021/nl304715p

204. Pease RF, Chou SY (2008) Lithography and Other Patterning Techniques for Future Electronics. Proc IEEE 96:248–270. doi: 10.1109/JPROC.2007.911853

205. Cao G (2004) Nanostructures and Nanomaterials: Synthesis, Properties, and Applications. 581.

206. Lyon JL, Fleming DA, Stone MB, et al. (2004) Synthesis of Fe Oxide Core/Au Shell Nanoparticles by Iterative Hydroxylamine Seeding. Nano Lett 4:719–723. doi: 10.1021/nl035253f

207. Liu J, Qiao SZ, Hu QH, (Max) Lu GQ (2011) Magnetic Nanocomposites with Mesoporous Structures: Synthesis and Applications. Small 7:425–443. doi: 10.1002/smll.201001402

208. Park J, An K, Hwang Y, et al. (2004) Ultra-large-scale syntheses of monodisperse nanocrystals. Nat Mater 3:891–5. doi: 10.1038/nmat1251

209. Jana NR, Chen Y, Peng X (2004) Size- and Shape-Controlled Magnetic (Cr, Mn, Fe, Co, Ni) Oxide Nanocrystals via a Simple and General Approach. Chem Mater 16:3931–3935. doi: 10.1021/cm049221k

210. Li Z, Sun Q, Gao M (2005) Preparation of Water-Soluble Magnetite Nanocrystals from Hydrated Ferric Salts in 2-Pyrrolidone: Mechanism Leading to Fe3O4. Angew Chemie 117:125–128. doi: 10.1002/ange.200460715

211. Li Z, Wei L, Gao MY, Lei H (2005) One-Pot Reaction to Synthesize Biocompatible Magnetite Nanoparticles. Adv Mater 17:1001–1005. doi: 10.1002/adma.200401545

212. Mikhaylova M, Kim DK, Bobrysheva N, et al. (2004) Superparamagnetism of magnetite nanoparticles: dependence on surface modification. Langmuir 20:2472–7.

213. Mandal M, Kundu S, Ghosh SK, et al. (2005) Magnetite nanoparticles with tunable gold or silver shell. J Colloid Interface Sci 286:187–194. doi: http://dx.doi.org/10.1016/j.jcis.2005.01.013

214. Lin J, Zhou W, Kumbhar A, et al. (2001) Gold-Coated Iron (Fe@Au) Nanoparticles: Synthesis, Characterization, and Magnetic Field-Induced Self-Assembly. J Solid State Chem 159:26–31. doi: http://dx.doi.org/10.1006/jssc.2001.9117

215. Lo CK, Xiao D, Choi MMF (2007) Homocysteine-protected gold-coated magnetic nanoparticles: synthesis and characterisation. J Mater Chem 17:2418–2427. doi: 10.1039/B617500G

216. Wang L, Luo J, Maye MM, et al. (2005) Iron oxide-gold core-shell nanoparticles and thin film assembly. J Mater Chem 15:1821–1832. doi: 10.1039/B501375E

217. Ban Z, Barnakov YA, Li F, et al. (2005) The synthesis of core-shell iron@gold nanoparticles and their characterization. J Mater Chem 15:4660–4662. doi: 10.1039/B504304B

218. Daniel M-C, Astruc D (2004) Gold Nanoparticles: Assembly, Supramolecular Chemistry, Quantum-Size-Related Properties, and Applications toward Biology, Catalysis, and Nanotechnology. Chem Rev 104:293–346. doi: 10.1021/cr030698+

219. Sapsford KE, Tyner KM, Dair BJ, et al. (2011) Analyzing nanomaterial bioconjugates: a review of current and emerging purification and characterization techniques. Anal Chem 83:4453–88. doi: 10.1021/ac200853a

220. Monopoli MP, Walczyk D, Campbell A, et al. (2011) Physical−Chemical Aspects of Protein Corona: Relevance to in Vitro and in Vivo Biological Impacts of Nanoparticles. J Am Chem Soc 133:2525–2534. doi: 10.1021/ja107583h

221. Jonkheijm P, Weinrich D, Schröder H, et al. (2008) Chemical strategies for generating protein biochips. Angew Chem Int Ed Engl 47:9618–47. doi: 10.1002/anie.200801711

222. Aubin-Tam M-E, Hamad-Schifferli K (2008) Structure and function of nanoparticle-protein conjugates. Biomed Mater 3:034001. doi: 10.1088/1748-6041/3/3/034001

223. Longo A, Carotenuto G, Palomba M, Nicola S De (2011) Dependence of Optical and Microstructure Properties of Thiol-Capped Silver Nanoparticles Embedded in Polymeric Matrix. Polymers (Basel) 3:1794–1804. doi: 10.3390/polym3041794

224. Veilleux JK, Duran LW (1996) Covalent Immobilization of Biomolecules to Preactivated Surfaces. IVD Technol Mag 26–31.

225. Weber C, Reiss S, Langer K (2000) Preparation of surface modified protein nanoparticles by introduction of sulfhydryl groups.Int J Pharm 211:67–78.doi:10.1016/S0378-5173(00)00590-1

226. Sigrist H, Collioud A, Clemence J-F, et al. (1995) Surface immobilization of biomolecules by light. Opt Eng 34:2339–2348.

227. Collioud A, Clemence JF, Saenger M, Sigrist H (1993) Oriented and covalent immobilization of target molecules to solid supports: Synthesis and application of a light-activatable and thiol-reactive cross-linking reagent. Bioconjug Chem 4:528–536. doi: 10.1021/bc00024a016

228. Gutmann O, Kuehlewein R, Reinbold S, et al. (2005) Fast and reliable protein microarray production by a new drop-in-drop technique. Lab Chip 5:675–81. doi: 10.1039/b418765b

229. Gutmann O, Kuehlewein R, Reinbold S, et al. (2004) A highly parallel nanoliter dispenser for microarray fabrication. Biomed Microdevices 6:131–7.

230. Hsieh H Ben, Fitch J, White D, et al. (2004) Ultra-high-throughput microarray generation and liquid dispensing using multiple disposable piezoelectric ejectors. J Biomol Screen 9:85–94. doi: 10.1177/1087057103260943

231. Strobl CJ, von Guttenberg Z, Wixforth A (2004) Nano- and pico-dispensing of fluids on planar substrates using SAW. IEEE Trans Ultrason Ferroelectr Freq Control 51:1432–6.

232. Maiti S, Shear JB, Williams RM, et al. (1997) Measuring serotonin distribution in live cells with three-photon excitation. Science 275:530–2.

233. Gryczynski I, Malak H, Lakowicz JR (1996) Three-photon excitation of a tryptophan derivative using a fs-Ti : Sapphire laser. Biospectroscopy 2:9–15. doi: 10.1002/(SICI)1520-6343(1996)2:1<9::AID-BSPY2>3.0.CO;2-6

234. Gryczynski I, Malak H, Lakowicz JR, et al. (1996) Fluorescence spectral properties of troponin C mutant F22W with one-, two-, and three-photon excitation. Biophys J 71:3448–53. doi: 10.1016/S0006-3495(96)79540-1

235. Zhou L, Ding F, Chen H, et al. (2012) Enhancement of Immunoassay's Fluorescence and Detection Sensitivity Using Three-Dimensional Plasmonic Nano-Antenna-Dots Array. Anal Chem 84:4489–4495. doi: 10.1021/ac3003215

236. Singh N, Jenkins GJS, Asadi R, Doak SH (2010) Potential toxicity of superparamagnetic iron oxide nanoparticles (SPION). Nano Rev. doi: 10.3402/nano.v1i0.5358

237. Hoskins C, Cuschieri A, Wang L (2012) The cytotoxicity of polycationic iron oxide nanoparticles: common endpoint assays and alternative approaches for improved understanding of cellular response mechanism. J Nanobiotechnology 10:15. doi: 10.1186/1477-3155-10-15

238. Pirie A (1971) Formation of N'-formylkynurenine in proteins from lens and other sources by exposure to sunlight. Biochem J 125:203–8.

239. Pirie A (1972) Fluorescence of N'-formylkynurenine and of protein exposed to sunlight. Biochem J 128:1365–7.

240. Willis KJ, Szabo AG (1991) Fluorescence decay kinetics of tyrosinate and tyrosine hydrogen-bonded complexes. J Phys Chem 95:1585–1589. doi: 10.1021/j100157a015

241. Pons T, Uyeda HT, Medintz IL, Mattoussi H (2006) Hydrodynamic dimensions, electrophoretic mobility, and stability of hydrophilic quantum dots. J Phys Chem B 110:20308–16. doi: 10.1021/jp065041h

242. Brar SK, Verma M (2011) Measurement of nanoparticles by light-scattering techniques. TrAC Trends Anal Chem 30:4–17. doi: http://dx.doi.org/10.1016/j.trac.2010.08.008

243. Filipe V, Hawe A, Jiskoot W (2010) Critical evaluation of Nanoparticle Tracking Analysis (NTA) by NanoSight for the measurement of nanoparticles and protein aggregates. Pharm Res 27:796–810. doi: 10.1007/s11095-010-0073-2

244. Figueiredo M (2013) Sizing Nanoparticles in Liquids: An Overview of Methods. In: Coelho J (ed) Drug Deliv. Syst. Adv. Technol. Potential. Appl. Pers. Treat. SE - 3. Springer Netherlands, pp 87–107

245. Carr B, Wright M (2013) Nanoparticle Tracking Analysis - A Review of Applications and Usage 2010 - 2012. Amesbury, Wiltshire, United Kingdom

246. Goldstein J, Newbury DE, Joy DC, et al. (2003) Scanning Electron Microscopy and X-ray Microanalysis: Third Edition. Springer US, New York, NY, USA

247. Johal MS (2011) Understanding Nanomaterials. CRC Press, Boca Raton, Florida, USA

248. Hall JB, Dobrovolskaia MA, Patri AK, McNeil SE (2007) Characterization of nanoparticles for therapeutics. Nanomedicine 2:789–803. doi: 10.2217/17435889.2.6.789

249. Bootz A, Vogel V, Schubert D, Kreuter J (2004) Comparison of scanning electron microscopy, dynamic light scattering and analytical ultracentrifugation for the sizing of poly(butyl cyanoacrylate) nanoparticles. Eur J Pharm Biopharm 57:369–375. doi: http://dx.doi.org/10.1016/S0939-6411(03)00193-0

250. Tom RT, Samal AK, Sreeprasad TS, Pradeep T (2007) Hemoprotein bioconjugates of gold and silver nanoparticles and gold nanorods: structure-function correlations. Langmuir 23:1320–5. doi: 10.1021/la061150b

251. Clogston JD, Patri AK (2011) Zeta Potential Measurement. In: McNeil SE (ed) Charact. Nanoparticles Intend. Drug Deliv. SE - 6. Humana Press, pp 63–70

252. Doane TL, Chuang C-H, Hill RJ, Burda C (2011) Nanoparticle ζ -Potentials. Acc Chem Res 45:317–326. doi: 10.1021/ar200113c

253. Xu R (2008) Progress in nanoparticles characterization: Sizing and zeta potential measurement. Particuology 6:112–115. doi: http://dx.doi.org/10.1016/j.partic.2007.12.002

254. Couvreur P, Dubernet C, Puisieux F (1995) Controlled drug delivery with nanoparticles : current possibilities and future trends. Eur J Pharm Biopharm 41:2–13.

8 Appendix

8.1 Absorption and fluorescence spectral characteristics of tryptophan, tyrosine and by-products of photo-oxidation

		Absorption Maximum (Abs^{max}) **Extinction Coefficient (ε)**	**Excitation Maximum (Exc^{max})**	**Emission Maximum (Em^{max})**
Tryptophan (Trp)		278, 287, (272) nm [a] ε^{278nm}= 5579 $M^{-1}.cm^{-1}$ ε^{287nm}= 4594 $M^{-1}.cm^{-1}$ ε^{272nm}= 5360 $M^{-1}.cm^{-1}$	282, 290 nm [b]	305-350 nm [b]
N'-Formylkynurenine	Ac-NFK-NH3 *Neutral*	261, 322 nm [c]		420-434 nm [c]
	NFK *Neutral/Acidic*	260, 321 nm [d]	265, 330 nm [e]	440 nm [e]
	NFK *Alkaline*		240, 315 nm [e]	400 nm [e]
Kynurenine	Ac-Kyn-NH3	258, 360 nm [c]		434-480 nm [c]
Tyrosine (Tyr)	*Neutral/Acidic*	275 nm [f] ε^{275nm}= 1400 $M^{-1}.cm^{-1}$	275 nm [b]	303 nm [b, c]
	Alkaline (Tyrosinate)	290 nm [f] ε^{290nm}= 2300 $M^{-1}.cm^{-1}$		345 nm [b, g]
Dityrosine	*Acidic*	284 nm [h] ε^{284nm}= 5400 $M^{-1}.cm^{-1}$	284 nm [h]	409 nm [h]
	Alkaline	316 nm [h]	317 nm [h]	407 nm [h]

		ε^{316nm}= 8600 $M^{-1}.cm^{-1}$		
	In proteins			400-401 nm [i]
Trityrosine	*Acidic*	286 nm [h]	286 nm [h]	409 nm [h]
		ε^{286nm}= 11000 $M^{-1}.cm^{-1}$		
	Alkaline	322 nm [h]	319 nm [h]	416 nm [h]
		ε^{322nm}= 11500 $M^{-1}.cm^{-1}$		
Pulcherosine	*Acidic*	282 nm [h]	283 nm [h]	416 nm [h]
		ε^{282nm}= 7700 $M^{-1}.cm^{-1}$		
	Alkaline	315 nm [h]	320 nm [h]	414 nm [h]
		ε^{315nm}= 9500 $M^{-1}.cm^{-1}$		

References: (a) [70]**; (b)** [71]**; (c)** [77]**; (d)** [238]**; (e)** [239]**; (f)** [79]**; (g)** [240]**; (h)** [85]**; (i)** [82]**.**

8.2 Characterization of nanoparticle bioconjugates - methodologies

It is important that the engineered nanoparticles retain its intrinsic properties during the bioconjugation process, and preserve their stability and performance. Therefore, their physicochemical properties have to be controlled by characterization techniques during the distinct steps of the engineering process, including the synthesis, coating, immobilization and purification/washing procedures. Furthermore, thorough characterization of the engineered nanomaterials is essential in order to verify if the nanoconstruct and its parts fit the design expectations.

Several physicochemical characteristics are relevant for the characterization of nanoparticle bioconjugates. These metrics include nanoparticle size and size distribution, shape and aspect ratio, aggregation/agglomeration state, chemical composition, surface characteristics (charge and presence of functional groups), stability and its optical and magnetic properties [149, 219]. On the other hand, bioconjugation procedure has also to be verified, which adds other features and metrics to the characterization process. It includes confirming the protein attachment to the nanoparticles and its nature, determining the average ratio of nanoparticle/biomolecule, and evaluating the structure and orientation of the proteins after attachment. Finally, characterization of nanoparticle bioconjugates also includes testing the activity of attached proteins and the function of the nanocarriers [219].

In order to characterize and analyse the components of the nanoparticle bioconjugates, several experimental techniques were used during this PhD work. It includes characterization techniques that are more commonly used for nanoparticles such as dynamic light scattering or scanning electron microscopy, and other more general methodologies such as UV visible absorbance spectroscopy and fluorescence spectroscopy and microscopy.

8.2.1 Dynamic Light Scattering

Dynamic light scattering (DLS) is a fast and routinely used method for determining nanoparticle size in solution. DLS can probe the size distribution of small particles, biomolecules (including some proteins), or polymers by the use a monochromatic light source (e.g. laser). The hydrodynamic diameter is determined by analyzing the light scattering properties of the particles in the irradiated solution. It is widely used since it is simple (the solution is usually illuminated in a disposable cuvette), nondestructive, fast (measurement within minutes) and inexpensive to run [187, 219].

The principle of DLS is to monitor the temporal fluctuations in the elastic scattering light intensity (Rayleigh scattering) resultant of the Brownian motion of the particles in solution [219]. Smaller particles move faster in solution generating fast fluctuations in intensity, whereas larger particles

move slower, resulting in slow intensity fluctuations. The intensity fluctuation data is then correlated to determine the diffusion coefficient of the particles, which is converted to the hydrodynamic diameter by the Stokes Einstein equation (scheme A.1) [241, 242]:

$$D_H = \frac{k_B T}{3\pi\eta D} \tag{A.1}$$

where D_H is the hydrodynamic diameter, D the translation diffusion coefficient, k_B the Boltzmann's constant, T the absolute temperature and η the viscosity of the solvent.

DLS can be used to determine the hydrodynamic diameter of samples in a broad range of particle concentrations (10^8 to 10^{12} particles/mL) and sizes (10 to 1000 nm) [219]. Despite its versatility, this technique may obscure the presence of smaller particles in samples containing different size populations. The experimental measurements depend on the light scattering of the particles in solution, which is proportional to sixth power of particle diameter according to the Rayleigh scattering regime. Therefore, particle size estimation with DLS is inclined towards larger particle sizes and the presence of dust particles or large agglomerates may compromise the measurement [219, 243]. As previously stated, DLS directly provides an intensity based distribution, which favors fractions of larger particles, and should be converted to a number based distribution (or volume) in order to have a real estimation of the particle size distributions in solution.

Furthermore, the hydrodynamic diameter of the particle obtained by DLS may not necessarily reflect the real size of a particle. The diffusion of the particles in solution may not be determined only by their Brownian motion and the size of the particle core. Other factors can influence the apparent diffusion of the particles, such as attached molecules, the ionic strength of the solvent, and particle shape. Additionally, Brownian motion theory assumes that the particles are spherical, which is not always true for engineered nanoparticles and this can result in over-estimation of particle size [242, 243].

8.2.2 Nanoparticle Tracking Analysis

Nanoparticle tracking analysis (NTA) is an interesting alternative or complementary method to DLS. This technique employs laser light scattering microscopy coupled with a CCD camera, which allows the real-time visualization and recording of nanoparticles in solution. Similarly to DLS, NTA explores the Brownian motion of particles in solution which are individually tracked by the NTA software in the recorded video frames [243, 244]. Particle movement is then related to particle size according to expression derived from the Stokes-Einstein (scheme A.2) [243] .

$$\overline{(x,y)^2} = \frac{2k_B T}{3r_H \pi\eta} \tag{A.2}$$

where r_H is the hydrodynamic radius, k_B the Boltzmann's constant, $\overline{(x,y)^2}$ the mean-squared speed of a particle, T the absolute temperature and η the viscosity of the solvent.

NTA allows determining the hydrodynamic diameters of particle suspensions in the size range 10-1000 nm operating at a concentration range of 10^7-10^{10} particles/mL [219, 245]. The lower size limit depends on particle constitution and refractive index, which will dictate its scattering properties according to the Rayleigh scattering regime. For materials with high refractive index, like colloidal gold or silver, it is possible to determine sizes down to 10-15 nm. In the case of materials of lower refractive index, e.g. of biological origin, the lower size limit may be only around 25-35 nm [245].

Unlike traditional light scattering techniques such as DLS, each scattering source is tracked separately during analysis, and not as an ensemble [219, 244]. Therefore, it is possible to resolve efficiently different populations in a polydisperse sample as the measurement directly provides number based frequency distributions [243, 244]. Thus, the measurements are not influenced by small amounts of large particles such as dust, one of the main disadvantages of DLS. Another advantage of NTA consists on the large area of detection that it provides. Together with user control of the quality and limits of detection area, it enables a more realistic representation of the particle populations in solution. Since NTA tracks particles within a known liquid volume, the relative particle concentration can also be estimated, which can be quite challenging to obtain when it is not possible to estimate the particle concentration by UV visible absorption (*vide infra*) [219, 244].

However, NTA has some limitations and is more complex and time consuming than traditional light scattering techniques. Additionally, in NTA the samples are injected to a special sample chamber where a laser beam is projected via a prism. This configuration might be a problem since the particles may interact with the bottom and top glass surfaces of the chamber and thus change their path and motion in solution, resulting in incorrect particle sizes. Like in DLS this method also assumes sphericity of the particles, which may lead to overestimated hydrodynamic diameter values.

8.2.3 Scanning Electron Microscopy (SEM) and Energy Dispersive X-ray Spectroscopy (EDX)

Scanning electron microscopy (SEM) is a surface imaging technique, which is commonly used to visualize and image nanostructures and to estimate nanoparticle size by subsequent image analysis. Electron microcopy uses beams of accelerated electrons and electrostatic or electromagnetic lenses to produce images of much higher resolution than traditional optical microscopy methods, based on the shorter wavelengths of electrons than visible light photons

[187, 246]. In SEM an incident electron beam is used to scan across the sample surface, interacting with it to produce signals to reveal the topographic details of the specimen surface and in some cases the atomic composition [247, 248].

Detection of secondary electrons is the most common imaging mode in SEM and can lead to a resolution lower than 1 nm. Secondary electrons are low energy electrons, which are dislodged from the sample upon collision with the high energy electrons of the incident beam (primary electrons) (inelastic scattering). This type of signal is resultant of a thin layer under the surface of the sample, and thus leads to a good topographic mapping of the surface. Another signal detectable by SEM is the backscattering of primary electrons, which occurs upon collision of the primary electrons with the atoms in the sample (elastic scattering). Backscatter electron detection is dependent on the atomic number of the elements and provides qualitative visual mapping of the sample surface composition [246, 247].

Another feature of SEM is the possibility to analyze the chemical composition of the specimen by coupling it with Energy Dispersive X-ray spectroscopy (EDX). This combined technique explores the characteristic X-rays emitted by the sample upon atomic excitation with the SEM electron beam (catholuminescence), which are collected by the EDX detector. The X-ray spectrum can subsequently be used to identify the atomic composition of the specimen based on of the characteristic energies of the X-rays produced by each atomic element. The X-rays signals can be collected within spot sizes of a few micrometers (or smaller), providing precise information on the atomic composition on that area [246].

SEM measurements must usually be performed under vacuum and in the absence of liquid. This has to be taken in to consideration when this technique is used to estimate the mean particle size of a nanoparticle suspension. The process of drying samples can cause shrinkage of the specimen and alter the characteristics of the nanomaterials [248, 249]. Another requirement of SEM is that the specimen is conductive, in order to avoid accumulation of charge on the sample surface. This is not usually a problem for unconjugated nanoparticles (containing elements such as Au or Fe). However, it can be more difficult to image bioconjugated nanomaterials containing non-conductive elements (e.g. buffer components), which tend to acquire charge and thus do not deflect efficiently the electron beam [248].

SEM is extremely useful for analyzing nanomaterials given the large depth of focus that the system provides, generating a detailed image of the 3D nanostructures in observation. The size, size distribution and shape of nanomaterials can be directly acquired from a SEM image. In particular, the directing imaging capability provided by SEM is useful to characterize nanoparticles with non-spherical shapes allowing a direct measure of the aspect ratio [170, 187, 219, 246, 250]. This is not possible to obtain through light-scattering techniques such as DLS and NTA. These techniques should be used together with SEM for thorough size and shape characterization of the

nanoparticle sample. Additionally, combining SEM with EDX allows a more detailed characterization and to verify for instance if the coating of nanoparticles was successful, as it provides the different elements within the individual nanoparticles.

8.2.4 Zeta Potential

The zeta (ζ) potential of particle is frequently used to characterize the surface charge properties of dispersed nanoparticles [142, 149, 187, 219]. In ionic solutions, the surface of charged particles is firmly bound to opposite charged ions forming a thin layer (stern layer), which is surrounded by an outer layer comprising loosely associated ions [187, 251]. These two layers constitute the electrical double layer. In solution, the movement of the charge particles (due to the Brownian motion or other external forces) shears ions that migrate with the particle charge in the diffuse layer from ions in solution outside the layer [187, 251]. The electric potential on the shear surface is the zeta potential. It can be determined by applying an electric field across the sample and measuring the velocity at which the charge particles move towards the electrode [219, 241].

Electrophoretic light scattering (ELS), is the most common technique used to estimate the zeta potential of nanoparticle dispersions and this method can be usually carried out in the same instrument as DLS. In this case, the instrument measures simultaneously the velocity of several charged particles in liquids under the electric field by laser light scattering, providing the electrophoretic mobility of the particle, which is then used to determine the zeta potential [252, 253].

Measurement of the zeta potential of a nanoparticle suspension gives information on the net charge of colloid in suspension and provides an indication on the nanoparticle stability in the solution. Nanoparticles with zeta potential values above ± 30mV were shown to be stable in solution, as the elevated surface charge leads to electrostatic repulsion between individual nanoparticles, thus preventing aggregation [219, 254]. Several factors affect nanoparticle stability and the zeta potential of nanoparticle solutions, including pH, concentration, ionic strength, temperature, and nature of the surface ligands and they should be taken into account when interpreting the achieved data [219, 241, 253].

8.2.5 UV Visible Absorption Spectroscopy and Localized Surface Plasmon Resonance

Spectroscopic techniques, such as UV visible absorption, are useful tools for nanoparticle characterization as they can provide an average bulk qualitative analysis of nanoparticle suspensions in a fast manner and without the need of extensive sample preparation. The intrinsic UV visible absorption of nanoparticle suspensions can be used to monitor pertinent properties of

the colloids, such as concentration, size and aggregation state (and therefore colloidal stability) and to confirm the presence of proteins upon bioconjugation.

Metallic nanoparticles, in particular gold, exhibit strong absorption in the visible region due to the LSPR band. As mentioned before, the surface plasmon band depends on a number of factors and is sensitive to size, shape and composition, aggregation state and also refractive index changes within the surface proximity [165, 219]. This phenomenon can also be used to probe protein binding of proteins to gold nanoparticles. Protein binding to gold nanoparticles can lead to small shifts (~5 nm) in the UV visible measured LPSR peak. These spectral changes can in some cases be sufficient to confirm nanoparticle interactions with other molecules and protein attachment [219].

The direct analysis of UV visible spectroscopy data can also provide additional information on nanoparticle bioconjugation with the proteins. This is possible when the protein UV visible profile remains identifiable when conjugated to nanoparticles. UV visible absorption spectroscopy can be used to detect the characteristic absorption bands of peptide bonds (at ~220 nm) and of the aromatic amino acid pool (~280 nm, tryptophan, tyrosine and phenylalanine). If the nanoparticle absorption is considerable in the spectral range of detection, then it is possible to estimate protein attachment indirectly, by measuring the amount protein free in solution before and after bioconjugation. The protein concentration can be determined either by using the protein absorbance at ~280 nm or by using a number of colorimetric assays (which usually have lower limits of detection). Several colorimetric reactive tests have been used to quantify the amount of protein through these types of procedures, such as the Bradford reagent and bicinchoninic acid assays. This type of tests usually relies on the change in the absorption maximum of a reactive dye upon binding to the protein in solution. Although these tests have not been specifically designed for nanoparticle bioconjugates, they have been applied for their analysis, allowing obtaining an estimation of the protein/nanoparticle binding ratio. Nonetheless it has been proven that nanoparticles can interfere with certain chemical assays and tests. Therefore, appropriate analysis of controls with bare nanoparticles (not bioconjugated) is crucial for a correct interpretation of the results [219].

8.2.6 Fluorescence Spectroscopy and Microscopy

Fluorescence based techniques, such as steady state fluorescence spectroscopy and fluorescence microscopy, are powerful and sensitive methods for biomolecular detection.

Similarly to UV visible absorbance spectroscopy, steady state fluorescence spectroscopy is a fast and practical method to obtain bulk information of the nanoparticle bioconjugate suspension. The emission spectrum obtained by steady state fluorescence spectroscopy can be used for multiple purposes, such as verifying the protein immobilization onto the nanoparticle surface and determining a number of parameters related to immobilization of biomolecules, such as

microenvironmental changes of the fluorescence probe altered upon immobilization. These metrics can include information regarding the local environment of the fluorophore, protein/nanoparticle coupling ratio, and conformation state of the protein [187, 219].

Fluorescence techniques are evidently restricted to the nanoparticle bioconjugate components which display an intrinsic or extrinsic fluorescence behavior. Usually the detection method is based on the biomolecule component, in this case the protein. The intrinsic fluorescence of the protein fluorophores, tryptophan, tyrosine and phenyalanine can be used to confirm the protein attachment to the nanoparticle's surface. Tryptophan in particular can provide supplementary information on the conformation and binding of the attached proteins. Tryptophan absorbs at ~280 nm and emits at 305-340 nm depending on the solvent polarity of the environment. Therefore, changes in the microenvironment of the tryptophan molecules can be detected as blue or red shifts in the maximum fluorescence emission peak .

Nevertheless, the detection of the intrinsic protein fluorophores is restricted to the UV region, which may not be practical for detection with some fluorescence techniques such as e.g. fluorescence microscopy (see below). Furthermore, the intrinsic fluorophore emission intensity may not be strong enough due to interference from the nanoparticle entities. In the case of insufficient optical signal of the intrinsic fluorophores, an extrinsic fluorophore probe can be coupled to the protein of interest (before or after bioconjugation). Nowadays, a broad range of fluorophore probes is commercially available for labeling proteins, displaying different excitation and emission wavelengths and high quantum yield (e.g. Alexa Fluor® from Molecular probes). These extrinsic fluorophores can easily be coupled to e.g. primary amine or thiol groups of the proteins. However, the labeling process itself might cause conformational changes of the protein and this should be taken into consideration for the characterizing procedure.

As previously mentioned, the nanoparticles may interfere with the fluorescence signal of the protein fluorophores. This might also be the case with extrinsic fluorescent probes as it is known that quenching or oppositely enhancement of fluorophore fluorescence can occur upon coupling to a metallic surface.

Fluorescence microscopy can provide extraordinary information and direct visualization of the fluorophores bound to nanoparticle bioconjugates. The setup of a fluorescence microscope allows the selective imaging of the fluorescence probes coupled to the surface. Therefore, it is possible to directly visualize and track the nanoparticle bioconjugates in suspension, if we are looking at a liquid sample. The nanoparticle sample can also be dried on a microscope slide, allowing to obtain an image with the position of the fluorophores. This image can be then co-localized with other microscopic images of the nanoparticles (e.g. dark field, SEM) to verify the attachment of the proteins to the nanoparticle surface.

8.3 Supporting scientific publication

Photonic Activation of Plasminogen induced by low dose UVB

Manuel Correia, Tørben Snabe, Viruthachalam Thiagarajan*, Steffen B. Petersen, and Maria Teresa Neves-Petersen*

PloS One, submitted May 2014.

Photonic Activation of Plasminogen induced by low dose UVB

Manuel Correia[1], Torben Snabe[1], Viruthachalam Thiagarajan[2,3], Steffen Bjørn Petersen[2,4,5], Maria Teresa Neves-Petersen[2,4]*

[1] Department of Physics and Nanotechnology, Aalborg University, DK-9220, Aalborg, Denmark

[2] International Iberian Nanotechnology Laboratory (INL), 4715-310 Braga, Portugal

[3] School of Chemistry, Bharathidasan University, Tiruchirappalli-620 024, India

[4] Medical Photonics Laboratory, Medical Faculty, Aalborg University, DK-9220, Aalborg, Denmark

[5] University at Buffalo, The State University of New York Buffalo, The Institute for Lasers, Photonics and Biophotonics, NY 14260-3000, USA

* To whom correspondence should be addressed: E-mail: nevespetersen@gmail.com. Telephone: +45 9940 8469, Fax: +45 9815 4008.

Short Title: Photonic Activation of Plasminogen induced by low dose UVB

Abstract

Activation of the proenzyme plasminogen to its active form plasmin is essential for several key mechanisms, among which the dissolution of blood clots. Plasminogen activation occurs naturally via enzymatic proteolysis. Here we report that plasminogen activation can be achieved with 280 nm light. A 2.6 fold increase in plasmin proteolytic activity was observed after brief 10 min of 280 nm illumination of human plasminogen in solution. Plasminogen activation is correlated with protein structural changes induced by UVB excitation of its aromatic residues (2.3 $W.m^{-2}$) due to light induced disruption of disulphide bridges and formation of photochemical products, e.g.dityrosine and N-formylkynurenine. Despite the existence of chemical modifications and structural changes, we observe that most of the protein fold is maintained after 10 min of 280 nm illumination (2.1 $W.m^{-2}$) since no major changes are observed in the near-UV circular dichroism spectrum of plasminogen. Far-UV circular dichroism spectroscopy shows some loss of secondary structure content upon UV exposure (33.4 % decrease in signal at 206 nm). Thermal unfolding CD studies show that plasminogen retains a native like thermal cooperative transition at ~70 ºC after UV-illumination. We propose that UVB activation of plasminogen occurs upon photo-cleavage of a functional allosteric disulphide bond in plasminogen, Cys737-Cys765. This disulphide bond is located in the catalytic domain of the protein and is in van der Waals contact with Trp761 (4.3 Å). The close spatial proximity makes the disruption of this disulphide bond very likely, whichmay occur upon direct electron transfer from UV excited Trp761. Reduction of Cys737-Cys765 would result in a likely conformational change in the catalytic site of the protein, rendering the site accessible to its substrate. The presented photonic mechanism of plasminogen activation has the potential to be used in clinical applications, possibly together with other enzymatic treatments for the elimination of blood clots.

Introduction

Human blood plasma contains a large number of proteins and enzymes that regulates thrombosis (blood coagulation) and thrombolysis (dissolution of coagulated blood). The key enzyme in thrombolysis is plasmin, formed after activation of the inactive proenzyme plasminogen. Plasmin is a trypsin-like serine protease, which degrades fibrin. Fibrin is a protein that spontaneously polymerises to form blood clots, a mesh-like structure that covers a wound. Plasmin secures blood fluidity upon dissolution of fibrin thrombi (blood clots). Plasmin also plays a role in tissue remodelling (e.g. wound healing), angiogenesis, ovulation, embryo implantation onto the uterus, activation of some growth hormones and metalloproteinases [1].

Plasminogen activation in humans occurs by proteolysis and is predominantly catalysed by two serine proteases – the tissue-type Plasminogen Activator (tPA) or the urokinase-type Plasminogen Activator (uPA). The tPA has large affinity for fibrin and is the main activator in blood. Since uPA has affinity for a specific plasma membrane receptor, it is responsible for localised plasminogen activation in tissues and vessel walls [2]. Plasminogen can also be activated by a complex consisting of free plasminogen or plasmin molecules in tight association with streptokinase or by staphylokinase alone [3]. Plasminogen activation using streptokinase is not the natural activation mechanism in humans but along with tPA and uPA it is used in clinical therapy as thrombolytical agent for treatment of blood clotting disorders, e.g. myocardical infarction [4].

The 3D structure of full-length native human plasminogen is displayed in Figure 1 (top panel). It contains seven domains with a total of 24 disulphide bonds. The N-terminal activation peptide (AP) comprises residues Glu1-Lys77 (Figure 1) and is stabilized by two disulphide bonds. It confers native plasminogen (also called Glu1-Pmg) its closed conformation [5]. Removal of this domain by proteolytic hydrolysis of Lys77-Lys78 peptide bond yields Lys78-Pmg [5,6], characterized by a less compact structure and that is more effectively activated than Glu1-Pmg [5,7]. Human plasminogen has five homologous triple-loop structures called kringles (K1 to K5, residues Lys78-Ala542, approximately 80 residues each, Figure 1) [6]. Each of the kringle domains is stabilized by three intra-chain disulphide bridges. Furthermore, the connection between kringle 2 and 3 is reinforced by the presence of an additional inter-kringle disulphide bridge (Cys169-Cys297) [6]. The kringle domains contain lysine binding sites (LBS) that bind fibrin. When fibrin is not present, plasminogen

adopts a closed and compact conformation. Upon binding to fibrin, plasminogen adopts an open conformation and is more easily activated [8]. The kringle domains interact with lysine-like ligands [5] and assist plasminogen in binding to large substrates (e.g. fibrin) [9], mammalian cells surfaces [10], bacterial proteins [11–13] and small ligands (e.g. Cl^-, α,ω-amino acids [14,15]). These interactions are also a part of the regulation mechanisms of plasminogen activation [5].

The inactive pro-enzyme domain of plasminogen is located at the C-terminus of the protein (Ala543-Asn791) [7] (Figure 1, top and bottom panels). It is a typical serine protease catalytic domain, homologous to trypsin [16], belonging to the chymotrypsin family of serine proteases [7] and is commonly called microplasminogen [7]. The catalytic domain of human plasminogen is displayed in Figure 1 (bottom panel). It contains four disulphide bonds and is has two subdomains, an N domain (displayed in green) and a C domain (displayed in blue). The active site residues His603, Asp646 and Ser741 (catalytic triad, CPK, in red) are located in a cleft at the junction of the two subdomains. Plasminogen catalytic activity is very reduced compared to plasmin, which is characterized by a 10^6 times higher catalytic efficiency (k_{cat}/K_M) [8]. Conversion of the proenzyme plasminogen to plasmin renders the serine protease domain active. The proteolytic activation of plasminogen occurs upon cleavage of a specific peptide bond (Arg561 – Val562), located in the so-called activation loop (see Figure 2, top panel) [5,6,8]. Most of the structural modifications which occur upon plasminogen proteolytic activation occur in the C subdomain (Figure 2, top panel), where the activation loop is (residues 558-566, in red) [8]. The activation loop is restrained by the disulphide bond Cys558-Cys566. Cleavage of the peptide bond Arg561-Val562 leads to a conformational change in two loops close to the catalytic triad: the oxyanion-stabilizing loop (residues 737-740, displayed as red ribbon) and the S1-entrance frame (residues 760-765, displayed as red ribbon) (see Figure 2, top panel) [8]. The two loops are linked together by the disulphide bond Cys737-Cys765. Upon proteolytic activation, the location and conformation of the disulphide bond Cys737-Cys765 changes, while the location of Cys558-Cys566 does not (Figure 2, top panel) [8]. Cys737-765 is characterized by a particular bond geometry, -RH Staple. Staple disulphide bonds have a high torsional potential energy, corresponding to regions of stress in a protein structure. Instead of acting as structure stabilizers, this type of disulphide bonds may have a functional redox role [17]. In fact, -RHStaple geometry has been associated to allosteric disulphide bonds in proteins [18]. These bonds are

functional disulphide bonds and they control protein function by mediating conformational change when they undergo reduction or oxidation [18].

Usually, disulphide bonds are reduced chemically, enzymatically, or electrochemically. Reduction of disulphide bonds can also occur upon UV excitation. In proteins, it can occur directly upon cystine excitation at ~250 nm (wavelength of maximum absorption for dimethylsulfide, model for cystine absorption [19]), or indirectly upon UV excitation of the side chains of aromatic residues such as tryptophan (Trp, Abs^{max} ~278 nm [20]), tyrosine (Tyr, Abs^{max} ~275 nm [21]) and phenylalanine (Abs^{max} ~257 nm [20]). Reduction of disulphide bridges upon UV excitation of aromatic residues has been shown for proteins such as cutinase and lysozyme [22–24], bovine serum albumin [25,26] prostate specific antigen [27], alpha-lactalbumin [28], antibody Fab fragments [29], and insulin [30]. Such mechanism is favoured by the spatial proximity between aromatic residues and disulphide bonds, which is a conserved structural feature in proteins [31]. Disulphide bond disruption upon UV excitation of aromatic residues can occur via electron transfer to cystines. Cystines can capture solvated electrons generated upon Trp and Tyr photoionization (scheme 1) or by direct electron transfer from ^{3}Trp and ^{3}Tyr triplet states formed upon UV excitation (scheme 2) [22,32,33]. Electron capture by cystines results in the formation of $RSSR^{\cdot-}$ (disulphide electron adduct) that can cleave to form a thiyl radical ($RS^{\cdot}$) and a thiol (RSH) (scheme 3) [22,32]. Furthermore, solvated electrons can interact with the peptide chain generating hydroxide ions and ketyl radicals (scheme 4), which can propagate along the peptide chain [34,35]. Entrapment of a ketyl radical by a disulfide bridge can yield a disulphide anion and lead to disulphide bridge breakage. Disulphide anion protonation can also lead to disulphide bond disruption (scheme 5) [32]. The thiyl radical $RS^{\cdot}$ formed upon disulphide bond disruption can react with other amino acids, oxygen, or a second thiyl radical reforming a disulphide bond either within a protein or between proteins leading to aggregation [36].

$$e^-_{aq} + RSSR \rightarrow RSSR^{\bullet -} \quad (1)$$

$$^3Tyr + RSSR \rightarrow Tyr^{\bullet +} + RSSR^{\bullet -} \quad (2)$$

$$RSSR^{\bullet -} \Leftrightarrow RS^{\bullet} + RS^{-} \quad (3)$$

126 $$e^{-}_{aq} + -CONH- \rightarrow OH^{-} + -\overset{\bullet}{C}(OH)NH- \quad (4)$$

127 $$RSSR^{\bullet -} + H^{+} \Leftrightarrow RS^{\bullet} + RSH \quad (5)$$

128 Besides disulphide bond disruption, UV excitation of Trp and Tyr in proteins can trigger other
129 photophysical and photochemical processes. It can lead to the formation of distinct Trp and Tyr side-
130 products such as N-formylkyneurenine (NFK), kyneurenine (Kyn), dityrosine (DT) and isodityrosine,
131 trityrosine and pulcherosine [36–38]. In Figure 3 and Table 1 are summarized the major
132 photoproducts generated upon Trp and Tyr photooxidation, their absorption and fluorescence
133 spectral characteristics.

134 Our study reports the consequences of 280nm excitation on the fluorescence properties, structure
135 and biofunctionality of plasminogen. Continuous UV exposure of plasminogen (2.3 $W.m^{-2}$) leads to
136 disulphide bond breakage mediated by Trp and Tyr excitation, and to the formation of dityrosine and
137 possibly NFK. Despite the onset of chemical modifications and structural changes, we observe that
138 most of the protein fold is maintained after 10 min of 280 nm illumination. Circular dichroism confirms
139 losses in secondary content of the protein, but not in the tertiary organization surrounding the protein
140 aromatic residues. The overall fold of the protein is also retained after 10 min illumination ($2.1W.m^{-2}$)
141 since the melting temperature of the protein does not change after illumination. We show that 280
142 nm illumination of human plasminogen also leads to its activation into plasmin. After only 10 min of
143 280 nm illumination a 2.6 fold increase in proteolytic activity was observed. This increase in
144 proteolytic activity is correlated with the likely UV light induced reduction of the allosteric disulphide
145 bond C737-C765.

146

Materials and Methods

Protein and buffer preparation

Milli-Q water was used for buffer preparation (conductivity below 0.2 $\mu S.cm^{-1}$).

Plasminogen from human plasma was purchased from Sigma-Aldrich (Sigma-Aldrich Danmark A/S, Copenhagen, Denmark) in powder form. In the majority of the experiments and unless stated differently we have used the Sigma-Aldrich plasminogen product P7999. The product was dissolved directly in 20 mM Lysine buffer pH 7.2 (Fluka, 62840) in order to make stock solutions and stored at ~-20 °C in 50-100 µl aliquots until use. Prior to use the protein aliquots were slowly thawed at 4-8°C before dilution in the experimental buffer.

Plasminogen concentrations were determined by Abs^{280nm} using a molar extinction coefficient of 152200 $M^{-1}.cm^{-1}$, estimated using the bioinformatic tool ProtParam (Expasy, [39], entry: uniProt sequence P00747 [AA 20-810] for human plasminogen).

Fluorescence Studies

UV illumination of plasminogen solutions was carried out in a RTC 2000 PTI spectrometer (Photon Technology International, Canada, Inc.347 Consortium Court London, Ontario, Canada) with a T-configuration, using a 75-W Xenon arc lamp coupled to a monochromator.

A 0.75 µM plasminogen work solution was prepared upon 36 X dilution of 27.3 µM plasminogen stock in 10 mM Tris HCl pH 8.0. Two mL of the work solution was placed in a quartz macro cuvette (1 cm path length) and continuously illuminated at 280 nm during 45 min. Emission and excitation spectra were recorded before and after illumination. Emission spectra were acquired with 280 nm, 295 nm, 325 nm, and 365 nm excitation. Excitation spectra were recorded with the emission fixed at 330 nm, 405 nm, 434 nm and 480 nm.

In order to collect the kinetics of fluorescence emission intensity at at 330 nm and 405 nm the experiment above was also carried out for different 280 nm illumination time periods. For each illumination session, a 0.55 µM plasminogen work solution was prepared upon 50 X dilution of 27.6 µM plasminogen stock onto 10 mM Tris HCl pH 8.0. Two mL of the work solution was placed in a

quartz macro cuvette (1 cm path length) and continuously illuminated at 280 nm during 10 min, 20 min, 30 min, or 45 min. A fresh sample was used for each illumination session. Time-based fluorescent emission kinetic traces (emission fixed at 330 nm or 405 in the detector) were obtained during continuous 280 nm excitation. Before and after each illumination session, emission spectra were acquired upon 325 nm excitation.

Slits (bandpass) were set to 5 nm. Lamp power at 280 nm was 148 µW at the sample location. The illumination spot was 0.64 cm^2. Irradiance was therefore 2.3 $W.m^{-2}$.

In all experiments, samples were magnetically stirred at 950 rpm in order to secure homogeneous illumination. Solution temperature was set to 20 °C using a Peltier element at the cuvette holder location.

Detection of thiol groups' concentration formed upon UV illumination of plasminogen

Plasminogen solutions were UV illuminated using the same experimental set-up, conditions and parameters as described in the previous section. Before each experiment, a plasminogen work solution (0.97 µM) was freshly prepared upon 40 X dilution of 38.7 µM plasminogen stock. Plasminogen samples (2 mL each) were illuminated at 280 nm in a quartz macro cuvette (1 cm path length) during 22.5 min, 45 min, 90 min, or 112.5 min.

Detection of free thiol groups was carried out using the Ellman's assay [30,40]. Ellman's reagent, 5,5'-dithiobis-2-nitrobenzoic acid (DTNB) was purchased from Molecular Probes (product D8451, Life Technologies, Naerum, Denmark). One hundred mM stock solution was prepared in DMSO and stored at 4 °C. After each illumination session, 1 mL of illuminated plasminogen solution was mixed with an excess of DTNB (10 µL of 100 mM stock solution). The molar ratio DTNB/plasminogen was ~1031. Four minutes after mixing the two components (sample kept in the dark), the absorbance intensity at 412 nm was measured in a UV/Visible spectrophotometer (UV1 VWR International—Thermo Electron Corporation, Thermo Fisher Scientific Inc. 81 Wyman Street Waltham, MA, USA), using a 1 cm path length quartz cuvette. Absorbance at 412 nm is due to the release of the product 2-nitro-5-thiobenzoate ion (TNB^{2-}) and is proportional to the amount of thiol groups present in

200 solution. The concentration of thiol groups was determined using an extinction molar coefficient for
201 TNB^{2-} of 14150 $M^{-1}.cm^{-1}$ at 412 nm [40].

202 ***Circular Dichroism measurements***

203 The plasminogen stock solutions (110 µM) were prepared in 20 mM Lysine Buffer and this time
204 stored at ~-80 °C until use. Plasminogen samples (100 µl, 10 µM) were made up in 50 mM Tris
205 buffer containing 100 mM NaCl, pH 7.4, and kept on ice all the time, except for illumination and
206 optical measurements at 20ºC.

207 UV illumination was carried out in a ChronosBH spectrometer (ISS) with a T-configuration, using a
208 300-W Xenon arc lamp coupled to a monochromator. For illumination, plasminogen samples (100µl,
209 10 µM) was placed in an 10 × 2 × 5 mm (length×width×height) inner volume quartz cell with self-
210 masking solid black walls and three clear quartz windows (Hellma) and continuously excited with 280
211 nm light for 10 min. The excitation beam was shaped to a rectangular area 2 x 10 mm (width x
212 Height) and passed centrally through the excitation volume. Excitation slits were set to 4 nm. The
213 irradiance was measured at 280 nm by an optical power meter (1917-R, Newport) placed in the
214 excitation beam leaving the cell (2.1 W/m^2). The temperature of the solution was kept at 20 °C using a
215 Peltier element at the cuvette holder location.

216 The CD measurements were carried out on a JASCO J-815 CD spectrometer (JASCO Corporation,
217 Ishikawa-cho Hachioji-shi, Tokyo, Japan). A fresh non-illuminated plasminogen sample (100µl, 10µM)
218 was prepared before the CD measurements. One hundred µL of 10 µM plasminogen solution (non
219 illuminated or 10 min illuminated at 280 nm) was placed in a quartz microcuvette with a path length of
220 0.1 cm and a CD spectrum was acquired between 400 and 185 nm (comprising both near and far UV
221 regions). The following parameters were set for the measurements: 1.0 nm band width, resolution 0.5
222 nm, 3 accumulations, scan speed 20 nm/min, sensitivity high, 16 s response time. The temperature
223 was always kept at 10 °C using a Peltier element at the cuvette holder's location. The buffer signal
224 was subtracted from all spectra.

225

Circular dichroism based protein thermal unfolding studies

The solution and protein preparation, and the experimental set-up, conditions and parameters used for UV illumination were the same as described in the previous section (Circular dichroism experiments).

The thermal unfolding of plasminogen samples (100µl, 10µM) was studied using CD spectroscopy by monitoring the intensity of the ellipticity signal of the protein during progressive heating at two different wavelengths (206 nm and 283 nm). The ellipticity intensity at 206 nm or 283 nm of a non illuminated plasminogen sample and of a UV illuminated plasminogen sample (10 min at 280 nm) was continuously monitored from 25ºC to 90ºC. The heating rate was 1ºC/min. A point was acquired every minute. Bandwidth was 1 nm and the response time was 16 s.

UV Activation of Plasminogen

In this experiment, the plasminogen product used was Sigma-Aldricht P5661 (lyophilized plasminogen). As before, the powder was dissolved in 20 mM Lysine buffer pH 7.2 in order to make 18 µM (~1.7 mg ml^{-1}) stock solutions and was stored at -20° C in 50 µL aliquots until use. A 50 µl aliquot was thawed slowly at 4-8 °C before diluting 5x (to 3.6 µM) in 10 mM Tris HCl pH 8.0.

For each experiment, approximately 55 µL of the 3.6 µM plasminogen sample was added to an "illumination chamber" comprised by a 1 mm thick quartz slide, a rubber o-ring (6 mm in diameter and 1.5 mm thick), and a plexi-glass back block. The illumination chamber was placed in a dark box with the UV transparent quartz slide facing towards the exit slit opening of a PTI (Photon Technology Int.) monochromator connected to a 75 W Xenon Arc lamp source. The monochromator was set at 280 nm (+/- 6nm). The distance from the slit opening to the quartz slide of the illumination chamber was 2 cm. The sample was illuminated for 10 minutes at 25 °C (+/- 0.5 °C). As a negative control, the same procedure (with approximately 55 µl sample in the illumination chamber) was carried out in the absence of UV illumination.

Plasmin Activity Measurements

A standard fluorescent substrate for testing the activity of a wide range of proteases (Molecular Probes, Enzcheck E-6639) was used. The substrate (casein based and labelled with Bodipy dye) was diluted according to the suppliers' instructions in 10 mM Tris HCl at pH 8.0.

45 µL of sample (illuminated or non-illuminated, preparation described in the section above) was mixed with 55 µL substrate solution in a black 96-well microtiter plate and incubated in darkness at ambient room temperature (20-23 °C). The samples were analysed in a SpectraMax XS Fluorescence Reader (excitation at 590 nm / emission at 640 nm with cut-off at 610 nm). The fluorescence emission intensity emitted by the fluorescent cleaved products was measured after 1 h and 22 h of incubation.

Data Analysis

Structure Analysis

The crystallography data used for the display of the 3D protein structure (Figures 1 and 2) and distance calculations was extracted from the PDB files 4A5T.pdb (full-length native human plasminogen, 3.49 Å resolution [41]) and 1BML.pdb (human plasmin catalytic domain in complex with streptokinase, 2.90 Å resolution [4]). Distances between Trp, Tyr residues and disulphide bonds, and among Tyr residues in native human plasminogen were calculated in Matlab R20120B after extracting the atomic xyz coordinates from the PDB file 4A5T.pdb. For the calculation of distances between aromatic residues (Trp and Tyr) and disulphide bonds we have considered the shortest distances between atoms of each pair of elements (Trp, Tyr and disulphide bonds). We have considered all the atoms in the disulphide bonds. In the case of Trp and Tyr, only the atoms belonging to the indole and benzene rings were considered. For the calculation of distances between Tyr residues, we have considered the shortest distances between the carbon atoms in the ortho-position(s) of the phenol group.

The fraction of disulphide bridges in human plasminogen and other proteins was obtained upon dividing the number of disulphide bridges found in a protein by the protein chain length (number of amino acids) and multiplying by 100 (Figure 4). The PDB dataset used for the calculation on Figure 4

(dependence of the average fraction of disulphide bridges on the protein chain length) has been published previously by our group [31].

The disulphide bonds of human plasminogen has been also analysed using the software tool *Disulphide Bond Analysis* available online from the webpage of the Adult Cancer Programme (University of New South Wales, Australia, [42]). The software provides different geometric measures, secondary structural information (including disulphide bond configuration) and solvent-accessibility values for the disulfide bonds of a protein upon uploading its xyz atomic coordinates. The PDB file 4A5T.pdb (full length native human plasminogen, 3.49 Å resolution [41]) was submitted to the online software for analysing the disulphide bonds in human plasminogen. The value considered for the total ASA of a Cys residue is 104 Å (Cys side chain). This value was estimated considering Cys in the tripeptide Gly-Cys-Gly with the main chain in an extended conformation [43].

Emission Spectra (280 nm, 295 nm, 325 nm, and 365 nm excitation)

Emission spectra were corrected by subtracting the spectra recorded for the buffer solution. Subsequently the spectra were smoothed using 5 points adjacent averaging, except for the emission spectra recorded upon 365 nm excitation, which were smoothed using a 7 points adjacent averaging. Normalized emission spectra were obtained by dividing each data point by the maximum intensity value in each spectrum.

Excitation Spectra (emission fixed at 330 nm, 405 nm, 434 nm and 480 nm)

The excitation spectra were first corrected for buffer contribution. The spectra with emission fixed at 405 nm, 434 nm and 480 nm were smoothed using adjacent averaging with 5, 7 and 9 points, respectively. Normalized excitation spectra were obtained by dividing each data point by the maximum intensity value in each spectrum.

Time-based fluorescence emission kinetic traces (emission at 405 nm and 330 nm)

The kinetic traces of fluorescence emission at 405 nm and 330 nm and excitation fixed at 280 nm (Figure 6B) were obtained directly during continuous 280 nm illumination of plasminogen (1 point acquired each 10 s; 90 min illumination time for 405 nm em.; 30 min 280 nm illumination time for 330

nm em.). The traces were normalized by dividing each data point by the emission intensity value at 0 min illumination time.

The kinetic trace of fluorescence emission at 405 nm upon excitation at 325 nm displayed in Figure 7 (insert) was obtained in a different way. The emission intensity values at 405 nm were obtained from the emission spectra recorded upon 325 nm excitation after 280nm illumination of the sample for different periods of time (10 min, 20 min, 30 min, 45 min, or 90 min).

Circular dichroism far and near UV spectra

The near UV CD part of the CD spectra (251-450 nm) was first corrected by baseline substraction. The baselines were created by interpolation (12 points for 0 min 280 nm ill. and 16 points for 10 min 280 nm ill.) using the Origin 8.0 tool peak analyser.

The full CD spectra data set (185-450 nm) was converted from the ellipticity machine units (milidegrees, mdeg) to mean residue ellipticity units [θ] ($deg.cm^2.dmol^{-1}$) using the formula:

Ellipticity [θ] in $deg.cm^2.dmol^{-1}$ = (milidegrees × mean residue weight) / (pathlenght in mm × concentration in $mg.mL^{-1}$).

The mean residue weight of a protein is obtained by dividing the molecular weight by the number of backbone amides (number of amino acids – 1 if the protein is not acetylated) [44].

The far UV CD spectra were analyzed using the online CD deconvolution tool Dichroweb (http://dichroweb.cryst.bbk.ac.uk/html/home.shtml, [45,46]) in order to estimate the secondary structure of the protein (Table 6). The deconvolution results were obtained using the algorithm CDSSTR [47–49] and the reference data set 4 [50], which provided the best fit for the experimental data.

Fitting procedures

The kinetic traces of fluorescence emission at 330 nm (280 nm exc., Figure 6B) and 405 nm (280 nm exc., Figure 6B, and 325 nm exc., Figure 7 insert) were fitted with an exponential function $F(t)= C_1 – C_2.e^{-kt}$ for the window 0-30 min and 0-45 min, respectively. $F(t)$ is the fluorescence emission intensity at 330 nm or 405 nm (a.u.) at 280 nm illumination time t (min), $C1$ and $C2$ are constants and k is the rate constant of fluorescence emission intensity decrease or increase (min^{-1}). The fitted parameter

values and corresponding errors, and root mean square error values obtained after fitting the 405 nm emission kinetic trace are displayed in Table 5. For the kinetic trace of fluorescence emission at 330 nm the fitted parameters were as follows. The root mean square error R^2 was 0.99262. The values recovered from the fitting for *C*1 and *C*2 were 7.37 ± 31.03 and 6.37 ± 31.03, respectively. The rate constants of fluorescence emission intensity decrease *k*1fitted value was -3.49E-04 ± 16.9E-04 min^{-1}.

The kinetics of thiol group formation versus 280 nm illumination time have also fitted according to an exponential function $y = y_0 - A.e^{-R0t}$, where *y* is the concentration of thiol groups (μM) at the 280 nm illumination time t(h), y_0 and *A* are constants and *R0* is the rate of thiol group formation (min^{-1}).

The circular dichroism thermal unfolding curves (ellipticity at 206 nm and 283 nm) were fitted using a modified Boltzmann function (for equation see Table 7). For the thermal unfolding curve obtained with ellipticity fixed at 206 nm, the fitting was done for the interval 60-90 °C. For the curve obtained with ellipticity fixed at 206 nm, the fitting was done for the data points 58.11-80.8 °C and 57.35-80.78 °C for non-illuminated and illuminated (10 min 280 nm) plasminogen samples, respectively. The fitting parameter x0 corresponds to the inflection point of the Boltzmann curve and the corresponding temperature is the melting point determined by circular dichroism.

Smoothing procedures, data fitting and plotting were done in Origin Pro 8.0.

Results

Bioinformatics

In Figure 1 (top panel) is presented the 3D crystal structure of native human plasminogen. The five kringles of the protein are visible (K1 to K5), as well as the activation peptide (AP) and the catalytic serine protease domain. Human plasminogen contains 19 Tyr, and 30 Trp and 24 disulphide bonds, which are distributed over all domains of the protein.

Aromatic Residues

A large fraction of the aromatic residues is located in close spatial proximity of disulphide bonds. In human plasminogen, 14 of the 19 Trp residues, and 26 of the 30 Tyr residues are situated less than 8 Å away from an disulphide bond (less than the average size of an amino acid, which is ~ 10 Å [51]. In Table 2 are listed the Trp,Tyr-disulphide bond pairs whose inter-distance is less than 6 Å (threshold distance defined considering direct Van der Waals contact distance ≤5.2 Å [52]. We can find Trp,Tyr-disulphide bond pairs in or close to Van der Waals contact in all protein domains. In Figure 1 (bottom panel) is displayed the catalytic domain of plasminogen, which contains 6 disulphide bonds, 6 Trp and 5 Tyr residues. In Table 3 are summarized the distances between Trp, Tyr residues and disulphide bonds in the serine protease domain (distance cut-off of 12 Å). Trp761 is the only Trp/Tyr residue in van der Waals contact (4.24 Å) to a SS bond, Cys737-Cys765 (Figures 1, bottom panel). The latter links the oxyanion stabilizing loop (residues 737-740) and the S1 entrance-frame (residues 760-765). Tyr774 is also quite close to Cys737-Cys765 (8.35 Å). The other disulphide important for plasminogen activation, Cys558-Cys566 (Figure 1, bottom pannel), which restrains the activation loop, has only one Trp/Tyr in close spatial proximity (Trp573, 9.06 Å away).

In human plasminogen, one third of the Tyr residues are less than 6 Å (threshold distance defined considering direct Van der Waals contact distance ≤5.2 Å [52] away from another Tyr residue (data not shown). Three clusters of Tyr residues can be identified, where the closest distance between single Tyr residues is less than 6 Å: Tyr359-Tyr366, Tyr146-Tyr154-Tyr156, and Tyr429-Tyr535-Tyr533-Tyr525 (data not shown). In Table 4 are displayed the shortest distances between the carbon atoms involved in possible dityrosine cross-linking (ortho position(s) of the phenol group) for these 3 clusters.

Disulphide Bonds

The characteristics of the disulphide bonds of native human plasminogen are summarized in Table S1. Two of the disulphide bonds of plasminogen have a –RHStaple geometry, Cys680-Cys747 and as already mentioned Cys737-Cys765, which is relevant for plasminogen activation. The disulphide bonds are ordered by increasing solvent-acessible surface area (ASA) of the Cys residues. Most of the disulphide bonds of plasminogen comprise cysteines with low ASA values. Out of the 24 disulphides, 15 of them have cysteine residues with ASA values lower than 7 Å, which corresponds to ~12 % of the total ASA of a Cys residue. Only 7 of the disulphide bonds comprise Cys residues with ASA values superior to 32 Å, corresponding to 31 % of the total ASA of a Cys residue. Among these disulphide bonds are Cys558-Cys566 and Cys737-Cys765, both relevant in plasminogen enzymatic activation. Cys737-Cys765 displays the second highest Cys ASA value, with 57 Å for Cys737 and 21 Å for Cys 765, corresponding to ~55 % and ~20 % of the total ASA of a Cys residue.

The fraction of disulphide bonds in plasminogen is displayed in Figure 4 together with the dependence of the average fraction of disulphide bridges on the protein chain length [31]. Human plasminogen contains 767 amino acids. For a protein of that chain length size (about 700-750 amino acids) we would expect an average fraction of disulphide bridges of ~0.1 %. However, the fraction of disulphide bridges obtained for human plasminogen is ~3 %, indicating that this protein exceptionally rich in disulphide bridges.

Steady State Fluorescence

Emission and excitation spectra were obtained prior and after illuminating human plasminogen with 280 nm (45 min, irradiance of 2.3 $W.m^{-2}$) in order to study the effects of continuous UV illumination on the fluorescence properties of the protein.

Excitation Spectra (emission 330 nm)

In Figure 5 is displayed the excitation spectra of plasminogen with fluorescence emission fixed at 330 nm, before and after continuous 280 nm illumination of the protein for 45 min. Both Trp and Tyr absorption contribute to this spectrum. Continuous 280 nm illumination leads to a decrease in the fluorescence excitation intensity. After 45 min of illumination, the excitation intensity at 283 nm

decreases by 10.6%. The correspondent normalized excitation spectra (data not shown) show no shift in the wavelength where maximum excitation intensity is observed (~283 nm).

Emission Spectra (excitation 280 nm)

The emission spectra of plasminogen recorded upon 280 nm illumination before and after 45 min of continuous 280 nm illumination are shown in Figure 6A. A decrease in the intensity of the fluorescence emission at ~330nm is observed after continuous UV illumination of the protein. Trp and Tyr residues in the protein contribute to the fluorescence emission observed from 305 to 345 nm. After 280 nm prolonged illumination, there is no wavelength shift of the most intense peak centered at ~331 nm. The emission intensity of plasminogen at 330 nm decreases by 9.4 % after 45 min of continuous 280 nm illumination. An increase of the fluorescence emission intensity at 375-450 nm is observed after continuous UV illumination at 280 nm (Figure 6A): fluorescence emission intensity increases by 144.3 % at 405 nm and 330.8 % at 434 nm.

In Figure 6B are displayed the kinetics of fluorescence emission intensity at 330 nm and 405 nm upon continuous 280 nm illumination. There is a progressive decrease of the Trp and Tyr fluorescence emission intensity (at 330 nm) with increasing 280 nm illumination, which is correlated with a progressive increase of fluorescence emission intensity at 405 nm. Fitting the experimental data (in red) reveals that both kinetics are exponential. The fit results are presented in Materials and Methods and Table 5. After 10 min of 280 nm illumination the fluorescence emission intensity decreases by 1.4 % at 330 nm and increases by 23.3 % at 405 nm. After 45 min, the increase in emission intensity at 405 nm (exc. 280 nm) is up to 41.9 %. This increase is lower than the calculated for the emission spectra (144.3 %, Figure 6A). The reason for this is that the emission spectra were corrected for the buffer contribution (Figure 6A) and the kinetics were not, as it is not possible to correct the time-dependent 405 nm emission intensity values for the buffer contribution. Therefore, the kinetic traces take into account the initial 405nm fluorescence from the buffer that is not present in the corrected emission spectra (Figure 6A). The initial 405 nm buffer fluorescence is due to the buffer component L-Lysine that fluoresces at 405 nm [53]. L-lysine fluorescence does not change along the 45 min of 280 nm illumination (data not shown).

Emission Spectra (excitation 325 nm)

In order to verify the formation of fluorescent photoproducts of Tyr and Trp such as DT (absorbance maximum, Abs^{max} at 316 nm, see Table 1) and NFK (Abs^{max} at 321 nm, see Table 1), emission spectra were obtained upon 325 nm excitation prior and after 45 min of 280 nm illumination (Figure 7). There is an increase in fluorescence emission intensity at 390-400 nm (exc. 325 nm) with continuous 280 nm illumination time. The fluorescence emission maximum is centred at ~396 nm, corresponding to the emission maximum of dityrosine (Em^{max} at 400-409 nm, see Table 1) and to a spectral region where NFK can also emit (for NFK, Em^{max} at 400-440 nm, see Table 1). The wavelength of maximum emission does not change with increasing 280 nm illumination time. After 45 min of continuous 280 nm illumination, the fluorescence emission intensity at 405 nm increases by 508.2 % (Figure 7).

The fluorescence emission intensity increase at 405 nm (325 nm exc.) with continuous 280 nm illumination follows a single exponential kinetics as can be observed in the insert of Figure 7. The 405 nm fuorescence emission increases by 40.5 and 66.8 % after 10 min and 45 min of illumination, respectivelly. The kinetics show a lower increase in emission intensity after 45 min than the obtained from the emission spectra (508.2 %, Figure 7). As explained in the previous section this occurs since the emission spectra are corrected for the buffer contribution and the kinetics are not.

In Table 5 are summarized the fitting parameters obtained upon fitting the kinetic traces of fluorescence emission increase at 405 nm (280 nm exc., Figure 6B; 325 nm exc., Figure 7 insert). The value obtained for the rate constant of fluorescence emission intensity increase *k* is similar for both excitation wavelengths (0.076 min^{-1} for 280 nm exc. and 0.082 min^{-1} for 325 nm exc.).

Emission Spectra (excitation 295 nm)

Figure 8 shows the effect of 280 nm continuous illumination (45 min) on the emission spectra of plasminogen obtained upon 295 nm excitation. Among the aromatic residues, only Trp is excited at 295 nm. After 45 min of 280 nm illumination, there is a 10.6 % decrease in fluorescence emission intensity at 330 nm. Normalization of the spectra (data not shown) shows that wavelength of maximum emission is 332 nm at illumination time 0 h and does not change with continuous UV illumination. After 45 min, the fluorescence emission intensity increases by 115.5 % at 405 nm and by 192.5 % at 434 nm.

Excitation Spectra (emission 405 nm)

Excitation spectra (emission fixed at 405 nm) were obtained before and after continuous 280 nm illumination (45 min) in order to investigate which fluorescent species contributed to the increase in fluorescence emission intensity at 405 nm (Figure 9). Before 280 nm illumination (0 min illumination), we can observe a single excitation peak centered at ~283 nm. Continuous 280 nm illumination leads to an increase in excitation intensity at 283 nm, and to the formation of a new peak, centred at ~321 nm. Both DT (Abs^{max} at 316 nm, see Table 1) and NFK (Abs^{max} at 321 nm, see Table 1) absorb at these wavelengths. After 45 min of 280 nm illumination, fluorescence excitation intensity increases by 151.4 % and 1706.9% at 283 nm and 325 nm, respectively.

Excitation Spectra (emission 434 nm)

In Figure 10 are displayed the excitation spectra (emission fixed at 434 nm) obtained before and after continuous 280 nm illumination (45 min). The spectra were recorded in order to verify the presence of NFK (Em^{max} at 434 nm in water and neutral pH, [38], see Table 1). At illumination time 0 min, an excitation peak can be observed with maximum centred at ~285 nm. After 45 min of illumination, we can observe both an increase in excitation intensity at 285 nm and the presence of a new peak, centred at ~320 nm. After 45 min, the excitation intensity at 283 nm (where DT absorbs, Abs^{max} at 284 nm, see Table 1, dityrosine still emits at 434 nm) increased 4.4 fold relative to illumination time 0 min. At 327 nm, where DT (Abs^{max} at 316 nm, see Table 1) and NFK (Abs^{max} at 321 nm, see Table 1) absorb, there is a 15.4 fold increase in excitation intensity.

Circular Dichroism measurements

Circular dichroism (CD) measurements were carried out in order to infer the effects of brief 280 nm illumination (10 min, irradiance of 2.1 $W.m^{-2}$) on the secondary and tertiary structure of plasminogen.

The far and near UV CD spectra of fresh (0 min 280 nm ill.) and UV illuminated plasminogen (10 min 280 nm ill.) are displayed in Figure 11. Continuous 280 nm illumination of the protein leads to spectral losses in the far UV region of the CD spectrum (185-250 nm, Figure 11). The far UV CD spectrum of fresh human plasminogen (280 nm ill. time 0 min) shows a single distinct positive peak at ~206 nm. 10 min of 280 nm illumination leads to a 3 nm red-shift of the peak to ~209 nm. The red-

shift is correlated with a decrease in ellipticity signal with UV-illumination. After 10 min of 280 nm illumination, the ellipticity signal at 206 nm decreases by 33.4 %. The secondary structural contents of both non illuminated and UV illuminated plasminogen were estimated upon deconvolution of the far-UV CD spectra (Table 6). The results show that the secondary structure of non illuminated human plasminogen is mostly constituted by β strand (76 %) and turns (17 %), while there is almost no presence of α helix (below 1 %). UV-illumination (10 min 280 nm) leads to loss of β strand features (down to 31 %), and a major increase in unordered structure (3 % to 37 %). The turn content also increases to 31 % with UV-illumination.

The near-UV CD spectrum of human plasminogen (251-350 nm, Figure 11) does not change considerably after 10 min of UV-illumination. The near-UV CD spectrum maximum of plasminogen remains constant with UV-illumination, at ~285 nm, region where mainly the protein aromatic residues absorb. Furthermore, after 10 min of illumination the ellipticity signal at 285 nm decreases only by 6 %.

Circular dichroism based protein thermal unfolding studies

The thermal unfolding curve of and the melting temperature of plasminogen samples were recovered using CD spectroscopy in order to see if the protein 3D fold is affected by brief UV illumination. The ellipticity intensity at 206 nm (far UV) and 283 nm (near UV) was continuously monitored from 25 ºC to 90ºC for a non-illuminated plasminogen sample (0 min 280 nm ill. time) and for an UV illuminated plasminogen sample (10 min 280 nm ill. time). The results are shown in Figure 12A and 12B (206 nm and 283 nm fixed wavelength, respectively).

Both non-illuminated and illuminated plasminogen samples show a similar thermal unfolding at 206 nm, with a rapid initial decrease in ellipticity intensity upon heating and a cooperative transition between 67-75 ºC. The ellipticity signal intensity of the illuminated sample is lower during the whole range (e.g. between 25 ºC and 60 ºC, this signal is in average 8.5 % lower for illuminated plasminogen). A thermal transition is clearly visible in both samples. The curves were fitted using a modified Boltzmann model (fitted data in red and blue in Figure 12A). The fitting results are displayed in Table 7. The melting temperature of the protein can be estimated from the temperature of mid-transition at 206 nm, corresponding to the fitting parameter *x*0. The estimated melting temperature

515 (206 nm thermal denaturation curve) is almost the same for the non-illuminated and 10 min
516 illuminated samples, 70.61 and 70.79 ºC, respectively.

517 Similarly, at 283 nm the thermal unfolding profile of plasminogen is not significantly affected by
518 10min of continuous 280 nm illumination (Figure 12B). For both non-illuminated and illuminated
519 samples there is a similar cooperative transition, occurring between 60 and 73 ºC, and there are no
520 major differences between the two curves in ellipticity signal during the thermal heating of the protein
521 (Figure 12B). Fitting of the curves with a modified Boltzmann model (Figure 12B and Table 7) shows
522 that the estimated melting temperatures at 283 nm are also very similar for non-illuminated and
523 illuminated plasminogen, of 70.34 and 69.98 ºC, respectively.

524 ***Thiol group's quantification***

525 The concentration of solvent accessible thiol groups in human plasminogen has been determined
526 with Ellman's assay for a non-illuminated sample and for samples previously illuminated at 280 nm
527 during 22.5-112.5 min (irradiance of 2.3 $W.m^{-2}$). The concentration of free thiol groups increases
528 exponentially with 280 nm continuous illumination (Figure 12). After 112.5 min of illumination, the
529 concentration of free thiol groups in human plasminogen is ~2.27 µM. Assuming that the formation of
530 free thiol groups follows a first order kinetics (as indicates the 1^{st} order exponential model used) it is
531 possible that more thiol groups are formed with increased 280 nm illumination time. The maximum
532 value of thiol concentration (detected with the Ellmann's reagent) can be estimated from the
533 exponential model ($y = y_0 - A.e^{-R0t}$) used for fitting and is given by y_0, which is of 2.29 µM.

534 ***Plasminogen UV activation***

535 The activity of illuminated (10 min, 280 nm) and non-illuminated (negative control) plasminogen was
536 tested by measuring the fluorescence signal of the fluorescent cleaved casein-Bodipy products after
537 1 hour and 22 hours of incubation in the dark. It is a standard procedure using this particular
538 substrate (Figure 14). After 1 h of incubation the fluorescence emitted from the cleaved products by
539 UV illuminated plasminogen is 1.6 fold larger than for non-illuminated plasminogen (negative
540 control). At 22 h of incubation, the fluorescence emission intensity of cleaved products by UV
541 illuminated plasminogen is 2.6 fold higher than for non-illuminated plasminogen (negative control),

while the fluorescence signal for the non-illuminated plasminogen sample remains constant compared to the previous reading.

Discussion

Human plasminogen is a complex molecule comprising seven folded domains. It contains a large number of aromatic residues, among which 19 Trp and 30 Tyr, which are present in all seven domains of the protein. The high number of aromatic residues makes this protein a likely target for photo-oxidation. Plasminogen architecture comprises 24 disulphide bonds, which have distinct functions within the protein, including e.g. stabilization of the kringle domains or restriction and recognition of the activation loop (see Introduction). For a protein of the size of plasminogen (769 amino acids), it is an exceptionally high number of disulphide bonds. It has an average fraction of disulphide bonds of 3 %, compared to the expected 0.1 % for a protein of that size (Figure 4). Data displayed in Figure 4 indicates that smaller proteins have usually higher average fraction of disulphide bonds values while the abundance of disulphide bonds is low in large proteins. A short protein has a hydrophobic core than a large protein and therefore depends to a larger extent on the structural stability provided by disulphide bridges. In plasminogen, disulphide bridges are ~30 times more abundant than expected for a protein of this length.

Most of these disulphide bonds have Trp or Tyr residues in close spatial proximity (≤ 8Å, see Results), which is a conserved structural feature in nature [31]. Additionally, in all the domains there is at least one aromatic residue less than 6 Å away from a disulphide bond (See Results), therefore close to the van der Waals contact distance between atoms (≤ 5.2 Å, [52]. This makes these disulphide bonds excellent targets for photo-induced cleavage [22]. Their proximity to aromatic residues favours the transfer of electrons formed upon upon UV excitation of aromatic residues (see Introduction) to the disulphide bonds. Hence, it is expected that several of the protein disulphide bonds are disrupted upon UV illumination, inducing conformational changes that can affect the functionality of the biomolecule.

Tryptophan and Tyrosine photobleaching

Prolonged UV illumination of plasminogen leads to decreasing amounts of intact Trp and Tyr molecules. A decrease in both excitation and emission intensity of Trp and Tyr (losses in intensity ~10-11 %, Figure 5, Figure 6A and Figure 8) has been observed upon 280 nm illumination (45 min). This suggests that these aromatic residues are progressively photo-bleached. Photobleaching of the

aromatics can imply the formation of new species, Trp and Tyr derivatives (see Figure 3), and the triggering of other photochemical and photophysical mechanisms, which will now be discussed.

Dityrosine and other tyrosine derivatives

A new species that strongly emits at 396 nm (exc. 325 nm, Figure 7) is progressively formed upon 280 nm illumination of plasminogen. These spectral features are consistent with the fluorescence characteristics of dityrosine (Em^{max} at 400-409 nm, see Table 1). The emission intensity increase at 396 nm is correlated with an increase in excitation intensity (em. 405 nm, Figure 9) at 2 separate peaks located at ~283 nm and ~321 nm. These wavelengths are in agreement with the absorption maxima of dityrosine ionic species at 283 nm (deprotonated form) and 315 nm (protonated form) [54,55], Table 1). In fact, we also observed an increase in the intensity at ~375-450 nm in the emission spectra recorded with excitation at 280 nm and 295 nm (Figure 6A and Figure 8). The formation of this new fluorescent species was monitored during 280 nm illumination by following the kinetics of fluorescence emission at 405 nm at the two relevant excitation wavelengths: 280 nm and 325 nm (Fig. 6 and 7, respectively). Both curves followed single exponential kinetics and had matching values for the kinetic constant *k* (fluorescence exponential emission increase) (Table 5). This indicates that at both excitation wavelengths (280 nm and 325 nm) we are monitoring the formation of the same fluorescent species via a first order reaction, which matches the mechanisms of dityrosine formation [30].

Dityrosine formation has been previously observed upon exposure of proteins to UV-light, e.g. in calmodulin [37,56], elastine hydrolysates [57], and insulin [30]. While in solution dityrosine emits at 407-409 nm, it has been observed that in proteins dityrosine emission is blue-shifted, being centered ~400 nm. This is true for calmodulin and insulin and is consistent with our observations in this work (em_{max} at 396 nm, Figure 7). The close spatial proximity between Tyr residues in plasminogen favours dityrosine formation (see Table 4). Furthermore, we have documented that three or even four Tyr residues are in favourable distance for Tyr cross-linking (Table 4), which could result in more than one Tyr cross-linking within the same chain. Pulcherosine and Trityrosine, which are trimers of Tyr formed upon Tyr radical cross-linking, have similar fluorescence characteristics compared to dityrosine (Table 1). Thus, these specii could also contribute to the observed emission intensity increase at 396 nm.

NFK and Kyn

Dityrosine is not the only species that can contribute to the strong increase in emission intensity at ~396 nm (exc. 325 nm, Figure 7) observed upon UV illumination of plasminogen. NFK, a Trp derivative (Figure 3), can fluoresces between 400 nm and 440 nm, depending on pH, neighbouring functional groups and solvent polarity (Table 1 and [38]). Fluorescence emission of the two formed species upon 280 nm illumination, NFK (Em^{max} between 400-440 nm) and dityrosine (Em^{max} at 400-409 nm) might overlap in the spectra obtained upon 325 nm excitation (Figure 7). The same is true for the excitation spectra obtained with emission fixed at 405 nm (Figure 9) and 434 nm (Figure 10), where the excitation peaks found at 283-286 nm and 327-326 nm might be resultant of dityrosine and NFK excitation. Absorption and excitation of NFK are also strongly dependent on experimental conditions. For instance, in solution at pH 7.4 NFK excitation peaks are centred at 265 nm and 330 nm, while at pH 11 these are centred at 240 nm and 315 nm (Table 1, [58]).

It is not likely that Kyn (another Trp derivative, see Introduction and Table 1) is formed upon prolonged UV illumination of human plasminogen. We did not detect any Kyn typical fluorescence during the fluorescence measurements that were carried out in this work (data not shown, emission spectra recorded with 365 nm excitation, and excitation spectra obtained with emission fixed at 480 nm).

Disulphide Bond Disruption

UV illumination of Trp and Tyr also leads to increasing amounts of free SH groups detected with the Ellman's assay (Figure 13). The close spatial proximity of aromatic residues and SS bonds in plasminogen favors the breakage of disulphide bonds upon UV illumination of neighboring aromatic residues. The proximity to disulphide bonds allows direct electron transfer from the aromatic residues to disulphide bonds (see Introduction, schemes 2 and 3). Photoionization of Trp and Tyr and subsequent formation of solvated e^-_{aq} may also be a mechanism involved in the photo induced breakage of disulphide bonds (See Introduction, schemes 1 and 3).

The formation of free disulphide groups upon continuous 280 nm illumination of plasminogen follows a single exponential kinetic. It indicates that the breakage of disulphide bonds is consistent with a first order reaction. The maximum value for the concentration of free and solvent accessible SH

groups is 2.29 µM. Considering that the protein concentration used for the Ellman's assay experiments was 0.97 µM, that plasminogen has 24 disulphide bonds, and that 1 SH group is formed per molecules bond disrupted (the other S atom is in a radical from), the maximum concentration of free thiol groups that could be present would be of 23.3 µM. Thus, we can conclude that at least two disulphide bonds have been disrupted in each plasminogen molecule after 280 nm illumination (Fig. 12). The number of disulphide bonds broken may be higher than estimated by the Ellman's assay. It has been reported that due to steric or electrostatic constraints, some protein sulfhydryls do not react with DTNB [59–61]. In fact, most of the cysteine residues involved in disulphide bonds in plasminogen have low ASA values (less than 12 % of the total Cys ASA, see Results) and it is not certain that the most solvent acessible disulphide bonds (7 of them have more than 31 % of total Cys ASA, see Results) are all cleaved upon UV-illumination.

UV light effects on secondary and tertiary structure of plasminogen

The chemical modifications on Trp, Tyr residues and the breakage of disulphide bonds that occur upon continuous UV exposure of plasminogen are likely to affect the native three-dimensional fold of the protein. The disulphide bonds of plasminogen have important structural roles (e.g. stabilization of the kringle domains, restriction and recognition of the activation loop etc). Furthermore, dimerization of Tyr residues (forming DT) can lead to intra- or inter-molecular cross-linking in proteins [37,62,63]. The possible conversion of Trp to NFK can also lead to protein structural damage, since NFK is also a photosensitizer that can generate reactive oxygen species (ROS) upon UV light absorption [64]. The fluorescent photo derivatives of Trp and Tyr are formed quickly upon UV illumination (Figures 6B and 7 insert). If we consider the fluorescence emission kinetics (em. 405 nm) recovered on Figures 6B and 7 as indicatives of DT and/or NFK formation we can estimate that after only 10 min of UV illumination ~56 % of the total possible DT and/or NFK products are already formed.

The impact of UV illumination on the secondary and tertiary structure of human plasminogen was evaluated using CD spectroscopy. We have observed a decrease in far UV CD ellipticity at 206 nm (33.4 %) and a 3 nm red-shift of the spectrum maximum after only 10 min of 280 nm illumination (Figure 11). This is consistent with the loss of protein secondary structure contents upon UV-illumination.

658 The secondary structural content of the protein was estimated upon deconvolution of the far UV CD
659 spectra with the CD. This analysis shows that non illuminated plasminogen contains a large fraction
660 of β strands (76 %) and turns (17 %), and almost no helical content (below 1%) (Table 6). This
661 numbers are in agreement with the structural motifs observed in the 3D crystal structure of native
662 human plasminogen, confirming that the deconvolution of the spectra worked well. Promotif analysis
663 of the crystal structure (recovered with PDBsum, http://www.ebi.ac.uk/pdbsum/, input file: 4A5T.pdb,
664 full-length native human plasminogen, 3.49 Å resolution [41]) shows that the native human
665 plasminogen secondary structure is mostly constituted by strands (19.3 %) and other types of
666 structure (73.9 %), including a great number of β and gamma turns (130 in total). Furthermore, the
667 helical content of the protein is low (6.7 % of the structure).

668 Deconvolution data (Table 6) indicates that the β strand content of human plasminogen is mostly
669 disarranged upon UV-illumination, resulting in an increase in unordered secondary structure. The
670 results also show a slight increase in turn content with UV illumination (17 % to 31 %), probably due
671 to disarrangement of β strands.

672 There is no doubt that UV illumination leads to losses in secondary structural features of
673 plasminogen. However, it is not likely that these structural changes will affect tremendously the
674 overall native fold of the protein. Human plasminogen retains a cooperative thermal unfolding
675 ellipticity curve at 206 nm even if it is previously exposed to 280nm for a short illumination period
676 (Figure 12A). Furthermore, the melting temperature recovered from the curves is similar for non-
677 illuminated and illuminated plasminogen: 70.61 ºC and 70.79 ºC respectively (Table 7).

678 Similarly, 10 min 280nm illumination did not lead to significant changes in the near UV CD features
679 of plasminogen. The near UV CD spectra of non-illuminated and illuminated plasminogen are both
680 centered at ~285 nm, where Tyr and Trp residues contribute. Most of the the CD signal of
681 plasminogen at 285 nm (~94 %) is retained after 10 min of UV illumination. Additionally, the near UV
682 (283 nm) CD thermal unfolding of human plasminogen is practically the same before and after 10
683 min of UV illumination. The two samples had similar cooperative thermal unfolding curves (Figure
684 12B) and concordant melting temperature values (70.34 ºC and 69.68 ºC before and after UV illum.,
685 respectively, Table 7). The data indicates that the local tertiary environment of Tyr and Trp residues
686 does not change considerably. This is supported by the Trp fluorescence data (Figure 8). There is no

687 change in the wavelength of maximum emission (332 nm) with 280 nm illumination, indicating no
688 changes in solvent accessibility and thus in the environment of the Trp residues.

689 ***UV light Activation of Plasminogen***

690 Brief UV illumination of plasminogen (10 min, 280 nm) results in an increase of detected cleaved
691 enzyme substrate (2.6 fold increase in fluorescence emission for 22 h of substrate incubation, Figure
692 14). It shows that the enzymatic activity of plasminogen is enhanced upon brief UV illumination and it
693 indicates that the proenzyme can be activated by UV exposure. The fact that the fluorescence signal
694 of the non-illuminated sample does not increase between these measurements, and that UV
695 activated plasminogen displays significant larger substrate degradation at both readings, indicates
696 that plasminogen is activated by brief 280nm illumination and that no or little activity is displayed by
697 the non-activated plasminogen (negative control).

698 We have observed that the overall fold of the protein is not compromised after exposing the protein
699 to a low UV-light dosage (CD studies, 10 min illumination at 280 nm, 2.1 $W.m^{-2}$). It is also relevant to
700 mention that the irradiance at 280nm used in our present study (Fluorescence studies and Ellman's
701 assay: 2.3 $W.m^{-2}$, CD studies 2.1 $W.m^{-2}$) is in the same order of magnitude than the total irradiance
702 of sunlight in the UVB region (280-315 nm), which is reported to be 0.78 W (annual average value
703 based on the data from ASTM G173-03 Air Mass 1.5 Reference Spectra, American Society for
704 Testing and Materials (ASTM) [30]).The used UVB dose proved to be the sufficient to induce limited
705 conformational changes that favour plasminogen activation, despite not affecting the overall
706 conformation of the protein. 280nm illumination of Trp and Tyr residues in human plasminogen leads
707 to the breakage of two or more disulphide bonds. If the breakage of these disulphide bonds occurs
708 within the serine protease domain it is likely that conformational changes occur inside and around
709 the active site upon UV illumination. Two disulphide bonds are particularly relevant for activation of
710 plasminogen to plasmin: Cys558-Cys566 and Cys737-Cys765. Cys558-Cys566 stabilizes the
711 activation loop (Figure 1B) and it has been proposed that it has a role in its recognition by uPA, tPA
712 and fibrin [65]. Furthermore, it has been proposed that the disulphide bond Cys558-Cys566 may be
713 important for the enzymatic specificity of plasminogen [4]. Trp573 is 9.06 Å away from this disulphide
714 bond, and it could mediate disruption of this disulphide bond. However, there are other Trp and Tyr
715 residues in closer proximity to other disulphide bonds in the catalytical domain that could be more

likely targets for photolysis (Table 3). Furthermore, it has been proven that the activity of plasmin does not depend on the presence of the Cys558-Cys566 disulphide bond [65].

Cys737-Cys765 is the only disulphide bond in the serine protease domain that has an aromatic residue within van der Waals distance (Trp761 at 4.24 Å) (Figure 1B), which makes it the most likely target of photolysis upon Trp excitation. It has also a Tyr residue in close proximity (Tyr 774, 8.35 Å away). Additionally, its pair of cysteine residues is one of the most solvent accessible in native human plasminogen and the most solvent accessible in the serine protease domain (ASA_{Cys737} = 57Å^2; ASA_{Cys765} = 21Å^2; see Table S1). This makes this Cys residues good acceptors of solvated electrons generated upon aromatic excitation. Cys737-Cys765 and Cys680-747 have an unique bond geometry among the disulphide bonds in plasminogen called –RHStaple [18]. As previously mentioned, this geometry is typical of allosteric disulphide bonds, known for controlling protein function by mediating conformational change via their reduction or oxidation [18]. Chen and Hogg report that one or more of the plasminogen disulphide bonds are redox-active [18]. Additionally, one of these redox-active disulphide bonds may be important in the mechanism of release of angiostatin, a fragment of plasmin and the precursor for an inhibitor of angiogenesis. It occurs upon reduction of the disulphide bonds in K5 (kringle 5) [18]. As previously mentioned Cys737-Cys765 holds together two important loops for plasminogen activation: the oxyanion stabilizing loop (residues 737-740) and the S1 entrance-frame (residues 760-765). These loops are located in a region close to the activation pocket and that suffers conformational changes upon activation. It is possible that the likely disruption of this disulphide bond induces a similar conformational change in plasminogen, rendering the catalytic site active (Figure 2). Several allosteric disulphide bonds have been identified in proteins involved in thrombosis and thrombolysis. In tissue factor, an important protein for the initiation of blood coagulation, it has been proven that the cleavage and formation of a particular allosteric disulphide bond (Cys186-Cys209) is crucial for changing between the different functions of this co-factor [66]. It is possible that in plasminogen/plasmin Cys737-Cys765 has a similar functional role, and depending on its redox state, induces the switch between inactive (plasminogen) and active (plasmin) protein.

743 The presented results show that plasminogen can be activated by low dose 280nm radiation.
744 Possible applications of UV induced activation of plasminogen are numerous – a few are mentioned
745 below:

746 – Activation of plasminogen using plasminogen activators is used in clinical practice for treatment of
747 patients with various vascular diseases. For situations where activation and/or enhanced
748 activation of plasminogen is needed, e.g. for clinical treatment of strokes, low dose UV activation
749 could be beneficial compared to infusion of the common (and expensive) plasminogen activator
750 proteins such as tPa or uPA.

751 – If plasminogen activation is inhibited due to a high amounts of tPA and/or uPA inhibitors therapies
752 based on infusions of these activators will not be effective for plasminogen activation. In contrast,
753 plasminogen activation via UV light would not be affected by the presence of tPA/uPA inhibitors.

754 – Catheters/tubes for draining blood/plasma e.g. from lung tissues often clot (Stevens and Tobias,
755 2001). Introducing UV activation locally through these catheters, e.g. by optical fibres in the
756 catheter construction or by constructing the catheter in a UV guiding material and introduce UV
757 light may reduce this critical problem.

758 The dangers of overexposure to sunlight have been well publicized, and there is reluctance for the
759 use of UV light in medical therapy. However, UV light has already been used to successfully treat a
760 number of diseases, including rickets, psoriasis, lupus vulgaris, vitiligo, atopic dermatitis and
761 localized scleroderma and jaundice [67]. The effects of UV light on biomolecules, cells and tissues
762 will depend on the energy delivered per unit area. Furthermore, it will also depend greatly on the
763 wavelength that is used. Skin cancer is the result of exposure to both UVB and UVA (315 – 400 nm)
764 radiation upon acute overdosing (causing sunburn) and lifelong cumulative exposure [68]. Melanoma
765 is most likely to be caused by UVA, while the UVB fraction of the solar radiation has mostly benign
766 effects such as erythema, melanogenesis (melanin production), vitamin D synthesis, and non-
767 melanoma skin cancer [69]. The health effects of UV exposure are dose and wavelength dependent.
768 It is our hope that the presented results will inspire the development of novel solutions based on UV
769 activation of plasminogen that could help patients with relevant diseases.

770

Acknowledgements

M.C. acknowledges the support from “Fundação para a Ciência e Tecnologia” (FCT) for the PhD grant (SFRH/BD/61012/2009) supported by “Programa Operacional Potencial Humano” (POPH) in the framework of “Quadro de Referência Estratégico Nacional” (QREN) and co-financed by the European Social Fund (“Fundo Social Europeu”, FSE).

References

1. Collen D (2001) Ham-Wasserman Lecture: Role of the Plasminogen System in Fibrin-Homeostasis and Tissue Remodeling. Hematology 2001: 1–9.

2. Christ G, Kostner K, Zehetgruber M, Binder BR, Gulba D, et al. (1999) Plasmin activation system in restenosis: role in pathogenesis and clinical prediction? J Thromb Thrombolysis 7: 277–285.

3. Parry MAA, Fernandez-Catalan C, Bergner A, Huber R, Hopfner K-P, et al. (1998) The ternary microplasmin–staphylokinase–microplasmin complex is a proteinase–cofactor–substrate complex in action. Nat Struct Biol 5: 917–923.

4. Wang X, Lin X, Loy JA, Tang J, Zhang XC (1998) Crystal Structure of the Catalytic Domain of Human Plasmin Complexed with Streptokinase. Science (80-) 281: 1662–1665.

5. Castellino FJ, Ploplis V a. (2005) Structure and function of the plasminogen/plasmin system. Thromb Haemost: 647–654.

6. Schaller J, Gerber SS (2011) The plasmin-antiplasmin system: structural and functional aspects. Cell Mol Life Sci 68: 785–801.

7. Peisach E, Wang J, de los Santos T, Reich E, Ringe D (1999) Crystal structure of the proenzyme domain of plasminogen. Biochemistry 38: 11180–11188.

8. Wang X, Terzyan S, Tang J, Loy J a, Lin X, et al. (2000) Human plasminogen catalytic domain undergoes an unusual conformational change upon activation. J Mol Biol 295: 903–914.

9. Suenson E, Thorsen S (1981) Secondary-site binding of Glu-plasmin, Lys-plasmin and miniplasmin to fibrin. Biochem J 197: 619–628.

10. Miles LA, Dahlberg CM, Plow EF (1988) The cell-binding domains of plasminogen and their function in plasma. J Biol Chem 263: 11928–11934.

11. Berge A, Sjöbring U (1993) PAM, a novel plasminogen-binding protein from Streptococcus pyogenes. J Biol Chem 268: 25417–25424.

12. D'Costa SS, Boyle MD (1998) Interaction of a group A Streptococcus within human plasma results in assembly of a surface plasminogen activator that contributes to occupancy of surface plasmin-binding structures. Microb Pathog 24: 341–349.

13. Wistedt AC, Kotarsky H, Marti D, Ringdahl U, Castellino FJ, et al. (1998) Kringle 2 mediates high affinity binding of plasminogen to an internal sequence in streptococcal surface protein PAM. J Biol Chem 273: 24420–24424.

14. Urano T, Sator de Serrano V, Chibber BA, Castellino FJ (1987) The control of the urokinase-catalyzed activation of human glutamic acid 1-plasminogen by positive and negative effectors. J Biol Chem 262: 15959–15964.

15. Urano T, Chibber BA, Castellino FJ (1987) The reciprocal effects of epsilon-aminohexanoic acid and chloride ion on the activation of human [Glu1]plasminogen by human urokinase. Proc Natl Acad Sci U S A 84: 4031–4034.

16. Novokhatny V (2008) Structure and activity of plasmin and other direct thrombolytic agents. Thromb Res 122 Suppl : S3–8.

17. Wouters MA, Fan SW, Haworth NL (2010) Disulfides as redox switches: from molecular mechanisms to functional significance. Antioxid Redox Signal 12: 53–91.

18. Chen VM, Hogg PJ (2006) Allosteric disulfide bonds in thrombosis and thrombolysis. J Thromb Haemost 4: 2533–2541.

19. Klitgaard S, Neves-Petersen MT, Petersen SB (2006) Quenchers induce wavelength dependence on protein fluorescence lifetimes. J Fluoresc 16: 595–609.

20. Fasman GD, editor (1976) Handbook of Biochemistry and Molecular Biology, Proteins, Volume I. 3rd ed. CRC Press, Cleveland, Ohio.

21. Creed D (1984) The photophysics and photochemistry of the near-uv absorbing amino acids–II. Tyrosine and its simple derivatives. Photochem Photobiol 39: 563–575.

22. Neves-Petersen MT, Klitgaard S, Pascher T, Skovsen E, Polivka T, et al. (2009) Flash photolysis of cutinase: identification and decay kinetics of transient intermediates formed upon UV excitation of aromatic residues. Biophys J 97: 211–226.

23. Neves-Petersen MT, Gryczynski Z, Lakowicz J, Fojan P, Pedersen S, et al. (2002) High probability of disrupting a disulphide bridge mediated by an endogenous excited tryptophan residue. Protein Sci 11: 588–600.

24. Neves-Petersen MT, Snabe T, Klitgaard S, Duroux M, Petersen SB (2006) Photonic activation of disulfide bridges achieves oriented protein immobilization on biosensor surfaces. Protein Sci 15: 343–351.

25. Skovsen E, Kold AB, Neves-Petersen MT, Petersen SB (2009) Photonic immobilization of high-density protein arrays using Fourier optics. Proteomics 9: 3945–3948.

26. Parracino A, Gajula GP, di Gennaro AK, Correia M, Neves-Petersen MT, et al. (2011) Photonic immobilization of BSA for nanobiomedical applications: creation of high density microarrays and superparamagnetic bioconjugates. Biotechnol Bioeng 108: 999–1010.

27. Parracino A, Neves-Petersen MT, di Gennaro AK, Pettersson K, Lövgren T, et al. (2010) Arraying prostate specific antigen PSA and Fab anti-PSA using light-assisted molecular immobilization technology. Protein Sci 19: 1751–1759.

28. Correia M, Neves-Petersen MTM, Parracino A, di Gennaro AK, Petersen SB (2012) Photophysics, photochemistry and energetics of UV light induced disulphide bridge disruption in apo-α-lactalbumin. J Fluoresc 22: 323–337.

29. Duroux M, Skovsen E, Neves-Petersen MT, Duroux L, Gurevich L, et al. (2007) Light-induced immobilisation of biomolecules as an attractive alternative to microdroplet dispensing-based arraying technologies. Proteomics 7: 3491–3499.

30. Correia M, Neves-Petersen MT, Jeppesen PB, Gregersen S, Petersen SB (2012) UV-light exposure of insulin: pharmaceutical implications upon covalent insulin dityrosine dimerization and disulphide bond photolysis. PLoS One 7: e50733.

31. Petersen MT, Jonson PH, Petersen SB (1999) Amino acid neighbours and detailed conformational analysis of cysteines in proteins. Protein Eng 12: 535–548.

857 32. Hoffman MZ, Hayon E (1972) One-electron reduction of the disulfide linkage in aqueous
858 solution. Formation, protonation, and decay kinetics of the RSSR- radical. J Am Chem Soc
859 94: 7950–7957.

860 33. McCormick ML, Gaut JP, Lin TS, Britigan BE, Buettner GR, et al. (1998) Electron
861 paramagnetic resonance detection of free tyrosyl radical generated by myeloperoxidase,
862 lactoperoxidase, and horseradish peroxidase. J Biol Chem 273: 32030–32037.

863 34. Bent D V, Hayon E (1975) Excited state chemistry of aromatic amino acids and related
864 peptides. III. Tryptophan. J Am Chem Soc 97: 2612–2619.

865 35. Bent D V, Hayon E (1975) Excited state chemistry of aromatic amino acids and related
866 peptides. I. Tyrosine. J Am Chem Soc 97: 2599–2606.

867 36. Kerwin BA, Remmele RL (2007) Protect from light : photodegradation and protein biologics.
868 96: 1468–1479. doi:10.1002/jps.

869 37. Malencik D a, Anderson SR (2003) Dityrosine as a product of oxidative stress and fluorescent
870 probe. Amino Acids 25: 233–247.

871 38. Fukunaga Y, Katsuragi Y, Izumi T, Sakiyama F (1982) Fluorescence characteristics of
872 kynurenine and N'-formylkynurenine. Their use as reporters of the environment of tryptophan
873 62 in hen egg-white lysozyme. J Biochem 92: 129–141.

874 39. Gasteiger E, Hoogland C, Gattiker A, Duvaud S, Wilkins MR, et al. (2005) Protein
875 Identification and Analysis Tools on the ExPASy Server. In: Walker JM, editor. The
876 Proteomics Protocols Handbook. Humana Press. pp. 571–607.

877 40. Riener CK, Kada G, Gruber HJ (2002) Quick measurement of protein sulfhydryls with
878 Ellman's reagent and with 4,4'-dithiodipyridine. Anal Bioanal Chem 373: 266–276.

879 41. Xue Y, Bodin C, Olsson K (2012) Crystal structure of the native plasminogen reveals an
880 activation-resistant compact conformation. J Thromb Haemost 10: 1385–1396.

881 42. Wong JWH, Hogg PJ (2010) Analysis of disulfide bonds in protein structures. J Thromb
882 Haemost 8: 2345.

883 43. Miller S, Janin J, Lesk AM, Chothia C (1987) Interior and surface of monomeric proteins. J
884 Mol Biol 196: 641–656.

885 44. Greenfield NJ (2006) Using circular dichroism spectra to estimate protein secondary
886 structure. Nat Protoc 1: 2876–2890.

887 45. Whitmore L, Wallace BA (2008) Protein secondary structure analyses from circular dichroism
888 spectroscopy: methods and reference databases. Biopolymers 89: 392–400.

889 46. Lobley A, Whitmore L, Wallace BA (2002) DICHROWEB: an interactive website for the
890 analysis of protein secondary structure from circular dichroism spectra. Bioinformatics 18:
891 211–212.

892 47. Compton LA, Johnson WC (1986) Analysis of protein circular dichroism spectra for secondary
893 structure using a simple matrix multiplication. Anal Biochem 155: 155–167.

894 48. Manavalan P, Johnson WC (1987) Variable selection method improves the prediction of
895 protein secondary structure from circular dichroism spectra. Anal Biochem 167: 76–85.

49. Sreerama N, Woody RW (2000) Estimation of protein secondary structure from circular dichroism spectra: comparison of CONTIN, SELCON, and CDSSTR methods with an expanded reference set. Anal Biochem 287: 252–260.

50. Janes RW (2009) Reference Datasets Circular Dichroism and Synchrotron Radiation Circular Dichroism Spectroscopy of Proteins. In: Wallace BA, Janes RW, editors. Modern Techniques in Circular Dichroism and Synchrotron Radiation Circular Dichroism Spectroscopy. IOS Press.

51. Bhushan B, editor (2007) Springer Handbook of Nanotechnology. Berlin, Heidelberg: Springer Berlin Heidelberg.

52. Li AJ, Nussinov R (1998) A set of van der Waals and coulombic radii of protein atoms for molecular and solvent-accessible surface calculation, packing evaluation, and docking. Proteins 32: 111–127.

53. Homchaudhuri L, Swaminathan R (2001) Novel Absorption and Fluorescence Characteristics of L-Lysine. Chem Lett 30: 844–845.

54. Lehrer SS, Fasman GD (1967) Ultraviolet irradiation effects in poly-L-tyrosine and model compounds. Identification of bityrosine as a photoproduct. Biochemistry 6: 757–767.

55. Malencik DA, Anderson SR (1991) Fluorometric characterization of dityrosine: complex formation with boric acid and borate ion. Biochem Biophys Res Commun 178: 60–67.

56. Malencik D a, Anderson SR (1987) Dityrosine formation in calmodulin. Biochemistry 26: 695–704.

57. Sionkowska A, Skopinska J, Wisniewski M, Leznicki A, Fisz J (2006) Spectroscopic studies into the influence of UV radiation on elastin hydrolysates in water solution. J Photochem Photobiol B 85: 79–84.

58. Pirie A (1972) Fluorescence of N'-formylkynurenine and of protein exposed to sunlight. Biochem J 128: 1365–1367.

59. Han MK, Roseman S, Brand L (1990) Sugar transport by the bacterial phosphotransferase system. Characterization of the sulfhydryl groups and site-specific labeling of enzyme I. J Biol Chem 265: 1985–1995.

60. Grassetti DR, Murray JF (1967) Determination of sulfhydryl groups with 2,2'- or 4,4'-dithiodipyridine. Arch Biochem Biophys 119: 41–49.

61. Wilson JM, Wu D, Motiu-DeGrood R, Hupe DJ (1980) A spectrophotometric method for studying the rates of reaction of disulfides with protein thiol groups applied to bovine serum albumin. J Am Chem Soc 102: 359–363.

62. Tew D, Montellano PRO De (1988) The Myoglobin Protein Radical.

63. Aeschbach R, Amadoò R, Neukom H (1976) Formation of dityrosine cross-links in proteins by oxidation of tyrosine residues. Biochim Biophys Acta - Protein Struct 439: 292–301.

64. Finley EL, Dillon J, Crouch RK, Schey KL (1998) Identification of tryptophan oxidation products in bovine alpha-crystallin. Protein Sci 7: 2391–2397.

65. Linde V, Nielsen LS, Foster DC, Petersen LC (1998) Elimination of the Cys558-Cys566 bond in Lys78-plasminogen--effect on activation and fibrin interaction. Eur J Biochem 251: 472–479.

66. Chen VM, Ahamed J, Versteeg HH, Berndt MC, Ruf W, et al. (2006) Evidence for activation of tissue factor by an allosteric disulfide bond. Biochemistry 45: 12020–12028.

67. World Health Organization (n.d.) The known health effects of UV. Ultrav Radiat INTERSUN Program - FAQ.

68. Webb AR, Engelsen O (n.d.) Calculated ultraviolet exposure levels for a healthy vitamin D status. Photochem Photobiol 82: 1697–1703.

69. Moan J (2001) Visible Light and UV radiation. In: Brune D, Hellborg R, Persson B, Paakkonen R, editors. Radiation at Home, Outdoors and in the Workplace. Oslo: Scandinavian Publisher. pp. 69–85.

70. Lakowicz JR, editor (2006) Principles of Fluorescence Spectroscopy. 3rd ed. Springer.

71. Pirie A (1971) Formation of N'-formylkynurenine in proteins from lens and other sources by exposure to sunlight. Biochem J 125: 203–208.

72. Willis KJ, Szabo AG (1991) Fluorescence decay kinetics of tyrosinate and tyrosine hydrogen-bonded complexes. J Phys Chem 95: 1585–1589.

73. Jacob JS, Cistola DP, Hsu FF, Muzaffar S, Mueller DM, et al. (1996) Human phagocytes employ the myeloperoxidase-hydrogen peroxide system to synthesize dityrosine, trityrosine, pulcherosine, and isodityrosine by a tyrosyl radical-dependent pathway. J Biol Chem 271: 19950–19956.

Figure Legends

Figure 1. Tertiary structure of native human plasminogen. Top panel: Full length native 3D structure of native human Glu1-Pmg. The activation peptide (AP), the 5 kringle domains (K1 to K5), and the serine protease domain (where the catalytic site is located) are highlighted with different colors. The 24 disulphide bonds are displayed in orange in stick configuration, and the Trp and Tyr residues are displayed in dark green in stick configuration. Bottom panel: detailed 3D structure of the serine protease domain of human Glu1-Pmg (Ala543-Asn791). The C and N subdomains of plasminogen are displayed in blue and green, respectively. The disulphide bonds are displayed in stick configuration (orange) and two important disulphide bonds are highlighted: Cys556-Cys566 and Cys737-Cys765. The Trp and Tyr residues in the Serine Protease domain are displayed in line configuration (dark green). The active site residues (catalytic triad His603, Asp646 and Ser741 for plasminogen) are displayed as red CPK (0.5 Å radius). The three important loops involved in plasminogen activation are displayed in red: the oxyanion stabilizing loop, the S1 entrance frame and the activation loop. The xyz atomic coordinates for 3D representation were extracted from the crystallized structures of Glu1-Pmg (4A5T.pdb) [41].

Figure 2. Proteolytic and photonic activation of plasminogen. 3D structures of the catalytic serine protease domain in plasminogen (to the left) and plasmin (to the right) (Ala543-Asn791). The xyz atomic coordinates for structural display were extracted from the crystallized structures of Glu1-Pmg (4A5T.pdb) [41] and activated plasminogen upon tight association with streptokinase (1BML.pdb) [4]. The C and N subdomains of plasminogen are displayed in blue and green, respectively. The disulphide bonds are displayed in stick configuration (orange) and two important disulphide bonds are highlighted: Cys556-Cys566 and Cys737-Cys765. The Trp and Tyr residues in the Serine Protease domain are displayed in line configuration (dark green). The active site residues (catalytic triad His603, Asp646 and Ser741 for plasminogen, His603, Asp646 and mutated Ala741 for plasmin) are displayed in CPK red (0.5 Å radius). The three important loops involved in plasminogen activation are displayed as red CPK: the oxyanion stabilizing loop, the S1 entrance frame and the

activation loop. Top panel: The peptide bond Arg561-Val562 (in pink) in the activation loop is cleaved upon streptokinase activation leading to a conformational change and activating the catalytic triad (plasmin image to the right). Bottom panel: we can see in more detail the region around the oxyanion stabilizing loop, the S1 entrance frame. We observe a conformational change upon plasminogen activation involving the disulphide bond Cys737-Cys765 and Trp 761. We assume that upon UV illumination of plasminogen, Trp761 transfers its excitation energy to Cys737-Cys765. This results in disruption of this disulphide bond, leading to a conformational change that renders the catalytic triad active.

Figure 3. Chemical Structures of tryptophan, tyrosine and of the most important side-products formed upon their photo-oxidation.

Figure 4. Dependence of the average fraction of disulphide bridges on protein chain length. The fraction of disulphide bridges was obtained by dividing the number of disulphide bridges found in a protein by the protein sequence length (number of amino acids) multiplied by 100. The fraction of disulphide bridges estimated for human plasminogen (in blue, 3.1 %, for 767 amino acids) is much higher than what would be expected for a protein of about that length (0.1 % for 700-750 amino acids).

Figure 5. Fluorescence excitation spectra of human plasminogen (330 nm emission). The excitation spectra (em. 330 nm) were obtained before and after 280 nm light continuous illumination (45 min) of human plasminogen in solution. After 45 min of 280 nm illumination there is a decrease in excitation intensity at ~283 nm. Small increasing arrows indicate the wavelengths of maximum absorption (Abs_{max}) of Trp and Tyr in solution.

Figure 6. Fluorescence emission of human plasminogen (280 nm excitation). A- Fluorescence emission spectra (280 nm exc.) obtained before and after 280 nm light continuous illumination (45 min) of human plasminogen in solution. 280 nm illumination leads both to a decrease in emission

intensity at 330 nm and to an increase in emission intensity between 375 nm and 450 nm. Small decreasing arrows indicate the wavelengths of maximum emission intensity (Em_{max}) of Trp, Tyr, DT and NFK in solution. **B-** Fluorescence emission intensity kinetic traces obtained at 330 nm and 405 nm (exc. 280 nm) upon continuous illumination of human plasminogen with 280 nm light. Fitting of the experimental trace obtained with emission fixed at 330 nm and 405 nm was carried out using an exponential function $F(t) = C1 - C2.e^{-kt}$. The fitted parameter values and corresponding errors, and root mean square error values were obtained after fitting the kinetic trace (Table 5 and Materials and Methods).

Figure 7. Fluorescence emission of human plasminogen (325 nm excitation). Fluorescence emission spectra (325 nm exc.) recorded before and after 280 nm light continuous illumination (45 min) of human plasminogen in solution. There is an increase in emission intensity at 396 nm with 280 nm ill time. Small decreasing arrows indicate the wavelengths of maximum emission intensity (Em_{max}) of DT and NFK in solution. **Insert-** Fluorescence emission intensity at 405 nm (exc. 325 nm) *vs* 280 nm illumination time. The experimental points were fitted to an exponential function $F(t) = C1 - C2.e^{-kt}$. Fitted parameter values and corresponding errors, and root mean square error values were obtained after fitting the kinetic trace (Table 5).

Figure 8. Fluorescence emission spectra of human plasminogen (295 nm excitation). Fluorescence emission spectra (295 nm exc.) recorded before and after 280 nm continuous illumination (45 min) of human plasminogen in solution. UV illumination of plasminogen results in a decrease in emission intensity at 330 nm and an increase in emission intensity between 375 nm and 450 nm. Small decreasing arrows indicate the wavelengths of maximum emission intensity (Em_{max}) of Trp, DT and NFK in solution.

Figure 9. Fluorescence excitation spectra of human plasminogen (405 nm emission). Fluorescence excitation spectra (emission at 405 nm) obtained before and after 280 nm continuous illumination (45 min) of human plasminogen in solution. There is an increase in excitation intensity at

1041 the peak located at ~283-284 nm and a new peak is formed at 321 nm upon 280 nm illumination.
1042 Small increasing arrows indicate the wavelengths of maximum absorption (Abs_{max}) of DT, Kyn and
1043 NFK in solution.

1044

1045 **Figure 10. Fluorescence excitation spectra of human plasminogen (434 nm emission).**
1046 Fluorescence excitation spectra (emission at 434 nm) obtained before and after 280 nm continuous
1047 illumination (45 min) of human plasminogen in solution. 280 nm illumination leads to an increase in
1048 excitation intensity at the peak located at ~285-286 nm and to the formation of a new peak at 320
1049 nm. Small increasing arrows indicate the wavelengths of maximum absorption (Abs_{max}) of DT, Kyn
1050 and NFK in solution.

1051

1052 **Figure 11. Far and near UV circular dichroism spectra of human plasminogen.** Far UV (185-
1053 250 nm) and near UV (250-350 nm) CD spectra were obtained before and after 280 nm light
1054 continuous illumination (10 min) of human plasminogen in solution. 280 nm illumination leads to a
1055 loss of far UV ellipticity signal at 206 nm (33.4 %) and to a red-shift in wavelength of maximum
1056 ellipticity (206 nm to 209 nm). There are almost no changes in the near UV CD spectrum of
1057 plasminogen with 280 nm illumination. After 10 min of 280 nm ill. the ellipticity signal at the
1058 wavelength of maximum ellipticity (285 nm) decreases only by 6 %.

1059

1060 **Figure 12. Circular dichroism thermal unfolding curves of human plasminogen.** The circular
1061 dichroims thermal unfolding curves of a non-illuminated plasminogen sample (0 min 280 nm ill. time)
1062 or a UV illuminated plasminogen sample (10 min 280 nm ill. time) were obtained upon heating from
1063 25 ºC to 90 ºC (1 $ºC.min^{-1}$). **A-** The ellipticity signal was constantly monitored at 206 nm. **B-** The
1064 ellipticity signal was constantly monitored at 283 nm. Both curves were fitted using a modified
1065 Boltzmann function (see Table 7). The melting temperature of the protein, which corresponds to the
1066 transition mid-point of each curve, was recovered from the fitting (parameter *x*0) and is displayed for
1067 each sample.

Figure 13. Increase in the concentration of detected free thiol groups (open circles) in human plasminogen UV-illumination. Detection of free thiol groups was carried out using the Ellman's assay after 280 nm light continuous illumination (22.5 min, 45 min, 90 min, or 112.5 min) of human plasminogen in solution. The experimental values were fitted using an exponential function $y = y_0 - A.e^{-R0t}$ (fitted curve in red), where y is the concentration of thiol groups (μM) at the 280 nm illumination time t (h), y_0 and A are constants and $R0$ is the rate of thiol group formation (h^{-1}). Fitted experimental parameters were: y_0 = 2.29 ± 0.07 μM, A = 3.78 ± 0.42 μM, $R0$ = 0.037 ± 0.005 min^{-1}. Root mean square error was 99.39 %.

Figure 14. Fluorescence signal presented by the digested substrate for plasminogen kept in the dark (10 min in the dark, negative control) and UV illuminated plasminogen (10 min 280 nm illumination). Fluorescence signal is used as a measure of degradation of the substrate and to acess plasmin activity. The fluorescence readings were performed after 1 hour and 22 hours which is standard procedure for the used Casein-based substrate. The background fluorescence signal from substrate blank was subtracted.

Tables

Table 1. Absorption and fluorescence spectral characteristics of tryptophan, tyrosine and the major side-products formed upon their photo-oxidation.

		Absorption Maximum (Abs^{max}) **Extinction Coefficient (ε)**	**Excitation Maximum (Exc^{max})**	**Emission Maximum (Em^{max})**
Tryptophan Trp		278, 287, (272) nm [a] ε^{278nm}= 5579 $M^{-1}.cm^{-1}$ ε^{287nm}= 4954 $M^{-1}.cm^{-1}$ ε^{272nm}= 5360 $M^{-1}.cm^{-1}$	282, 290 nm [b]	305-350 nm [b]
N'-Formylkynurenine NFK	Ac-NFK-NH3 *Neutral*	261, 322 nm [c]		420-434 nm [c]
	NFK *Neutral/Acidic*	260, 321 nm [d]	265, 330 nm [e]	440 nm [e]
	NFK *Alkaline*		240, 315 nm [e]	400 nm [e]
Kynurenine Kyn	Ac-Kyn-NH3	258, 360 nm [c]		434-480 nm [c]
Tyrosine Tyr	*Neutral/Acidic*	275 nm [f] ε^{275nm}= 1400 $M^{-1}.cm^{-1}$	275 nm [b]	303 nm [b, c]
	Alkaline (Tyrosinate)	290 nm [f] ε^{290nm}= 2300 $M^{-1}.cm^{-1}$		345 nm [b, g]
Dityrosine DT	*Acidic*	284 nm [h] ε^{284nm}= 5400 $M^{-1}.cm^{-1}$	284 nm [h]	409 nm [h]
	Alkaline	316 nm [h] ε^{316nm}= 8600 $M^{-1}.cm^{-1}$	317 nm [h]	407 nm [h]
	In proteins			400-401 nm [i]
Trityrosine TriTyr	*Acidic*	286 nm [h] ε^{286nm}= 11000 $M^{-1}.cm^{-1}$	286 nm [h]	409 nm [h]
	Alkaline	322 nm [h] ε^{322nm}= 11500 $M^{-1}.cm^{-1}$	319 nm [h]	416 nm [h]
Pulcherosine Pul	*Acidic*	282 nm [h] ε^{282nm}= 7700 $M^{-1}.cm^{-1}$	283 nm [h]	416 nm [h]
	Alkaline	315 nm [h] ε^{315nm}= 9500 $M^{-1}.cm^{-1}$	320 nm [h]	414 nm [h]

References: (a) [20]; (b) [70]; (c) [38]; (d) [71]; (e) [58]; (f) [21]; (g) [72]; (h) [73]; (i) [37].

Table 2. Shortest spatial distances between disulphide bonds and aromatic residues (tryptophan and tyrosine) in full-length native human plasminogen.

Protein Domain	Disulphide Bond	Aromatic Residue	Distance (Å)
AP	C34-C42	Y6	4.48
	C30-C54	Y47	4.18
K1	C133-C145	W108	5.83
		W144	5.93
K2	C215-C238	Y174	5.87
K3	C256-C333	Y254	4.13
	C277-C316	W280	5.74
K4	C407-C430	Y366	5.60
K5	C483-C524	W486	5.76
	C512-C536	Y470	5.87
Serine Protease Domain	C737-C765	W761	4.23

The shortest distances (< 6 Å) between atoms of each pair of elements (Trp, Tyr and disulphide bonds) were considered. For Trp and Tyr residues, only the atoms belonging to the indole and benzene rings were considered.

Table 3. Shortest spatial distances between disulphide bonds and aromatic residues (tryptophan and tyrosine) in the serine protease domain of human plasminogen.

Disulphide Bond	Aromatic Residue	Distance (Å)
C548-C666	W573	11.54
	W575	7.05
	Y672	11.97
	Y753	8.12
C558-C566	**W573**	**9.06**
C588-C604	W685	9.92
	W761	7.18
	Y614	7.30
C680-C747*	W573	9.44
	W575	10.25
	Y672	7.48
	Y753	7.25
C710-C726	Y774	7.06
C737-C765*	**W761**	**4.24**
	Y774	**8.35**

The shortest distances (<12 Å) between atoms of each pair of elements (Trp, Tyr and disulphide bonds) were considered. For Trp and Tyr residues, only the atoms belonging to the indole and benzene rings were considered.

* -RH Staple disulphide bonds.

In bold: disulphide bonds relevant for plasminogen activation.

Table 4. Shortest spatial distances between tyrosine residues in full-length native human plasminogen.

Tyr1	Tyr2	Distance (Å)
	Cluster 1	
Tyr359	Tyr366	7.64
	Cluster 2	
Tyr146	Tyr154	6.32
Tyr154	Tyr156	3.86
	Cluster 3	
Tyr429	Tyr535	4.41
Tyr525	Tyr533	6.00
Tyr533	Tyr535	5.94

The shortest distances between the carbon atoms in the ortho-position(s) of the phenol were considered.

Table 5. Parameter values recovered upon fitting the fluorescence emission kinetic traces recorded with fixed emission at 405 nm (exc. 280, Figure 6B; or exc. 325 nm, Figure 7 insert).

Fitting Equation		$F(t) = C1 - C2.e^{-kt}$	
		exc. 280 nm	**exc. 325 nm**
Fitting Parameters	R^2	0.99936	0.96489
	$C1$	1.43 ± 5.26E-4	1.65 ± 0.05
	$C2$	-0.43 ± 6.68E-4	-0.64 ± 0.07
	k (min^{-1})	0.076 ± 3.36E-4	0.082 ± 0.022

Table 6. Quantification of the secondary structure of human plasminogen samples (non-illuminated, 0 min; UV illuminated, 10 min at 280 nm) obtained upon far UV CD spectra deconvolution with the algorithm CDSTRR.

280 nm ill. time	Fraction of Secondary Structure Content							NRMSD
	α helix (regular)	α helix (distorted)	β strand (regular)	β strand (distorted)	Turns	Unordered	Total	
0 min	-2 %	1 %	51 %	25 %	17 %	3 %	95 %	0.018
10 min	-2%	2 %	18 %	13 %	31 %	37 %	99 %	0.035

Table 7. Parameter values obtained upon fitting the circular dichroism thermal unfolding curves (ellipticity at 206 nm, Figure 12A; ellipticity at 283 nm, Figure 12B) of human plasminogen with a modified Boltzmann function.

Fitting Equation		$y = A2 + B2.x + \frac{(A1 + B1.x - A2 + B2.x)}{\left(1 + \exp\left(\frac{x - x0}{dx}\right)\right)}$			
Ellipticity		**206 nm**		**283 nm**	
280 nm illumination time		**0 min**	**10 min**	**0 min**	**10 min**
Fitting Parameters	R^2	0.9936	0.99114	0.99973	0.99986
	A1	109.94 ± 8.03	77.37 ± 8.92	3.45 ± 0.12	2.84 ± 0.11
	B1	50.89 ± 2.88	53.75 ± 3.02	-4.47 ± 0.18	-4.66 ± 0.14
	A2	-1.18 ± 0.13	-0.72 ± 0.14	-0.05 ± 0.002	-0.05 ± 0.002
	B2	0.016 ± 0.034	-0.10 ± 0.04	0.04 ± 0.002	0.04 ± 0.002
	x0	**70.61 ± 0.14**	**70.79 ± 0.23**	**70.34 ± 0.05**	**69.68 ± 0.05**
	dx	1.36 ± 0.10	1.71 ± 0.16	1.43 ± 0.04	1.83 ± 0.04

Figure 1
Click here to download high resolution image

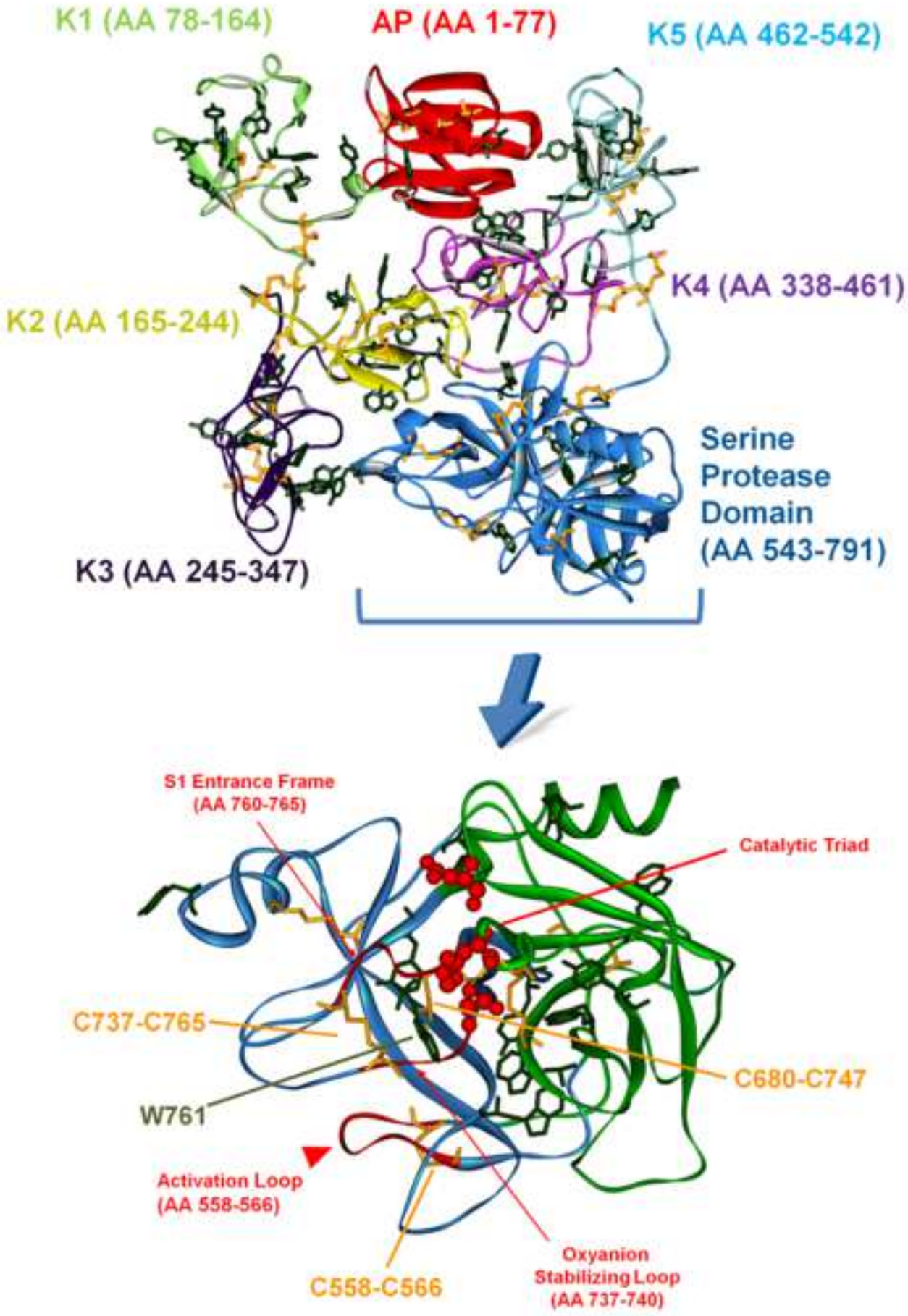

Figure 2
Click here to download high resolution image

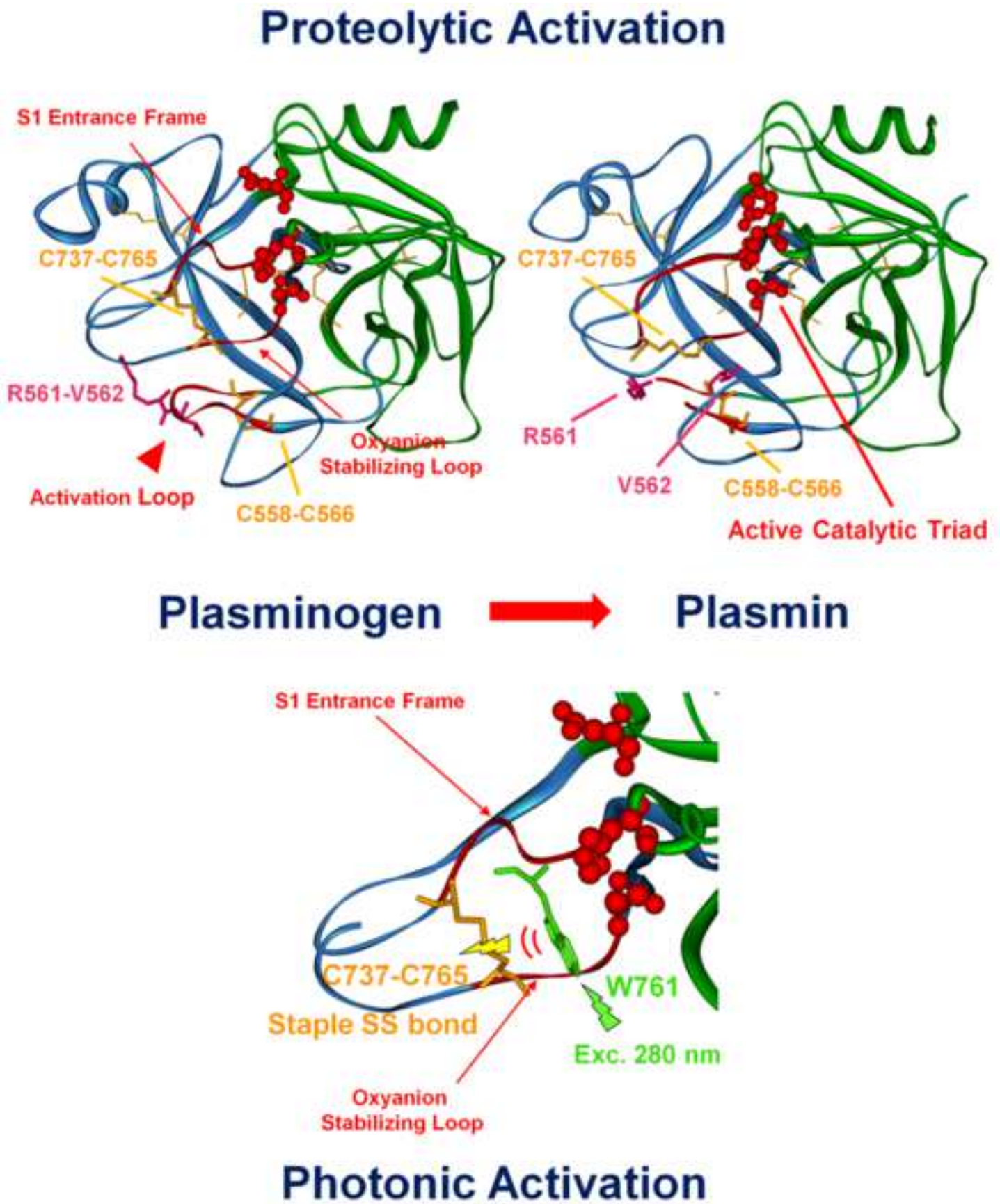

Figure 3

Click here to download high resolution image

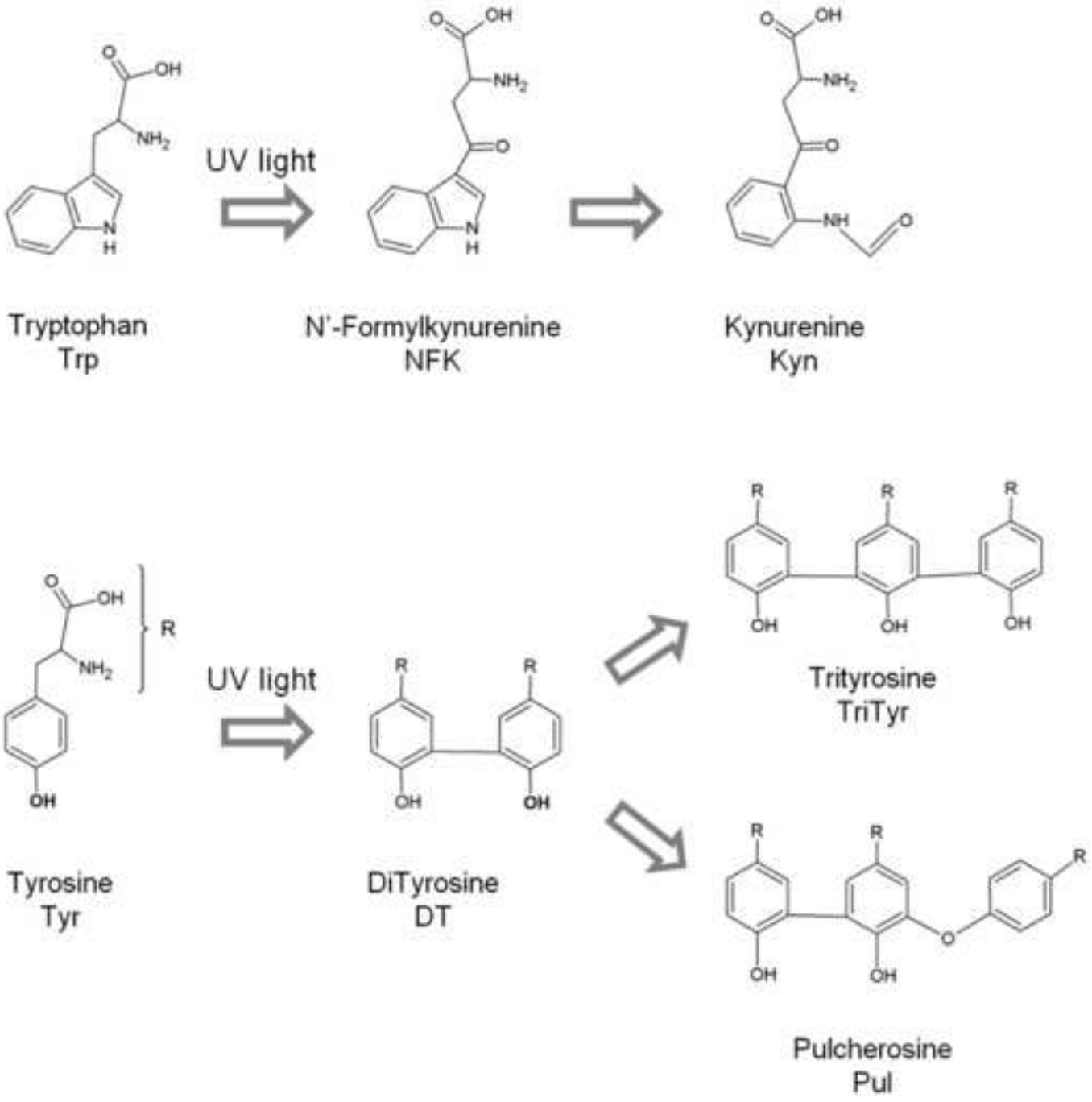

Figure 4
Click here to download high resolution image

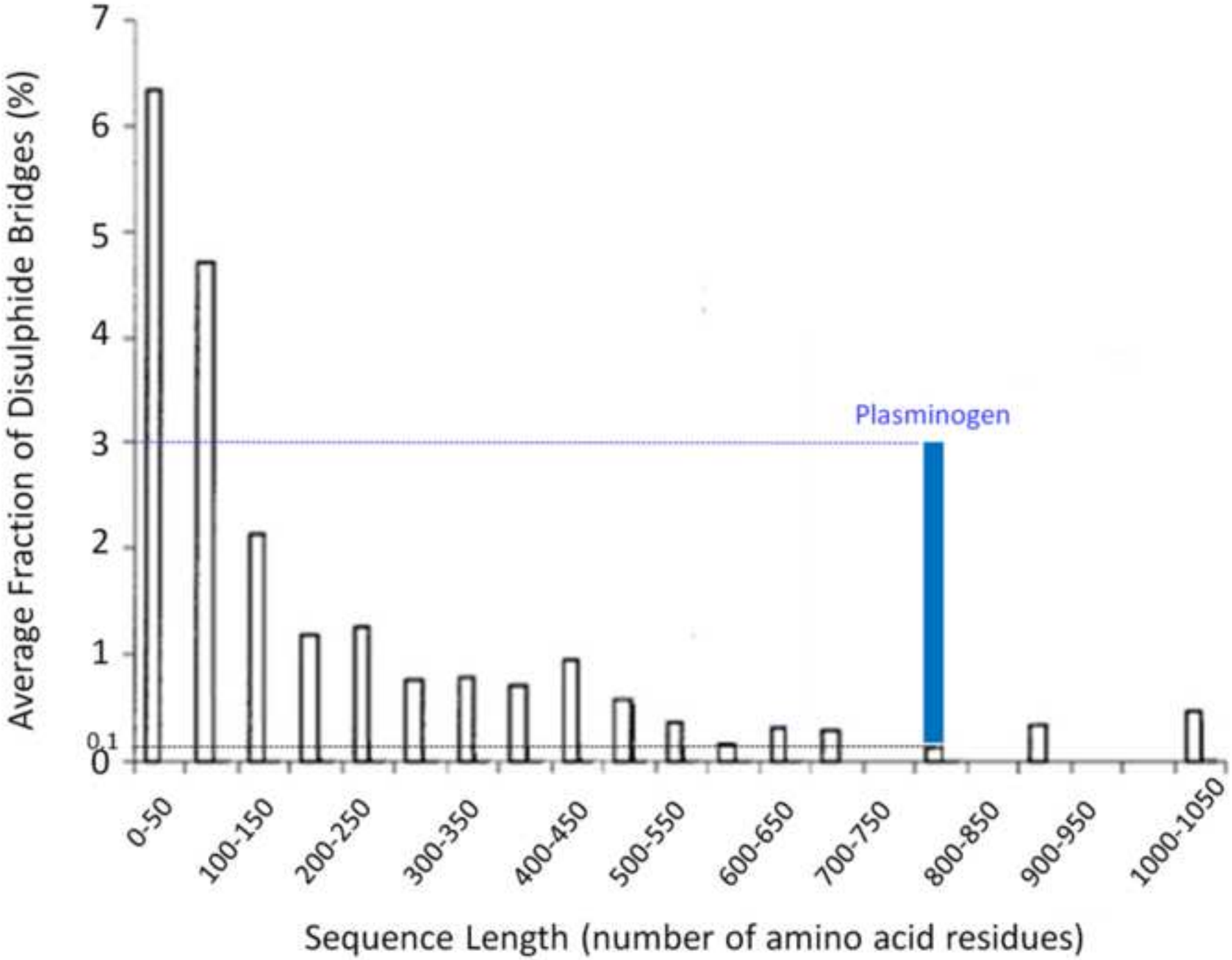

Figure 5
Click here to download high resolution image

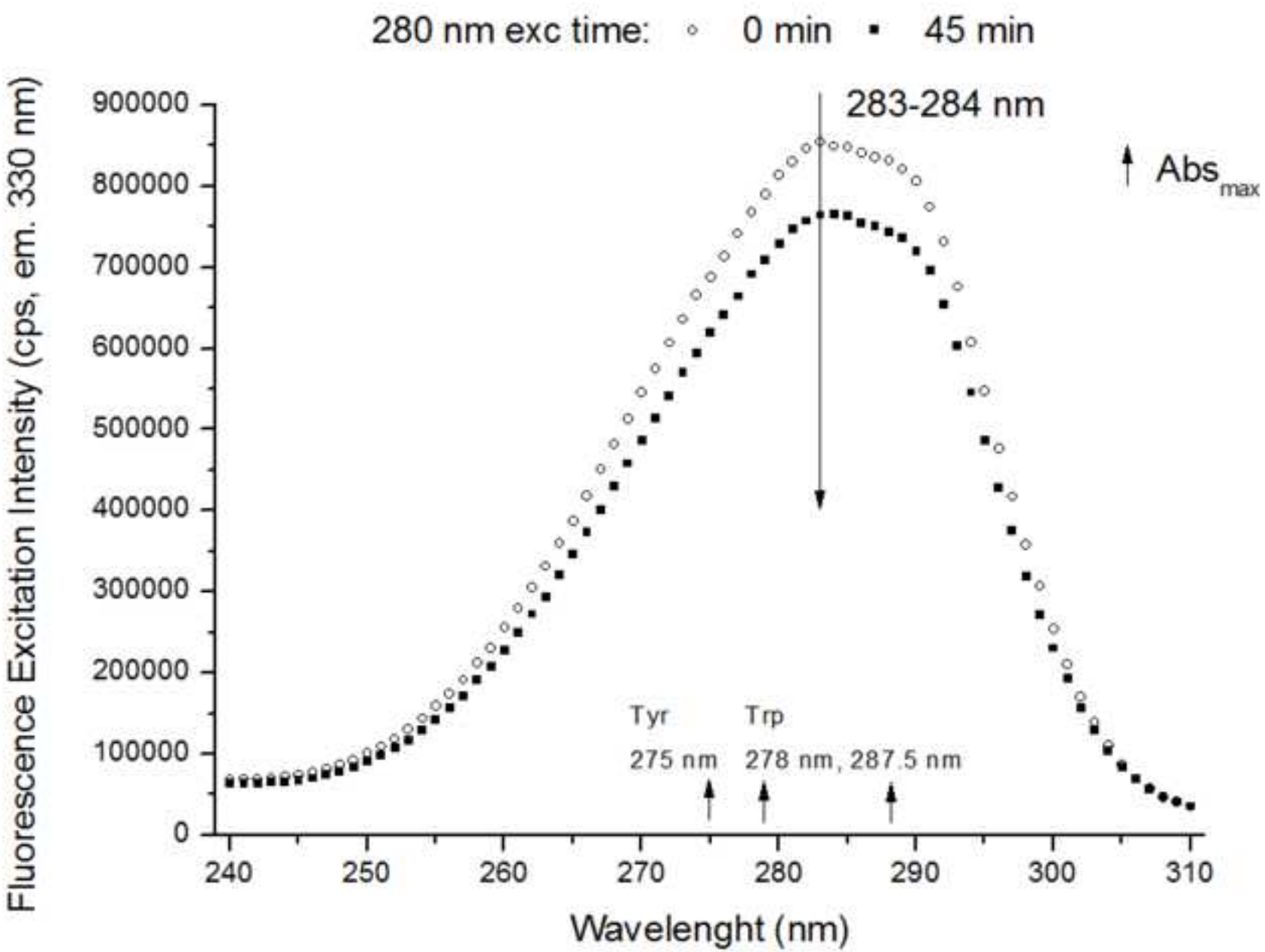

Figure 6

Click here to download high resolution image

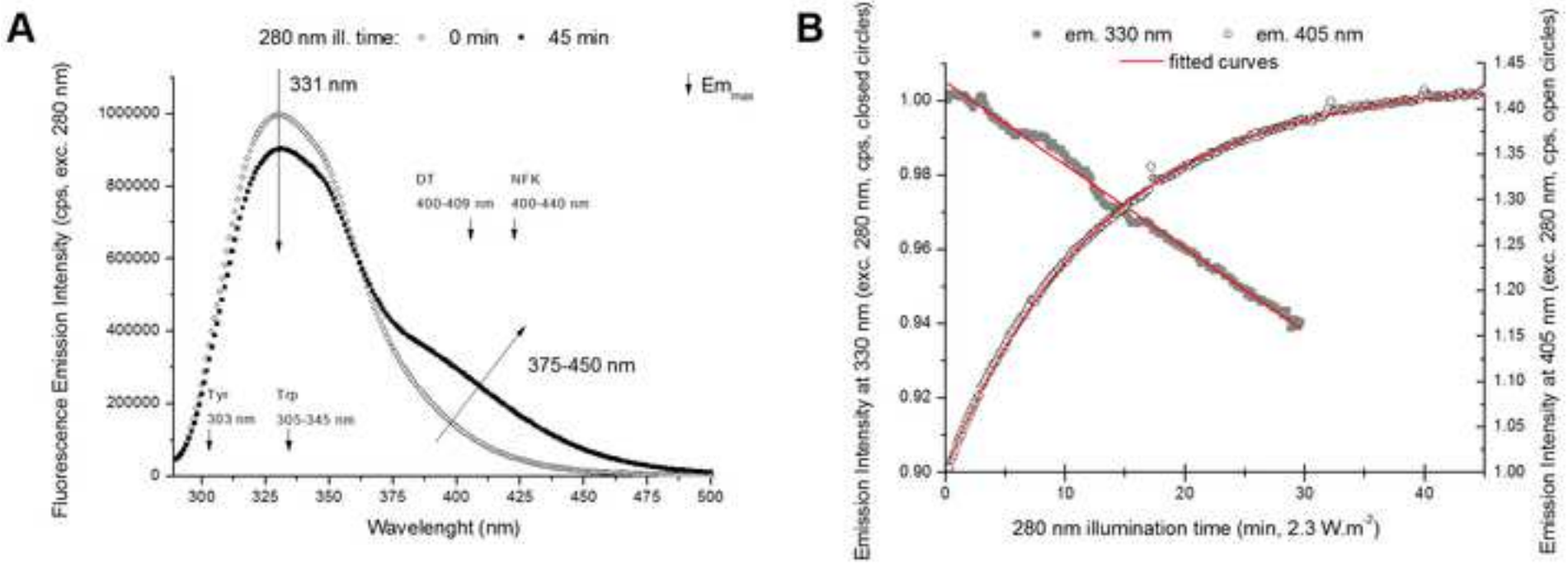

Figure 7
Click here to download high resolution image

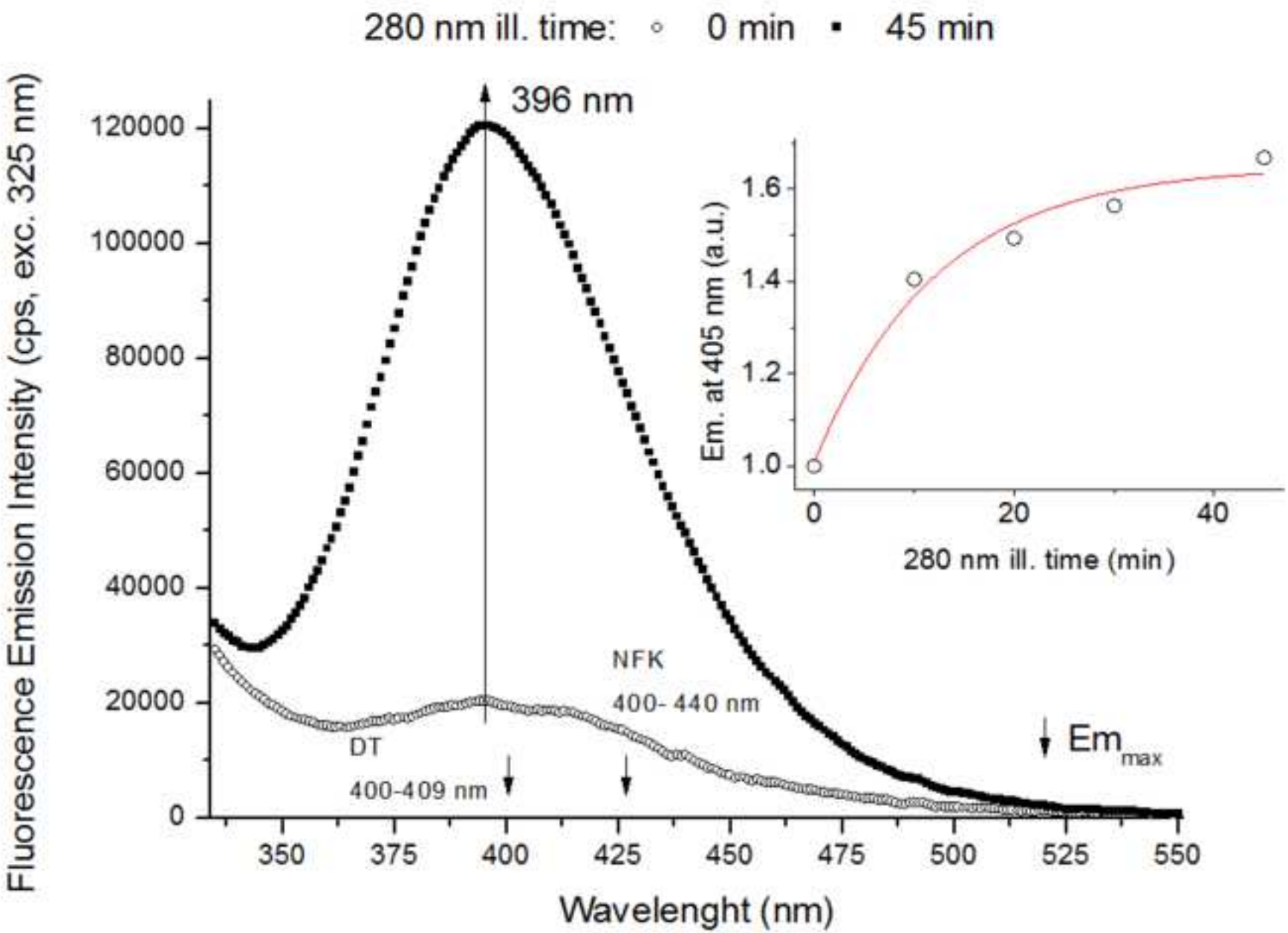

Figure 8

Click here to download high resolution image

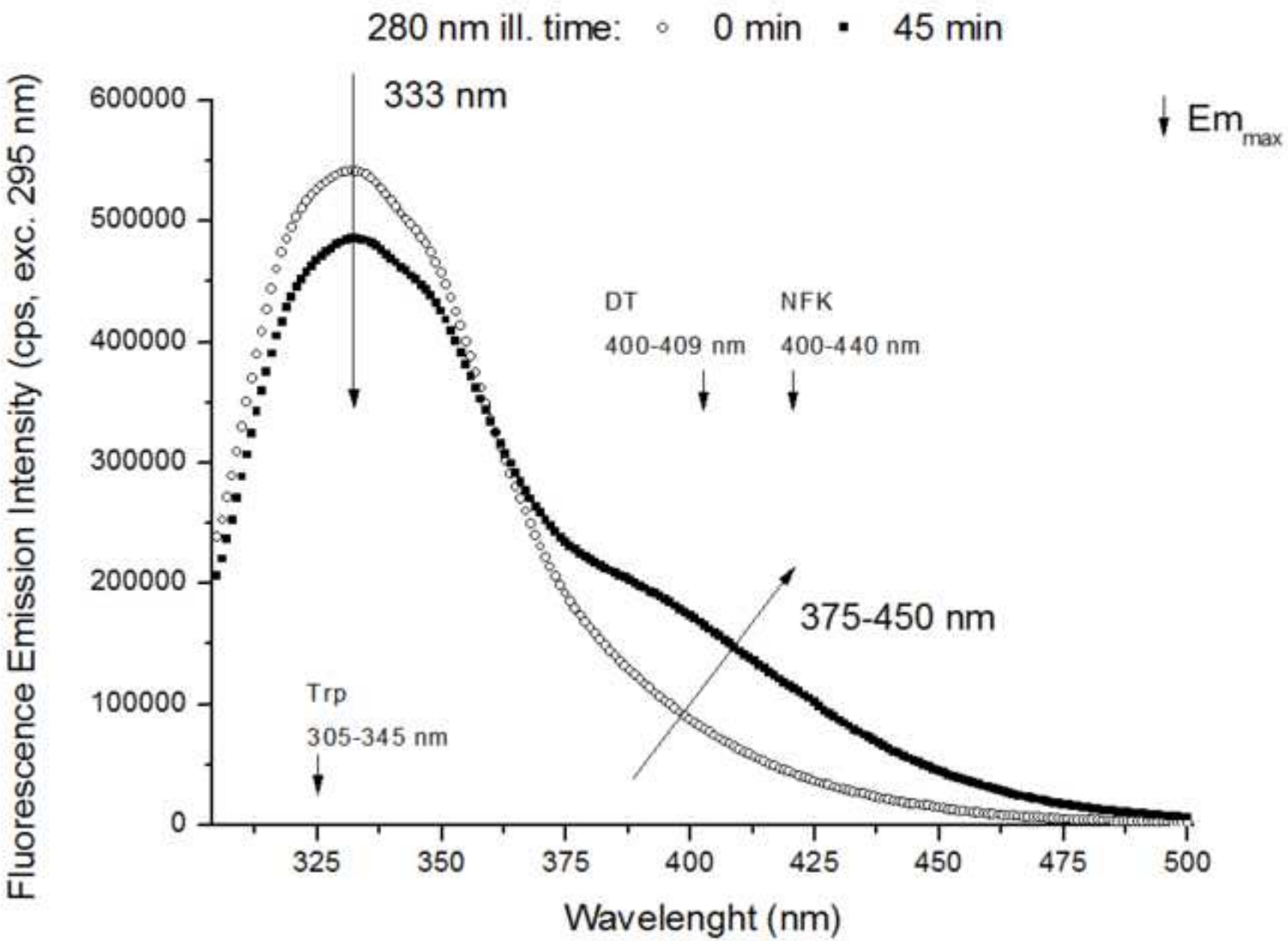

Figure 9
Click here to download high resolution image

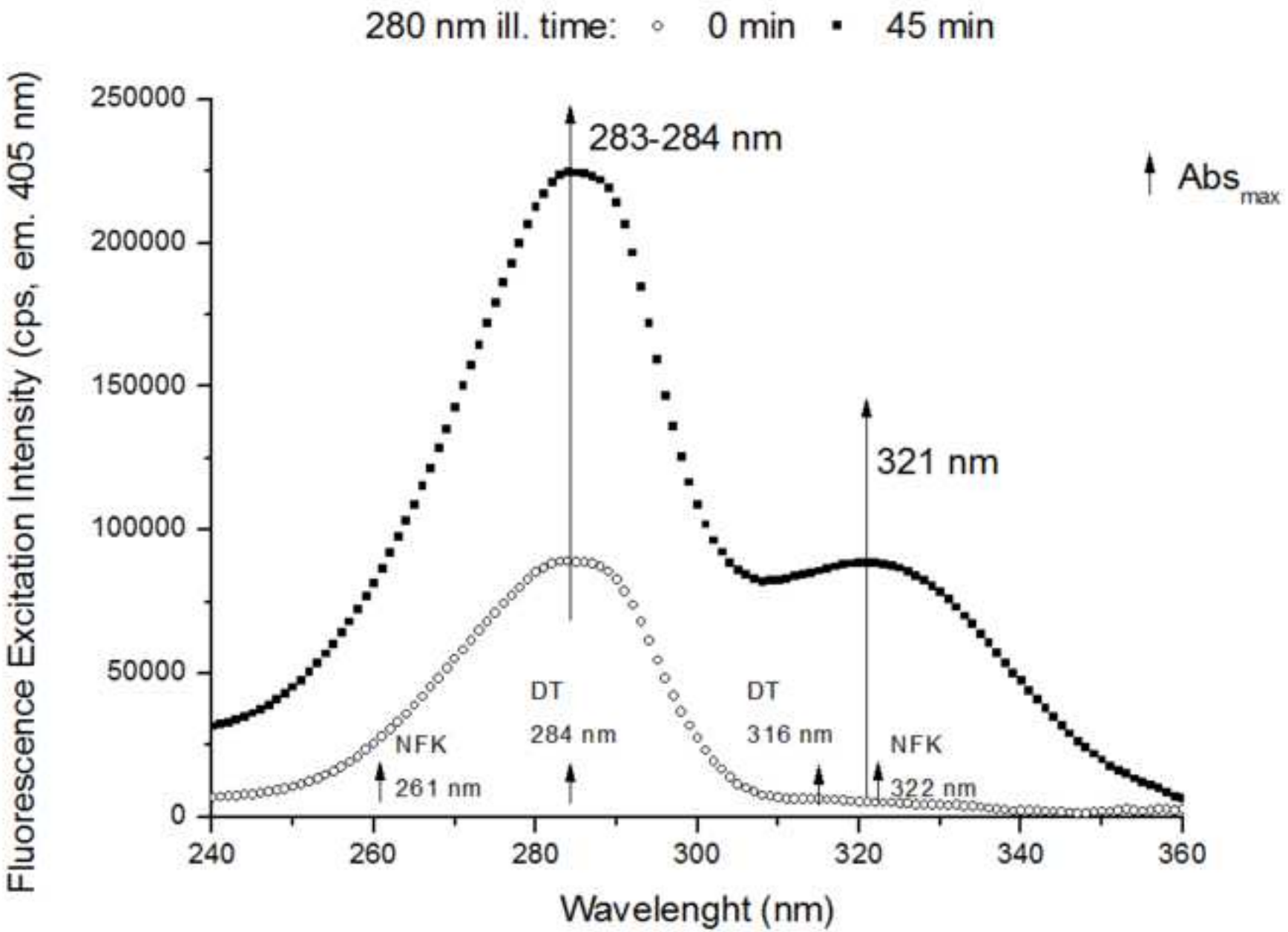

Figure 10
Click here to download high resolution image

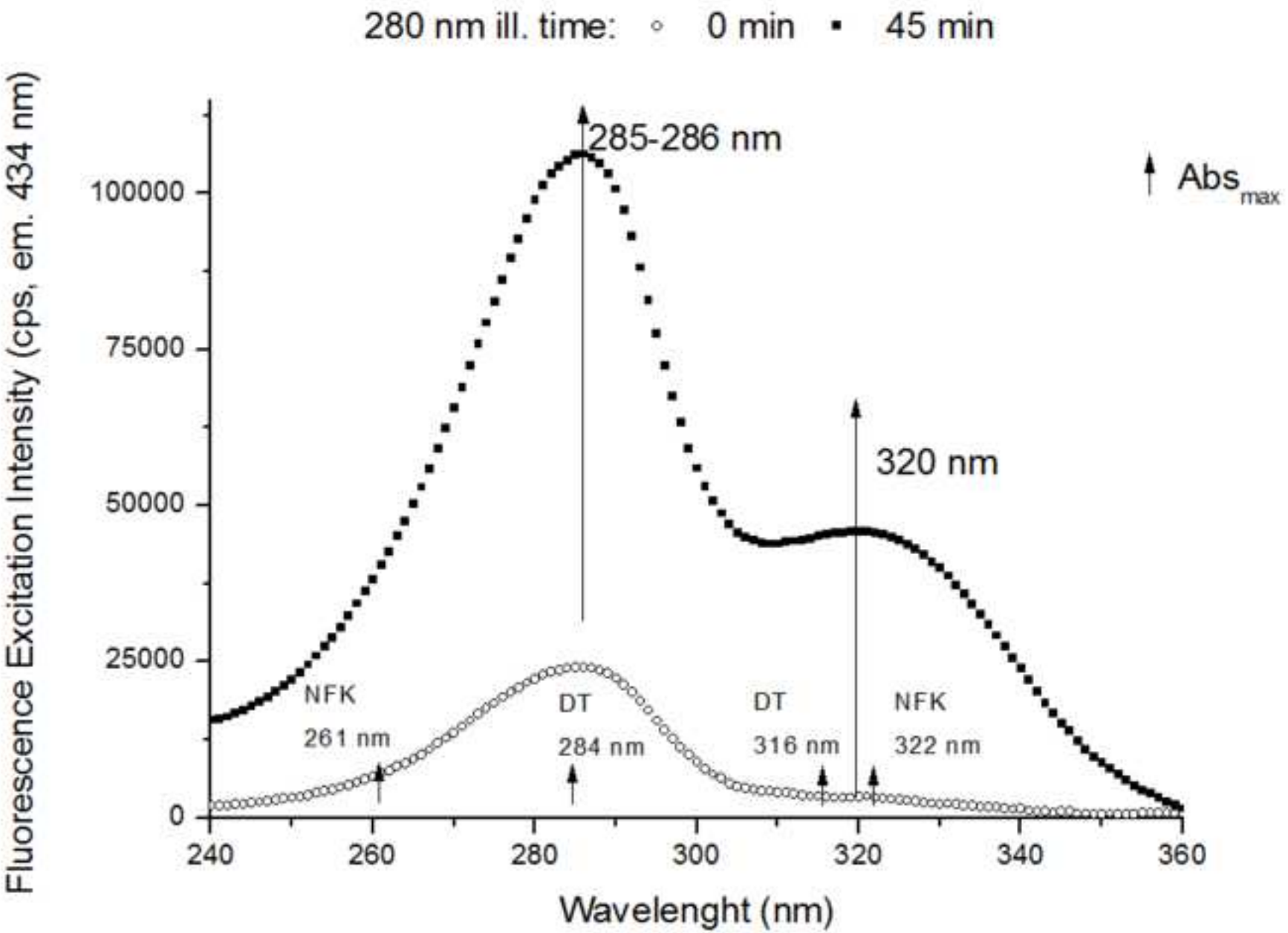

Figure 11
Click here to download high resolution image

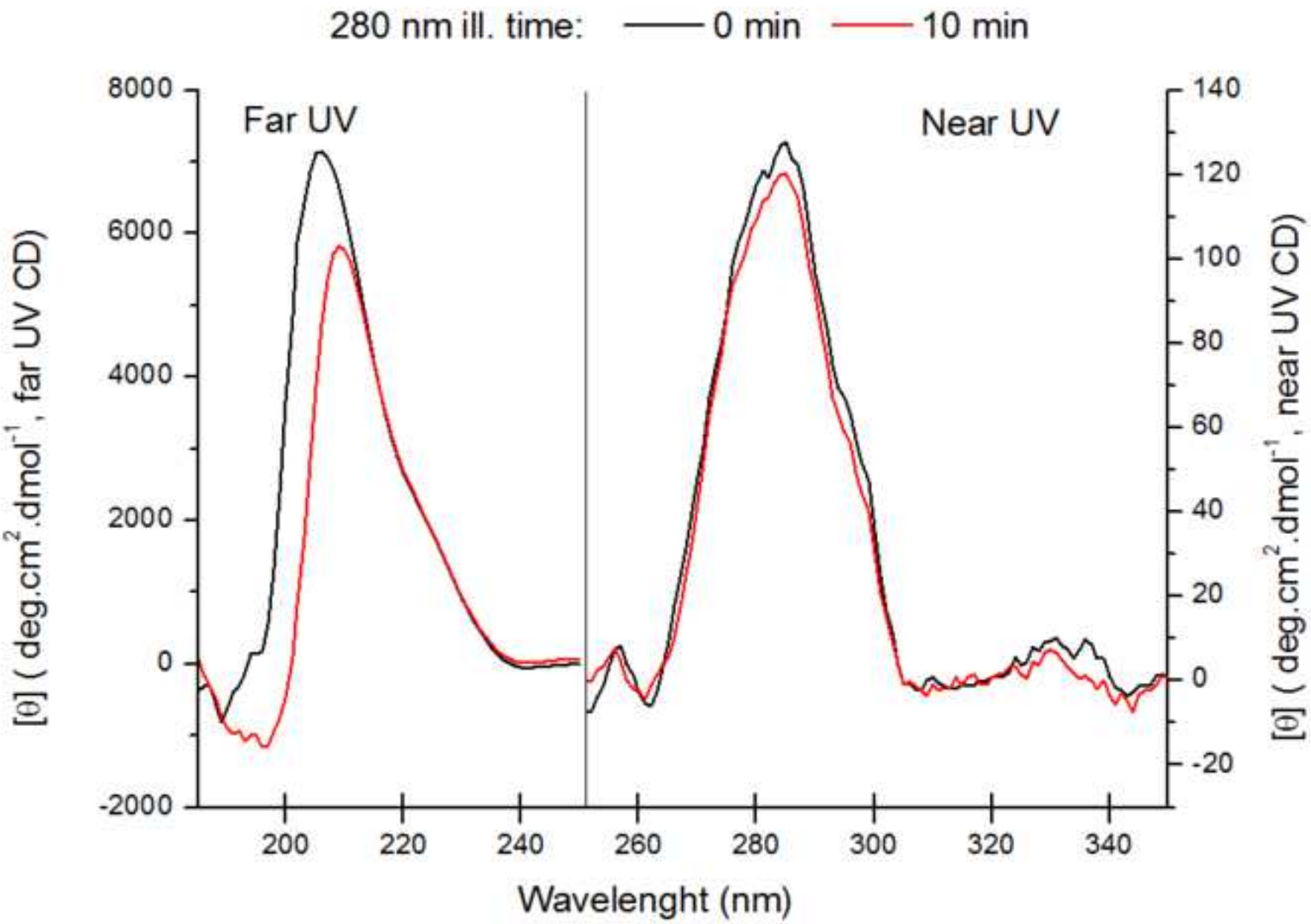

Figure 12
Click here to download high resolution image

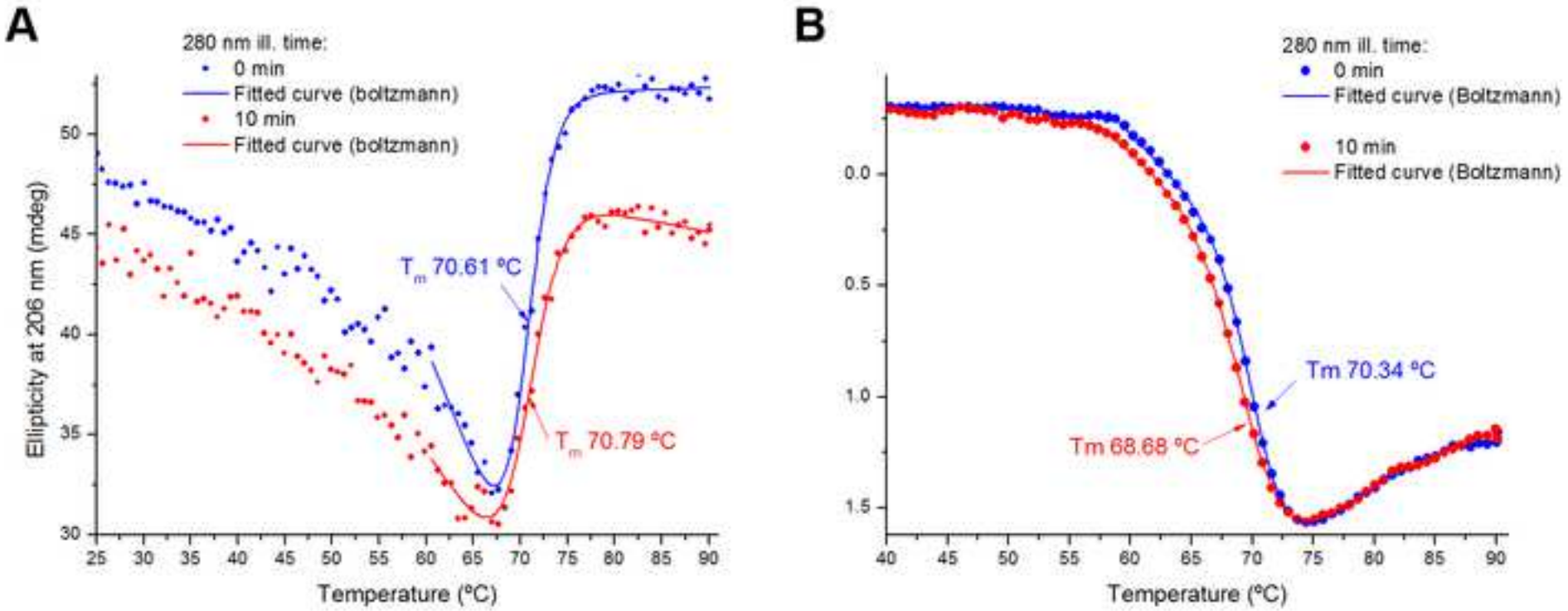

Figure 13
Click here to download high resolution image

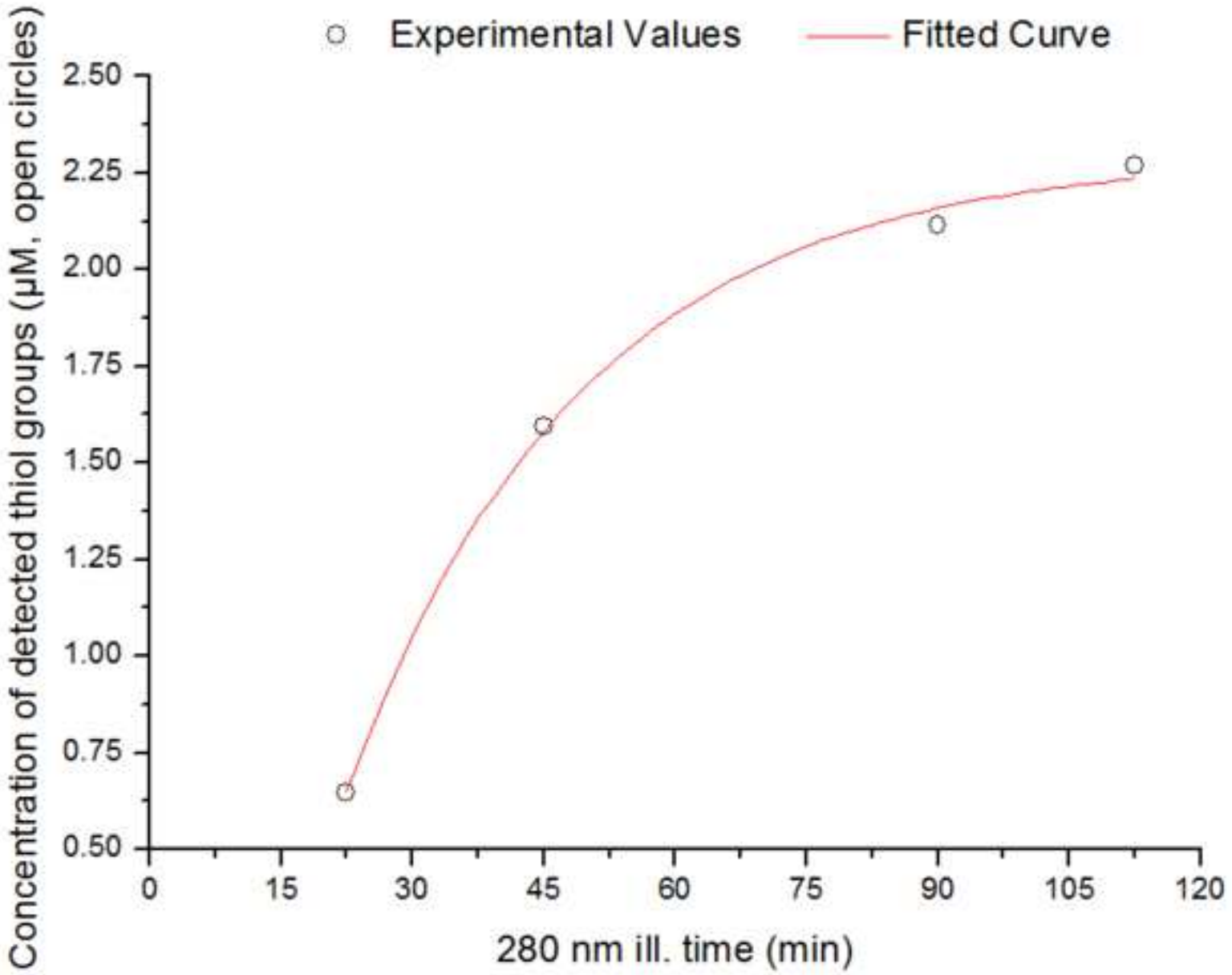

Figure 14
Click here to download high resolution image